

Research Reports from the Communications Research Laboratory  
at Ilmenau University of Technology

*Yao Cheng*

**Advanced Multi-Dimensional  
Signal Processing for  
Wireless Systems**





**ILMENAU** UNIVERSITY OF TECHNOLOGY



Fakultät für Elektrotechnik und Informationstechnik  
der Technischen Universität Ilmenau

ADVANCED MULTI-DIMENSIONAL  
SIGNAL PROCESSING FOR  
WIRELESS SYSTEMS

October 11, 2016

*Yao Cheng*  
*geboren am 26.10.1985 in Jinan*

Dissertation zur Erlangung des  
akademischen Grades Doktor-Ingenieur (Dr.-Ing)

---

Anfertigung im: Fachgebiet Nachrichtentechnik  
Institut für Informationstechnik  
Fakultät für Elektrotechnik und Informationstechnik

Gutachter: Univ.-Prof. Dr.-Ing. Martin Haardt  
Prof. Dr. Didier Le Ruyet, Conservatoire National des Arts et Métiers  
Prof. Dr. Ana Isabel Pérez-Neira, Universitat Politècnica de Catalunya

Vorgelegt am: 11.01.2016

Verteidigt am: 05.10.2016

Verf.-Nr.: EI386

urn:nbn:de:gbv:ilm1-2016000488



This work is licensed under a Creative Commons Attribution  
Noncommercial-No Derivative Works 3.0 License  
<http://creativecommons.org/licenses/by-nc-nd/3.0/>.

---

## Acknowledgements

Being the author of this thesis, I would say I never regard myself as the sole contributor. A lot of people deserve my gratitude. It is their kind and generous help, support, and concern that has led to the completion of this work as well as my wonderful and life-changing experience as a Ph.D. candidate.

First, I would like to express my deepest gratitude to my supervisor, Prof. Martin Haardt, for providing me with this precious opportunity to pursue the Doctor's degree in the first place, for continuously supporting and encouraging me, and for inspiring me with countless brilliant ideas while training me to be independent and creative as well. In addition to his immense knowledge, his incredible industriousness, his persistent pursuit of perfection, his great sense of responsibility, and his warm personality have not only shown me what a successful researcher and leader should be like but also deeply moved me, making me thinking constantly about what I should improve, with him as the role model. It is really my fortune having had him as my supervisor and mentor.

My sincere thanks also goes to Prof. Didier Le Ruyet and Prof. Ana Isabel Pérez-Neira, who have spent time and effort reviewing my thesis and have come a long way to Ilmenau to attend the defense, showing their kind support and encouragement. Their insightful and constructive comments have contributed to the improvement of the thesis and have shed light on future research directions that I could pursue next. In addition, having the opportunity to cooperate with both of them in the European project EMPHAtiC is wonderful, and it is absolutely a valuable and important experience for me.

I would also like to thank the rest of my dissertation examination committee, Prof. Heiko O. Jacobs, Prof. Jochen Seitz, and Prof. Gerald Schuller, for their kind help, patience, and support.

I owe a debt of gratitude to my former and current colleagues as well. In particular, I am truly grateful for the generous and enlightening guidance from Dr. Florian Römer whose tremendous help and encouragement all along have meant a lot to me. Special thanks also goes to Dr. Nuan Song for being like a big sister to me and for kindly giving me both research-wise and life-wise advice, among many other things. In addition, I would like to thank Bin Song, Bilal Zafar, Jens Steinwandt, Jianhui Li, Jianshu Zhang, Keke Zu, Kristina Naskovska, Marko Hennhöfer, Mike Wolf, Peng Li, Sheng Li, Sher Ali Cheema. I apologize for not being able to name everyone in person. I have been so lucky to work with

you all in the past years and really appreciate every technical or private discussion and exchange of ideas we have had. My sincere appreciation also goes to Ms. Christina Patotschka and Mr. Wolfgang Erdtmann, for always attaching warm smiles and kind words to every answer to my questions, to every complicated form you helped me with, and to every computer or printer related problem you helped revolve.

Last but not the least, I would like to thank my family who have made all of this happen. Words can hardly describe how grateful I am having such cool parents. Thank you for providing me with endless support in various ways, for creating a carefree and breezy life style that has made me feel real contented and happy ever since I was a little girl, and for never pushing me for good grades but insisting on raising me up as a kind and hardworking person with integrity. I would also like to express my deep appreciation to my beloved husband, Shuhao Si, for putting so much effort into making me feel like home in a place thousands miles away from our actual homes, for acting in so many roles beyond a caring husband also as a dear friend and a patient father, for accompanying me in the advent of every new phase of my life, and for making my everyday so much more colorful and delightful while promising it is gonna be even better. Finally, a few compliment words to our little boy, Weichen, who, as a ten-month-old baby, can hardly understand what I am saying right now. Still, thank you for being there for me and backing me up, inside my belly and outside as well, in every difficult and stressful moment during my preparation of this thesis and the final defense. The smile constantly hanging on your cute little face is the most fabulous rainbow of my life.

---

## Abstract

The thriving development of wireless communications calls for innovative and advanced signal processing techniques targeting at an enhanced performance in terms of reliability, throughput, robustness, efficiency, flexibility, etc.. This thesis addresses such a compelling demand and presents new and intriguing progress towards fulfilling it. We mainly concentrate on two advanced multi-dimensional signal processing challenges for wireless systems that have attracted tremendous research attention in recent years, multi-carrier Multiple-Input Multiple-Output (MIMO) systems and multi-dimensional harmonic retrieval.

As the key technologies of wireless communications, the numerous benefits of MIMO and multi-carrier modulation, e.g., boosting the data rate and improving the link reliability, have long been identified and have ignited great research interest. In particular, the Orthogonal Frequency Division Multiplexing (OFDM)-based multi-user MIMO downlink with Space-Division Multiple Access (SDMA) combines the twofold advantages of MIMO and multi-carrier modulation. It is the essential element of IEEE 802.11ac and will also be crucial for the fifth generation of wireless communication systems (5G). Although past investigations on scheduling and precoding design for multi-user MIMO downlink systems have been fruitful, new advances are desired that exploit the multi-carrier nature of the system in a more efficient manner or aim at a higher spectral efficiency. On the other hand, a Filter Bank-based Multi-Carrier modulation (FBMC) featuring a well-concentrated spectrum and thus a low out-of-band radiation is regarded as a promising alternative multi-carrier scheme to OFDM for an effective utilization of spectrum fragments, e.g., in 5G or broadband Professional Mobile Radio (PMR) networks. Unfortunately, the existing transmit-receive processing schemes for FBMC-based MIMO systems suffer from limitations in several aspects, e.g., with respect to the number of supported receive antennas (dimensionality constraint) and channel frequency selectivity. The forms of MIMO settings that have been investigated are still limited to single-user MIMO and simplified multi-user MIMO systems. More advanced techniques are therefore demanded to alleviate the constraints imposed on the state-of-the-art. More sophisticated MIMO scenarios are yet to be explored to further corroborate the benefits of FBMC.

In the context of multi-dimensional harmonic retrieval, it has been demonstrated that a higher estimation accuracy can be achieved by using tensors to preserve and exploit the multi-dimensional nature of the data, e.g., for model order estimation and subspace estimation. Crucial pending topics include how to further incorporate statistical robustness and how to

handle time-varying scenarios in an adaptive manner.

In Part I of this thesis, we first present an efficient and flexible transmission strategy for OFDM-based multi-user MIMO downlink systems. It consists of a spatial scheduling scheme, efficient multi-carrier ProSched (EMC-ProSched), with an effective scheduling metric tailored for multi-carrier systems and two new precoding algorithms, linear precoding-based geometric mean decomposition (LP-GMD) and low complexity coordinated beamforming (LoCCoBF). These two new precoding schemes can be flexibly chosen according to the dimensions of the system. We also develop a system-level simulator where the parameters for the link-to-system level interface can be calibrated according to a certain standardization framework, e.g., IEEE 802.11ac. Numerical results show that the proposed transmission strategy, apart from guaranteeing the scheduling fairness and a small signaling overhead, achieves a much higher throughput than the state-of-the-art and requires a lower complexity.

The remainder of Part I is dedicated to Filter Bank-based Multi-Carrier with Offset Quadrature Amplitude Modulation (FBMC/OQAM)-based MIMO systems. We begin with a thorough overview of FBMC. Then we present new transmit-receive processing techniques for FBMC/OQAM-based MIMO settings ranging from the single-user MIMO case to the Coordinated Multi-Point (CoMP) downlink considering various degrees of channel frequency selectivity. The use of widely linear processing is first investigated. A two-step receiver is designed for FBMC/OQAM-based point-to-point MIMO systems with low frequency selective channels. It exhibits a significant performance superiority over the linear MMSE receiver. The rationale in this two-step receiver is that the intrinsic interference is first mitigated to facilitate the exploitation of the non-circularity residing in the signals. It sheds light upon further studies on widely linear processing for FBMC/OQAM-based systems. Moreover, two coordinated beamforming algorithms are devised for FBMC/OQAM-based point-to-point MIMO systems to relieve the dimensionality constraint of existing schemes that the number of transmit antennas must be larger than the number of receive antennas. The channel on each subcarrier is assumed to be flat fading, which is categorized as the class of intermediate frequency selective channels. With the Channel State Information at the Transmitter (CSIT) known, the precoder designed based on a Zero Forcing (ZF) criterion or the maximization of the Signal-to-Leakage-plus-Noise-Ratio (SLNR) is jointly and iteratively computed with the receiver, leading to an effective mitigation of the intrinsic interference inherent in FBMC/OQAM-based systems. The benefits of the coordinated beamforming concept are successfully translated into the FBMC/OQAM-based multi-user MIMO downlink and the CoMP downlink. Three intrinsic interference mitigating coordinated beamforming (IIM-CBF) schemes are developed. The first two IIM-CBF schemes are proposed for FBMC/OQAM-based multi-user MIMO downlink



---

settings with different dimensions and are able to effectively suppress the Multi-User Interference (MUI) as well as the intrinsic interference. A novel FBMC/OQAM-based CoMP concept is established via the third IIM-CBF scheme which enables the joint transmission of adjacent cells to the cell edge users to combat the strong interference as well as the heavy path loss and to boost the cell edge throughput. The performance of the proposed algorithms is evaluated via extensive numerical simulations. Their convergence behavior is studied, and the complexity issue is also addressed. In addition, the stronger resilience of FBMC over OFDM against frequency misalignments is demonstrated. Furthermore, we cover the case of highly frequency selective channels and provide solutions to the very challenging task of suppressing the MUI, the Inter-Symbol Interference (ISI), as well as the Inter-Carrier Interference (ICI) and supporting per-user multi-stream transmissions. Several design criteria of the multi-tap precoders are devised including the Mean Squared Error (MSE) minimization as well as the Signal-to-Leakage-Ratio (SLR) and SLNR maximization. By rendering a larger computational load at the base station, only single-tap spatial receive filters are required at the user terminals with a weaker computational capability, which enhances the applicability of the proposed schemes in real-world multi-user MIMO downlink systems.

Part II focuses on the context of multi-dimensional harmonic retrieval. We demonstrate the incorporation of statistical robustness into multi-dimensional model order estimation schemes by substituting the sample covariance matrices of the unfoldings of the measurement tensor with robust covariance estimates. It is observed that in the presence of a very severe contamination of the measurements due to brief sensor failures, the robustified tensor-based model order estimation schemes lead to a satisfactory estimation accuracy. This philosophy of introducing statistical robustness also inspires robust versions of parameter estimation algorithms. Last but not the least, we present a generic framework for Tensor-based subspace Tracking via Kronecker-structured projections (TeTraKron) for time-varying multi-dimensional harmonic retrieval problems. It allows to extend arbitrary matrix-based subspace tracking schemes to track the tensor-based subspace estimate in an elegant and efficient manner. By including forward-backward-averaging, we show that TeTraKron can also be employed to devise real-valued tensor-based subspace tracking algorithms. Taking a few matrix-based subspace tracking approaches as an example, a remarkable improvement of the tracking accuracy is observed in case of the TeTraKron-based tensor extensions. The performance of ESPRIT-type parameter estimation schemes is also assessed where the subspace estimates obtained by the proposed TeTraKron-based subspace tracking algorithms are used. We observe that Tensor-ESPRIT combined with a tensor-based subspace tracking scheme significantly outperforms the combination of standard ESPRIT and the corresponding matrix-based subspace tracking

method. These results open the way for robust multi-dimensional big data signal processing applications in time-varying environments.

---

## Zusammenfassung

Die florierende Entwicklung der drahtlosen Kommunikation erfordert innovative und fortschrittliche Signalverarbeitungsalgorithmen, die auf eine verbesserte Performance hinsichtlich der Zuverlässigkeit, des Durchsatzes, der Effizienz und weiterer Faktoren abzielen. Die vorliegende Arbeit befasst sich mit der Lösung dieser Herausforderungen und präsentiert neue und faszinierende Fortschritte, um diesen Herausforderungen zu erfüllen. Hauptsächlich konzentrieren wir uns auf zwei innovative Aspekte der mehrdimensionalen Signalverarbeitung für drahtlose Systeme, denen in den letzten Jahren große Aufmerksamkeit in der Forschung geschenkt wurde. Das sind Mehrträgerverfahren für *Multiple-Input Multiple-Output* (MIMO) Systeme und die mehrdimensionale harmonische Schätzung (*Harmonic Retrieval*).

Da es sich bei MIMO-Systemen und Mehrträgerverfahren um Schlüsseltechnologien der drahtlosen Kommunikation handelt, sind ihre zahlreichen Vorteile seit langem bekannt und haben ein großes Forschungsinteresse geweckt. Zu diesen Vorteilen zählen zum Beispiel die Steigerung der Datenrate und die Verbesserung der Verbindungszuverlässigkeit. Insbesondere OFDM-basierte MIMO *Downlink* Systeme für mehrere Teilnehmer (*Multi-User MIMO Downlink Systems*), die durch SDMA (*Space-Division Multiple Access*) getrennt werden, kombinieren die Vorteile von MIMO-Systemen mit denen von Mehrträger-Modulationsverfahren. Sie sind wesentliche Elemente des IEEE 802.11ac Standards und werden ebenfalls für 5G (die fünfte Mobilfunkgeneration) ausschlaggebend sein. Obwohl die bisherigen Arbeiten über das *Precoding* (Vorcodierung) für solche *Multi-User MIMO Downlink* Systeme schon fruchtbare Ergebnisse zeigten, werden neue Fortschritte benötigt, die den Mehrträger-Charakter des Systems in einer effizienteren Weise ausnutzen oder auf eine höhere spektrale Effizienz des Gesamtsystems abzielen.

Andererseits gilt die Filterbank-basierte Mehrträger Modulation (*Filter Bank-based Multi-Carrier modulation*, FBMC) mit einem gut konzentrierten Spektrum und einer somit niedrigen *Out-of-band Leakage* als eine vielversprechende Alternative zu OFDM. FBMC ermöglicht eine effiziente Nutzung von Fragmenten im Frequenzspektrums, z. B. in 5G oder Breitband *Professional Mobile Radio* (PMR) Netzwerken. Jedoch leiden die vorhandenen Verfahren zur Sende- und Empfangs-Verarbeitung für FBMC-basierte MIMO Systeme unter Einschränkungen in Bezug auf mehrere Aspekte, wie z. B. der erlaubten Dimensionalität des Systems und der zulässigen Frequenzselektivität des Kanals. Die Formen der MIMO Einstellungen, die in der Literatur untersucht wurden, sind noch begrenzt auf MIMO-Systeme für einzelne Teilnehmer

und vereinfachte *Multi-User MIMO* Systeme. Fortschrittlichere Techniken sind daher erforderlich, die diese Einschränkungen der existierenden Verfahren aufheben. MIMO-Szenarien, die weniger Einschränkungen unterliegen, müssen außerdem untersucht werden, um die Vorteile von FBMC zu weiter herauszuarbeiten.

Im Rahmen der mehrdimensionalen harmonischen Schätzung (*Harmonic Retrieval*) hat sich gezeigt, dass eine höhere Genauigkeit bei der Schätzung durch Tensoren erreicht werden kann. Das liegt daran, dass die Darstellung mehrdimensionaler Signale mit Tensoren eine natürlichere Beschreibung und eine gute Ausnutzung ihrer mehrdimensionalen Struktur erlaubt, z. B. für die Modellordnungsschätzung und die Unterraumschätzung. Wichtige offene Themen umfassen die statistische Robustheit und wie man die Schätzung in zeitlich variierenden Szenarien adaptiv gestalten kann.

In Teil I dieser Arbeit präsentieren wir zunächst eine effiziente und flexible Übertragungsstrategie für OFDM-basierten *Multi-User MIMO Downlink* Systeme. Sie besteht aus einer räumlichen *Scheduling*-Methode, der effizienten Mehrträger ProSched (*Efficient Multi-Carrier ProSched*, EMC-ProSched) Erweiterung mit einer effektiven *Scheduling*-Metrik, die auf Mehrträger-Systeme zugeschnitten wird. Weiterhin werden zwei neuartige *Precoding* Algorithmen vorgestellt, die lineare *Precoding*-basierte geometrische Mittelwert-Zerlegung (*Linear Precoding-based Geometric Mean Decomposition*, LP-GMD) und ein *Coordinated Beamforming* Algorithmus geringer Komplexität (*Low Complexity Coordinated Beamforming*, LoCCoBF). Diese beiden neuen *Precoding*-Verfahren können flexibel entsprechend den Abmessungen des Systems gewählt werden. Wir entwickeln auch einen *System Level*-Simulator, in dem die Parameter für das *Link-to-System Level Interface* kalibriert werden können. Diese Kalibrierung ist Standard-spezifisch, z. B. kann der Standard IEEE 802.11ac gewählt werden. Numerische Ergebnisse zeigen, dass diese Übertragungsstrategie *Scheduling* Fairness garantiert, einen weitaus höheren Durchsatz als die existierenden Verfahren erzielt, eine geringere Komplexität besitzt und nur einen geringen Signalisierungs-overhead erfordert.

Der Schwerpunkt des Rests von Teil I bilden MIMO Systeme basierend auf Filter Bank-basierten Mehrträger-Verfahren mit *Offset Quadrature Amplitude Modulation* (FBMC/OQAM). Es wird ein umfassender Überblick über FBMC gegeben. Nachfolgend werden für verschiedene FBMC/OQAM-basierte MIMO Varianten neue Verfahren zur Send- und Empfangs-Verarbeitung entwickelt, die unterschiedliche Grade von Frequenz-Selektivität des Kanals voraussetzen. Zunächst wird die Verwendung von weitgehend linearer Verarbeitung (*widely linear processing*) untersucht. Ein Zwei-Schritt-Empfänger wird für FBMC/OQAM-basierte MIMO Systeme mit einzelnen Teilnehmern entwickelt. Hierbei ist die Frequenz-Selektivität des Kanals niedrig. Verglichen mit linearen MMSE-Empfänger ist die Leistung des Zwei-

---

Schritt-Empfängers viel besser. Das Grundprinzip dieser Zwei-Schritt-Empfänger ist zuerst die Verringerung der intrinsischen Interferenz, um die Ausnutzung von nicht-zirkulären Signalen zu ermöglichen. Es motiviert weitere Studien über weitgehend lineare Verfahren für FBMC/OQAM-basierte Systeme. Darüber hinaus werden zwei *Coordinated Beamforming*-Algorithmen für FBMC/OQAM-basierte MIMO Systeme mit einzelnen Teilnehmern entwickelt. Sie verzichten auf die Einschränkung der Dimensionalität der bestehenden Methode, bei der die Anzahl der Sendeantennen größer als die Anzahl der Empfangsantennen sein muss. Der Kanal auf jedem Träger wird als flacher Schwund (*Flat Fading*) modelliert, was einer Klassifizierung als “*intermediate frequency selective channel*” entspricht. Unter der Kenntnis der Kanalzustandsinformation am Sender (*Channel-State-Information at the Transmitter*, CSIT) basiert die Vorcodierung entweder auf einem *Zero Forcing* (ZF) Kriterium oder auf der Maximierung der *Signal-to-Leakage-plus-Noise-Ratio* (SLNR). Die Vorcodierungsvektoren und die Empfangsvektoren werden gemeinsam und iterativ berechnet. Daher führen die zwei *Coordinated Beamforming*-Algorithmen zu einer wirksamen Verringerung der intrinsischen Interferenz in FBMC/OQAM-basierten Systemen.

Die Vorteile der *Coordinated Beamforming*-Konzepte werden in FBMC/OQAM-basierten *Multi-User MIMO Downlink* Systeme und koordinierte Mehrpunktverbindung (*Coordinated Multi-Point*, CoMP-Konzepte) eingebracht. Dafür werden drei intrinsische Interferenz mildern- de koordinierte Beamforming-Verfahren (*Intrinsic Interference Mitigating Coordinated Beamforming*, IIM-CBF) vorgeschlagen. Die ersten beiden IIM-CBF Algorithmen werden für die FBMC/OQAM-basierten *Multi-User MIMO Downlink* Varianten mit unterschiedlichen Dimensionen entwickelt. Es wird gezeigt, dass diese Verfahren zu einer Abschwächung der Multi-User-Interferenz (MUI) sowie einer Verringerung der intrinsischen Interferenz führen. Bei der dritten IIM-CBF Methode wird ein neuartiges FBMC/OQAM-basiertes-CoMP Konzept vorgestellt. Dieses wird durch die gemeinsame Übertragung von benachbarten Zellen zu Teilnehmern, die sich am Zellenrand befinden, ermöglicht, um den Daten-Durchsatz am Zellenrand zu erhöhen. Die Leistungsfähigkeit der vorgeschlagenen Algorithmen wird durch umfangreiche numerische Simulationen evaluiert. Das Konvergenzverhalten wird untersucht sowie das Thema der Komplexität angesprochen. Außerdem wird die geringere Anfälligkeit von FBMC verglichen mit OFDM gegenüber Frequenzsynchronisationsfehlern demonstriert. Darüber hinaus wird auf die FBMC/OQAM-basierten *Multi-User MIMO Downlink* Systeme mit stark frequenzselektiven Kanälen eingegangen. Dafür werden Lösungen erarbeitet, die für die Unterdrückung der MUI, der Inter-Symbol Interferenz (ISI) sowie der Inter-Carrier Interferenz (ICI) anwendbar sind. Mehrere Kriterien der *multi-tap* Vorcodierung werden entwickelt, beispielsweise die *Mean Squared Error* (MSE) Minimierung sowie die *Signal-to-Leakage-Ratio* (SLR)

und die SLNR Maximierung. An Endgeräten, die eine schwächere Rechenleistung besitzen als sie an der Basisstation vorhanden ist, wird dadurch nur ein *single-tap* Empfangsfilter benötigt.

Teil II der Arbeit konzentriert sich auf die mehrdimensionale harmonische Schätzung (*Harmonic Retrieval*). Der Einbau von statistischer Robustheit in mehrdimensionale Modellordnungsschätzverfahren wird demonstriert. Das wird durch den Ersatz der Kovarianz-Matrizen der *Unfoldings* der Tensoren der Messdaten durch robuste Schätzungen der Kovarianz-Matrizen erreicht. Es ist festzustellen, dass in der Gegenwart von einer sehr schweren Kontamination der Messungen durch kurzzeitige Ausfälle der Sensoren die robusten Tensor-basierten Modellordnungsschätzungsverfahren eine zufriedenstellende Schätzgenauigkeit erreichen. Diese Philosophie der Einführung der statistischen Robustheit inspiriert auch robuste Versionen von Parameterschätzalgorithmen. Weiterhin wird ein generisches *Framework* für das Tensor-basierte Unterraum-Tracking mit Hilfe von Kronecker-strukturierten Projektionen (*Tensor-based subspace Tracking via Kronecker-structured projections*, TeTraKron) vorgestellt, das für die mehrdimensionale harmonische Schätzung in zeitlich variierenden Szenarien angewendet werden kann. Es ermöglicht die Erweiterung einer beliebigen Matrix-basierten Unterraum *Tracking* Methode, um den Tensor-basierten Unterraum in einer eleganten und effizienten Weise zu schätzen. Durch die Einbeziehung der Vorwärts-Rückwärts-Mittelwertbildung (*Forward-Backward Averaging*) wird gezeigt, dass mit Hilfe von TeTraKron reellwertige Tensor-basierte Unterraum *Tracking* Algorithmen entwickelt werden können. Für alle untersuchten Beispiele von Matrix-basierten Unterraum *Tracking* Ansätzen konnte eine wesentliche Verbesserung der Schätzgenauigkeit bei den TeTraKron-basierten Tensor Erweiterungen beobachtet werden. Die Leistungsfähigkeit von ESPRIT-artigen Parameterschätzalgorithmen, bei der die Unterraumschätzungen der entwickelten TeTraKron-basierte Unterraum *Tracking* Methoden verwendet werden, wird auch untersucht. Die Genauigkeit einer Kombination von Tensor-ESPRIT und einem Tensor-basierten Unterraum *Tracking* Verfahren übertrifft deutlich die von Standard ESPRIT und dem entsprechenden Matrix-basierten Unterraum *Tracking* Verfahren. Diese Ergebnisse eröffnen neue Wege für die robuste mehrdimensionale Big Data Signalverarbeitung in zeitlich veränderlichen Szenarien.

# Contents

<b>Acknowledgements</b>	<b>v</b>
<b>Abstract</b>	<b>vii</b>
<b>Zusammenfassung</b>	<b>xi</b>
<b>Contents</b>	<b>xv</b>
<b>List of Figures</b>	<b>xix</b>
<b>List of Tables</b>	<b>xxvi</b>
<b>1. Introduction</b>	<b>1</b>
1.1. Motivation and state-of-the-art . . . . .	1
1.2. Major contributions . . . . .	8
1.3. Notation . . . . .	15
<b>I. Transmit-receive strategies for multi-carrier single-user and multi-user MIMO systems</b>	<b>17</b>
<b>2. Efficient scheduling and precoding for the CP-OFDM-based multi-user MIMO downlink</b>	<b>20</b>
2.1. Introduction . . . . .	20
2.2. CP-OFDM-based multi-user MIMO downlink system model . . . . .	25
2.3. Efficient multi-carrier ProSched (EMC-ProSched) . . . . .	27
2.4. Linear precoding-based geometric mean decomposition (LP-GMD) . . . . .	34
2.5. Low complexity coordinated beamforming (LoCCoBF) . . . . .	40
2.6. IEEE 802.11ac system-level simulator . . . . .	44
2.7. Simulation results . . . . .	45
2.8. Summary . . . . .	54
<b>3. Introduction of Filter Bank-based Multi-Carrier modulation (FBMC)</b>	<b>57</b>
3.1. Motivation . . . . .	57

3.2. Fundamentals of FBMC/OQAM . . . . .	60
3.3. MIMO techniques for FBMC/OQAM-based systems: challenges . . . . .	66
3.4. Summary . . . . .	74
<b>4. Exploring widely linear processing in single-user MIMO FBMC/OQAM systems</b>	<b>75</b>
4.1. Introduction . . . . .	75
4.2. Preliminaries . . . . .	76
4.3. Two-step receiver combining linear and widely linear processing . . . . .	79
4.4. Simulation results . . . . .	82
4.5. Summary . . . . .	86
<b>5. Coordinated beamforming for single-user MIMO FBMC/OQAM systems</b>	<b>88</b>
5.1. Introduction . . . . .	88
5.2. Data model and review of state-of-the-art schemes . . . . .	90
5.3. Coordinated beamforming-based transmission strategy . . . . .	92
5.4. Towards a non-error floor multi-stream beamforming design . . . . .	96
5.5. Simulation results . . . . .	102
5.6. Summary . . . . .	107
<b>6. Intrinsic interference mitigating coordinated beamforming for the FBMC/OQAM-based downlink</b>	<b>108</b>
6.1. Introduction . . . . .	109
6.2. FBMC/OQAM-based multi-user MIMO downlink system model . . . . .	112
6.3. Coordinated beamforming for the single-cell multi-user MIMO downlink . . . . .	117
6.4. Coordinated beamforming for the CoMP downlink . . . . .	123
6.5. Simulation results . . . . .	128
6.6. Summary . . . . .	139
<b>7. FBMC/OQAM-based multi-user MIMO downlink with highly frequency selective channels</b>	<b>141</b>
7.1. Introduction . . . . .	142
7.2. System model . . . . .	144
7.3. Iterative design of MMSE-based precoders and real-valued receive spatial filters	147
7.4. Signal-to-Leakage-Ratio (SLR)-based precoders and real-valued receive spatial filters . . . . .	151
7.5. Enabling per-user multi-stream transmissions . . . . .	153



---

7.6. Simulation results . . . . .	160
7.7. Summary . . . . .	169
<b>II. Tensor-based model order estimation and subspace tracking for multi-dimensional harmonic retrieval</b>	<b>170</b>
<b>8. Robust multi-dimensional model order estimation in the presence of brief sensor failures</b>	<b>172</b>
8.1. Introduction . . . . .	172
8.2. Tensor algebra . . . . .	174
8.3. Data model . . . . .	178
8.4. Robust multi-dimensional model order estimation . . . . .	180
8.5. Robust $R$ -D Exponential Fitting Test . . . . .	186
8.6. Simulation results . . . . .	189
8.7. Summary . . . . .	195
<b>9. Tensor subspace Tracking via Kronecker structured projections (TeTraKron)</b>	<b>196</b>
9.1. Introduction . . . . .	196
9.2. Data model for the matrix-based and the tensor-based subspace estimation . . .	199
9.3. Tensor subspace Tracking via Kronecker structured projections (TeTraKron) . .	201
9.4. Examples . . . . .	206
9.5. Simulation results . . . . .	214
9.6. Summary . . . . .	224
<b>10. Conclusions and future work</b>	<b>227</b>
<b>Appendix A. Glossary of acronyms, symbols, and notation</b>	<b>234</b>
A.1. Acronyms . . . . .	234
A.2. Symbols and notation . . . . .	236
A.3. Frequently used notation in each chapter . . . . .	237
<b>Appendix B. Derivation of Exponential Effective SINR Mapping (EESM) for binary signaling</b>	<b>244</b>
<b>Appendix C. Evaluation of the accuracy of Exponential Effective SINR Mapping (EESM)</b>	<b>247</b>
<b>Appendix D. Modulation and Coding Schemes (MCSs) specified in IEEE 802.11ac</b>	<b>250</b>

---

<b>Appendix E. Derivation of the widely linear MMSE receiver</b>	<b>251</b>
<b>Appendix F. Proof of Theorem 9.3.1 [RHD14]</b>	<b>254</b>
<b>Appendix G. Avoiding matrix inversion in TeTraKron-PAST</b>	<b>255</b>
<b>Bibliography</b>	<b>258</b>

## List of Figures

1.1. The evolution of data throughput requirements for PMR networks . . . . .	5
2.1. Maximum achievable throughput of the IEEE 802.11 standards family (the years in the x-axis labels indicate when the standards were published) . . . . .	23
2.2. Illustration of the multi-user MIMO downlink . . . . .	26
2.3. Illustration of the tree-based sorting scheme . . . . .	28
2.4. PER versus SNR curves for SISO transmissions over the AWGN channel for the 10 IEEE 802.11ac MCSs; the SNR is defined as $E_s/N_0$ , where $E_s$ represents the symbol energy, and $N_0$ denotes the noise spectral density . . . . .	46
2.5. Block diagram of the system-level simulator . . . . .	46
2.6. CCDF of the system throughput of a 16-user scenario with the PSDU size as 500,000 B when the proposed transmission strategy is employed . . . . .	48
2.7. Fairness comparison between Round Robin and EMC-ProSched in a 16-user scenario . . . . .	49
2.8. System throughput of a 16-user scenario with the PSDU size as 500,000 B where EMC-ProSched, EMC-ProSched with exhaustive search, and Round Robin are compared . . . . .	50
2.9. Comparison of the number of calculations of the scheduling metric (considering one channel realization) in case of EMC-ProSched that employs the tree-based sorting scheme and the exhaustive search of all possible user combinations . . . . .	51
2.10. System throughput of a 64-user scenario with the PSDU size as 500,000 B where EMC-ProSched and the user selection scheme in [SK10] are compared . . . . .	52
2.11. CCDF of the system throughput when LP-GMD is employed for a 16-user scenario with the PSDU size as 100,000 B and EMC-ProSched as the scheduling algorithm . . . . .	53
2.12. System throughput when LP-GMD-RBD is employed for a 32-user scenario with the PSDU size as 500,000 B with and without power loading (“LP-GMD-RBD PL” represents LP-GMD-RBD with the MMSE-based power loading in the legend) . . . . .	54

2.13. CCDF of the system throughput and the number of iterations in a 16-user scenario when LoCCoBF is employed with the PSDU size as 500,000 B and EMC-ProSched as the scheduling algorithm . . . . .	55
3.1. Comparison of the power spectral density of FBMC and CP-OFDM; the normalized frequency is obtained by dividing the actual frequency by the subcarrier spacing . . . . .	58
3.2. Future PMR broadband in coexistence and cohabitation with current systems [RBB <sup>+</sup> 13]; BB – broadband, UE – user equipment . . . . .	59
3.3. OQAM staggering for subcarriers with odd indices (top) and even indices (bottom)	60
3.4. Illustration of the data symbols after the OQAM staggering in FBMC/OQAM-based systems; $\Delta f$ represents the subcarrier spacing, whereas $T$ denotes the symbol period . . . . .	61
3.5. Block diagram of a SISO FBMC/OQAM system . . . . .	61
3.6. Illustration of the multi-user MIMO uplink setting and the block-wise subcarrier allocation . . . . .	71
3.7. Comparison between FBMC/OQAM and CP-OFDM for a two-user uplink scenario in the presence of symbol timing offsets in the range of $(T/8, T/4)$ (GB – guard band in terms of the number of subcarriers) . . . . .	72
3.8. Comparison between FBMC/OQAM and CP-OFDM for a 2-user uplink scenario in the presence of residual CFOs (normalized by the subcarrier spacing) .	73
4.1. Block diagram of the proposed two-step receiver . . . . .	81
4.2. BER vs. SNR for the case where $M_T = M_R = 2$ (“MMSE + WL-MMSE 1” and “MMSE + WL-MMSE 2” correspond to the two versions of the two-step receiver where the estimated interference is obtained by using (4.13) and (4.14), respectively; “WL-MMSE ideal” corresponds to an ideal case where the interference component is completely canceled) . . . . .	83
4.3. BER vs. SNR for the case where $M_T = M_R = 4$ (“MMSE + WL-MMSE 1” and “MMSE + WL-MMSE 2” correspond to the two versions of the two-step receiver where the estimated interference is obtained by using (4.13) and (4.14), respectively; “WL-MMSE ideal” corresponds to an ideal case where the interference component is completely canceled) . . . . .	84

---

4.4. BER vs. SNR for the case where $M_T = M_R = 2$ (“MMSE + WL-MMSE 1” and “MMSE + WL-MMSE 2” correspond to the two versions of the two-step receiver where the estimated interference is obtained by using (4.13) and (4.14), respectively) . . . . .	85
4.5. BER vs. SNR for the case where $M_T = M_R = 4$ (“MMSE + WL-MMSE 2” corresponds to the version of the two-step receiver where the estimated interference is obtained by using (4.14); “MMSE-ML” corresponds to the scheme combining MMSE and ML in [ZLB10]) . . . . .	86
5.1. Comparison of the BER performances of different schemes in a system where $M_T = M_R = 6$ , $d = 5$ , and the ITU Ped-A channel is considered; CBF - coordinated beamforming . . . . .	102
5.2. Comparison of the BER performances of different schemes in a system where $M_T = 6$ , $M_R = 7$ , $d = 5$ , and the ITU Ped-A channel is considered; CBF - coordinated beamforming . . . . .	103
5.3. Comparison of the BER performances of different schemes in a system where $M_T = M_R = 4$ , $d = 3$ , and the ITU Veh-A channel is considered; CBF - coordinated beamforming . . . . .	104
5.4. Comparison of the BER performances of different schemes in a system where $M_T = 6$ , $M_R = 7$ , $d = 5$ , and the ITU Veh-A channel is considered; CBF - coordinated beamforming . . . . .	105
5.5. CCDF of the number of iterations in case of the two coordinated beamforming schemes in a system where $M_T = 6$ , $M_R = 7$ , $d = 5$ , and the ITU Veh-A channel is considered; CBF - coordinated beamforming . . . . .	106
6.1. Illustration of the multi-user MIMO downlink setting with linear precoding on a per-subcarrier basis (time and frequency indices ignored in the notation of data vectors, precoding and decoding matrices) . . . . .	113
6.2. An example of a two-cell CoMP downlink scenario where a cell interior user and two cell edge users are served in each cell . . . . .	124
6.3. Comparison of the BER performances of different schemes in a multi-user MIMO system where $Q = 2$ , $M_T^{(\text{BS})} = M_R^{(\text{tot})} = 8$ , $d = 6$ , the ITU Veh-A channel is considered; $E_s$ denotes the energy of each 16 QAM symbol, and $N_0$ represents the noise power spectral density . . . . .	130

---

6.4.	Comparison of the BER performances of different schemes in a multi-user MIMO downlink system where $Q = 2$ , $M_T^{(\text{BS})} = 8$ , $M_R^{(\text{tot})} = 10$ , $d = 6$ , and the ITU Ped-A channel is considered; $E_s$ denotes the energy of each 16 QAM symbol, and $N_0$ represents the noise power spectral density . . . . .	131
6.5.	Comparison of the BER performances of different schemes in a multi-user MIMO downlink system where $Q = 3$ , $M_T^{(\text{BS})} = 8$ , $M_R^{(\text{tot})} = 9$ , $d = 6$ , and the ITU Ped-A channel is considered; $E_s$ denotes the energy of each 16 QAM symbol, and $N_0$ represents the noise power spectral density . . . . .	132
6.6.	CCDF of the number of iterations required for IIM-CBF 2 and LoCCoBF in multi-user MIMO FBMC/OQAM and CP-OFDM-based downlink systems with different settings, respectively, and the ITU Ped-A channel is considered . . . .	133
6.7.	Comparison of the BER performances of different schemes in a multi-user MIMO downlink system in the presence of residual CFO (unit: subcarrier spacing) where $Q = 4$ , $M_T^{(\text{BS})} = 8$ , $M_R^{(\text{tot})} = 12$ , $d = 8$ , and the ITU Ped-A channel is considered; $E_s$ denotes the energy of each 16 QAM symbol, and $N_0$ represents the noise power spectral density . . . . .	134
6.8.	Comparison of the sum rate performances of different schemes in the CoMP downlink where the total number of users in two adjacent cells is 5, and the ITU Ped-A channel is considered . . . . .	137
6.9.	CCDF of the number of iterations required for different coordinated beamforming schemes in the CoMP downlink system where the total number of users in two adjacent cells is 5, and the ITU Ped-A channel or the ITU Veh-A channel is considered . . . . .	138
6.10.	Comparison of the sum rate performances of different coordinated beamforming schemes in the CoMP downlink where the total number of users in three adjacent cells is 7, and the ITU Ped-A channel is considered . . . . .	139
7.1.	Precoding of the signals for the $U$ users onto $M_T$ transmit antennas for subcarrier $\ell$	145
7.2.	Block diagram of the transmitter side of the subcarrier model . . . . .	146
7.3.	Block diagram of the receiver side of the subcarrier model considering the $r$ -th receive antenna of the $j$ -th user . . . . .	147
7.4.	Precoding of multiple data streams of each of the $U$ users onto $M_T$ transmit antennas for subcarrier $\ell$ . . . . .	154
7.5.	Block diagram of the transmitter side of the subcarrier model considering the $k$ -th subcarrier . . . . .	155

---

7.6. BER performance in different multi-user MIMO downlink settings where $U = 2$ , $M_{R_1} = M_{R_2} = 2$ , $M_T = 8$ or $4$ , and $\alpha = 0.025$ . . . . .	161
7.7. CCDF of the number of iterations of the iterative design in Section 7.3 and the final value of $\Delta(\mathbf{g})$ in different multi-user MIMO downlink settings where $U = 2$ , $M_{R_1} = M_{R_2} = 2$ , $M_T = 8, 6$ or $4$ , $B = 5$ , and $\alpha = 0.025$ . . . . .	162
7.8. BER performance in a multi-user MIMO downlink setting where $U = 2$ , $M_{R_1} = M_{R_2} = 3$ , $M_T = 6$ . . . . .	163
7.9. BER performance in multi-user MIMO downlink settings where $U = 2$ , $M_{R_1} = M_{R_2} = 3$ , $M_T = 6$ , $D_1 = D_2 = 2$ . . . . .	164
7.10. BER performance of the SLNR-based precoding method in multi-user MIMO downlink settings where $U = 2$ , $M_{R_1} = M_{R_2} = 2$ or $M_{R_1} = M_{R_2} = 3$ , $M_T = 8$ , $D_1 = D_2 = 2$ . . . . .	165
7.11. BER performance in multi-user MIMO downlink settings where $U = 2$ , $M_{R_1} = M_{R_2} = 5$ , $M_T = 8$ , $D_1 = D_2 = 3$ . . . . .	168
8.1. Illustration of the unfoldings of a $4 \times 5 \times 3$ tensor in the forward column ordering	175
8.2. Illustration of the unfoldings of a $4 \times 5 \times 3$ tensor in the reverse cyclical ordering	175
8.3. $r$ -mode products between a three-way tensor $\mathcal{A}$ and a matrix . . . . .	176
8.4. Illustration of a three-way identity tensor $\mathcal{I}_{4,3}$ . . . . .	177
8.5. Illustration of the concatenation of two three-way tensors along the $r$ -modes . .	178
8.6. Construction of the measurement tensor from the measurement matrix in the 2-D case . . . . .	179
8.7. Influence functions of two covariance estimators, the sample covariance estimator (left) and the M-estimator (right) at the bivariate complex normal distribution [ZKCM12] . . . . .	180
8.8. Illustration of the calculation of the global eigenvalues . . . . .	184
8.9. Top: global eigenvalues and predicted global eigenvalues obtained in robust $R$ -D EFT by applying the exponential approximation for $M_1 = 5$ , $M_2 = 5$ , $M_3 = 5$ , $N = 5$ , $d = 1$ , and $\text{SNR} = 0$ dB in the presence of a brief sensor failure; bottom: global eigenvalues and predicted global eigenvalues obtained in $R$ -D EFT for the same scenario . . . . .	187
8.10. Probability of correct detection versus SNR for $M_1 = 5$ , $M_2 = 7$ , $M_3 = 9$ , $N = 10$ , $d = 3$ in the presence of a brief sensor failure modeled by randomly replacing a single entry of the measurement tensor with a complex i.i.d. impulsive noise that obeys a complex zero mean Gaussian distribution with variance of $\kappa\sigma_n^2$ , where $\sigma_n^2$ represents the variance of the noise, and $\kappa = 50$ . . . . .	189

---

8.11. Probability of correct detection versus SNR for $M_1 = 7$ , $M_2 = 7$ , $M_3 = 7$ , $M_4 = 7$ , $N = 7$ , $d = 4$ in the presence of a brief sensor failure modeled by randomly replacing a single entry of the measurement tensor with a complex i.i.d. impulsive noise that obeys a complex zero mean Gaussian distribution with variance of $\kappa\sigma_n^2$ , where $\sigma_n^2$ represents the variance of the noise, and $\kappa = 50$ . . . . .	190
8.12. Probability of correct detection versus SNR for $M_1 = 5$ , $M_2 = 5$ , $M_3 = 5$ , $N = 5$ , $d = 3$ without sensor failure and the performances of the original $R$ -D EFT and the robustified $R$ -D EFT are compared . . . . .	191
8.13. Probability of correct detection versus SNR for $M_1 = 5$ , $M_2 = 5$ , $M_3 = 5$ , $N = 5$ , $d = 3$ in the presence of a brief sensor failure modeled by randomly replacing 2 % of the entries of the measurement tensor with a complex i.i.d. impulsive noise that obeys a complex zero mean Gaussian distribution with variance of $\kappa\sigma_n^2$ , where $\sigma_n^2$ represents the variance of the noise, and $\kappa = 50$ . . . . .	192
8.14. Probability of correct detection versus SNR for $M_1 = 5$ , $M_2 = 5$ , $M_3 = 5$ , $M_4 = 5$ , $N = 5$ , $d = 2$ in the presence of a brief sensor failure modeled by randomly replacing a single entry of the measurement tensor with a complex i.i.d. impulsive noise that obeys a complex zero mean Gaussian distribution with variance of $\kappa\sigma_n^2$ , where $\sigma_n^2$ represents the variance of the noise, and $\kappa = 50$ . . . . .	193
8.15. Probability of correct detection versus the percentage of contamination at SNR = 0 dB for a 3-D scenario $M_1 = 5$ , $M_2 = 5$ , $M_3 = 5$ , $N = 5$ , and $d = 3$ in the presence of a brief sensor failure modeled by randomly replacing a certain percentage of the entries in the measurement tensor with a complex i.i.d. impulsive noise that obeys a complex zero mean Gaussian distribution with variance of $\kappa\sigma_n^2$ , where $\sigma_n^2$ represents the variance of the noise, and $\kappa = 50$ . . . . .	194
9.1. Illustration of the spatial frequencies of the three sources over the course of 1000 snapshots. The first two sources cross, whereas the third source stays stationary	217
9.2. LPA (in radians) for three moving sources on a $9 \times 9$ URA at an SNR of 0 dB; averaged over 100 trials . . . . .	218
9.3. LPA (in radians) for three moving sources on a $7 \times 7$ URA at an SNR of 0 dB; averaged over 100 trials . . . . .	219
9.4. LPA (in radians) for three moving sources on a $9 \times 9$ URA at an SNR of 0 dB where FAPI and its tensor extensions are employed; averaged over 100 trials . .	220
9.5. Illustration of the spatial frequencies of the three sources over the course of 1000 snapshots. The first two sources cross, whereas the third source stays stationary	221



9.6.	LPA (in radians) for three-dimensional harmonic retrieval problem of size $7 \times 7 \times 7$ at an SNR of 0 dB; three moving sources; FBA - forward-backward-averaging; averaged over 100 trials . . . . .	222
9.7.	LPA (in radians) for three moving sources on a $7 \times 7$ URA at an SNR of 0 dB; sources correlated with $\rho = 0.7$ ; FBA - forward-backward-averaging; averaged over 1000 trials . . . . .	223
9.8.	RMSE of spatial frequencies for three moving sources on a $7 \times 7$ URA at an SNR of 0 dB; sources correlated with $\rho = 0.7$ ; FBA - forward-backward-averaging, SE - Standard ESPRIT, UE - Unitary ESPRIT, STE - Standard Tensor-ESPRIT, UTE - Unitary Tensor-ESPRIT; averaged over 1000 trials . . . . .	224
9.9.	Averaged spatial frequency estimates of the first mode and error bars for three moving sources on a $7 \times 7$ URA at an SNR of 0 dB; sources correlated with $\rho = 0.7$ ; FBA - forward-backward-averaging, SE - Standard ESPRIT, UE - Unitary ESPRIT, STE - Standard Tensor-ESPRIT, UTE - Unitary Tensor-ESPRIT; averaged over 1000 trials . . . . .	225
9.10.	Averaged spatial frequency estimates of the second mode and error bars for three moving sources on a $7 \times 7$ URA at an SNR of 0 dB; sources correlated with $\rho = 0.7$ ; FBA - forward-backward-averaging, SE - Standard ESPRIT, UE - Unitary ESPRIT, STE - Standard Tensor-ESPRIT, UTE - Unitary Tensor-ESPRIT; averaged over 1000 trials . . . . .	226
C.1.	Comparison of EESM and the instantaneous SNR method for MCS 1 . . . . .	247
C.2.	CCDF of the measured throughput and the estimated throughput by employing EESM for MCS 3 in a single-user 4-by-4 MIMO setting . . . . .	248
C.3.	Channel frequency response of IEEE 802.11ac channel Model D . . . . .	249
G.1.	Complexity comparison between the version with the $d \times d$ matrix inversion and the version of avoiding the matrix inversion in terms of FLOPs for updating the $r$ -mode subspace estimates . . . . .	256

## List of Tables

2.1. Proposed transmission strategy . . . . .	43
2.2. IEEE 802.11ac OFDM parameters (80 MHz transmission) . . . . .	47
3.1. Coefficients $c_{i,\ell}$ representing the system impulse response determined by the synthesis and analysis filters [Bel10] (the PHYDYAS prototype filter [PHY] used with the overlapping factor $K = 4$ ) . . . . .	64
3.2. Summary of the focuses and major outcomes of Chapters 4, 5, 6, and 7 . . . . .	70
6.1. Acronyms of the proposed intrinsic interference mitigating coordinated beam-forming (IIM-CBF) schemes and the corresponding scenarios . . . . .	112
8.1. Breakdown points and properties of the influence functions of the sample co-variance matrix, the S-estimator, the M-estimator, the MM-estimator . . . . .	182
9.1. Summary of the PAST algorithm [Yan95b] . . . . .	207
9.2. Summary of the tensor-based PAST algorithm for updating the $r$ -mode subspace estimates . . . . .	209
9.3. Summary of the PASTd algorithm [Yan95b] where $\hat{\mathbf{u}}_i(n)$ represents the $i$ -th column of $\hat{\mathbf{U}}_s(n)$ , and $d_i(n)$ is the $i$ -th element of $\mathbf{d}(n)$ . . . . .	210
9.4. Summary of the tensor-based version of the PASTd algorithm for updating the $r$ -mode subspace estimates . . . . .	211
9.5. Summary of the tensor-based version of the exponential window FAPI algorithm [BDR05] for updating the $r$ -mode subspace estimates . . . . .	213
9.6. Summary of TeTraKron-PAST, TeTraKron-PASTd, TeTraKron-PAST II, TeTraKron-PASTd II, and TeTraKron-FAPI . . . . .	215
9.7. Summary of TeTraKron-PAST with FBA and TeTraKron-FAPI with FBA . . . . .	216
D.1. IEEE 802.11ac MCSs (80 MHz, single data stream, and the length of CP is 800 ns); $N_{\text{DBPS}}$ denotes the number of data bits per OFDM symbol . . . . .	250

---

# 1. Introduction

## 1.1. Motivation and state-of-the-art

In 1895, Guglielmo Marconi transmitted the three-dot Morse code for the letter “S” over a distance of three kilometers using electromagnetic waves, which has preluded the ever-growing attention on wireless communications. Especially the past few decades have witnessed the rapid and prosperous development of wireless communications that caters for the booming demand of higher data rates, increasing spectral efficiency, greater robustness, etc.. It has stimulated and also has been in turn supported by emerging advanced signal processing techniques.

As one of the essential enabling technologies for wireless communications, the variety of advantages of Multiple-Input Multiple-Output (MIMO) where multiple transmit antennas and multiple receive antennas are used have long been well acknowledged. It is the key element of wireless communication standards such as IEEE 802.11n and LTE. A diversity of signal processing schemes were designed, and performance bounds were established for single-user MIMO systems [Tel99a], [GJJV03], [ZT03], [Ala98], [TJC02], [GSS<sup>+</sup>03], [PGNB04]. These pioneering works corroborated the predicted benefits of the MIMO technology. For instance, the rich scattering environment provides independent transmission paths such that the spatial diversity gain is exploited to alleviate the sensitivity to fading and the spatial multiplexing gain promises a significant boost in the channel capacity. Due to a coherent combining effect of the wireless signals at the receiver, array gain is achieved, contributing to an enhanced resistance to noise and an improved coverage. Moreover, the interference mitigation can be achieved by exploiting the spatial dimensions in MIMO systems. On the other hand, limitations of the single-user MIMO were also revealed. For instance, in general the antenna elements are required to be sufficiently distant from each other, e.g., half a wavelength, to reduce the influence of mutual coupling and to fully exploit the MIMO benefits. However, the receiver for the downlink is very likely to be size-constrained. This issue has not only motivated advanced antenna designs for single-user MIMO systems but also led considerable research attention to another form of MIMO, multi-user MIMO with Space-Division Multiple Access (SDMA) [Tel99b], [SPSH04], [SSH04], [SCA<sup>+</sup>05], [SH08], [RFH08]. On the downlink of multi-user MIMO systems, the base station serves multiple user terminals at the same time and on the same frequency. Such a high-capacity achieving technology demands effective spatial scheduling and multi-user interference mitigation algorithms. Due to the fact that the spatial

capacity of the base station is limited and the spatial signatures of the user terminals play an crucial role in user separation, spatial scheduling is performed to select SDMA user groups with an appropriate size and isolate users with a high spatial correlation into different SDMA user groups. Then, precoding techniques serve to suppress the multi-user interference, turning the multi-user MIMO downlink into parallel and independent single-user settings.

Another remarkable innovation in modern wireless communications is believed to be the introduction of multi-carrier modulation, which further boosts the data rate, enhances the resilience against critical propagation conditions, and contributes to improved link reliability. One of the most popular and widely used multi-carrier modulation schemes is Orthogonal Frequency Division Multiplexing with the Cyclic Prefix insertion (CP-OFDM). Its intriguing features include great robustness against multi-path fading, an efficient implementation, and the capability of turning the frequency selective channels into parallel flat fading subchannels such that sophisticated receiver designs are avoided. Consequently, CP-OFDM has been adopted in a variety of communication standards and products. For example, it was for the first time introduced to the IEEE 802.11 standards family when deployed in IEEE 802.11a in 1999. As the most recent amendment to the IEEE 802.11 specifications, IEEE 802.11ac, published in December 2013, promises a significant increase of the maximum achievable throughput by combining the twofold benefits of the SDMA-based multi-user MIMO downlink and CP-OFDM.

There have been a number of user scheduling and precoding algorithms proposed in the literature for multi-user MIMO downlink systems. For some scheduling techniques, e.g., [LTSL10], it is required that precoding is first employed on each possible user group to predict the scheduling performance and then to determine the best user group. The resulting computational complexity is therefore prohibitive, especially when the total number of users is large. Another type of scheduling schemes [PKP11] avoid such a high computational load by assuming that the precoding vectors are generated according to a codebook shared by the base station and the user terminals. But this assumption prevents these approaches from being applied in systems where such codebooks are not available. Targeting at a low complexity and a high flexibility, the ProSched scheme [FDH07], employs a capacity related scheduling metric and uses the concept of orthogonal projections such that neither the pre-calculation of the precoding matrices nor certain codebooks for precoding is necessary. The scheduling metric in ProSched was originally designed for a single subcarrier. In [FDH07], the use of ProSched in a multi-carrier system is addressed, and it treats each subcarrier as a virtual user in the scheduling process, leading to a high complexity and a large signaling overhead. These limitations of existing algorithms motivate the development of new efficient user scheduling

schemes for multi-carrier multi-user MIMO downlink systems.

On the other hand, linear precoding algorithms such as Block Diagonalization (BD) [SSH04] and Regularized Block Diagonalization (RBD) [SH08], [SHGJ06] have laid foundation for research on multi-user MIMO downlink linear precoding designs. The philosophy of these schemes consists of two subsequent steps, the multi-user interference suppression and the tuning of the performance of each resulting single-user transmission. Decoupling each equivalent single-user MIMO channel into parallel subchannels enables the transmission of multiple data streams to each user. A certain power allocation scheme, e.g., the water filling algorithm [PNG03], can be further employed. Consequently, suitable Modulation and Coding Schemes (MCSs) need to be selected for individual data streams according to their distinct Signal-to-Noise-Ratios (SNRs). Using the same MCS across all the data streams would lead to the fact that the Packet Error Rate (PER) performance is dominated by the weakest subchannel. The implementation of unequal MCSs, on the other hand, results in a large signaling overhead. Therefore, in communication standards such as IEEE 802.11ac [WG813], it is specified that equal MCSs should be applied on the spatial streams sent to each user to avoid the loss in spectral efficiency. These facts have sparked the interest in devising new linear precoding techniques that support the same MSC on all data streams and in the meantime exhibit a performance superiority to the state-of-the-art.

One issue with the BD algorithm [SSH04] is the dimensionality constraint which states that BD cannot be employed if the aggregated number of receive antennas at the user terminals exceeds the number of transmit antennas at the base station. Some approaches such as RBD [SH08] and the leakage-based precoding scheme [STS07] are able to alleviate this dimensionality constraint but still suffer from a severe performance degradation as the total number of receive antennas increases. To break through this bottle-neck of the precoding design, the concept of coordinated beamforming was first introduced in [SSH04], which opened the way for the development of linear precoding schemes featuring a greater flexibility. The coordinated beamforming algorithm proposed in [CMIH08] achieves a satisfactory sum rate performance by jointly and iteratively optimizing the transmit and receive beamformers. To overcome the limit in [CMIH08] that only a single spatial stream is allowed for each user, a flexible coordinated beamforming (FlexCoBF) algorithm [SRH10b] was developed, where the design criterion of the transmit and receive beamformers can be selected flexibly. Moreover, by interpreting the coordinated beamforming task as a special joint matrix transformation, called “sequentially drilled” joint congruence transformation (SeDJoCo), a semi-algebraic solution has also been proposed, presenting a new perspective of the precoding design for multi-user MIMO downlink systems [YSRH12]. As computational complexity is one of the biggest concerns with respect

to an iterative algorithm, it is of great interest and importance to, for instance, devise ways of lowering the number of iterations, and to therefore find coordinated beamforming schemes that experience both a high flexibility (in the sense that the number of receive antennas at the user terminals is not restricted) and a satisfactory efficiency.

Although widely deployed in various state-of-the-art communication standards, CP-OFDM suffers from several drawbacks, such as high out-of-band radiation and vulnerability to the loss of synchronization, that give rise to the pursuit of alternative multi-carrier modulation schemes. One promising substitute of CP-OFDM is Filter Bank-based Multi-Carrier modulation (FBMC). By employing spectrally well-concentrated synthesis and analysis filter banks at the transmitter and the receiver [SSL02], [Bel01], respectively, FBMC is endowed with a much better spectral containment and a much lower out-of-band leakage compared to CP-OFDM. Accordingly, FBMC is more immune to time as well as frequency misalignments and contributes to effective utilization of spectrum holes. With these advantageous features, FBMC has found applications in numerous contexts, e.g., cognitive radio networks [SB10] and asynchronous communication scenarios [FPT08], [SSWB<sup>+</sup>11]. In addition, FBMC plays a significant role in several international projects [PHY], [EMP], [5GN], [MET]. Among them, the European project EMPhAtiC [EMP] addresses the evolution of data throughput requirements for Professional Mobile Radio (PMR) systems depicted in Figure 1.1 and proposes a novel broadband PMR concept [RBB<sup>+</sup>13]. There the key element is FBMC, since it enables an effective use of spectrum fragments to accommodate broadband communication services without acquiring new frequency bands.

As the FBMC scheme that has received the most research attention, Filter Bank-based Multi-Carrier with Offset Quadrature Amplitude Modulation (FBMC/OQAM) leads to a higher spectral efficiency compared to CP-OFDM. It is due to the fact that the insertion of a CP is not required. In FBMC/OQAM-based systems, the in-phase and quadrature components of each complex-valued QAM modulated data symbol are staggered by half of the symbol period [SSL02]. Assuming ideal propagation conditions, i.e., an AWGN channel, the desired signal and the intrinsic interference are separated in the real domain and the pure imaginary domain, respectively [Bel10]. This is regarded as a special type of orthogonality in FBMC/OQAM-based systems. It has been established that the degree of the frequency selectivity of the propagation channel plays a significant role in the design of FBMC/OQAM-based MIMO schemes. Some publications on the receiver design for point-to-point MIMO FBMC/OQAM systems consider the case of low frequency selective channels where the frequency response of the channel stays almost constant across neighboring subcarriers and time instants. As a consequence, the orthogonality of FBMC/OQAM systems is preserved. The

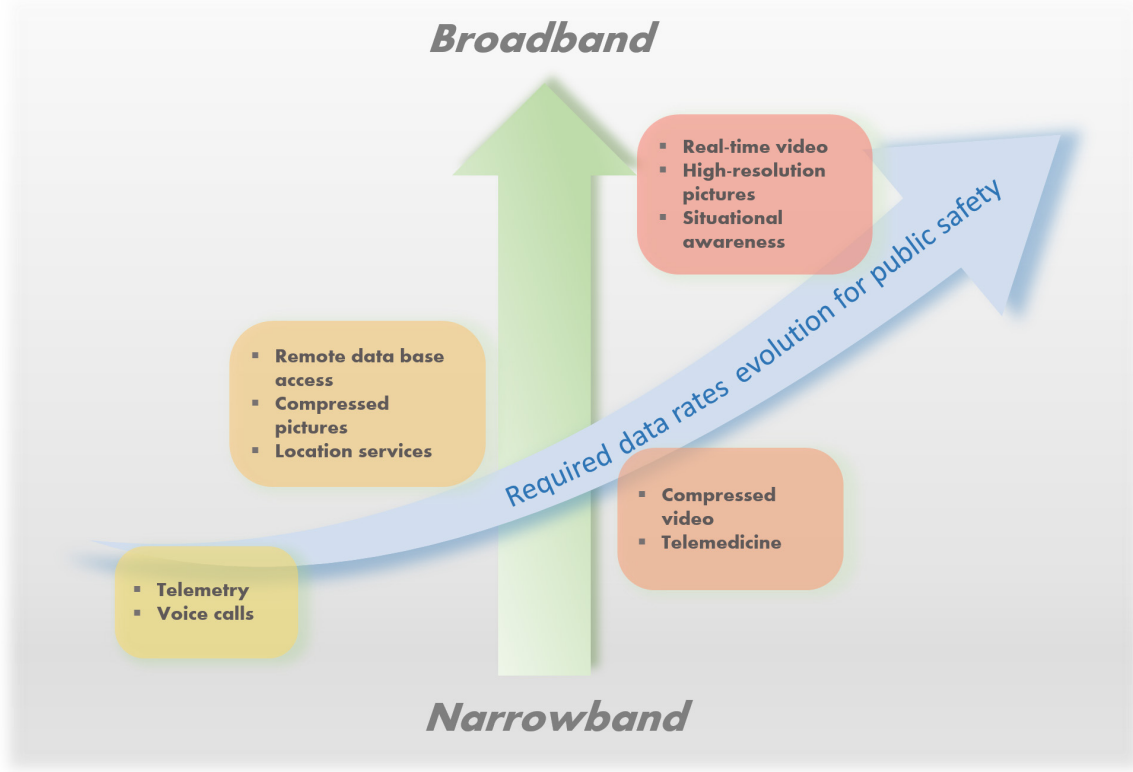


Figure 1.1.: The evolution of data throughput requirements for PMR networks

resulting per-subcarrier data model of a MIMO FBMC/OQAM system becomes similar to that of its CP-OFDM-based counterpart. The only difference is that the equivalent transmit signal consists of the desired signal and the intrinsic interference that are isolated in the real domain and the pure imaginary domain, respectively. Such a formulation of the data model alleviates the difficulty of the intrinsic interference mitigation which is regarded as the major challenge in the design of FBMC/OQAM-based MIMO techniques. It has facilitated the development of the Maximum Likelihood (ML)-based receiver [ZLB10] and its variants as well as enhanced versions [ZL11a], [ZL11b]. They follow the philosophy that the intrinsic interference is first suppressed and the ML detection is applied on the resulting signal. Note that the data signals of an FBMC/OQAM system show non-circularity. Thus, there exists the potential of exploiting the benefits of widely linear processing [PC95]. The case of low frequency selective channels is a promising starting point. Based on a similar rationale to the ML-based receivers (i.e., by using a two-step receiver), the incorporation of widely linear processing to MIMO

FBMC/OQAM systems is an interesting and important innovation.

Endeavors have also been made to relax the constraint on the frequency selectivity of the propagation channel by exploiting the Channel State Information at the Transmitter (CSIT). A Zero Forcing (ZF)-based precoder has been proposed in [CPN13b] and [CPN13a] for point-to-point MIMO FBMC/OQAM systems. It is able to achieve the intrinsic interference elimination assuming that the channel on each subcarrier can be treated as flat fading. Combining this ZF-based concept with Tomlinson-Harashima precoding (THP) and the BD algorithm [SSH04] has yielded two precoding schemes for FBMC/OQAM-based multi-user Multiple-Input Single-Output (MISO) and MIMO downlink systems [CPN13c], [CPNM13]. Unfortunately, due to the fact that these methods follow the theory of the ZF-based precoder to mitigate the intrinsic interference, they have inherited its drawback with respect to the dimensionality. It has been pointed out in [CPN13a] that the ZF-based precoding scheme can only be employed in a point-to-point MIMO FBMC/OQAM system where the number of receive antennas does not exceed the number of transmit antennas. In addition, it fails to achieve a satisfactory performance in a symmetric MIMO setting (where the number of transmit antennas is equal to the number of receive antennas). These observations call for dimensionality constraint resolving techniques for both the FBMC/OQAM-based point-to-point and multi-user MIMO systems. On the other hand, in case of CP-OFDM-based systems, the fruitful outcome of the research on SDMA schemes for multi-user MIMO downlink systems has motivated and has built the foundation for the thriving development of Coordinated Multi-Point (CoMP) techniques. It predicts a similar trend in case of FBMC/OQAM and stimulates the design of FBMC/OQAM-based CoMP schemes.

Some results have also been reported on FBMC/OQAM-based MIMO schemes in the presence of highly frequency selective channels. In this case, the task of mitigating the inter-carrier interference as well as the inter-symbol interference and separating the data streams is very challenging. One way to accomplish it is to resort to multi-tap equalization. A per-subcarrier Minimum Mean Squared Error (MMSE)-based multi-tap equalizer was proposed in [IL09], whereas two joint designs of multi-tap precoders and decoders were presented in [CPN14b] by exploiting both the CSIT and the Channel State Information at the Receiver (CSIR). Alternatively, [MG14] introduced an architecture for the implementation of MIMO precoders and receivers where multiple parallel stages are combined on a per-subcarrier level. Each stage is constructed using the successive derivatives of the prototype pulse. Note that the aforementioned techniques were all devised for point-to-point FBMC/OQAM-based MIMO systems. The multi-user downlink setting with highly frequency selective channels is of great interest as well. Yet only MISO scenarios have been recently studied in the literature [HFDL13], [NBSN14]



where the number of receiver antennas at each user terminal is restricted to one. Therefore, FBMC/OQAM-based multi-user MIMO downlink systems in the presence of highly frequency selective channels remain to be explored. Advanced transmit-receive processing schemes are to be tailored to enable per-user multiple-stream transmissions and to achieve the mitigation of the inter-carrier interference, the inter-symbol interference as well as the multi-user interference.

The multi-channel nature of communications due to, e.g., the fact that MIMO and multi-carrier technologies have been incorporated, demands advanced and efficient ways of processing the resulting multi-dimensional data. For instance, the parameter estimation step that follows channel sounding [HTR04] is a multi-dimensional harmonic retrieval problem. There the channels are sampled in multiple dimensions with respect to time, frequency, polarization and space, resulting in multi-dimensional measurements based on which the parameters are estimated. In general, to estimate the frequencies of multi-dimensional harmonics that are sampled on a multi-dimensional lattice is referred to as multi-dimensional harmonic retrieval. In addition to MIMO channel sounding, it has been encountered in numerous application fields such as Direction-Of-Arrival (DOA) estimation in the context of array signal processing (e.g., using a Uniform Rectangular Array (URA)), MIMO radar [NS10], 2-D nuclear magnetic resonance spectroscopy [BL86], the initial ranging process for Orthogonal Frequency Division Multiple Access (OFDMA) uplink systems (used to identify multiple users as well as to estimate the corresponding timing and/or frequency offsets for the adjustment/alignment) [LM15], high-resolution localization of multiple frequency-hopped spread-spectrum signals in Code-Division Multiple Access (CDMA)-based systems [LSS02], discontinuous (or multiple) motion estimation in computer vision as well as in video communications [CGN98]. By representing multi-dimensional data in multi-way arrays and preserving the multi-dimensional structure inherent in the data, tensor-based signal processing techniques offer fundamental advantages compared to their matrix-based counterparts in terms of identifiability, uniqueness, etc.. The multilinear rank reduction contributes to more efficient denoising and a higher accuracy in, for example, subspace estimation or model order estimation [HRD08], [dCHRD07], [dCRHdS11].

Model order estimation schemes accomplish the essential first step of subspace-based estimation techniques which find applications in a great many scientific fields ranging from communications to imaging processing. In recent years, multi-dimensional extensions of matrix-based model order estimation methods including Akaike's Information Criterion (AIC), Minimum Description Length (MDL) [WK85], and the Exponential Fitting Test (EFT) [QBLH06], have been developed [dCHRD07], [dCRHdS11]. The superior performance of the resulting tensor-based algorithms,  $R$ -D AIC,  $R$ -D MDL, and  $R$ -D EFT, is evident. It has been observed that

when the measurement data are only corrupted by Gaussian noise, these  $R$ -D model order estimation schemes yield a satisfactory estimation accuracy. An evaluation of their performance in a more critical and practical scenario, e.g., where a fraction of the measurements are severely contaminated due to brief sensor failures, is compelling. Furthermore, it has not yet been revealed in the literature how to introduce robustness to tensor-based model order estimation approaches.

Given multi-dimensional signals, one can take advantage of their  $R$ -D structure by using tensors to store and manipulate these signals. Higher-Order Singular Value Decomposition (HOSVD)-based signal subspace estimates experience an enhanced accuracy and lead to an improved performance of the parameter estimation [HRD08]. The resulting gain was also shown analytically in [RBHW09], [RHD14]. In time-varying scenarios, it is then desirable to adaptively track the accordingly time-varying signal subspace. The pursuit of matrix-based subspace tracking schemes is hardly a new endeavor. It can be traced back to the 1970s [Ows78], and a number of algorithms have been devised ever since then targeting at a fast adaption, a good steady-state behavior as well as a low computational complexity [Oja82], [Yan95b], [AAM02], [BDR05]. The previous success in matrix-to-tensor extensions suggests the design of a generic framework for extending matrix-based subspace tracking schemes to the tensor case which leads to comparable performance gains while keeping the increase in complexity moderate.

### 1.2. Major contributions

Reviewing recent developments of signal processing techniques in several aspects of wireless communications inspires new innovations that show superiority over the state-of-the-art in terms of performance, flexibility, efficiency, robustness, extent of the applicability, etc.. Strongly motivated, the main objectives of this thesis are as follows:

- *Design enhanced spatial scheduling and precoding techniques for CP-OFDM-based multi-user MIMO downlink systems as well as up-to-date system-level performance evaluation tools*

The challenges posed on the multi-user MIMO downlink user scheduling due to the use of multi-carrier modulation schemes are evident. We propose a new spatial scheduling algorithm tailored in light of the multi-carrier nature of the system to achieve a high efficiency and a promising performance. As ubiquitous Wireless Local Area Network (WLAN) standards such as IEEE 802.11ac call for an enhanced flexibility in the multi-user MIMO downlink precoding, we devise linear precoding schemes that support an

equal MCS implementation on all spatial streams or that resolve the well-known dimensionality issue with many existing precoding algorithms yielding an improved efficiency. Moreover, we develop a system-level performance evaluation tool for CP-OFDM-based multi-user MIMO downlink systems with an effective and accurate link-to-system mapping mechanism that can be tuned to ensure the compatibility with a certain communication standard, e.g., IEEE 802.11ac.

- *Broaden and expand the road map for the development of transmit-receive processing in FBMC/OQAM-based MIMO systems*

As the merits of FBMC/OQAM become widely acknowledged and its applications encompass an ever-increasing number of fields, it is compelling to develop more mature and well-rounded signal processing techniques such that the fundamental advantages of FBMC/OQAM are thoroughly exploited. Thus, we design new transmit-receive processing schemes for both FBMC/OQAM-based single-user MIMO and multi-user MIMO downlink systems to alleviate the constraints in various aspects (e.g., dimensionality, frequency selectivity of the propagation channel) that are imposed on state-of-the-art algorithms. On the other hand, new areas and directions are explored. We exploit the non-circularity of the signals and introduce the benefits of widely linear processing to MIMO FBMC/OQAM systems. New progress is made for more sophisticated communication scenarios that are more prone to synchronization errors and would significantly benefit from the strong robustness of FBMC against time or frequency misalignments. More specifically, we propose a novel FBMC/OQAM-based CoMP technique that enables the joint transmission of adjacent cells to cell edge users and is very effective in combating the intra-cell interference, the inter-cell interference, as well as the intrinsic interference. Furthermore, we present extensive numerical results corroborating the theory that FBMC is more immune to synchronization errors and in turn strengthen the motivation of using FBMC.

- *Incorporate robustness into multi-dimensional model order estimation and find a solution to the adaptive subspace estimation in time-varying multi-dimensional harmonic retrieval problems*

The successful multi-dimensional extension of several matrix-based model order estimation methods on the one hand validates the benefits of using tensors to store and manipulate multi-dimensional data. On the other hand, it also sparks the interest in assessing the performance of tensor-based model order estimation schemes in critical scenarios where the measurement data suffer from some severe contamination. In addition to such

a performance evaluation, we develop robustified versions of the tensor-based model order estimation algorithms. Moreover, in time-varying multi-dimensional harmonic retrieval problems, it is desired that the subspace estimation is performed in an adaptive manner and feeds tensor-based signal subspace estimates to the subsequent parameter estimation steps. In this regard, we pursue a generic multi-dimensional extension of matrix-based subspace tracking schemes that leads to tensor gains.

Based on the communications contexts that are dealt with, we divided this thesis into two parts with Part I focusing on multi-carrier single-user as well as multi-user MIMO systems and Part II on multi-dimensional harmonic retrieval problems. The main contributions and the outline of this thesis are briefly highlighted in the following.

The first part of the thesis focuses on transmit and receive processing in multi-carrier MIMO systems. Two multi-carrier modulation schemes are considered, CP-OFDM which is widely used for high-data rate transmissions in mobile communication systems nowadays, and FBMC that has received great research attention recently due to its well-concentrated spectrum. We present the challenges in the design of suitable transmit-receive strategies for multi-carrier MIMO settings and thereafter discuss how these problems have been tackled.

Chapter 2 is devoted to scheduling and precoding for CP-OFDM-based multi-user MIMO downlink systems with SDMA. A new transmission strategy that consists of a spatial scheduling algorithm and two precoding algorithms is presented. The scheduling algorithm, called efficient multi-carrier ProSched (EMC-ProSched), adopts a novel and effective scheduling metric for each user and can efficiently search for a suitable group of users to be served at the same time on the same frequency. To handle different antenna configurations, two precoding techniques are designed. For the case where the number of transmit antennas at the base station is not smaller than the total number of receive antennas at the user terminals, the linear precoding-based geometric mean decomposition (LP-GMD) algorithm is proposed. It suppresses the multi-user interference and enables an effective implementation of the same MCS on all spatial streams of each user. Consequently a smaller signaling overhead is required compared to the case where a different MCS is applied on each spatial stream. When the total number of receive antennas at the user terminals exceeds the number of transmit antennas at the base station, we propose the low complexity coordinated beamforming (LoCCoBF) algorithm to accomplish the goal of the multi-user interference mitigation and to achieve a high capacity. By exploiting the correlation of the channels of neighboring subcarriers, the LoCCoBF algorithm experiences an enhanced efficiency. This coordinated beamforming concept has also inspired the design of transmit-receive strategies for FBMC/OQAM-based MIMO systems in Chapters 5 and 6. A system-level simulator with a link-to-system interface is further developed. It can be tuned

to fit into the framework of the IEEE 802.11ac standard to evaluate the performance of the proposed transmission strategy. Numerical simulations indicate that a promising performance can be achieved by employing the proposed transmission strategy. The results mentioned above have been published in [CLZ<sup>+</sup>12], [LCZ<sup>+</sup>12], [CLZ<sup>+</sup>14], and have been released as patents [DCL<sup>+</sup>c], [DCL<sup>+</sup>a], [DCL<sup>+</sup>b].

Chapter 3 presents basics of FBMC which is the multi-carrier modulation scheme considered in the remaining chapters of Part I of this thesis. We start with an overview of appealing features of FBMC that give rise to its applications in various fields. Then, fundamentals of FBMC/OQAM from the point of view of signal processing are provided by presenting the data model of an FBMC/OQAM-based Single-Input Single-Output (SISO) system. To further pave the way for the subsequent chapters, we address challenges in the design of transmit-receive processing schemes for FBMC/OQAM-based MIMO systems. It is also pointed out that the frequency selectivity of the propagation channel plays an important part.

Hence, in the following chapters of Part I, we first start with the case of low frequency selective channels in Chapter 4 and investigate the use of widely linear processing in point-to-point MIMO FBMC/OQAM systems. Due to the fact that the data in FBMC/OQAM-based systems show non-circularity, exploiting widely linear processing potentially provides a gain over linear processing. The concept of a two-step receiver combining linear processing and widely linear processing is presented in Chapter 4. In the first step we cancel the intrinsic interference that prevents us from exploiting the benefits of widely linear processing. Two ways of estimating the interference components are developed and compared. In the second step, a widely linear MMSE receiver is employed taking into account the residual interference. A significant gain over the linear processing-based receiver is demonstrated via numerical simulations. These results have been published in [CPN13b].

Chapter 5 is also dedicated to point-to-point FBMC/OQAM-based MIMO systems. In contrast to Chapter 4, we consider the case of intermediate frequency selective channels. The limit imposed on the two-step receiver with regard to the frequency selectivity of the propagation channel is therefore relaxed. Consequently, it is only required that the channel on each sub-carrier can be treated as flat fading. The CSIT is exploited for the mitigation of the intrinsic interference residing in FBMC/OQAM-based systems. To enable reliable transmissions when the number of transmit antennas does not exceed the number of receive antennas, we first present a joint and iterative procedure to calculate the precoding matrix and the decoding matrix for each subcarrier. Such results have laid the basis for the design of the intrinsic interference mitigating coordinated beamforming (IIM-CBF) schemes in FBMC/OQAM-based multi-user MIMO downlink systems as a focus of Chapter 6. Aiming at a more effective mitiga-

tion of the intrinsic interference, in this chapter we further introduce an enhanced version of the coordinated beamforming scheme, where a Signal-to-Leakage-plus-Noise-Ratio (SLNR)-based metric is used to compute the precoding matrices. Simulation results show that the proposed algorithms outperform the existing transmission strategies for MIMO FBMC/OQAM systems. It is also observed that in addition to featuring a well-localized spectrum and a higher spectral efficiency, by employing the proposed coordinated beamforming schemes, the MIMO FBMC/OQAM system achieves a similar Bit Error Rate (BER) performance as its CP-OFDM-based counterpart. These results have been published in [CLH14b], [CPNCH15].

In Chapter 6 we take it one step further to discuss the design of transmission strategies for the downlink of FBMC/OQAM-based multi-user MIMO systems (as an FBMC/OQAM-based counterpart of the multi-user MIMO downlink setting considered in Chapter 2) and CoMP systems. Our goal is to alleviate the dimensionality constraint imposed on the state-of-the-art solutions for FBMC/OQAM-based Space-Division Multiple Access (SDMA) that the total number of receive antennas of the users must not exceed the number of transmit antennas at the base station. First, a single-cell multi-user MIMO downlink system is considered, and two IIM-CBF algorithms are proposed for the case where the number of transmit antennas at the base station is equal to the total number of receive antennas of the users and the case where the former is smaller than the latter, respectively. The central idea is to jointly and iteratively calculate the precoding matrix and the decoding matrix for each subcarrier to mitigate the multi-user interference as well as the intrinsic interference inherent in FBMC/OQAM-based systems. Second, for a CoMP downlink scenario where partial coordination among the base stations is considered, the application of the coordinated beamforming concept is further investigated. An appropriate IIM-CBF technique is proposed. Simulation results show that that by employing the proposed IIM-CBF schemes, the FBMC/OQAM systems achieve a similar BER performance as its CP-OFDM-based counterpart with the LoCCoBF algorithm presented in Chapter 2 while exhibiting superiority in terms of a higher spectral efficiency, a greater robustness against synchronization errors, and a lower out-of-band radiation. In the presence of residual carrier frequency offsets, the superiority of the FBMC/OQAM systems over the CP-OFDM based systems is demonstrated, which corroborates the theoretical analysis that the FBMC/OQAM systems are more immune to the lack of perfect synchronization. In addition, numerical results with respect to the convergence behavior of the proposed IIM-CBF techniques are presented, and the computational complexity issue is also addressed. The aforementioned results have been published in [CLH14b], [CLH14a], [CLH14d].

Chapter 7 focuses on the case of highly frequency selective channels and presents novel SDMA solutions to FBMC/OQAM-based multi-user MIMO downlink systems. As reviewed

in the previous chapter, Chapter 6, most of the state-of-the-art solutions for FBMC/OQAM-based multi-user downlink settings have been developed assuming that the channel on each subcarrier can be treated as flat fading. The IIM-CBF schemes presented in Chapter 6 have the advantage of alleviating the dimensionality constraint such that the number of receive antennas is not restricted. Following this contribution, in this chapter we turn to the more challenging case of highly frequency selective propagation channels. First, to overcome the limits on the number of receive antennas per user terminal that are imposed on the existing solutions, we present two approaches for FBMC/OQAM-based multi-user MIMO downlink settings where a single data stream is sent to each user. The first design of precoders and equalizers is iterative and Minimum Mean Squared Error (MMSE)-based. The second is a closed-form design based on the maximization of the Signal-to-Leakage-Ratio (SLR). Then we provide solutions for per-user multi-stream transmissions in FBMC/OQAM-based multi-user MIMO downlink systems under highly frequency selective propagation conditions. An SLNR-based metric is proposed, and it is tailored for the downlink of FBMC/OQAM-based multi-user MIMO settings. At the base station, per-subcarrier fractionally spaced multi-tap precoders are computed based on this metric to mitigate the multi-user interference, the inter-symbol interference, as well as the inter-carrier interference and to map the multiple data streams for each user to the transmit antennas. With the base station carrying most of the computational load, each user terminal only employs a Zero Forcing (ZF)-based one-tap spatial equalizer to recover the desired streams. Numerical simulations show that the proposed schemes achieve satisfactory performances in various multi-user MIMO downlink scenarios with highly frequency selective channels. They significantly outperform the existing algorithms that require the channel on each subcarrier to be flat fading. The aforementioned results have been published in [CBHN15a] and [CBHN15b].

Part II of this thesis is dedicated to novel and advanced multi-dimensional signal processing techniques in the context of multi-dimensional harmonic retrieval. The compelling demand of statistically robust tensor-based model order estimation schemes and tensor-based subspace tracking methods for time-varying scenarios is addressed. Then we present new progress towards fulfilling such a demand.

Model order estimation is a long standing topic in the field of signal processing. In recent years, the prosperous development of tensor-based signal processing has sparked great research attention on multi-dimensional model order estimation. By preserving and exploiting the multi-dimensional nature of the data, multi-dimensional model order estimation schemes exhibit performance superiority over their conventional matrix-based counterparts. Nevertheless, approaches that have been devised assuming a Gaussian noise distribution are very

sensitive to brief sensor failures that cause contamination to the measurement data. We address this issue in Chapter 8 and present designs of robust multi-dimensional model order estimation schemes that show strong resilience against brief sensor failures. First, robust versions of  $R$ -D Akaike’s Information Criterion (AIC),  $R$ -D Minimum Description Length (MDL), and the  $R$ -D Exponential Fitting Test (EFT) are developed, where the robust MM-estimates of the covariance matrices of the unfoldings of the multi-dimensional data are used. Moreover, forward-backward averaging is incorporated into the construction of a real-valued measurement tensor, leading to a further enhancement of the robust multi-dimensional model order estimation schemes. The unfoldings of the real-valued data tensor are used as the input of the robust covariance estimator instead of stacking the real and imaginary parts of the unfoldings of the original complex-valued measurement tensor. Such enhanced versions of robust  $R$ -D AIC, robust  $R$ -D MDL, and robust  $R$ -D EFT experience an improved performance and a reduced computational complexity. Numerical simulations are performed to demonstrate the promising performances of these tensor-based robust model order selection techniques in the presence of brief sensor failures. The aforementioned results have been published in [MCR<sup>+</sup>12] and [CH13a].

Chapter 9 presents a generic framework for Tensor-based subspace Tracking via Kronecker-structured projections (TeTraKron). TeTraKron allows to extend arbitrary matrix-based subspace tracking schemes to track the tensor-based subspace estimate. The latter can be computed via a structured projection applied to the matrix-based subspace estimate which enforces the multi-dimensional structure in a computationally efficient fashion. This projection is tracked by considering all matrix rearrangements of the signal tensor jointly, which can be efficiently realized via parallel processing. In addition, we incorporate forward-backward-averaging and find a similar link between the real-valued matrix-based and tensor-based subspace estimation. This enables the tracking of the real-valued tensor-based subspace estimate via a similar Kronecker-structured projection applied to the real-valued matrix-based subspace estimate. In time-varying multi-dimensional harmonic retrieval problems, the TeTraKron-based subspace tracking schemes outperform the original matrix-based subspace tracking algorithms as well as the batch solutions provided by the SVD and the HOSVD as benchmarks. Moreover, incorporating forward-backward-averaging leads to an improved accuracy of the subspace tracking, and only real-valued processing is involved. Furthermore, we evaluate the performances of ESPRIT-type parameter estimation schemes where the subspace estimates obtained by the proposed TeTraKron-based subspace tracking algorithms are used for the tracking of spatial frequencies in time-varying scenarios. The aforementioned results have been published in [RKCH13] and [CRKH14].



## 1.3. Notation

To facilitate the distinction between scalars, vectors, matrices, and tensors, the following notation is used throughout the thesis: scalars are represented by italic letters, vectors by lower-case bold-faced letters, matrices by upper-case bold-faced letters, and tensors as bold-faced calligraphic letters. We use the superscripts  $\text{T}$ ,  $\text{H}$ ,  $^{-1}$ , and  $^*$  for transpose, Hermitian transpose, matrix inversion, and complex conjugate, respectively. An  $M \times M$  identity matrix is symbolized by  $\mathbf{I}_M$ . A matrix denoted by  $\mathbf{I}_{M \times d}$  ( $M > d$ ) has the form  $\mathbf{I}_{M \times d} = \begin{bmatrix} \mathbf{I}_d & \mathbf{0}_{d \times (M-d)} \end{bmatrix}^{\text{T}}$ . The trace and Frobenius norm of a matrix are denoted by  $\text{Tr}\{\cdot\}$  and  $\|\cdot\|_{\text{F}}$ , respectively, whereas the absolute value is represented by  $|\cdot|$ . The two-norm of a vector is denoted by  $\|\cdot\|$ . The operator  $\text{blkdiag}\{\cdot\}$  creates a block-diagonal concatenation of its input matrices. Moreover,  $\text{Re}\{\cdot\}$  symbolizes the real part of the input argument, while  $\text{Im}\{\cdot\}$  represents the imaginary part. The discrete convolution is symbolized by  $*$ . For a matrix  $\mathbf{A}$ ,  $\mathbf{A}(m, n)$  denotes its  $(m, n)$ -th entry. The Kronecker product is represented via  $\otimes$  and the Khatri-Rao (columnwise Kronecker) product via  $\diamond$ . The operator  $\text{Tri}\{\cdot\}$  calculates the upper/lower triangular part of its argument and copies its Hermitian transpose to the other lower/upper triangular part [Yan95b]. Moreover,  $\text{off}(\cdot)$  indicates an operation of keeping all off-diagonal elements of its input matrix while setting its diagonal elements to zero. We use  $\mathcal{P}\{\cdot\}$  to represent the operator of computing the principal eigenvector of a matrix which corresponds to the maximal eigenvalue. The Big O notation  $\mathcal{O}\{\cdot\}$  that is frequently used in complexity theory describes the asymptotic behavior of a function, i.e., it indicates how fast a function grows or declines. For instance, given a function  $f(n) = 3n^2 + 2n + 5$  (which could present the computation time, the number of steps, or the number of multiplications, etc., that are required in a certain algorithm), to describe its growth rate as  $n$  approaches infinity, one can say that  $f(n)$  grows at the order of  $n^2$  and write  $f(n) = \mathcal{O}\{n^2\}$ .

An  $R$ -way tensor with size  $I_r$  along mode  $r = 1, 2, \dots, R$  is represented as  $\mathcal{A} \in \mathbb{C}^{I_1 \times I_2 \times \dots \times I_R}$ . We use  $\mathcal{A}(i_1, i_2, \dots, i_R)$  to denote its  $(i_1, i_2, \dots, i_R)$ -th element. The  $r$ -mode vectors of  $\mathcal{A}$  are obtained by varying the  $r$ -th index from 1 to  $I_r$  and keeping all other indices fixed. Aligning all  $r$ -mode vectors as the columns of a matrix yields the  $r$ -mode unfolding of  $\mathcal{A}$  which is denoted by  $[\mathcal{A}]_{(r)} \in \mathbb{C}^{I_r \times I_{r+1} \times \dots \times I_R \times I_1 \times \dots \times I_{r-1}}$ . The order of the columns is arbitrary as long as it is chosen consistently. Throughout this thesis, the reverse cyclical ordering, as proposed in [dLdMV00], is used. In this rule for the ordering, we start with varying the  $(r-1)$ -th index, keep decreasing to the first index, continue with the  $R$ -th index, and proceed backwards until reaching the  $(r+1)$ -th index. The  $r$ -mode product between a tensor  $\mathcal{A}$  and a matrix  $\mathbf{U}$  is written as  $\mathcal{A} \times_r \mathbf{U}$ . It is computed by multiplying all  $r$ -mode vectors of  $\mathcal{A}$  with  $\mathbf{U}$ . In other

words,  $[\mathcal{A} \times_r \mathbf{U}]_{(r)} = \mathbf{U} \cdot [\mathcal{A}]_{(r)}$ . The  $r$ -rank of a tensor  $\mathcal{A}$  is the rank of the  $r$ -mode unfolding matrix  $[\mathcal{A}]_{(r)}$ . The tensor  $\mathcal{I}_{R,d}$  is an  $R$ -dimensional identity tensor of size  $d \times d \times \dots \times d$ , which is equal to one if all  $R$  indices are equal and zero otherwise. In addition,  $[\mathcal{A} \sqcup_r \mathcal{B}]$  symbolizes the concatenation of two tensors  $\mathcal{A}$  and  $\mathcal{B}$  along the  $r$ -th mode [HRD08].

A list of symbols and notation used in this thesis is provided in Appendix A.2. In addition, we summarize the frequently used notation of each chapter in Appendix A.3.

## **Part I.**

**Transmit-receive strategies for multi-carrier  
single-user and multi-user MIMO systems**

This part of the thesis is devoted to transmit and receive processing in multi-carrier Multiple-Input Multiple-Output (MIMO) systems. We consider two multi-carrier modulation schemes, the widely used Orthogonal Frequency Division Multiplexing with the Cyclic Prefix insertion (CP-OFDM) and Filter Bank-based Multi-Carrier modulation (FBMC) that has attracted great research attention recently due to its well-concentrated spectrum. We address the challenges in the design of suitable transmit-receive strategies for multi-carrier MIMO settings and thereafter discuss how these problems have been tackled.

Chapter 2 presents an efficient and flexible transmission strategy for CP-OFDM-based multi-user MIMO downlink systems. It consists of a scheduling stage and a precoding stage to select a suitable Space-Division Multiple Access (SDMA) user group and to mitigate the Multi-User Interference (MUI). One spatial scheduling scheme and two linear precoding algorithms are developed targeting at an enhanced performance as well as improved efficiency and flexibility.

Chapter 3 provides a thorough overview of FBMC which is the multi-carrier modulation scheme considered in the remainder of this part of the thesis. It is pointed out that the frequency selectivity of the propagation channel plays an important role in the design of transmit-receive processing schemes for Filter Bank-based Multi-Carrier with Offset Quadrature Amplitude Modulation (FBMC/OQAM)-based MIMO systems. Hence, in the following chapters, we start with the case of low frequency selective channels in Chapter 4. The concept of a two-step receiver combining linear processing and widely linear processing is proposed for point-to-point FBMC/OQAM-based MIMO systems. Chapter 5 focuses on single-user MIMO settings as well and presents two coordinated beamforming schemes, where the Channel State Information at the Transmitter (CSIT) is exploited. The channel on each subcarrier is assumed to be flat fading, categorized as the case of intermediate frequency selective channels. It is demonstrated that the proposed coordinated beamforming algorithms are effective in mitigating the intrinsic interference in FBMC/OQAM-based MIMO systems where the number of transmit antennas does not exceed the number of receive antennas and the state-of-the-art fails to provide a satisfactory performance.

In Chapter 6 we discuss the design of transmit-receive strategies for FBMC/OQAM-based multi-user MIMO downlink systems and Coordinated Multi-Point downlink (CoMP) systems. Three intrinsic interference mitigating coordinated beamforming (IIM-CBF) schemes are developed. Consequently, we are able to alleviate the dimensionality constraint imposed on the existing solutions for FBMC/OQAM-based multi-user MIMO downlink settings that the total number of receive antennas of the users must not exceed the number of transmit antennas at the base station. In addition, a novel FBMC/OQAM-based CoMP concept is established for the first time. In the presence of residual carrier frequency offsets, the superiority of

the FBMC/OQAM-based systems over the CP-OFDM-based systems is also demonstrated. Finally, FBMC/OQAM-based multi-user MIMO downlink systems with highly frequency selective channels are covered in Chapter 7. We devise multi-tap precoders at the base station and simple single-tap spatial receive filters at the user terminals to achieve the suppression of the MUI, the Inter-Symbol Interference (ISI), and the Inter-Carrier Interference (ICI). In contrast to the state-of-the-art schemes, multiple receive antennas at each user terminal are supported, and per-user multi-stream transmissions are enabled as well.

## 2. Efficient scheduling and precoding for the CP-OFDM-based multi-user MIMO downlink

In this chapter, a new transmission strategy that consists of a spatial scheduling algorithm and two precoding algorithms is presented for Orthogonal Frequency Division Multiplexing (OFDM)-based multi-user Multiple-Input Multiple-Output (MIMO) systems. The scheduling algorithm, called efficient multi-carrier ProSched (EMC-ProSched), adopts a novel and effective scheduling metric for each user and can efficiently search for a suitable group of users to be served at the same time on the same frequency. Two precoding techniques are then designed to handle different antenna configurations. For the case where the number of transmit antennas at the Base Station (BS) is not smaller than the total number of receive antennas at the user terminals, the linear precoding-based geometric mean decomposition (LP-GMD) algorithm is proposed. It suppresses the Multi-User Interference (MUI) and enables an effective implementation of the same Modulation and Coding Scheme (MCS) on all spatial streams of each user. Consequently a smaller signaling overhead is required compared to the case where a different MCS is applied on each spatial stream. When the total number of receive antennas at the user terminals exceeds the number of transmit antennas at the BS, we propose the low complexity coordinated beamforming (LoCCoBF) algorithm to accomplish the goal of the MUI mitigation and to achieve a high capacity. This coordinated beamforming concept has also inspired the design of transmit-receive strategies for Filter Bank-based Multi-Carrier modulation (FBMC)-based MIMO systems in Chapters 5 and 6. A system-level simulator with a link-to-system interface is further developed under the framework of the IEEE 802.11ac standard to evaluate the performance of the proposed transmission strategy. Numerical simulations indicate that a promising performance can be achieved by employing the proposed transmission strategy. The results mentioned above have been published in [CLZ<sup>+</sup>12], [LCZ<sup>+</sup>12], [CLZ<sup>+</sup>14], and have been released as patents [DCL<sup>+</sup>c], [DCL<sup>+</sup>a], [DCL<sup>+</sup>b].

### 2.1. Introduction

Multi-user Multiple-Input Multiple-Output (MIMO) systems have the potential of combining the high capacity achievable by MIMO processing with the benefits of Space-Division Multiple Access (SDMA) [Tel99b], [SPSH04]. Constrained by the processing ability and the Quality of Service (QoS) requirement of standards, only a limited number of users can be served

simultaneously. Hence, for the downlink of a multi-user MIMO system (cf. Figure 2.2) with a large number of users, spatial scheduling algorithms can be employed to select a suitable SDMA user group to be served simultaneously, and precoding algorithms can then be used to mitigate the Multi-User Interference (MUI) [SSH04], [SH08], [RFH08], [SCA<sup>+</sup>05], [FDH07].

The main task of spatial scheduling algorithms is to separate users with a high spatial correlation into different SDMA groups. In [PKP11], a scheduling algorithm is proposed where the beamforming vectors are generated with a common codebook shared by the Base Station (BS) and the user terminals. However, such a codebook is not available for some systems constructed under the framework of certain standards such as the IEEE 802.11ac [WG813]. In the scheduling algorithm developed in [LTSL10], precoding matrices for each possible user group are required to be pre-calculated which leads to an unaffordable computational complexity. In [FDH07], the ProSched scheme which can avoid the pre-calculation of the precoding matrices by using a capacity related scheduling metric, is initially developed for one subcarrier. In a multi-carrier system, ProSched has been proposed to treat each subcarrier as a virtual user. However, it suffers from a high complexity and a large signaling overhead.

After determining the user group to be served, linear precoding algorithms such as Block Diagonalization (BD) [SSH04] and Regularized Block Diagonalization (RBD) [SH08], [SHGJ06] can be used to suppress the MUI and tune the performance of each equivalent single-user transmission. It is known that the Singular Value Decomposition (SVD) can be used to decompose a single-user MIMO channel into multiple parallel subchannels to transmit multiple data streams. The water filling algorithm can be employed to assign the transmit power of each subchannel to achieve the channel capacity [PNG03]. It should be noted that these subchannels will have very different Signal-to-Noise-Ratios (SNRs) [LHJ05]. In order to achieve the channel capacity, different Modulation and Coding Schemes (MCSs) should be used in different subchannels. In practice, unequal MCSs across subchannels of each user will introduce a large signaling overhead. However, if the same MCS is used on all the subchannels, the Packet Error Rate (PER) performance will be dominated by the weakest subchannel. Therefore, in order to enable the implementation of the same MCS across all the subchannels and fully utilize the transmit power, in [LHJ05] and [LJH05], the Geometric Mean Decomposition (GMD) technique has been employed for single-user systems to decompose the MIMO channel into multiple subchannels with identical SNRs. The GMD of a matrix  $\mathbf{H} \in \mathbb{C}^{m \times n}$  with rank  $r$  is expressed as  $\mathbf{H} = \mathbf{Q}\mathbf{R}\mathbf{Z}^H$ , where  $\mathbf{R} \in \mathbb{R}^{r \times r}$  represents a real-valued upper triangular matrix with diagonal elements all equal to the geometric mean of the positive singular values of  $\mathbf{H}$ . The matrices  $\mathbf{Q}$  and  $\mathbf{Z}$  have orthonormal columns [LHJ05]. In addition to its aforementioned application in point-to-point MIMO systems, GMD is also employed in the design of precoders

for inter-symbol interference suppression [ZKMW02] and for the generation of test matrices with prescribed singular values [KS00]. In [LHL08], BD-GMD has been proposed to recursively decompose the multi-user MIMO channel such that the subchannels for each user have identical SNRs. However, the recursive procedure for the decomposition leads to a high computational complexity. In addition, BD-GMD is only a decomposition algorithm, and it has to be combined with some precoding technique, such as Tomlinson-Harashima precoding (THP) [LHL08].

It is known that many linear precoding algorithms require that the number of transmit antennas at the BS is not smaller than the total number of receive antennas at the user terminals [SSH04]. In multi-user MIMO systems where the total number of users to be served is large and each user is equipped with multiple antennas, this antenna constraint becomes a bottle-neck of the precoding techniques. Although some existing algorithms such as RBD [SH08], can relax this antenna constraint, its performance degrades heavily with an increasing aggregated number of receive antennas at the user terminals [SRH10b]. The concept of coordinated beamforming was introduced in [SSH04] to overcome this antenna constraint by initializing the receive beamforming matrix for each user using the dominant left singular vectors of the channel matrix from the BS to this user. The transmit beamforming matrices are then calculated using the resulting equivalent multi-user channel matrix. Since this scheme has only two steps (no iterative computations required), it has a low complexity, however, at the price of a degradation in the performance. The coordinated beamforming algorithm proposed in [CMIH08] jointly and iteratively optimizes the transmit and receive beamforming matrices. It achieves a good sum rate performance but suffers from a high complexity. In addition, this algorithm allows only one spatial stream transmitted to each user. In [SRH10b], the flexible coordinated beamforming (FlexCoBF) algorithm is developed to iteratively calculate beamforming matrices for a subcarrier when the antenna constraint is not fulfilled. Although FlexCoBF allows transmitting multiple spatial streams to each user, it requires a large number of iterations. A closed-form expression for the coordinated beamforming was proposed in [CMJH08]. However, it can only be applied for a system where the base station is equipped with two transmit antennas and the number of users is two. Further in [YSRH12], it is shown that the coordinated beamforming task for the multi-user MIMO downlink can be transformed into a “sequentially drilled” joint congruence (SeDJoCo) problem. The resulting SeDJoCo-based coordinated beamforming scheme computes the transmit-receive beamformers directly for an arbitrary number of transmit antennas and is regarded as a closed-form approach. For both these methods, the number of data streams transmitted to each user is restricted to one.

Although a variety of scheduling and precoding algorithms has been proposed in the lit-



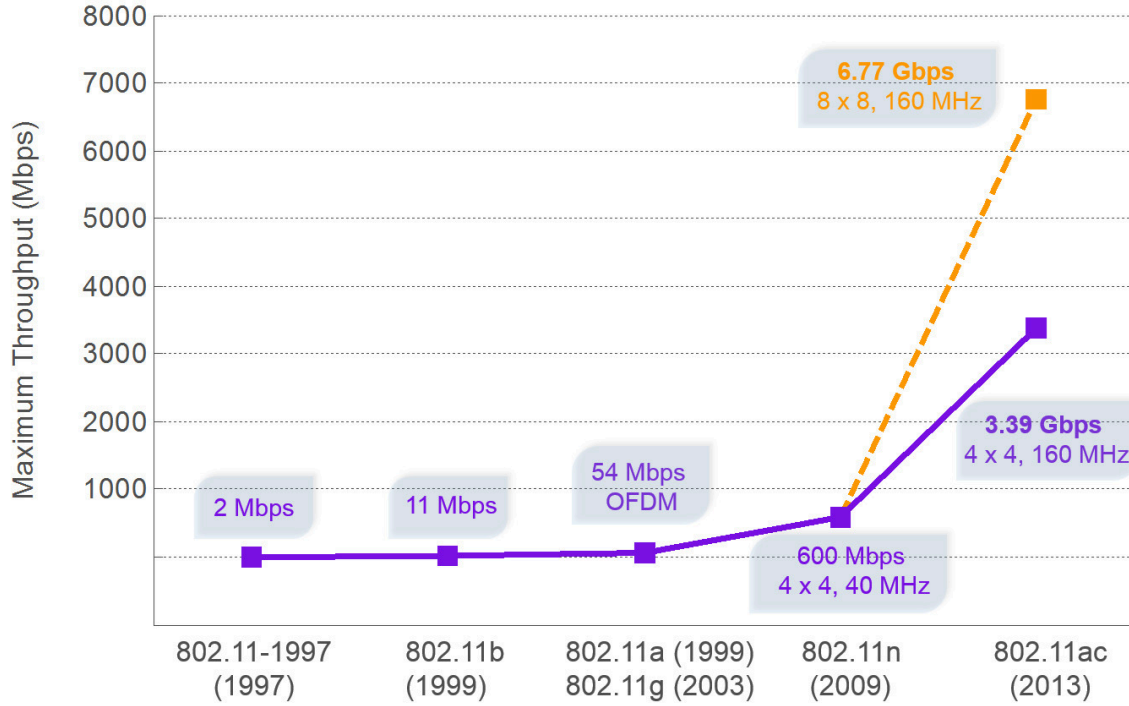


Figure 2.1.: Maximum achievable throughput of the IEEE 802.11 standards family (the years in the x-axis labels indicate when the standards were published)

erature as reviewed above, it is hardly addressed if such schemes can be suitably applied in multi-user MIMO downlink systems compatible with a certain communications standard. In fact, the benefits of the multi-user MIMO downlink with SDMA have attracted great attention of the IEEE 802 LAN/MAN Standards Committee. Published in December 2013, IEEE 802.11ac [WG813] is an amendment to the IEEE 802.11 specification for Wireless Local Area Networks (WLANs). It builds upon IEEE 802.11n [WG809], operates in the 5 GHz band, and targets primarily a significant increase of data rates required for, e.g., high-definition video and mobile voice applications. Figure 2.1 illustrates the throughput improvement along the development of the IEEE 802.11 standards family for WLAN. OFDM was first deployed in IEEE 802.11a, whereas the support of multi-stream transmissions (up to four spatial streams) was first introduced in IEEE 802.11n. In addition to the support of wider channel bandwidths, an increased number of spatial streams (up to eight spatial streams), and higher-order modulation, a very important enhancement of IEEE 802.11ac is the addition of multi-user MIMO.

These features of IEEE 802.11ac lead to a remarkable increase of the maximum achievable throughput which is evident in Figure 2.1. Since technical proposals for IEEE 802.11ac were started to be considered in November 2008, draft specifications have motivated the design of new compatible transmit-receive processing schemes for multi-user MIMO downlink systems. On the other hand, the development of system-level performance evaluation tools in the context of IEEE 802.11ac is also intriguing.

In the sequel, we present a new framework of an efficient and flexible transmission strategy that accomplishes the tasks of spatial scheduling and precoding for multi-carrier multi-user MIMO downlink systems with the IEEE 802.11ac specifications taken into account [CLZ<sup>+</sup>14]. Our major focus is on a scenario where the total number of users is much larger than the maximum number of users that can be served at the same time and on the same frequency without any constraint on antenna configurations. The proposed transmission strategy consists of a scheduling stage and a precoding stage. In the scheduling stage, the efficient multi-carrier ProSched (EMC-ProSched) algorithm determines the most suitable user group using an efficient tree-based sorting algorithm and a novel and effective scheduling metric inspired by the philosophy of the link-to-system mapping with well-calibrated parameters. A comparison in terms of the computational complexity is made between the proposed EMC-ProSched and the ProSched [FDH07] which treats each subcarrier of each user as a virtual user. In the precoding stage, we distinguish two cases:

- **Case 1:** the total number of receive antennas of the user terminals *does not exceed* the number of transmit antennas at the BS
- **Case 2:** the total number of receive antennas of the user terminals *exceeds* the number of transmit antennas at the BS

Then, for **Case 1**, the linear precoding-based geometric mean decomposition (LP-GMD) algorithm is proposed to suppress the MUI at the BS and decompose each equivalent single-user MIMO channel into multiple parallel sub-channels that have the same Signal-to-Interference-plus-Noise-Ratio (SINR). Consequently, the implementation of the same MCS is enabled on different spatial streams of each user. This scheme is especially suitable for IEEE 802.11ac systems where equal MCS across the subchannels of each user is required [WG813]. In addition, a Minimum Mean Squared Error (MMSE) power loading strategy is designed to enable a better power balancing between different users and further improve the system performance. It is then elaborated how the decoding matrices can be obtained at the user terminals. The concept of LP-GMD has been picked up in [PRPF15], and the advantages of LP-GMD are thus corroborated. For **Case 2**, the low complexity coordinated beamforming (LoCCoBF)

algorithm is developed to jointly and iteratively optimize the transmit and receive beamformers. By exploiting the correlation of the channels of neighboring subcarriers, the LoCCoBF algorithm has an enhanced efficiency. Chapters 5 and 6 of this thesis suggest that there also exist some dimensionality constraints on state-of-the-art MIMO techniques for Filter Bank-based Multi-Carrier modulation (FBMC)-based MIMO systems. The investigations leading to LoCCoBF have paved the way for the design of transmit-receive processing schemes presented in Chapters 5 and 6 that are able to overcome these dimensionality limits. Moreover, the construction of the link-to-system interface in the system-level simulator under the framework of the IEEE 802.11ac is described in detail. The importance of employing the MMSE-based power loading in practice is pointed out. Furthermore, a detailed complexity analysis of the proposed algorithms is carried out, and a thorough evaluation of the proposed algorithms is performed via simulations.

In this chapter, we start with a brief introduction of the system model of CP-OFDM-based multi-user MIMO downlink settings in Section 2.2. Then, the proposed EMC-ProSched algorithm is detailed in Section 2.3. In Section 2.4, the LP-GMD algorithm is described for **Case 1** with the focus on two versions, LP-GMD-BD and LP-GMD-RBD. Section 2.5 presents the LoCCoBF scheme that is designed for **Case 2**. In order to examine the proposed transmission strategy in an efficient and flexible manner, a system-level simulator with a link-to-system interface is designed for the IEEE 802.11ac standard, as described in Section 2.6. The benefits of the proposed transmission strategy are demonstrated through numerical simulations in Section 2.7. Finally, the conclusions are drawn in Section 2.8.

## 2.2. CP-OFDM-based multi-user MIMO downlink system model

We consider the downlink of a multi-user MIMO system with one BS equipped with  $M_T$  transmit antennas and  $N$  user terminals. A scheduling algorithm is first employed to select  $K$  users out of  $N$  users and assign them to one SDMA group, i.e., these  $K$  users are served at the same time and on the same frequency. We set the indices of the selected users as  $i = 1, 2, \dots, K$  for the following introduction of the precoding process. The number of receive antennas of each user is then denoted by  $M_{R_i}$ , and the total number of receive antennas for one SDMA group is  $M_R = \sum_{i=1}^K M_{R_i}$ . Figure 2.2 illustrates such a multi-user MIMO downlink setting. Assuming perfect synchronization, the channel is modeled as a perfectly tuned Orthogonal Frequency Division Multiplexing (OFDM) channel without any inter-carrier interference. The number of data subcarriers is denoted by  $N_{SD}$  as in IEEE 802.11ac [WG813]. It is worth noting that all the  $N_{SD}$  subcarriers are utilized for the transmissions of data to each of the selected  $K$

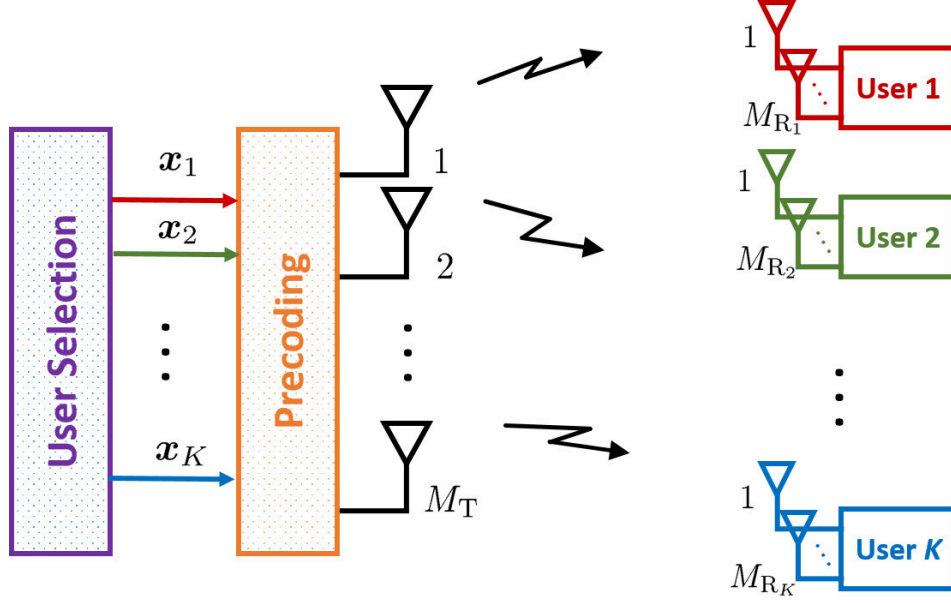


Figure 2.2.: Illustration of the multi-user MIMO downlink

users. In other words, the BS transmits to all the  $K$  users on each of the  $N_{\text{SD}}$  subcarriers simultaneously, i.e., the selected  $K$  users are solely spatially multiplexed. At a certain time instant, the channel between the BS and the  $i$ -th user on a certain subcarrier<sup>1</sup> is denoted by  $\mathbf{H}_i \in \mathbb{C}^{M_{R_i} \times M_T}$ . The joint channel matrix is given by

$$\mathbf{H} = \begin{bmatrix} \mathbf{H}_1^T & \mathbf{H}_2^T & \dots & \mathbf{H}_K^T \end{bmatrix}^T \in \mathbb{C}^{M_R \times M_T}. \quad (2.1)$$

In this chapter, perfect Channel State Information at the Transmitter (CSIT) is always assumed. The transmitted signal for the  $i$ -th user is defined as a  $d_i$ -dimensional vector  $\mathbf{x}_i$ . These vectors are stacked into the vector  $\mathbf{x} = [\mathbf{x}_1^T, \mathbf{x}_2^T, \dots, \mathbf{x}_K^T]^T \in \mathbb{C}^{d \times 1}$  with  $d = \sum_{i=1}^K d_i$ , where  $d \leq M_T$  and  $d_i \leq M_{R_i}$  for  $i = 1, 2, \dots, K$ . For the  $i$ -th user, a precoding matrix  $\mathbf{F}_i \in \mathbb{C}^{M_T \times d_i}$  is calculated

<sup>1</sup>Note that the precoding is performed on a subcarrier basis. The index of subcarriers is then ignored in the notation of the channel matrices when describing the precoding algorithms. To detail the proposed scheduling technique in Section 2.3 dedicated to such a multi-carrier system, the subcarrier indices of the channel matrices are included.

at the BS, and the joint precoding matrix can be expressed as

$$\mathbf{F} = \begin{bmatrix} \mathbf{F}_1, & \mathbf{F}_2, & \dots, & \mathbf{F}_K \end{bmatrix} \in \mathbb{C}^{M_T \times d}. \quad (2.2)$$

The precoding matrix is employed to suppress the MUI while taking a transmit power constraint into account. At the user terminals, decoding matrices  $\mathbf{D}_i \in \mathbb{C}^{M_{R_i} \times d_i}$  are employed. The joint block-diagonal decoding matrix containing the decoding matrices of the users is denoted by  $\mathbf{D}$  and takes the following form

$$\mathbf{D} = \begin{bmatrix} \mathbf{D}_1 & \mathbf{0} & \dots & \mathbf{0} \\ \mathbf{0} & \mathbf{D}_2 & \dots & \mathbf{0} \\ \vdots & \vdots & \ddots & \vdots \\ \mathbf{0} & \mathbf{0} & \dots & \mathbf{D}_K \end{bmatrix}. \quad (2.3)$$

Finally, the  $d$ -dimensional joint received vector is given by

$$\mathbf{y} = \mathbf{D}^H (\mathbf{H} \mathbf{F} \mathbf{x} + \mathbf{n}), \quad (2.4)$$

where  $\mathbf{y} = [\mathbf{y}_1^T, \mathbf{y}_2^T, \dots, \mathbf{y}_K^T]^T$ ,  $\mathbf{y}_i \in \mathbb{C}^{d_i \times 1}$  represents the received vector of the  $i$ -th user, and  $\mathbf{n} \in \mathbb{C}^{M_R \times 1}$  denotes the vector of the Additive White Gaussian Noise (AWGN) containing zero mean i.i.d. circularly symmetric Gaussian random variables with variance  $\sigma_n^2$ .

The major challenge of the transmission strategy design for such a multi-carrier multi-user MIMO downlink is to adopt efficient and effective spatial scheduling algorithms and precoding algorithms such that the SDMA benefits are fully exploited, the MUI at the user terminals is mitigated, and most of the computations are carried out at the BS.

## 2.3. Efficient multi-carrier ProSched (EMC-ProSched)

The proposed EMC-ProSched scheme consists of three major steps: setting up the possible user groups, calculating the scheduling metrics, and selecting the user group with the maximum sum metric. In addition, to ensure the fairness of the scheduling, a proportional fairness-based extension is also developed for the EMC-ProSched algorithm. Instead of carrying out an exhaustive search of all possible user groups, the tree-based sorting algorithm [FDH07] is utilized to produce candidate user groups featuring the maximum sum metric for all possible group sizes from one to the maximum supported size of the precoder. The maximum possible group size can also be determined by a certain communications standard (e.g., the maximum group size is 4 as in the IEEE 802.11ac specifications [WG813]). In Figure 2.3, we depict the

tree-based sorting scheme employed for user grouping in a simple five-user example. To avoid

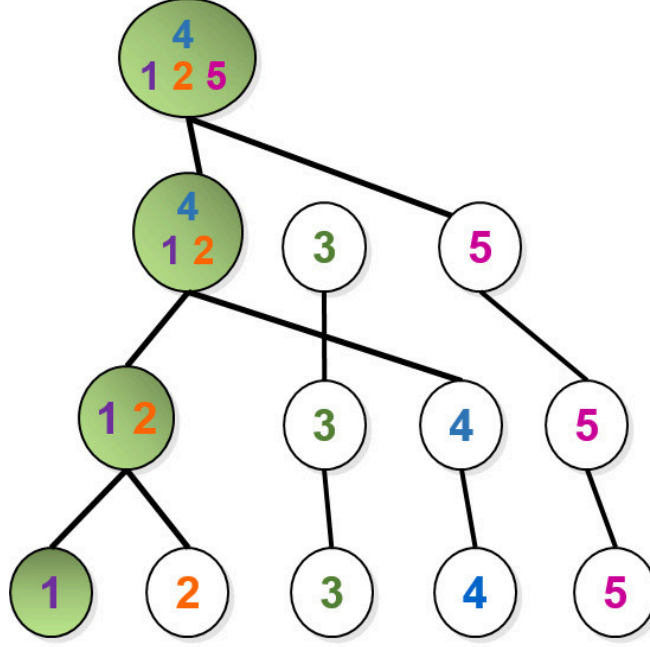


Figure 2.3.: Illustration of the tree-based sorting scheme

the pre-calculation of the precoding matrices, we employ the interpretation of the precoding process based on the orthogonal projection as developed in [FDH07]. Then, for every possible user group, a new scheduling metric designed based on the Exponential Effective SINR Mapping (EESM) [JKWF10] is calculated for each user (rather than for each subcarrier of one user as in [FDH07]) in the presence of a possible user group. Finally, the sum metrics of the candidate user groups with different sizes are compared and the group with the largest sum metric is selected and served. Note that the optimum group size is also determined.

### 2.3.1. Metric calculation

Now, the metric calculation for the user selection will be detailed. We define the channel matrix for the  $i$ -th user on the  $j$ -th subcarrier as  $\mathbf{H}_{i,j}$  and use  $\mathbf{F}_{i,j} \in \mathbb{C}^{M_T \times d_i}$  to denote the precoding matrix for the  $i$ -th user on the  $j$ -th subcarrier. The number of users in the current user set  $\mathcal{S}$  as a candidate SDMA user group is denoted by  $K^{(\mathcal{S})}$ . Assuming the BD algorithm [SSH04] is employed as the precoding technique, the equivalent single-user channel matrix

after the MUI elimination on the  $j$ -th subcarrier for the  $i$ -th user present in the user set  $\mathcal{S}$  is represented as

$$\mathbf{H}_{i,j}^{(\text{eq})} = \mathbf{H}_{i,j} \tilde{\mathbf{V}}_{i,j}^{(0)}, \quad i = 1, \dots, K^{(\mathcal{S})}, \quad j = 1, \dots, N_{\text{SD}}, \quad (2.5)$$

where the columns of  $\tilde{\mathbf{V}}_{i,j}^{(0)}$  form an orthonormal basis of the common null space of all the other users present in the user set  $\mathcal{S}$ .

It has been shown in [FDH07] that when the BD algorithm [SSH04] is employed, the norm of the equivalent channel after precoding equals the norm of the projected channel

$$\left\| \mathbf{H}_{i,j} \tilde{\mathbf{V}}_{i,j}^{(0)} \right\|_{\text{F}}^2 = \left\| \mathbf{H}_{i,j} \tilde{\mathbf{P}}_{i,j} \right\|_{\text{F}}^2, \quad (2.6)$$

$$i = 1, \dots, K^{(\mathcal{S})}, \quad j = 1, \dots, N_{\text{SD}},$$

where  $\tilde{\mathbf{P}}_{i,j}$  is a projection matrix that serves to project the channel matrix of the  $i$ -th user on the  $j$ -th subcarrier  $\mathbf{H}_{i,j}$  onto the common null space of the other co-channel users. When using other linear precoding algorithms for the multi-user MIMO downlink aiming at the MUI mitigation, this relationship holds approximately. To further avoid the calculation of the projection matrices for all possible user combinations and thus achieve a low complexity, we adopt the following approximation [Hal62]

$$\tilde{\mathbf{P}}_{i,j} \approx (\mathbf{P}_{1,j} \cdot \mathbf{P}_{2,j} \cdots \mathbf{P}_{i-1,j} \cdot \mathbf{P}_{i+1,j} \cdots \mathbf{P}_{K^{(\mathcal{S})},j})^p, \quad p \rightarrow \infty, \quad (2.7)$$

where  $\mathbf{P}_{i,j}$  is the projection matrix on the  $i$ -th user's null space (on the  $j$ -th subcarrier) which can be obtained by performing the SVD of the  $i$ -th user's channel matrix on the  $j$ -th subcarrier  $\mathbf{H}_{i,j}$ . Note that it is sufficient to choose the projection order<sup>2</sup>  $p$  between 1 and 3 [FDH07].

Hence, by using such an orthogonal projection-based interpretation of the precoding process and the repeated projection approximation, we obtain  $\left\| \mathbf{H}_{i,j}^{(\text{eq})} \right\|_{\text{F}}$ , the Frobenius norm of the equivalent single-user channel matrix on the  $j$ -th subcarrier for the  $i$ -th user present in the user set  $\mathcal{S}$  without performing the precoding. With the perfect CSIT, an SVD-based transmission scheme can be applied to the equivalent single-user transmissions. Assume that the number of spatial streams transmitted to the  $i$ -th user on the  $j$ -th subcarrier,  $d_i$  as denoted previously, is chosen as the rank of  $\mathbf{H}_{i,j}^{(\text{eq})}$ . The channel gains on these spatial streams are then the  $d_i$  non-zero eigenvalues of  $\mathbf{H}_{i,j}^{(\text{eq})} \mathbf{H}_{i,j}^{(\text{eq})\text{H}}$  when the SVD-based transmission scheme is adopted. Note that one of the goals of the proposed efficient scheduling algorithm is to avoid the calculation of the precoding matrices. The optimum power allocation on the spatial streams of each user

<sup>2</sup>In the simulations the results of which are presented in Section 2.7, the projection order  $p$  is chosen as 1.

cannot be determined without the knowledge of the channel gain on each spatial stream. Thus, for the spatial scheduling process equal power is assumed to be allocated to each spatial stream for simplicity. Therefore, knowing  $\|\mathbf{H}_{i,j}^{(\text{eq})}\|_{\text{F}}$ , we obtain the receive SINR averaged over the  $d_i$  spatial streams of the  $i$ -th user present in the user set  $\mathcal{S}$  on the  $j$ -th subcarrier as

$$\rho_{i,j}^{(\mathcal{S})} = \frac{P_{\text{T}} \cdot \text{Tr} \left\{ \mathbf{H}_{i,j}^{(\text{eq})} \mathbf{H}_{i,j}^{(\text{eq})\text{H}} \right\}}{K(\mathcal{S}) d_i^2 \sigma_n^2} = \frac{P_{\text{T}} \cdot \|\mathbf{H}_{i,j}^{(\text{eq})}\|_{\text{F}}^2}{K(\mathcal{S}) d_i^2 \sigma_n^2} \quad (2.8)$$

$$i = 1, \dots, K(\mathcal{S}), \quad j = 1, \dots, N_{\text{SD}},$$

where  $P_{\text{T}}$  is the transmit power allocated on each subcarrier, and  $\text{Tr}\{\cdot\}$  denotes the trace of the input matrix. Note that equal power is assigned on the subcarriers, i.e.,  $P_{\text{T}} = P_{\text{T,tot}}/N_{\text{SD}}$ , where  $P_{\text{T,tot}}$  is the total transmit power. It is known that using a link-to-system mapping scheme, a metric of the link quality can be acquired from a collection of data measuring the instantaneous channel state, such as the SINRs on all the data streams and across all the subcarriers in a multi-carrier system. Inspired by this idea, we propose to extract an effective SINR as an estimate of the quality of transmissions involving a candidate user group and use it as the scheduling metric. Here the EESM scheme is employed which has been shown to contribute to a relatively accurate link-to-system interface for OFDM-based systems. The derivation of EESM in case of binary signaling is based on the Union-Chernoff bound of the pairwise error probabilities [Eri03] and can be found in Appendix B. Note that for higher-order modulation or an arbitrary MCS, determining the exact expression for EESM is not straightforward. Nevertheless, via link-level simulations, the MCS-dependent parameters in EESM can be calibrated.

Based on the EESM scheme, we represent the effective SINR for the transmission of the  $i$ -th user in the presence of the user set  $\mathcal{S}$  by using the averaged SINRs across the spatial streams on each subcarrier obtained from (2.8) for simplicity

$$\rho_i^{(\mathcal{S})} = -\beta_2 \ln \left( \frac{1}{N_{\text{SD}}} \sum_{j=1}^{N_{\text{SD}}} \exp \left( -\frac{\rho_{i,j}^{(\mathcal{S})}}{\beta_1} \right) \right), \quad i = 1, \dots, K(\mathcal{S}), \quad (2.9)$$

where  $\beta_1$  and  $\beta_2$  are system-dependent parameters obtained from calibrations. The detailed calibration procedures are presented in Section 2.6 where the system-level simulator is developed. The results for the evaluation of the accuracy of EESM are included in Appendix C. It is worth mentioning that in the evaluation of the performance of multi-carrier systems, parallel transmissions on different subcarriers are sometimes assumed as independent for simplicity.



Then the performance is measured by averaging over certain metrics (e.g., rate, or SINR) for all the subcarriers, and the averaged metric is used for the scheduling purpose. However, in some practical cases, for instance, when the channel shows obvious frequency selectivity and the information symbols at the transmitter are not independently coded (e.g., a convolutional encoder is applied), the aforementioned assumption does not hold anymore. It might also lead to an overoptimistic estimate of the system performance which is not an effective metric for a scheduling algorithm. By comparison, our proposed scheduling metric utilizes well-calibrated parameters and provides a more accurate measure of the performance of the transmissions which feature each candidate user group in such a multi-carrier system.

Thereby, based on (2.6), (2.7), (2.8) and (2.9), the scheduling metric for the  $i$ -th user in the presence of a set of users  $\mathcal{S}$ ,  $i = 1, \dots, K^{(\mathcal{S})}$ , can be calculated as

$$\rho_i^{(\mathcal{S})} = -\beta_2 \ln \left( \frac{1}{N_{\text{SD}}} \sum_{j=1}^{N_{\text{SD}}} \exp \left( -\frac{P_{\text{T}} \cdot \|\mathbf{H}_{i,j} \tilde{\mathbf{P}}_{i,j}\|_{\text{F}}^2}{\beta_1 K^{(\mathcal{S})} d_i^2 \sigma_n^2} \right) \right). \quad (2.10)$$

The EMC-ProSched sum metric of the candidate user set  $\mathcal{S}$  is then

$$\eta^{(\mathcal{S})} = \sum_{i=1}^{K^{(\mathcal{S})}} \rho_i^{(\mathcal{S})}. \quad (2.11)$$

Note that the Frobenius norm of the projected channel  $\|\mathbf{H}_{i,j} \tilde{\mathbf{P}}_{i,j}\|_{\text{F}}$  also indicates the spatial correlation among the users. A higher spatial correlation results in a smaller Frobenius norm of the projected channel and hence a smaller scheduling metric. Thus, the task of avoiding the allocation of users with a high spatial correlation into one SDMA group is fulfilled.

### 2.3.2. Fairness consideration

In order to further take the fairness of the scheduling into account, the scheduling metric expressed in (2.11) can be extended using one of the known fairness algorithms. Here we present one extension of the EMC-ProSched scheduling metric based on the proportional fairness algorithm. The scheduling metric for the  $i$ -th user in the presence of a set of users  $\mathcal{S}$  is then normalized by its long-term average metric. Accordingly, the sum metric of the user set  $\mathcal{S}$  is written as

$$\eta^{(\mathcal{S})} = \sum_{i=1}^{K^{(\mathcal{S})}} \frac{\rho_i^{(\mathcal{S})}}{\bar{\rho}_i}, \quad (2.12)$$

where  $\bar{\rho}_i$  is the average of the user metrics of the previous  $m$  time slots. We define  $\bar{\rho}_i(n)$  for the  $n$ -th time slot as

$$\bar{\rho}_i(n) = \frac{1}{m} \sum_{\mu=n-m}^{n-1} \rho_i(\mu). \quad (2.13)$$

In the  $\mu$ -th time slot, if the  $i$ -th user is selected, then  $\rho_i(\mu)$  is set to its metric calculated for its presence in the selected group. Conversely, if the  $i$ -th user is not selected in the  $\mu$ -th time slot,  $\rho_i(\mu)$  is set to zero. With this proportional fairness-based extension, the scheduling fairness is enhanced by taking into account previous scheduling results while determining the users to be served in the present scheduling process.

### 2.3.3. Complexity analysis

The complexity of the proposed scheduling algorithm is mainly determined by the calculation of the SVDs. This is due to the fact that the SVD for an  $N_{\text{row}}$ -by- $N_{\text{col}}$  dimensional matrix experiences a complexity proportional to  $\min(N_{\text{row}} \cdot N_{\text{col}}^2, N_{\text{row}}^2 \cdot N_{\text{col}})$ . In the proposed EMC-ProSched scheme, only  $(N \cdot N_{\text{SD}})$  SVDs are required at the beginning of each scheduling process for all the possible user groups. By comparison, for the conventional spatial scheduling algorithms where the calculation of the precoding matrices for all the user combinations is required [LTSL10], [KRO<sup>+</sup>11], assuming the SDMA group size is fixed to  $K$ , the number of SVDs needed to accomplish the same scheduling task is

$$\begin{aligned} & N_{\text{SD}} \times [(N-1) \times 2 + (N-2) \times 3 + \dots + (N-K+1) \times K] \\ &= N_{\text{SD}} \times \left[ \left( \frac{1}{2} K(K+1) - 1 \right) N - \frac{1}{3} K(K^2-1) \right]. \end{aligned}$$

For example, in a system with  $N = 16$  users, the number of data subcarriers  $N_{\text{SD}}$  is 234 as specified in the IEEE 802.11ac standard for an 80 MHz transmission [WG813], and the SDMA group size is set to  $K = 4$  users. The number of SVDs required for EMC-ProSched is only 3744. On the other hand for the conventional scheduling algorithms requiring the calculation of the precoding matrices for all the user combinations, the same scheduling task involves 29016 SVDs. Compared to these spatial scheduling algorithms, the proposed EMC-ProSched scheme has a much lower complexity especially for multi-carrier systems with a large number of data subcarriers.

Note that the ProSched algorithm [FDH07] initially proposed for one subcarrier is also based on the orthogonal projections to avoid a prohibitive large number of required SVDs. However, when applied in a multi-carrier system, the ProSched algorithm treats subcarriers as virtual users. It experiences an unaffordable computational complexity to search for a suitable group

of virtual users among the total  $N \cdot N_{SD}$  virtual users. In addition, by treating the subcarriers as virtual users, the number of users served will be different from one subcarrier to another. This feature requires much more information exchange between the BS and the user terminals, and a huge signaling overhead is unavoidable. Also, at each time slot, serving some selected subcarriers but not all subcarriers for one user is not compatible with the IEEE 802.11ac specifications [WG813].

#### 2.3.4. Cross-layer aspects

EMC-ProSched, a spatial scheduling algorithm, is proposed as the first stage of the physical layer (PHY) transmission scheme for the multi-user MIMO downlink which is the major focus of this chapter. It accomplishes the task of the SDMA user group selection mainly by exploring the spatial correlation of the users such that the multi-user diversity is better exploited, while the impacts of multi-carrier transmissions are also taken into account. However, in practice link layer retransmission mechanisms such as Automatic Repeat Request (ARQ) and Hybrid Automatic Repeat Request (HARQ) are used to handle erroneous packet transmissions. This gives rise to the concern of considering possible effects of retransmissions in the scheduling process when a certain ARQ/ HARQ scheme is employed. In such a case, retransmissions are involved in the scheduling procedure as well as new transmissions. If a higher priority is granted to retransmissions, it can be reflected in the design of the scheduling metric. In [ZV05], modifications to a scheduler are proposed by taking into consideration the retransmission information in the cases where simple ARQ and Chase combining are used, respectively. They provide some insights into a cross-layer extension of the proposed EMC-ProSched algorithm. Moreover, the impact of the SINR increment per retransmission to that of the first transmission is also worth attention, since EMC-ProSched employs an SINR-based scheduling metric. The HARQ combining gain model proposed in [FK12] and its modified versions in [CCKC06] for both the Chase combining scheme and the incremental redundancy scheme can be referred to.

Hence, to adapt EMC-ProSched to systems where retransmission mechanisms are considered as future work, the aforementioned SINR increment can be incorporated into an extension of the scheduling metric. In addition, a weighted version of the scheduling metric can be devised, where the weights are computed based on, for instance, estimates of the packet error rates for retransmissions and new transmissions [ZV05]. Consequently, a higher priority can be provided to retransmissions as they might be more prone to experience a higher SINR due to the HARQ combining gain.

## 2.4. Linear precoding-based geometric mean decomposition (LP-GMD)

After selecting the user group to be served, linear precoding algorithms are employed to mitigate the MUI. Since the precoding is performed on a per-subcarrier basis, the index of subcarriers is ignored in the notation of channel matrices and precoding matrices similar as in Section 2.2. For **Case 1** where  $M_T \geq M_R$ , we propose the LP-GMD algorithm. Let us follow the generic philosophy of the calculation of the linear precoding matrix as explained in [SH08]. The calculation can be divided into two steps, the MUI cancellation or suppression and the system performance optimization. Thus, the precoding matrix  $\mathbf{F}$  can be expressed as

$$\mathbf{F} = \gamma \mathbf{F}_a \mathbf{F}_b, \quad (2.14)$$

where  $\mathbf{F}_a = [\mathbf{F}_{a_1}, \mathbf{F}_{a_2}, \dots, \mathbf{F}_{a_K}] \in \mathbb{C}^{M_T \times M_x}$  with  $\mathbf{F}_{a_i} \in \mathbb{C}^{M_T \times M_{x_i}}$  serves to cancel or suppress the MUI, and the block-diagonal matrix  $\mathbf{F}_b = \text{blkdiag}\{\mathbf{F}_{b_1}, \mathbf{F}_{b_2}, \dots, \mathbf{F}_{b_K}\} \in \mathbb{C}^{M_x \times d}$  with  $\mathbf{F}_{b_i} \in \mathbb{C}^{M_{x_i} \times d_i}$  is used to further tune the system performance for each user separately. Here  $\text{blkdiag}\{\cdot\}$  denotes a block-diagonal concatenation of its input matrices. We define  $M_x = \sum_{i=1}^K M_{x_i}$  and assume that  $M_{x_i} \leq d$ . Due to the fact that after the MUI mitigation the multi-user MIMO downlink setting is decoupled into  $K$  equivalent independent single-user settings,  $M_{x_i}$  can be treated as the resulting equivalent number of transmit antennas for the  $i$ -th user ( $i = 1, 2, \dots, K$ ). Different MUI suppression schemes lead to various values of  $M_{x_i}$ . The parameter  $\gamma$  is chosen such that the total transmit power constraint is fulfilled. In the proposed LP-GMD algorithm, which follows this generic philosophy, the matrix  $\mathbf{F}_a$  is firstly calculated by suitable MUI suppression algorithms to mitigate the MUI, and then the matrix  $\mathbf{F}_b$  is computed by using the GMD algorithm to enable an equal MCS implementation across the spatial streams for each user. It should be noted that the MUI suppression algorithm can be selected flexibly in the LP-GMD algorithm, and two versions will be given in what follows, called LP-GMD-BD and LP-GMD-RBD. In addition, an MMSE-based power loading strategy is developed for the LP-GMD schemes to further enhance their performances.

### 2.4.1. LP-GMD-BD

First, we follow the strategy of the BD algorithm to calculate the matrix  $\mathbf{F}_a$ , and we call this approach LP-GMD-BD. By substituting (2.14) into the joint received vector (2.4), we can

express the received vector for the  $i$ -th user as

$$\mathbf{y}_i = \gamma \mathbf{D}_i^H \mathbf{H}_i \mathbf{F}_{a_i} \mathbf{F}_{b_i} \mathbf{x}_i + \bar{\mathbf{n}}_i + \sum_{j=1, j \neq i}^K \gamma \mathbf{D}_i^H \mathbf{H}_i \mathbf{F}_{a_j} \mathbf{F}_{b_j} \mathbf{x}_j, \quad (2.15)$$

where  $\bar{\mathbf{n}}_i = \mathbf{D}_i^H \mathbf{n}_i$ , and the last term on the right hand side of the equation represents the MUI. The design criterion for  $\mathbf{F}_a$  is to mitigate this interference term. It has been pointed out in [SSH04] that for the  $i$ -th user  $\mathbf{F}_{a_i}$  can be calculated such that it lies in the common null space of the other users' channel matrices. Let us define the matrix  $\widetilde{\mathbf{H}}_i \in \mathbb{C}^{(M_R - M_{R_i}) \times M_T}$  as the joint matrix that consists of all the other users' channel matrices, which is given by

$$\widetilde{\mathbf{H}}_i = \begin{bmatrix} \mathbf{H}_1^T, & \dots, & \mathbf{H}_{i-1}^T, & \mathbf{H}_{i+1}^T, & \dots, & \mathbf{H}_K^T \end{bmatrix}^T. \quad (2.16)$$

The zero MUI constraint forces the precoding matrix of the  $i$ -th user  $\mathbf{F}_{a_i}$  to lie in the null space of  $\widetilde{\mathbf{H}}_i$ . Assuming the rank of  $\widetilde{\mathbf{H}}_i$  is  $\widetilde{L}_i$ , by performing the SVD of  $\widetilde{\mathbf{H}}_i$ , we have

$$\widetilde{\mathbf{H}}_i = \widetilde{\mathbf{U}}_i \widetilde{\Sigma}_i \begin{bmatrix} \widetilde{\mathbf{V}}_i^{(1)} & \widetilde{\mathbf{V}}_i^{(0)} \end{bmatrix}^H \in \mathbb{C}^{(M_R - M_{R_i}) \times M_T}, \quad (2.17)$$

where  $\widetilde{\mathbf{V}}_i^{(1)} \in \mathbb{C}^{M_T \times \widetilde{L}_i}$  contains the first  $\widetilde{L}_i$  right singular vectors, and  $\widetilde{\mathbf{V}}_i^{(0)} \in \mathbb{C}^{M_T \times (M_T - \widetilde{L}_i)}$  contains the last  $M_T - \widetilde{L}_i$  right singular vectors which form an orthogonal basis for the null space of  $\widetilde{\mathbf{H}}_i$ . Therefore, the matrix  $\mathbf{F}_{a_i}$  for the  $i$ -th user is identified as

$$\mathbf{F}_{a_i} = \widetilde{\mathbf{V}}_i^{(0)} \in \mathbb{C}^{M_T \times (M_T - \widetilde{L}_i)}. \quad (2.18)$$

It should be noted that this result leads to  $\widetilde{\mathbf{H}}_i \mathbf{F}_{a_i} = \mathbf{0} \in \mathbb{R}^{(M_R - M_{R_i}) \times (M_T - \widetilde{L}_i)}$ , i.e.,  $\mathbf{H}_j \mathbf{F}_{a_i} = \mathbf{0} \in \mathbb{R}^{M_{R_j} \times (M_T - \widetilde{L}_i)}$  with  $j \neq i$ . Hence, the received vector of the  $i$ -th user can then be expressed as

$$\mathbf{y}_i = \gamma \mathbf{D}_i^H \mathbf{H}_i \mathbf{F}_{a_i} \mathbf{F}_{b_i} \mathbf{x}_i + \bar{\mathbf{n}}_i. \quad (2.19)$$

The equivalent channel of the  $i$ -th user denoted by  $\mathbf{H}_i^{(\text{eq})}$  is then expressed as

$$\mathbf{H}_i^{(\text{eq})} = \mathbf{H}_i \widetilde{\mathbf{V}}_i^{(0)} \in \mathbb{C}^{M_{R_i} \times (M_T - \widetilde{L}_i)}. \quad (2.20)$$

Note that  $\mathbf{H}_i^{(\text{eq})}$  equivalently corresponds to the channel of a single user system with  $M_T - \widetilde{L}_i$  transmit antennas and  $M_{R_i}$  receive antennas, where  $M_T - \widetilde{L}_i \geq M_{R_i}$ . Hence, the GMD algorithm can be employed to the equivalent single-user MIMO transmissions. The GMD of

the equivalent channel matrix of the  $i$ -th user can be expressed as [LHJ05]

$$\mathbf{H}_i^{(\text{eq})} = \mathbf{Q}_i \mathbf{R}_i \mathbf{Z}_i^H, \quad (2.21)$$

where  $\mathbf{Q}_i^H \mathbf{Q}_i = \mathbf{Z}_i^H \mathbf{Z}_i = \mathbf{I}_L$  ( $\mathbf{Q}_i \in \mathbb{C}^{M_{R_i} \times L}$  and  $\mathbf{Z}_i \in \mathbb{C}^{(M_T - \tilde{L}_i) \times L}$ ), assuming that the rank  $L$  matrix  $\mathbf{H}_i^{(\text{eq})}$  has non-zero singular values  $\lambda_l$ , with  $l = 1, \dots, L$ . The  $L$ -by- $L$  matrix  $\mathbf{R}_i$  is an upper triangular matrix with real-valued and equal entries on its diagonal, i.e.,  $r_{nn} = \bar{\lambda} = (\prod_{l=1}^L \lambda_l)^{1/L}$  as the geometric mean of the  $L$  singular values [LHJ05], where  $n = 1, \dots, L$ . The GMD<sup>3</sup> of  $\mathbf{H}_i^{(\text{eq})}$  can be calculated starting with the SVD of  $\mathbf{H}_i^{(\text{eq})}$  given by

$$\mathbf{H}_i^{(\text{eq})} = \mathbf{U}_i^{(\text{eq})} \mathbf{\Lambda}_i^{(\text{eq})} \mathbf{V}_i^{(\text{eq})H}. \quad (2.22)$$

Then the upper triangular matrix  $\mathbf{R}_i$  is constructed as explained in [LJH05]

$$\mathbf{R}_i = \tilde{\mathbf{Q}}_i \mathbf{\Lambda}_i^{(\text{eq})} \tilde{\mathbf{Z}}_i^H, \quad (2.23)$$

where  $\tilde{\mathbf{Q}}_i \in \mathbb{C}^{L \times L}$  and  $\tilde{\mathbf{Z}}_i \in \mathbb{C}^{L \times L}$  are unitary matrices. Each of them equals the product of a sequence of orthogonal matrices constructed using a symmetric permutation and a pair of Givens rotations [LHJ05]. By combining (2.22) and (2.23), the matrix  $\mathbf{Q}_i$  and  $\mathbf{Z}_i$  are expressed as

$$\mathbf{Q}_i = \mathbf{U}_i^{(\text{eq})} \tilde{\mathbf{Q}}_i^H \in \mathbb{C}^{M_{R_i} \times L}, \quad (2.24)$$

$$\mathbf{Z}_i = \mathbf{V}_i^{(\text{eq})} \tilde{\mathbf{Z}}_i^H \in \mathbb{C}^{(M_T - \tilde{L}_i) \times L}. \quad (2.25)$$

The matrix  $\mathbf{F}_{b_i}$  in the LP-GMD scheme is defined as

$$\mathbf{F}_{b_i} = \mathbf{Z}_i \in \mathbb{C}^{(M_T - \tilde{L}_i) \times L}. \quad (2.26)$$

Let us use  $\tilde{\mathbf{y}}_i$  as a short-hand notation for the signal received by the  $i$ -th user before decoding written as

$$\begin{aligned} \tilde{\mathbf{y}}_i &= \gamma \mathbf{H}_i^{(\text{eq})} \mathbf{F}_{b_i} \mathbf{x}_i + \mathbf{n}_i \\ &= \gamma (\mathbf{Q}_i \mathbf{R}_i \mathbf{Z}_i^H) \mathbf{Z}_i \mathbf{x}_i + \mathbf{n}_i \\ &= \gamma \mathbf{Q}_i \mathbf{R}_i \mathbf{x}_i + \mathbf{n}_i, \end{aligned} \quad (2.27)$$

such that  $\mathbf{y}_i = \mathbf{D}_i^H \tilde{\mathbf{y}}_i$ . The equivalent channel in (2.27) identified as  $\mathbf{Q}_i \mathbf{R}_i$  can be acquired by

---

<sup>3</sup>The MATLAB implementation of the GMD is available at [H<sup>+</sup>03].

performing channel estimation at the  $i$ -th user. Via a QR decomposition of this  $M_{R_i}$ -by- $L$  equivalent channel matrix<sup>4</sup>,  $\mathbf{Q}_i$  is obtained and employed as the decoding matrix for the  $i$ -th user, i.e.,

$$\mathbf{D}_i = \mathbf{Q}_i \in \mathbb{C}^{M_{R_i} \times L}. \quad (2.28)$$

Therefore, with (2.27) and (2.28) the received signal of the  $i$ -th user expressed in (2.19) is further written as

$$\begin{aligned} \mathbf{y}_i &= \mathbf{Q}_i^H \tilde{\mathbf{y}}_i \\ &= \gamma \mathbf{Q}_i^H \mathbf{Q}_i \mathbf{R}_i \mathbf{x}_i + \tilde{\mathbf{n}}_i \\ &= \gamma \mathbf{R}_i \mathbf{x}_i + \tilde{\mathbf{n}}_i. \end{aligned} \quad (2.29)$$

Recall that  $\mathbf{R}_i$  is an upper triangular matrix with equal diagonal elements. After adopting a Successive Interference Cancellation (SIC) receiver, all spatial streams for the  $i$ -th user experience the same gain and the same noise variance resulting in the same SINR. The implementation of the same MCS is consequently enabled on the spatial streams of each user. As the number of receive antennas at a user terminal is rather limited, applying an SIC receiver does not induce much additional computational effort. Furthermore, it has been shown in [LJH05] that when the number of receive antennas at the user terminals is moderate, the error propagation incurred by the SIC receiver can be ignored.

Note that the LP-GMD algorithm is proposed as one promising solution for multi-user MIMO downlink transmissions where it is desired (e.g., due to certain constraints by standardization or the pursuit of a smaller signaling overhead) that the same MCS is used on all spatial streams for each user. Here we treat the case where all possible spatial modes for each user are switched on, i.e., the number of spatial streams transmitted to each user equals the rank of the equivalent single-user channel after the MUI mitigation. As future work, it is also of interest to extend the LP-GMD scheme to the case where more than one but not all spatial modes are used and equal MCS is enabled on them.

---

<sup>4</sup>The QR decomposition of a matrix  $\mathbf{A} \in \mathbb{C}^{m \times n}$  that has full column rank written as  $\mathbf{A} = \mathbf{Q}\mathbf{R}$  is unique when the diagonal elements of  $\mathbf{R}$  are positive [GvL96]. Note that in our case the real-valued matrix  $\mathbf{R}_i$  is indeed required to have positive diagonal entries. Hence, assuming the equivalent channel  $\mathbf{Q}_i^H \mathbf{R}_i$  is perfectly estimated,  $\mathbf{Q}_i$  and  $\mathbf{R}_i$  are the unique outcome of the QR decomposition of this equivalent channel.

In addition, the number of spatial streams transmitted to the  $i$ -th user  $d_i$  is chosen to be the rank of the equivalent single-user channel  $\mathbf{H}_i^{(\text{eq})}$  to achieve the full multiplexing gain.

### 2.4.2. LP-GMD-RBD

In what follows, we present LP-GMD-RBD, in which the calculation of the matrix  $\mathbf{F}_a$  follows the philosophy of the RBD algorithm [SH08]. We start from the equivalent combined channel matrix of all users after the MUI mitigation, which is given by

$$\mathbf{H}\mathbf{F}_a = \begin{bmatrix} \mathbf{H}_1\mathbf{F}_{a_1} & \mathbf{H}_1\mathbf{F}_{a_2} & \dots & \mathbf{H}_1\mathbf{F}_{a_K} \\ \mathbf{H}_2\mathbf{F}_{a_1} & \mathbf{H}_2\mathbf{F}_{a_2} & \dots & \mathbf{H}_2\mathbf{F}_{a_K} \\ \vdots & \vdots & \ddots & \vdots \\ \mathbf{H}_K\mathbf{F}_{a_1} & \mathbf{H}_K\mathbf{F}_{a_2} & \dots & \mathbf{H}_K\mathbf{F}_{a_K} \end{bmatrix}, \quad (2.30)$$

where the  $i$ -th user's effective channel is represented as  $\mathbf{H}_i\mathbf{F}_{a_i}$ , and the interference generated to the other users is determined by  $\widetilde{\mathbf{H}}_i\mathbf{F}_{a_i}$  with  $\widetilde{\mathbf{H}}_i$  defined in (2.16). Here the matrix  $\mathbf{F}_{a_i}$  is chosen such that the off-diagonal block matrices of the equivalent combined channel matrix of all users after the MUI cancellation converge to zero as the SNR increases. According to [SH08]  $\mathbf{F}_{a_i}$  can be written as

$$\mathbf{F}_{a_i} = \widetilde{\mathbf{V}}_i \left( \widetilde{\mathbf{\Sigma}}_i^T \widetilde{\mathbf{\Sigma}}_i + \frac{M_R \sigma_n^2}{P_T} \mathbf{I}_{M_T} \right)^{-1/2} \in \mathbb{C}^{M_T \times M_T}, \quad (2.31)$$

where  $\widetilde{\mathbf{V}}_i \in \mathbb{C}^{M_T \times M_T}$  and  $\widetilde{\mathbf{\Sigma}}_i \in \mathbb{C}^{(M_R - M_{R_i}) \times M_T}$  are obtained from the SVD of  $\widetilde{\mathbf{H}}_i$  given by

$$\widetilde{\mathbf{H}}_i = \widetilde{\mathbf{U}}_i \widetilde{\mathbf{\Sigma}}_i \widetilde{\mathbf{V}}_i^H \in \mathbb{C}^{(M_R - M_{R_i}) \times M_T}. \quad (2.32)$$

Recall that  $P_T$  is the transmit power allocated on each subcarrier, and  $\sigma_n^2$  is the noise power in the bandwidth of each subcarrier at the receiver. In the high SNR regime, the off-diagonal block matrices of the equivalent combined channel matrix of all users  $\mathbf{H}\mathbf{F}_a$  converge to zero, i.e.,  $\mathbf{H}_j\mathbf{F}_{a_i} \approx \mathbf{0}$  with  $j \neq i$ ,  $i, j = 1, 2, \dots, K$ .

After determining the matrix  $\mathbf{F}_a$ , the LP-GMD-RBD scheme also arrives at the equivalent single-user MIMO channels. The GMD algorithm can then be employed to obtain the matrices  $\mathbf{F}_{b_i}$  as in (2.26). Note that the methods to obtain  $\mathbf{F}_a$  are not limited to the two approaches we show here. Other linear MUI suppression algorithms fitted into the multi-user MIMO linear precoding philosophy represented by (2.14) can be employed in the LP-GMD scheme.

### 2.4.3. Complexity Analysis

The proposed LP-GMD algorithm consists of two parts, which are the MUI suppression and the GMDs of the equivalent single-user MIMO channel matrices. For all the LP-GMD versions,



the second step requires  $K$  times the calculation of the GMD. The complexity of the first step depends on the complexity of the chosen MUI suppression algorithm for multi-user MIMO systems. For example, in LP-GMD-BD, the complexity of the MUI suppression is mainly determined by the  $K$  calculations of SVDs of the  $(M_R - M_{R_i})$ -by- $M_T$  joint matrices expressed in (2.16). In LP-GMD-RBD, the MUI mitigation procedure requires not only  $K$  SVDs of the  $(M_R - M_{R_i})$ -by- $M_T$  joint matrices, but also the calculation of the expressions shown in (2.31) for each user. Note that for the work of BD-GMD combined with THP [LHL08], the matrix decomposition of the  $K$ -user MIMO channel requires  $K$  times the calculation of the GMD and a recursion process, while the non-linear THP algorithm experiences a higher complexity than linear precoding algorithms such as BD and RBD. In [ZdH13], low-complexity BD-type precoding algorithms have been devised based on a channel inversion technique, QR decompositions, and lattice reductions. Employing these schemes to achieve the MUI mitigation in LP-GMD can lead to versions of LP-GMD that have a lower computational complexity compared to LP-GMD-BD and LP-GMD-RBD.

#### 2.4.4. MMSE-based Power Loading

Note that the goal of LP-GMD is to balance the power across the subchannels of each user. In order to further assign the power efficiently to all the users, an MMSE-based power loading strategy is developed in this section for a further enhancement of the LP-GMD algorithm.

For the  $i$ -th user, let us define a diagonal matrix  $\Sigma_i \in \mathbb{C}^{d_i \times d_i}$  such that the entries on its diagonal are the same as the diagonal elements of  $\mathbf{R}_i$  obtained from the GMD of the  $i$ -th user's equivalent channel after the MUI mitigation. We further define a matrix  $\Sigma_e$  as

$$\Sigma_e = \begin{bmatrix} \Sigma_1 & \mathbf{0} & \dots & \mathbf{0} \\ \mathbf{0} & \Sigma_2 & \dots & \vdots \\ \vdots & \vdots & \ddots & \vdots \\ \mathbf{0} & \mathbf{0} & \dots & \Sigma_K \end{bmatrix} \in \mathbb{R}^{d \times d}. \quad (2.33)$$

The matrix  $\mathbf{F}_b$  after applying the proposed power loading strategy is then identified as

$$\mathbf{F}_b = \text{blkdiag} \{ \mathbf{Z}_1, \mathbf{Z}_2, \dots, \mathbf{Z}_K \} \cdot \mathbf{\Lambda} \in \mathbb{C}^{M_x \times d}, \quad (2.34)$$

where matrices  $\mathbf{Z}_i$  with  $i = 1, 2, \dots, K$  are obtained by the GMD algorithm as in (2.26), and

$\mathbf{\Lambda} \in \mathbb{R}^{d \times d}$  denotes the power loading matrix given by [SH08]

$$\mathbf{\Lambda} = \left( \mathbf{\Sigma}_e^T \mathbf{\Sigma}_e + \frac{M_R \sigma_n^2}{P_T} \mathbf{I}_d \right)^{-1} \cdot \mathbf{\Sigma}_e^T \in \mathbb{R}^{d \times d}. \quad (2.35)$$

By employing such a power loading matrix, the “weak” users are enhanced, while the “strong” ones are weakened. Consequently the degradation caused by the weak users dominating the PER performance is avoided. Moreover, it should be noted that in multi-user transmissions in practice under a certain standard framework, such as the IEEE 802.11ac, the manner of the integration of the payload belonging to different users into the physical layer packet must be taken into account. When the sizes of the payload of different users are on the same level to ensure the fairness, unequal MCSs across different users will cause some overhead due to the requirement of padding bits [WG813]. When such an MMSE-based power loading strategy is employed, the power is balanced over all the users such that the probability that a lower MCS is applied to some users while a higher to others is reduced. The power efficiency is thereby enhanced by reducing the power loss caused by the overhead.

## 2.5. Low complexity coordinated beamforming (LoCCoBF)

In **Case 2**, where the total number of receive antennas at the  $K$  users selected by performing the EMC-ProSched algorithm is larger than the number of transmit antennas at the BS, the proposed precoding algorithm low complexity coordinated beamforming (LoCCoBF) is employed. Note that for precoding algorithms such as BD, which achieve the MUI suppression by letting each user transmit in all the other users’ common null space, under the condition that  $M_R > M_T$ , such a null space is in general empty. Therefore, we define an equivalent joint channel matrix  $\mathbf{H}_e$  for the  $K$  users, that is given by

$$\mathbf{H}_e = \begin{bmatrix} \mathbf{D}_1^H \mathbf{H}_1 \\ \vdots \\ \mathbf{D}_K^H \mathbf{H}_K \end{bmatrix} \in \mathbb{C}^{d \times M_T}, \quad (2.36)$$

where  $\mathbf{H}_i$ ,  $i = 1, 2, \dots, K$ , is the channel matrix for the  $i$ -th user on a certain subcarrier at a certain time instant as defined in Section 2.2. Recall that  $\mathbf{D}_i \in \mathbb{C}^{M_{R_i} \times d_i}$  and  $d_i \leq M_{R_i}$ , where  $i = 1, 2, \dots, K$ , is the receive beamforming matrix. Due to the fact that the total number of spatial streams  $d = \sum_{i=1}^K d_i$  does not exceed the number of transmit antennas, i.e.,  $d \leq M_T$ , the aforementioned dimensionality constraint is then relaxed by performing precoding on the equivalent channel matrix defined in (2.36). The main idea of coordinated beamforming al-

gorithms is that the transmit and receive beamformers are updated iteratively based on an initialized receive beamforming matrix until a stopping criterion is satisfied to achieve the goal of the MUI suppression [SRH10b], [CMIH08]. In our proposed LoCCoBF algorithm, we further take into account the correlation among the channels of different subcarriers. The receive beamforming matrices calculated for the adjacent subcarrier are employed as the receive beamforming matrices for the initialization step of the current subcarrier to reduce the computational complexity. The LoCCoBF algorithm is summarized as follows:

- **Step 1:** Initialize the receive beamforming matrices  $\mathbf{D}_i^{(0)}$  with  $i = 1, 2, \dots, K$ , set the iteration index  $p$  to zero, and set a threshold  $\epsilon$  for the stopping criterion. If the current subcarrier is the first one, the receive beamforming matrices are generated randomly; otherwise, set the receive beamforming matrices as the receive beamforming matrices calculated for the previous subcarrier.

- **Step 2:** Set  $p \leftarrow p + 1$  and calculate the equivalent joint channel matrix  $\mathbf{H}_e^{(p)}$  in the  $p$ -th iteration as

$$\mathbf{H}_e^{(p)} = \left[ \mathbf{H}_{e_1}^{(p)\text{T}}, \mathbf{H}_{e_2}^{(p)\text{T}}, \dots, \mathbf{H}_{e_K}^{(p)\text{T}} \right]^{\text{T}}, \quad (2.37)$$

where  $\mathbf{H}_{e_i}^{(p)} = \mathbf{D}_i^{(p-1)\text{H}} \mathbf{H}_i$  is the equivalent channel matrix for the  $i$ -th user in the  $p$ -th iteration.

- **Step 3:** Calculate the transmit beamforming matrix in the  $p$ -th iteration using the equivalent joint channel matrix  $\mathbf{H}_e^{(p)}$ . For the  $i$ -th user, let us first define the matrix  $\widetilde{\mathbf{H}}_{e_i}^{(p)}$  as

$$\widetilde{\mathbf{H}}_{e_i}^{(p)} = \left[ \mathbf{H}_{e_1}^{(p)\text{T}}, \dots, \mathbf{H}_{e_{i-1}}^{(p)\text{T}}, \mathbf{H}_{e_{i+1}}^{(p)\text{T}}, \dots, \mathbf{H}_{e_K}^{(p)\text{T}} \right]^{\text{T}}, \quad (2.38)$$

which contains the equivalent channel matrices of all the other users obtained in **Step 2**.

Then the transmit beamforming matrix  $\mathbf{F}_i^{(p)}$  in the  $p$ -th iteration for the  $i$ -th user is obtained as  $\mathbf{F}_i^{(p)} = \widetilde{\mathbf{V}}_{e_i}^{(p,0)}$ , where  $\widetilde{\mathbf{V}}_{e_i}^{(p,0)}$  contains the  $d_i$  singular vectors which form an orthonormal basis for the null space of  $\widetilde{\mathbf{H}}_{e_i}^{(p)}$ .

- **Step 4:** Calculate the receive beamforming matrix in the  $p$ -th iteration using the channel after precoding  $\mathbf{H}_i \mathbf{F}_i^{(p)}$  for the  $i$ -th user. When using the MMSE receiver,  $\mathbf{D}_i^{(p)}$  then has the form

$$\mathbf{D}_i^{(p)} = \left( \mathbf{H}_i \mathbf{F}_i^{(p)} \mathbf{F}_i^{(p)\text{H}} \mathbf{H}_i^{\text{H}} + \sigma_n^2 \mathbf{I}_{M_{R_i}} \right)^{-1} \mathbf{H}_i \mathbf{F}_i^{(p)}. \quad (2.39)$$

- **Step 5:** Calculate the term  $\text{MUI}(\mathbf{H}_e^{(p)} \mathbf{F}^{(p)})$  defined as

$$\text{MUI}(\mathbf{H}_e^{(p)} \mathbf{F}^{(p)}) = \left\| \text{off}(\mathbf{H}_e^{(p)} \mathbf{F}^{(p)}) \right\|_F^2, \quad (2.40)$$

where  $\text{off}(\cdot)$  indicates an operation of keeping all off-diagonal elements of its input matrix while setting its diagonal elements to zero. This term measures the residual MUI and the inter-stream interference. If  $\text{MUI}(\mathbf{H}_e^{(p)} \mathbf{F}^{(p)}) < \epsilon$ , the convergence has been achieved, and the iterative procedure comes to the end. Otherwise go back to **Step 2**.

Via numerical investigations as in [SRH13], it can be shown that there exist rare cases where the convergence of LoCCoBF is not achieved. For most of these cases, though the residual MUI still stays above the threshold  $\epsilon$  after a number of iterations, the value is already on a level which leads to a performance as good as in the case where the convergence is achieved. Therefore, a maximum number of iterations is set to handle these cases. The iterative procedure is manually terminated if the residual MUI does not fall below the threshold when the number of iterations reaches this maximum number. Moreover, other stopping criteria, such as the change of the transmit beamforming matrices expressed as  $\|\mathbf{F}^{(p)} - \mathbf{F}^{(p-1)}\|_F^2$  [CMIH08], can also be employed.

It is worth mentioning that in the LoCCoBF algorithm, by jointly updating the precoding and decoding matrices at the BS, we obtain the precoding matrices in the case where  $M_R > M_T$ . It is not required that the user terminals are informed of their decoding matrices. The user terminals can obtain the CSI via channel estimation and use this to tune their decoding matrices.

In addition, the proposed LoCCoBF algorithm presents in a more general sense a framework of coordinated beamforming, and more flexibility is allowed in computing the transmit and receive beamforming matrices. For instance, in **Step 3** of LoCCoBF the precoding matrix is calculated to mitigate the MUI and the number of spatial streams transmitted to each user  $d_i$  is chosen as the rank of the resulting equivalent single-user channel  $\mathbf{H}_i \mathbf{F}_i^{(p)}$  to achieve the full spatial multiplexing gain. One might also incorporate transmit processing techniques (beamforming techniques and spatial multiplexing techniques) originally designed for single-user MIMO transmissions into the calculation of the precoding matrix of LoCCoBF. Consequently, the number of spatial streams for each user can be adapted according to the transmission qualities in terms of, e.g., the spatial rank of the equivalent single-user channel after the MUI suppression and the SNR level.

To this end, the proposed transmission strategy is summarized in Table 2.1.

Table 2.1.: Proposed transmission strategy

<b>Stage 1: Scheduling</b>	
<b>Step 1</b>	Set the SDMA group size as $K^{(S)} = 1$ Calculate the sum metric defined in (2.11) for all possible user groups Select the best one identified as $\mathcal{S}_1^{(\text{opt})}$ with the maximum sum metric
<b>Step 2</b>	Set $K^{(S)} = K^{(S)} + 1$ , and add one of the remaining users to the selected user group with the group size $(K^{(S)} - 1)$ Calculate the sum metric using (2.11) for all the new possible user groups Select the best one identified as $\mathcal{S}_{K^{(S)}}^{(\text{opt})}$ with the maximum sum metric
<b>Step 3</b>	Compare $K^{(S)}$ with the total number of user terminals in the system $N$ and the maximum allowed SDMA group size $K_{\max}$ <ul style="list-style-type: none"> <li>• If <math>K^{(S)} &lt; \min(N, K_{\max})</math>, go back to <b>Step 2</b></li> <li>• If <math>K^{(S)} = \min(N, K_{\max})</math>, compare the sum metrics of the optimum user groups with different sizes and select the one with the maximum sum metric</li> </ul>
<b>Stage 2: Precoding</b>	
<b>Step 1</b>	Compare the number of transmit antennas at the BS $M_T$ with the total number of receive antennas of the user terminals in the user group selected in <b>Stage 1</b> $M_R$
<b>Step 2</b>	Calculate the precoding matrices <ul style="list-style-type: none"> <li>• If <b>Case 1</b> (<math>M_T \geq M_R</math>), employ LP-GMD-BD detailed in Section 2.4.1 or LP-GMD-RBD in Section 2.4.2</li> <li>• If <b>Case 2</b> (<math>M_T &lt; M_R</math>), employ LoCCoBF described in Section 2.5</li> </ul>

## 2.6. IEEE 802.11ac system-level simulator

A MATLAB system-level simulator using a link-to-system interface has been developed under the IEEE 802.11ac [WG813] framework. With the aid of this simulator, the system and user throughput of multi-carrier multi-user MIMO downlink transmissions on one of the IEEE 5 GHz bands with a bandwidth of 20 MHz, 40 MHz, or 80 MHz can be demonstrated. For each independent run, a new channel realization is generated with the parameters concerning the channel and the antennas. The generation of the channel is based on the MATLAB implementation package of the IEEE 802.11n channel models [SD04] and follows the modification instructions [IEE10] for the IEEE 802.11ac multi-user scenarios. A scheduling algorithm first selects a user group to be served, and precoding is then performed on the selected users. Using the calculated precoding and decoding matrices, the equivalent channel matrix and the equivalent noise covariance matrix are obtained. The SINRs are computed on each subcarrier across all the spatial streams.

With the knowledge of the SINRs on the  $i$ -th spatial stream and  $j$ -th data subcarrier, denoted by  $\rho_{i,j}$ ,  $i = 1, 2, \dots, N_{\text{SS}}$  and  $j = 1, 2, \dots, N_{\text{SD}}$ , the main idea of the link-to-system mapping is to first map all these SINRs to a scalar value known as the Link Quality Metric (LQM). In our case, the effective SINR denoted by  $\rho_{\text{eff}}$  is employed as the LQM, and it is then used to estimate the PER for this specific channel state according to the AWGN link-level performance. In the light of this statement, an accurate effective SINR mapping has to fulfill the following approximate equivalence

$$P_e^{\text{fading}}(\{\rho_{1,1}, \dots, \rho_{i,j}, \dots, \rho_{N_{\text{SS}}, N_{\text{SD}}}\}) \approx P_e^{\text{AWGN}}(\rho_{\text{eff}}), \quad (2.41)$$

where  $P_e$  stands for the PER. Here the EESM scheme is adopted (see Appendix B and C for the derivation of EESM in case of binary signaling and the evaluation of the accuracy of this scheme). This method was originally used in [Eri03] and has been later applied in the construction of other system-level simulators such as [IWR10]. Consequently, the expression of the effective SINR is given by

$$\rho_{\text{eff}} = -\beta_2 \ln \left( \frac{1}{N_{\text{SS}} \cdot N_{\text{SD}}} \sum_{j=1}^{N_{\text{SD}}} \sum_{i=1}^{N_{\text{SS}}} \exp \left( -\frac{\rho_{i,j}}{\beta_1} \right) \right), \quad (2.42)$$

where  $\beta_1$  and  $\beta_2$  depend on the MCS and the channel model. Hence, they need to be calibrated. In [Eri03], these two parameters are treated as equal to each other, i.e.,  $\beta_1 = \beta_2 = \beta$ . For each MCS, link-level simulations are performed using  $N_c$  channel realizations. For the  $k$ -th channel realization, a PER denoted by  $P_e^{(k)}$  is obtained,  $k = 1, 2, \dots, N_c$ . By mapping  $P_e^{(k)}$  onto a

PER versus SNR curve of transmissions over the AWGN channel with the same MCS applied, an equivalent “measured” SINR  $\rho_m^{(k)}$  for the  $k$ -th channel realization is acquired. Meanwhile, according to (2.42) with a certain value of  $\beta$  an effective SINR  $\rho_{\text{eff}}^{(k)}(\beta)$  can be calculated using the SINRs on different subcarriers across all the spatial streams for the  $k$ -th channel realization. Seeking the approximate equivalence in (2.41),  $\beta$  is then chosen as the numerical solution of the following optimization problem

$$\beta_{\text{opt}} = \arg \min_{\beta} \left\{ \sum_{k=1}^{N_c} \left| \log(\rho_{\text{eff}}^{(k)}(\beta)) - \log(\rho_m^{(k)}) \right|^2 \right\}. \quad (2.43)$$

The parameter  $\beta$  obtained from such calibration procedures guarantees that the approximate equivalence expressed in (2.41) is fulfilled, leading to an accurate estimate of the link performance in terms of the PER.

In the IEEE 802.11ac, 10 MCSs (coding rate from 1/2 to 5/6, BPSK to 256-QAM) are specified [WG813] (see Appendix D for more details on the 10 MCSs). To further enhance the accuracy of the effective SINR mapping for higher-order modulation formats, such as 64-QAM and 256-QAM, we carry out a two-dimensional calibration, turning (2.43) into

$$(\beta_1^{(\text{opt})}, \beta_2^{(\text{opt})}) = \arg \min_{(\beta_1, \beta_2)} \left\{ \sum_{k=1}^{N_c} \left| \log(\rho_{\text{eff}}^{(k)}(\beta_1, \beta_2)) - \log(\rho_m^{(k)}) \right|^2 \right\}. \quad (2.44)$$

The PER versus SNR curves for all the 10 IEEE 802.11ac MCSs over the AWGN channel are obtained via link-level simulations and are shown in Figure 2.4. These curves play an important role in the parameter calibration of the EESM scheme as well as the link-to-system mapping itself.

In addition, a fast link adaptation procedure is adopted in our simulator such that one of the 10 specified MCSs [WG813] is selected according to the link quality reflected by the estimates of the PER. Here the threshold PER for the MCS switching is set to 0.01 [JKWF10], [IST07]. Finally, the PHY throughput with the PHY preamble taken into account is calculated by using the estimate of the PER for a channel realization with the suitable MCS applied. We present the block diagram of the system-level simulator described above in Figure 2.5.

## 2.7. Simulation results

In the following, simulation results of 80 MHz transmissions are shown. Table 2.2 presents the corresponding OFDM parameters [WG813]. The noise power density is calculated assuming room temperature 290 K as the noise temperature. The IEEE 802.11ac channel Model D

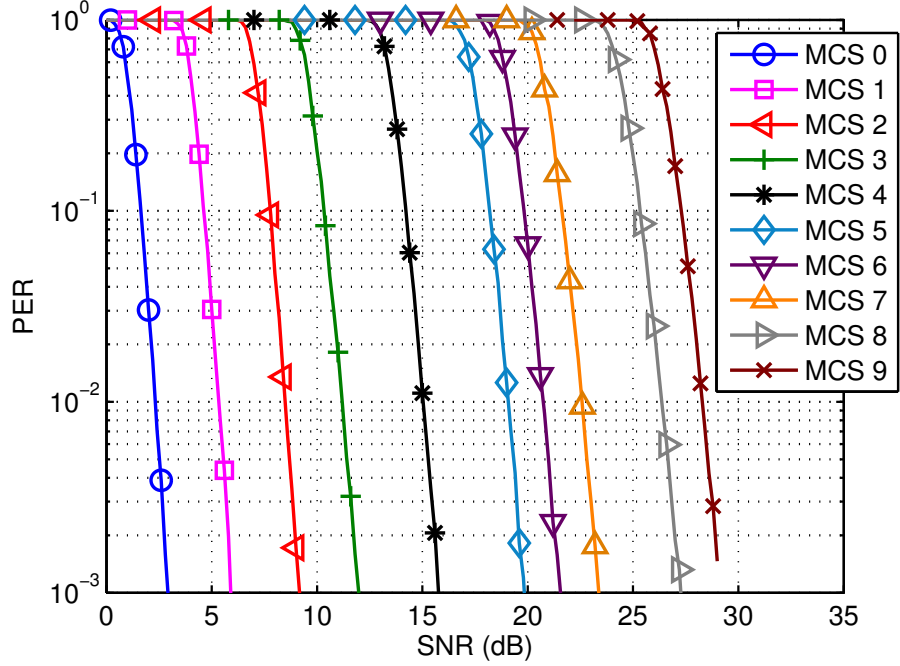


Figure 2.4.: PER versus SNR curves for SISO transmissions over the AWGN channel for the 10 IEEE 802.11ac MCSs; the SNR is defined as  $E_s/N_0$ , where  $E_s$  represents the symbol energy, and  $N_0$  denotes the noise spectral density



Figure 2.5.: Block diagram of the system-level simulator

that represents an indoor scenario [IEE04] is adopted. The BS is equipped with 8 transmit antennas [WG813], i.e.,  $M_T = 8$ . The transmit power is set to 25 dBm for all the plots of the Complementary Cumulative Distribution Function (CCDF) of the throughput. If not specifically stated, the size of the Physical Layer Service Data Unit (PSDU) that is the PHY payload is set to 500,000 B (Bytes) in the simulations.

First, a 16-user scenario is considered. Here the maximum allowed SDMA group size is 4



Table 2.2.: IEEE 802.11ac OFDM parameters (80 MHz transmission)

Parameter	Value
carrier frequency	5.21 GHz
total bandwidth	80 MHz
number of data subcarriers	234
subcarrier spacing	0.3125 MHz
symbol duration	4 $\mu$ s
length of the cyclic prefix	800 ns

[WG813], i.e.,  $K_{\max} = 4$ . The BS transmits 2 spatial streams to each of the  $K$  users selected by the scheduling algorithm, i.e.,  $d_i = 2$ , where  $i = 1, 2, \dots, K$ . Among the 16 users, there are 12 users each of which is equipped with 2 receive antennas, while two of the other users have 3 receive antennas each and the remaining two have 4 receive antennas each. Note that under such an antenna configuration, the relation between the number of transmit antennas at the BS  $M_T$  and the total number of receive antennas at the selected users  $M_R$  is arbitrary. In such a scenario, we compare our proposed transmission strategy, EMC-ProSched combined with LP-GMD or LoCCoBF to two others, the Round Robin scheduling scheme combined with the FlexCoBF algorithm and the RBD algorithm, respectively. Note that in the proposed transmission strategy as summarized in Table 2.1, after the EMC-ProSched algorithm determines the user group that will be served, LP-GMD is employed to perform the precoding when  $M_T \geq M_R$ , while the LoCCoBF algorithm deals with the opposite case, i.e.,  $M_T < M_R$ . Figure 2.6 presents the CCDF of the system throughput for the aforementioned three transmission strategies. We observe that the proposed transmission strategy yields the best performance. This is due to fact that the proposed EMC-ProSched is a much more effective scheduling algorithm by applying a novel scheduling metric inspired by the link-to-system mapping. Together with well-calibrated parameters, it contributes to an accurate prediction of the performances of multi-carrier transmissions. By comparison, the Round Robin scheme selects a fixed number of users (here set to  $K_{\max} = 4$ ) every time slot by cycling through the 16 users one by one in the system without taking into account the spatial correlation of the users. Moreover, the benefits of the proposed transmission strategy partially come from the precoding stage as well. The LP-GMD algorithm enables an effective equal MCS implementa-

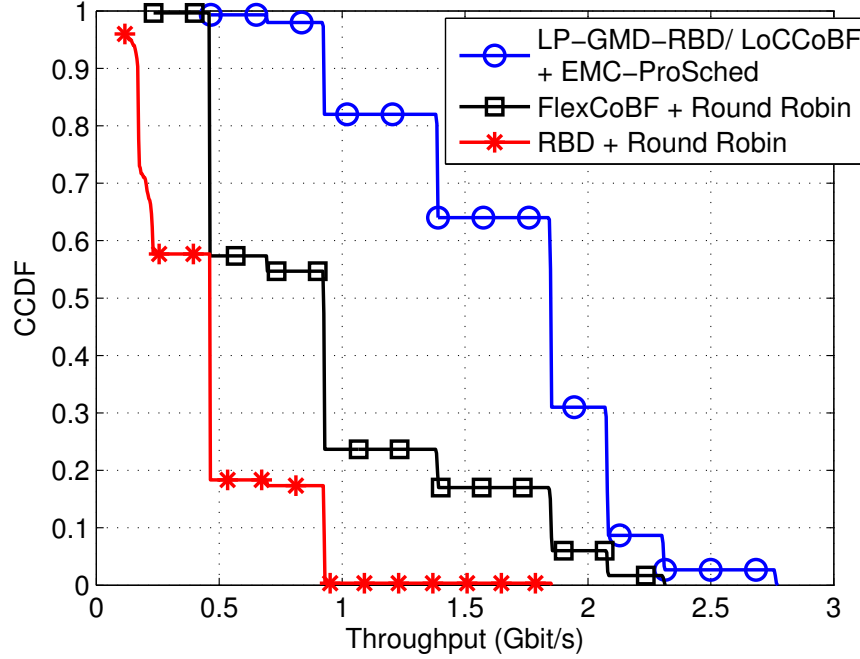


Figure 2.6.: CCDF of the system throughput of a 16-user scenario with the PSDU size as 500,000 B when the proposed transmission strategy is employed

tion over the spatial streams of each user, and a joint optimization of the transmit and receive beamformers is involved in the LoCCoBF algorithm. The proposed two algorithms are superior to their counterparts in the other two transmission strategies. Furthermore, the dynamic selection of the precoding algorithm also counts as one of the advantages of our developed transmission strategy. In addition, the fairness extension of the scheduling metric expressed in (2.12) is adopted. Figure 2.7 depicts the probability of transmission with respect to each of the 16 users in case of Round Robin and EMC-ProSched as the scheduling algorithm, respectively. We can see that by taking into account the scheduling results in the previous 20 time slots, the EMC-ProSched scheme guarantees the scheduling fairness in the sense that each user is served at a similar probability.

In the second and the third experiments, we concentrate on the scheduling stage of the transmission strategy. Note that in the EMC-ProSched algorithm, a sub-optimum tree-based sorting scheme is employed to avoid the prohibitive complexity of the optimum exhaustive search among all possible user combinations. Here, a comparison is made between the proposed EMC-ProSched and a “special” version of EMC-ProSched where the candidate user groups

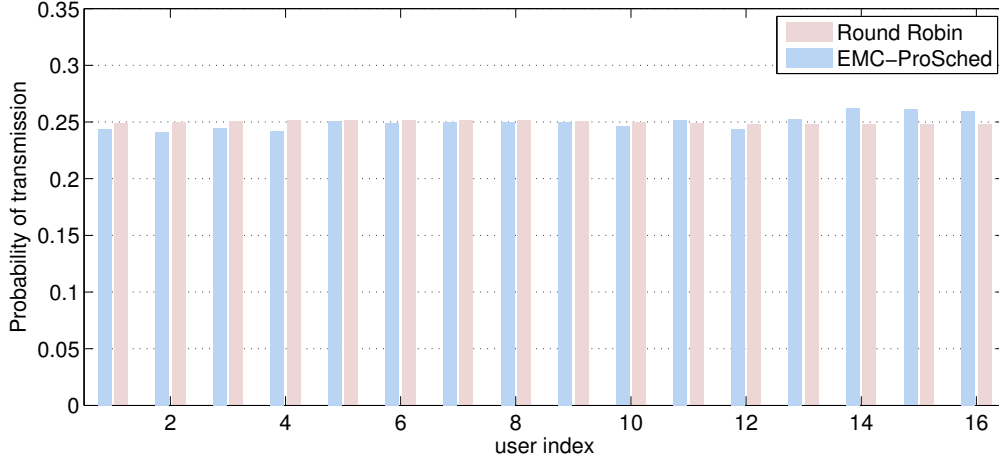


Figure 2.7.: Fairness comparison between Round Robin and EMC-ProSched in a 16-user scenario

are determined by an exhaustive search while keeping the calculation of the scheduling metric unchanged. In addition, the Round Robin scheme is also considered in the comparison. A 16-user scenario is simulated, and the scheduling algorithms serve to select 4 users at a time. Each of the 16 users is equipped with 2 receive antennas, i.e.,  $M_{R_i} = 2$ ,  $i = 1, 2, \dots, 16$ . Here 2 spatial streams are transmitted to each of the 4 users selected by the scheduling algorithm. The two versions of the LP-GMD algorithm, LP-GMD-BD and LP-GMD-RBD, are employed as the precoding algorithm. Figure 2.8 presents the performance comparison in terms of the system throughput versus the transmit power. In EMC-ProSched, by employing the tree-based sorting algorithm, the number of calculations of the scheduling metric for each channel realization is  $\sum_{k=1}^{K_{\max}} (N - k + 1)$ . By contrast, the exhaustive search of all possible user combinations with respect to the user group sizes that do not exceed  $K_{\max}$  requires  $\sum_{k=1}^{K_{\max}} \binom{N}{k}$  calculations of

the scheduling metric, where  $\binom{n}{r} = \frac{n!}{(n-r)!r!}$  represents the number of possible combinations of  $r$  objects from a set of  $n$  objects, and  $n!$  denotes the factorial of  $n$ . Considering an example where  $K_{\max} = 4$ , and the total number of users in the multi-user MIMO downlink setting ranges from 5 to 100, we plot the number of calculations of the scheduling metric in case of EMC-ProSched and the exhaustive search, respectively, in Figure 2.9. It can be easily seen that the exhaustive search leads to a much higher complexity compared to the tree-based sorting scheme used in EMC-ProSched. On the other hand, in Figure 2.8, we can see that the gap

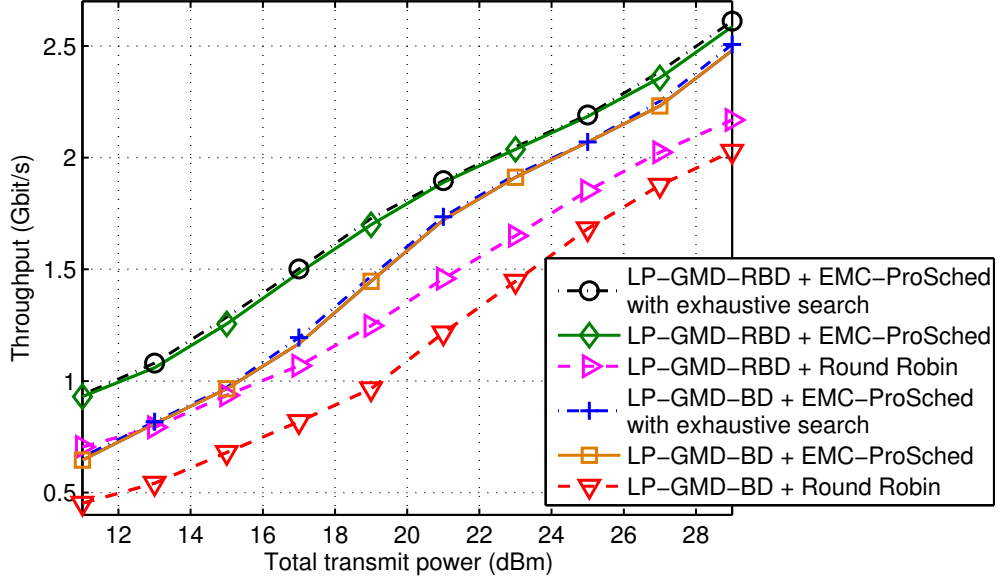


Figure 2.8.: System throughput of a 16-user scenario with the PSDU size as 500,000 B where EMC-ProSched, EMC-ProSched with exhaustive search, and Round Robin are compared

between our EMC-ProSched with the low-complexity tree-based sorting scheme and the version with the exhaustive search is very small, indicating that the EMC-ProSched algorithm finds a very good trade-off between the complexity and performance. Moreover, this gap on the other hand implies the effectiveness of the designed scheduling metric for multi-carrier systems. Also, we can see that the proposed EMC-ProSched algorithm significantly outperforms the Round Robin scheme. It is worth mentioning that, in this scenario, the original ProSched algorithm [FDH07] cannot be employed as totally 3744 (16 users with 234 data carriers) virtual users need to be considered, and the complexity is unaffordable in practice. In addition, ProSched assigns subcarriers rather than real users into an SDMA group, and this feature is not compatible with the IEEE 802.11ac standard [WG813].

We further make a comparison of EMC-ProSched and another scheduling algorithm proposed in [SK10] (in Table II of [SK10], the antenna selection procedure is not considered) which selects user groups also based on the spatial correlation of the users. To distinguish with the previously presented examples, a 64-user scenario is simulated. EMC-ProSched and the scheduling scheme in [SK10] are employed to select suitable SDMA user groups, while LP-GMD-BD and LP-GMD-RBD are used as the precoding algorithm. The other simulation parameters are the same as in the second experiment. We plot the system throughput with

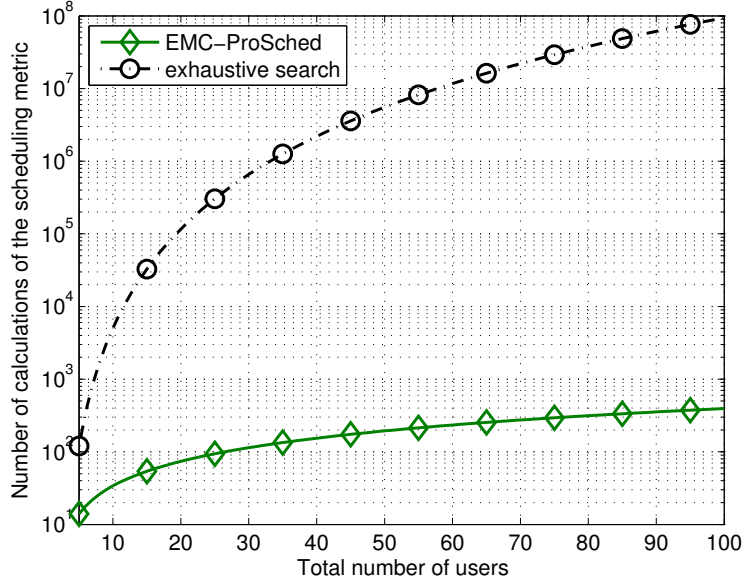


Figure 2.9.: Comparison of the number of calculations of the scheduling metric (considering one channel realization) in case of EMC-ProSched that employs the tree-based sorting scheme and the exhaustive search of all possible user combinations

respect to different transmit powers in Figure 2.10. It can be observed that the proposed EMC-ProSched algorithm provides a better performance compared to the user selection scheme developed in [SK10]. As both schemes take into account the spatial correlation of the users when selecting a user group, the superiority of EMC-ProSched to a large extent results from the fact that it uses a more effective scheduling metric for multi-carrier systems. On the other hand, EMC-ProSched employs the orthogonal projection such that the complexity caused by computing SVDs is avoided when analyzing the spatial correlation of users in candidate SDMA user groups.

To further evaluate the performance of the proposed LP-GMD scheme, we consider the same 16-user scenario as for Figure 2.8 but fix the scheduling algorithm to EMC-ProSched. It serves to select 4 users out of the total 16 users, and precoding is performed on the selected user group by employing BD [SSH04], RBD [SH08], and the proposed two versions of the LP-GMD algorithm LP-GMD-BD and LP-GMD-RBD, respectively. The PSDU size is set to 100,000 B in this example. As shown in Figure 2.11, we compare the CCDF of the system throughput when these precoding algorithms are applied. It can be found that the LP-GMD schemes provide much higher system throughput compared to BD and RBD. The maximum

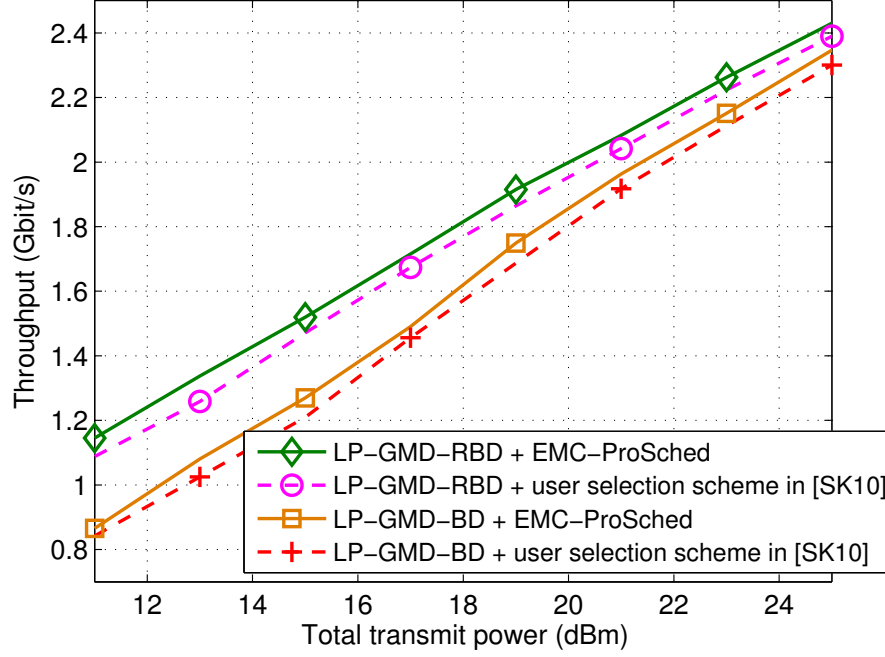


Figure 2.10.: System throughput of a 64-user scenario with the PSDU size as 500,000 B where EMC-ProSched and the user selection scheme in [SK10] are compared

throughput that can be achieved when LP-GMD is employed is around 2.7 Gbps.

We now continue to examine the MMSE-based power loading strategy developed for the LP-GMD schemes. In a 32-user scenario, EMC-ProSched and the Round Robin scheme, respectively, are employed to assign 4 users to an SDMA group. Each of the 32 users is equipped with 2 receive antennas. The BS transmits 2 spatial streams to each of the 4 selected users. Figure 2.12 presents the system throughput when LP-GMD-RBD with equal power allocation across the users and with the MMSE-based power loading presented in Section 2.4.4 (represented by “LP-GMD-RBD PL” in the legend of Figure 2.12) as well as the RBD algorithm are employed. It can be seen that the power loading provides a noticeable gain over the LP-GMD-RBD scheme with equal power allocation. As pointed out already in Section 2.4.4, the proposed MMSE-based power loading strategy helps to reduce the amount of padding bits due to the implementation of unequal MCSs across different users by balancing the power assigned to these users. Therefore, the performance gain of the LP-GMD schemes with the MMSE power loading partially comes from the reduction of the power loss due to the overhead, i.e., an improvement of the power utilization efficiency. On the other hand, by enhancing the

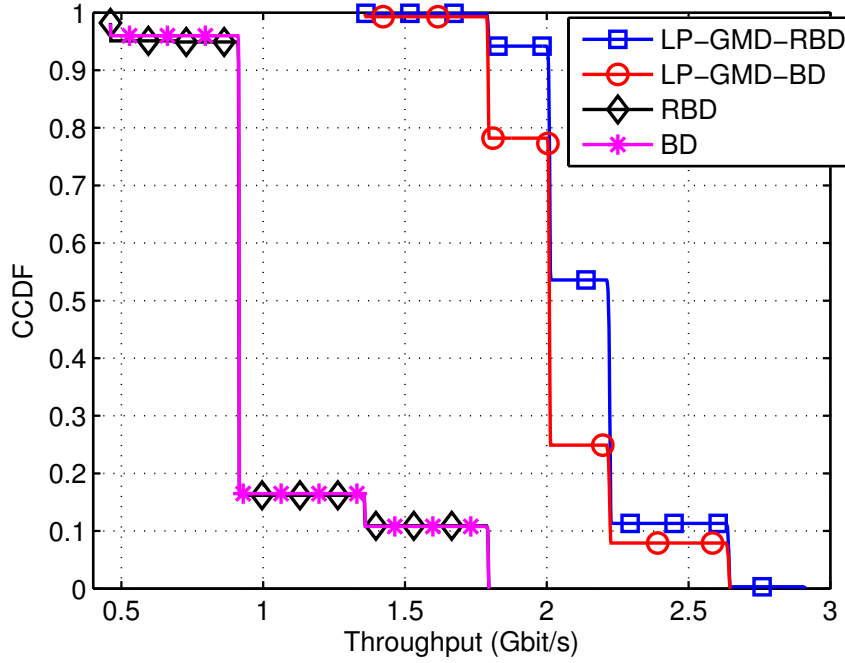


Figure 2.11.: CCDF of the system throughput when LP-GMD is employed for a 16-user scenario with the PSDU size as 100,000 B and EMC-ProSched as the scheduling algorithm

“weak” users, the MMSE-based power loading scheme helps to solve the problem that the PER performance is dominated by that of the “weak” users. Similarly as observed in Figure 2.11, the proposed LP-GMD-RBD greatly outperforms the RBD algorithm. Also, in such a 32-user scenario, the superiority of EMC-ProSched over the Round Robin Scheme is even more pronounced.

In the last experiment, with the scheduling algorithm fixed to EMC-ProSched, a comparison between the proposed LoCCoBF and another iterative linear precoding algorithm FlexCoBF [SRH10b] is presented. The EMC-ProSched algorithm serves to select 4 users out of the total 16 users at a time. The BS transmits 2 spatial streams to each of the 4 users selected by EMC-ProSched. Each user has 4 receive antennas. Thus, in this scenario, the total number of receive antennas of the users served at a time is 16 and exceeds the number of transmit antennas at the BS. The CCDF of the system throughput for FlexCoBF (BD as the precoding algorithm and MMSE receiver is adopted) [SRH10b] and the proposed LoCCoBF both employed in combination with the proposed EMC-ProSched algorithm is presented on the left-hand side of Figure 2.13. It can be observed that the LoCCoBF algorithm outperforms FlexCoBF. The reason is that instead of randomly initializing the receive beamforming matrices as in Flex-

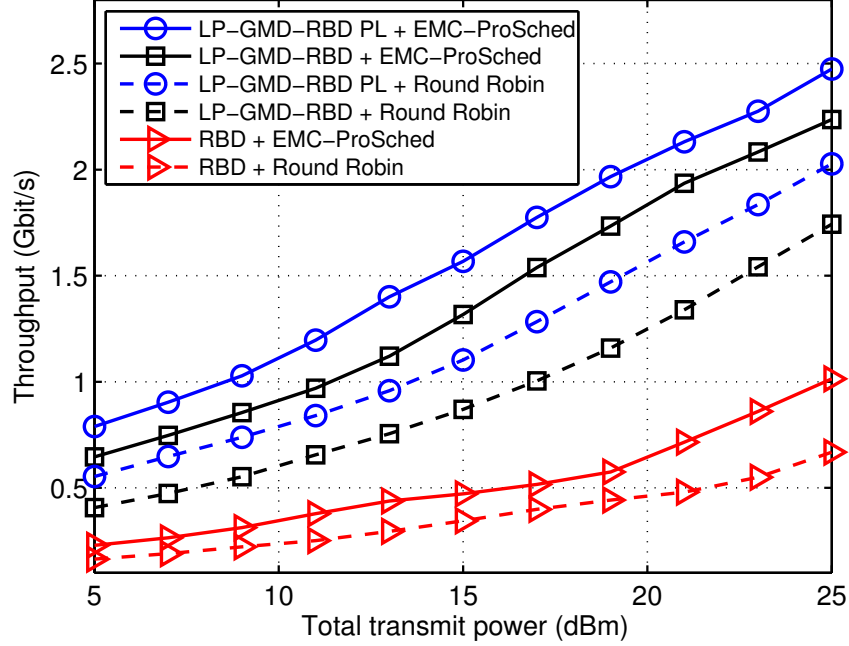


Figure 2.12.: System throughput when LP-GMD-RBD is employed for a 32-user scenario with the PSDU size as 500,000 B with and without power loading (“LP-GMD-RBD PL” represents LP-GMD-RBD with the MMSE-based power loading in the legend)

CoBF, the proposed LoCCoBF algorithm uses the receive beamforming matrices calculated for the previous subcarrier and thus exploits the correlation of neighboring subcarriers.

On the right-hand side of Figure 2.13, we further show the comparison between the proposed LoCCoBF algorithm and FlexCoBF in terms of the CCDF of the number of iterations. The maximum number of iterations is set to 50 in this experiment. The average number of iterations required by LoCCoBF is 9, while for FlexCoBF it is 14. Since the computational complexity per iteration is similar for LoCCoBF and FlexCoBF, we can see that the LoCCoBF algorithm requires a lower complexity while providing a better performance.

## 2.8. Summary

In this chapter, we have presented an efficient and flexible transmission strategy for multi-carrier multi-user MIMO downlink systems consisting of a spatial scheduling algorithm and two precoding algorithms. The spatial scheduling algorithm EMC-ProSched is able to assign the users efficiently by using a novel and effective scheduling metric based on the philosophy



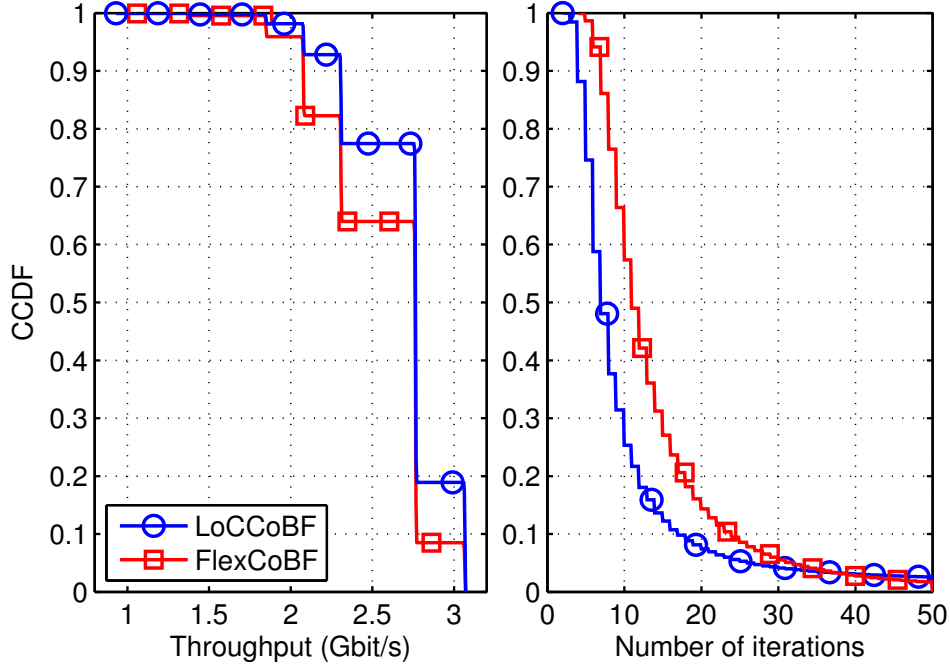


Figure 2.13.: CCDF of the system throughput and the number of iterations in a 16-user scenario when LoCCoBF is employed with the PSDU size as 500,000 B and EMC-ProSched as the scheduling algorithm

of the link-to-system mapping. A linear precoding algorithm, called LP-GMD, is proposed to allow the transmission of multiple data streams to each user with the same MCS and thereby reduces the required signaling overhead compared to the case where unequal MCSs are employed on different data streams. BD and RBD versions of the LP-GMD algorithm are developed, while other suitable MUI mitigation schemes can also be flexibly adopted in LP-GMD. An MMSE-based power loading algorithm is further introduced in the LP-GMD schemes which assigns transmit power across different users to achieve a higher power efficiency by reducing the number of padding bits. The second proposed precoding algorithm LoCCoBF also contributes to the flexibility of the proposed transmission strategy, as it is able to suppress the MUI in scenarios where the number of transmit antennas at the BS is smaller than the total number of receive antennas at the user terminals. In order to examine the proposed transmission strategy, a system-level simulator has been developed under the IEEE 802.11ac framework with a link-to-system interface as well as a fast link adaptation procedure included. Simulation results indicate that the proposed transmission strategy outperforms the analyzed

state-of-the-art transmission strategies and can achieve a very high system throughput.

---

### 3. Introduction of Filter Bank-based Multi-Carrier modulation (FBMC)

This chapter provides an introduction of Filter Bank-based Multi-Carrier modulation (FBMC). It is regarded as an alternative multi-carrier modulation scheme to Orthogonal Frequency Division Multiplexing with the Cyclic Prefix insertion (CP-OFDM) which is considered in Chapter 2. We start with an overview of intriguing features of FBMC that give rise to its applications in various fields. Then, fundamentals of Filter Bank-based Multi-Carrier with Offset Quadrature Amplitude Modulation (FBMC/OQAM) from the point of view of signal processing are provided by presenting the data model of an FBMC/OQAM-based Single-Input Single-Output (SISO) system. To further pave the way for the subsequent chapters, we address challenges in the design of transmit-receive processing schemes for FBMC/OQAM-based Multiple-Input Multiple-Output (MIMO) systems.

#### 3.1. Motivation

Multi-carrier transmissions provide high data rates demanded by modern communications and have the capability of combating hostile propagation conditions. CP-OFDM is a very popular multi-carrier modulation scheme that has been widely adopted in a variety of communication standards and products, e.g., the Wireless Local Area Network (WLAN) radio interfaces IEEE 802.11a, g, n, ac as well as Digital Video Broadcasting-Terrestrial (DVB-T). It features great robustness against multi-path fading and an efficient implementation. By turning the frequency selective channel into parallel flat fading subchannels, simple one-tap equalizers are employed at the receiver of CP-OFDM-based systems. Nevertheless, CP-OFDM suffers from high out-of-band leakage due to the use of a rectangular pulse in the time domain for shaping filtering. The insertion of a CP is required in CP-OFDM-based systems, leading to a reduced spectral efficiency. Moreover, CP-OFDM is sensitive to synchronization errors. It is thus not a suitable multi-carrier modulation scheme for communication scenarios where perfect synchronization is hardly guaranteed, e.g., the uplink of multi-user MIMO systems. These issues with CP-OFDM give rise to the trend of the development of new advanced multi-carrier modulation schemes. A very promising alternative to CP-OFDM that has attracted great research attention is FBMC, our focus for the rest of the first part of this thesis.

FBMC employs spectrally well-concentrated synthesis and analysis filter banks at the transmitter and at the receiver [SSL02], [Bel01], respectively. This feature contributes to its concentrated spectrum and thus a much lower out-of-band radiation compared to CP-OFDM. The comparison between the Power Spectral Density (PSD) of FBMC and that of CP-OFDM is depicted in Figure 3.1. Consequently, FBMC is endowed with a strong robustness against

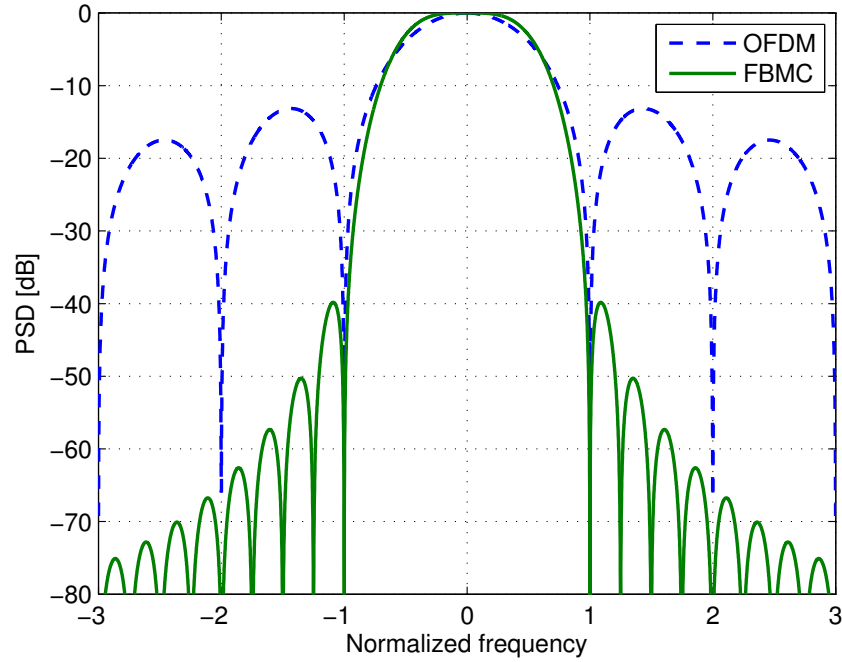


Figure 3.1.: Comparison of the power spectral density of FBMC and CP-OFDM; the normalized frequency is obtained by dividing the actual frequency by the subcarrier spacing

time and frequency misalignments. It also renders an effective and flexible use of spectrum holes. These merits of FBMC have sparked significant research interest in its applications in various contexts, e.g., asynchronous scenarios [FPT08], [SSWB<sup>+</sup>11], and cognitive radio networks [SB10]. FBMC/OQAM is one of the FBMC schemes which has been investigated most in the literature. FBMC/OQAM-based systems exhibit a higher spectral efficiency compared to their CP-OFDM-based counterparts, as the insertion of the CP is not required. As the focus of the following chapters in the first part of the thesis, the basics of FBMC/OQAM are introduced in detail in Section 3.2. It is also worth noting that FBMC plays an important role in several international projects [PHY], [EMP], [5GN], [MET].

The European project EMPHAtiC [EMP] has investigated the application of FBMC in future

Professional Mobile Radio (PMR) systems [RBB<sup>+</sup>13]. Public safety organizations resort to PMR systems for everyday operational needs and exceptional planned events such as sports and cultural events. They are also used for exceptional unplanned events, e.g., for disaster relieve. Currently deployed PMR systems, e.g., TETRA and TETRAPOL in Europe and a large part of the world, mainly offer low data rate services, such as voice communications. The limited achievable throughput is due to a small frequency bandwidth. Unfortunately, with only narrow-band transmissions deployed, these current PMR networks cannot support critical missions and services requiring much higher data throughputs, such as video streaming, high-resolution file transfer, enhanced transfer of medical aid information. Such a significant increase of the demand for higher data throughputs is illustrated in Figure 1.1. In commercial communication networks, broadband techniques have long been enabled to deliver high data rates. Hence, to keep up with the evolution of data throughput requirements, current PMR systems have to be upgraded to support broadband transmissions. The EMPhAtiC project [EMP] has addressed this trend and has proposed a novel broadband PMR concept as depicted in Figure 3.2. Although acquiring new frequency bands is one way to accommodate broadband

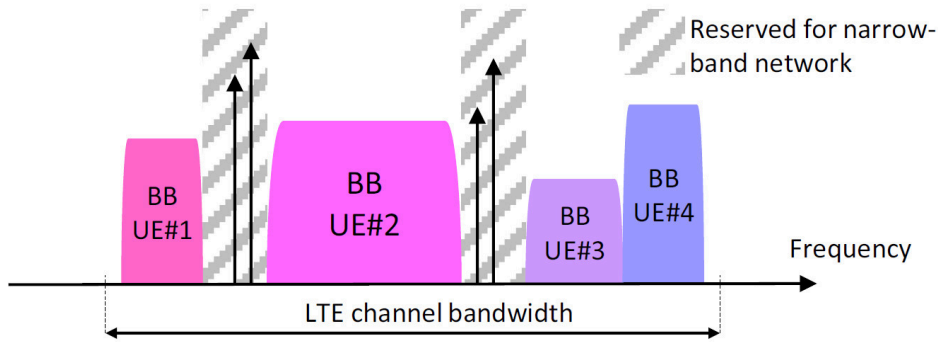


Figure 3.2.: Future PMR broadband in coexistence and cohabitation with current systems [RBB<sup>+</sup>13]; BB – broadband, UE – user equipment

communication services, building a coexistence scenario is the core idea here, i.e., broadband data services are fitted into a frequency band that has been already occupied by narrow-band networks. This concept features an effective utilization of spectrum fragments but consequently demands a multi-carrier modulation scheme that leads to an agile spectrum. Otherwise, as indicated in Figure 3.2, large guard bands would be necessary to avoid the interference to adjacent systems, resulting in undesired loss of spectral efficiency. With a well-concentrated spectrum, FBMC has been regarded as the perfect fit for advanced broadband PMR networks.

### 3.2. Fundamentals of FBMC/OQAM

As addressed previously, FBMC/OQAM is the focus of the remaining chapters in the first part of the thesis. In the sequel, we start by presenting the data model of an FBMC/OQAM-based SISO setting to introduce the basics of FBMC/OQAM that are crucial for our discussions in the following chapters.

On the transmitter side of a SISO FBMC/OQAM-based system, the real part and the imaginary part of the QAM modulated data symbols  $s_k[m]$  are staggered by half of the symbol period  $T/2$  as illustrated in Figure 3.3. The resulting data symbol  $d_k[n]$  on the  $k$ -th

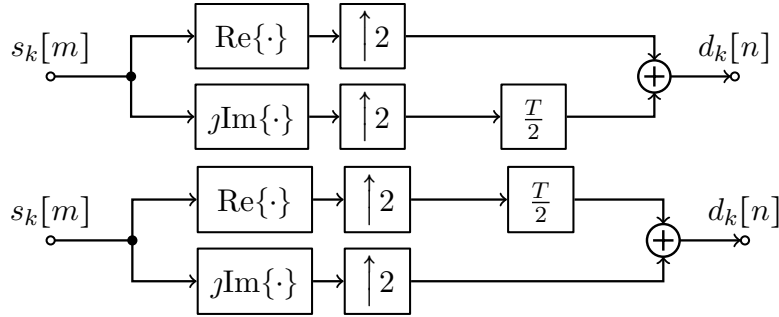


Figure 3.3.: OQAM staggering for subcarriers with odd indices (top) and even indices (bottom)

subcarrier and at the  $n$ -th time instant (with the sampling period as half of the symbol period  $T/2$ ) fulfills

$$\begin{aligned} d_{2\ell-1}[2m-1] &= \text{Re}\{s_{2\ell-1}[m]\} \\ d_{2\ell-1}[2m] &= j\text{Im}\{s_{2\ell-1}[m]\} \\ d_{2\ell}[2m-1] &= j\text{Im}\{s_{2\ell}[m]\} \\ d_{2\ell}[2m] &= \text{Re}\{s_{2\ell}[m]\}. \end{aligned}$$

Thus, for the case where  $(k+n)$  is even, the data symbol  $d_k[n]$  is real-valued. On the other hand, when  $(k+n)$  is odd,  $d_k[n]$  is pure imaginary. As we will see later, this is a very important property of the data symbols after the OQAM staggering in FBMC/OQAM-based systems. Its illustration is provided in Figure 3.4.

Next, signals for different subcarriers are multiplexed by a Synthesis Filter Bank (SFB). At the receiver, signals from the subchannels are separated by an Analysis Filter Bank (AFB) as shown in Figure 3.5. It is worth mentioning that the FBMC/OQAM-based system is equivalent to a modulated transmultiplexer. Thus, the SFB and the AFB can be efficiently implemented

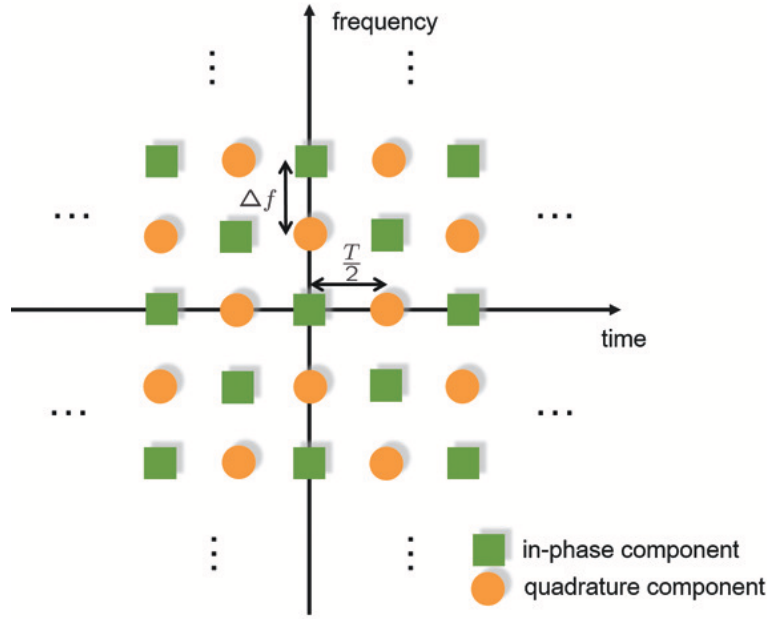


Figure 3.4.: Illustration of the data symbols after the OQAM staggering in FBMC/OQAM-based systems;  $\Delta f$  represents the subcarrier spacing, whereas  $T$  denotes the symbol period

based on the Inverse Fast Fourier Transform (IFFT) and the Fast Fourier Transform (FFT), respectively [SSL02]. As the implementation issues of FBMC/OQAM are beyond the scope of this chapter, the reader is referred to [Bel10] and [SSL02] for more details. The pulse shaping

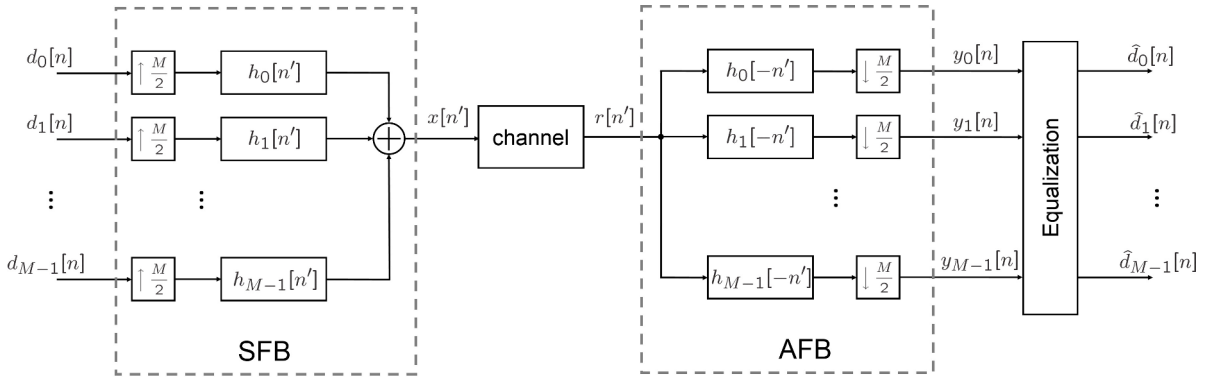


Figure 3.5.: Block diagram of a SISO FBMC/OQAM system

filter of the  $k$ -th subcarrier takes the following form

$$h_k[l_P] = h_P[l_P] \exp\left(j \frac{2\pi}{M} k \left(l_P - \frac{L_P - 1}{2}\right)\right),$$

$$l_P = 0, 1, \dots, L_P - 1, \quad (3.1)$$

where  $h_P[l_P]$  is the prototype filter of length  $L_P$ , and  $M$  denotes the number of subcarriers. The length of the prototype filter is  $L_P = KM + c$ , where  $K$  represents the overlapping factor, and typical values for  $c$  are  $\{-1, 0, 1\}$ . As the overlapping factor is larger, the pulse in the frequency domain shows a more favorable decaying behavior. In the literature, several prototype filters with a well-confined spectrum for  $K \leq 4$  have been designed [SSL02], [Bel11].

Let  $h^{(\text{ch})}$  represent the impulse response of the propagation channel between the transmitter and the receiver. Note that the signal on the  $k$ -th subcarrier is contaminated by interference from the  $(k-1)$ -th as well as the  $(k+1)$ -th subcarrier and noise. The equivalent channel impulse response for the signal that is transmitted on the  $\ell$ -th subcarrier and passed through the analysis filter for the  $k$ -th subcarrier can be expressed as

$$h_{\ell,k}[n] = \left[ h_\ell[l_P] * h^{(\text{ch})}[l_P] * h_k[-l_P] \right]_{l_P = n \frac{M}{2}} \quad (3.2)$$

with  $*$  representing the discrete convolution. Here the effects of the transmit filter, the propagation channel, the receive filter as well as the upsampling and downsampling operations are included. The resulting number of taps of this equivalent channel is

$$Q = \left\lceil \frac{2(L_P - 1) + L_{\text{ch}}}{M/2} \right\rceil, \quad (3.3)$$

where  $L_{\text{ch}}$  denotes the length of the channel impulse response.

The received signal on the  $k$ -th subcarrier and at the  $n$ -th time instant is written as

$$y_k[n] = \sum_{\ell=k-1}^{k+1} h_{\ell,k}[n] * d_\ell[n] + n_k[n], \quad (3.4)$$

where  $n_k[n]$  denotes the noise component. By comparison, for CP-OFDM-based systems with perfect synchronization, as long as the length of the CP is not smaller than the length of the propagation channel, the received signal on a certain subcarrier at a certain time instant does not suffer from either the inter-carrier interference nor the inter-symbol interference. In case of FBMC/OQAM-based systems, on the other hand, the degree of the frequency selectivity of the channel plays an important role in the further interpretation of the data model shown in



(3.4) and consequently the design of transmit-receive processing schemes. Let us distinguish three cases with respect to the degree of the frequency selectivity of the propagation channel as follows:

- *Highly frequency selective channels*: the channel on each subcarrier is frequency selective

In this first case, the data model remains as shown in (3.4). To mitigate the inter-carrier interference and the inter-symbol interference, over-interpolated filterbanks can be employed to introduce some redundancy that enables the complete interference cancellation [LP01]. However, due to the redundancy, the spectral efficiency is lowered. On the other hand, in critically sampled FBMC/OQAM-based systems, the inter-carrier interference and the inter-symbol interference are suppressed by resorting to multi-tap equalization techniques. Traditional equalization algorithms can be directly applied in FBMC/OQAM-based systems [FBL03], [LLS08] but suffer from a high computational complexity. By contrast, the per-subcarrier equalization schemes [ISRR07], [WBN08a], [WBN08b] [BWN09], require less computational effort. Recently, a parallel multi-stage equalizer has been proposed aiming at a good trade-off between the computational complexity and the performance [MMP13].

- *Intermediate frequency selective channels*: the channel on each subcarrier is almost flat fading

As the channel on each subcarrier can be treated as flat fading, let us denote the frequency response of the channel for the  $\ell$ -th subcarrier and the  $i$ -th time instant as  $H_\ell^{(\text{ch})}[i]$ . With the overlapping factor  $K = 4$ , the received signal  $y_k[n]$  given by (3.4) is then reformulated as

$$y_k[n] = \sum_{i=n-3}^{n+3} \sum_{\ell=k-1}^{k+1} H_\ell^{(\text{ch})}[i] \cdot c_{i,\ell} \cdot d_\ell[i] + n_k[n], \quad (3.5)$$

where  $c_{i,\ell}$  ( $\ell = k-1, k, k+1$  and  $i = n-3, \dots, n+3$ ) represent the system impulse response determined by the synthesis and analysis filters. They can be computed via

$$c_{i,\ell} = [h_\ell[l_P] * h_k[-l_P]]_{l_P=i\frac{M}{2}}. \quad (3.6)$$

When the PHYDYAS prototype filter [PHY] is employed, the coefficients  $c_{i,\ell}$  ( $\ell = k-1, k, k+1$  and  $i = n-3, \dots, n+3$ ) are presented in Table 3.1. It can be seen that the coefficient  $c_{i,\ell}$  is either real-valued or pure imaginary, and the real-valued coefficients and the pure imaginary ones (for  $(i,\ell) \neq (n,k)$ ) appear in an alternate manner along the

		Time						
		$n - 3$	$n - 2$	$n - 1$	$n$	$n + 1$	$n + 2$	$n + 3$
Frequency	$k - 1$	0.043j	-0.125	-0.206j	0.239	0.206j	-0.125	-0.043j
	$k$	-0.067	0	0.564	1	0.564	0	-0.067
	$k + 1$	-0.043j	-0.125	0.206j	0.239	-0.206j	-0.125	0.043j

Table 3.1.: Coefficients  $c_{i,\ell}$  representing the system impulse response determined by the synthesis and analysis filters [Bel10] (the PHYDYAS prototype filter [PHY] used with the overlapping factor  $K = 4$ )

time as well as the frequency direction. Now let us take one step further and write the received signal  $y_k[n]$  as

$$y_k[n] = H_k^{(\text{ch})}[n] \cdot d_k[n] + \sum_{\substack{i=n-3 \\ (i,\ell) \neq (n,k)}}^{n+3} \sum_{\ell=k-1}^{k+1} H_\ell^{(\text{ch})}[i] c_{i,\ell} d_\ell[i] + n_k[n]. \quad (3.7)$$

Here the first term is the desired signal component, whereas the second term corresponds to the inter-carrier interference as well as the inter-symbol interference, in the literature usually called intrinsic interference in FBMC/OQAM-based systems. In case of ideal propagation conditions (an AWGN channel), i.e.,  $H_\ell^{(\text{ch})}[i] = 1$ , where  $\ell = k - 1, k, k + 1$  and  $i = n - 3, \dots, n + 3$ , the received signal  $y_k[n]$  becomes

$$y_k[n] = d_k[n] + \sum_{\substack{i=n-3 \\ (i,\ell) \neq (n,k)}}^{n+3} \sum_{\ell=k-1}^{k+1} c_{i,\ell} d_\ell[i] + n_k[n]. \quad (3.8)$$

Recall the property of the data symbols after the OQAM staggering as depicted in Figure 3.4 that  $d_k[n]$  is either real-valued or pure imaginary depending on whether  $(k + n)$  is even or odd. For the case where  $(k + n)$  is even, the desired signal on the  $k$ -th subcarrier and at the  $n$ -th time instant  $d_k[n]$  is real-valued, while the terms  $c_{i,\ell} d_\ell[i]$  in (3.8) that contribute to the intrinsic interference are pure imaginary provided that the prototype pulse satisfies the perfect reconstruction property [Bel10]. On the other hand, when  $(k + n)$  is odd, the desired signal on the  $k$ -th subcarrier and at the  $n$ -th time instant  $d_k[n]$  is pure imaginary, and the intrinsic interference is real-valued. Since these two cases are equivalent to each other, let us simply focus on the case where  $(k + n)$  is

even in the following. As the desired signal and the intrinsic interference are separated in the real domain and the pure imaginary domain, respectively, the intrinsic interference can be canceled by taking the real part of the received signal  $y_k[n]$ . This is a special type of orthogonality inherent in FBMC/OQAM-based systems.

Later in Section 3.3, we will revisit this case where the channel on each subcarrier can be treated as flat fading but considering MIMO settings. This model (represented via (3.7)) is very often used to make the design of transmit-receive processing schemes with CSIT for MIMO FBMC/OQAM systems easier to tackle while keeping the assumption on the channel frequency selectivity practical.

- *Low frequency selective channels*: the channels on neighboring subcarriers and at adjacent time instants almost stay constant

In this case, the degree of the frequency selectivity of the channel is low in the sense that the channel stays almost constant across adjacent subcarriers. It does not vary during consecutive symbol periods either, i.e.,

$$H_k^{(\text{ch})}[n] \approx H_\ell^{(\text{ch})}[i], \\ \ell = k-1, k, k+1, \quad i = n-3, \dots, n+3.$$

Consequently, taking the case where  $(k+n)$  is even as an example, the data model in case of intermediate frequency selective channels given by (3.7) can be written as

$$y_k[n] = H_k^{(\text{ch})}[n] \cdot (d_k[n] + ju_k[n]) + n_k[n] \quad (3.9)$$

with

$$u_k[n] = \text{Im} \left\{ \sum_{\substack{i=n-3 \\ (i,\ell) \neq (n,k)}}^{n+3} \sum_{\ell=k-1}^{k+1} c_{i,\ell} d_\ell[i] \right\}. \quad (3.10)$$

Here the desired signal  $d_k[n]$  and the intrinsic interference  $ju_k[n]$  are real-valued and pure imaginary, respectively. Therefore, when the propagation channel has a low degree of frequency selectivity, the data model of a SISO FBMC/OQAM system can be simplified to a large extent and is in a form quite similar to that of a CP-OFDM-based system. As long as the Channel State Information at the Receiver (CSIR) is available, after equalization, the elimination of the intrinsic interference is easily achieved by taking the real part of the resulting signal. As we will discuss in detail later in Section 3.3, this

case has been frequently considered in the literature on the receiver design for MIMO FBMC/OQAM systems.

### 3.3. MIMO techniques for FBMC/OQAM-based systems: challenges

In this section, we turn to FBMC/OQAM-based MIMO settings. In contrast to the previous section, let us start with the case of low and intermediate frequency selective channels. In a MIMO system with  $M_T$  transmit antennas and  $M_R$  receive antennas, let  $H_k^{(q,p)}[n]$  denote the frequency response of the channel between the  $p$ -th transmit antenna and the  $q$ -th receive antenna. We define the following channel matrix  $\mathbf{H}_k[n]$  for the  $k$ -th subcarrier and the  $n$ -th time instant

$$\mathbf{H}_k[n] = \begin{bmatrix} H_k^{(1,1)}[n] & H_k^{(1,2)}[n] & \cdots & H_k^{(1,M_T)}[n] \\ H_k^{(2,1)}[n] & H_k^{(2,2)}[n] & \cdots & H_k^{(2,M_T)}[n] \\ \vdots & \vdots & \ddots & \vdots \\ H_k^{(M_R,1)}[n] & H_k^{(M_R,2)}[n] & \cdots & H_k^{(M_R,M_T)}[n] \end{bmatrix} \in \mathbb{C}^{M_R \times M_T}. \quad (3.11)$$

Note that since the two cases where  $(k+n)$  is even and  $(k+n)$  is odd, respectively, are equivalent to each other. From now on, we simply focus on the former in our discussions in the sequel. In case of low frequency selective channels, based on (3.9), the  $M_R$ -dimensional received vector  $\mathbf{y}_k[n]$  is expressed as

$$\mathbf{y}_k[n] = \mathbf{H}_k[n] \cdot (\mathbf{d}_k[n] + j\mathbf{u}_k[n]) + \mathbf{n}_k[n], \quad (3.12)$$

where

$$\mathbf{u}_k[n] = \text{Im} \left\{ \sum_{i=n-3}^{n+3} \sum_{\substack{\ell=k-1 \\ (i,\ell) \neq (n,k)}}^{k+1} c_{i,\ell} \mathbf{d}_\ell[i] \right\} \in \mathbb{R}^{M_T}. \quad (3.13)$$

Here  $\mathbf{d}_k[n] \in \mathbb{R}^{M_T}$ , and  $\mathbf{n}_k[n] \in \mathbb{C}^{M_R}$  denotes the AWGN vector. The data model given by (3.12) can be further simplified by ignoring the time and frequency indices, i.e., the received vector on a certain subcarrier and at a certain time instant takes the following form

$$\mathbf{y} = \mathbf{H} \cdot (\mathbf{d} + j\mathbf{u}) + \mathbf{n}. \quad (3.14)$$

This expression looks very similar to the data model of a MIMO CP-OFDM system where the transmissions on different subcarriers can be treated as independent and parallel. The only difference is that the signal component consists of the real-valued desired signal and the pure imaginary intrinsic interference as well. It is thus intuitive to employ receive processing strategies that have been devised for MIMO CP-OFDM systems followed by a real-part extraction operation. In [ZLB10] an MMSE-based equalizer is first employed to obtain an estimate of the intrinsic interference such that it can be eliminated from the received signal. Then Maximum Likelihood (ML) detection is performed on the resulting signal. Aiming at an enhancement on the performance of the aforementioned MMSE-ML scheme [ZLB10], in [ZL11b] a recursive ML method is proposed to further exploit the output of the MMSE-ML detector, leading to a more accurate estimate of the intrinsic interference and thus a more effective interference cancellation. Focusing on the case of coded data, the two schemes mentioned above are accordingly adapted [ZL11a]. In pursuit of a reduced complexity, the partial interference cancellation approach is designed in [ZL11b], featuring a receiver composed of a tentative detector providing decisions which serve to partially cancel the interference and a Viterbi detector.

For the receiver design in FBMC/OQAM-based MIMO systems, the existence of the intrinsic interference is an obstacle. Considering the case of low frequency selective channels as in the publications mentioned above enables the formulation of the data model into (3.14). Consequently, the aforementioned special orthogonality in FBMC/OQAM-based systems that the desired signal and the intrinsic interference are separated in the real domain and the imaginary domain is still preserved and can be exploited. It is thus not necessary to resort to complicated multi-tap equalization schemes to achieve the interference mitigation. State-of-the-art methods originally devised for CP-OFDM-based MIMO systems can be applied, which facilitates the receiver design in FBMC/OQAM-based MIMO systems, e.g., the ML-based receivers for FBMC/OQAM [ZLB10], [ZL11a], [ZL11b]. In Chapter 4 of this thesis, we will also focus on the case of low frequency selective channels and discuss the application of widely linear processing in point-to-point MIMO FBMC/OQAM systems. The fact that the data symbols in FBMC/OQAM-based systems exhibit non-circularity has given rise to the exploitation of the benefits of widely linear processing. In Chapter 4, it is described in detail how the issue with the intrinsic interference is resolved and how a gain is achieved over linear processing by employing widely linear processing.

When the channel on each subcarrier can be treated as flat fading, based on (3.7), the

received vector is written as

$$\mathbf{y}_k[n] = \underbrace{\mathbf{H}_k[n]\mathbf{d}_k[n]}_{\text{desired signal}} + \underbrace{\sum_{i=n-3}^{n+3} \sum_{\ell=k-1}^{k+1} \mathbf{H}_\ell[i]c_{i,\ell}\mathbf{d}_\ell[i]}_{\text{intrinsic interference}} + \mathbf{n}_k[n], \quad (\ell, i) \neq (k, n). \quad (3.15)$$

This more practical assumption on the frequency selectivity of the channel renders the intrinsic interference mitigation more challenging. It is obviously not possible to extract a “virtual” transmitted signal component that consists of the real-valued desired signal and the pure imaginary interference as in (3.14) for the case of low frequency selective channels. Hence, the authors of [CPN13b] and [CPN13a] have proposed to exploit the CSIT and have devised a Zero Forcing (ZF)-based precoder to achieve the elimination of the intrinsic interference in point-to-point MIMO FBMC/OQAM systems. Later the philosophy of the ZF-based precoder has been applied to downlink settings of multi-user Multiple-Input Single-Output (MISO) and MIMO systems. It is combined with the Tomlinson-Harashima precoding (THP) [CPN13c] or the Block Diagonalization (BD) algorithm [CPNM13] to suppress both the intrinsic interference and the multi-user interference.

Chapter 5 and Chapter 6 of this thesis concentrate on the same scenario where the channel on each subcarrier can be treated as flat fading. FBMC/OQAM-based point-to-point MIMO systems are first considered in Chapter 5. The ZF-based precoder [CPN13b] is known to suffer from the dimensionality constraint that the number of transmit antennas  $M_T$  must not be smaller than the number of receive antennas  $M_R$ . Chapter 5 provides solutions to this problem by introducing two coordinated beamforming schemes that are able to overcome this dimensionality constraint. On the other hand, Chapter 6 is dedicated to the design of transmit-receive strategies for FBMC/OQAM-based multi-user MIMO downlink systems. There we will present three intrinsic interference mitigating coordinated beamforming (IIM-CBF) schemes that show a superiority over existing transmit-receive processing algorithms in various aspects. In addition, a novel FBMC/OQAM-based Coordinated Multi-Point (CoMP) technique will also be discussed.

In case of FBMC/OQAM-based MIMO systems with highly frequency selective channels, based on (3.4), the received signal on the  $q$ -th receive antenna, where  $q = 1, 2, \dots, M_R$ , is expressed as

$$y_k^{(q)}[n] = \sum_{p=1}^{M_T} \sum_{\ell=k-1}^{k+1} h_{\ell,k}^{(q,p)}[n] * d_\ell^{(p)}[n] + n_k^{(q)}[n], \quad (3.16)$$

where  $h_{\ell,k}^{(q,p)}[n]$  represents the equivalent channel impulse response between the  $p$ -th transmit antenna and the  $q$ -th receive antenna similar to (3.2). It incorporates the effects of the transmit filter of the  $\ell$ -th subcarrier  $h_{\ell}[l_P]$ , the propagation channel  $h^{(q,p)}[l_P]$  (between the  $p$ -th transmit antenna and the  $q$ -th receive antenna), the receive filter on the  $k$ -th subcarrier  $h_k[l_P]$  as well as the upsampling and downsampling operations. It proves to be a very tough task to mitigate the inter-carrier interference, the inter-symbol interference, and the inter-antenna interference. In [IL09], a per-subcarrier MMSE-based multi-tap equalizer has been developed, and SIC as well as ordered Successive Interference Cancellation (SIC) techniques have been adapted to the context of FBMC/OQAM to recover the transmitted data streams. On the other hand, finite impulse response per-subcarrier equalizers have been devised based on the frequency sampling approach [IILR11]. To exploit the CSIT as well, [CPN14b] has presented two joint designs of multi-tap precoders and decoders for FBMC/OQAM-based MIMO systems that are devised based on the criterion of minimizing the sum mean square error. An alternative architecture for the implementation of MIMO precoders and linear receivers has been proposed in [MG14], where multiple parallel stages are combined on a per-subcarrier level. Each stage is constructed using the successive derivatives of the prototype pulse.

The publications mentioned above have provided solutions for point-to-point MIMO transmissions in FBMC/OQAM-based systems in the presence of highly frequency selective channels. In Chapter 7 of this thesis, we focus on the more sophisticated FBMC/OQAM-based multi-user MIMO downlink. As mentioned in the previous text, the case where the channel on each subcarrier is flat fading will be considered in Chapter 6. Chapter 7, instead, turns to the case of more critical highly frequency selective propagation conditions and addresses the mitigation of the inter-carrier interference, the inter-symbol interference as well as the multi-user interference.

To this end, in Table 3.2 we provide a summary of the focuses and major outcomes of the following chapters in the first part of this thesis that are dedicated to MIMO techniques for FBMC/OQAM-based systems.

Due to the intrinsic interference inherent in FBMC/OQAM-based systems, the design of transmit processing and receive processing schemes appears to be more complicated than that for CP-OFDM-based systems. Especially when the propagation channels exhibit severe frequency selectivity, sophisticated algorithms are required for the interference mitigation, demanding more computation effort compared to CP-OFDM-based systems. In spite of these issues with FBMC/OQAM, it is still a very promising choice of multi-carrier modulation schemes in a variety of communications scenarios. In the following, let us take the uplink of multi-user MIMO systems as an example and look at the performance comparison of FBMC/OQAM and

Table 3.2.: Summary of the focuses and major outcomes of Chapters 4, 5, 6, and 7

Chapter	Scenarios	Channel frequency selectivity	Schemes
Chapter 4	point-to-point MIMO	low frequency selective	two-step receiver combining linear and widely linear processing
Chapter 5	point-to-point MIMO	intermediate frequency selective	two coordinated beamforming-based transmit-receive strategies
Chapter 6	multi-user MIMO downlink and coordinated multi-point downlink	intermediate frequency selective	three intrinsic interference mitigating coordinated beamforming schemes
Chapter 7	multi-user MIMO downlink	highly frequency selective	iterative and closed-form designs of multi-tap linear precoders and spatial receive filters

CP-OFDM in the presence of time or frequency misalignments [CLH14c]. A three-user case is illustrated in Figure 3.6. Here the  $U$  users each assigned to a group of subcarriers transmit to a single base station simultaneously. Each node is equipped with multiple antennas. A block-wise fashion of the subcarrier allocation as depicted in Figure 3.6 is adopted. Each user is assigned consecutive subcarriers, and a guard band can be employed to achieve the isolation of the transmissions from different users to the base station. Either FBMC/OQAM or CP-OFDM is used as the multi-carrier modulation scheme. As it is very difficult to ensure that the signals from different users arrive at the base station simultaneously, the exact symbol timing is usually not sufficiently warranted. In addition, frequency synchronization errors contaminate the orthogonality between subcarriers, resulting in serious performance degradation as well. Note that Carrier Frequency Offsets (CFOs) can be estimated by using training symbols in both CP-OFDM and FBMC/OQAM-based transmissions. For instance, a maximum likelihood estimator in the frequency domain was developed in [Moo94], and it helps in compensating CFOs caused by phase noise, Doppler frequency shift, and physical limitations of oscillators. However, a perfect estimation of the CFO is still unavailable, and the residual



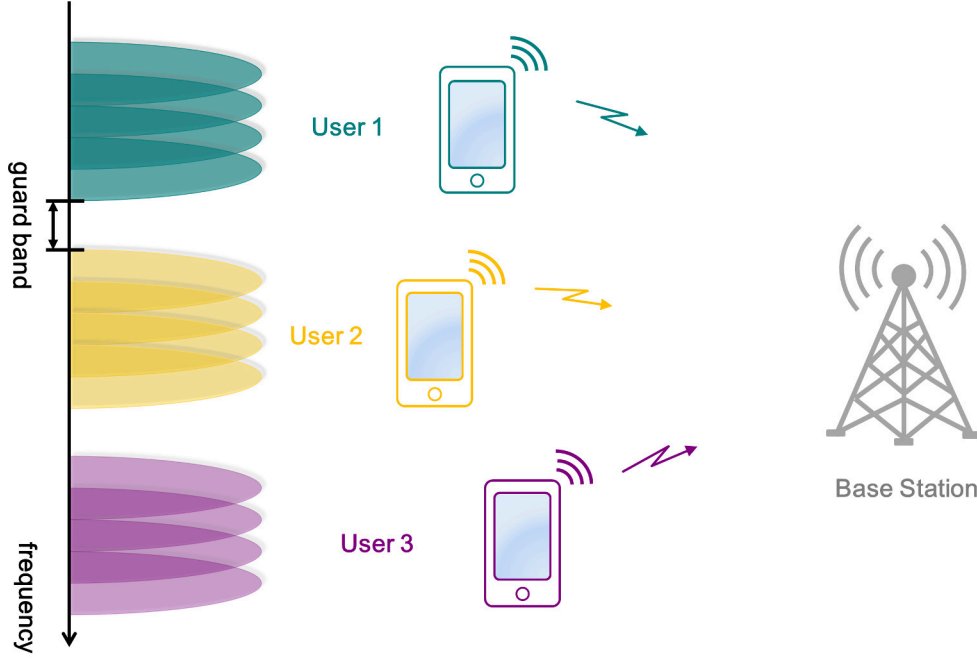


Figure 3.6.: Illustration of the multi-user MIMO uplink setting and the block-wise subcarrier allocation

CFOs remain.

First, we consider a two-user uplink scenario that suffers from symbol timing offsets. The two users and the base station are each equipped with two antennas. The ITU Pedestrian-A (Ped-A) channel [ITU97] is employed. The subcarrier spacing is 15 kHz, and the FFT size is 512. Here the length of the CP for CP-OFDM is set to  $T/8$ . In case of FBMC/OQAM, the PHYDYAS prototype filter [PHY] is used, and the overlapping factor is chosen as  $K = 4$ . The data symbols are drawn from a 4 QAM constellation. A linear MMSE receiver is employed at the base station in both the FBMC/OQAM-based and the CP-OFDM-based systems. For FBMC/OQAM-based systems, we consider the data model given by (3.14) and rely on the real-part extraction that follows the MMSE receiver to mitigate the intrinsic interference. Let  $\mathbf{H}_u$  denote the channel between the  $u$ -th user and the base station on a certain subcarrier and at a certain time instant, where  $u = 1, 2, \dots, U$ . The MMSE receiver is given by

$$\mathbf{W}_u = \left( \mathbf{H}_u \mathbf{H}_u^H + \sigma_n^2 \mathbf{I}_{M_{R_u}} \right)^{-1} \mathbf{H}_u, \quad (3.17)$$

where  $\sigma_n^2$  and  $M_{R_u}$  represent the noise variance and the number of receive antennas of the

$u$ -th user, respectively. Here the symbol timing offset with respect to each user is assumed to be uniformly distributed in the range of  $(T/8, T/4)$ . Figure 3.7 shows the corresponding numerical results in terms of the Bit Error Rate (BER) performance. The impacts of different

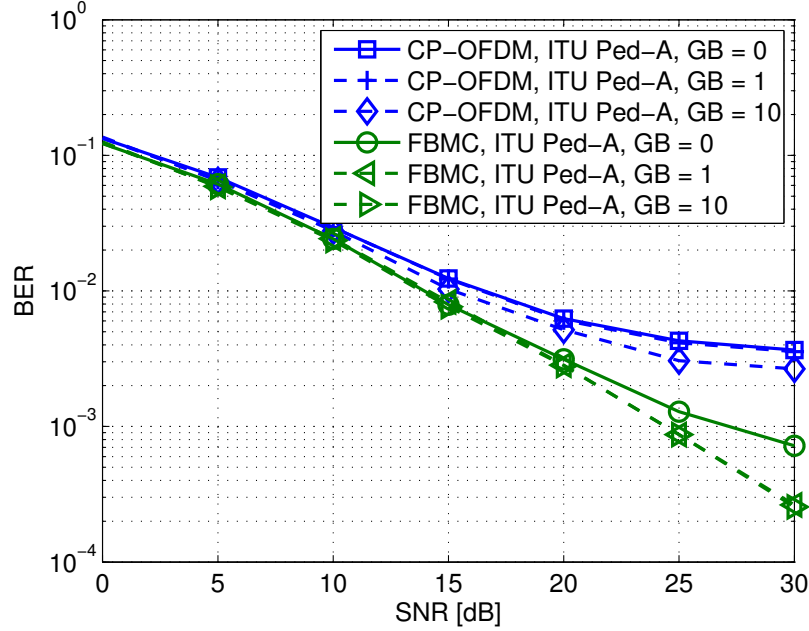


Figure 3.7.: Comparison between FBMC/OQAM and CP-OFDM for a two-user uplink scenario in the presence of symbol timing offsets in the range of  $(T/8, T/4)$  (GB - guard band in terms of the number of subcarriers)

sizes of the guard band on CP-OFDM and FBMC/OQAM are illustrated, respectively. It can be seen that when there is no guard band, FBMC/OQAM significantly outperforms CP-OFDM. With a single subcarrier as the guard band, a performance improvement is observed in case of FBMC/OQAM, while for CP-OFDM the gain compared to the zero-guard-band case is negligible. As the size of the guard band is increased to 10 subcarriers, we can only see a very slight improvement for CP-OFDM, and it still suffers from an error floor. On the other hand, it can be observed that for FBMC/OQAM when one subcarrier is used as the guard band, the performance is as good as that in the case of 10 subcarriers. These results corroborate the theory that as FBMC/OQAM-based systems are endowed with an agile spectrum (cf. Figure 3.1), guard bands with very small sizes suffice to isolate groups of subcarriers for different users or services. It has been reported in [CLH14c] that similar observations obtained in a four-user scenario also confirm that FBMC/OQAM is more robust

against symbol timing offsets compared to CP-OFDM. Moreover, the size of the guard band required to separate different groups of subcarriers is substantially smaller than that for CP-OFDM.

Now let us look at a two-user uplink setting where residual CFOs are present. Here the ITU Vehicular-A (Veh-A) channel [ITU97] is employed. The users are assumed to be perfectly synchronized in the time domain. The rest of the simulation parameters remain the same as in the previous example. In the simulations, the residual CFO (normalized by the subcarrier spacing) is drawn uniformly from the range  $(0, 0.1)$  or  $(0, 0.15)$ . Figure 3.8 shows the BER performances of CP-OFDM and FBMC/OQAM in the presence of the residual CFOs. As the maximum pos-

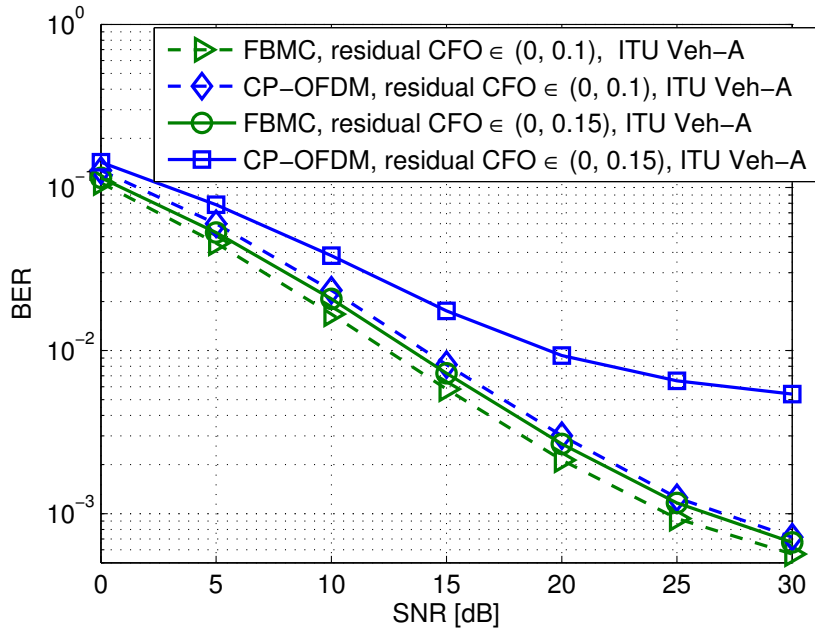


Figure 3.8.: Comparison between FBMC/OQAM and CP-OFDM for a 2-user uplink scenario in the presence of residual CFOs (normalized by the subcarrier spacing)

sible value of the residual CFOs (normalized by the subcarrier spacing) is increased to 0.15, we observe a significant performance degradation for CP-OFDM due to inter-carrier interference. By comparison, FBMC/OQAM shows a stronger resilience against frequency misalignments, as the performance loss is much smaller compared to that of CP-OFDM when the residual carrier frequency offset increases. Meanwhile, FBMC/OQAM outperforms CP-OFDM in both cases. It should be noted that in addition to the frequency misalignments, another factor that affects the performance of FBMC/OQAM is the multi-path channel considered in this

example. Since the data model given by (3.14) is only valid in case of low frequency selective channels, the single-tap linear MMSE receiver followed by the real part extraction does not suffice to effectively eliminate the intrinsic interference and thus fails to provide a satisfactory performance. When more sophisticated transmit-receive processing schemes are employed, a performance improvement can be expected. Later in Chapter 6, we will also demonstrate the robustness of FBMC/OQAM against the residual CFO in the downlink of multi-user MIMO systems.

## 3.4. Summary

We have started this chapter by addressing the motivation behind the use of FBMC. Taking the application of FBMC in future broadband PMR systems as an example, we have introduced a novel broadband PMR concept. It has been also explained that FBMC featuring a well-contained spectrum contributes to the effective utilization of the spectrum fragments demanded by the broadband PMR. Then with a focus on FBMC/OQAM, its basics have been introduced by presenting the data model of a SISO FBMC/OQAM system. Three cases with respect to the degree of the frequency selectivity of the propagation channels have been discussed, as it plays a crucial role in the formulation of the data model. The extension to MIMO settings for each case has been elaborated. The challenges in the design of MIMO transmit-receive processing techniques have been pointed out, and a brief review of state-of-the-art algorithms in each case has been provided. Moreover, we have presented a “roadmap” for the rest of the first part of the thesis specifying the motivations, the communications scenarios, and the major contributions of each chapter. Last but not the least, an asynchronous multi-user MIMO uplink scenario has been investigated as an example to demonstrate the superiority of FBMC over CP-OFDM in terms of the robustness against synchronization errors in the time domain and the frequency domain. These results justify the advantages of FBMC despite the issue that it demands the design of more complicated transmit-receive strategies compared to CP-OFDM.

---

## 4. Exploring widely linear processing in single-user MIMO FBMC/OQAM systems

Due to the fact that the data in Filter Bank-based Multi-Carrier with Offset Quadrature Amplitude Modulation (FBMC/OQAM)-based systems show non-circularity, exploiting widely linear processing potentially provides a gain over linear processing. This inspires our investigation on the use of widely linear processing in Multiple-Input Multiple-Output (MIMO) FBMC/OQAM systems in this chapter. The concept of a two-step receiver combining linear processing and widely linear processing is presented. In the first step we cancel the intrinsic interference that prevents us from exploiting the benefits of widely linear processing. Two ways of estimating the interference components are developed and compared. In the second step, a widely linear MMSE receiver is employed taking into account the residual interference. A significant gain over the linear processing-based receiver is demonstrated via numerical simulations. These results have been published in [CH13b].

### 4.1. Introduction

Filter Bank-based Multi-Carrier modulation (FBMC) is regarded as a promising alternative to Orthogonal Frequency Division Multiplexing with the Cyclic Prefix insertion (CP-OFDM). In contrast to CP-OFDM based systems, the insertion of a CP is not needed in systems employing Filter Bank-based Multi-Carrier with Offset Quadrature Amplitude Modulation (FBMC/OQAM), leading to a higher spectral efficiency. Moreover, FBMC reduces the side-lobes by using spectrally well-contained synthesis and analysis filter banks in the transmultiplexer configuration [SSL02], [Bel01]. Consequently it is able to avoid a high level of out-of-band radiation which CP-OFDM suffers from. These advantages of FBMC give rise to great research attention on its use in different contexts, such as cognitive radio and Professional Mobile Radio (PMR) networks, where an effective utilization of the available fragmented spectrum is required as explained in Chapter 3. In FBMC/OQAM systems, the real and imaginary parts of each complex-valued data symbol are staggered by half of the symbol period [SSL02]. Therefore, the desired signal and the intrinsic interference are separated in the real domain and the pure imaginary domain, respectively.

However, the intrinsic interference in Multiple-Input Multiple-Output (MIMO) FBMC/OQAM systems is known as an obstacle of applying a variety of MIMO processing techniques often

used when CP-OFDM is employed as the multi-carrier scheme. Widely linear processing is among one of them, while the use of OQAM gives rise to the potential of exploiting its benefits [GSL03]. Widely linear filtering achieves a gain compared to conventional linear filtering in the case where either the correlation of the observation with its complex-conjugated version or the correlation of the observation with the complex-conjugated desired variable is non-zero [PC95]. The transmission of real-valued data symbols over a complex-valued channel is among such scenarios. Previous works, such as [CPN13b], have brought attention to the potential of employing widely linear processing in FBMC/OQAM systems. Nevertheless, it has not been explicitly established how to deal with the presence of the intrinsic interference such that the benefits of widely linear processing can be fully exploited. On the other hand, [ZLB10] points out that mitigating the intrinsic interference enables the application of Maximum Likelihood (ML) detection in MIMO transmissions with FBMC/OQAM.

Our emphasis in this chapter is on the use of widely linear processing in MIMO FBMC/OQAM systems. A two-step receiver is proposed where linear processing and widely linear processing are combined. In the first step, a linear MMSE receiver is applied. An estimate of the intrinsic interference term is obtained either by using the output of the linear MMSE receiver directly or via a reconstruction process by employing the already detected symbols. After the intrinsic interference term is canceled, a widely linear MMSE receiver is employed in the second step. It is derived taking into consideration the residual interference. Extensive simulations are performed to evaluate the performance of the proposed two-step receiver.

This chapter is organized as follows. In Section 4.2, we first briefly introduce non-circular signals and the concept of widely linear processing followed by the data model of a point-to-point MIMO FBMC/OQAM system. Then the proposed two-step receiver is detailed in Section 4.3. Numerical results are presented in Section 4.4, before conclusions are drawn in Section 4.5.

## 4.2. Preliminaries

### 4.2.1. Non-circular signals and widely linear processing

Let us denote a complex-valued random vector by  $\mathbf{v} = \mathbf{v}_I + j\mathbf{v}_Q \in \mathbb{C}^M$ , where  $\mathbf{v}_I, \mathbf{v}_Q \in \mathbb{R}^M$  are zero-mean random vectors. The autocorrelation matrix and the pseudo-autocorrelation matrix of  $\mathbf{v}$  are written as

$$\Phi_{vv} = E\{\mathbf{v}\mathbf{v}^H\}$$

and

$$\Phi_{vv^*} = \mathbb{E}\{\mathbf{v}\mathbf{v}^T\},$$

respectively. The complex-valued random vector  $\mathbf{v}$  is proper or second-order circular if  $\Phi_{vv^*}$  is an all-zero matrix. Otherwise, it is called improper or non-circular [NM93]. By employing some modulation formats, such as Binary Phase Shift Keying (BPSK), Amplitude Shift Keying (ASK), or OQAM, the resulting data signals exhibit non-circularity which may be exploited by widely linear processing at the receiver. It is important to note that for an improper vector  $\mathbf{v}$ , its second-order statistics are described by both  $\Phi_{vv}$  and  $\Phi_{vv^*}$ . By stacking  $\mathbf{v}$  itself and its complex conjugate  $\mathbf{v}^*$ , a complex-valued augmented vector  $\tilde{\mathbf{v}}$  is obtained as

$$\tilde{\mathbf{v}} = \begin{bmatrix} \mathbf{v}^T & \mathbf{v}^H \end{bmatrix}^T \in \mathbb{C}^{2M}. \quad (4.1)$$

Moreover, the autocorrelation matrix of  $\tilde{\mathbf{v}}$ , also as an augmented version of the autocorrelation matrix of  $\mathbf{v}$ , is identified as

$$\Phi_{\tilde{\mathbf{v}}\tilde{\mathbf{v}}} = \begin{bmatrix} \Phi_{vv} & \Phi_{vv^*} \\ \Phi_{vv^*}^* & \Phi_{vv}^* \end{bmatrix} \in \mathbb{C}^{2M \times 2M}. \quad (4.2)$$

When  $\mathbf{v}$  is non-circular,  $\Phi_{\tilde{\mathbf{v}}\tilde{\mathbf{v}}}$  fully characterizes its second-order statistics. This also corresponds to the principle of widely linear filtering [PC95] where the filter outputs of the input signal and its complex conjugate are combined, leading to an improved performance.

#### 4.2.2. System model

Consider a point-to-point MIMO FBMC/OQAM system with  $M_T$  transmit antennas and  $M_R$  receive antennas. The case of low frequency selective channels is considered throughout this chapter. As already addressed in Section 3.2, the change of the channel frequency response across adjacent subcarriers and during consecutive symbol periods can be ignored. The  $M_R$ -dimensional received vector  $\mathbf{y}_k[n]$  on the  $k$ -th subcarrier and at the  $n$ -th time instant for the case where  $(k+n)$  is even is expressed as

$$\mathbf{y}_k[n] = \mathbf{H}_k[n] \cdot (\mathbf{d}_k[n] + j\mathbf{u}_k[n]) + \mathbf{n}_k[n], \quad (4.3)$$

where

$$j\mathbf{u}_k[n] = \sum_{i=n-3}^{n+3} \sum_{\substack{\ell=k-1 \\ (i,\ell) \neq (n,k)}}^{k+1} c_{i,\ell} \mathbf{d}_\ell[i]. \quad (4.4)$$

Here the PHYDYAS prototype filter [PHY] is used, and the overlapping factor is chosen to be  $K = 4$ . The coefficients  $c_{i,\ell}$  represent the system impulse response determined by the synthesis and analysis filters (cf. Table 3.1). The desired signal  $\mathbf{d}_k[n]$  is real-valued, whereas  $\mathbf{u}_k[n] \in \mathbb{R}^{M_T}$ , i.e., the intrinsic interference  $j\mathbf{u}_k[n]$  is pure imaginary provided that the prototype pulse satisfies the perfect reconstruction property [Bel10]. On the other hand, when  $(k+n)$  is odd, the transmitted signal  $\mathbf{d}_k[n]$  on the  $k$ -th subcarrier and at the  $n$ -th time instant is pure imaginary, and the received signal  $\mathbf{y}_k[n]$  takes the following form

$$\mathbf{y}_k[n] = \mathbf{H}_k[n] \cdot (\mathbf{d}_k[n] + \mathbf{u}_k[n]) + \mathbf{n}_k[n], \quad (4.5)$$

where

$$\mathbf{u}_k[n] = \sum_{\substack{i=n-3 \\ (i,\ell) \neq (n,k)}}^{n+3} \sum_{\ell=k-1}^{k+1} c_{i,\ell} \mathbf{d}_\ell[i] \mathbf{u}_k[n] \in \mathbb{R}^{M_T}. \quad (4.6)$$

Here the intrinsic interference is real-valued, and the desired signal  $\mathbf{d}_k[n]$  is pure imaginary, i.e.,  $\mathbf{d}_k[n] = j\text{Im}\{\mathbf{d}_k[n]\}$ . Alternatively, (4.5) can be reformulated into

$$\mathbf{y}_k[n] = \mathbf{H}'_k[n] \cdot (\mathbf{d}'_k[n] + j\mathbf{u}'_k[n]) + \mathbf{n}_k[n], \quad (4.7)$$

where

$$\begin{aligned} \mathbf{H}'_k[n] &= j\mathbf{H}_k[n] \\ \mathbf{d}'_k[n] &= \text{Im}\{\mathbf{d}_k[n]\} \in \mathbb{R}^{M_T} \\ \mathbf{u}'_k[n] &= -\mathbf{u}_k[n] \in \mathbb{R}^{M_T}. \end{aligned}$$

Comparing (4.3) with (4.7), it can be seen that the two cases where  $(k+n)$  is even and odd, respectively, are actually equivalent to each other. Therefore, in the sequel, we focus on the case where  $(k+n)$  is even, and the desired signal is real-valued, while the intrinsic interference is pure imaginary. The received vector on the  $k$ -th subcarrier and at the  $n$ -th time instant is then written as<sup>1</sup>

$$\mathbf{y} = \mathbf{H}(\mathbf{d} + j\mathbf{u}) + \mathbf{n} \in \mathbb{C}^{M_R}, \quad (4.8)$$

---

<sup>1</sup>In this expression the index of the subcarrier and the index of the time instant are ignored for simplicity of notation. These indices only appear when explaining the intrinsic interference caused by adjacent subcarriers and time instants (see (4.9)).



where  $\mathbf{d} \in \mathbb{R}^{M_T}$  is the desired signal on the  $k$ -th subcarrier and at the  $n$ -th time instant (alternatively written as  $\mathbf{d}_k[n]$ ),  $\mathbf{u} \in \mathbb{R}^{M_T}$  and  $j\mathbf{u}$  is the pure imaginary intrinsic interference given by

$$j\mathbf{u} = \sum_{i=n-3}^{n+3} \sum_{\ell=k-1}^{k+1} c_{i,\ell} \cdot \mathbf{d}_\ell[i], \quad j \neq k \text{ and } i \neq n. \quad (4.9)$$

Moreover,  $\mathbf{H} \in \mathbb{C}^{M_R \times M_T}$  contains the channel gains between each transmit antenna and each receive antenna, and  $\mathbf{n}$  denotes the additive white Gaussian noise vector with variance  $\sigma_n^2$ .

When a linear MMSE receiver is employed, the desired symbols can be obtained as [ZLB10]

$$\hat{\mathbf{s}} = \mathbf{W}_{\text{MMSE}}^H \cdot \mathbf{y}, \quad (4.10)$$

$$\hat{\mathbf{d}} = \text{Re}\{\hat{\mathbf{s}}\}. \quad (4.11)$$

To apply widely linear processing, the obstacle is the pure imaginary intrinsic interference. In the sequel, we devise a two-step receiver to tackle this problem such that the benefits of widely linear processing can be exploited.

### 4.3. Two-step receiver combining linear and widely linear processing

We propose a two-step receiving procedure where linear processing and widely linear processing are combined. First, a linear MMSE receiver is applied to the received signal. The goal of the first step is to obtain an estimate of the intrinsic interference  $j\hat{\mathbf{u}}$ . Assuming perfect channel state information at the receiver, the estimated interference component can be subtracted from the received signal as

$$\tilde{\mathbf{y}} = \mathbf{H}(\mathbf{d} + j\mathbf{u}) - \mathbf{H} \cdot j\hat{\mathbf{u}} + \mathbf{n} = \mathbf{H}(\mathbf{d} + j\boldsymbol{\epsilon}) + \mathbf{n}, \quad (4.12)$$

where  $j\boldsymbol{\epsilon} = j(\mathbf{u} - \hat{\mathbf{u}})$  is the pure imaginary residual interference. We present two ways of obtaining an estimate of the interference. The first method is to directly take the imaginary part of the output of the linear MMSE receiver on the  $k$ -th subcarrier and at the  $n$ -th time instant as

$$j\hat{\mathbf{u}} = j \cdot \text{Im}\{\mathbf{W}_{\text{MMSE}}^H \cdot \mathbf{y}\}. \quad (4.13)$$

On the other hand, the idea of the second scheme is to construct an estimate of the interference by using the already detected data symbols shown as follows

$$j\hat{\mathbf{u}} = \sum_{i=n-3}^{n+3} \sum_{j=k-1}^{k+1} c_{ij} \cdot \check{\mathbf{d}}_j[i], \quad j \neq k \text{ and } i \neq n, \quad (4.14)$$

where the  $\check{\mathbf{d}}_j[i]$  are obtained by modulating the information bits detected from  $\hat{\mathbf{d}}$  using OQAM.

In the second step, a widely linear MMSE receiver is employed on the resulting equivalent received signal  $\tilde{\mathbf{y}}$  and its complex conjugate. The detected desired signal is accordingly expressed as

$$\tilde{\mathbf{d}} = \text{Re} \left\{ \begin{bmatrix} \mathbf{W}_1^H & \mathbf{W}_2^H \end{bmatrix} \cdot \begin{bmatrix} \tilde{\mathbf{y}} \\ \tilde{\mathbf{y}}^* \end{bmatrix} \right\}, \quad (4.15)$$

where

$$\mathbf{W}_1 = \left( \mathbf{R}_{\tilde{\mathbf{y}}\tilde{\mathbf{y}}} - \mathbf{R}_{\tilde{\mathbf{y}}\tilde{\mathbf{y}}^*} \cdot \mathbf{R}_{\tilde{\mathbf{y}}\tilde{\mathbf{y}}^*}^*{}^{-1} \cdot \mathbf{R}_{\tilde{\mathbf{y}}\tilde{\mathbf{y}}}^* \right)^{-1} \cdot \left( \mathbf{H} - \mathbf{R}_{\tilde{\mathbf{y}}\tilde{\mathbf{y}}^*} \cdot \mathbf{R}_{\tilde{\mathbf{y}}\tilde{\mathbf{y}}}^*{}^{-1} \cdot \mathbf{H}^* \right)$$

and

$$\mathbf{W}_2 = \left( \mathbf{R}_{\tilde{\mathbf{y}}\tilde{\mathbf{y}}^*}^* - \mathbf{R}_{\tilde{\mathbf{y}}\tilde{\mathbf{y}}}^* \cdot \mathbf{R}_{\tilde{\mathbf{y}}\tilde{\mathbf{y}}}^{-1} \cdot \mathbf{R}_{\tilde{\mathbf{y}}\tilde{\mathbf{y}}^*} \right)^{-1} \cdot \left( \mathbf{H}^* - \mathbf{R}_{\tilde{\mathbf{y}}\tilde{\mathbf{y}}^*}^* \cdot \mathbf{R}_{\tilde{\mathbf{y}}\tilde{\mathbf{y}}}^{-1} \cdot \mathbf{H} \right).$$

Here  $\mathbf{R}_{\tilde{\mathbf{y}}\tilde{\mathbf{y}}}$  and  $\mathbf{R}_{\tilde{\mathbf{y}}\tilde{\mathbf{y}}^*}$  are the autocorrelation matrix of the equivalent received signal  $\tilde{\mathbf{y}}$  and its pseudo-autocorrelation matrix (the correlation matrix of  $\tilde{\mathbf{y}}$  and  $\tilde{\mathbf{y}}^*$ ), respectively. The detailed derivations are presented in Appendix E.

Let  $P_s$  denote the power per symbol at each transmit antenna. The covariance matrix and the pseudo-covariance matrix of the desired signal  $\mathbf{d} \in \mathbb{R}^{M_T}$  are

$$\mathbb{E}\{\mathbf{d} \cdot \mathbf{d}^H\} = \mathbb{E}\{\mathbf{d} \cdot \mathbf{d}^T\} = \frac{P_s}{2} \mathbf{I}_{M_T}. \quad (4.16)$$

Assuming that the residual interference is uncorrelated with the desired signal and the noise as well, i.e.,

$$\mathbb{E}\{\mathbf{d} \cdot \boldsymbol{\epsilon}^H\} = \mathbb{E}\{\mathbf{d} \cdot \boldsymbol{\epsilon}^T\} = \mathbf{0} \in \mathbb{R}^{M_T \times M_T} \quad (4.17)$$

$$\mathbb{E}\{\boldsymbol{\epsilon} \cdot \mathbf{n}^H\} = \mathbf{0} \in \mathbb{R}^{M_T \times M_R}, \quad (4.18)$$

we obtain

$$\mathbf{R}_{\tilde{\mathbf{y}}\tilde{\mathbf{y}}} = \mathbf{H} \cdot \left( \frac{P_s}{2} \mathbf{I}_{M_T} + \mathbf{R}_{\boldsymbol{\epsilon}\boldsymbol{\epsilon}} \right) \cdot \mathbf{H}^H + \sigma_n^2 \mathbf{I}_{M_R}, \quad (4.19)$$

and

$$\mathbf{R}_{\tilde{\mathbf{y}}\tilde{\mathbf{y}}^*} = \mathbf{H} \cdot \left( \frac{P_s}{2} \mathbf{I}_{M_T} - \mathbf{R}_{\boldsymbol{\epsilon}\boldsymbol{\epsilon}} \right) \cdot \mathbf{H}^T. \quad (4.20)$$

Here the covariance matrix of the residual interference related term  $\boldsymbol{\epsilon}$  denoted by  $\mathbf{R}_{\boldsymbol{\epsilon}\boldsymbol{\epsilon}}$  is cal-

culated as

$$\mathbf{R}_{\epsilon\epsilon} \approx \frac{1}{N} \sum_{l=1}^N (\mathbf{u}_l - \hat{\mathbf{u}}_l) \cdot (\mathbf{u}_l - \hat{\mathbf{u}}_l)^H, \quad (4.21)$$

where  $N$  is the number of observations. Note that a more effective covariance matrix estimation method, e.g., [SW14], can be employed such that a more accurate estimate of the covariance matrix of  $\epsilon$  can be obtained. Alternatively, as future work, it would also be interesting to find an analytical expression of  $\mathbf{R}_{\epsilon\epsilon}$ . This would facilitate the use of the proposed two-step receiver in practice, for example, its implementation in a demonstrator. In any case, it is worth mentioning that compared to the amount of the residual intrinsic interference, the accuracy of the covariance matrix estimation for  $\epsilon$  appears to have a relatively minor impact on the performance of the two-step receiver. A block diagram that illustrates the two-step receiver introduced above is shown in Figure 4.1.

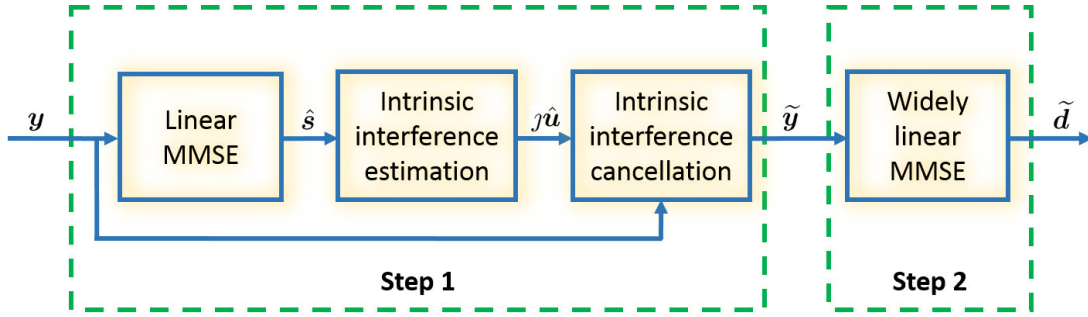


Figure 4.1.: Block diagram of the proposed two-step receiver

Notice that to obtain an estimate of the intrinsic interference using (4.14) there is a delay since three future multi-carrier symbols have to be detected and used (cf. also Table 3.1). By making use of only two detected future symbols or even one, the delay is consequently smaller at the price of a performance degradation due to a larger residual interference term. This issue is further analyzed and discussed in Section 4.4 where the simulation results are shown.

With a focus on point-to-point MIMO FBMC/OQAM systems, we have devised a way of dealing with the intrinsic interference and thus enabling the use of widely linear processing. In fact, it also inspires the design of widely linear processing-based techniques in more complicated communication scenarios. For instance, in uplink transmissions where cooperative MIMO is used, FBMC/OQAM is regarded as a promising alternative to CP-OFDM as the latter suffers from performance degradation due to the lack of synchronization in both the time and the frequency domain. The robustness of FBMC/OQAM in uplink transmissions with timing and frequency misalignments between the nodes has been numerically shown in [FPT08],

[SSWB<sup>+</sup>11], [CLH14c], and in Section 3.3. It is thus interesting to investigate how widely linear processing can be incorporated into a cooperative MIMO FBMC/OQAM system. In such a case, relay nodes assist the transmissions from the source or sources to the destination such that the source signals arrive at the destination through a number of independent paths and are constructively combined. Unlike the point-to-point MIMO scenario where multiple antennas at the transmit and receive nodes provide spatial diversity, the relay nodes form a virtual antenna array which enhances the reliability of the transmissions without requiring multiple antennas at the nodes. To exploit the cooperative diversity of such a system, distributed beamforming is an effective technique. Compared to linear distributed beamforming algorithms, it is reported in [SH13] that by applying widely linear processing a significant gain can be obtained. However, it should be noted that when FBMC/OQAM is used and amplify-and-forward is considered as the relaying scheme, the overall interference term observed at the destination that results from the intrinsic interference induced in all phases of the transmissions is a challenge. By employing decode-and-forward instead, the intrinsic interference can then be mitigated at the relay nodes based on the idea introduced in this section such that the benefits due to the second-order non-circular property of the equivalently real-valued desired signals can be exploited.

#### 4.4. Simulation results

In what follows, we evaluate the Bit Error Rate (BER) performance of the proposed two-step receiver for MIMO FBMC/OQAM systems. The number of subcarriers is 512, and the subcarrier spacing is 15 kHz. The bandwidth is 5 MHz. Each subchannel is considered as Rayleigh flat fading. Perfect channel state information at the receiver is assumed. In addition, the PHYDYAS prototype filter with the overlapping factor  $K = 4$  [PHY] is employed. The data symbols are drawn from a 4 QAM constellation. For the estimation of the covariance matrix of the residual interference related term  $\epsilon$ ,  $N$  in (4.21) is set to 250 in the simulations as the number of training symbols. First, a scenario where  $M_T = M_R = 2$  is considered. Figure 4.2 presents a comparison between the BER performances of the linear MMSE receiver (as represented by (4.10) and (4.11)) and the proposed two-step receiver combining both linear processing and widely linear processing. Here  $\text{SNR} = P_T/\sigma_n^2$ , and the transmit power  $P_T = M_T \cdot P_s$ . Note that in the legend of the figure “MMSE + WL-MMSE 1” and “MMSE + WL-MMSE 2” correspond to the two versions of the two-step receiver where the estimated interference is obtained by using (4.13) and (4.14), respectively. We also illustrate in Figure 4.2 an ideal case where the interference component is completely canceled, i.e.,  $\epsilon = \mathbf{0}$  in (4.12), corresponding to the legend “WL-MMSE ideal”. A performance improvement is observed by

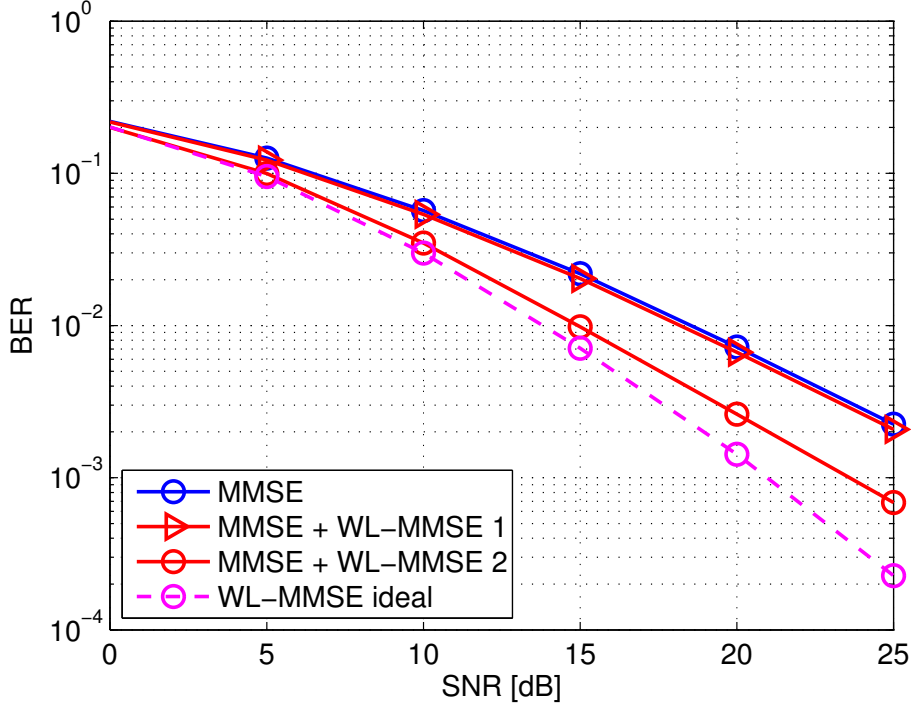


Figure 4.2.: BER vs. SNR for the case where  $M_T = M_R = 2$  (“MMSE + WL-MMSE 1” and “MMSE + WL-MMSE 2” correspond to the two versions of the two-step receiver where the estimated interference is obtained by using (4.13) and (4.14), respectively; “WL-MMSE ideal” corresponds to an ideal case where the interference component is completely canceled)

employing our proposed two-step receiver based on (4.12), (4.14) and (4.15) compared to the case where the linear MMSE receiver is used. It can also be seen that when the interference is estimated by using (4.13), the achieved gain over the linear MMSE receiver is negligible due to a relatively high level of the residual interference. In addition to the non-zero residual interference, the violation of the assumptions (4.17) and (4.18) as well as the approximation of  $\mathbf{R}_{\epsilon\epsilon}$  also contribute to the gap between the performance of the two-step receiver and the ideal case plotted for the purpose of comparison.

In the second example, we consider a  $M_T = M_R = 4$  scenario and illustrate the corresponding results in Figure 4.3. Similar observations as in the first experiment are obtained. Moreover, it is shown that by increasing the number of transmit and receive antennas, the gain achieved by the proposed two-step receiver over the linear MMSE receiver is even more significant when the estimated interference is obtained based on (4.14).

Now we concentrate on the two-step receiver where the intrinsic interference is estimated

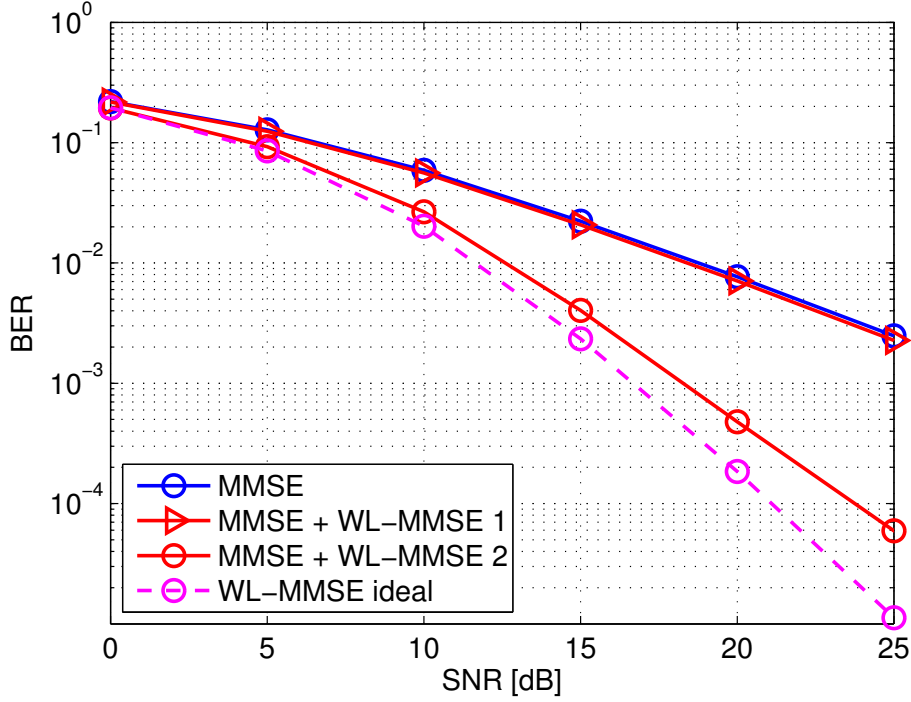


Figure 4.3.: BER vs. SNR for the case where  $M_T = M_R = 4$  (“MMSE + WL-MMSE 1” and “MMSE + WL-MMSE 2” correspond to the two versions of the two-step receiver where the estimated interference is obtained by using (4.13) and (4.14), respectively; “WL-MMSE ideal” corresponds to an ideal case where the interference component is completely canceled)

according to the second scheme as in (4.14). Its performance is evaluated when a smaller number of detected future multi-carrier symbols is used, and the intrinsic interference is thus only partially canceled. The simulation parameters are the same as in the first experiment. It can be observed in Figure 4.4 that when two detected future symbols are used, the performance degradation compared to the case where all three future symbols contributing to the intrinsic interference are considered is quite small. As the delay is further reduced to one symbol, i.e., only one detected future symbol is used, the gap in the performance, which is around 2 dB, is still on an acceptable level. However, when no detected future symbols are utilized at all, the amount of the residual interference is large, and the performance degrades heavily. Still, it outperforms the version of the two-step receiver based on the first scheme of estimating the intrinsic interference as in (4.13).

Finally, we present a comparison between the proposed two-step receiver and the MMSE-ML scheme in [ZLB10]. In this technique, the intrinsic interference is also first mitigated by

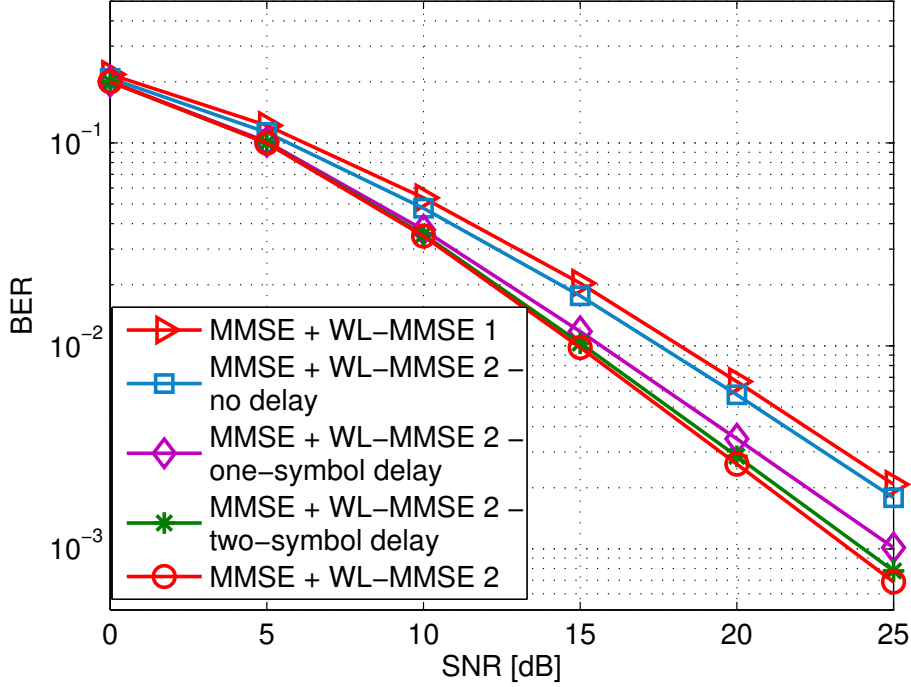


Figure 4.4.: BER vs. SNR for the case where  $M_T = M_R = 2$  (“MMSE + WL-MMSE 1” and “MMSE + WL-MMSE 2” correspond to the two versions of the two-step receiver where the estimated interference is obtained by using (4.13) and (4.14), respectively)

using the output of a linear MMSE receiver, and the ML detection is applied afterwards. In this example, the scenario is the same as for Figure 4.3. For the purpose of comparison, the versions of the two-step receiver with less delay are also considered. The results are shown in Figure 4.5. We can observe that the proposed two-step receiver significantly outperforms the MMSE-ML scheme even when the intrinsic interference is only partially canceled and a smaller delay is incurred. Although the MMSE-ML technique provides a better performance compared to the version of the two-step receiver without taking advantage of any detected future symbols and thus causing no delay, the ML detection in MMSE-ML leads to a higher computational complexity in contrast to the widely linear processing part of the two-step receiver. In addition, the fact that the two-step receiver achieves a superior performance over the linear MMSE receiver inspires an enhanced version of the MMSE-ML scheme in [ZLB10]. The proposed two-step receiver can be incorporated into the first step of the MMSE-ML approach to replace the linear MMSE receiver, contributing to an improved performance.

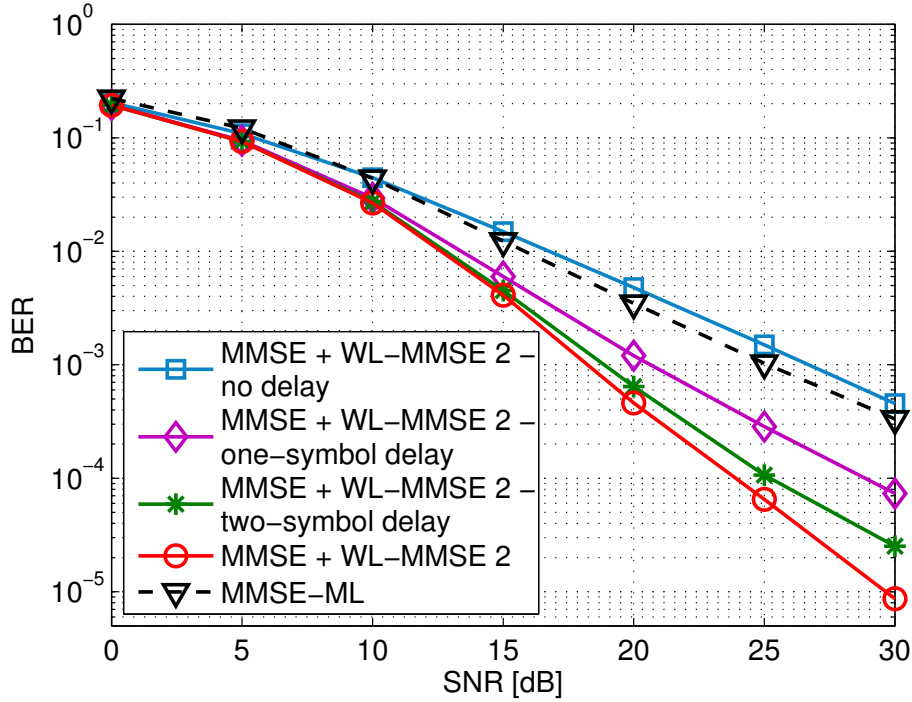


Figure 4.5.: BER vs. SNR for the case where  $M_T = M_R = 4$  (“MMSE + WL-MMSE 2” corresponds to the version of the two-step receiver where the estimated interference is obtained by using (4.14); “MMSE-ML” corresponds to the scheme combining MMSE and ML in [ZLB10])

## 4.5. Summary

In this chapter, we have presented a two-step receiver for a point-to-point MIMO FBMC/OQAM system. The intrinsic interference term is first estimated by using the output of a linear MMSE receiver and then subtracted from the received signal. A widely linear MMSE receiver is further applied on the resulting signal. Two schemes of estimating the intrinsic interference are presented and analyzed via simulations. In the first scheme, an estimate of the intrinsic interference is obtained by directly taking the imaginary part of the output of the linear MMSE receiver. It causes no delay in the processing but fails to provide a performance improvement compared to the case of a linear MMSE receiver. On the other hand, the second scheme uses the detected adjacent multi-carrier symbols. The two-step receiver with this scheme achieves a very promising performance. Since the knowledge of detected future symbols is required, some delay is incurred. We could cope with this issue by using a smaller number of detected



future symbols with a slightly degraded performance.

For future work, the statistics of the residual interference could be analyzed such that estimates of the covariance matrix of the residual interference could be obtained. In addition, the extension of the proposed scheme to cooperative MIMO FBMC/OQAM systems based on the remarks at the end of Section 4.3 is also interesting.

## 5. Coordinated beamforming for single-user MIMO FBMC/OQAM systems

This chapter is devoted to coordinated beamforming-based transmit-receive processing schemes for point-to-point Multiple-Input-Multiple-Output (MIMO) Filter Bank-based Multi-Carrier with Offset Quadrature Amplitude Modulation (FBMC/OQAM) systems. Assuming that channel frequency responses on neighboring subcarriers are almost constant, the two-step receiver as a combination of linear and widely linear processing discussed in Chapter 4 can be employed. In this chapter, the limit imposed on the two-step receiver with regard to the frequency selectivity of the propagation channel is relaxed. Consequently, it is only required that the channel on each subcarrier can be treated as flat fading. The Channel State Information at the Transmitter (CSIT) is exploited for the mitigation of the intrinsic interference residing in FBMC/OQAM-based systems. To enable reliable transmissions when the number of transmit antennas does not exceed the number of receive antennas, we first present a joint and iterative procedure to calculate the precoding matrix and the decoding matrix for each subcarrier. Such results have laid the basis for the design of the intrinsic interference mitigating coordinated beamforming (IIM-CBF) schemes in FBMC/OQAM-based multi-user MIMO downlink systems as a focus of Chapter 6.

Aiming at a more effective mitigation of the intrinsic interference, in this chapter we further introduce an enhanced version of the coordinated beamforming scheme, where a Signal-to-Leakage-plus-Noise-Ratio (SLNR)-based metric is used to compute the precoding matrices. Simulation results show that the proposed algorithms outperform the existing transmission strategies for MIMO FBMC/OQAM systems. It is also observed that in addition to featuring a well-localized spectrum and a higher spectral efficiency, by employing the proposed coordinated beamforming schemes, the MIMO FBMC/OQAM system achieves a similar Bit Error Rate (BER) performance as its CP-OFDM-based counterpart. These results have been published in [CLH14b], [CPNCH15].

### 5.1. Introduction

Filter Bank-based Multi-Carrier modulation (FBMC) is widely known as a promising alternative multi-carrier modulation scheme to Orthogonal Frequency Division Multiplexing with the Cyclic Prefix insertion (CP-OFDM). Thanks to the use of spectrally well-confined synthe-

sis and analysis filter banks at the transmitter and at the receiver [SSL02], [Bel01], FBMC features a concentrated spectrum and a much lower out-of-band radiation compared to CP-OFDM. Moreover, it is not required to insert the CP in systems where Filter Bank-based Multi-Carrier with Offset Quadrature Amplitude Modulation (FBMC/OQAM) is employed, which contributes to an improved spectral efficiency compared to CP-OFDM-based systems. The benefits of adopting FBMC have been demonstrated in a variety of contexts, such as asynchronous scenarios [FPT08], [SSWB<sup>+</sup>11], cognitive radio networks [SB10], and broadband Professional Mobile Radio (PMR) systems [RBB<sup>+</sup>13].

In the previous chapter, we have addressed the issue of exploiting the benefits of widely linear processing in point-to-point MIMO FBMC/OQAM systems. As low frequency selective channels are considered, the channel frequency response can be approximated as constant across the neighboring subcarriers that contribute to the intrinsic interference. Consequently, the data model can be formulated such that the desired signal and the intrinsic interference are separated in the real domain and in the pure imaginary domain, respectively. Then, the intrinsic interference is canceled by taking the real part of the resulting signal after the equalization. Perfect Channel State Information (CSI) is only assumed at the receiver side. In this chapter, however, we investigate more practical scenarios where the constraint on the frequency selectivity of the propagation channels is alleviated. It is only required the the channel frequency response remains constant on each subcarrier, while it can differ over adjacent subcarriers, categorized as the class of intermediate frequency selective channels in Chapter 3. In such cases, the task of mitigating the intrinsic interference becomes more challenging. Nevertheless, we present in this chapter effective transmit-receive processing techniques that are tailored for FBMC/OQAM-based MIMO systems by exploiting the knowledge of the CSI at both the transmitter and the receiver side.

In [CPN13b], a Zero Forcing (ZF)-based approach has been proposed for multi-stream transmissions in a single-user MIMO FBMC/OQAM system with intermediate frequency selective channels. More details on the performance analysis of this algorithm have been presented in [CPN13a]. However, the work in [CPN13b] and [CPN13a] is limited to the case where the number of receive antennas  $M_R$  does not exceed the number of transmit antennas  $M_T$ . In addition, the authors have shown numerically and have also pointed out that their proposed approach only provides a satisfactory performance in an asymmetric configuration, i.e., when  $M_T$  is larger than  $M_R$ .

In the context of the multi-user MIMO downlink with Space-Division Multiple Access (SDMA), coordinated beamforming techniques [CLZ<sup>+</sup>14], [SRH13] have been proposed to cope with the dimensionality constraint imposed on Block Diagonalization (BD)-based precoding

algorithms [SSH04]. Inspired by these works, we design a coordinated beamforming algorithm for point-to-point MIMO FBMC/OQAM systems without restricting the number of transmit antennas  $M_T$  and the number of receive antennas  $M_R$  [CLH14b]. Assuming perfect Channel State Information at the Transmitter (CSIT), the precoding matrix and the decoding matrix are calculated jointly in an iterative procedure for each subcarrier. Different choices of the decoding matrix in the initialization step are recommended for different scenarios. Then we also present an enhanced version of the coordinated beamforming scheme [CPNCH15], where the precoders are computed to maximize the Signal-to-Leakage-plus-Noise-Ratio (SLNR) given the equalizers. Based on the MMSE criterion, the equalizers are further updated. In addition, we address the impact of the initialization of the equalizers in specific MIMO settings. This approach achieves a more effective elimination of the intrinsic interference inherent in FBMC/OQAM-based systems and thus does not lead to an error floor due to the existence of residual intrinsic interference.

The investigation on transmit-receive processing for point-to-point MIMO FBMC/OQAM systems that we present in this chapter can be regarded as a crucial stepping stone for the design of transmit-receive strategies in FBMC/OQAM-based multi-user MIMO scenarios, which is the focus of Chapters 6 and 7.

We organize the rest of this chapter as follows: Section 5.2 introduces the data model of a point-to-point MIMO FBMC/OQAM system where the channel on each subcarrier is assumed to be flat fading. Two existing algorithms are also reviewed. We then describe the coordinated beamforming scheme in detail in Section 5.3, whereas Section 5.4 is devoted to the enhanced coordinated beamforming approach that effectively avoids an error floor. Numerical results are presented in Section 5.5, before a brief summary is provided in Section 5.6.

## 5.2. Data model and review of state-of-the-art schemes

We consider a point-to-point MIMO FBMC/OQAM system where the channel on each subcarrier can be treated as flat fading [CPN13b], [CPN13a]. The number of transmit antennas and the number of receive antennas are denoted by  $M_T$  and  $M_R$ , respectively. The received signal on the  $k$ -th subcarrier and at the  $n$ -th time instant is written as follows

$$\mathbf{y}_k[n] = \mathbf{H}_k[n]\mathbf{F}_k[n]\mathbf{d}_k[n] + \sum_{i=n-3}^{n+3} \sum_{\ell=k-1}^{k+1} \mathbf{H}_\ell[i]\mathbf{F}_\ell[i]c_{i,\ell}\mathbf{d}_\ell[i] + \mathbf{n}_k[n], \quad (\ell, i) \neq (k, n), \quad (5.1)$$

where  $\mathbf{d}_k[n] \in \mathbb{R}^d$  is the desired signal on the  $k$ -th subcarrier and at the  $n$ -th time instant when  $(k+n)$  is even<sup>1</sup>, and  $d$  denotes the number of spatial streams. The terms  $c_{i,\ell}\mathbf{d}_\ell[i]$  contribute to the intrinsic interference and are pure imaginary, where  $\ell = k-1, k, k+1$ ,  $i = n-3, \dots, n+3$ , and  $(\ell, i) \neq (k, n)$ . The coefficients  $c_{i,\ell}$  represent the system impulse response determined by the synthesis and analysis filters (cf. Table 3.1). The PHYDYAS prototype filter [PHY] is used, and the overlapping factor is chosen to be  $K = 4$ . For more details about FBMC/OQAM-based systems, the reader is referred to Chapter 3 and [Bel10]. Here  $\mathbf{H}_k[n] \in \mathbb{C}^{M_R \times M_T}$  contains the frequency response of the channel between each transmit antenna and each receive antenna, and  $\mathbf{n}_k[n]$  denotes the additive white Gaussian noise vector containing zero mean i.i.d. circularly symmetric Gaussian random variables with variance  $\sigma_n^2$ . In addition,  $\mathbf{F}_k[n] \in \mathbb{C}^{M_T \times d}$  represents the precoding matrix that maps the spatial streams to the transmit antennas.

### 5.2.1. Straightforward extension of the transmission strategy as in case of CP-OFDM

In several publications on MIMO FBMC/OQAM systems, such as [ZLB10] and [CH13b], it is assumed that the channels on adjacent subcarriers are almost the same. The received signal on the  $k$ -th subcarrier and at the  $n$ -th time instant can be accordingly approximated as

$$\mathbf{y}_k[n] = \mathbf{H}_k[n] \mathbf{F}_k[n] \tilde{\mathbf{d}}_k[n] + \mathbf{n}_k[n], \quad (5.2)$$

where  $\tilde{\mathbf{d}}_k[n]$  contains the real-valued desired signal and the pure imaginary interference

$$\tilde{\mathbf{d}}_k[n] = \mathbf{d}_k[n] + \sum_{i=n-3}^{n+3} \sum_{\ell=k-1}^{k+1} c_{i,\ell} \mathbf{d}_\ell[i], \quad (\ell, i) \neq (k, n). \quad (5.3)$$

Considering  $\tilde{\mathbf{d}}_k[n]$  as an equivalent transmitted signal, (5.2) resembles the data model of a MIMO CP-OFDM system. Consequently, transmission strategies that have been developed for MIMO CP-OFDM systems can be straightforwardly extended to MIMO FBMC/OQAM systems where only one additional step is required, i.e., taking the real part of the resulting signal after the multiplication by the decoding matrix

$$\hat{\mathbf{d}}_k[n] = \text{Re} \{ \mathbf{D}_k^H[n] \mathbf{y}_k[n] \}, \quad (5.4)$$

<sup>1</sup>For the case where  $(k+n)$  is odd, the desired signal on the  $k$ -th subcarrier and at the  $n$ -th time instant is pure imaginary, while intrinsic interference is real. As the two cases are essentially equivalent to each other, we only take the case where  $(k+n)$  is even to describe the proposed algorithm in this chapter.

where  $\mathbf{D}_k[n] \in \mathbb{C}^{M_R \times d}$  is the decoding matrix on the  $k$ -th subcarrier and at the  $n$ -th time instant. Here  $\text{Re}\{\cdot\}$  symbolizes the real part of the input argument, while  $\text{Im}\{\cdot\}$  is used in the following text to represent the imaginary part.

### 5.2.2. Zero forcing-based approach

In [CPN13b] and [CPN13a], the precoding matrix is designed such that the intrinsic interference (corresponding to the second term on the right hand side of (5.1)) can be canceled by taking the real part of the received signal. Let us expand the real part of the received signal on the  $k$ -th subcarrier and at the  $n$ -th time instant

$$\begin{aligned} \text{Re}\{\mathbf{y}_k[n]\} = & \text{Re}\{\mathbf{H}_k[n]\mathbf{F}_k[n]\}\mathbf{d}_k[n] + (-1) \cdot \sum_{i=n-3}^{n+3} \sum_{\ell=k-1}^{k+1} \text{Im}\{\mathbf{H}_\ell[i]\mathbf{F}_\ell[i]\} \text{Im}\{c_{i,\ell}\mathbf{d}_\ell[i]\} \\ & + \text{Re}\{\mathbf{n}_k[n]\}, \quad (\ell, i) \neq (k, n). \end{aligned} \quad (5.5)$$

The precoding matrix  $\mathbf{F}$  for each subcarrier and each time instant is calculated such that

$$\text{Im}\{\mathbf{H}\mathbf{F}\} = \mathbf{0}, \quad (5.6)$$

where  $\mathbf{H}$  represents the channel matrix on the same subcarrier and at the same time instant, and the time as well as the subcarrier indices are ignored, as the precoding concept is on a per-subcarrier basis. Define a matrix  $\check{\mathbf{H}}$  as

$$\check{\mathbf{H}} = \begin{bmatrix} \text{Im}\{\mathbf{H}\} & \text{Re}\{\mathbf{H}\} \end{bmatrix} \in \mathbb{R}^{M_R \times 2M_T}. \quad (5.7)$$

The stacked version of the real part and the imaginary part of the precoding matrix  $\mathbf{F}$ , i.e.,  $\begin{bmatrix} \text{Re}\{\mathbf{F}\}^T & \text{Im}\{\mathbf{F}\}^T \end{bmatrix}^T$ , should lie in the null space of  $\check{\mathbf{H}}$ , such that  $\text{Im}\{\mathbf{H}\mathbf{F}\} = \mathbf{0}$ . However, this approach is designed only for scenarios where  $M_T \geq M_R$ . In addition, it is observed in the numerical results presented in [CPN13a] and is also pointed out in [CPN13b] that in a symmetric case where  $M_T = M_R$ , this scheme does not lead to a good Bit Error Rate (BER) performance.

## 5.3. Coordinated beamforming-based transmission strategy

Therefore, we propose to jointly and iteratively update the precoding matrix and the decoding matrix to alleviate the dimensionality constraint on the precoding algorithm in [CPN13b], i.e., scenarios where  $M_T \leq M_R$  will be dealt with. First, an equivalent channel matrix  $\mathbf{H}_{\text{eq}}$  is

defined as

$$\mathbf{H}_{\text{eq}} = \mathbf{D}^T \mathbf{H} \in \mathbb{C}^{d \times M_T}, \quad (5.8)$$

where  $\mathbf{D} \in \mathbb{R}^{M_R \times d}$  is the real-valued decoding matrix. In addition, we decouple the precoding matrix into two parts, i.e.,

$$\mathbf{F} = \mathbf{F}_1 \mathbf{F}_2 \in \mathbb{C}^{M_T \times d}, \quad (5.9)$$

where  $\mathbf{F}_1 \in \mathbb{C}^{M_T \times M_x}$  and  $\mathbf{F}_2 \in \mathbb{R}^{M_x \times d}$ .

The proposed coordinated beamforming algorithm is summarized as follows:

- **Step 1:** Initialize the decoding matrix  $\mathbf{D}^{(0)} \in \mathbb{R}^{M_R \times d}$ , set the iteration index  $p$  to zero, and set a threshold  $\epsilon$  for the stopping criterion<sup>2</sup>. The decoding matrix is generated randomly if the current subcarrier is the first one; otherwise set the decoding matrix as the one calculated for the previous subcarrier [CLZ<sup>+</sup>14].

- **Step 2:** Set  $p \leftarrow p + 1$  and calculate the equivalent channel matrix  $\mathbf{H}_{\text{eq}}^{(p)}$  in the  $p$ -th iteration as

$$\mathbf{H}_{\text{eq}}^{(p)} = \mathbf{D}^{(p-1)T} \mathbf{H} \in \mathbb{C}^{d \times M_T}. \quad (5.10)$$

Define a matrix  $\check{\mathbf{H}}_{\text{eq}}^{(p)}$

$$\check{\mathbf{H}}_{\text{eq}}^{(p)} = \begin{bmatrix} \text{Im} \left\{ \mathbf{H}_{\text{eq}}^{(p)} \right\} & \text{Re} \left\{ \mathbf{H}_{\text{eq}}^{(p)} \right\} \end{bmatrix} \in \mathbb{R}^{d \times 2M_T}. \quad (5.11)$$

- **Step 3:** Calculate the precoding matrix  $\mathbf{F}^{(p)} = \mathbf{F}_1^{(p)} \mathbf{F}_2^{(p)}$  for the  $p$ -th iteration. First, we perform the Singular Value Decomposition (SVD) of  $\check{\mathbf{H}}_{\text{eq}}^{(p)}$  as

$$\check{\mathbf{H}}_{\text{eq}}^{(p)} = \mathbf{U}_1^{(p)} \boldsymbol{\Sigma}_1^{(p)} \mathbf{V}_1^{(p)T}. \quad (5.12)$$

Denoting the rank of  $\check{\mathbf{H}}_{\text{eq}}^{(p)}$  as  $r^{(p)}$ , we define  $\mathbf{V}_{1,0}^{(p)} \in \mathbb{R}^{2M_T \times M_x}$  as containing the last  $M_x = 2M_T - r^{(p)}$  right singular vectors that form an orthonormal basis for the null space of  $\check{\mathbf{H}}_{\text{eq}}^{(p)}$ . Hence, the first part of the precoding matrix for the  $p$ -th iteration  $\mathbf{F}_1^{(p)}$  can be obtained via

$$\mathbf{V}_{1,0}^{(p)} = \begin{bmatrix} \text{Re} \left\{ \mathbf{F}_1^{(p)} \right\} \\ \text{Im} \left\{ \mathbf{F}_1^{(p)} \right\} \end{bmatrix} \in \mathbb{R}^{2M_T \times M_x}, \quad (5.13)$$

such that  $\text{Im} \left\{ \mathbf{H}_{\text{eq}}^{(p)} \mathbf{F}_1^{(p)} \right\} = \mathbf{0}$ . To further calculate the second part of the precoding matrix in the  $p$ -th iteration  $\mathbf{F}_2^{(p)}$ , the following equivalent channel matrix after the can-

<sup>2</sup> The threshold  $\epsilon$  is set to  $10^{-4}$  in our simulations.

cancellation of the intrinsic interference for the  $p$ -th iteration is defined as

$$\widetilde{\mathbf{H}}_{\text{eq}}^{(p)} = \text{Re} \left\{ \mathbf{H}_{\text{eq}}^{(p)} \mathbf{F}_1^{(p)} \right\} \in \mathbb{R}^{d \times M_x}. \quad (5.14)$$

Further calculate the SVD of  $\widetilde{\mathbf{H}}_{\text{eq}}^{(p)}$ , and define  $\mathbf{V}_{2,1}^{(p)} \in \mathbb{R}^{M_x \times d}$  as containing the first  $d$  right singular vectors. Thereby,  $\mathbf{F}_2^{(p)}$  is obtained as  $\mathbf{F}_2^{(p)} = \mathbf{V}_{2,1}^{(p)}$ .

- **Step 4:** Update the decoding matrix based on the equivalent channel matrix after the cancellation of the intrinsic interference where only the processing at the transmitter is considered

$$\widetilde{\mathbf{H}}_{\text{eq,tx}}^{(p)} = \text{Re} \left\{ \mathbf{H} \mathbf{F}^{(p)} \right\} \in \mathbb{R}^{M_R \times d}. \quad (5.15)$$

When the MMSE receiver<sup>3</sup> is used, the decoding matrix has the following form

$$\mathbf{D}^{(p)} = \widetilde{\mathbf{H}}_{\text{eq,tx}}^{(p)} \left( \widetilde{\mathbf{H}}_{\text{eq,tx}}^{(p)\text{T}} \widetilde{\mathbf{H}}_{\text{eq,tx}}^{(p)} + \sigma_n^2 \mathbf{I}_d \right)^{-1}. \quad (5.16)$$

- **Step 5:** Calculate the term  $\Delta(\mathbf{F})$  defined as

$$\Delta(\mathbf{F}) = \left\| \mathbf{F}^{(p)} - \mathbf{F}^{(p-1)} \right\|_{\text{F}}^2, \quad (5.17)$$

which measures the change of the precoding matrix  $\mathbf{F}$ . If  $\Delta(\mathbf{F}) < \epsilon$ , the convergence is achieved, and the iterative procedure terminates. Otherwise go back to **Step 2**.

It is important to note that in the special case where  $M_T = M_R = d + 1$ , we propose to compute the decoding matrix in the initialization step as follows. Then it is observed that the coordinated beamforming technique only needs two iterations to converge<sup>4</sup>. First, calculate the SVD of  $\check{\mathbf{H}} \in \mathbb{R}^{M_R \times 2M_T}$  as defined in (5.7), and let  $\mathbf{V}_{1,0}^{(0)}$  contain the last  $(2M_T - M_R)$  right singular vectors. Defining  $\mathbf{F}_1^{(0)}$  via

$$\mathbf{V}_{1,0}^{(0)} = \begin{bmatrix} \text{Re} \left\{ \mathbf{F}_1^{(0)} \right\} \\ \text{Im} \left\{ \mathbf{F}_1^{(0)} \right\} \end{bmatrix}, \quad (5.18)$$

---

<sup>3</sup>Other receivers, such as zero forcing or maximum ratio combining, can also be employed in this coordinated beamforming algorithm.

<sup>4</sup>Since the stopping criterion is defined based on the change of the precoding matrix (5.17), the algorithm converging within two iterations means that the precoding matrix is barely changed in the second iteration. In other words, though not proved analytically, after initializing the decoding matrices via (5.19), only one iteration (performing **Step 2 – 4**) is enough to obtain the precoding and decoding matrices.



we compute  $\mathbf{U}_{2,1}^{(0)} \in \mathbb{R}^{M_R \times d}$  from the SVD of  $\text{Re}\{\mathbf{H}\mathbf{F}_1^{(0)}\}$  such that it contains the first  $d$  left singular vectors. Then the decoding matrix for the initialization step is chosen as

$$\mathbf{D}^{(0)} = \mathbf{U}_{2,1}^{(0)}. \quad (5.19)$$

Here we choose real-valued decoding matrices for the coordinated beamforming scheme described above. To explain the reason behind such a feature of this approach, let us start by looking at the more general case where the decoding matrix  $\mathbf{D}_k[n]$  is not restricted to be real-valued. Then, we write the signal after the receive processing as

$$\mathbf{r}_k[n] = \mathbf{D}_k^H[n] \cdot \mathbf{y}_k[n], \quad (5.20)$$

with  $\mathbf{y}_k[n]$  defined in (5.1). Focusing the case where  $(k+n)$  is even, the real part of  $\mathbf{r}_k[n]$  is taken to obtain an estimate of the desired signal, i.e.,

$$\text{Re}\{\mathbf{r}_k[n]\} = \text{Re}\{\mathbf{D}_k[n]\}^T \cdot \text{Re}\{\mathbf{y}_k[n]\} + \text{Im}\{\mathbf{D}_k[n]\}^T \cdot \text{Im}\{\mathbf{y}_k[n]\}, \quad (5.21)$$

where  $\text{Re}\{\mathbf{y}_k[n]\}$  and  $\text{Im}\{\mathbf{y}_k[n]\}$  are expressed as

$$\text{Re}\{\mathbf{y}_k[n]\} = \overbrace{\text{Re}\{\mathbf{H}_k[n]\mathbf{F}_k[n]\} \mathbf{d}_k[n]}^{\text{desired signal}} + \overbrace{(-1) \cdot \sum_{\substack{i=n-3 \\ (\ell,i) \neq (k,n)}}^{n+3} \sum_{\ell=k-1}^{k+1} \text{Im}\{\mathbf{H}_\ell[i]\mathbf{F}_\ell[i]\} \text{Im}\{c_{i,\ell}\mathbf{d}_\ell[i]\}}^{\text{intrinsic interference}} + \text{Re}\{\mathbf{n}_k[n]\}$$

and

$$\text{Im}\{\mathbf{y}_k[n]\} = \overbrace{\text{Im}\{\mathbf{H}_k[n]\mathbf{F}_k[n]\} \mathbf{d}_k[n]}^{\text{desired signal}} + \overbrace{\sum_{\substack{i=n-3 \\ (\ell,i) \neq (k,n)}}^{n+3} \sum_{\ell=k-1}^{k+1} \text{Re}\{\mathbf{H}_\ell[i]\mathbf{F}_\ell[i]\} \text{Im}\{c_{i,\ell}\mathbf{d}_\ell[i]\}}^{\text{intrinsic interference}} + \text{Im}\{\mathbf{n}_k[n]\},$$

respectively. Consequently, via precoding and decoding, it has to be guaranteed that  $\text{Re}\{\mathbf{r}_k[n]\}$  is interference-free, and in the meantime the desired signal is recovered. Recall that precoding and decoding are performed on a per-subcarrier basis, i.e., the precoding matrix and the decoding matrix on a certain subcarrier at a certain time instant are solely determined by the channel on the same subcarrier at the same time instant. This allows us to ignore the time and subcarrier indices in the notation of the channel matrices, the precoding matrices, and the decoding matrices. Thus, the following has to be achieved via the design of the precoding

matrix and the decoding matrix on a certain subcarrier at a certain time instant

$$\text{Re}\{\mathbf{D}\}^T \cdot \text{Im}\{\mathbf{H} \cdot \mathbf{F}\} - \text{Im}\{\mathbf{D}\}^T \cdot \text{Re}\{\mathbf{H} \cdot \mathbf{F}\} = \mathbf{0} \quad (5.22)$$

$$\text{Re}\{\mathbf{D}\}^T \cdot \text{Re}\{\mathbf{H} \cdot \mathbf{F}\} + \text{Im}\{\mathbf{D}\}^T \cdot \text{Im}\{\mathbf{H} \cdot \mathbf{F}\} = \mathbf{\Sigma}, \quad (5.23)$$

where  $\mathbf{\Sigma}$  denotes a real-valued diagonal matrix. In other words, the matrix  $\begin{bmatrix} \text{Re}\{\mathbf{D}\}^T & \text{Im}\{\mathbf{D}\}^T \end{bmatrix}$  has to lie in the null space of  $\begin{bmatrix} \text{Im}\{\mathbf{H} \cdot \mathbf{F}\}^T & -\text{Re}\{\mathbf{H} \cdot \mathbf{F}\}^T \end{bmatrix}^T$  and in the signal space of  $\begin{bmatrix} \text{Re}\{\mathbf{H} \cdot \mathbf{F}\}^T & \text{Im}\{\mathbf{H} \cdot \mathbf{F}\}^T \end{bmatrix}^T$ . By contrast, when the decoding matrices are chosen as real-valued, the conditions given via (5.22) and (5.23) become

$$\mathbf{D}^T \cdot \text{Im}\{\mathbf{H} \cdot \mathbf{F}\} = \mathbf{0} \quad (5.24)$$

$$\mathbf{D}^T \cdot \text{Re}\{\mathbf{H} \cdot \mathbf{F}\} = \mathbf{\Sigma}. \quad (5.25)$$

In fact, in each iteration of the proposed coordinated beamforming algorithm, the precoding matrix  $\mathbf{F}$  is first computed such that (5.24) is fulfilled. Then, the decoding matrix  $\mathbf{D}$  is updated by using (5.25) as a criterion. When the convergence is achieved, the conditions given via (5.24) and (5.25) are approximately fulfilled. Nevertheless, we have found in numerical simulations that in case of the complex-valued decoding matrices, the convergence of a similar iterative procedure where the precoding matrix  $\mathbf{F}$  and the decoding matrix  $\mathbf{D}$  are updated as mentioned above cannot be achieved, i.e., the conditions (5.22) and (5.23) cannot be satisfied at the same time. Therefore, real-valued decoding matrices are used in the proposed coordinated beamforming algorithm which leads to a satisfactory performance as demonstrated in Section 5.5.

## 5.4. Towards a non-error floor multi-stream beamforming design

After the receive processing, we obtain the estimate of the desired signal as follows

$$\begin{aligned} \hat{\mathbf{d}}_k[n] = & \mathbf{D}_k^T[n] \cdot \text{Re}\{\mathbf{H}_k[n] \cdot \mathbf{F}_k[n]\} \cdot \mathbf{d}_k[n] \\ & + (-1) \cdot \mathbf{D}_k^T[n] \cdot \sum_{i=n-3}^{n+3} \sum_{\ell=k-1}^{k+1} \text{Im}\{\mathbf{H}_\ell[i] \cdot \mathbf{F}_\ell[i]\} \cdot \text{Im}\{c_{i,\ell} \cdot \mathbf{d}_\ell[i]\} \\ & + \mathbf{D}_k^T[n] \cdot \text{Re}\{\mathbf{n}_k[n]\}, \quad (\ell, i) \neq (k, n). \end{aligned} \quad (5.26)$$

According to the philosophy of the coordinated beamforming approach presented in the previous section, the following is achieved

$$\mathbf{D}_\ell^T[i] \cdot \text{Im} \{ \mathbf{H}_\ell[i] \cdot \mathbf{F}_\ell[i] \} = \mathbf{0}. \quad (5.27)$$

When the channel is not constant across adjacent subcarriers and consecutive symbol periods, it cannot be guaranteed that

$$\begin{aligned} \mathbf{D}_\ell[i] &= \mathbf{D}_k[n], \\ \ell &= k-1, k, k+1, \quad i = n-3, \dots, n+3, \quad (\ell, i) \neq (k, n). \end{aligned}$$

Consequently, the component with respect to the intrinsic interference in (5.26) is not completely eliminated, since

$$\mathbf{D}_k^T[n] \cdot \text{Im} \{ \mathbf{H}_\ell[i] \cdot \mathbf{F}_\ell[i] \} \neq \mathbf{0}. \quad (5.28)$$

The resulting residual intrinsic interference has impact on the performance at the high SNR regime.

Therefore, we propose to enhance the coordinated beamforming algorithm presented in the previous section via an SLNR-based design of the precoders. Given an initialization of the real-valued decoding matrices  $\mathbf{D}_k^{(0)}[n]$  for all subcarriers and time instants of interest, the SLNR-based metric takes the following form

$$\text{SLNR}_{k,n} = \frac{\left\| \mathbf{D}_k^{(0)T}[n] \cdot \text{Re} \{ \mathbf{H}_k[n] \cdot \mathbf{F}_k[n] \} \right\|_F^2}{\sum_{\substack{i=n-3 \\ (i,\ell) \neq (n,k)}}^{n+3} \sum_{\ell=k-1}^{k+1} |c_{i,\ell}|^2 \cdot \left\| \mathbf{D}_\ell^{(0)T}[i] \cdot \text{Im} \{ \mathbf{H}_k[n] \cdot \mathbf{F}_k[n] \} \right\|_F^2 + \frac{N_0}{E_s} \cdot \left\| \mathbf{D}_k^{(0)}[n] \right\|_F^2}, \quad (5.29)$$

where  $E_s$  denotes the energy of each QAM symbol, and  $N_0$  represents the noise power spectral density. Let us first find the linear expressions for the real part and the imaginary part extraction

$$\text{Re} \{ \mathbf{H}_k[n] \cdot \mathbf{F}_k[n] \} = \hat{\mathbf{H}}_k[n] \cdot \bar{\mathbf{F}}_k[n] \quad (5.30)$$

$$\text{Im} \{ \mathbf{H}_k[n] \cdot \mathbf{F}_k[n] \} = \check{\mathbf{H}}_k[n] \cdot \bar{\mathbf{F}}_k[n] \quad (5.31)$$

where

$$\hat{\mathbf{H}}_k[n] = \begin{bmatrix} \text{Re}\{\mathbf{H}_k[n]\} & -\text{Im}\{\mathbf{H}_k[n]\} \end{bmatrix} \quad (5.32)$$

$$\check{\mathbf{H}}_k[n] = \begin{bmatrix} \text{Im}\{\mathbf{H}_k[n]\} & \text{Re}\{\mathbf{H}_k[n]\} \end{bmatrix} \quad (5.33)$$

$$\bar{\mathbf{F}}_k[n] = \begin{bmatrix} \text{Re}\{\mathbf{F}_k[n]\} \\ \text{Im}\{\mathbf{F}_k[n]\} \end{bmatrix}. \quad (5.34)$$

For a matrix  $\mathbf{A}$ ,  $\|\mathbf{A}\|_{\text{F}}^2 = \text{Tr}\{\mathbf{A}^{\text{H}} \cdot \mathbf{A}\}$ . Based on this property and the normalization that  $\|\mathbf{F}_k[n]\|_{\text{F}}^2 = d$ , the metric can be reformulated as

$$\text{SLNR}_{k,n} = \frac{\text{Tr}\{\bar{\mathbf{F}}_k^{\text{T}}[n] \cdot \mathbf{P}_k[n] \cdot \bar{\mathbf{F}}_k[n]\}}{\text{Tr}\{\bar{\mathbf{F}}_k^{\text{T}}[n] \cdot \mathbf{Q}_k[n] \cdot \bar{\mathbf{F}}_k[n]\}}, \quad (5.35)$$

where

$$\mathbf{P}_k[n] = \hat{\mathbf{H}}_k^{\text{T}}[n] \cdot \mathbf{D}_k^{(0)}[n] \cdot \mathbf{D}_k^{(0)\text{T}}[n] \cdot \hat{\mathbf{H}}_k[n] \quad (5.36)$$

$$\mathbf{Q}_k[n] = \sum_{\substack{i=n-3 \\ (i,\ell) \neq (n,k)}}^{n+3} \sum_{\ell=k-1}^{k+1} |c_{i,\ell}|^2 \cdot \check{\mathbf{H}}_k^{\text{T}}[n] \cdot \mathbf{D}_\ell^{(0)}[i] \cdot \mathbf{D}_\ell^{(0)\text{T}}[i] \cdot \check{\mathbf{H}}_k[n] + \frac{1}{d} \cdot \frac{N_0}{E_s} \cdot \|\mathbf{D}_k^{(0)}[n]\|_{\text{F}}^2 \cdot \mathbf{I}_{2M_{\text{T}}}. \quad (5.37)$$

The precoders can be obtained via the following optimization problem

$$\arg \max_{\bar{\mathbf{F}}_k[n]} \text{SLNR}_{k,n} \quad (5.38)$$

$$\text{s. t.} \quad \|\bar{\mathbf{F}}_k[n]\|_{\text{F}}^2 = d \quad (5.39)$$

$$\bar{\mathbf{F}}_k^{\text{T}}[n] \cdot \mathbf{P}_k[n] \cdot \bar{\mathbf{F}}_k[n] \rightarrow \text{diagonal}, \quad (5.40)$$

which can be solved by computing the generalized eigenvalue decomposition of the matrix pair  $\{\mathbf{P}_k[n], \mathbf{Q}_k[n]\}$  [STS07]. Then, the  $d$  columns of  $\bar{\mathbf{F}}_k[n]$  are obtained as the  $d$  generalized eigenvectors that correspond to the  $d$  largest generalized eigenvalues.

The design criterion of the receive processing is to minimize the MMSE. To update  $\mathbf{D}_k[n]$  given the precoding matrices, the following optimization problem is formulated

$$\arg \min_{\mathbf{D}_k[n]} \text{MSE}_{k,n}, \quad (5.41)$$

where

$$\begin{aligned}
 \text{MSE}_{k,n} &= \mathbb{E} \left\{ \left\| \hat{\mathbf{d}}_k[n] - \mathbf{d}_k[n] \right\|^2 \right\} \\
 &= \frac{E_s}{2} \cdot \text{Tr} \left\{ \mathbf{I}_d - 2 \cdot \mathbf{D}_k^T[n] \cdot \hat{\mathbf{H}}_k[n] \cdot \bar{\mathbf{F}}_k[n] \right\} \\
 &\quad + \text{Tr} \left\{ \mathbf{D}_k^T[n] \cdot \left( \sum_{\substack{i=n-3 \\ (i,\ell) \neq (n,k)}}^{n+3} \sum_{\ell=k-1}^{k+1} \frac{E_s}{2} \cdot |c_{i,\ell}|^2 \cdot \check{\mathbf{H}}_\ell[i] \cdot \bar{\mathbf{F}}_\ell[i] \cdot \bar{\mathbf{F}}_\ell^T[i] \cdot \check{\mathbf{H}}_\ell^T[i] \right) \cdot \mathbf{D}_k[n] \right\} \\
 &\quad + \text{Tr} \left\{ \mathbf{D}_k^T[n] \cdot \left( \frac{E_s}{2} \cdot \hat{\mathbf{H}}_k[n] \cdot \bar{\mathbf{F}}_k[n] \cdot \bar{\mathbf{F}}_k^T[n] \cdot \hat{\mathbf{H}}_k^T[n] + \frac{N_0}{2} \cdot \mathbf{I}_{M_R} \right) \cdot \mathbf{D}_k[n] \right\}. \quad (5.42)
 \end{aligned}$$

The solution is given by

$$\begin{aligned}
 \mathbf{D}_k[n] &= \left( \sum_{\substack{i=n-3 \\ (i,\ell) \neq (n,k)}}^{n+3} \sum_{\ell=k-1}^{k+1} |c_{i,\ell}|^2 \cdot \check{\mathbf{H}}_\ell[i] \cdot \bar{\mathbf{F}}_\ell[i] \cdot \bar{\mathbf{F}}_\ell^T[i] \cdot \check{\mathbf{H}}_\ell^T[i] \right. \\
 &\quad \left. + \hat{\mathbf{H}}_k[n] \cdot \bar{\mathbf{F}}_k[n] \cdot \bar{\mathbf{F}}_k^T[n] \cdot \hat{\mathbf{H}}_k^T[n] + \frac{N_0}{E_s} \cdot \mathbf{I}_{M_R} \right)^{-1} \cdot \hat{\mathbf{H}}_k[n] \cdot \bar{\mathbf{F}}_k[n]. \quad (5.43)
 \end{aligned}$$

Note that we have observed via numerical simulations that a simplified version of the MMSE-based receiver leads to the same performance as (5.43). It can be expressed as

$$\mathbf{D}_k[n] = \left( \hat{\mathbf{H}}_k[n] \cdot \bar{\mathbf{F}}_k[n] \cdot \bar{\mathbf{F}}_k^T[n] \cdot \hat{\mathbf{H}}_k^T[n] + \frac{N_0}{E_s} \cdot \mathbf{I}_{M_R} \right)^{-1} \cdot \hat{\mathbf{H}}_k[n] \cdot \bar{\mathbf{F}}_k[n]. \quad (5.44)$$

This implies that it is the SLNR-based precoder that is in charge of mitigating the Inter-Symbol Interference (ISI) and the Inter-Carrier Interference (ICI).

To this end, we summarize the proposed SLNR-based coordinated beamforming algorithm as follows:

- **Step 1:** Initialize the real-valued decoding matrices  $\mathbf{D}_k^{(0)}[n] \in \mathbb{R}^{M_R \times d}$  for all the subcarriers randomly, set the iteration index  $p$  to zero, and set a threshold  $\epsilon$  for the stopping criterion.
- **Step 2:** Set  $p \leftarrow p+1$  and compute the precoding matrices  $\mathbf{F}_k^{(p)}[n]$  for all the subcarriers based on the SLNR-based beamforming design described above. The columns of  $\bar{\mathbf{F}}_k^{(p)}[n]$  are computed as the generalized eigenvectors associated with the  $d$  largest generalized

eigenvalues of the matrix pair

$$\left\{ \mathbf{P}_k^{(p)}[n], \mathbf{Q}_k^{(p)}[n] \right\}, \quad (5.45)$$

where

$$\mathbf{P}_k^{(p)}[n] = \hat{\mathbf{H}}_k^T[n] \cdot \mathbf{D}_k^{(p-1)}[n] \cdot \mathbf{D}_k^{(p-1)T}[n] \cdot \hat{\mathbf{H}}_k[n] \quad (5.46)$$

$$\begin{aligned} \mathbf{Q}_k^{(p)}[n] = & \sum_{\substack{i=n-3 \\ (i,\ell) \neq (n,k)}}^{n+3} \sum_{\ell=k-1}^{k+1} |c_{i,\ell}|^2 \cdot \check{\mathbf{H}}_k^T[n] \cdot \mathbf{D}_\ell^{(p-1)}[i] \cdot \mathbf{D}_\ell^{(p-1)T}[i] \cdot \check{\mathbf{H}}_k[n] \\ & + \frac{1}{d} \cdot \frac{N_0}{E_s} \cdot \left\| \mathbf{D}_k^{(p-1)}[n] \right\|_F^2 \cdot \mathbf{I}_{2M_T}. \end{aligned} \quad (5.47)$$

Here  $\hat{\mathbf{H}}_k[n]$  and  $\check{\mathbf{H}}_k[n]$  are as defined in (5.32) and (5.33), respectively. The precoding matrices are normalized such as the transmit power constraint is fulfilled.

- **Step 3:** Update the decoding matrices  $\mathbf{D}_k^{(p)}[n]$  for *all the subcarriers*. Based on the MMSE-based receiver described previously,  $\mathbf{D}_k^{(p)}[n]$  are computed as

$$\begin{aligned} \mathbf{D}_k^{(p)}[n] = & \left( \sum_{\substack{i=n-3 \\ (i,\ell) \neq (n,k)}}^{n+3} \sum_{\ell=k-1}^{k+1} |c_{i,\ell}|^2 \cdot \check{\mathbf{H}}_\ell[i] \cdot \bar{\mathbf{F}}_\ell^{(p)}[i] \cdot \bar{\mathbf{F}}_\ell^{(p)T}[i] \cdot \check{\mathbf{H}}_\ell^T[i] \right. \\ & \left. + \hat{\mathbf{H}}_k[n] \cdot \bar{\mathbf{F}}_k^{(p)}[n] \cdot \bar{\mathbf{F}}_k^{(p)T}[n] \cdot \hat{\mathbf{H}}_k^T[n] + \frac{N_0}{E_s} \cdot \mathbf{I}_{M_R} \right)^{-1} \cdot \hat{\mathbf{H}}_k[n] \cdot \bar{\mathbf{F}}_k^{(p)}[n], \end{aligned} \quad (5.48)$$

or as

$$\mathbf{D}_k^{(p)}[n] = \left( \hat{\mathbf{H}}_k[n] \cdot \bar{\mathbf{F}}_k^{(p)}[n] \cdot \bar{\mathbf{F}}_k^{(p)T}[n] \cdot \hat{\mathbf{H}}_k^T[n] + \frac{N_0}{E_s} \cdot \mathbf{I}_{M_R} \right)^{-1} \cdot \hat{\mathbf{H}}_k[n] \cdot \bar{\mathbf{F}}_k^{(p)}[n]. \quad (5.49)$$

- **Step 4:** Track the variation of the residual interference to determine the termination of the algorithm. The following term that provides a measure of the inter-stream interference, the ISI, and the ICI at the  $p$ -th iteration can be defined

$$\begin{aligned} \xi^{(p)} = & \frac{1}{M} \sum_{k=0}^{M-1} \left\| \text{off} \left( \mathbf{D}_k^{(p)T}[n] \cdot \hat{\mathbf{H}}_k[n] \cdot \bar{\mathbf{F}}_k^{(p)}[n] \right) \right\|_F^2 \\ & + \frac{1}{M} \sum_{q=0}^{M-1} \sum_{\substack{i=n-3 \\ (i,\ell) \neq (n,k)}}^{n+3} \sum_{\ell=k-1}^{k+1} |c_{i,\ell}|^2 \cdot \left\| \mathbf{D}_k^{(p)T}[n] \cdot \check{\mathbf{H}}_k[n] \cdot \bar{\mathbf{F}}_k^{(p)}[n] \right\|_F^2, \end{aligned} \quad (5.50)$$

where  $\text{off}(\cdot)$  denotes an operation of replacing all elements on the diagonal of the input matrix by zeros. Then, we approximate the slope of the variation of the residual interference via [CPN14a]

$$\xi^{(p)'} = \frac{|\xi^{(p)} - \xi^{(p-1)}|}{\xi^{(p-1)}}. \quad (5.51)$$

If  $\xi^{(p)'} < \epsilon$ , terminate the iterative procedure. Otherwise go back to **Step 2** and further update the precoding matrices and decoding matrices. Alternatively, a stopping criterion based on the change of the precoding matrices [CLH14b] can also be employed.

It is worth noting that a joint-subcarrier processing is involved, i.e., the precoding matrices and decoding matrices for all the subcarriers are updated jointly. By contrast, the coordinated beamforming algorithm in [CLH14b] and introduced in Section 5.3 is on a per-subcarrier basis. The lack of the joint-subcarrier processing leads to its failure of effectively mitigating the ICI. In addition, we have observed that rendering the decoding matrices as complex-valued in this SLNR-based coordinated beamforming algorithm results in a much worse performance compared to the real-valued design described above. On the one hand, adopting complex-valued decoding matrices keeps the full degrees of freedom. On the other hand, it becomes even more challenging to suppress the interference in both the real domain and the imaginary domain. As the impact of the latter consequence overweighs that of the former, the performance is degraded compared to the real-valued design of the decoding matrices.

In special cases where  $M_T = M_R = d + 1$ , we have also observed that by initializing  $\mathbf{D}_k^{(0)}[n]$  similarly as (5.19), the iterative approach boils down to a two-step one. In the first step, compute the SVD of  $\tilde{\mathbf{H}}_k[n] = \begin{bmatrix} \text{Im}\{\mathbf{H}_k[n]\} & \text{Re}\{\mathbf{H}_k[n]\} \end{bmatrix} \in \mathbb{R}^{M_R \times 2M_T}$  and obtain  $\mathbf{V}_{k1,0}^{(0)}[n]$  containing the last  $(2M_T - M_R)$  right singular vectors. We further obtain  $\mathbf{U}_{k2,1}^{(0)}[n] \in \mathbb{R}^{M_R \times d}$  containing the first  $d$  left singular vectors of  $\text{Re}\{\mathbf{H}_k[n]\mathbf{F}_k^{(0)}[n]\}$ , where  $\mathbf{F}_k^{(0)}[n]$  is defined via

$$\mathbf{V}_{k1,0}^{(0)} = \begin{bmatrix} \text{Re}\{\mathbf{F}_k^{(0)}[n]\} \\ \text{Im}\{\mathbf{F}_k^{(0)}[n]\} \end{bmatrix}. \quad (5.52)$$

Then, the real-valued decoding matrices  $\mathbf{D}_k^{(0)}[n]$  for *all the subcarriers* are computed as

$$\mathbf{D}_k^{(0)}[n] = \mathbf{U}_{k2,1}^{(0)}[n]. \quad (5.53)$$

In the second step, the  $d$  columns of  $\bar{\mathbf{F}}_k[n]$  are obtained as the  $d$  generalized eigenvectors of the matrix pair  $\{\mathbf{P}_k[n], \mathbf{Q}_k[n]\}$  that correspond to the  $d$  largest generalized eigenvalues, where

$P_k[n]$  and  $Q_k[n]$  are calculated via (5.36) and (5.37), respectively. The decoding matrices  $D_k[n]$  are finally obtained via (5.43) or the simplified version (5.44).

## 5.5. Simulation results

In this section, we evaluate the Bit Error Rate (BER) performance of the proposed coordinated beamforming techniques. For all examples, the number of subcarriers is 1024, the sampling frequency is 11.2 MHz, and the bandwidth is 10 MHz. In case of CP-OFDM, the length of the CP is set to 1/8 of the symbol period. Moreover, the PHYDYAS prototype filter [PHY] with the overlapping factor  $K = 4$  is employed. The data symbols are drawn from a 16 QAM constellation. In the legend of the figures, we use “FBMC/OQAM CBF” and “FBMC/OQAM SLNR-based CBF” to present the coordinated beamforming schemes that we have discussed in Section 5.3 and Section 5.4, respectively.

First, we consider a point-to-point MIMO system where  $M_T = M_R = 6$ , and  $d = 5$ . The ITU Pedestrian-A (Ped-A) channel [ITU97] is adopted. The BER performances of three schemes for MIMO FBMC/OQAM systems are presented and also compared to that of a MIMO CP-OFDM system in Figure 5.1. It can be found that the coordinated beamforming technique

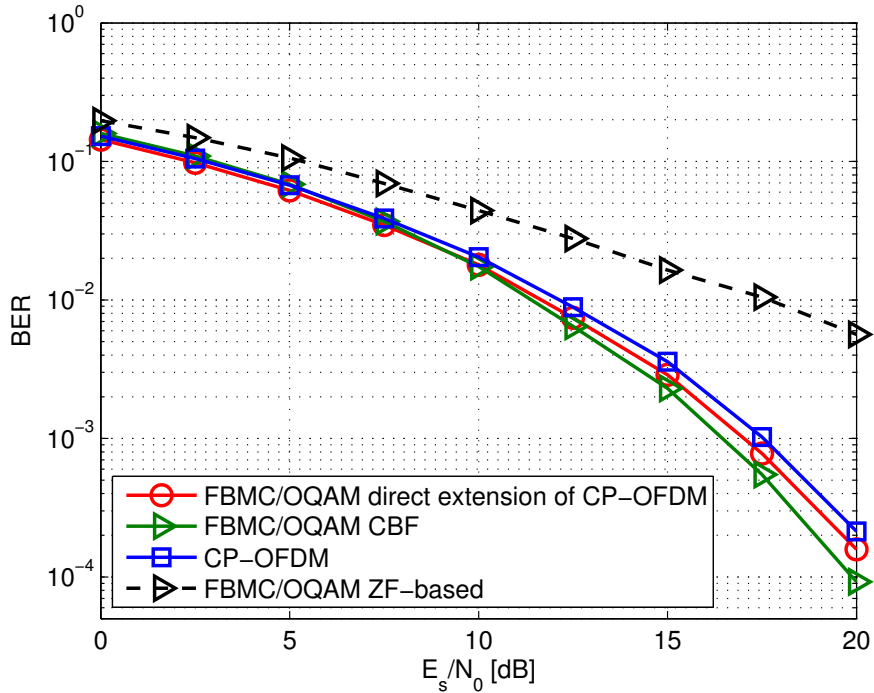


Figure 5.1.: Comparison of the BER performances of different schemes in a system where  $M_T = M_R = 6$ ,  $d = 5$ , and the ITU Ped-A channel is considered; CBF - coordinated beamforming



presented in Section 5.3 yields the best performance. Note that the decoding matrix is initialized as (5.19). In this case, we observe that it takes only two iterations to converge. On the other hand, the transmission scheme that is a straightforward extension of the CP-OFDM case as described in Section 5.2.1 relies on the assumption that the channel frequency responses remain the same across adjacent subcarriers. As the ITU Ped-A channel exhibits frequency selectivity and such an assumption is therefore violated, the performance of this scheme degrades especially in the high Signal-to-Noise-Ratio (SNR) regime. It can also be observed that in this symmetric scenario, the ZF-based precoding algorithm<sup>5</sup> proposed in [CPN13b] performs much worse compared to the other schemes.

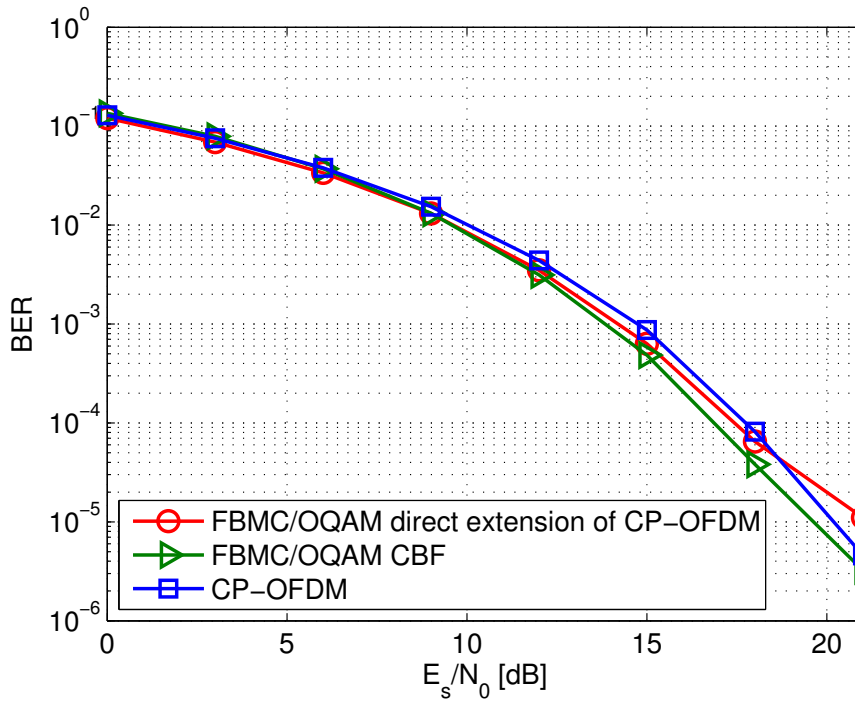


Figure 5.2.: Comparison of the BER performances of different schemes in a system where  $M_T = 6$ ,  $M_R = 7$ ,  $d = 5$ , and the ITU Ped-A channel is considered; CBF - coordinated beamforming

The second example focuses on another point-to-point MIMO setting where the number of

<sup>5</sup>In the implementation of this algorithm, only the ZF-based step that ensures the cancellation of the intrinsic interference is considered. The remaining part of the transmit processing (spatial mapping) and the receive processing (MMSE receiver) are chosen to be the same as the other schemes for the purpose of a fair comparison. Note that the performance of the precoding algorithm proposed in [CPN13b] is dominated by the ZF-based step.

receive antennas  $M_R = 7$  exceeds the number of transmit antennas  $M_T = 6$ . The ITU Ped-A channel [ITU97] is adopted. Note that the precoding technique in [CPN13b] that is only designed for the case where  $M_T \geq M_R$  cannot be employed in such a scenario. In case of the coordinated beamforming technique presented in Section 5.3,  $\epsilon$  for the stopping criterion is set to  $10^{-4}$ , and the maximum number of iterations is 50. In Figure 5.2, the performance of the MIMO FBMC/OQAM system where the proposed coordinated beamforming technique is employed is slightly better than that of the MIMO CP-OFDM system due to the fact that no insertion of the CP is required. The convergence behavior of this scheme is discussed later in the last experiment (cf. Figure 5.5).

In the following, let us assess the performance of the SLNR-based coordinated beamforming algorithm discussed in Section 5.4. We first look at a symmetric point-to-point MIMO setting where  $M_T = M_R = 4$ ,  $d = 3$ , and the ITU Vehicular-A (Veh-A) channel [ITU97] is adopted. In such a scenario where the condition  $M_T = M_R = d + 1$  is fulfilled, we have observed that the two coordinated beamforming schemes presented in Section 5.3 and Section 5.4 can be treated as a two-step method that demands no iterative procedures. Figure 5.3 depicts a BER performance comparison of various approaches. Due to the fact that the ITU Veh-A channel

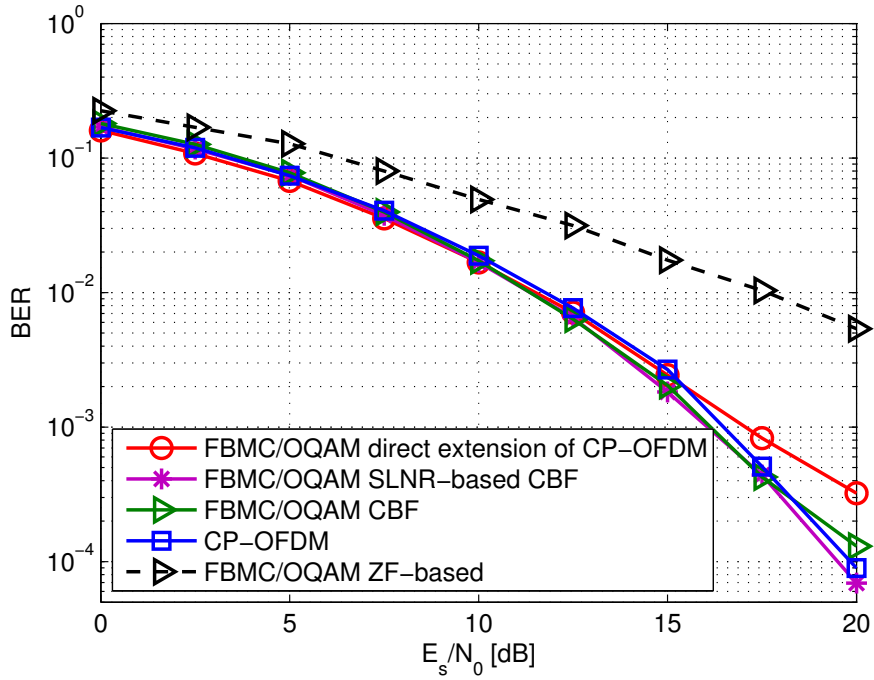


Figure 5.3.: Comparison of the BER performances of different schemes in a system where  $M_T = M_R = 4$ ,  $d = 3$ , and the ITU Veh-A channel is considered; CBF - coordinated beamforming

shows more severe frequency selective fading compared to the ITU Ped-A channel, the BER

curve with respect to the coordinated beamforming scheme presented in Section 5.3 tends to suffer from an error floor in the high SNR regime caused by residual intrinsic interference. On the other hand, the SLNR-based scheme motivated by the aforementioned observation achieves a satisfactory performance thanks to its stronger capability in intrinsic interference mitigation. Similarly as in the first example, the performance of the ZF-based approach [CPN13b] is much worse than those of the other schemes in this symmetric point-to-point MIMO setting. The performance inferiority of the transmission scheme that is a straightforward extension of the CP-OFDM case as described in Section 5.2.1 is more noticeable in this experiment since the more frequency selective ITU Veh-A channel is used.

Finally, we revisit the point-to-point MIMO setting considered for Figure 5.2. Here the ITU Veh-A channel [ITU97] is employed. The rest of the parameters remain the same as for Figure 5.2. It can be seen in Figure 5.4 that in the high SNR regime, the SLNR-based

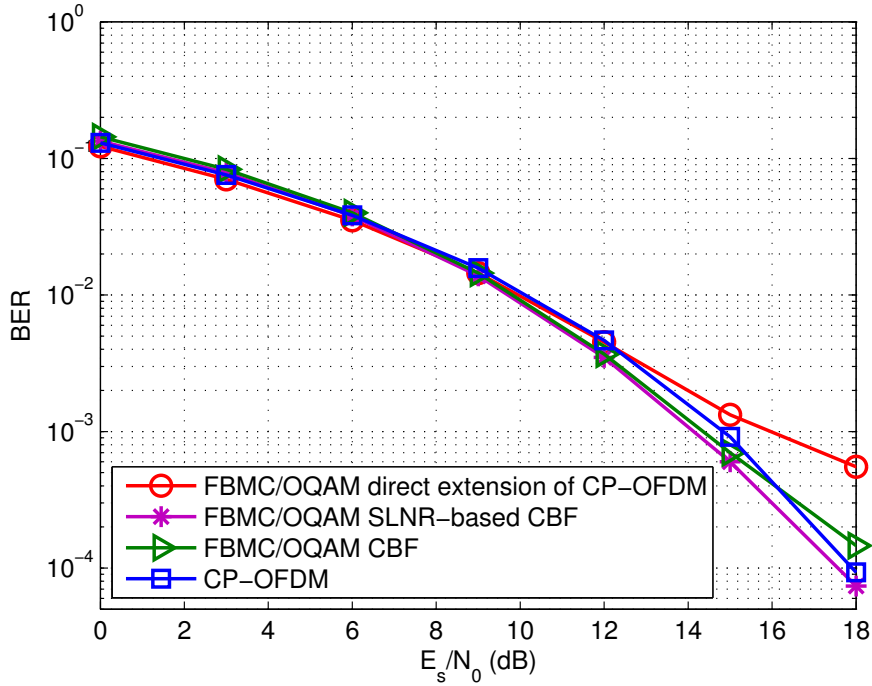


Figure 5.4.: Comparison of the BER performances of different schemes in a system where  $M_T = 6$ ,  $M_R = 7$ ,  $d = 5$ , and the ITU Veh-A channel is considered; CBF - coordinated beamforming

coordinated beamforming scheme outperforms the method that also employs the similar coordinate beamforming concept but a ZF-based precoder. The gain achieved by the former over CP-OFDM-based systems can be observed as well. It is due to the intriguing feature of FBMC/OQAM-based systems that the insertion of the CP is not required. For both co-

ordinated beamforming schemes, the maximum number of iterations is 50. In case of the coordinated beamforming technique presented in Section 5.3,  $\epsilon$  for the stopping criterion is set to  $10^{-4}$ , whereas for the SLNR-based scheme the threshold for the approximated slope of the variation of the residual interference is set to 0.01. In Figure 5.5, we plot the Complementary Cumulative Distribution Function (CCDF) of the number of iterations required for convergence in case of these two coordinated beamforming schemes. It can be observed that the

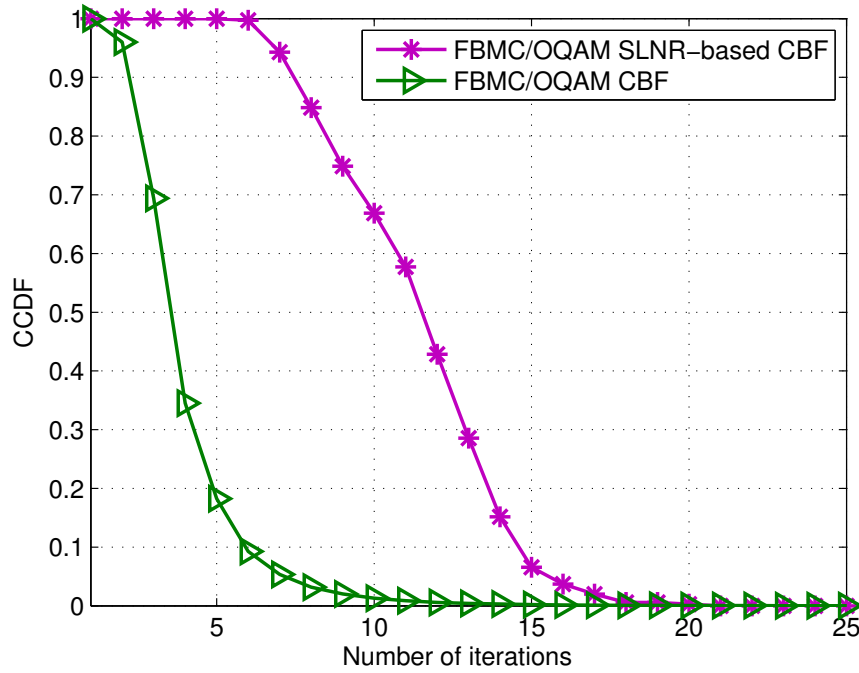


Figure 5.5.: CCDF of the number of iterations in case of the two coordinated beamforming schemes in a system where  $M_T = 6$ ,  $M_R = 7$ ,  $d = 5$ , and the ITU Veh-A channel is considered; CBF - coordinated beamforming

coordinated beamforming scheme introduced in Section 5.3 does not require a large number of iterations to achieve the convergence, indicating an acceptable computational complexity. The performance superiority of the SLNR-based approach comes at a price. To more effectively suppress the intrinsic interference, a joint-subcarrier processing is involved in the SLNR-based scheme. This is very likely to lead to the fact that it takes a larger number of iterations for convergence in case of the SLNR-based scheme compared to the other per-subcarrier coordinated beamforming method.

## 5.6. Summary

In this chapter, we have discussed two coordinated beamforming algorithms for point-to-point MIMO FBMC/OQAM systems designed to alleviate the constraints imposed on the state-of-the-art schemes, e.g., the dimensionality limit or the strict requirement for channels whose frequency responses do not change across adjacent subcarriers. In these two approaches, the calculation of the precoding matrix and the decoding matrix is carried out jointly in an iterative manner. Nevertheless, it is not required that the receiver is informed of the decoding matrix. As an example, the MMSE receiver of the resulting equivalent channel can be used. The first method computes the precoding matrix based on a ZF concept, whereas an SLNR maximizing precoder is devised in the second scheme that is able to more effectively mitigate the intrinsic interference. Numerical results show that these proposed techniques outperform the state-of-the-art algorithms with an acceptable additional complexity. For a special scenario where  $M_T = M_R = d + 1$ , it is observed that both coordinated beamforming algorithms require only two iterations to converge.

## 6. Intrinsic interference mitigating coordinated beamforming for the FBMC/OQAM-based downlink

With the fundamentals of Filter Bank-based Multi-Carrier modulation (FBMC) introduced in Chapter 3, widely linear processing and coordinated beamforming-based transmit-receive schemes have been presented in Chapter 4 and Chapter 5 for point-to-point Multiple-Input Multiple-Output (MIMO) systems where Filter Bank-based Multi-Carrier with Offset Quadrature Amplitude Modulation (FBMC/OQAM) is employed. In this chapter we take it one step further to discuss the design of transmission strategies for the downlink of FBMC/OQAM-based multi-user MIMO systems (as an FBMC/OQAM-based counterpart of the multi-user MIMO downlink setting considered in Chapter 2) and Coordinated Multi-Point (CoMP) systems. Our goal is to alleviate the dimensionality constraint imposed on the state-of-the-art solutions for FBMC/OQAM-based space division multiple access that the total number of receive antennas of the users must not exceed the number of transmit antennas at the base station. First, a single-cell multi-user MIMO downlink system is considered, and two intrinsic interference mitigating coordinated beamforming (IIM-CBF) algorithms are proposed for the case where the number of transmit antennas at the base station is equal to the total number of receive antennas of the users and the case where the former is smaller than the latter, respectively. The central idea is to jointly and iteratively calculate the precoding matrix and the decoding matrix for each subcarrier to mitigate the multi-user interference as well as the intrinsic interference inherent in FBMC/OQAM-based systems. Second, for a CoMP downlink scenario where partial coordination among the base stations is considered, the application of coordinated beamforming-based transmission schemes is further investigated. An appropriate IIM-CBF technique is proposed. Simulation results show that by employing the proposed IIM-CBF schemes, the FBMC/OQAM systems achieve a similar Bit Error Rate (BER) performance as its Orthogonal Frequency Division Multiplexing (OFDM)-based counterpart with the LoCCoBF algorithm presented in Chapter 2 while exhibiting superiority in terms of a higher spectral efficiency, a greater robustness against synchronization errors, and a lower out-of-band radiation. In addition, numerical results with respect to the convergence behavior of the proposed IIM-CBF techniques are presented, and the computational complexity issue is also addressed. The aforementioned results have been published in [CLH14b], [CLH14a], [CLH14d].

## 6.1. Introduction

As a promising alternative to Orthogonal Frequency Division Multiplexing with the Cyclic Prefix insertion (CP-OFDM), Filter Bank-based Multi-Carrier modulation (FBMC) has received great research attention in recent years. By using spectrally well-contained synthesis and analysis filter banks at the transmitter and at the receiver [SSL02], [Bel01], FBMC has an agile spectrum. Thereby, the out-of-band radiation is lower compared to CP-OFDM, and it is consequently beneficial to choose FBMC over CP-OFDM for asynchronous scenarios [FPT08], [SSWB<sup>+</sup>11], or to achieve an effective utilization of spectrum holes [SB10], [SB12]. Moreover, in systems where Filter Bank-based Multi-Carrier with Offset Quadrature Amplitude Modulation (FBMC/OQAM) is employed, the fact that the insertion of the CP is not required as in CP-OFDM-based systems leads to a higher spectral efficiency.

In FBMC/OQAM systems, the real and imaginary parts of each complex-valued data symbol are staggered by half of the symbol period [SSL02], [Bel10] such that the desired signal and the intrinsic interference are separated in the real domain and in the pure imaginary domain, respectively. Different approaches of canceling the intrinsic interference have been proposed based on different assumptions on the frequency selectivity of the channel. In [ZLB10] and [CH13b] where receive processing techniques have been developed for Multiple-Input Multiple-Output (MIMO) FBMC/OQAM systems, it is assumed that the channel frequency responses of adjacent subcarriers stay constant. Consequently, the intrinsic interference is canceled by taking the real part of the resulting signal after the equalization.

To alleviate the constraint on the frequency selectivity of the channel, a Zero Forcing (ZF)-based approach has been proposed in [CPN13b] for multi-stream transmissions in a MIMO FBMC/OQAM system where the channel is not restricted to flat fading. More details of the performance analysis of this algorithm have been presented in [CPN13a]. However, the work in [CPN13b] and [CPN13a] is limited to the case where the number of receive antennas does not exceed the number of transmit antennas. In addition, the authors have shown numerically and have also pointed out that their proposed approach only provides a satisfactory performance in an asymmetric configuration, i.e., when the number of transmit antennas is larger than the number of receive antennas. Based on the concept of mitigating the intrinsic interference mentioned above for point-to-point MIMO FBMC/OQAM systems, the authors in [CPN13c] have adapted the conventional spatial Tomlinson Harashima precoder (STHP) to an FBMC/OQAM-based Multiple-Input Single-Output Broadcast Channel (MISO-BC) which results in a new non-linear precoder. It is known that non-linear precoders have a higher computational complexity compared to linear precoders. Moreover, the non-linear precoding

technique in [CPN13c] is restricted to the case where each user is equipped with only a single receive antenna. On the other hand, a Block Diagonalization (BD)-based linear precoder has been developed in [CPNM13] for the FBMC/OQAM-based multi-user MIMO downlink with Space-Division Multiple Access (SDMA). It adopts the central idea of BD [SSH04] to mitigate the multi-user interference and then uses the ZF-based approach [CPN13b] to deal with the intrinsic interference cancellation for the resulting equivalent single-user transmissions. Consequently, this algorithm inherits the drawback of the ZF-based scheme such that it also fails to achieve a good performance in a symmetric multi-user MIMO downlink setting, where the number of transmit antennas at the base station is equal to the total number of receive antennas of the users. In addition, this linear precoder suffers from the dimensionality constraint that the total number of receive antennas of the users must not exceed the number of transmit antennas at the base station. Note that similarly as in these publications, we focus on scenarios where the channel on each subcarrier is flat fading in this chapter, while Chapter 7 is devoted to the case of highly frequency selective propagation conditions. On the other hand, in the aforementioned publications on the FBMC/OQAM-based multi-user downlink, the impact of the residual Carrier Frequency Offsets (CFOs) has not been investigated.

To the best of our knowledge, FBMC/OQAM-based Coordinated Multi-Point (CoMP) techniques have not been studied in the literature. In the context of CP-OFDM the corresponding research has been very fruitful, and CoMP is known as one of the advanced communication techniques that are able to provide benefits of reduced intercell interference and enhanced cell edge throughput [LSC<sup>+</sup>12], [VPW10], [SRH13], [ZCA09], [KLL<sup>+</sup>09]. Here we focus on downlink CoMP and the schemes that belong to the category of joint transmission [LSC<sup>+</sup>12]. When the full cooperation between the base stations of adjacent cells is assumed, the Channel State Information (CSI) and signals for all users are shared by the base stations. In this case, a virtual multi-user MIMO downlink setting is formed, where the transmit antennas are geographically separated. Thereby, the transmission strategies that have been developed for the single cell multi-user MIMO downlink can be employed. Nevertheless, such a full cooperation scheme is not practical due to many issues, for example, it requires excessive information exchange resulting in a large signaling overhead, and the CSI of all users is very hard to acquire [SRH13]. As a more realistic solution, partial cooperation schemes have been proposed in [SRH13], [ZCA09], [BH07], where the users are classified into two categories, cell [or in some papers [SRH13], [ZCA09] cluster that consists of multiple cells] interior users and cell (cluster) edge users. The base stations of adjacent cells (clusters) transmit the same signals to the cell (cluster) edge users, and coordinated beamforming techniques that rely on the limited cooperation between the cells (clusters) (e.g., the exchange of the beamforming matrices



for cell (cluster) edge users) are employed to suppress the intra-cell (cluster) and inter-cell (cluster) interference. For these downlink CoMP scenarios, it is more likely that the total number of receive antennas of the users served by one base station is larger than the number of transmit antennas. Thus, transmission strategies that are able to tackle such a case are required. Note that in the aforementioned publications on CP-OFDM-based downlink CoMP, perfect synchronization is assumed. However, the asynchronous nature of the interference in the downlink CoMP setting is emphasized in [ZMM<sup>+</sup>08]. It has been shown in [ZMM<sup>+</sup>08] that the lack of perfect synchronization causes a performance degradation. Such a fact greatly motivates the use of FBMC as a replacement of CP-OFDM, as FBMC is more robust against synchronization errors compared to CP-OFDM.

In this chapter, we present the design of intrinsic interference mitigating coordinated beamforming (IIM-CBF) schemes for the FBMC/OQAM-based multi-user MIMO downlink systems and CoMP downlink systems without restricting the configuration with respect to the number of transmit antennas and the number of receive antennas. First, considering the symmetric single-cell multi-user MIMO downlink setting where the number of transmit antennas  $M_T^{(BS)}$  at the base station is equal to the total number of receive antennas of the users  $M_R^{(tot)}$ , we propose to compute the precoding matrix and the decoding matrix jointly in an iterative procedure for each subcarrier. Different choices of the decoding matrix in the initialization step are recommended for different scenarios. The resulting scheme is called IIM-CBF 1. For CP-OFDM-based multi-user MIMO downlink systems, there have been some publications on coordinated beamforming techniques [CLZ<sup>+</sup>14], [SRH13] proposed to cope with the dimensionality constraint imposed on BD-based precoding algorithms [SSH04]. Inspired by these works, the IIM-CBF 2 scheme specifically for FBMC/OQAM-based systems is developed to alleviate the same dimensionality constraint that all state-of-the-art transmission strategies for FBMC/OQAM-based multi-user downlink settings suffer from. It handles the mitigation of the multi-user interference as well as the intrinsic interference. Moreover, we investigate FBMC/OQAM-based CoMP techniques for the first time and provide an extension of the IIM-CBF 2 scheme designed for the FBMC/OQAM-based multi-user MIMO downlink system, namely “IIM-CBF 3”. To evaluate the performance of the proposed IIM-CBF algorithms, we have performed extensive simulations. The BER as well as sum rate performances are shown, and the convergence behavior of the developed coordinated beamforming techniques is also investigated via numerical results. It can be observed that the number of iterations required for the convergence in these IIM-CBF schemes is acceptable. Thus, the additional computational complexity is not prohibitive compared to the closed-form algorithms which fail in scenarios where the total number of receive antennas of the users exceeds the number of transmit an-

Table 6.1.: Acronyms of the proposed intrinsic interference mitigating coordinated beamforming (IIM-CBF) schemes and the corresponding scenarios

Acronyms	Configurations	Interference Type
IIM-CBF 1	multi-user MIMO downlink, $M_T^{(\text{BS})} = M_R^{(\text{tot})}$	intrinsic, multi-user
IIM-CBF 2	multi-user MIMO downlink, $M_T^{(\text{BS})} < M_R^{(\text{tot})}$	intrinsic, multi-user
IIM-CBF 3	CoMP downlink	intrinsic, intra/inter-cell

tennas. In addition, we also investigate the effects of the residual CFOs and demonstrate the superiority of the FBMC/OQAM-based system over its CP-OFDM-based counterpart in the tolerance of the synchronization errors. In Table 6.1, we summarize the proposed IIM-CBF schemes.

The remainder of the chapter is organized as follows: Section 6.2 introduces the data model of a single-cell multi-user MIMO FBMC/OQAM system and reviews two state-of-the-art transmission strategies for such a system. In Section 6.3, the two proposed algorithms IIM-CBF 1 and IIM-CBF 2 are described in detail for the case where the number of transmit antennas at the base station is equal to the total number of receive antennas of the users and the case where the former is smaller than the latter, respectively. Section 6.4 focuses on the CoMP downlink and presents another coordinated beamforming-based transmission scheme, IIM-CBF 3. Numerical results are shown in Section 6.5, before conclusions are drawn in Section 6.6.

## 6.2. FBMC/OQAM-based multi-user MIMO downlink system model

In a multi-user MIMO downlink system where SDMA is employed as illustrated in Figure 6.1, one base station equipped with  $M_T^{(\text{BS})}$  transmit antennas transmits to  $Q$  users at the same time and on the same frequency. The number of receive antennas of the  $q$ -th user is denoted by  $M_{R_q}$ , and the total number of receive antennas of all users served simultaneously is then  $M_R^{(\text{tot})} = \sum_{q=1}^Q M_{R_q}$ . Assuming that the channel on each subcarrier can be treated as flat fading [CPN13b], [CPN13a], [CPNM13], the combined receive vector on the  $k$ -th subcarrier and at the  $n$ -th time instant is denoted by  $\mathbf{y}_k[n] = \begin{bmatrix} \mathbf{y}_{1,k}^T[n] & \mathbf{y}_{2,k}^T[n] & \cdots & \mathbf{y}_{Q,k}^T[n] \end{bmatrix}^T \in \mathbb{C}^{M_R^{(\text{tot})}}$  where

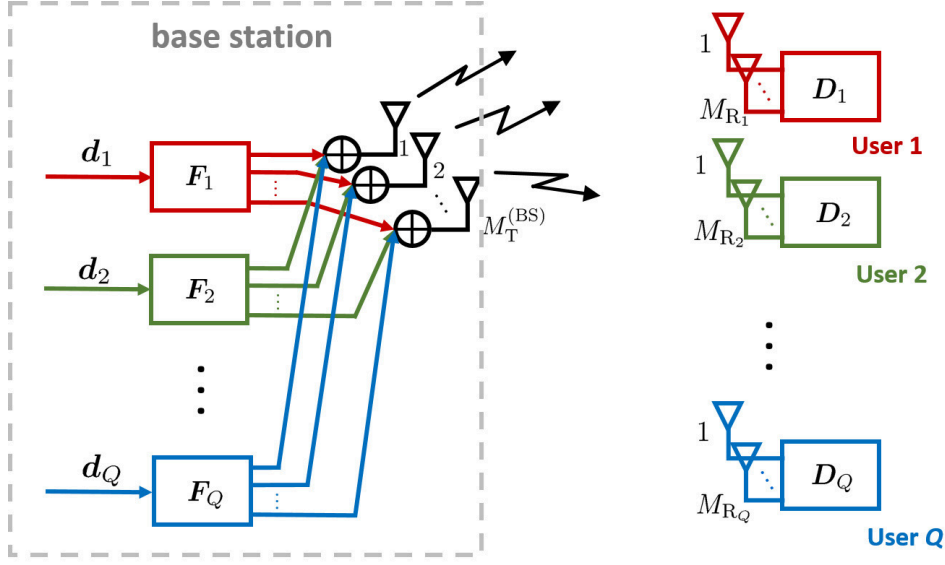


Figure 6.1.: Illustration of the multi-user MIMO downlink setting with linear precoding on a per-subcarrier basis (time and frequency indices ignored in the notation of data vectors, precoding and decoding matrices)

the received signals of all  $Q$  users are stacked and can be represented by

$$\mathbf{y}_k[n] = \mathbf{H}_k[n] \mathbf{F}_k[n] \mathbf{d}_k[n] + \sum_{i=n-3}^{n+3} \sum_{\ell=k-1}^{k+1} \mathbf{H}_\ell[i] \mathbf{F}_\ell[i] c_{i,\ell} \mathbf{d}_\ell[i] + \mathbf{n}_k[n], \quad (\ell, i) \neq (k, n). \quad (6.1)$$

Here  $\mathbf{H}_k[n] \in \mathbb{C}^{M_R^{(\text{tot})} \times M_T^{(\text{BS})}}$  denotes the combined channel matrix of all  $Q$  users<sup>1</sup> and is written as

$$\mathbf{H}_k[n] = \begin{bmatrix} \mathbf{H}_{1,k}^T[n] & \mathbf{H}_{2,k}^T[n] & \cdots & \mathbf{H}_{Q,k}^T[n] \end{bmatrix}^T, \quad (6.2)$$

where  $\mathbf{H}_{q,k}[n] \in \mathbb{C}^{M_{R_q} \times M_T^{(\text{BS})}}$  represents the channel frequency response between the base station and the  $q$ -th user,  $q = 1, 2, \dots, Q$ . The data vector  $\mathbf{d}_k[n] \in \mathbb{R}^d$  with the total number of spatial streams  $d = \sum_{q=1}^Q d_q$  is expressed as

$$\mathbf{d}_k[n] = \begin{bmatrix} \mathbf{d}_{1,k}^T[n] & \mathbf{d}_{2,k}^T[n] & \cdots & \mathbf{d}_{Q,k}^T[n] \end{bmatrix}^T, \quad (6.3)$$

<sup>1</sup>Here we only provide the formulas of the channel matrices, precoding matrices, and data vectors on the  $k$ -th subcarrier and at the  $n$ -th time instant explicitly. In case of the  $\ell$ -th subcarrier and the  $i$ -th time instant, the corresponding expressions can be obtained by replacing  $k$  and  $n$  with  $\ell$  and  $i$ , respectively.

where  $\mathbf{d}_{q,k}[n] \in \mathbb{R}^{d_q}$  denotes the desired signal for the  $q$ -th user on the  $k$ -th subcarrier and at the  $n$ -th time instant when  $(k+n)$  is even<sup>2</sup>, and  $d_q$  denotes the number of spatial streams sent to the  $q$ -th user. The terms  $c_{i,\ell}\mathbf{d}_\ell[i]$  in (6.1) contribute to the intrinsic interference and are pure imaginary if the prototype pulse satisfies the perfect reconstruction property [Bel10], [CPN13c], where  $\ell = k-1, k, k+1, i = n-3, \dots, n+3$ , and  $(\ell, i) \neq (k, n)$ . The coefficients  $c_{i,\ell}$  (cf. Table 3.1) represent the system impulse response determined by the synthesis and analysis filters. The PHYDYAS prototype filter [PHY] is used, and the overlapping factor is chosen to be  $K = 4$ . For more details about FBMC/OQAM systems, the reader is referred to [Bel10]. Moreover,  $\mathbf{n}_k[n] \in \mathbb{C}^{M_R^{(\text{tot})}}$  denotes the combined additive white Gaussian noise vector with variance  $\sigma_n^2$ , and the noise is assumed to be spatially uncorrelated. For the  $q$ -th user, the noise autocorrelation matrix is written as  $\sigma_n^2 \mathbf{I}_{M_{Rq}}$ .

Furthermore,  $\mathbf{F}_k[n] \in \mathbb{C}^{M_T^{(\text{BS})} \times d}$  contains the precoding matrices for all users

$$\mathbf{F}_k[n] = \begin{bmatrix} \mathbf{F}_{1,k}[n]\mathbf{G}_{1,k}[n] & \mathbf{F}_{2,k}[n]\mathbf{G}_{2,k}[n] & \cdots & \mathbf{F}_{Q,k}[n]\mathbf{G}_{Q,k}[n] \end{bmatrix}, \quad (6.4)$$

where  $\mathbf{F}_{q,k}[n] \in \mathbb{C}^{M_T^{(\text{BS})} \times M_{Tq}^{(\text{eq})}}$ ,  $q = 1, 2, \dots, Q$ , are calculated to mitigate the multi-user interference by employing, e.g., BD [SSH04] such that a multi-user MIMO downlink system is decoupled into parallel equivalent single-user transmissions. Here  $M_{Tq}^{(\text{eq})}$  symbolizes the resulting equivalent number of transmit antennas for the  $q$ -th user. It is determined by the precoding scheme employed to suppress the multi-user interference, which will be explained in detail in Section 6.3. In addition,  $\mathbf{G}_{q,k}[n] \in \mathbb{C}^{M_{Tq}^{(\text{eq})} \times d_q}$ ,  $q = 1, 2, \dots, Q$ , are the transmit beamforming matrices for the equivalent single-user systems. Note that throughout this chapter equal power allocation on the spatial streams and subcarriers is assumed.

### 6.2.1. Straightforward extension of the transmission strategy as in case of CP-OFDM

In some publications on MIMO FBMC/OQAM systems, such as [ZLB10] and [CH13b], it is assumed that the channel stays constant across adjacent subcarriers and during consecutive

<sup>2</sup>For the case where  $(k+n)$  is odd, the desired signal on the  $k$ -th subcarrier and at the  $n$ -th time instant is pure imaginary, while the intrinsic interference is real providing that the prototype pulse satisfies the perfect reconstruction property [Bel10], [CPN13c]. As the two cases are essentially equivalent to each other, we only take the case where  $(k+n)$  is even to describe the algorithms in this chapter. In addition, each entry in the data vector corresponds to either the in-phase component or the quadrature component of a QAM symbol that is assumed to have unit energy.

symbol periods, i.e.,

$$\begin{aligned} \mathbf{H}_k[n] &= \mathbf{H}_\ell[i], \\ \ell &= k-1, k, k+1, \quad i = n-3, \dots, n+3. \end{aligned}$$

Since the precoding is performed on a per-subcarrier basis, i.e., the calculation of the precoding matrices for a certain subcarrier is solely determined by the channel on the same subcarrier, the precoding matrices are also the same on adjacent subcarriers. Therefore, the combined received signal on the  $k$ -th subcarrier and at the  $n$ -th time instant can be expressed as

$$\mathbf{y}_k[n] = \mathbf{H}_k[n] \mathbf{F}_k[n] \tilde{\mathbf{d}}_k[n] + \mathbf{n}_k[n], \quad (6.5)$$

where  $\tilde{\mathbf{d}}_k[n]$  contains the real-valued desired signal and the pure imaginary intrinsic interference

$$\tilde{\mathbf{d}}_k[n] = \mathbf{d}_k[n] + \sum_{i=n-3}^{n+3} \sum_{\ell=k-1}^{k+1} c_{i,\ell} \mathbf{d}_\ell[i], \quad (\ell, i) \neq (k, n). \quad (6.6)$$

Considering  $\tilde{\mathbf{d}}_k[n]$  as an equivalent transmitted signal, (6.5) resembles the data model of a CP-OFDM-based multi-user MIMO downlink system. Consequently, transmission strategies that have been developed for multi-user MIMO CP-OFDM downlink systems can be straightforwardly extended to their FBMC/OQAM-based counterparts where only one additional step is required, i.e., taking the real part of the resulting signal after the multiplication by the decoding matrix

$$\hat{\mathbf{d}}_k[n] = \text{Re} \{ \mathbf{D}_k^H[n] \mathbf{y}_k[n] \}, \quad (6.7)$$

where  $\mathbf{D}_k[n] \in \mathbb{C}^{M_R^{(\text{tot})} \times d}$  is the combined block-diagonal decoding matrix on the  $k$ -th subcarrier and at the  $n$ -th time instant that contains the decoding matrices  $\mathbf{D}_{q,k}[n] \in \mathbb{C}^{M_{R_q} \times d_q}$ ,  $q = 1, 2, \dots, Q$ , for the  $Q$  users, respectively. It is worth mentioning that there is no cooperation among the users, and the decoding matrix for each user is computed separately.

The concept of this transmission scheme is simple, does not induce much additional processing compared to CP-OFDM-based systems, and directly applies the state-of-the-art transmit as well as receive processing techniques developed for the CP-OFDM-based multi-user MIMO downlink. Nevertheless, it relies on the impractical assumption that the channel is flat fading and time invariant. In case of frequency selective channels, this transmission strategy fails to completely eliminate the intrinsic interference inherent in FBMC/OQAM systems and thus suffers from a performance degradation as also shown in Section 6.5.

### 6.2.2. Block diagonalization-based approach

In [CPNM13] a BD-based precoding algorithm has been proposed for FBMC/OQAM-based multi-user MIMO downlink systems, where  $M_T^{(\text{BS})} \geq M_R^{(\text{tot})}$ . First, the BD algorithm [SSH04] is used to calculate the first part of the precoding matrix  $\mathbf{F}_{q,k}[n]$ ,  $q = 1, 2, \dots, Q$ , for the  $Q$  users to mitigate the multi-user interference. By rendering  $\mathbf{F}_{q,k}[n]$  for the  $q$ -th user to lie in the null space of all the other users' combined channel matrix, it is ensured that

$$\mathbf{H}_{g,k}[n] \cdot \mathbf{F}_{q,k}[n] = \mathbf{0} \quad \in \mathbb{C}^{M_{R_q} \times M_{T_q}^{(\text{eq})}}, \quad g \neq q. \quad (6.8)$$

Consequently, the received signal of the  $q$ -th user is expressed as

$$\begin{aligned} \mathbf{y}_{q,k}[n] &= \mathbf{H}_{q,k}[n] \mathbf{F}_{q,k}[n] \mathbf{G}_{q,k} \mathbf{d}_{q,k}[n] + \sum_{i=n-3}^{n+3} \sum_{\ell=k-1}^{k+1} \mathbf{H}_{q,\ell}[i] \mathbf{F}_{q,\ell}[i] \mathbf{G}_{q,\ell}[i] c_{i,\ell} \mathbf{d}_{q,\ell}[i] + \mathbf{n}_{q,k}[n], \\ &\quad (\ell, i) \neq (k, n), \end{aligned} \quad (6.9)$$

where  $\mathbf{H}_{q,k}[n] \mathbf{F}_{q,k}[n] \in \mathbb{C}^{M_{R_q} \times M_{T_q}^{(\text{eq})}}$ ,  $q = 1, 2, \dots, Q$ , can be treated as the equivalent channels for parallel single-user transmissions. Recall that here the terms  $c_{i,\ell} \mathbf{d}_{q,\ell}[i]$  ( $\ell = k-1, k, k+1$ ,  $i = n-3, \dots, n+3$ , and  $(\ell, i) \neq (k, n)$ ) are pure imaginary,  $\text{Re}\{c_{i,\ell} \mathbf{d}_{q,\ell}[i]\} = \mathbf{0}$ . Let us expand the real part of the received signal of the  $q$ -th user

$$\begin{aligned} \text{Re}\{\mathbf{y}_{q,k}[n]\} &= \text{Re}\{\mathbf{H}_{q,k}[n] \mathbf{F}_{q,k}[n] \mathbf{G}_{q,k}\} \mathbf{d}_{q,k}[n] \\ &\quad + (-1) \cdot \sum_{i=n-3}^{n+3} \sum_{\ell=k-1}^{k+1} \text{Im}\{\mathbf{H}_{q,\ell}[i] \mathbf{F}_{q,\ell}[i] \mathbf{G}_{q,\ell}[i]\} \text{Im}\{c_{i,\ell} \mathbf{d}_{q,\ell}[i]\} \\ &\quad + \text{Re}\{\mathbf{n}_{q,k}[n]\}, \quad (\ell, i) \neq (k, n). \end{aligned} \quad (6.10)$$

To cancel the intrinsic interference, the second term on the right hand side of (6.10) should be rendered as zero. This can be achieved by computing the second part of the precoding matrix, i.e.,  $\mathbf{G}_{q,k}[n]$ , such that [CPNM13]

$$\text{Im}\{\mathbf{H}_q \mathbf{F}_q \mathbf{G}_q\} = \mathbf{0} \quad \in \mathbb{C}^{M_{R_q} \times d_q}, \quad (6.11)$$

where  $\mathbf{F}_q \mathbf{G}_q$  represents the precoding matrix for the  $q$ -th user on a certain subcarrier and at a certain time instant, and  $\mathbf{H}_q$  denotes the channel matrix for the  $q$ -th user on the same subcarrier and at the same time instant. From now on, the time and frequency indices are ignored as the precoding is performed on a per-subcarrier basis. It should be noted that the optimization of the power allocation is originally incorporated in the BD-based technique

[CPNM13]. Nevertheless, this part of the algorithm is not reviewed in detail here, since optimizing the power allocation is beyond the scope of this thesis and equal power allocation is assumed. In the simulations section, when using the BD-based technique as a benchmark scheme, equal power allocation is also adopted to ensure a fair comparison.

This approach outperforms the straightforward extension of the CP-OFDM case in the sense that it is able to tolerate a certain level of the frequency selectivity of the channel. However, it suffers from the dimensionality constraint that the number of transmit antennas at the base station has to be larger than or equal to the total number of receive antennas of the users, i.e.,  $M_T^{(\text{BS})} \geq M_R^{(\text{tot})}$ . For the case where  $M_T^{(\text{BS})} = M_R^{(\text{tot})}$ , this scheme is not able to provide a satisfactory performance as shown later in the simulation section.

### 6.3. Coordinated beamforming for the single-cell multi-user MIMO downlink

Based on the philosophy on the precoding design for multi-user MIMO downlink settings first proposed in [SH08], the precoding matrix for each user is decomposed into two parts as already shown in (6.4). For the  $q$ -th user, the first part  $\mathbf{F}_q$  eliminates the multi-user interference<sup>3</sup>. The second part  $\mathbf{G}_q$  plays the role of the transmit beamforming matrix for each equivalent single-user transmission after the multi-user interference cancellation. Due to the fact that the intrinsic interference resides in FBMC/OQAM-based systems, we propose to further decouple  $\mathbf{G}_q$  into two parts, i.e.,

$$\mathbf{G}_q = \mathbf{G}_{q,1} \mathbf{G}_{q,2} \in \mathbb{C}^{M_{Tq}^{(\text{eq})} \times d_q}, \quad (6.12)$$

where  $\mathbf{G}_{q,1} \in \mathbb{C}^{M_{Tq}^{(\text{eq})} \times M_{xq}}$  is computed to suppress the intrinsic interference, and  $\mathbf{G}_{q,2} \in \mathbb{R}^{M_{xq} \times d_q}$  is used for the spatial mapping.

#### 6.3.1. The IIM-CBF 1 algorithm

We first propose a coordinated beamforming-based transmission scheme IIM-CBF 1 for symmetric multi-user MIMO downlink settings where  $M_T^{(\text{BS})} = M_R^{(\text{tot})}$ . BD [SSH04] is employed to calculate the first part of the precoding matrices  $\mathbf{F}_q \in \mathbb{C}^{M_T^{(\text{BS})} \times M_{Tq}^{(\text{eq})}}$ ,  $q = 1, 2, \dots, Q$ . For the  $q$ -th user, define a matrix  $\widetilde{\mathbf{H}}_q \in \mathbb{C}^{(M_R^{(\text{tot})} - M_{Rq}) \times M_T^{(\text{BS})}}$  as

$$\widetilde{\mathbf{H}}_q = \begin{bmatrix} \mathbf{H}_1^T & \cdots & \mathbf{H}_{q-1}^T & \mathbf{H}_{q+1}^T & \cdots & \mathbf{H}_Q^T \end{bmatrix}^T, \quad (6.13)$$

<sup>3</sup>In IIM-CBF 3 for the CoMP downlink,  $\mathbf{F}_q$  suppresses both the intra-cell interference and the inter-cell interference.

which contains the channel matrices of all the other users. Computing the Singular Value Decomposition (SVD) of  $\widetilde{\mathbf{H}}_q$  gives

$$\widetilde{\mathbf{H}}_q = \widetilde{\mathbf{U}}_q \widetilde{\Sigma}_q \begin{bmatrix} \widetilde{\mathbf{V}}_{(1,0)} & \widetilde{\mathbf{V}}_{(q,0)} \end{bmatrix}^H, \quad (6.14)$$

where  $\widetilde{\mathbf{V}}_{(q,0)}$  contains the last  $M_{T_q}^{(\text{eq})}$  right singular vectors. They form an orthonormal basis for the null space of  $\widetilde{\mathbf{H}}_q$  [SSH04]. Then, the precoding matrix  $\mathbf{F}_q$  for the  $q$ -th user is obtained as

$$\mathbf{F}_q = \widetilde{\mathbf{V}}_{(q,0)} \in \mathbb{C}^{M_T^{(\text{BS})} \times M_{T_q}^{(\text{eq})}}. \quad (6.15)$$

The resulting equivalent number of transmit antennas  $M_{T_q}^{(\text{eq})} = M_T^{(\text{BS})} - \sum_{g=1, g \neq q}^Q M_{R_g}$  is equal to  $M_{R_q}$ . The reader is referred [SSH04] for more details of the BD algorithm.

For the  $q$ -th user, we propose to use the coordinated beamforming scheme introduced in Section 5.3 for point-to-point MIMO FBMC/OQAM systems such that the second part of its precoding matrix  $\mathbf{G}_q$  and its decoding matrix are jointly and iteratively updated. An equivalent channel matrix  $\mathbf{H}_{e_q}$  is defined as

$$\mathbf{H}_{e_q} = \mathbf{D}_q^T \mathbf{H}_q \mathbf{F}_q \in \mathbb{C}^{d_q \times M_{T_q}^{(\text{eq})}}, \quad (6.16)$$

where  $\mathbf{D}_q \in \mathbb{R}^{M_{R_q} \times d_q}$  is the real-valued decoding matrix. The proposed coordinated beamforming algorithm is summarized as follows:

- **Step 1:** Initialize the decoding matrix  $\mathbf{D}_q^{(0)} \in \mathbb{R}^{M_{R_q} \times d_q}$ , set the iteration index  $p$  to zero, and set a threshold  $\epsilon$  for the stopping criterion<sup>4</sup>. The decoding matrix is generated randomly if the current subcarrier is the first one; otherwise set the decoding matrix as the one calculated for the previous subcarrier [CLZ<sup>+</sup>14].
- **Step 2:** Set  $p \leftarrow p + 1$  and calculate the equivalent channel matrix  $\mathbf{H}_{e_q}^{(p)}$  in the  $p$ -th iteration as

$$\mathbf{H}_{e_q}^{(p)} = \mathbf{D}_q^{(p-1)T} \mathbf{H}_q \mathbf{F}_q \in \mathbb{C}^{d_q \times M_{T_q}^{(\text{eq})}}, \quad (6.17)$$

where  $\mathbf{F}_q$  is calculated via (6.15). Define a matrix

$$\check{\mathbf{H}}_{e_q}^{(p)} = \begin{bmatrix} \text{Im} \{ \mathbf{H}_{e_q}^{(p)} \} & \text{Re} \{ \mathbf{H}_{e_q}^{(p)} \} \end{bmatrix} \in \mathbb{R}^{d_q \times 2M_{T_q}^{(\text{eq})}}. \quad (6.18)$$

<sup>4</sup>If not stated otherwise, the threshold  $\epsilon$  for the stopping criterion is set to  $10^{-5}$  in this chapter.



- **Step 3:** Calculate the precoding matrix  $\mathbf{G}_q^{(p)} = \mathbf{G}_{q,1}^{(p)} \mathbf{G}_{q,2}^{(p)}$  for the  $p$ -th iteration. First, we perform the SVD of  $\check{\mathbf{H}}_{e_q}^{(p)}$  as

$$\check{\mathbf{H}}_{e_q}^{(p)} = \mathbf{U}_{q,1}^{(p)} \boldsymbol{\Sigma}_{q,1}^{(p)} \mathbf{V}_{q,1}^{(p)\top}. \quad (6.19)$$

Denoting the rank of  $\check{\mathbf{H}}_{e_q}^{(p)}$  as  $r_q^{(p)}$ , we define  $\mathbf{V}_{q,1,0}^{(p)} \in \mathbb{R}^{2M_{T_q}^{(\text{eq})} \times M_{x_q}}$  as containing the last  $M_{x_q} = 2M_{T_q}^{(\text{eq})} - r_q^{(p)}$  right singular vectors that form an orthonormal basis for the null space of  $\check{\mathbf{H}}_{e_q}^{(p)}$ . Hence,  $\mathbf{G}_{q,1}^{(p)}$  for the  $p$ -th iteration can be obtained via

$$\mathbf{V}_{1,0}^{(p)} = \begin{bmatrix} \text{Re} \left\{ \mathbf{G}_{q,1}^{(p)} \right\} \\ \text{Im} \left\{ \mathbf{G}_{q,1}^{(p)} \right\} \end{bmatrix} \in \mathbb{R}^{2M_{T_q}^{(\text{eq})} \times M_{x_q}}, \quad (6.20)$$

such that  $\text{Im} \left\{ \mathbf{H}_{e_q}^{(p)} \mathbf{G}_{q,1}^{(p)} \right\} = \mathbf{0}$ . To further calculate  $\mathbf{G}_{q,2}^{(p)}$ , the following equivalent channel matrix after the cancellation of the intrinsic interference for the  $p$ -th iteration is defined as

$$\widetilde{\mathbf{H}}_{e_q}^{(p)} = \text{Re} \left\{ \mathbf{H}_{e_q}^{(p)} \mathbf{G}_{q,1}^{(p)} \right\} \in \mathbb{R}^{d_q \times M_{x_q}}. \quad (6.21)$$

Further calculate the SVD of  $\widetilde{\mathbf{H}}_{e_q}^{(p)}$ , and define  $\mathbf{V}_{q,2,1}^{(p)} \in \mathbb{R}^{M_{x_q} \times d_q}$  as containing the first  $d_q$  right singular vectors. Thereby,  $\mathbf{G}_{q,2}^{(p)}$  is obtained as  $\mathbf{G}_{q,2}^{(p)} = \mathbf{V}_{q,2,1}^{(p)}$ .

- **Step 4:** Update the decoding matrix based on the equivalent channel matrix after the cancellation of the intrinsic interference where only the processing at the transmitter is considered

$$\widetilde{\mathbf{H}}_{\text{etx}_q}^{(p)} = \text{Re} \left\{ \mathbf{H}_q \mathbf{F}_q \mathbf{G}_q^{(p)} \right\} \in \mathbb{R}^{M_{R_q} \times d_q}. \quad (6.22)$$

When the MMSE receiver<sup>5</sup> is used, the decoding matrix has the following form

$$\mathbf{D}_q^{(p)} = \widetilde{\mathbf{H}}_{\text{etx}_q}^{(p)} \left( \widetilde{\mathbf{H}}_{\text{etx}_q}^{(p)\top} \widetilde{\mathbf{H}}_{\text{etx}_q}^{(p)} + \sigma_n^2 \mathbf{I}_{d_q} \right)^{-1}. \quad (6.23)$$

- **Step 5:** Calculate the term  $\Delta(\mathbf{G}_q)$  defined as

$$\Delta(\mathbf{G}_q) = \left\| \mathbf{G}_q^{(p)} - \mathbf{G}_q^{(p-1)} \right\|_{\text{F}}^2, \quad (6.24)$$

which measures the change of the precoding matrix  $\mathbf{G}_q$ . If  $\Delta(\mathbf{G}_q) < \epsilon$ , the convergence

<sup>5</sup>Other receivers, such as zero forcing or maximum ratio combining, can also be employed in this coordinated beamforming algorithm.

is achieved, and the iterative procedure terminates. Otherwise go back to **Step 2**.

It is important to note that in the special case where  $M_{T_q}^{(\text{eq})} = M_{R_q} = d_q + 1$ , we propose to compute the decoding matrix in the initialization step as follows. Then it is observed that the coordinated beamforming technique only needs two iterations to converge<sup>6</sup>. First, calculate the SVD of  $\check{\mathbf{H}}_q \in \mathbb{R}^{M_{R_q} \times 2M_{T_q}^{(\text{eq})}}$

$$\check{\mathbf{H}}_q = \begin{bmatrix} \text{Im}\{\mathbf{H}_q \mathbf{F}_q\} & \text{Re}\{\mathbf{H}_q \mathbf{F}_q\} \end{bmatrix}, \quad (6.25)$$

and let  $\mathbf{V}_{q,1,0}^{(0)}$  contain the last  $(2M_{T_q}^{(\text{eq})} - M_{R_q})$  right singular vectors. Defining  $\mathbf{G}_{q,1}^{(0)}$  via

$$\mathbf{V}_{q,1,0}^{(0)} = \begin{bmatrix} \text{Re}\{\mathbf{G}_{q,1}^{(0)}\} \\ \text{Im}\{\mathbf{G}_{q,1}^{(0)}\} \end{bmatrix}, \quad (6.26)$$

we compute  $\mathbf{U}_{q,2,1}^{(0)} \in \mathbb{R}^{M_{R_q} \times d_q}$  from the SVD of  $\text{Re}\{\mathbf{H}_q \mathbf{F}_q \mathbf{G}_{q,1}^{(0)}\}$  such that it contains the first  $d_q$  left singular vectors. Then the decoding matrix for the initialization step is chosen as

$$\mathbf{D}_q^{(0)} = \mathbf{U}_{q,2,1}^{(0)}. \quad (6.27)$$

### 6.3.2. The IIM-CBF 2 algorithm

In multi-user MIMO FBMC/OQAM downlink systems where the total number of receive antennas of the users  $M_R^{(\text{tot})}$  exceeds the number of transmit antennas at the base station  $M_T^{(\text{BS})}$ , the BD algorithm [SSH04] or the BD-based technique [CPNM13] cannot be employed to achieve the multi-user interference or the intrinsic interference suppression. Therefore, we propose another iterative procedure to jointly compute the precoding matrix and the decoding matrix. Let us first define an equivalent combined channel matrix after the decoding at the user terminals as

$$\mathbf{H}_e = \begin{bmatrix} \mathbf{D}_1^T \mathbf{H}_1 \\ \mathbf{D}_2^T \mathbf{H}_2 \\ \vdots \\ \mathbf{D}_Q^T \mathbf{H}_Q \end{bmatrix} \in \mathbb{C}^{d \times M_T^{(\text{BS})}}. \quad (6.28)$$

<sup>6</sup>Since the stopping criterion is defined based on the change of the precoding matrix (6.24), the fact that the algorithm converges within two iterations means that the precoding matrix is barely changed in the second iteration. In other words, though not proved analytically, after initializing the decoding matrices via (6.27), only one iteration (performing Step 2 – 4) is enough to obtain the precoding and decoding matrices.

Unlike the coordinated beamforming schemes in [SRH13] or [CLZ<sup>+</sup>14], we choose real-valued decoding matrices<sup>7</sup>  $\mathbf{D}_q \in \mathbb{R}^{M_{R_q} \times d_q}$ ,  $q = 1, 2, \dots, Q$ . Although the BD-based concept cannot be employed on the physical channel due to the dimensionality constraint, it can be used on this equivalent channel. The proposed IIM-CBF 2 algorithm for the FBMC/OQAM-based multi-user MIMO downlink system is described in detail as follows:

- **Step 1:** Initialize the decoding matrices  $\mathbf{D}_q^{(0)} \in \mathbb{R}^{M_{R_q} \times d_q}$  ( $q = 1, \dots, Q$ ), set the iteration index  $p$  to zero, and set a threshold  $\epsilon$  for the stopping criterion. If the current subcarrier is the first one, the decoding matrices are generated randomly; otherwise, set the decoding matrices as those calculated for the previous subcarrier [CLZ<sup>+</sup>14].
- **Step 2:** Set  $p \leftarrow p + 1$  and calculate the equivalent channel matrix  $\mathbf{H}_e^{(p)}$  in the  $p$ -th iteration as

$$\mathbf{H}_e^{(p)} = \begin{bmatrix} \mathbf{H}_{e_1}^{(p)\top} & \mathbf{H}_{e_2}^{(p)\top} & \dots & \mathbf{H}_{e_Q}^{(p)\top} \end{bmatrix}^\top, \quad (6.29)$$

where  $\mathbf{H}_{e_q}^{(p)} = \mathbf{D}_q^{(p-1)\top} \mathbf{H}_q$  is the equivalent channel matrix for the  $q$ -th user in the  $p$ -th iteration.

- **Step 3:** Calculate the precoding matrices  $\mathbf{F}_q^{(p)}$  ( $q = 1, \dots, Q$ ) in the  $p$ -th iteration to cancel the multi-user interference based on the BD algorithm [SSH04]. For the  $q$ -th user, define a matrix  $\widetilde{\mathbf{H}}_{e_q}^{(p)} \in \mathbb{C}^{(d-d_q) \times M_T^{(\text{BS})}}$  as

$$\widetilde{\mathbf{H}}_{e_q}^{(p)} = \begin{bmatrix} \mathbf{H}_{e_1}^{(p)\top} & \dots & \mathbf{H}_{e_{q-1}}^{(p)\top} & \mathbf{H}_{e_{q+1}}^{(p)\top} & \dots & \mathbf{H}_{e_Q}^{(p)\top} \end{bmatrix}^\top, \quad (6.30)$$

which contains the equivalent channel matrices of all the other users that are calculated in **Step 2**. The precoding matrix  $\mathbf{F}_q^{(p)}$  for the  $q$ -th user in the  $p$ -th iteration is obtained as  $\mathbf{F}_q^{(p)} = \widetilde{\mathbf{V}}_{e_{(q,0)}}^{(p)} \in \mathbb{C}^{M_T^{(\text{BS})} \times M_{T_q}^{(\text{eq})}}$ , where  $\widetilde{\mathbf{V}}_{e_{(q,0)}}^{(p)}$  contains the last  $M_{T_q}^{(\text{eq})}$  right singular vectors that form an orthonormal basis for the null space of  $\widetilde{\mathbf{H}}_{e_q}^{(p)}$  [SSH04]. To this end, the multi-user MIMO downlink transmission is decoupled into parallel equivalent single-user MIMO transmissions that will be considered in the following steps.

- **Step 4:** Define a matrix  $\check{\mathbf{H}}_{e_q}^{(p)} \in \mathbb{R}^{d_q \times 2M_{T_q}^{(\text{eq})}}$  for the  $q$ -th user based on its equivalent channel matrix  $\mathbf{H}_{e_q}^{(p)} \mathbf{F}_q^{(p)}$  after the cancellation of the multi-user interference

$$\check{\mathbf{H}}_{e_q}^{(p)} = \begin{bmatrix} \text{Im} \left\{ \mathbf{H}_{e_q}^{(p)} \mathbf{F}_q^{(p)} \right\} & \text{Re} \left\{ \mathbf{H}_{e_q}^{(p)} \mathbf{F}_q^{(p)} \right\} \end{bmatrix}. \quad (6.31)$$

<sup>7</sup>Although great effort has been spent on devising an IIM-CBF scheme where the decoding matrices are complex-valued, this attempt has not been successful. The reason might be that when adopting complex-valued decoding matrices, it becomes more challenging to mitigate the intrinsic interference in both the real domain and the imaginary domain, in spite of the fact that the full degrees of freedom are kept.

- **Step 5:** Calculate the precoding matrix  $\mathbf{G}_q^{(p)} = \mathbf{G}_{q,1}^{(p)} \mathbf{G}_{q,2}^{(p)}$  for the  $q$ -th user in the  $p$ -th iteration. First, we perform the SVD of  $\tilde{\mathbf{H}}_{e_q}^{(p)}$  and obtain  $\mathbf{V}_{q,1,0}^{(p)} \in \mathbb{R}^{2M_{T_q}^{(\text{eq})} \times M_{x_q}}$  as containing the last  $M_{x_q} = 2M_{T_q}^{(\text{eq})} - r_q^{(p)}$  right singular vectors that form an orthonormal basis for the null space of  $\tilde{\mathbf{H}}_{e_q}^{(p)}$ , where  $r_q^{(p)}$  denotes the rank of  $\tilde{\mathbf{H}}_{e_q}^{(p)}$ . Hence,  $\mathbf{G}_{q,1}^{(p)} \in \mathbb{C}^{M_{T_q}^{(\text{eq})} \times M_{x_q}}$  can be obtained via

$$\mathbf{V}_{q,1,0}^{(p)} = \begin{bmatrix} \text{Re} \left\{ \mathbf{G}_{q,1}^{(p)} \right\} \\ \text{Im} \left\{ \mathbf{G}_{q,1}^{(p)} \right\} \end{bmatrix} \in \mathbb{R}^{2M_{T_q}^{(\text{eq})} \times M_{x_q}} \quad (6.32)$$

such that (6.11) is fulfilled to achieve the mitigation of the intrinsic interference.

Now we define the following equivalent channel matrix after canceling the intrinsic interference for the  $q$ -th user in the  $p$ -th iteration

$$\bar{\mathbf{H}}_{e_q}^{(p)} = \text{Re} \left\{ \mathbf{H}_{e_q}^{(p)} \mathbf{F}_q^{(p)} \mathbf{G}_{q,1}^{(p)} \right\} \in \mathbb{R}^{d_q \times M_{x_q}}. \quad (6.33)$$

Further calculate the SVD of  $\bar{\mathbf{H}}_{e_q}^{(p)}$  and define  $\mathbf{V}_{q,2,1}^{(p)} \in \mathbb{R}^{M_{x_q} \times d_q}$  as containing the first  $d_q$  right singular vectors. Then  $\mathbf{G}_{q,2}^{(p)}$  is obtained as  $\mathbf{G}_{q,2}^{(p)} = \mathbf{V}_{q,2,1}^{(p)}$ .

- **Step 6:** Update the decoding matrix for each user based on the real-valued equivalent channel matrix where the processing at the transmitter and the procedure of taking the real part of the receive signal are taken into account

$$\mathbf{H}_{\text{etx}_q}^{(p)} = \text{Re} \left\{ \mathbf{H}_q \mathbf{F}_q^{(p)} \mathbf{G}_q^{(p)} \right\} \in \mathbb{R}^{M_{R_q} \times d_q}, \quad q = 1, \dots, Q. \quad (6.34)$$

When the MMSE receiver is used, the update of the real-valued decoding matrix in the  $p$ -th iteration for the  $q$ -th user has the following form:

$$\mathbf{D}_q^{(p)} = \mathbf{H}_{\text{etx}_q}^{(p)} \left( \mathbf{H}_{\text{etx}_q}^{(p)\text{T}} \mathbf{H}_{\text{etx}_q}^{(p)} + \sigma_n^2 \mathbf{I}_{d_q} \right)^{-1}. \quad (6.35)$$

- **Step 7:** Calculate the term  $\xi^{(p)}$  that measures the residual multi-user and the inter-stream interference for the  $p$ -th iteration defined as

$$\xi^{(p)} = \left\| \text{off} \left( \mathbf{D}^{(p)\text{T}} \text{Re} \left\{ \mathbf{H} \mathbf{F}^{(p)} \right\} \right) \right\|_{\text{F}}^2, \quad (6.36)$$

where  $\text{off}(\cdot)$  indicates an operation of keeping all off-diagonal elements of its input matrix while setting its diagonal elements to zero. If  $\xi^{(p)} < \epsilon$ , the convergence is achieved, and

the iterative procedure terminates. Otherwise go back to **Step 2**.

Note that the stopping criterion similar as (6.24) that tracks the change of the precoding matrix can also be adopted<sup>8</sup>. In addition, for both IIM-CBF schemes proposed in this section and Section 6.3.1, it is not required that the users are informed of the decoding matrices that are obtained at the base station while computing the precoding matrices. After the users acquire the information of the effective channel via channel estimation, the receive processing can be performed. For example, the MMSE receiver of the effective channel for each user can be employed according to (6.35).

## 6.4. Coordinated beamforming for the CoMP downlink

In this section, we focus on a CoMP downlink setting based on [SRH13]. Note that in [SRH13] a clustered cellular scenario is considered where each cluster contains multiple cells. Since full cooperation is assumed in each cluster, the downlink transmissions for each cluster resemble those of the single-cell multi-user MIMO downlink. Thereby, we simplify the scenario description of the CoMP downlink and only consider joint transmission of adjacent cells. It is assumed that the cell interior users only receive signals from their own base station and suffer only from the intra-cell interference, i.e., the multi-user interference as in the single-cell multi-user MIMO downlink scenarios. On the other hand, both the intra-cell interference and the inter-cell interference have an impact on the cell edge users. To assist the cell edge users to combat the interference and also deal with the greater path loss compared to the cell interior users, the base stations of the adjacent cells transmit the same signals to each cell edge user. An example of a two-cell FBMC/OQAM-based CoMP downlink scenario is illustrated in Figure 6.2. Assume that Cell 1 and Cell 2 are equipped with  $M_T^{(\text{BS1})}$  and  $M_T^{(\text{BS2})}$  transmit antennas, respectively. The number of users served by each cell is denoted as  $Q$ . The received signal on the  $k$ -th subcarrier and at the  $n$ -th time instant of the  $q$ -th user of Cell 1 as a cell interior user is expressed as

$$\begin{aligned} \mathbf{y}_{q,k}[n] = & \mathbf{H}_{q,k,(1)}[n] \mathbf{F}_{k,(1)}[n] \mathbf{d}_{k,(1)}[n] + \sum_{i=n-3}^{n+3} \sum_{\ell=k-1}^{k+1} \mathbf{H}_{q,\ell,(1)}[i] \mathbf{F}_{\ell,(1)}[i] c_{i,\ell} \mathbf{d}_{\ell,(1)}[i] \\ & + \mathbf{n}_{q,k}[n], \quad (\ell, i) \neq (k, n), \end{aligned} \quad (6.37)$$

---

<sup>8</sup>These two stopping criteria require different thresholds for the convergence. In this chapter, we only present numerical results obtained when the stopping criterion as in (6.36) is employed, and the threshold  $\epsilon$  is set to  $10^{-5}$ .

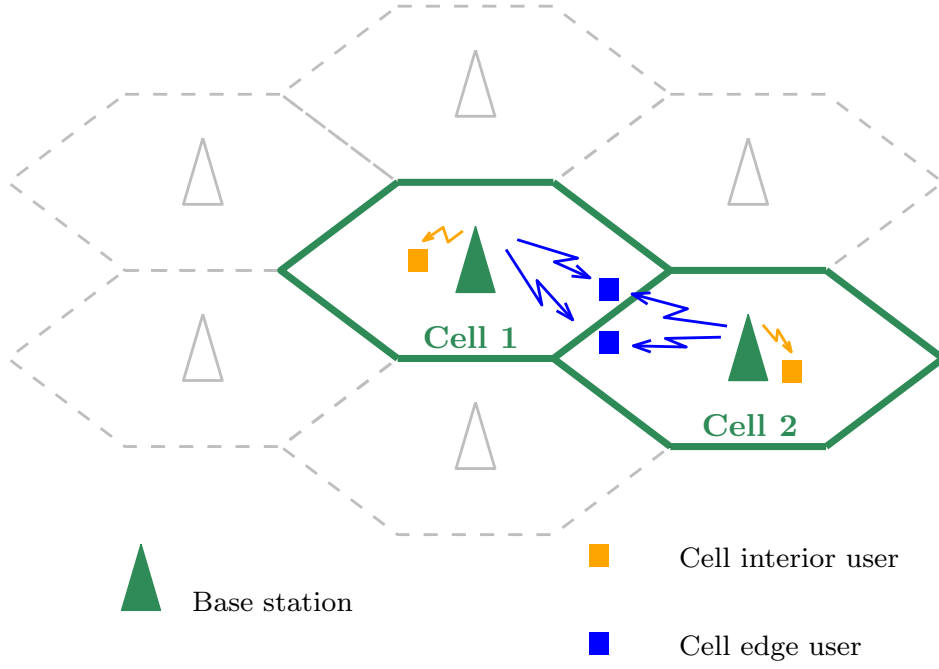


Figure 6.2.: An example of a two-cell CoMP downlink scenario where a cell interior user and two cell edge users are served in each cell

where  $\mathbf{H}_{g,k,(1)}[n] \in \mathbb{C}^{M_{R_q} \times M_T^{(\text{BS1})}}$  represents the channel matrix between the base station of Cell 1 and the  $g$ -th user with  $M_{R_q}$  receive antennas,  $\mathbf{F}_{k,(1)}[n]$  symbolizes the precoding matrix for Cell 1, and  $\mathbf{d}_{k,(1)}[n]$  contains the signals for all users served by Cell 1. It can be seen that for a cell interior user, assuming that the inter-cell interference is negligible, the transmission from the base station in its own cell is the same as in a single-cell multi-user MIMO downlink system (cf. (6.1)). For the  $g$ -th user that is a cell edge user and receives the same signals from both Cell 1 and Cell 2, its received signal on the  $k$ -th subcarrier and at the  $n$ -th time instant has the following form

$$\begin{aligned} \mathbf{y}_{g,k}[n] = & \mathbf{H}_{g,k,(1)}[n] \mathbf{F}_{k,(1)}[n] \mathbf{d}_{k,(1)}[n] + \sum_{i=n-3}^{n+3} \sum_{\ell=k-1}^{k+1} \mathbf{H}_{g,\ell,(1)}[i] \mathbf{F}_{\ell,(1)}[i] c_{i,\ell} \mathbf{d}_{\ell,(1)}[i] + \\ & \mathbf{H}_{g,k,(2)}[n] \mathbf{F}_{k,(2)}[n] \mathbf{d}_{k,(2)}[n] + \sum_{i=n-3}^{n+3} \sum_{\ell=k-1}^{k+1} \mathbf{H}_{g,\ell,(2)}[i] \mathbf{F}_{\ell,(2)}[i] c_{i,\ell} \mathbf{d}_{\ell,(2)}[i] \\ & + \mathbf{n}_{g,k}[n], \quad (\ell, i) \neq (k, n). \end{aligned} \quad (6.38)$$

Here the channel matrix, precoding matrix, and the data vector with respect to Cell 2 are denoted similarly as in (6.37) only with “(2)” in the subscripts. Note that  $\mathbf{d}_{g,k,(1)}[n] = \mathbf{d}_{g,k,(2)}[n]$ ,

i.e., the signals from Cell 1 and Cell 2 transmitted to the  $g$ -th user<sup>9</sup> are the same. To enable such FBMC/OQAM-based CoMP downlink transmissions, the mitigation of the intra-cell, inter-cell, and intrinsic interference has to be achieved. Therefore, we propose the following IIM-CBF 3 scheme that is an extension of the approach described in Section 6.3.2 and is also the outcome of adapting the Extended FlexCoBF algorithm for CP-OFDM-based systems in [SRH13] to FBMC/OQAM-based systems.

Consider  $M$  cells, and the  $m$ -th cell serves  $Q_m$  users simultaneously,  $m = 1, 2, \dots, M$ . It is assumed that for the  $m$ -th cell the users  $1, 2, \dots, L_m$  are cell interior users, while the remaining  $(Q_m - L_m)$  users are cell edge users. The proposed IIM-CBF 3 scheme is summarized as follows:

- **Step 1:** Initialize the real-valued decoding matrices  $\mathbf{D}_{q,m}^{(0)}$  ( $q = 1, \dots, Q_m$ ) for the  $m$ -th cell, where  $m = 1, \dots, M$ . Set the iteration index  $p$  to zero, and set a threshold  $\epsilon$  for the stopping criterion. If the current subcarrier is the first one, the decoding matrices are generated randomly; otherwise, set the decoding matrices as those calculated for the previous subcarrier [CLZ<sup>+</sup>14].

- **Step 2:** Set  $p \leftarrow p + 1$  and calculate the equivalent channel matrix  $\mathbf{H}_{e_m}^{(p)}$  in the  $p$ -th iteration as

$$\mathbf{H}_{e_m}^{(p)} = \begin{bmatrix} \mathbf{H}_{e_{(1,m)}}^{(p)\top} & \mathbf{H}_{e_{(2,m)}}^{(p)\top} & \dots & \mathbf{H}_{e_{(Q_m,m)}}^{(p)\top} \end{bmatrix}^\top, \quad (6.39)$$

where  $\mathbf{H}_{e_{(q,m)}}^{(p)} = \mathbf{D}_{q,m}^{(p-1)\top} \mathbf{H}_{q,m}$  is the equivalent channel matrix for the  $q$ -th user in the  $p$ -th iteration.

- **Step 3:** Calculate the precoding matrices  $\mathbf{F}_{q,m}^{(p)} \mathbf{G}_{q,m}^{(p)}$  ( $q = 1, \dots, Q_m$ ) following **Step 3 - Step 5** of Section 6.3.2 to achieve the suppression of the multi-user interference and the intrinsic interference.
- **Step 4:** Update the decoding matrix for each user based on the real-valued equivalent channel matrix where the processing at the transmitter and the procedure of taking the real part of the receive signal are taken into account.

1. For the  $q$ -th user that is a cell interior user of the  $m$ -th cell, its equivalent channel matrix  $\mathbf{H}_{\text{etx}(q,m)}^{(p)}$  is calculated as

$$\mathbf{H}_{\text{etx}(q,m)}^{(p)} = \text{Re} \left\{ \mathbf{H}_{q,m} \mathbf{F}_{q,m}^{(p)} \mathbf{G}_{q,m}^{(p)} \right\}. \quad (6.40)$$

<sup>9</sup>In this example, we assume that the indices of each cell edge user in Cell 1 and Cell 2 are the same to facilitate the description of the scenario.

2. For the  $q$ -th user that is a cell edge user, define a set  $\mathcal{S}_{q,m}$  that contains the indices of the cells that simultaneously transmit the same signals to the  $q$ -th user. Then its equivalent channel matrix is expressed as

$$\mathbf{H}_{\text{etx}(q,m)}^{(p)} = \sum_{r \in \mathcal{S}_{q,m}} \text{Re} \left\{ \mathbf{H}_{q_r,r} \mathbf{F}_{q_r,r}^{(p)} \mathbf{G}_{q_r,r}^{(p)} \right\}, \quad (6.41)$$

where  $q_r$  represents the index of the  $q$ -th user of the  $m$ -th cell in the  $r$ -th cell, and  $q_m = q$  following this definition. It is required that the base station of the  $m$ -th cell is informed by the  $r$ -th cell,  $r \in \mathcal{S}_{q,m}$  and  $r \neq m$ , of the corresponding real-valued equivalent channel matrices after the precoding and the operation of taking the real part of the received signal. In summary, the cooperation of the adjacent cells involves the knowledge of the signals for all cell edge users. It also requires the exchange of these real-valued equivalent channel matrices that are used to compute the decoding matrix for each cell edge user, which can be achieved by adopting the two exchange mechanisms proposed in [SRH13].

Afterwards, when a single data stream is transmitted to each user, the decoding matrix for the  $q$ -th user in the  $p$ -th iteration can be obtained by employing the MRC receiver or the MMSE receiver of the its equivalent channel matrix  $\mathbf{H}_{\text{etx}(q,m)}^{(p)}$ . On the other hand, when there exist users to which multiple data streams are transmitted, we propose to use the ZF receiver<sup>10</sup>

$$\mathbf{D}_{q,m}^{(p)} = \mathbf{H}_{\text{etx}(q,m)}^{(p)} \left( \mathbf{H}_{\text{etx}(q,m)}^{(p)\text{T}} \mathbf{H}_{\text{etx}(q,m)}^{(p)} \right)^{-1}. \quad (6.42)$$

- **Step 5:** Calculate the term  $\xi_m^{(p)}$  for the  $m$ -th cell that measures the residual multi-user and the inter-stream interference for the  $p$ -th iteration. When a single data stream is transmitted to each user,  $\xi_m^{(p)}$  is defined as

$$\xi_m^{(p)} = \left\| \text{off} \left( \mathbf{D}_m^{(p)\text{T}} \cdot \text{Re} \left\{ \mathbf{H}_m \mathbf{F}_m^{(p)} \right\} \right) \right\|_{\text{F}}^2, \quad (6.43)$$

where  $\text{off}(\cdot)$  indicates an operation of keeping all off-diagonal elements of its input matrix while setting its diagonal elements to zero. Moreover,  $\mathbf{D}_m^{(p)}$ ,  $\mathbf{H}_m$ , and  $\mathbf{F}_m^{(p)}$  denote the

---

<sup>10</sup>In such scenarios where multiple data streams are transmitted to at least one user, by employing the MMSE or the MRC criterion to update the decoding matrices in IIM-CBF 3, convergence cannot be achieved.

Note that the IIM-CBF 3 scheme can be employed when multiple data streams are sent to either cell edge users or cell interior users only. The convergence cannot be achieved when transmitting multiple data streams to all users.



block diagonal combined decoding matrix in the  $p$ -th iteration, the combined channel matrix, and the precoding matrix in the  $p$ -th iteration for the  $m$ -th cell, respectively.

When multiple data streams are transmitted to at least one of the cell edge users, we propose to express the term  $\xi_m^{(p)}$  as

$$\begin{aligned} \xi_m^{(p)} = & \sum_{q=1}^{L_m} \left( \left\| \text{off} \left( \mathbf{D}_{q,m}^{(p)\top} \cdot \text{Re} \left\{ \mathbf{H}_{q,m} \mathbf{F}_{q,m}^{(p)} \mathbf{G}_{q,m}^{(p)} \right\} \right) \right\|_{\text{F}}^2 + \sum_{g=1, g \neq q}^{Q_m} \left\| \mathbf{D}_{q,m}^{(p)\top} \cdot \text{Re} \left\{ \mathbf{H}_{q,m} \mathbf{F}_{g,m}^{(p)} \mathbf{G}_{g,m}^{(p)} \right\} \right\|_{\text{F}}^2 \right) \\ & + \sum_{q=L_m+1}^{Q_m} \left( \left\| \text{off} \left( \mathbf{D}_{q,m}^{(p)\top} \cdot \sum_{r \in \mathcal{S}_{q,m}} \text{Re} \left\{ \mathbf{H}_{q,r} \mathbf{F}_{q,r}^{(p)} \mathbf{G}_{q,r}^{(p)} \right\} \right) \right\|_{\text{F}}^2 \right. \\ & \left. + \sum_{g=1, g \neq q}^{Q_m} \left\| \mathbf{D}_{q,m}^{(p)\top} \cdot \text{Re} \left\{ \mathbf{H}_{q,m} \mathbf{F}_{g,m}^{(p)} \mathbf{G}_{g,m}^{(p)} \right\} \right\|_{\text{F}}^2 \right). \end{aligned} \quad (6.44)$$

On the right-hand side of (6.44), the first term corresponds to the residual inter-stream interference of each cell interior user, while the second term represents the residual multi-user interference that it still suffers from. For each cell edge user, the third term on the right-hand side of (6.44) measures its residual inter-stream interference. Here we take into account the fact that coordinated adjacent cells transmit the same signals to the cell edge user simultaneously. Recall that  $\mathcal{S}_{q,m}$  contains the indices of the cells that serve the  $q$ -th user of the  $m$ -th cell. Moreover, the forth term corresponds to the residual multi-user interference that affects each cell edge user.

If  $\xi_m^{(p)} < \epsilon$ , the convergence is achieved, and the iterative procedure terminates. Otherwise go back to **Step 2**.

As mentioned before, this coordinated beamforming scheme is designed based on the CoMP technique in [SRH13]. Nevertheless, due to the fact that the intrinsic interference is inherent in FBMC/OQAM systems, we have proposed to incorporate the additional processing to suppress the intrinsic interference. Moreover, different choices of the stopping criterion are recommended for single-stream transmissions and multiple-stream transmissions, respectively.

The proposed three IIM-CBF schemes have been summarized in Table 6.1. These three algorithms are all based on the concept of jointly and iteratively computing the precoding matrix and decoding matrix. In addition, they mitigate the intra-cell and inter-cell interference as well as the intrinsic interference in a ZF fashion. Nevertheless, the three schemes are designed for different configurations and deal with different types of interference. IIM-CBF 1 is developed

for symmetric single-cell FBMC/OQAM-based multi-user MIMO downlink settings. In this scenario, BD can still be employed to cancel the multi-user interference. Therefore, in IIM-CBF 1 only the precoding matrix for each equivalent single user transmission (i.e.,  $\mathbf{G}_q$  for the  $q$ -th user) is computed via the iterative procedure to suppress the intrinsic interference. On the other hand, IIM-CBF 2 is proposed to overcome the dimensionality constraint that  $M_R^{(\text{tot})}$  must not exceed  $M_T^{(\text{BS})}$  in the single-cell FBMC/OQAM-based multi-user MIMO downlink. The complete precoding matrix (i.e., for the  $q$ -th user  $\mathbf{F}_q \mathbf{G}_q$ ) that mitigates the multi-user interference and the intrinsic interference is computed iteratively and jointly with the decoding matrix. Unlike the first two schemes, IIM-CBF 3, as a novel FBMC/OQAM-based CoMP technique, is devised to enable the joint transmission of adjacent cells and to mitigate both the intra-cell interference and the inter-cell interference. In the meantime, it is able to achieve the suppression of the intrinsic interference inherent in FBMC/OQAM-based systems. Although the three IIM-CBF schemes exhibit satisfactory capabilities in alleviating the dimensionality constraint and in combating different types of interference, a complete elimination of the intrinsic interference that is inherent in FBMC/OQAM-based systems is not achieved. We revisit this issue in Section 6.5.2. It is worth noting that compared to the transmission strategy reviewed in Section 6.2.1, the residual intrinsic interference in case of the IIM-CBF schemes is much smaller, which is reflected in the performance comparison in Section 6.5. Throughout this chapter, equal power allocation is considered. A direct implementation of optimal power allocation schemes developed for CP-OFDM-based systems suffers from the loss of optimality due to the residual intrinsic interference existing in FBMC/OQAM-based multi-user MIMO downlink systems where the IIM-CBF algorithms are employed. Although the power optimization issue is beyond the scope of this thesis, it is of interest to devise power allocation schemes which are tailored for FBMC/OQAM-based multi-user MIMO downlink systems by taking into account the methods of the multi-user and intrinsic interference mitigation as well as possible residual interference.

## 6.5. Simulation results

In this section, we evaluate the Bit Error Rate (BER) and the sum rate performances of the proposed IIM-CBF techniques in various simulation settings. For all examples, the number of subcarriers is 128, and the subcarrier spacing is 15 kHz. The bandwidth is 1.25 MHz. In case of CP-OFDM, the length of the CP is set to 1/8 of the symbol period. The ITU Pedestrian-A (Ped-A) channel or the ITU Vehicular-A (Veh-A) channel [ITU97] is adopted. Moreover, the PHYDYAS prototype filter [PHY] with the overlapping factor  $K = 4$  is employed. The data

symbols are drawn from a 16 QAM constellation. Perfect CSI is assumed at the transmitter and at the receiver.

### 6.5.1. Single-cell multi-user MIMO downlink

In the first experiment, a symmetric single-cell multi-user MIMO downlink setting is considered, where the base station is equipped with  $M_T^{(BS)} = 8$  transmit antennas, each of the two users has 4 receive antennas, and the number of spatial streams transmitted to each user is 3. The BER (averaged over all data streams and all users) performances of the three schemes for FBMC/OQAM-based systems are presented and also compared to that of a CP-OFDM-based system in Figure 6.3. It can be found that IIM-CBF 1 described in Section 6.3.1 yields the best performance. The multi-user interference is first mitigated by using the BD algorithm [SSH04], and the precoding matrix and the decoding matrix are computed jointly and iteratively for each of the resulting  $4 \times 4$  equivalent point-to-point transmissions. Note that the decoding matrix is initialized as (6.27). In this case, we observe that it takes only two iterations to converge. On the other hand, the transmission scheme that is a straightforward extension of BD [SSH04] for the CP-OFDM case as described in Section 6.2.1 relies on the assumption that the channel frequency responses remain the same across adjacent subcarriers. As the ITU Veh-A channel exhibits frequency selectivity and such an assumption is therefore violated, the performance of this scheme degrades especially in the high Signal-to-Noise-Ratio (SNR) regime. We can also observe that in this symmetric scenario, the BD-based precoding algorithm<sup>11</sup> proposed in [CPNM13] performs much worse compared to the other schemes.

In the second and the third examples, we consider single-cell multi-user MIMO downlink settings where the base station equipped with  $M_T^{(BS)} = 8$  transmit antennas simultaneously serves two users and three users, i.e.,  $Q = 2$  and 3, respectively. Each of the two users in the second scenario has 5 receive antennas, and the number of data streams transmitted to each user is 3. On the other hand, the three users in the third scenario are equipped with 3 receive antennas each, and two data streams are transmitted to each of the three users. Note that for such  $M_R^{(tot)} > M_T^{(BS)}$  configurations, the transmission strategy proposed in [CPNM13] and briefly reviewed in Section 6.2.2 cannot be employed. Figure 6.4 and Figure 6.5 show the BER curves for these two scenarios, respectively. Two techniques are considered for the FBMC/OQAM-based system, i.e., IIM-CBF 2 presented in Section 6.3.2 and a direct extension

<sup>11</sup>In the implementation of this algorithm, after the cancellation of the multi-user interference by using BD, only the ZF-based step that ensures the cancellation of the intrinsic interference is considered. The remaining part of the transmit processing (spatial mapping) and the receive processing (MMSE receiver) are chosen to be the same as the other schemes for the purpose of a fair comparison. Note that the performance of the precoding algorithm proposed in [CPNM13] is dominated by the BD and ZF-based steps.

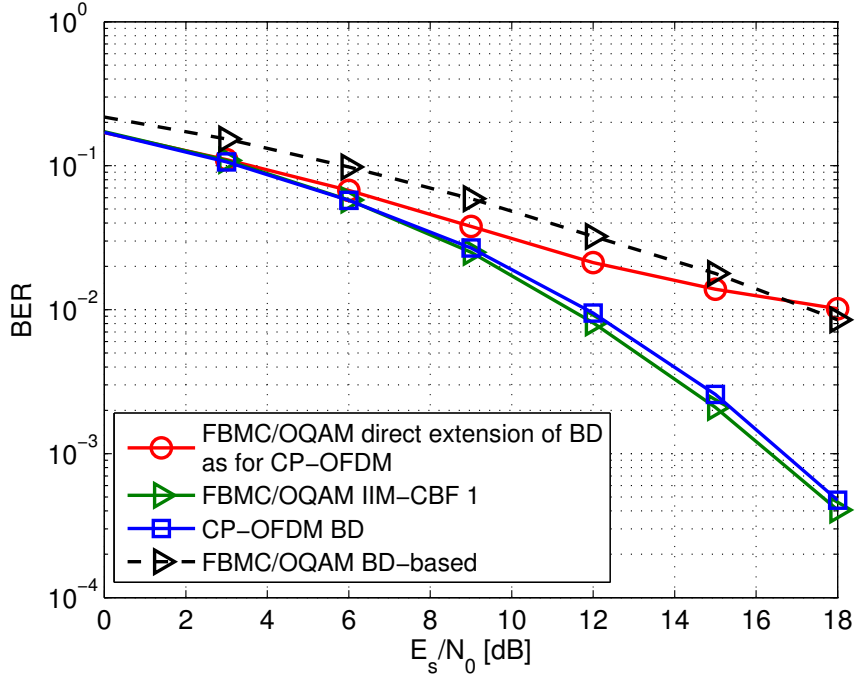


Figure 6.3.: Comparison of the BER performances of different schemes in a multi-user MIMO system where  $Q = 2$ ,  $M_T^{(BS)} = M_R^{(tot)} = 8$ ,  $d = 6$ , the ITU Veh-A channel is considered;  $E_s$  denotes the energy of each 16 QAM symbol, and  $N_0$  represents the noise power spectral density

(cf. Section 6.2.1) of the LoCCoBF algorithm [CLZ<sup>+</sup>14] originally designed for the case of CP-OFDM and described in detail in Section 2.5 of this thesis. For the purpose of comparison, we also present the BER performance of a CP-OFDM-based system with the same configuration where LoCCoBF is employed. For both the proposed IIM-CBF 2 scheme and LoCCoBF,  $\epsilon$  for the stopping criterion is set to  $10^{-5}$ , and the maximum number of iterations<sup>12</sup> is 50. It can be observed that the performance of the FBMC/OQAM-based multi-user MIMO downlink system where IIM-CBF 2 is employed is slightly better than its CP-OFDM-based counterpart due to the fact that no insertion of the CP is required. The other transmission scheme for

<sup>12</sup>Via numerical simulations, it has been observed that there exist rare cases where it takes a large number of iterations for the stopping criteria of the IIM-CBF schemes to be fulfilled. Therefore, a maximum number of iterations is set to handle these cases. The iterative procedure is manually terminated if the stopping criteria are not fulfilled when the number of iterations reaches this maximum number. Taking IIM-CBF 2 as an example, its stopping criterion corresponds to the residual interference. We have observed that when the algorithm is manually terminated, though the residual interference is above the threshold, its value is already so small that the performance is not affected much. Except for this simple way of setting a maximum number of iterations, the termination of the iterative procedure can also be determined based on the variation of the residual interference (in case of IIM-CBF 2 and IIM-CBF 3) or the change of the precoding matrix (in case of IIM-CBF 1) as the number of iterations increases.

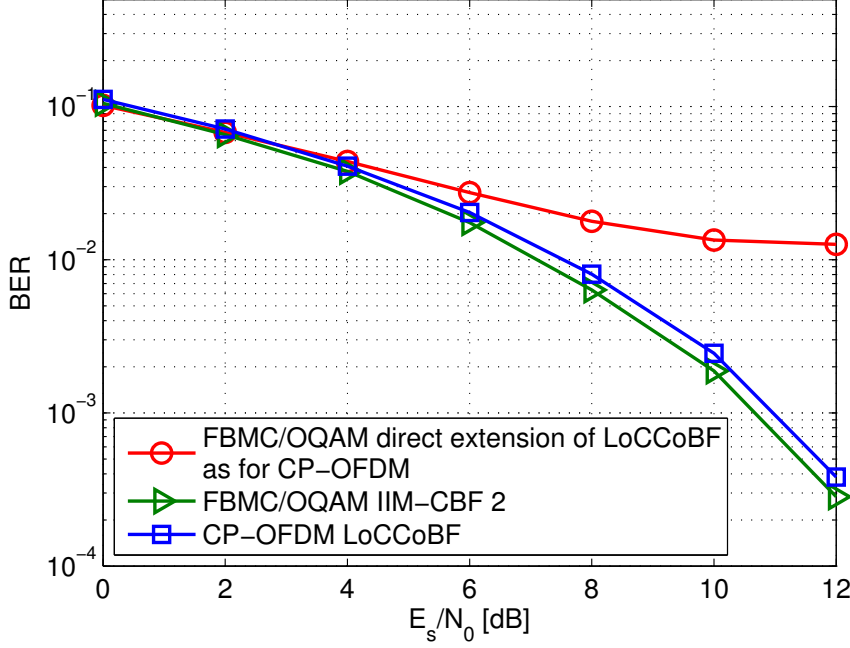


Figure 6.4.: Comparison of the BER performances of different schemes in a multi-user MIMO downlink system where  $Q = 2$ ,  $M_T^{(\text{BS})} = 8$ ,  $M_R^{(\text{tot})} = 10$ ,  $d = 6$ , and the ITU Ped-A channel is considered;  $E_s$  denotes the energy of each 16 QAM symbol, and  $N_0$  represents the noise power spectral density

the FBMC/OQAM-based system suffers from a performance degradation due to the frequency selectivity of the channel. By assuming that the channel stays constant across the neighboring subcarriers, the multi-user interference and the intrinsic interference cannot be eliminated even for high SNRs.

In addition, the convergence behavior of IIM-CBF 2 for the single-cell multi-user MIMO FBMC/OQAM downlink system where  $M_R^{(\text{tot})} > M_T^{(\text{BS})}$  is investigated. The Complementary Cumulative Distribution Function (CCDF) of the number of iterations required to achieve the convergence of the IIM-CBF 2 scheme presented in Section 6.3.2 and LoCCoBF for the case of CP-OFDM is illustrated in Figure 6.6. The three-user scenario used for Figure 6.5 is considered. By comparison, we also plot the same set of results for a four-user case, i.e.,  $Q = 4$ . The base station has 8 transmit antennas, and each of the four users is equipped with 3 receive antennas and receives 2 data streams. Thereby, the total number of the receive antennas of the users  $M_R^{(\text{tot})} = 12$ , and all spatial degrees of freedom are exploited. It can be observed that for

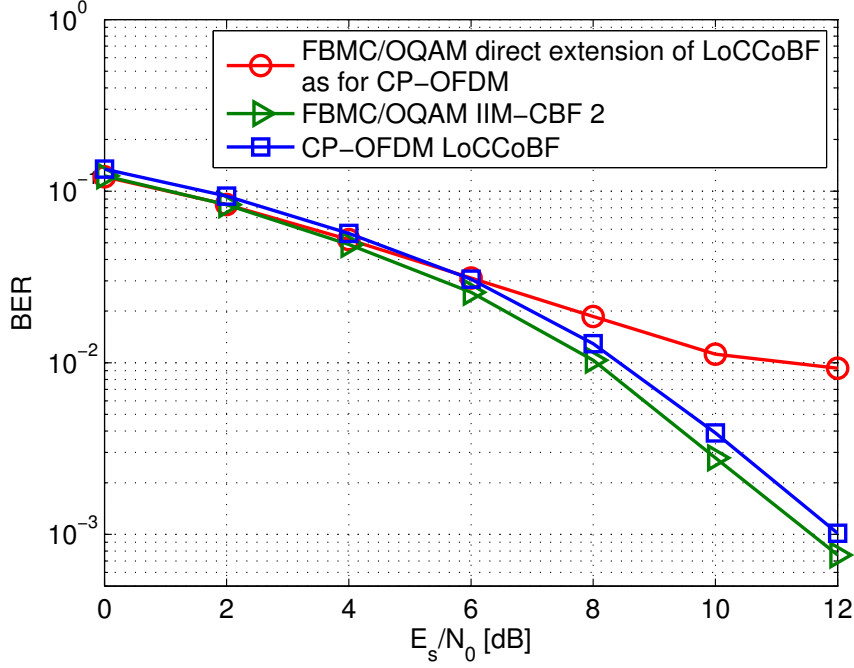


Figure 6.5.: Comparison of the BER performances of different schemes in a multi-user MIMO downlink system where  $Q = 3$ ,  $M_T^{(BS)} = 8$ ,  $M_R^{(tot)} = 9$ ,  $d = 6$ , and the ITU Ped-A channel is considered;  $E_s$  denotes the energy of each 16 QAM symbol, and  $N_0$  represents the noise power spectral density

the three-user scenario IIM-CBF 2 converges within 6 iterations in almost all of the cases. As the number of users  $Q$  and consequently the total number of receive antennas  $M_R^{(tot)}$  increase, the number of iterations needed for the convergence becomes slightly larger. Nevertheless, the convergence is achieved within 10 iterations. Moreover, we can see from the comparison of the proposed IIM-CBF 2 technique for the FBMC/OQAM-based system and LoCCoBF for the case of CP-OFDM that the number of iterations required for the convergence for both schemes is similar. Hence, compared to the CP-OFDM-based multi-user MIMO downlink setting, employing such an IIM-CBF technique in the FBMC/OQAM-based system where  $M_R^{(tot)} > M_T^{(BS)}$  does not result in an increased number of iterations for the convergence. Only the processing dedicated to the elimination of the intrinsic interference contributes to a slight additional complexity.

Furthermore, we consider again the four-user single-cell multi-user MIMO downlink system (as used for Figure 6.6) and investigate the impact of the residual CFO. The IIM-CBF 2 scheme

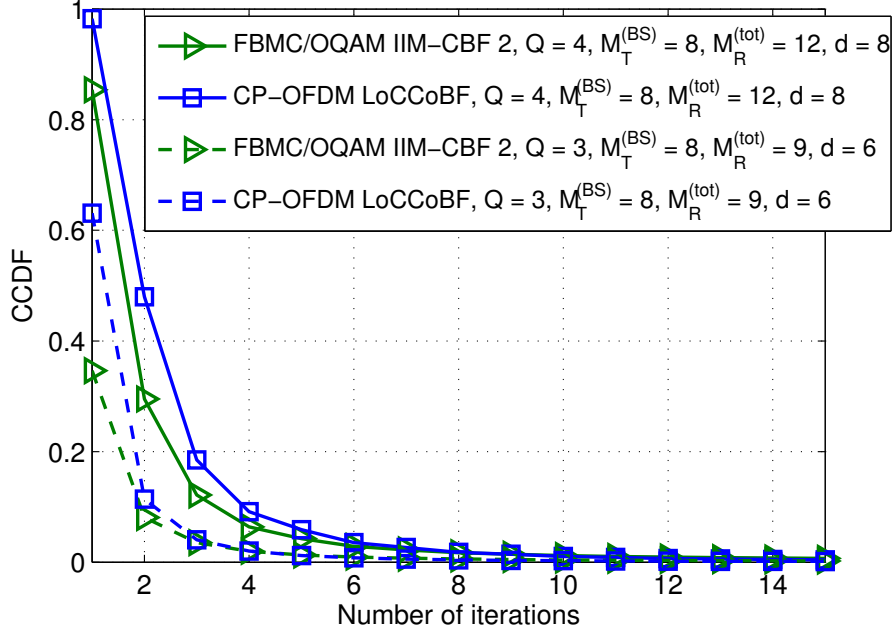


Figure 6.6.: CCDF of the number of iterations required for IIM-CBF 2 and LoCCoBF in multi-user MIMO FBMC/OQAM and CP-OFDM-based downlink systems with different settings, respectively, and the ITU Ped-A channel is considered

for the FBMC/OQAM-based system and LoCCoBF for CP-OFDM are considered. In addition, it is assumed that the residual CFO (normalized by the subcarrier spacing) ranges<sup>13</sup> either from 0 to 0.1 or from 0 to 0.15. Figure 6.7 illustrates the corresponding BER performances of these two schemes in the presence of the residual CFO. Notice that the CP-OFDM-based system suffers from a severe performance degradation. In contrast, the FBMC/OQAM-based system with IIM-CBF 2 significantly outperforms its CP-OFDM-based counterpart, and it exhibits a greater robustness against the synchronization errors in the frequency domain.

### 6.5.2. CoMP downlink

In the sequel, the performance of the FBMC/OQAM-based CoMP downlink is assessed. Transmissions in cooperative cells are assumed to be perfectly synchronized. Instead of the BER, we choose to use the sum rate performance as the evaluation approach. We start with a two-cell scenario consisting of 5 users in total. Each cell equipped with 4 transmit antennas serves 3

<sup>13</sup>In the simulations, the residual CFO is drawn uniformly from the range (0, 0.1) or (0, 0.15)

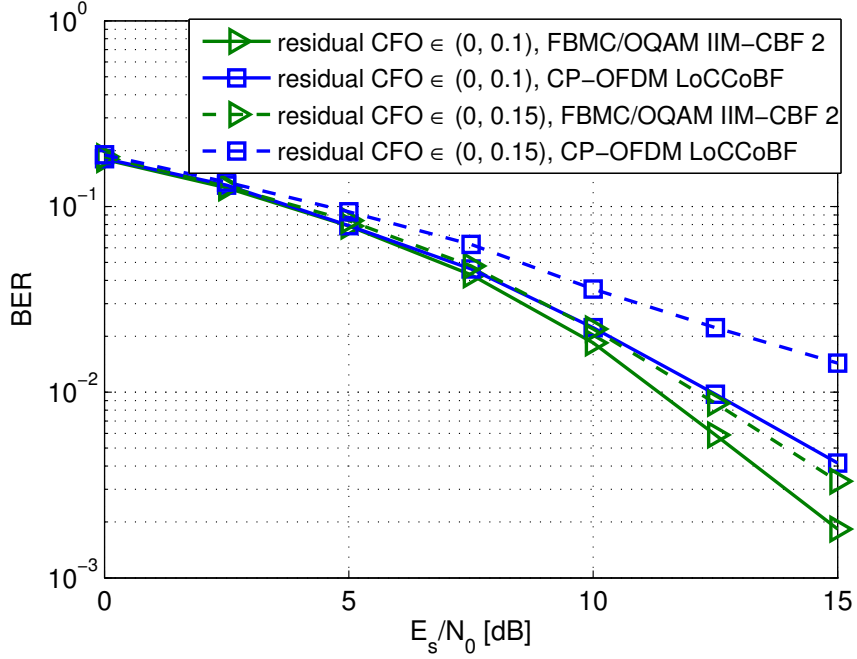


Figure 6.7.: Comparison of the BER performances of different schemes in a multi-user MIMO downlink system in the presence of residual CFO (unit: subcarrier spacing) where  $Q = 4$ ,  $M_T^{(BS)} = 8$ ,  $M_R^{(tot)} = 12$ ,  $d = 8$ , and the ITU Ped-A channel is considered;  $E_s$  denotes the energy of each 16 QAM symbol, and  $N_0$  represents the noise power spectral density

users each with 2 receive antennas, which forms a  $4 \times 6$  multi-user downlink setting. Among the three users, two are cell interior users, and one is a cell edge user. A single data stream is transmitted to each cell interior user, and two data streams are transmitted to the cell edge user, i.e., for each cell full spatial multiplexing is considered. The pathloss of the transmission to the cell edge users is assumed to be 10 times bigger than that for the cell interior users [SRH13]. To calculate the sum rate for both the FBMC/OQAM and the CP-OFDM cases, we first compute an instantaneous Signal-to-Interference-plus-Noise-Ratio (SINR) on each data stream for each subcarrier. In case of the FBMC/OQAM-based multi-user MIMO downlink where IIM-CBF 2 is employed, the decoded signal is written as

$$\begin{aligned} \hat{\mathbf{d}}_k[n] &= \mathbf{D}_k^T[n] \cdot \text{Re} \left\{ \mathbf{H}_k[n] \mathbf{F}_k[n] \mathbf{d}_k[n] + \sum_{i=n-3}^{n+3} \sum_{\ell=k-1}^{k+1} \mathbf{H}_\ell[i] \mathbf{F}_\ell[i] c_{i,\ell} \mathbf{d}_\ell[i] + \mathbf{n}_k[n] \right\} \\ &= \mathbf{D}_k^T[n] \cdot \text{Re} \{ \mathbf{H}_k[n] \mathbf{F}_k[n] \} \mathbf{d}_k[n] + \mathbf{D}_k^T[n] \cdot \text{Im} \left\{ - \sum_{i=n-3}^{n+3} \sum_{\ell=k-1}^{k+1} \mathbf{H}_\ell[i] \mathbf{F}_\ell[i] \right\} \bar{c}_{i,\ell} \bar{\mathbf{d}}_\ell[i] \end{aligned}$$



$$+ \mathbf{D}_k^T[n] \cdot \text{Re} \{ \mathbf{n}_k[n] \}, \quad (\ell, i) \neq (k, n). \quad (6.45)$$

where

$$\begin{aligned} \bar{c}_{i,\ell} &= \text{Im} \{ c_{i,\ell} \}, \quad \bar{\mathbf{d}}_\ell[i] = \mathbf{d}_\ell[i], \quad \text{when } (\ell + i) \text{ is even,} \\ \bar{c}_{i,\ell} &= c_{i,\ell}, \quad \bar{\mathbf{d}}_\ell[i] = \text{Im} \{ \mathbf{d}_\ell[i] \}, \quad \text{when } (\ell + i) \text{ is odd.} \end{aligned}$$

Note that as mentioned in Section 6.2, for the case where  $(\ell + i)$  is even, the signal  $\mathbf{d}_\ell[i]$  on the  $\ell$ -th subcarrier and at the  $i$ -th time instant is real, while the corresponding coefficient  $c_{i\ell}$  is pure imaginary (cf. Table 3.1). On the contrary, when  $(\ell + i)$  is odd,  $\mathbf{d}_\ell[i]$  and  $c_{i\ell}$  are pure imaginary and real, respectively. This explains the definitions of  $\bar{c}_{i,\ell}$  and  $\bar{\mathbf{d}}_\ell[i]$  shown above. Let us further write (6.45) as

$$\hat{\mathbf{d}}_k[n] = \mathbf{H}_k^{(\text{eff})}[n] \mathbf{d}_k[n] + \sum_{i=n-3}^{n+3} \sum_{\ell=k-1}^{k+1} \mathbf{H}_\ell^{(\text{int})}[i] \bar{\mathbf{d}}_\ell[i] + \tilde{\mathbf{n}}_k[n], \quad (\ell, i) \neq (k, n), \quad (6.46)$$

where

$$\begin{aligned} \mathbf{H}_k^{(\text{eff})}[n] &= \mathbf{D}_k^T[n] \cdot \text{Re} \{ \mathbf{H}_k[n] \mathbf{F}_k[n] \} \in \mathbb{R}^{d \times d}, \\ \mathbf{H}_\ell^{(\text{int})}[i] &= \mathbf{D}_k^T[n] \cdot \text{Im} \{ -\mathbf{H}_\ell[i] \mathbf{F}_\ell[i] \} \bar{c}_{i,\ell} \in \mathbb{R}^{d \times d}, \\ \tilde{\mathbf{n}}_k[n] &= \mathbf{D}_k^T[n] \cdot \text{Re} \{ \mathbf{n}_k[n] \}. \end{aligned}$$

To calculate the SINR denoted by  $\gamma_{r,k}$  for the  $r$ -th data stream on the  $k$ -th subcarrier, where  $r = 1, \dots, d$ , the entry  $(r, r)$  of  $\mathbf{H}_k^{(\text{eff})}[n]$  determines the effective gain for the  $r$ -th data stream, while the entries  $(r, u)$  ( $u = 1, \dots, d, u \neq r$ ) of  $\mathbf{H}_k^{(\text{eff})}[n]$  determine the residual multi-user and inter-stream interference. In addition, the elements of the  $r$ -th row of  $\mathbf{H}_\ell^{(\text{int})}[i]$  provide a measure of the residual intrinsic interference. Notice that only when  $\mathbf{D}_k[n] = \mathbf{D}_\ell[i]$  ( $\ell = k - 1, k, k + 1, i = n - 3, \dots, n + 3$ , and  $(\ell, i) \neq (k, n)$ ),  $\mathbf{H}_\ell^{(\text{int})}[i]$  is rendered as zero, and the intrinsic interference is completely eliminated. Due to the fact that the channel is not flat fading, the aforementioned condition is not fulfilled, leading to the existence of the residual intrinsic interference. The noise component can be extracted from the scaled covariance matrix of  $\tilde{\mathbf{n}}_k[n]$

$$\mathbf{R}_{\tilde{\mathbf{n}}_k}[n] = \mathbf{D}_k^T[n] \cdot \frac{d \cdot \sigma_n^2}{2 \cdot P_T} \mathbf{I}_{M_R} \cdot \mathbf{D}_k[n], \quad (6.47)$$

where  $P_T$  denotes the transmit power allocated on each subcarrier. As mentioned previously, equal power allocation is assumed on all subcarriers and data streams. Therefore,  $\gamma_{r,k}$  is computed as

$$\gamma_{r,k} = \frac{\left(\mathbf{H}_k^{(\text{eff})}[n](r, r)\right)^2}{\sum_{u=1, u \neq r}^d \left(\mathbf{H}_k^{(\text{eff})}[n](r, u)\right)^2 + \sum_{i=n-3}^{n+3} \sum_{\substack{\ell=k-1 \\ (\ell, i) \neq (k, n)}}^{k+1} \sum_{u=1}^d \left(\mathbf{H}_\ell^{(\text{int})}[i](r, u)\right)^2 + \left(\mathbf{R}_{\widetilde{n}\widetilde{n}_k}[n](r, r)\right)^2}. \quad (6.48)$$

The sum rate (bps/Hz) is then approximated as

$$R_{\text{sum}} = \frac{1}{N_c} \sum_{k=1}^{N_c} \sum_{r=1}^d \log_2(1 + \gamma_{r,k}), \quad (6.49)$$

where  $N_c$  is the total number of subcarriers. For the case of CP-OFDM, the sum rate can be computed similarly, but the residual intrinsic interference term does not exist. Moreover, the  $\text{Re}\{\cdot\}$  operation is not used.

On the other hand, when a transmission scheme that is a straightforward extension of the CP-OFDM case (cf. Section 6.2.1) is adopted, the residual intrinsic interference results from the violation of the assumption that the channels of adjacent subcarriers should be the same. Therefore, the effective channel that determines the intrinsic interference caused by the signal on the  $\ell$ -th subcarrier and at the  $i$ -th time instant to that on the  $k$ -th subcarrier and at the  $n$ -th time instant, where  $(\ell, i) \neq (k, n)$  is expressed as

$$\mathbf{H}_\ell^{(\text{int})}[i] = \text{Im} \left\{ \mathbf{D}_k^H[n] \mathbf{H}_\ell[i] \mathbf{F}_\ell[i] - \mathbf{D}_k^H[n] \mathbf{H}_k[n] \mathbf{F}_k[n] \right\} \bar{c}_{i,\ell}. \quad (6.50)$$

Then the sum rate for this case can be calculated accordingly. It is worth mentioning that in case of the downlink of the CoMP system, the fact that adjacent cells send the same signal to each cell edge user should be taken into account in the sum rate calculation, while the rest resembles the aforementioned case of the multi-user MIMO downlink system.

To this end, we use Figure 6.8 to illustrate the sum rate performances of two transmission schemes for the FBMC/OQAM-based CoMP downlink systems described at the beginning of this section. Here  $\text{SNR} = P_T/\sigma_n^2$ , where  $P_T$  is the per-subcarrier transmit power of each cell. The CP-OFDM-based system where Extended FlexCoBF<sup>14</sup> is employed is also considered for comparison. It can be seen that IIM-CBF 3 leads to a slightly better performance of

<sup>14</sup>In the implementation of Extended FlexCoBF [SRH13], we adopt the same mechanism of initializing the decoding matrices as in the LoCCoBF algorithm [CLZ<sup>+</sup>14] such that the correlation of the channels of adjacent subcarriers is exploited, and consequently the number of iterations required for the convergence is reduced.

the FBMC/OQAM-based system in contrast to the CP-OFDM-based system. The reason is that the former has a higher spectral efficiency compared to the latter, since no cyclic prefix is required. This observation also implies the effectiveness of the proposed transmission strategy IIM-CBF 3 in mitigating the intra-cell and inter-cell interference as well as the intrinsic interference. By comparison, when a transmission strategy originally designed for CP-OFDM, here Extended FlexCoBF, is straightforwardly extended to the FBMC/OQAM system, and the channel is frequency selective, the performance is much worse than that of the proposed IIM-CBF 3 scheme due to a much higher level of the residual interference.

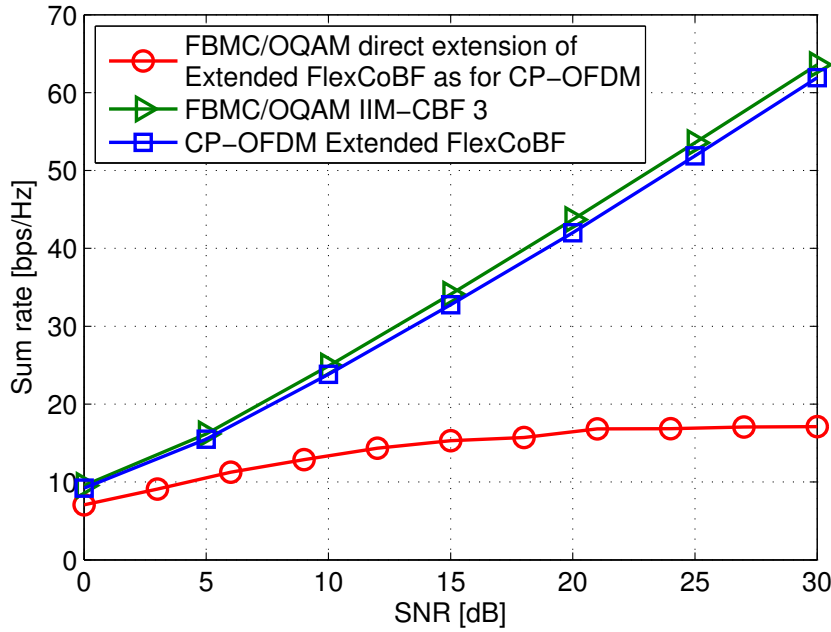


Figure 6.8.: Comparison of the sum rate performances of different schemes in the CoMP down-link where the total number of users in two adjacent cells is 5, and the ITU Ped-A channel is considered

Moreover, Figure 6.9 depicts the CCDF of the number of iterations required for the IIM-CBF 3 technique to converge. For all the evaluated schemes,  $\epsilon$  used for the stopping criterion is set to  $10^{-5}$ , and the iterative procedure is manually terminated when the number of iterations reaches 50. Two types of the frequency selective channel, ITU Ped-A and Veh-A are considered. Recall that in the initialization step of IIM-CBF 3, the decoding matrices calculated for the previous subcarrier are used to initialize the decoding matrices for the current subcarrier. Thereby, the lower the frequency selectivity of the channel is, the more effective becomes such

a choice of the initial decoding matrices, which leads to a smaller number of iterations required for the convergence of the coordinated beamforming algorithm. Consequently, we observe in Figure 6.9 that compared to the case of the ITU Veh-A channel which is more frequency selective, the number of iterations that are needed by the coordinated beamforming schemes to converge in case of the ITU Ped-A channel is slightly smaller. However, even when the ITU Veh-A is considered as the propagation channel, the proposed IIM-CBF 3 technique converges within 15 iterations in almost all of the cases.

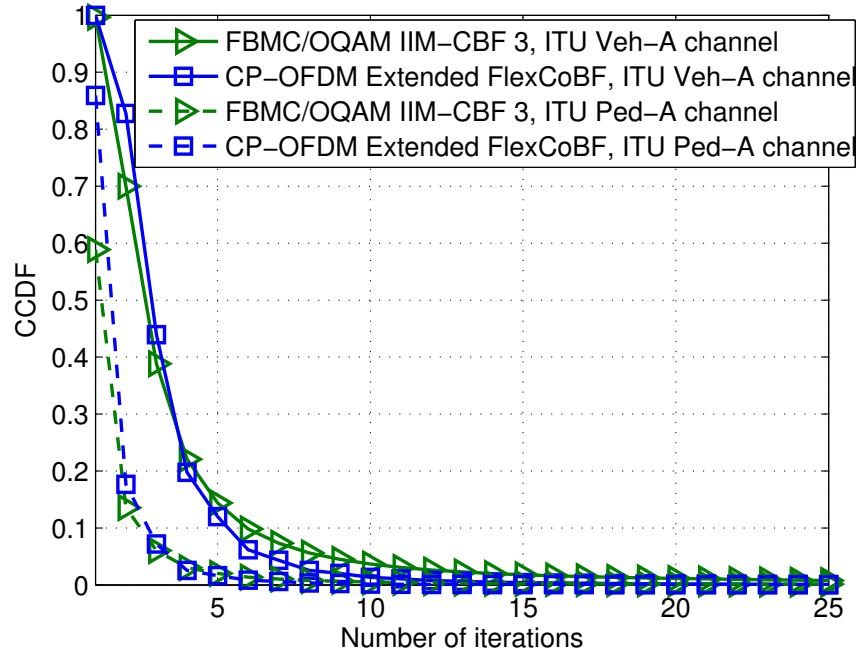


Figure 6.9.: CCDF of the number of iterations required for different coordinated beamforming schemes in the CoMP downlink system where the total number of users in two adjacent cells is 5, and the ITU Ped-A channel or the ITU Veh-A channel is considered

Finally, a three-cell CoMP downlink scenario is considered. Each cell equipped with 4 transmit antennas serves 3 users each with 2 receive antennas. This leads to a  $4 \times 6$  multi-user downlink setting. Among the three users, two are cell interior users, and one is a cell edge user. A single data stream is transmitted to each cell interior user, and two data streams are transmitted to the cell edge user. The numerical results with respect to the sum rate performance are shown in Figure 6.10. Similar observations are obtained as in Figure 6.8.

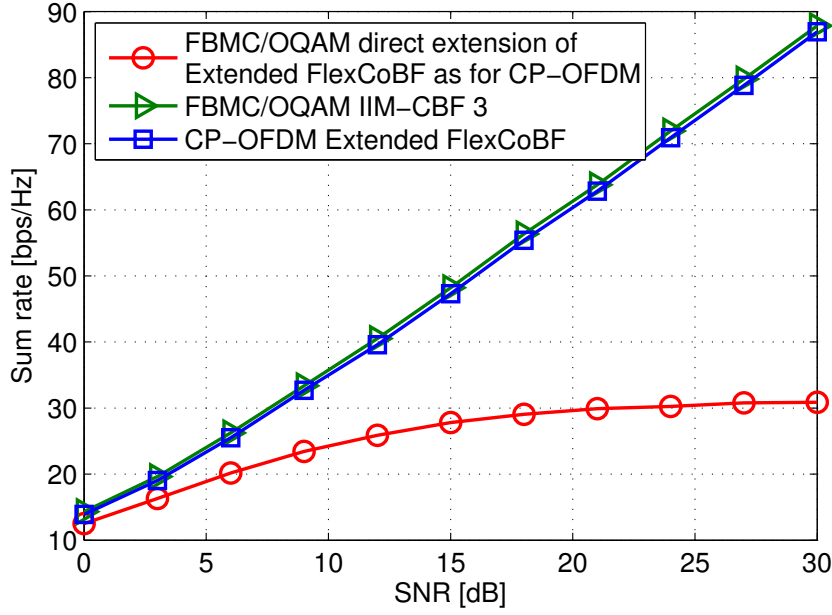


Figure 6.10.: Comparison of the sum rate performances of different coordinated beamforming schemes in the CoMP downlink where the total number of users in three adjacent cells is 7, and the ITU Ped-A channel is considered

## 6.6. Summary

In this chapter, we have shown three IIM-CBF-based transmission schemes for the downlink of FBMC/OQAM-based multi-user MIMO systems and CoMP systems as summarized in Table 6.1. The first algorithm that is called IIM-CBF 1 is designed for a multi-user MIMO FBMC/OQAM downlink system where  $M_T^{(BS)} = M_R^{(tot)}$ . We have employed an iterative procedure to jointly compute the precoding matrix and the decoding matrix of each equivalent single-user transmission that results from the elimination of the multi-user interference. On the other hand, the IIM-CBF 2 technique has been proposed as a solution to the problem that the state-of-the-art transmission strategies for the downlink of FBMC/OQAM-based multi-user MIMO systems fail to work when  $M_R^{(tot)} > M_T^{(BS)}$ . Moreover, we have conducted an investigation of FBMC/OQAM-based CoMP downlink systems for the first time [CLH14d]. With a focus on the case of partial cooperation of adjacent cells, the scheme, IIM-CBF 3, has been designed to enable the joint transmission of base stations in adjacent cells and combat both the intra-cell and the inter-cell interference. It is worth noting that in addition to the suppression of the multi-user interference, these three proposed IIM-CBF schemes are effective in

mitigating the intrinsic interference that is inherent in FBMC/OQAM-based systems without assuming that the propagation channel is almost flat fading. To demonstrate the advantages of the three IIM-CBF algorithms, their BER and sum rate performances have been shown in different settings. Via the simulation results, it has been shown that the FBMC/OQAM-based multi-user MIMO and CoMP downlink systems where IIM-CBF 1, IIM-CBF 2, or IIM-CBF 3 is employed achieve a similar performance compared to their CP-OFDM-based counterparts but with a higher spectral efficiency and a greater robustness against misalignments in the frequency domain. In addition, we have numerically analyzed the convergence of the IIM-CBF techniques. It leads to the conclusion that the additional complexity is quite acceptable as the price of alleviating the aforementioned dimensionality constraint.

---

## 7. FBMC/OQAM-based multi-user MIMO downlink with highly frequency selective channels

In this chapter, we present novel designs of transmit and receive processing for Filter Bank-based Multi-Carrier with Offset Quadrature Amplitude Modulation (FBMC/OQAM)-based multi-user Multiple-Input Multiple-Output (MIMO) downlink systems with highly frequency selective channels. As reviewed in the previous chapter, Chapter 6, most of the state-of-the-art solutions for FBMC/OQAM-based multi-user downlink settings have been developed assuming that the channel on each subcarrier can be treated as flat fading. The coordinated beamforming-based transmission strategies presented in Chapter 6 have the advantage of alleviating the dimensionality constraint that the total number of receive antennas at the user terminals should not exceed the number of transmit antennas at the base station. Following this contribution, in this chapter we turn to the more challenging case of highly frequency selective propagation channels. First, to overcome the limits on the number of receive antennas per user terminal that are imposed on the existing solutions, we present two approaches for FBMC/OQAM-based multi-user MIMO downlink settings where a single data stream is sent to each user. The first design of precoders and equalizers is iterative and Minimum Mean Squared Error (MMSE)-based. The second is a closed-form design based on the maximization of the Signal-to-Leakage-Ratio (SLR). Then we provide solutions for per-user multi-stream transmissions in FBMC/OQAM-based multi-user MIMO downlink systems under highly frequency selective propagation conditions. A Signal-to-Leakage-plus-Noise-Ratio (SLNR)-based metric is proposed, and it is tailored for the downlink of FBMC/OQAM-based multi-user MIMO settings. At the base station, per-subcarrier fractionally spaced multi-tap precoders are computed based on this metric to mitigate the Multi-User Interference (MUI), the Inter-Symbol Interference (ISI), as well as the Inter-Carrier Interference (ICI) and to map the multiple data streams of each user to the transmit antennas. With the base station carrying most of the computational load, each user terminal only employs a Zero Forcing (ZF)-based one-tap spatial equalizer to recover the desired streams. Numerical simulations show that the proposed schemes achieve satisfactory performances in various multi-user MIMO downlink scenarios with highly frequency selective channels. They significantly outperform the existing algorithms that require the channel on each subcarrier to be flat fading. The aforementioned results have been published in [CBHN15a] and [CBHN15b].

## 7.1. Introduction

Featuring an agile spectrum, Filter Bank-based Multi-Carrier modulation (FBMC) has attracted great research attention recently. Its use of spectrally well-concentrated synthesis and analysis filter banks at the transmitter and at the receiver contributes to a significantly reduced out-of-band leakage compared to Orthogonal Frequency Division Multiplexing with the Cyclic Prefix insertion (CP-OFDM). In addition, unlike CP-OFDM-based systems, Filter Bank-based Multi-Carrier with Offset Quadrature Amplitude Modulation (FBMC/OQAM)-based systems are able to achieve a higher spectral efficiency, as the insertion of the CP is not required. Therefore, FBMC is considered as a favorable replacement of CP-OFDM especially in asynchronous scenarios [FPT08], [SSWB<sup>+</sup>11] and broadband Professional Mobile Radio (PMR) systems [RBB<sup>+</sup>13] as addressed in Chapter 3.

To exploit the benefits of both this advanced multi-carrier scheme and the multi-user downlink with Space-Division Multiple Access (SDMA), there have been several proposals in the literature that shed light on appropriate designs of transmission strategies for FBMC/OQAM-based multi-user downlink settings. Most of these state-of-the-art solutions rely on the assumption that the channel on each subcarrier can be treated as flat fading. Among them, the spatial Tomlinson Harashima precoder-based non-linear precoding scheme in [CPN13c] allows only one receive antenna at each user terminal and is more prone to a high computational complexity compared to linear precoders. On the other hand, a Block Diagonalization (BD)-based linear precoder has been developed in [CPNM13] for the FBMC/OQAM-based multi-user MIMO downlink. It adopts the central idea of BD [SSH04] to mitigate the Multi-User Interference (MUI) and then uses the Zero Forcing (ZF)-based approach [CPN13b] to deal with the intrinsic interference cancellation for the resulting equivalent single-user transmissions. Furthermore, the coordinated beamforming-based transmission strategies devised in [CLH14b], [CLH14d], and also presented in Chapter 6, have the advantage of alleviating the dimensionality constraint such that the number of receive antennas is not restricted. Nevertheless, the violation of the assumption that the channel on each subcarrier is flat fading results in a performance degradation of the aforementioned techniques.

Focusing on the case of highly frequency selective channels, the linear precoder in [HFDL13] has a structure of a filter applied on each subcarrier and its two adjacent subcarriers at twice the symbol rate. In [NBSN14], two different Minimum Mean Square Error (MMSE)-based approaches have been devised for FBMC/OQAM-based multi-user Multiple-Input Single-Output (MISO) downlink systems also considering highly frequency selective channels. A closed-form solution is provided in the first scheme, where one complex-valued fractionally spaced multi-



tap precoder for each user on each subcarrier is applied at the transmitter and a single-tap real-valued weight at the receiver. The second scheme involves a joint transmitter and receiver design via an iterative procedure, where now the equalizer at the receiver side is also complex-valued fractionally spaced multi-tap. Similar to [HF DL13], the two methods in [NBSN14] are restricted to the case where each user is equipped with a single receive antenna.

Stemming from the problem formulation in [NBSN14], we first develop an iterative approach for FBMC/OQAM-based multi-user MIMO downlink systems under highly frequency selective propagation conditions. MMSE-based multi-tap precoders are designed to effectively mitigate the MUI, the Inter-Symbol Interference (ISI), and the Inter-Carrier Interference (ICI). At each user terminal equipped with multiple antennas, only a receive spatial filter is applied. Via an iterative design, the precoders and the receive spatial filters are jointly optimized. Then, we further propose a novel closed-form Signal-to-Leakage-Ratio (SLR)-based design of the precoders that can be conveniently extended to the case of multiple spatial streams per user. Via numerical results, it is observed that the proposed schemes achieve a very promising performance in case of highly frequency selective channels. They significantly outperform the state-of-the-art approaches that suffer from impractical restrictions on the channel frequency selectivity. By allowing multiple antennas at each user terminal, the benefits of the MIMO technology are exploited. Afterwards, we present a thorough and general system model of the FBMC/OQAM-based multi-user MIMO downlink setting considering highly frequency selective channels. Each user terminal is equipped with multiple receive antennas, and the transmission of multiple spatial streams to each user is enabled. A Signal-to-Leakage-plus-Noise-Ratio (SLNR)-based multi-tap precoding scheme is devised to mitigate the MUI, the ISI, and the ICI. Consequently, the base station with a relatively stronger computational capability is in charge of combating the interference, while at the user terminals, only single-tap zero-forcing (ZF)-based receive filters are employed to recover their desired signals. Numerical simulations have been performed to evaluate the performance of the proposed SLNR-based transmission strategy.

The remainder of this chapter is organized as follows: the data model of FBMC/OQAM-based multi-user MIMO downlink settings with highly frequency selective channels is introduced in Section 7.2 where a single spatial stream is sent to each user terminal. Section 7.3 and Section 7.4 present an iterative design and a closed-form design of the linear multi-tap precoders and the real-valued single-tap spatial receive filters, respectively. In Section 7.5, we discuss how the transmission of multiple data streams to each user terminal is enabled via the design of SLNR maximization-based precoders and ZF-based receive filters. Simulation results are provided in Section 7.6, before this chapter is summarized in Section 7.7.

## 7.2. System model

In the multi-user MIMO downlink setting (cf. Figure 6.1 for an illustration of multi-user MIMO downlink systems with one-tap linear precoding and decoding<sup>1</sup>), one base station serves  $U$  users simultaneously. The number of transmit antennas is denoted by  $M_T$ , whereas the  $j$ -th user is equipped with  $M_{R_j}$  receive antennas. The total number of receive antennas of all users is denoted by  $M_R = \sum_{j=1}^U M_{R_j}$ . We start by considering the case where one data stream is transmitted to each user. Multi-tap precoding filters at the base station and equalizers at the user terminals are designed to mitigate the MUI, the ISI, and the ICI as well as to recover the desired signals.

After the OQAM staggering (cf. Figure 3.3), the signal transmitted to the  $j$ -th user on the  $\ell$ -th subcarrier is denoted by  $d_\ell^{(j)}[n]$ ,  $j = 1, 2, \dots, U$ . The impulse response of its corresponding precoding filter is symbolized by  $b_\ell^{(i,j)}[n]$ ,  $i = 1, 2, \dots, M_T$ , while  $B$  denotes the length of the precoding filters. The precoding process is depicted in Figure 7.1, where the precoded signal on the  $\ell$ -th subcarrier and for the  $i$ -th transmit antenna is expressed as

$$x_\ell^{(i)}[n] = \sum_{s=1}^U \left( b_\ell^{(i,s)}[n] * d_\ell^{(s)}[n] \right). \quad (7.1)$$

Here we use  $*$  to denote the discrete convolution. Then the resulting signals are multiplexed by the Synthesis Filter Banks (SFBs). In this chapter, highly frequency selective channels are considered, and  $h_{\text{ch}}^{(i,j,r)}$  represents the impulse response of the propagation channel between the  $i$ -th transmit antenna and the  $r$ -th receive antenna of the  $j$ -th user. Note that the signal on the  $k$ -th subcarrier is contaminated by interference from the  $(k-1)$ -th and the  $(k+1)$ -th subcarriers. Let  $h_\ell[l_P]$  and  $h_k[l_P]$  denote the pulse shaping filter of the  $\ell$ -th subcarrier and the  $k$ -th subcarrier, respectively. The equivalent channel impulse response for the signal that is transmitted on the  $\ell$ -th subcarrier from the  $i$ -th transmit antenna to the  $r$ -th receive antenna and passed through the analysis filter for the  $k$ -th subcarrier can be expressed as

$$h_{\ell,k}^{(i,j,r)}[n] = \left[ h_\ell[l_P] * h_{\text{ch}}^{(i,j,r)}[l_P] * h_k[-l_P] \right]_{l_P=n\frac{M}{2}}, \quad (7.2)$$

where the effects of the transmit filter, the propagation channel, the receive filter, and the upsampling as well as the downsampling operations are included. The resulting number of

---

<sup>1</sup>In Chapter 6, the number of users is denoted by  $Q$ . Throughout this chapter, however, we use  $U$  to denote the number of users, while  $Q$  represents the number of taps of the equivalent channel defined in (7.3). In Appendix A.3, we provide a list of frequently used notation in each chapter.

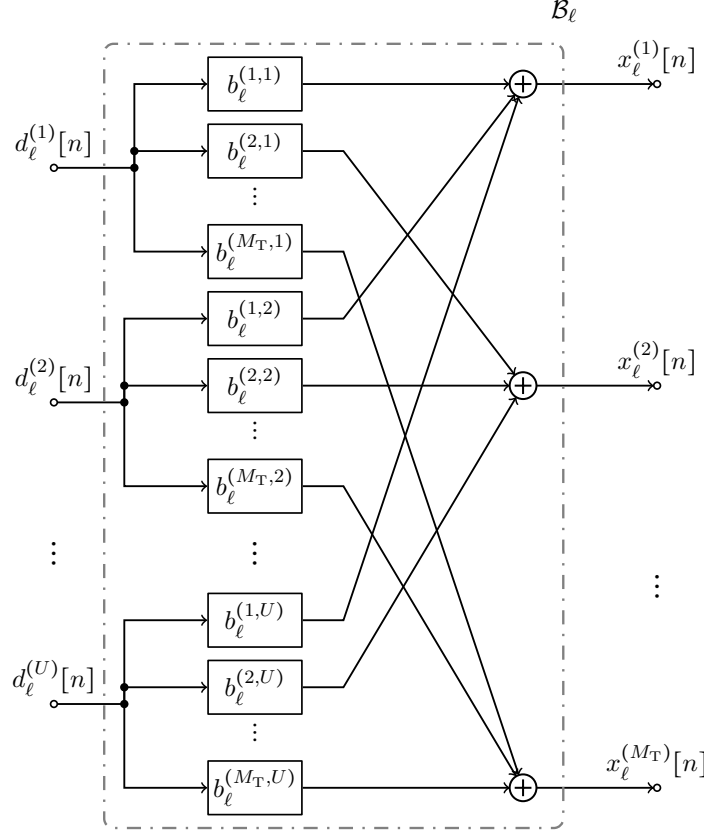


Figure 7.1.: Precoding of the signals for the  $U$  users onto  $M_T$  transmit antennas for subcarrier  $\ell$

taps of this equivalent channel is

$$Q = \left\lceil \frac{2(L_P - 1) + L_{\text{ch}}}{M/2} \right\rceil, \quad (7.3)$$

where  $L_{\text{ch}}$  denotes the length of the channel impulse response,  $L_P$  is the length of the prototype filter, and  $M$  represents the number of subcarriers. For the  $r$ -th receive antenna of the  $j$ -th user, an equalizer is applied, and its impulse response is represented by  $g_k^{(j,r)}[n]$ , where  $j = 1, 2, \dots, U$ , and  $r = 1, 2, \dots, M_{R_j}$ . Thus, the recovered signal of the  $j$ -th user on the  $k$ -th subcarrier is written as

$$\hat{d}_k^{(j)}[n] = \sum_{r=1}^{M_{R_j}} g_k^{(j,r)}[n] * \left( \sum_{i=1}^{M_T} \sum_{\ell=k-1}^{k+1} \left( h_{\ell,k}^{(i,j,r)}[n] * \sum_{s=1}^U \left( b_{\ell}^{(i,s)}[n] * d_{\ell}^{(s)}[n] \right) \right) + \hat{\eta}_k^{(j,r)}[n] \right),$$

where  $\hat{\eta}_k^{(j,r)}[n]$  denotes the filtered Additive White Gaussian Noise (AWGN)

$$\hat{\eta}_k^{(j,r)}[n] = \left[ h_k[l_P] * \eta^{(j,r)}[l_P] \right]_{l_P = n \frac{M}{2}} \quad (7.4)$$

with  $\eta^{(j,r)}[l_P]$  representing the AWGN with variance  $\sigma_n^2$ . It is worth mentioning that the precoding at the base station and the receive filtering at each user terminal are on a per-subcarrier basis. An equivalent subcarrier model can be derived. The block diagrams of its transmitter side and receiver side are presented in Figure 7.2 and Figure 7.3, respectively.

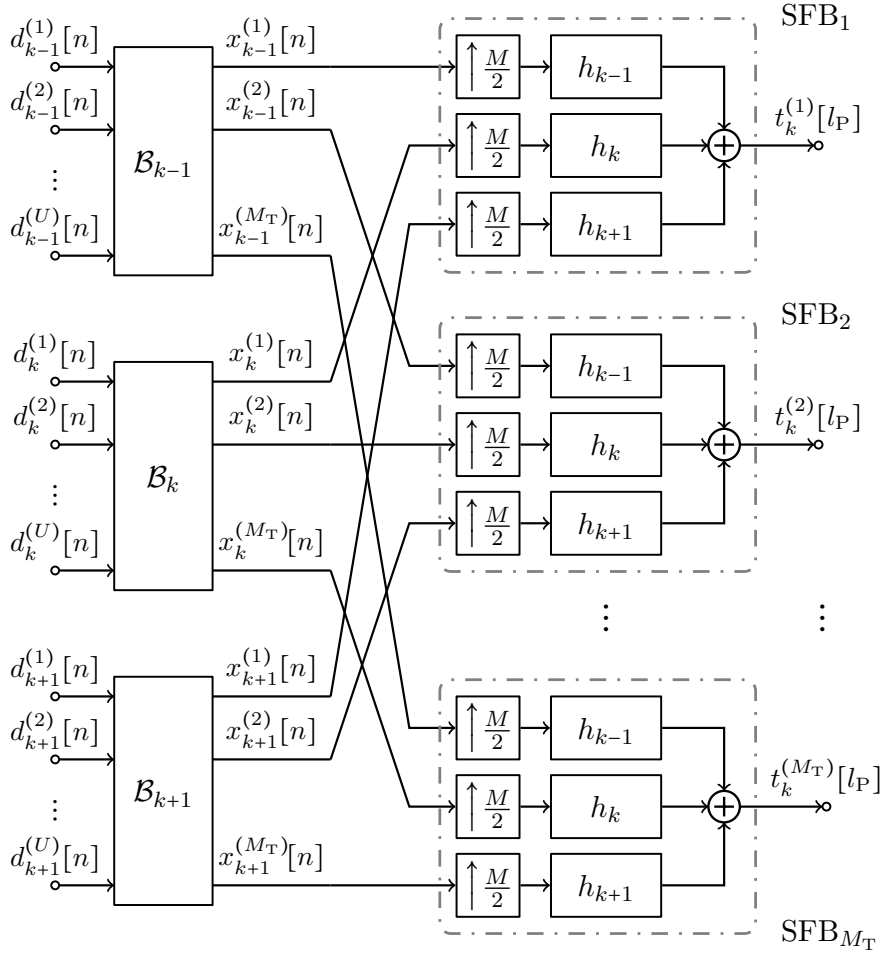


Figure 7.2.: Block diagram of the transmitter side of the subcarrier model

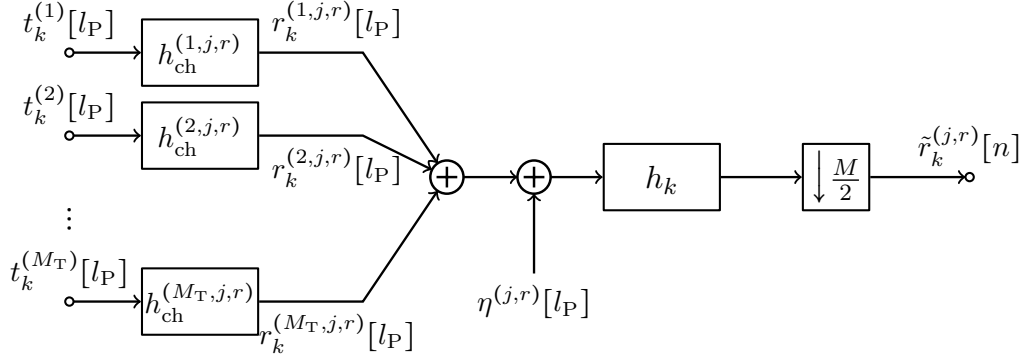


Figure 7.3.: Block diagram of the receiver side of the subcarrier model considering the  $r$ -th receive antenna of the  $j$ -th user

### 7.3. Iterative design of MMSE-based precoders and real-valued receive spatial filters

In this section, we present an iterative design of the precoders and the receive filters. The precoders are devised to mitigate the MUI, the ISI, and the ICI. At each user terminal, only a real-valued single-tap spatial filter is applied. Thus, the recovered desired signal  $\hat{d}_k^{(j)}[n]$  is expressed in a matrix-vector formulation as follows

$$\hat{d}_k^{(j)}[n] = \sum_{r=1}^{M_{Rj}} g_k^{(j,r)} \cdot \left( \sum_{\ell=k-1}^{k+1} \sum_{s=1}^U \mathbf{d}_\ell^{(s)\top}[n] \cdot \mathbf{H}_{\ell,k}^{(j,r)} \cdot \mathbf{b}_\ell^{(s)} + \hat{\eta}_k^{(j,r)}[n] \right), \quad (7.5)$$

where

$$\mathbf{b}_\ell^{(s)} = \begin{bmatrix} \mathbf{b}_\ell^{(1,s)\top} & \mathbf{b}_\ell^{(2,s)\top} & \dots & \mathbf{b}_\ell^{(M_T,s)\top} \end{bmatrix}^\top \in \mathbb{C}^{M_T \cdot B} \quad (7.6)$$

contains the  $M_T \cdot B$  coefficients of the precoding filter for the  $s$ -th user on the  $\ell$ -th subcarrier, and

$$\mathbf{H}_{\ell,k}^{(j,r)} = \begin{bmatrix} \mathbf{H}_{\ell,k}^{(1,j,r)} & \mathbf{H}_{\ell,k}^{(2,j,r)} & \dots & \mathbf{H}_{\ell,k}^{(M_T,j,r)} \end{bmatrix} \in \mathbb{C}^{(B+Q-1) \times M_T \cdot B} \quad (7.7)$$

with  $\mathbf{H}_{\ell,k}^{(i,j,r)} \in \mathbb{C}^{(B+Q-1) \times B}$ ,  $i = 1, 2, \dots, M_T$ , representing a Toeplitz matrix of the equivalent channel coefficients  $h_{\ell,k}^{(i,j,r)}[n]$  expressed as

$$\mathbf{H}_{\ell,k}^{(i,j,r)} = \begin{bmatrix} h_{\ell,k}^{(i,j,r)}[0] & 0 & \dots & 0 \\ h_{\ell,k}^{(i,j,r)}[1] & h_{\ell,k}^{(i,j,r)}[0] & \dots & 0 \\ \vdots & h_{\ell,k}^{(i,j,r)}[1] & \ddots & \vdots \\ h_{\ell,k}^{(i,j,r)}[Q-1] & \vdots & \ddots & 0 \\ 0 & h_{\ell,k}^{(i,j,r)}[Q-1] & \ddots & h_{\ell,k}^{(i,j,r)}[0] \\ 0 & 0 & \ddots & h_{\ell,k}^{(i,j,r)}[1] \\ \vdots & \vdots & \ddots & \vdots \\ 0 & 0 & \dots & h_{\ell,k}^{(i,j,r)}[Q-1] \end{bmatrix}. \quad (7.8)$$

The data vector  $\mathbf{d}_\ell^{(s)}[n] \in \mathbb{C}^{B+Q-1}$  contains consecutive data symbols and takes the following form

$$\mathbf{d}_\ell^{(s)}[n] = \begin{cases} \begin{bmatrix} \alpha_\ell^{(s)}[m] & j\beta_\ell^{(s)}[m] & \alpha_\ell^{(s)}[m-1] & \dots \end{bmatrix}^T, & k \text{ is odd} \\ \begin{bmatrix} j\beta_\ell^{(s)}[m] & \alpha_\ell^{(s)}[m] & j\beta_\ell^{(s)}[m-1] & \dots \end{bmatrix}^T, & k \text{ is even} \end{cases}, \quad (7.9)$$

where  $\alpha_\ell^{(s)}[m] = \text{Re}\{s_\ell^{(s)}[m]\}$  and  $\beta_\ell^{(s)}[m] = \text{Im}\{s_\ell^{(s)}[m]\}$  with unit variance, i.e.,  $\alpha_\ell^{(s)}[m]$  and  $\beta_\ell^{(s)}[m]$  represent the in-phase component and the quadrature component of the QAM modulated signal  $s_\ell^{(s)}[m]$ , respectively.

In addition,  $g_k^{(j,r)}$  denotes the real-valued coefficient of the spatial filter for the signal on the  $k$ -th subcarrier received by the  $r$ -th receive antenna of the  $j$ -th user. The recovered signal  $\hat{\alpha}_k^{(j)}[m]$  is obtained as

$$\hat{\alpha}_k^{(j)}[m] = \sum_{r=1}^{M_{Rj}} g_k^{(j,r)} \cdot \text{Re} \left\{ \left( \sum_{\ell=k-1}^{k+1} \sum_{s=1}^U \mathbf{d}_\ell^{(s)T}[n] \cdot \mathbf{H}_{\ell,k}^{(j,r)} \cdot \mathbf{b}_\ell^{(s)} + \hat{\eta}_k^{(j,r)}[n] \right) \right\}, \quad (7.10)$$

In case of  $\hat{\beta}_k^{(j)}[m]$ , it is obtained by taking the imaginary part of (7.5). Since both cases are equivalent to each other, we focus on the case of  $\hat{\alpha}_k^{(j)}[m]$  in the sequel.

In this iterative design, the precoders and the spatial filters are updated alternately. First given the spatial filter, the expression of the estimated desired signal of the  $j$ -th user on the

$k$ -th subcarrier can be written as

$$\hat{\alpha}_k^{(j)}[m] = \text{Re} \left\{ \sum_{\ell=k-1}^{k+1} \sum_{s=1}^U \mathbf{d}_\ell^{(s)\top} [n] \cdot \check{\mathbf{H}}_{\ell,k}^{(j)} \cdot \mathbf{b}_\ell^{(s)} + \sum_{r=1}^{M_{R,j}} g_k^{(j,r)} \cdot \hat{\eta}_k^{(j,r)} [n] \right\}, \quad (7.11)$$

where  $\check{\mathbf{H}}_{\ell,k}^{(j)} = \sum_{r=1}^{M_{R,j}} g_k^{(j,r)} \cdot \mathbf{H}_{\ell,k}^{(j,r)}$  is a short-hand notation. The precoder for the  $j$ -th user on the  $k$ -th subcarrier that minimizes the mean square error and the leakage can be obtained via the following optimization problem [NBSN14]

$$\mathbf{b}_k^{(j)} = \arg \min_{\mathbf{b}_k^{(j)}} \mathbb{E} \left\{ \left| \hat{\alpha}_k^{(j)}[m] - \alpha_k^{(j)}[m - \nu] \right|^2 + c_k^{(j)} + u_k^{(j)} \right\}, \quad (7.12)$$

where  $\nu = \left\lceil \frac{B+Q-1}{2} \right\rceil$  is the (integer) delay of the system. The value of  $\nu$  is chosen based on the criterion of selecting the symbol with the highest contribution [CPN11], [CPN13b]. The terms  $c_k^{(j)}$  and  $u_k^{(j)}$  measure the interference caused by the signal for the  $j$ -th user on the  $k$ -th subcarrier to the adjacent subcarriers and the other users, respectively. They take the following forms

$$c_k^{(j)} = \sum_{r=1}^{M_{R,j}} \sum_{\ell=k-1, \ell \neq k}^{k+1} \left| \text{Im} \left\{ \mathbf{d}_k^{(j)\top} [n] \cdot \mathbf{H}_{\ell,k}^{(j,r)} \cdot \mathbf{b}_k^{(j)} \right\} \right|^2 \quad (7.13)$$

$$u_k^{(j)} = \sum_{s=1, s \neq j}^U \sum_{r=1}^{M_{R,s}} \left( \sum_{\ell=k-1, \ell \neq k}^{k+1} \left| \text{Im} \left\{ \mathbf{d}_k^{(j)\top} [n] \cdot \mathbf{H}_{\ell,k}^{(s,r)} \cdot \mathbf{b}_k^{(j)} \right\} \right|^2 + \left| \text{Re} \left\{ \mathbf{d}_k^{(j)\top} [n] \cdot \mathbf{H}_{k,k}^{(s,r)} \cdot \mathbf{b}_k^{(j)} \right\} \right|^2 \right). \quad (7.14)$$

Let us define  $\tilde{\mathbf{d}}_k^{(j)} \in \mathbb{R}^{B+Q-1}$  such that

$$\mathbf{d}_k^{(j)} = \mathbf{J}_k \cdot \tilde{\mathbf{d}}_k^{(j)}, \quad (7.15)$$

where the diagonal matrix  $\mathbf{J}_k \in \mathbb{C}^{(B+Q-1) \times (B+Q-1)}$  has “1” and “ $j$ ” alternately appearing on its diagonal. This property of  $\mathbf{J}_k$  results from the structure of the data vector expressed in (7.9). Similarly as in [NBSN14], the following linear expressions for the real part and the imaginary part of the interference terms in (7.13) and (7.14) can be obtained

$$\text{Re} \left\{ \mathbf{d}_k^{(j)\top} [n] \cdot \mathbf{H}_{k,k}^{(s,r)} \cdot \mathbf{b}_k^{(j)} \right\} = \tilde{\mathbf{d}}_k^{(j)\top} \cdot \boldsymbol{\Psi}_{k,k}^{(s,r)} \cdot \boldsymbol{\xi}_k^{(j)} \quad (7.16)$$

$$\text{Im} \left\{ \mathbf{d}_k^{(j)\top} [n] \cdot \mathbf{H}_{\ell,k}^{(s,r)} \cdot \mathbf{b}_k^{(j)} \right\} = \tilde{\mathbf{d}}_k^{(j)\top} \cdot \boldsymbol{\Phi}_{\ell,k}^{(s,r)} \cdot \boldsymbol{\xi}_k^{(j)} \quad (7.17)$$

where

$$\Psi_{k,k}^{(s,r)} = \begin{bmatrix} \text{Re} \{ \mathbf{J}_k \cdot \mathbf{H}_{k,k}^{(s,r)} \} & -\text{Im} \{ \mathbf{J}_k \cdot \mathbf{H}_{k,k}^{(s,r)} \} \end{bmatrix} \quad (7.18)$$

$$\Phi_{\ell,k}^{(s,r)} = \begin{bmatrix} \text{Im} \{ \mathbf{J}_k \cdot \mathbf{H}_{\ell,k}^{(s,r)} \} & \text{Re} \{ \mathbf{J}_k \cdot \mathbf{H}_{\ell,k}^{(s,r)} \} \end{bmatrix} \quad (7.19)$$

$$\xi_k^{(j)} = \begin{bmatrix} \text{Re} \{ \mathbf{b}_k^{(j)} \} \\ \text{Im} \{ \mathbf{b}_k^{(j)} \} \end{bmatrix}. \quad (7.20)$$

The linear expression for the operation of taking the real part in (7.11) can be similarly obtained via defining

$$\check{\Psi}_{\ell,k}^{(j)} = \begin{bmatrix} \text{Re} \{ \mathbf{J}_k \cdot \check{\mathbf{H}}_{\ell,k}^{(j)} \} & -\text{Im} \{ \mathbf{J}_k \cdot \check{\mathbf{H}}_{\ell,k}^{(j)} \} \end{bmatrix}. \quad (7.21)$$

Assume that data symbols are uncorrelated, and the desired signal and the noise are uncorrelated. After inserting (7.11), (7.13), and (7.14) into the optimization problem defined via (7.12), it can be further reformulated using (7.16) – (7.21). Then, taking the derivative with respect to  $\xi_k^{(j)}$  and setting it to zero yield

$$\xi_k^{(j)} = \left( \check{\Psi}_{k,k}^{(j)\text{T}} \cdot \check{\Psi}_{k,k}^{(j)} + \sum_{s=1}^U \sum_{r=1}^{M_{R_s}} \sum_{\ell=k-1, \ell \neq k}^{k+1} \Phi_{\ell,k}^{(s,r)\text{T}} \cdot \Phi_{\ell,k}^{(s,r)} + \sum_{s=1, s \neq j}^U \sum_{r=1}^{M_{R_s}} \Psi_{k,k}^{(s,r)\text{T}} \cdot \Psi_{k,k}^{(s,r)} \right)^{-1} \cdot \check{\Psi}_{k,k}^{(j)\text{T}} \cdot \mathbf{e}_\nu, \quad (7.22)$$

where  $\mathbf{e}_\nu \in \mathbb{C}^{B+Q-1}$  is a unit vector with its  $\nu$ -th element as one. The delay of the system  $\nu$  has been defined in (7.12). To solve the problem that the matrix might be ill-conditioned, we add  $\alpha \cdot \mathbf{I}_{2 \cdot M_{T \cdot B}}$  in the matrix inversion involved in (7.22) with  $\alpha > 0$  as a regularization factor. The impact of  $\alpha$  on the performance of the proposed scheme is investigated in Section 7.6.

After computing the precoders, we turn to update the spatial filters assuming that the MUI, the ISI, and the ICI have been canceled completely, i.e.,  $\hat{\alpha}_k^{(j)}[m]$  takes the following form in the noiseless case

$$\hat{\alpha}_k^{(j)}[m] = \text{Re} \left\{ \mathbf{d}_k^{(j)\text{T}}[n] \cdot \sum_{r=1}^{M_{R_j}} g_k^{(j,r)} \cdot \mathbf{H}_{k,k}^{(j,r)} \cdot \mathbf{b}_k^{(j)} \right\}. \quad (7.23)$$

Define a vector  $\mathbf{g}_k^{(j)} \in \mathbb{R}^{M_{R_j}}$  that contains the  $M_{R_j}$  coefficients of the spatial filter of the  $j$ -th user on the  $k$ -th subcarrier, i.e.,

$$\mathbf{g}_k^{(j)} = \begin{bmatrix} g_k^{(j,1)} & g_k^{(j,2)} & \dots & g_k^{(j,M_{R_j})} \end{bmatrix}^{\text{T}}. \quad (7.24)$$



The Maximum Ratio Combining (MRC) is used as the criterion for the spatial filter. Therefore,  $\mathbf{g}_k^{(j)}$  can be obtained as

$$\mathbf{g}_k^{(j)} = \check{\mathbf{h}}_{k,k}^{(j)}, \quad (7.25)$$

where the  $r$ -th element of  $\check{\mathbf{h}}_{k,k}^{(j)}$ ,  $r = 1, 2, \dots, M_{R_j}$ , is given by

$$\check{h}_{k,k}^{(j,r)} = \text{Re} \left\{ \mathbf{e}_\nu^T \cdot \mathbf{H}_{k,k}^{(j,r)} \cdot \mathbf{b}_k^{(j)} \right\}. \quad (7.26)$$

In this proposed iterative scheme,  $\mathbf{g}_k^{(s)}$  ( $s = 1, 2, \dots, U$ ) that contains the  $M_{R_s}$  real-valued coefficients of the receive spatial filter of the  $s$ -th user on the  $k$ -th subcarrier is initialized randomly. To determine the termination of the iterative procedure, we propose to use the following stopping criterion. The term  $\Delta(\mathbf{g})$  that tracks the change of the receive spatial filters is defined as

$$\Delta(\mathbf{g}) = \sum_{s=1}^U \left\| \mathbf{g}_k^{(s,p)} - \mathbf{g}_k^{(s,p-1)} \right\|^2, \quad (7.27)$$

where  $\mathbf{g}_k^{(s,p)}$  and  $\mathbf{g}_k^{(s,p-1)} \in \mathbb{R}^{M_{R_s}}$  contain the coefficients of the receive spatial filter of the  $s$ -th user computed in the  $p$ -th iteration and the  $(p-1)$ -th iteration, respectively. A threshold denoted by  $\epsilon$  is set to  $10^{-5}$  in the simulations. At the end of each iteration,  $\Delta(\mathbf{g})$  is calculated and compared to  $\epsilon$ . If  $\Delta(\mathbf{g}) < \epsilon$ , the algorithm terminates, and the precoders are obtained. Otherwise, the iterative procedure continues, and the precoders as well as the receive filters are further updated.

## 7.4. Signal-to-Leakage-Ratio (SLR)-based precoders and real-valued receive spatial filters

Similar to the iterative design, we again consider a real-valued spatial filter at each user node. Instead of jointly and iteratively updating the precoder and the spatial filter, we propose a closed-form SLR-based linear precoder to reduce the complexity. A MRC-based spatial filter is employed at each user node. The effective channel with respect to the  $r$ -th receive antenna of the  $j$ -th user for the  $k$ -th subcarrier is given by

$$\mathbf{h}_{k,k}^{(\text{eff}),j,r} = \mathbf{\Psi}_{k,k}^{(j,r)T} \cdot \mathbf{e}_\nu \in \mathbb{R}^{2 \cdot M_T \cdot B}. \quad (7.28)$$

The ISI for the signal of the  $j$ -th user on the  $k$ -th subcarrier is measured via

$$\begin{aligned} \text{ISI}_k^{(j)} &= \mathbb{E} \left\{ \sum_{r=1}^{M_{R,j}} \left| \tilde{\mathbf{d}}_k^{(j)\top} \cdot \boldsymbol{\Psi}_{k,k}^{(\text{int}),j,r} \cdot \boldsymbol{\xi}_k^{(j)} \right|^2 \right\} \\ &= \boldsymbol{\xi}_k^{(j)\top} \cdot \sum_{r=1}^{M_{R,j}} \boldsymbol{\Psi}_{k,k}^{(\text{int}),j,r\top} \cdot \boldsymbol{\Psi}_{k,k}^{(\text{int}),j,r} \cdot \boldsymbol{\xi}_k^{(j)}, \end{aligned} \quad (7.29)$$

where

$$\boldsymbol{\Psi}_{k,k}^{(\text{int}),j,r} = \mathbf{J}_{\text{int}}^{(\nu)} \cdot \boldsymbol{\Psi}_{k,k}^{(j,r)} \in \mathbb{R}^{(B+Q-1) \times 2 \cdot M_T \cdot B}. \quad (7.30)$$

Here  $\mathbf{J}_{\text{int}}^{(\nu)} \in \mathbb{R}^{(B+Q-1) \times (B+Q-1)}$  is constructed by replacing the  $\nu$ -th row of a  $(B+Q-1)$ -by- $(B+Q-1)$  identity matrix by an all-zeros vector. The interference that is leaked to the adjacent subcarriers and other users by the signal for the  $j$ -th user on the  $k$ -th subcarrier can be represented as  $\mathbb{E} \{ c_k^{(j)} + u_k^{(j)} \}$ , where  $c_k^{(j)}$  and  $u_k^{(j)}$  are given by (7.13) and (7.14), respectively. It is expressed as

$$\begin{aligned} \mathbb{E} \{ c_k^{(j)} + u_k^{(j)} \} &= \boldsymbol{\xi}_k^{(j)\top} \cdot \left( \sum_{r=1}^{M_{R,j}} \sum_{\ell=k-1, \ell \neq k}^{k+1} \boldsymbol{\Phi}_{\ell,k}^{(j,r)\top} \cdot \boldsymbol{\Phi}_{\ell,k}^{(j,r)} \right. \\ &\quad \left. + \sum_{s=1, s \neq j}^U \sum_{r=1}^{M_{R,s}} \sum_{\ell=k-1, \ell \neq k}^{k+1} \boldsymbol{\Phi}_{\ell,k}^{(s,r)\top} \cdot \boldsymbol{\Phi}_{\ell,k}^{(s,r)} + \sum_{s=1, s \neq j}^U \sum_{r=1}^{M_{R,s}} \boldsymbol{\Psi}_{k,k}^{(s,r)\top} \cdot \boldsymbol{\Psi}_{k,k}^{(s,r)} \right) \cdot \boldsymbol{\xi}_k^{(j)} \\ &= \boldsymbol{\xi}_k^{(j)\top} \cdot \left( \sum_{s=1}^U \sum_{r=1}^{M_{R,s}} \sum_{\ell=k-1, \ell \neq k}^{k+1} \boldsymbol{\Phi}_{\ell,k}^{(s,r)\top} \cdot \boldsymbol{\Phi}_{\ell,k}^{(s,r)} + \sum_{s=1, s \neq j}^U \sum_{r=1}^{M_{R,s}} \boldsymbol{\Psi}_{k,k}^{(s,r)\top} \cdot \boldsymbol{\Psi}_{k,k}^{(s,r)} \right) \cdot \boldsymbol{\xi}_k^{(j)}. \end{aligned} \quad (7.31)$$

Consequently, the SLR on the  $k$ -th subcarrier for the  $j$ -th user denoted by  $\text{SLR}_k^{(j)}$  is given by

$$\text{SLR}_k^{(j)} = \frac{\boldsymbol{\xi}_k^{(j)\top} \cdot \mathbf{A}_k^{(j)} \cdot \boldsymbol{\xi}_k^{(j)}}{\boldsymbol{\xi}_k^{(j)\top} \cdot \mathbf{C}_k^{(j)} \cdot \boldsymbol{\xi}_k^{(j)}} \quad (7.32)$$

where

$$\mathbf{A}_k^{(j)} = \sum_{r=1}^{M_{R,j}} \mathbf{h}_{k,k}^{(\text{eff}),j,r} \cdot \mathbf{h}_{k,k}^{(\text{eff}),j,r\top}$$

$$C_k^{(j)} = \sum_{s=1}^U \sum_{r=1}^{M_{R,s}} \sum_{\ell=k-1, \ell \neq k}^{k+1} \Phi_{\ell,k}^{(s,r)\text{T}} \cdot \Phi_{\ell,k}^{(s,r)} + \sum_{s=1, s \neq j}^U \sum_{r=1}^{M_{R,s}} \Psi_{k,k}^{(s,r)\text{T}} \cdot \Psi_{k,k}^{(s,r)} + \sum_{r=1}^{M_{R,j}} \Psi_{k,k}^{(\text{int}),j,r\text{T}} \cdot \Psi_{k,k}^{(\text{int}),j,r}. \quad (7.33)$$

The precoder for the  $j$ -th user on the  $k$ -th subcarrier is obtained via

$$\xi_k^{(j)} = \arg \max_{\xi_k^{(j)}} \text{SLR}_k^{(j)}. \quad (7.34)$$

The solution is given by

$$\xi_k^{(j)} = \mathcal{P} \left\{ C_k^{(j)(-1)} \cdot A_k^{(j)} \right\}, \quad (7.35)$$

where  $\mathcal{P}\{\cdot\}$  represents the operator of computing the principal eigenvector of a matrix which corresponds to the maximal eigenvalue. Similarly as for the iterative design, we introduce a regularization factor  $\alpha$  in the matrix inversion involved in (7.35).

As the MUI, the ISI, and the ICI are mitigated by the SLR-based precoders at the base station, each user terminal then applies the MRC-based spatial filter given by (7.25) and (7.26).

## 7.5. Enabling per-user multi-stream transmissions

In this section, we consider the case where multiple data streams are transmitted to each user and present a Signal-to-Leakage-plus-Noise-Ratio (SLNR) maximization-based design of precoders that enables per-user multi-stream transmissions. First, we generalize the data model introduced in Section 7.2 where a single data stream is assumed to be sent to each user to the current scenario. Let  $D_j$  symbolize the number of data streams for the  $j$ -th user. The total number of data streams is  $D = \sum_{j=1}^U D_j$ . Note that the same number of data streams are sent on each subcarrier. After the OQAM staggering [SSL02] (cf. Figure 3.3), the  $q$ -th data stream transmitted to the  $s$ -th user on the  $\ell$ -th subcarrier is denoted by  $d_\ell^{(s,q)}[n]$ ,  $q = 1, 2, \dots, D_s$ , and  $s = 1, 2, \dots, U$ . Moreover, the impulse response of the precoding filter for  $d_\ell^{(s,q)}[n]$  is symbolized by  $b_\ell^{(i,s,q)}[n]$ ,  $i = 1, 2, \dots, M_T$ , while  $B$  denotes the length of the precoding filters. Figure 7.4 illustrates this per-subcarrier precoding procedure, where the precoded signal on the  $\ell$ -th subcarrier and for the  $i$ -th transmit antenna is given by

$$x_\ell^{(i)}[n] = \sum_{s=1}^U \sum_{q=1}^{D_s} \left( b_\ell^{(i,s,q)}[n] * d_\ell^{(s,q)}[n] \right). \quad (7.36)$$

Then, the resulting signals are multiplexed by SFBs.

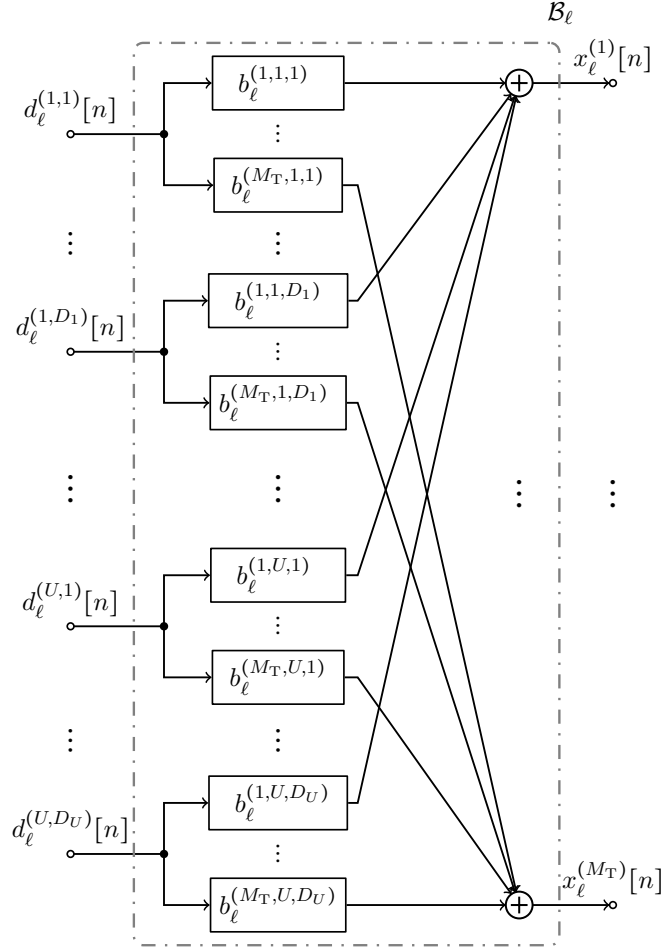


Figure 7.4.: Precoding of multiple data streams of each of the  $U$  users onto  $M_T$  transmit antennas for subcarrier  $\ell$

For the  $r$ -th receive antenna of the  $j$ -th user on the  $k$ -th subcarrier, equalizers are applied. The impulse response of the corresponding equalizer that recovers the  $p$ -th data stream ( $p = 1, 2, \dots, D_j$ ) is represented by  $g_k^{(j,r,p)}[n]$ , where  $j = 1, 2, \dots, U$ , and  $r = 1, 2, \dots, M_{R_j}$ . The recovered  $p$ -th data stream of the  $j$ -th user on the  $k$ -th subcarrier can be written as

$$\hat{d}_k^{(j,p)}[n] = \sum_{r=1}^{M_{R_j}} g_k^{(j,r,p)}[n] * \left( \sum_{i=1}^{M_T} \left( \sum_{\ell=k-1}^{k+1} h_{\ell,k}^{(i,j,r)}[n] * \sum_{s=1}^U \sum_{q=1}^{D_s} \left( b_{\ell}^{(i,s,q)}[n] * d_{\ell}^{(s,q)}[n] \right) \right) + \hat{\eta}_k^{(j,r)}[n] \right), \quad (7.37)$$

where  $\hat{\eta}_k^{(j,r)}[n]$  denotes the filtered AWGN. The block diagram of the transmitter side of an equivalent subcarrier model is presented in Figure 7.5. For the receiver side, the block diagram resembles that shown in Figure 7.3.

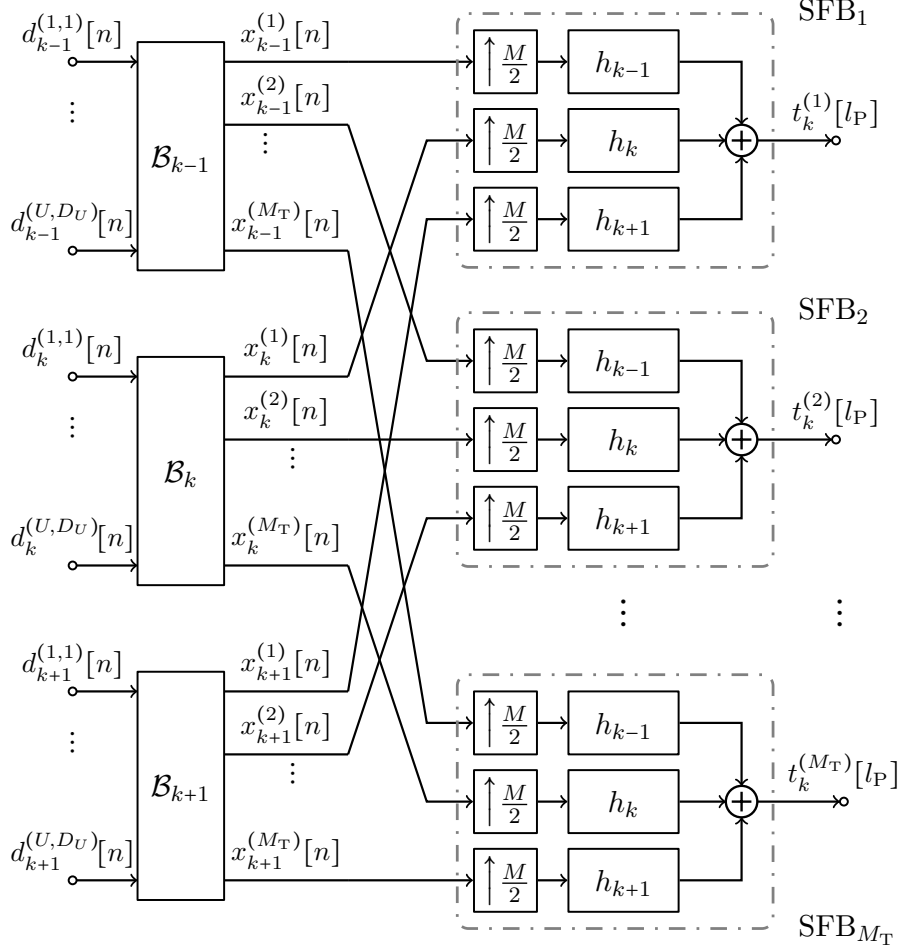


Figure 7.5.: Block diagram of the transmitter side of the subcarrier model considering the  $k$ -th subcarrier

Now we design SLNR-based precoders to mitigate the MUI, the ISI, and the ICI. To keep the computational burden at each user terminal low, single-tap spatial receive filters are employed, and they are assumed to be real-valued. Therefore, we can further express the recovered desired

signal  $\hat{d}_k^{(j,p)}[m]$  in the following matrix-vector formulation

$$\hat{d}_k^{(j,p)}[m] = \sum_{r=1}^{M_{R,j}} g_k^{(j,r,p)} \cdot \sum_{\ell=k-1}^{k+1} \sum_{s=1}^U \sum_{q=1}^{D_s} \mathbf{d}_\ell^{(s,q)\top}[n] \cdot \mathbf{H}_{\ell,k}^{(j,r)} \cdot \mathbf{b}_\ell^{(s,q)} + \hat{\eta}_k^{(j,r)}[n], \quad (7.38)$$

where

$$\mathbf{b}_\ell^{(s,q)} = \begin{bmatrix} \mathbf{b}_\ell^{(1,s,q)\top} & \mathbf{b}_\ell^{(2,s,q)\top} & \dots & \mathbf{b}_\ell^{(M_T,s,q)\top} \end{bmatrix}^\top \in \mathbb{C}^{M_T \cdot B} \quad (7.39)$$

contains the  $M_T \cdot B$  coefficients of the precoding filters for the  $q$ -th data stream that is transmitted to the  $s$ -th user on the  $\ell$ -th subcarrier, and

$$\mathbf{H}_{\ell,k}^{(j,r)} = \begin{bmatrix} \mathbf{H}_{\ell,k}^{(1,j,r)} & \mathbf{H}_{\ell,k}^{(2,j,r)} & \dots & \mathbf{H}_{\ell,k}^{(M_T,j,r)} \end{bmatrix} \in \mathbb{C}^{(B+Q-1) \times M_T \cdot B} \quad (7.40)$$

with  $\mathbf{H}_{\ell,k}^{(i,j,r)} \in \mathbb{C}^{(B+Q-1) \times B}$ ,  $i = 1, 2, \dots, M_T$ , representing a Toeplitz matrix of the equivalent channel coefficients  $h_{\ell,k}^{(i,j,r)}[n]$  given by (7.8). Moreover,  $g_k^{(j,r,p)}$  denotes the real-valued coefficient of the spatial filter used to recover the  $p$ -th data stream on the  $k$ -th subcarrier from the signals received by the  $r$ -th receive antenna of the  $j$ -th user. The data vector  $\mathbf{d}_\ell^{(s,q)}[n] \in \mathbb{C}^{B+Q-1}$  contains consecutive data symbols of the  $q$ -th data stream for the  $s$ -th user and is written as

$$\mathbf{d}_\ell^{(s,q)}[n] = \begin{cases} \begin{bmatrix} \alpha_\ell^{(s,q)}[m] & j\beta_\ell^{(s,q)}[m] & \alpha_\ell^{(s,q)}[m-1] & \dots \end{bmatrix}^\top, & k \text{ is odd} \\ \begin{bmatrix} j\beta_\ell^{(s,q)}[m] & \alpha_\ell^{(s,q)}[m] & j\beta_\ell^{(s,q)}[m-1] & \dots \end{bmatrix}^\top, & k \text{ is even} \end{cases}, \quad (7.41)$$

where  $\alpha_\ell^{(s,q)}[m] = \text{Re}\{s_\ell^{(s,q)}[m]\}$  and  $\beta_\ell^{(s,q)}[m] = \text{Im}\{s_\ell^{(s,q)}[m]\}$  with unit variance, i.e.,  $\alpha_\ell^{(s,q)}[m]$  and  $\beta_\ell^{(s,q)}[m]$  are the in-phase component and the quadrature component of the QAM modulated signal  $s_\ell^{(s,q)}[m]$ , respectively. Due to the fact that the receive spatial filters are real-valued, the recovered signal  $\hat{\alpha}_k^{(j,p)}$  is obtained as

$$\hat{\alpha}_k^{(j,p)}[m] = \sum_{r=1}^{M_{R,j}} g_k^{(j,r,p)} \cdot \text{Re} \left\{ \sum_{\ell=k-1}^{k+1} \sum_{s=1}^U \sum_{q=1}^{D_s} \mathbf{d}_\ell^{(s,q)\top}[n] \cdot \mathbf{H}_{\ell,k}^{(j,r)} \cdot \mathbf{b}_\ell^{(s,q)} + \hat{\eta}_k^{(j,r)}[n] \right\}. \quad (7.42)$$

To obtain  $\hat{\beta}_k^{(j,p)}[m]$ , on the other hand, we take the imaginary part of (7.38). Since both cases are equivalent to each other, we focus on the case of  $\hat{\alpha}_k^{(j,p)}[m]$  in the sequel.

First, let us use the terms  $c_k^{(j)}$  and  $u_k^{(j)}$  to measure the total interference power caused by the signal of the  $j$ -th user from the  $k$ -th subcarrier on the adjacent subcarriers and the other

users, respectively. They take the following forms

$$c_k^{(j)} = \mathbb{E} \left\{ \sum_{r=1}^{M_{R,j}} \sum_{\ell=k-1, \ell \neq k}^{k+1} \sum_{q=1}^{D_j} \left| \text{Im} \left\{ \mathbf{d}_k^{(j,q)\top} [n] \cdot \mathbf{H}_{\ell,k}^{(j,r)} \cdot \mathbf{b}_k^{(j,q)} \right\} \right|^2 \right\} \quad (7.43)$$

$$u_k^{(j)} = \mathbb{E} \left\{ \sum_{s=1, s \neq j}^U \sum_{r=1}^{M_{R,s}} \sum_{q=1}^{D_j} \left( \sum_{\ell=k-1, \ell \neq k}^{k+1} \left| \text{Im} \left\{ \mathbf{d}_k^{(j,q)\top} [n] \cdot \mathbf{H}_{\ell,k}^{(s,r)} \cdot \mathbf{b}_k^{(j,q)} \right\} \right|^2 + \left| \text{Re} \left\{ \mathbf{d}_k^{(j,q)\top} [n] \cdot \mathbf{H}_{k,k}^{(s,r)} \cdot \mathbf{b}_k^{(j,q)} \right\} \right|^2 \right) \right\}. \quad (7.44)$$

Define  $\tilde{\mathbf{d}}_k^{(j,q)}[n] \in \mathbb{R}^{B+Q-1}$  such that

$$\mathbf{d}_k^{(j,q)}[n] = \mathbf{J}_k \cdot \tilde{\mathbf{d}}_k^{(j,q)}[n], \quad (7.45)$$

where the diagonal matrix  $\mathbf{J}_k \in \mathbb{C}^{(B+Q-1) \times (B+Q-1)}$  has “1” and “j” alternately appearing on its diagonal. Similarly as in [NBSN14] and also as in the case where a single spatial stream is sent to each user (cf. Section 7.3 and Section 7.4), the following linear expressions for the real part and the imaginary part of the interference terms in (7.43) and (7.44) can be obtained

$$\text{Re} \left\{ \mathbf{d}_k^{(j,q)\top} [n] \cdot \mathbf{H}_{k,k}^{(s,r)} \cdot \mathbf{b}_k^{(j,q)} \right\} = \tilde{\mathbf{d}}_k^{(j,q)\top} [n] \cdot \boldsymbol{\Psi}_{k,k}^{(s,r)} \cdot \boldsymbol{\xi}_k^{(j,q)} \quad (7.46)$$

$$\text{Im} \left\{ \mathbf{d}_k^{(j,q)\top} [n] \cdot \mathbf{H}_{\ell,k}^{(s,r)} \cdot \mathbf{b}_k^{(j,q)} \right\} = \tilde{\mathbf{d}}_k^{(j,q)\top} [n] \cdot \boldsymbol{\Phi}_{\ell,k}^{(s,r)} \cdot \boldsymbol{\xi}_k^{(j,q)} \quad (7.47)$$

where  $\boldsymbol{\Psi}_{k,k}^{(s,r)} \in \mathbb{R}^{(B+Q-1) \times 2 \cdot M_T \cdot B}$ ,  $\boldsymbol{\Phi}_{\ell,k}^{(s,r)} \in \mathbb{R}^{(B+Q-1) \times 2 \cdot M_T \cdot B}$ , and  $\boldsymbol{\xi}_k^{(j,q)} \in \mathbb{R}^{2 \cdot M_T \cdot B}$  are defined as

$$\boldsymbol{\Psi}_{k,k}^{(s,r)} = \begin{bmatrix} \text{Re} \left\{ \mathbf{J}_k \cdot \mathbf{H}_{k,k}^{(s,r)} \right\} & -\text{Im} \left\{ \mathbf{J}_k \cdot \mathbf{H}_{k,k}^{(s,r)} \right\} \end{bmatrix} \quad (7.48)$$

$$\boldsymbol{\Phi}_{\ell,k}^{(s,r)} = \begin{bmatrix} \text{Im} \left\{ \mathbf{J}_k \cdot \mathbf{H}_{\ell,k}^{(s,r)} \right\} & \text{Re} \left\{ \mathbf{J}_k \cdot \mathbf{H}_{\ell,k}^{(s,r)} \right\} \end{bmatrix} \quad (7.49)$$

$$\boldsymbol{\xi}_k^{(j,q)} = \begin{bmatrix} \text{Re} \left\{ \mathbf{b}_k^{(j,q)} \right\} \\ \text{Im} \left\{ \mathbf{b}_k^{(j,q)} \right\} \end{bmatrix}. \quad (7.50)$$

In addition, we introduce

$$\Xi_k^{(j)} = \begin{bmatrix} \xi_k^{(j,1)} & \xi_k^{(j,2)} & \dots & \xi_k^{(j,D_j)} \end{bmatrix} \in \mathbb{R}^{2 \cdot M_T \cdot B \times D_j} \quad (7.51)$$

for the  $j$ -th user and the  $k$ -th subcarrier such that the  $D_j$  columns of  $\Xi_k^{(j)}$  correspond to the precoders for the  $D_j$  data streams that are transmitted to the  $j$ -th user on the  $k$ -th subcarrier.

Assuming that the data symbols are uncorrelated, we reformulate the terms  $c_k^{(j)}$  and  $u_k^{(j)}$  as follows

$$\begin{aligned} c_k^{(j)} &= \sum_{q=1}^{D_j} \xi_k^{(j,q)\top} \cdot \left( \sum_{r=1}^{M_{R_j}} \sum_{\ell=k-1, \ell \neq k}^{k+1} \Phi_{\ell,k}^{(j,r)\top} \cdot \Phi_{\ell,k}^{(j,r)} \right) \cdot \xi_k^{(j,q)} \\ &= \text{Tr} \left\{ \Xi_k^{(j)\top} \cdot \left( \sum_{r=1}^{M_{R_j}} \sum_{\ell=k-1, \ell \neq k}^{k+1} \Phi_{\ell,k}^{(j,r)\top} \cdot \Phi_{\ell,k}^{(j,r)} \right) \cdot \Xi_k^{(j)} \right\}, \end{aligned} \quad (7.52)$$

$$\begin{aligned} u_k^{(j)} &= \sum_{q=1}^{D_j} \xi_k^{(j,q)\top} \cdot \left( \sum_{s=1, s \neq j}^U \sum_{r=1}^{M_{R_s}} \left( \sum_{\ell=k-1, \ell \neq k}^{k+1} \Phi_{\ell,k}^{(s,r)\top} \cdot \Phi_{\ell,k}^{(s,r)} + \Psi_{k,k}^{(s,r)\top} \cdot \Psi_{k,k}^{(s,r)} \right) \right) \cdot \xi_k^{(j,q)} \\ &= \text{Tr} \left\{ \Xi_k^{(j)\top} \cdot \left( \sum_{s=1, s \neq j}^U \sum_{r=1}^{M_{R_s}} \left( \sum_{\ell=k-1, \ell \neq k}^{k+1} \Phi_{\ell,k}^{(s,r)\top} \cdot \Phi_{\ell,k}^{(s,r)} + \Psi_{k,k}^{(s,r)\top} \cdot \Psi_{k,k}^{(s,r)} \right) \right) \cdot \Xi_k^{(j)} \right\}, \end{aligned}$$

where  $\text{Tr}\{\cdot\}$  symbolizes the trace of the input matrix.

Moreover, the ISI for the signal of the  $j$ -th user on the  $k$ -th subcarrier is measured via

$$\begin{aligned} \text{ISI}_k^{(j)} &= \mathbb{E} \left\{ \sum_{r=1}^{M_{R_j}} \sum_{q=1}^{D_j} \left| \tilde{\mathbf{d}}_k^{(j,q)\top} [n] \cdot \Psi_{k,k}^{(\text{int}),j,r} \cdot \xi_k^{(j,q)} \right|^2 \right\} \\ &= \text{Tr} \left\{ \Xi_k^{(j)\top} \cdot \sum_{r=1}^{M_{R_j}} \Psi_{k,k}^{(\text{int}),j,r\top} \cdot \Psi_{k,k}^{(\text{int}),j,r} \cdot \Xi_k^{(j)} \right\}, \end{aligned} \quad (7.53)$$

where

$$\Psi_{k,k}^{(\text{int}),j,r} = \mathbf{J}_{\text{int}}^{(\nu)} \cdot \Psi_{k,k}^{(j,r)} \in \mathbb{R}^{(B+Q-1) \times 2 \cdot M_T \cdot B}. \quad (7.54)$$

Here  $\mathbf{J}_{\text{int}}^{(\nu)} \in \mathbb{R}^{(B+Q-1) \times (B+Q-1)}$  is constructed by replacing the  $\nu$ -th row of a  $(B+Q-1)$ -by-



$(B + Q - 1)$  identity matrix by an all-zeros vector, where  $\nu = \lceil \frac{B+Q-1}{2} \rceil$  is the (integer) delay of the system.

The effective channel with respect to the  $r$ -th receive antenna of the  $j$ -th user for the  $k$ -th subcarrier is given by

$$\mathbf{h}_{k,k}^{(\text{eff}),j,r} = \mathbf{\Psi}_{k,k}^{(j,r)\text{T}} \cdot \mathbf{e}_\nu \in \mathbb{R}^{2 \cdot M_{\text{T}} \cdot B}, \quad (7.55)$$

where  $\mathbf{e}_\nu \in \mathbb{R}^{B+Q-1}$  denotes a unit vector with its  $\nu$ -th element as one. Finally, the SLNR on the  $k$ -th subcarrier for the  $j$ -th user is expressed as

$$\text{SLNR}_k^{(j)} = \frac{\text{Tr} \left\{ \mathbf{\Xi}_k^{(j)\text{T}} \cdot \mathbf{A}_k^{(j)} \cdot \mathbf{\Xi}_k^{(j)} \right\}}{\text{Tr} \left\{ \mathbf{\Xi}_k^{(j)\text{T}} \cdot \mathbf{C}_k^{(j)} \cdot \mathbf{\Xi}_k^{(j)} \right\}}, \quad (7.56)$$

where

$$\begin{aligned} \mathbf{A}_k^{(j)} &= \sum_{r=1}^{M_{\text{R}_j}} \mathbf{h}_{k,k}^{(\text{eff}),j,r} \cdot \mathbf{h}_{k,k}^{(\text{eff}),j,r\text{T}} \\ \mathbf{C}_k^{(j)} &= \left( \sum_{s=1}^U \sum_{r=1}^{M_{\text{R}_s}} \sum_{\substack{\ell=k-1 \\ \ell \neq k}}^{k+1} \mathbf{\Phi}_{\ell,k}^{(s,r)\text{T}} \cdot \mathbf{\Phi}_{\ell,k}^{(s,r)} + \sum_{\substack{s=1 \\ s \neq j}}^U \sum_{r=1}^{M_{\text{R}_s}} \mathbf{\Psi}_{k,k}^{(s,r)\text{T}} \cdot \mathbf{\Psi}_{k,k}^{(s,r)} + \sum_{r=1}^{M_{\text{R}_j}} \mathbf{\Psi}_{k,k}^{(\text{int}),j,r\text{T}} \cdot \mathbf{\Psi}_{k,k}^{(\text{int}),j,r} + \rho \cdot \mathbf{I}_{2 \cdot M_{\text{T}} \cdot B} \right). \end{aligned}$$

Here  $\rho = 0.5 \cdot \frac{1}{D_j} \cdot M_{\text{R}_j} \cdot \gamma \cdot \sigma_n^2$  with  $\sigma_n^2$  representing the noise variance and  $\gamma$  resulting from the filtering as well as the downsampling operation as illustrated in Figure 7.3. The  $D_j$  columns of  $\mathbf{\Xi}_k^{(j)}$  that maximizes  $\text{SLNR}_k^{(j)}$  are obtained as the  $D_j$  generalized eigenvectors of the pair  $\{\mathbf{A}_k^{(j)}, \mathbf{C}_k^{(j)}\}$  as defined in (7.56) that correspond to the  $D_j$  largest generalized eigenvalues [STS07], [HMVS01]. Then  $\mathbf{\Xi}_k^{(j)}$  is scaled such that  $\text{Tr} \left\{ \mathbf{\Xi}_k^{(j)\text{T}} \cdot \mathbf{\Xi}_k^{(j)} \right\} = D_j$  is fulfilled.

At each user terminal, assuming that the MUI, the ISI, and the ICI have been eliminated,  $\hat{\alpha}_k^{(j,p)}[m]$  can be written as follows in the noiseless case

$$\hat{\alpha}_k^{(j,p)}[m] = \sum_{r=1}^{M_{\text{R}_j}} g_k^{(j,r,p)} \cdot \text{Re} \left\{ \sum_{q=1}^{D_j} \mathbf{d}_k^{(j,q)\text{T}}[n] \cdot \mathbf{H}_{k,k}^{(j,r)} \cdot \mathbf{b}_k^{(j,q)} \right\}. \quad (7.57)$$

The effective channel for the  $D_j$  spatial streams of the  $j$ -th user on the  $k$ -th subcarrier is given by  $\check{\mathbf{H}}_{k,k}^{(j)} \in \mathbb{R}^{M_{\text{R}_j} \times D_j}$ , and its  $(r, q)$ -th entry,  $r = 1, 2, \dots, M_{\text{R}_j}$ ,  $q = 1, 2, \dots, D_j$ , is written as

$$\check{h}_{k,k}^{(j,r,q)} = \text{Re} \left\{ \mathbf{e}_\nu^{\text{T}} \cdot \mathbf{H}_{k,k}^{(j,r)} \cdot \mathbf{b}_k^{(j,q)} \right\}. \quad (7.58)$$

Now define a matrix  $\mathbf{G}_k^{(j)} \in \mathbb{R}^{M_{R_j} \times D_j}$  such that it contains the coefficients of the single-tap spatial receive filter for the  $j$ -th user on the  $k$ -th subcarrier, i.e.,  $g_k^{(j,r,p)}$  is its  $(r, q)$ -th entry,  $r = 1, 2, \dots, M_{R_j}$ ,  $q = 1, 2, \dots, D_j$ . With Zero Forcing (ZF) as the criterion,  $\mathbf{G}_k^{(j)}$  is computed as

$$\mathbf{G}_k^{(j)} = \check{\mathbf{H}}_{k,k}^{(j)} \cdot \left( \check{\mathbf{H}}_{k,k}^{(j)\top} \cdot \check{\mathbf{H}}_{k,k}^{(j)} \right)^{-1}. \quad (7.59)$$

## 7.6. Simulation results

In this section, we evaluate the performance of the proposed transmitter and receiver designs in various multi-user MIMO downlink settings. The total number of subcarriers is 128, whereas the number of subcarriers with data symbols is 72 [DPS11]. The subcarrier spacing is set to 15 kHz, and the bandwidth is 1.4 MHz. The data symbols are drawn from the 16 QAM constellation.

First, we employ the WINNER Phase II spatial channel model based on the 3GPP as in [NBSN14]. The maximum channel impulse response length is approximately  $L_{\text{ch}} = 22$  samples. A two-user scenario is considered, and each user is equipped with two receive antennas, i.e.,  $U = 2$ , and  $M_{R_1} = M_{R_2} = 2$ . The number of transmit antennas at the base station  $M_T = 8$  or 4. The matrix inversion regularization factor is chosen as 0.025. Figure 7.6 depicts the Bit Error Rate (BER) performances of the MMSE-based iterative design and the closed-form SLR-based design. The former slightly outperforms the latter with the price of a higher computational complexity due to the iterative procedure. Still, the average number of iterations required for convergence is only around three. Moreover, it is observed that as the number of transmit antennas increases, the BER performance is better. A larger number of transmit antennas leads to more spatial degrees of freedom for the users that are simultaneously served in such an SDMA setting. Consequently, the MUI caused by each users to the other users is more effectively mitigated. The resulting ICI is smaller, too. On the other hand, even with only a single tap, i.e.,  $B = 1$ , the performance superiority of both proposed schemes over the BD-based technique [CPNM13] is significant. It is due to the fact that the BD-based scheme was devised assuming that the channel on each subcarrier is flat fading. As this assumption is violated in this example, it suffers from a severe performance degradation.

In addition, the Complementary Cumulative Distribution Function (CCDF) of the number of iterations required for convergence of the iterative design in Section 7.3 is illustrated at the top of Figure 7.7, while the CCDF of the final value (recorded as the algorithm terminates) of the term  $\Delta(\mathbf{g})$  (defined via (7.27)) is shown at the bottom of Figure 7.7. Here we consider

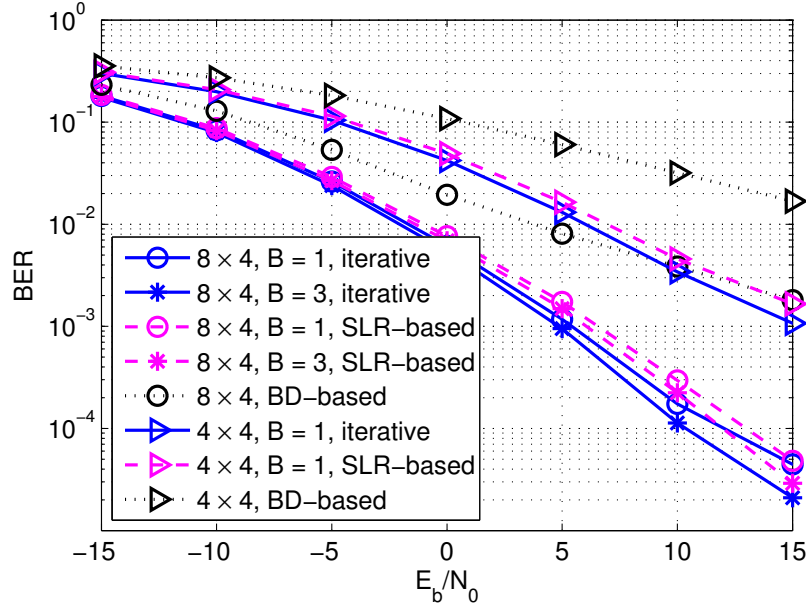


Figure 7.6.: BER performance in different multi-user MIMO downlink settings where  $U = 2$ ,  $M_{R_1} = M_{R_2} = 2$ ,  $M_T = 8$  or  $4$ , and  $\alpha = 0.025$

similar two-user scenarios as for Figure 7.6, where  $U = 2$ ,  $M_{R_1} = M_{R_2} = 2$ ,  $M_T = 8, 6$ , or  $4$ , and  $\alpha = 0.025$ . The length of the precoder  $B$  is set to 5. It can be seen that the algorithm converges within five iterations at a probability of around 90 % regardless of the number of transmit antennas considered in this example. It is also worth noting that the number of iterations required for convergence is barely affected by the length of the precoders or the MIMO settings.

Via Figure 7.8, the impact of the length of the precoders and the choice of the regularization factor is investigated. Longer precoders contribute to a superior capability in mitigating the MUI, the ICI, and the ISI. Hence, the BER performance of the proposed iterative approach becomes better, as the length of the precoding filters  $B$  increases. Nevertheless, by increasing the length from five to nine, the performance improvement is already very small. In addition, it is observed that a larger value for the matrix inversion regularization factor leads to a better performance in the low Signal-to-Noise-Ratio (SNR) regime, while there is an error floor in the high SNR regime. Similar observations also apply to the closed-form SLR-based design. The reason is that a larger value for the regularization factor results in larger residual ISI and residual leakage due to approximation errors induced by the regularization procedure. Unlike

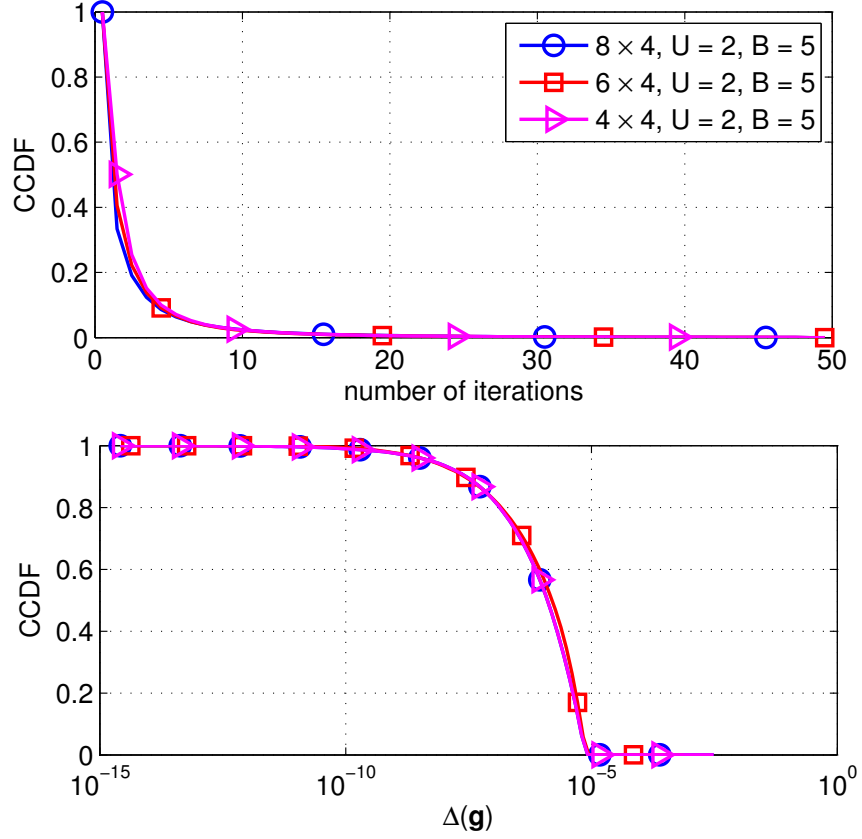


Figure 7.7.: CCDF of the number of iterations of the iterative design in Section 7.3 and the final value of  $\Delta(\mathbf{g})$  in different multi-user MIMO downlink settings where  $U = 2$ ,  $M_{R_1} = M_{R_2} = 2$ ,  $M_T = 8, 6$  or  $4$ ,  $B = 5$ , and  $\alpha = 0.025$

the low SNR regime, in the high SNR regime the residual interference (residual ISI and leakage) dominates instead of the noise. Hence, this observation inspires the design of an SNR-related regularization factor as future work. For all the values of the lengths of the precoders  $B$  and the choice of the regularization factor considered in this example, the iterative scheme achieves a much better performance compared to the IIM-CBF 1 scheme in Section 6.3.1 as well as in [CLH14d] and the BD-based technique [CPNM13].

In the sequel, the performance of the SLNR maximization-based design of precoders is assessed in multi-user MIMO downlink settings where per-user multi-stream transmissions are supported. The ITU Vehicular-B (Veh-B) channel [ITU97] is used. The maximum channel

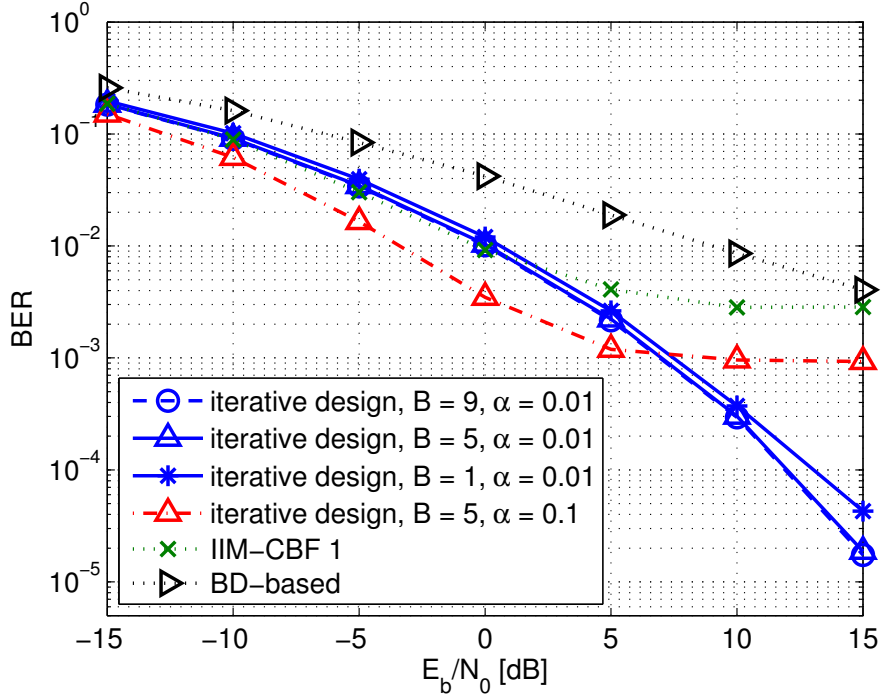


Figure 7.8.: BER performance in a multi-user MIMO downlink setting where  $U = 2$ ,  $M_{R_1} = M_{R_2} = 3$ ,  $M_T = 6$

impulse length is approximately  $L_{\text{ch}} = 47$  samples, indicating that the simulated scenarios are very critical with highly frequency selective channels.

A two-user scenario is considered in the first example. The base station is equipped with six transmit antennas, whereas each of the two users has three receive antennas, i.e.,  $M_T = 6$ , and  $M_{R_1} = M_{R_2} = 3$ . Two data streams are transmitted to each user. The BER performance of the proposed SLNR-based multi-tap precoding scheme is shown in Figure 7.9. Different lengths of the precoder, i.e., different values for  $B$ , are considered. It can be observed that as the length of the precoder is longer, a better performance is achieved due to a more effective mitigation of the MUI, ISI, and ICI. Nevertheless, increasing the length of the precoder from 9 to 11 only leads to a very slight improvement. With  $B = 5$ , the performance is already satisfactory over the range of the uncoded BER that is of interest. For the purpose of comparison, the IIM-CBF 1 scheme in Section 6.3.1 as well as in [CLH14d] and the BD-based method [CPNM13] have also been simulated. Note that these two approaches rely on the assumption that the channel on each subcarrier is flat fading. Since this assumption is violated, and the propagation channel is

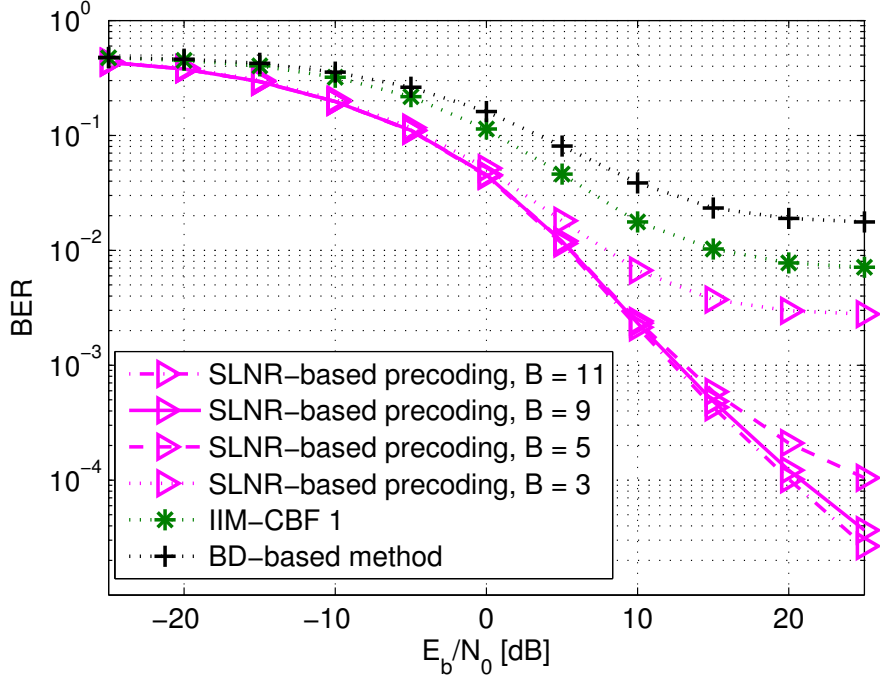


Figure 7.9.: BER performance in multi-user MIMO downlink settings where  $U = 2$ ,  $M_{R_1} = M_{R_2} = 3$ ,  $M_T = 6$ ,  $D_1 = D_2 = 2$

highly frequency selective, they fail to effectively suppress the interference. Therefore, we can see in Figure 7.9 that the proposed SLNR-based precoding algorithm significantly outperforms IIM-CBF 1 and the BD-based method even when  $B = 3$ .

In the second example, we evaluate the performance of the SLNR-based precoder in two other multi-user MIMO downlink scenarios, and the results are presented in Figure 7.10. It can be observed that the SLNR-based precoding scheme provides a satisfactory performance in these settings, too. As the number of receive antennas of each user terminal increases, the spatial degrees of freedom that are exploited for the mitigation of the MUI are reduced. On the other hand, a larger number of receive antennas brings a higher diversity gain. As the former effect dominates, the BER performance in case of the  $M_{R_1} = M_{R_2} = 2$  setting is slightly better than that of the  $M_{R_1} = M_{R_2} = 3$  setting.

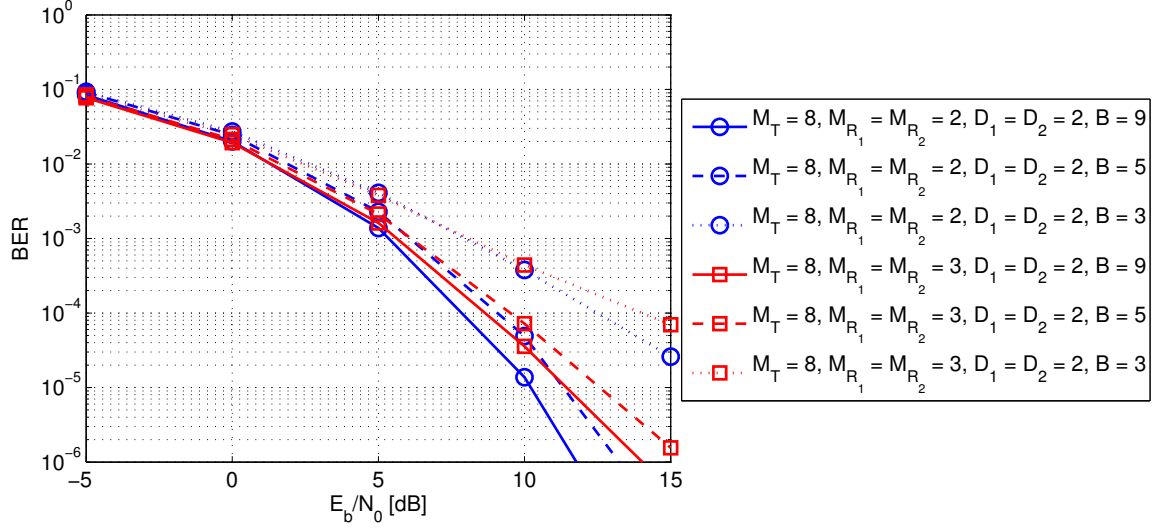


Figure 7.10.: BER performance of the SLNR-based precoding method in multi-user MIMO downlink settings where  $U = 2$ ,  $M_{R_1} = M_{R_2} = 2$  or  $M_{R_1} = M_{R_2} = 3$ ,  $M_T = 8$ ,  $D_1 = D_2 = 2$

### Extension of the SLNR-based scheme for overloaded multi-user MIMO downlink systems

In fact, the above observation in Figure 7.10 has inspired an SLNR maximization-based coordinated beamforming design where the precoders and the receive filters are computed jointly and iteratively. It is attractive for FBMC/OQAM-based multi-user MIMO downlink scenarios where  $M_R > D$ . In particular, for overloaded multi-user MIMO downlink settings where  $M_T < M_R$ , this iterative approach leads to a satisfactory performance. With the real-valued receive filters known, i.e.,  $g_\ell^{(j,r,p)}$  for the  $p$ -th data stream and the  $r$ -th receive antenna of the  $j$ -th user on the  $\ell$ -th subcarrier is known, the following equivalent channel matrix is computed

$$\check{\mathbf{H}}_{\ell,k}^{(j,p)} = \sum_{r=1}^{M_{R_j}} g_\ell^{(j,r,p)} \cdot \mathbf{H}_{\ell,k}^{(j,r)}. \quad (7.60)$$

Accordingly, the terms,  $c_k^{(j)}$  and  $u_k^{(j)}$  that measure the total interference power caused by the signal of the  $j$ -th user from the  $k$ -th subcarrier on the adjacent subcarriers and the other users,

respectively, are expressed as

$$c_k^{(j)} = \mathbb{E} \left\{ \sum_{p=1}^{D_j} \sum_{\ell=k-1, \ell \neq k}^{k+1} \sum_{q=1}^{D_j} \left| \text{Im} \left\{ \mathbf{d}_k^{(j,q)\top} [n] \cdot \check{\mathbf{H}}_{\ell,k}^{(j,p)} \cdot \mathbf{b}_k^{(j,q)} \right\} \right|^2 \right\} \quad (7.61)$$

$$u_k^{(j)} = \mathbb{E} \left\{ \sum_{s=1, s \neq j}^U \sum_{p=1}^{D_s} \sum_{q=1}^{D_j} \left( \sum_{\ell=k-1, \ell \neq k}^{k+1} \left| \text{Im} \left\{ \mathbf{d}_k^{(j,q)\top} [n] \cdot \check{\mathbf{H}}_{\ell,k}^{(s,p)} \cdot \mathbf{b}_k^{(j,q)} \right\} \right|^2 \right. \right. \\ \left. \left. + \left| \text{Re} \left\{ \mathbf{d}_k^{(j,q)\top} [n] \cdot \check{\mathbf{H}}_{k,k}^{(s,p)} \cdot \mathbf{b}_k^{(j,q)} \right\} \right|^2 \right) \right\}. \quad (7.62)$$

They are further reformulated as

$$c_k^{(j)} = \sum_{q=1}^{D_j} \boldsymbol{\xi}_k^{(j,q)\top} \cdot \left( \sum_{p=1}^{D_j} \sum_{\ell=k-1, \ell \neq k}^{k+1} \check{\boldsymbol{\Phi}}_{\ell,k}^{(j,p)\top} \cdot \check{\boldsymbol{\Phi}}_{\ell,k}^{(j,p)} \right) \cdot \boldsymbol{\xi}_k^{(j,q)} \\ = \text{Tr} \left\{ \boldsymbol{\Xi}_k^{(j)\top} \cdot \left( \sum_{p=1}^{D_j} \sum_{\ell=k-1, \ell \neq k}^{k+1} \check{\boldsymbol{\Phi}}_{\ell,k}^{(j,p)\top} \cdot \check{\boldsymbol{\Phi}}_{\ell,k}^{(j,p)} \right) \cdot \boldsymbol{\Xi}_k^{(j)} \right\}, \quad (7.63)$$

$$u_k^{(j)} = \sum_{q=1}^{D_j} \boldsymbol{\xi}_k^{(j,q)\top} \cdot \left( \sum_{s=1, s \neq j}^U \sum_{p=1}^{D_s} \left( \sum_{\ell=k-1, \ell \neq k}^{k+1} \check{\boldsymbol{\Phi}}_{\ell,k}^{(s,p)\top} \cdot \check{\boldsymbol{\Phi}}_{\ell,k}^{(s,p)} + \check{\boldsymbol{\Psi}}_{k,k}^{(s,p)\top} \cdot \check{\boldsymbol{\Psi}}_{k,k}^{(s,p)} \right) \right) \cdot \boldsymbol{\xi}_k^{(j,q)} \\ = \text{Tr} \left\{ \boldsymbol{\Xi}_k^{(j)\top} \cdot \left( \sum_{s=1, s \neq j}^U \sum_{p=1}^{D_s} \left( \sum_{\ell=k-1, \ell \neq k}^{k+1} \check{\boldsymbol{\Phi}}_{\ell,k}^{(s,p)\top} \cdot \check{\boldsymbol{\Phi}}_{\ell,k}^{(s,p)} + \check{\boldsymbol{\Psi}}_{k,k}^{(s,p)\top} \cdot \check{\boldsymbol{\Psi}}_{k,k}^{(s,p)} \right) \right) \cdot \boldsymbol{\Xi}_k^{(j)} \right\},$$

where  $\check{\boldsymbol{\Psi}}_{k,k}^{(s,p)} \in \mathbb{R}^{(B+Q-1) \times 2 \cdot M_T \cdot B}$  and  $\check{\boldsymbol{\Phi}}_{\ell,k}^{(s,p)} \in \mathbb{R}^{(B+Q-1) \times 2 \cdot M_T \cdot B}$  are defined as

$$\check{\boldsymbol{\Psi}}_{k,k}^{(s,p)} = \begin{bmatrix} \text{Re} \left\{ \mathbf{J}_k \cdot \check{\mathbf{H}}_{k,k}^{(s,p)} \right\} & -\text{Im} \left\{ \mathbf{J}_k \cdot \check{\mathbf{H}}_{k,k}^{(s,p)} \right\} \end{bmatrix} \quad (7.64)$$

$$\check{\boldsymbol{\Phi}}_{\ell,k}^{(s,p)} = \begin{bmatrix} \text{Im} \left\{ \mathbf{J}_k \cdot \check{\mathbf{H}}_{\ell,k}^{(s,p)} \right\} & \text{Re} \left\{ \mathbf{J}_k \cdot \check{\mathbf{H}}_{\ell,k}^{(s,p)} \right\} \end{bmatrix}. \quad (7.65)$$

Moreover,  $\boldsymbol{\xi}_k^{(j,q)} \in \mathbb{R}^{2 \cdot M_T \cdot B}$  contains the stacking of the real part and the imaginary part of  $\mathbf{b}_k^{(j,q)}$  as defined in (7.50), and  $\boldsymbol{\xi}_k^{(j,q)}$  ( $q = 1, 2, \dots, D_j$ ) constitute the  $D_j$  columns of  $\boldsymbol{\Xi}_k^{(j)} \in \mathbb{R}^{2 \cdot M_T \cdot B \times D_j}$  as defined in (7.51). On the other hand, the ISI for the signal of the  $j$ -th user on the  $k$ -th



subcarrier is given by

$$\begin{aligned} \text{ISI}_k^{(j)} &= \mathbb{E} \left\{ \sum_{p=1}^{D_j} \sum_{q=1}^{D_j} \left| \tilde{d}_k^{(j,q)\text{T}}[n] \cdot \check{\Psi}_{k,k}^{(\text{int}),j,p} \cdot \xi_k^{(j,q)} \right|^2 \right\} \\ &= \text{Tr} \left\{ \Xi_k^{(j)\text{T}} \cdot \sum_{p=1}^{D_j} \check{\Psi}_{k,k}^{(\text{int}),j,p\text{T}} \cdot \check{\Psi}_{k,k}^{(\text{int}),j,p} \cdot \Xi_k^{(j)} \right\}, \end{aligned} \quad (7.66)$$

where

$$\check{\Psi}_{k,k}^{(\text{int}),j,p} = \mathbf{J}_{\text{int}}^{(\nu)} \cdot \check{\Psi}_{k,k}^{(j,p)} \in \mathbb{R}^{(B+Q-1) \times 2 \cdot M_{\text{T}} \cdot B} \quad (7.67)$$

with  $\mathbf{J}_{\text{int}}^{(\nu)}$  defined in (7.54). The effective channel with respect to the  $p$ -th data stream of the  $j$ -th user for the  $k$ -th subcarrier is given by

$$\check{\mathbf{h}}_{k,k}^{(\text{eff}),j,p} = \check{\Psi}_{k,k}^{(j,p)\text{T}} \cdot \mathbf{e}_\nu \in \mathbb{R}^{2 \cdot M_{\text{T}} \cdot B}, \quad (7.68)$$

where  $\mathbf{e}_\nu \in \mathbb{R}^{B+Q-1}$  denotes a unit vector with its  $\nu$ -th element as one. Then the SLNR on the  $k$ -th subcarrier for the  $j$ -th user is expressed as

$$\text{SLNR}_k^{(j)'} = \frac{\text{Tr} \left\{ \Xi_k^{(j)\text{T}} \cdot \mathbf{A}_k^{(j)'} \cdot \Xi_k^{(j)} \right\}}{\text{Tr} \left\{ \Xi_k^{(j)\text{T}} \cdot \mathbf{C}_k^{(j)'} \cdot \Xi_k^{(j)} \right\}}, \quad (7.69)$$

where

$$\mathbf{A}_k^{(j)'} = \sum_{p=1}^{D_j} \check{\mathbf{h}}_{k,k}^{(\text{eff}),j,p} \cdot \check{\mathbf{h}}_{k,k}^{(\text{eff}),j,p\text{T}} \quad (7.70)$$

$$\begin{aligned} \mathbf{C}_k^{(j)'} &= \sum_{s=1}^U \sum_{p=1}^{D_s} \sum_{\substack{\ell=k-1 \\ \ell \neq k}}^{k+1} \check{\Phi}_{\ell,k}^{(s,p)\text{T}} \cdot \check{\Phi}_{\ell,k}^{(s,p)} + \sum_{\substack{s=1 \\ s \neq j}}^U \sum_{p=1}^{D_s} \check{\Psi}_{k,k}^{(s,p)\text{T}} \cdot \check{\Psi}_{k,k}^{(s,p)} + \sum_{p=1}^{D_j} \check{\Psi}_{k,k}^{(\text{int}),j,p\text{T}} \cdot \check{\Psi}_{k,k}^{(\text{int}),j,p} + \rho \cdot \mathbf{I}_{2 \cdot M_{\text{T}} \cdot B}. \end{aligned} \quad (7.71)$$

Here  $\rho = 0.5 \cdot \gamma \cdot \sigma_n^2$  with  $\sigma_n^2$  representing the noise variance and  $\gamma$  resulting from the filtering as well as the downsampling operation as illustrated in Figure 7.3. The solution of this optimization problem is similar to that of (7.56).

Notice that to compute the precoder for the  $k$ -th subcarrier, the knowledge of the coefficients of the receive filters for its adjacent subcarriers is required (cf. the first item of  $\mathbf{C}_k^{(j)'} in (7.71)). Therefore, compared to the closed-form SLNR-based scheme in Section 7.5, apart$

from the difference that the method described right above requires iterative procedures, joint-subcarrier processing is involved. For the initialization, the receive filters for each user on *all the subcarriers* are generated randomly. At each iteration, the precoders on *all the subcarriers* are computed successively. Then the receive filters on *all the subcarriers* are further updated according to (7.59) in a sequential manner as well. In Figure 7.11 we present some preliminary results with respect to this new iterative approach. Here a two-user FBMC/OQAM-based multi-user MIMO downlink setting is considered, where  $M_{R_1} = M_{R_2} = 5$ ,  $M_T = 8$ ,  $D_1 = D_2 = 3$ . The remaining simulation parameters are the same as for Figure 7.10. In the legend, we

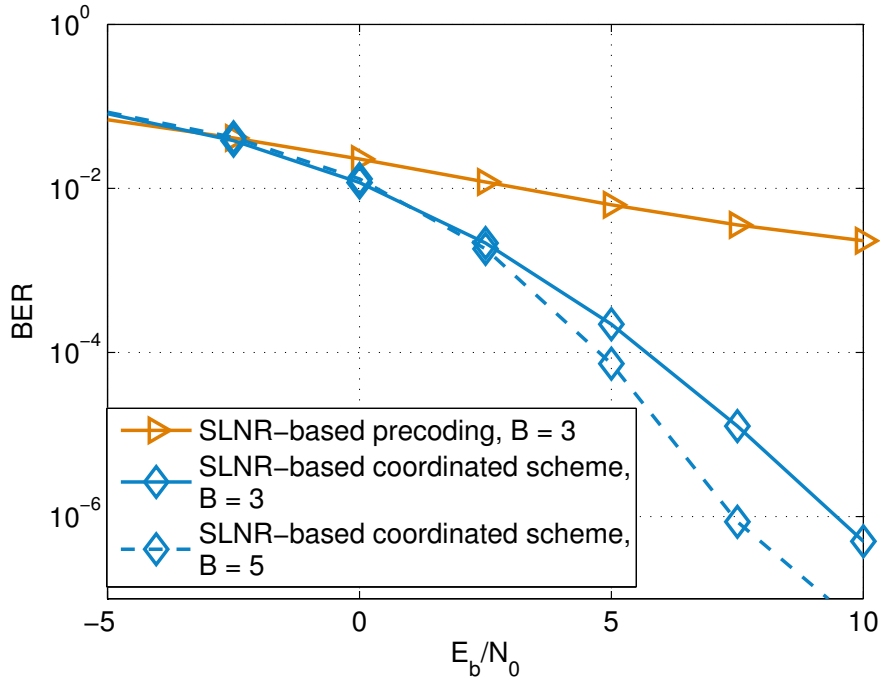


Figure 7.11.: BER performance in multi-user MIMO downlink settings where  $U = 2$ ,  $M_{R_1} = M_{R_2} = 5$ ,  $M_T = 8$ ,  $D_1 = D_2 = 3$

refer to the iterative design presented in this section as SLNR-based coordinated scheme. It can be observed that in such an overloaded multi-user MIMO downlink system where the number of receive antennas at the user terminals exceeds the number of transmit antennas at the base station, the SLNR-based coordinated scheme leads to a much better performance compared to the closed-form SLNR-based algorithm. To obtain these preliminary results, we set the number of iterations to 20 for the SLNR-based coordinated method. For future work, a

suitable stopping criterion can be devised based on, e.g., tracking the change of the precoders or the receive filters or measuring the residual interference.

## 7.7. Summary

We focus on FBMC/OQAM-based multi-user MIMO downlink systems with highly frequency selective channels in this chapter. Assuming a single data stream is sent to each user, we have presented two designs of precoders and equalizers. The first one is an iterative approach where the MMSE-based precoders and the MRC-based receive spatial filters are jointly computed. In the second scheme, we have devised closed-form SLR-based precoders for the base station and a similar MRC-based receive processing for each user terminal. Both schemes are developed to effectively mitigate the MUI, the ISI, and the ICI in critical highly frequency selective propagation conditions. From the numerical results it can be concluded that the first approach provides a slightly better performance compared to the second method, at the cost of a higher complexity due to the joint transceiver design. In addition, it has been addressed how to enable the transmission of multiple data streams to each user terminal via precoding that is designed to maximize the SLNR. All the proposed approaches show a considerable performance improvement over the state-of-the-art schemes that do not consider the channel frequency selectivity inside each subcarrier. Finally, we have also presented an SLNR-based coordinated design of the precoders and the receive filters, and we have shown its advantageous performance in overloaded multi-user MIMO downlink systems. This SLNR-based coordinated scheme can be extended to the downlink of coordinated multi-point systems with highly frequency selective channels.

## **Part II.**

### **Tensor-based model order estimation and subspace tracking for multi-dimensional harmonic retrieval**

Part II of this thesis concentrates on the context of multi-dimensional harmonic retrieval. New advances in multi-dimensional signal processing are presented towards fulfilling the compelling demand of statistically robust tensor-based model order estimation schemes and tensor-based subspace tracking methods for time-varying scenarios.

We first discuss the incorporation of statistical robustness into multi-dimensional model order estimation in Chapter 8. Robustified versions of  $R$ -D Akaike's Information Criterion (AIC),  $R$ -D Minimum Description Length (MDL), and the  $R$ -D Exponential Fitting Test (EFT) are developed. They are able to provide reliable estimates of the model order even when the measurement data suffer from a very severe contamination due to, e.g., brief sensor failures.

Chapter 9 presents a framework for Tensor-based subspace Tracking via Kronecker-structured projections (TeTraKron). TeTraKron allows to extend arbitrary matrix-based subspace tracking schemes to track the tensor-based subspace estimate. It can also be employed to devise tensor-based real-valued subspace tracking algorithms featuring an enhanced tracking accuracy and a reduced computational complexity. The performance of ESPRIT-type parameter estimation schemes is evaluated where the subspace estimates obtained by the proposed TeTraKron-based subspace tracking algorithms are used for the tracking of spatial frequencies in time-varying scenarios.

## 8. Robust multi-dimensional model order estimation in the presence of brief sensor failures

Model order estimation is a long standing topic in the field of signal processing. In recent years, the prosperous development of tensor-based signal processing has sparked great research attention on multi-dimensional model order estimation. By preserving and exploiting the multi-dimensional nature of the data, multi-dimensional model order estimation schemes exhibit performance superiority over their conventional matrix-based counterpart methods. Nevertheless, approaches that have been devised assuming a Gaussian noise distribution are very sensitive to brief sensor failures that cause contamination to the measurement data. We address this issue in this chapter and present robust multi-dimensional model order estimation schemes that show strong resilience against brief sensor failures. First, robust versions of  $R$ -D Akaike's Information Criterion (AIC),  $R$ -D Minimum Description Length (MDL), and  $R$ -D Exponential Fitting Test (EFT) are developed, where the robust MM-estimates of the covariance matrices of the unfoldings of the multi-dimensional data are used. Moreover, forward-backward averaging is incorporated into the construction of a real-valued measurement tensor, leading to a further enhancement of the robust multi-dimensional model order estimation schemes. The unfoldings of the real-valued data tensor are used as the input of the robust covariance estimator instead of stacking the real and imaginary parts of the unfoldings of the original complex-valued measurement tensor. Such enhanced versions of robust  $R$ -D AIC, robust  $R$ -D MDL, and robust  $R$ -D EFT experience an improved performance and a reduced computational complexity. Numerical simulations are performed to demonstrate the promising performances of these tensor-based robust model order selection techniques in the presence of brief sensor failures. The aforementioned results have been published in [MCR<sup>+</sup>12] and [CH13a].

### 8.1. Introduction

Subspace-based estimation techniques find their applications in a variety of scientific fields including radar, sonar, communications, channel modeling, image processing, and so on. To estimate the parameters in multi-dimensional harmonic retrieval problems, tensor-based approaches have been developed [HRD08]. It is shown that a Higher-Order Singular Value Decomposition (HOSVD) based low-rank approximation of the measurement tensor contributes to a more accurate estimate of the signal subspace compared to matrix-based methods [HRD08].

To accomplish the crucial first step of these tensor-based multi-dimensional subspace-based estimation schemes, higher-dimensional extensions of the matrix-based model order selection techniques, such as Akaike's Information Criterion (AIC), Minimum Description Length (MDL) [WK85], and Exponential Fitting Test (EFT) [QBLH06], have been proposed accordingly [dCRHdS11], [dCHRD07]. These tensor-based algorithms, known as  $R$ -D AIC,  $R$ -D MDL, and  $R$ -D EFT, better exploit the multi-dimensional structure inherent in the measurement data. Therefore, an improved performance is achieved by using these tensor-based model order selection techniques compared to the matrix-based schemes.

The aforementioned  $R$ -D model order estimation techniques are able to provide reliable estimates of the model order in the case where the measurements are only corrupted by Gaussian noise. However, when a fraction of the measurement data suffers from contamination lasting in a very short time duration due to, e.g., brief sensor failures, these schemes break down and thus fail to accurately estimate the model order [MCR<sup>+</sup>12]. Hence, we present robustified versions of the  $R$ -D AIC algorithm and the  $R$ -D MDL algorithm for these situations. The key idea is to replace the sample covariance matrix of each unfolding of the measurement tensor by a robust estimate of the covariance matrix obtained via a highly efficient and robust covariance estimator, e.g., the MM-estimator [ZKCM12]. To tackle the problem that the MM-estimator can only be applied to real-valued data, we propose to extract the real and imaginary parts of the unfoldings of the data tensor and stack them to form a real-valued input for the MM-estimator. Moreover, a robustified version of  $R$ -D EFT is developed based on the same concept of introducing the statistical robustness as in robust  $R$ -D AIC and robust  $R$ -D MDL.

Motivated by the application of forward-backward averaging in high-resolution parameter estimation techniques [HRD08], we propose enhanced versions of robust  $R$ -D AIC, robust  $R$ -D MDL, and robust  $R$ -D EFT. Incorporating forward-backward averaging combined with the subsequent manipulations offers an alternative way of obtaining real-valued data required by the MM-estimator. This brings in additional benefits in terms of an enhanced performance and a reduced computational complexity compared to the original robust  $R$ -D model order selection schemes. Furthermore, the performances of the proposed robust  $R$ -D model order selection techniques are demonstrated via numerical simulations.

The remainder of this chapter is organized as follows. Section 8.2 provides a brief introduction of tensor notation as well as important tensor operations that are used in Part II of this thesis. In Section 8.3, the data model of a multi-dimensional harmonic retrieval problem considered in this chapter is introduced. Then we present the concept of the robustified multi-dimensional model order selection and robust  $R$ -D AIC as well as robust  $R$ -D MDL in Section 8.4.1. In Section 8.4.2 we further explain how an enhancement is introduced to ro-

bust  $R$ -D AIC and robust  $R$ -D MDL by incorporating forward-backward averaging. Moreover, the proposed robust  $R$ -D EFT is described in detail in Section 8.5. Section 8.6 presents the simulation results, before conclusions are drawn in Section 8.7.

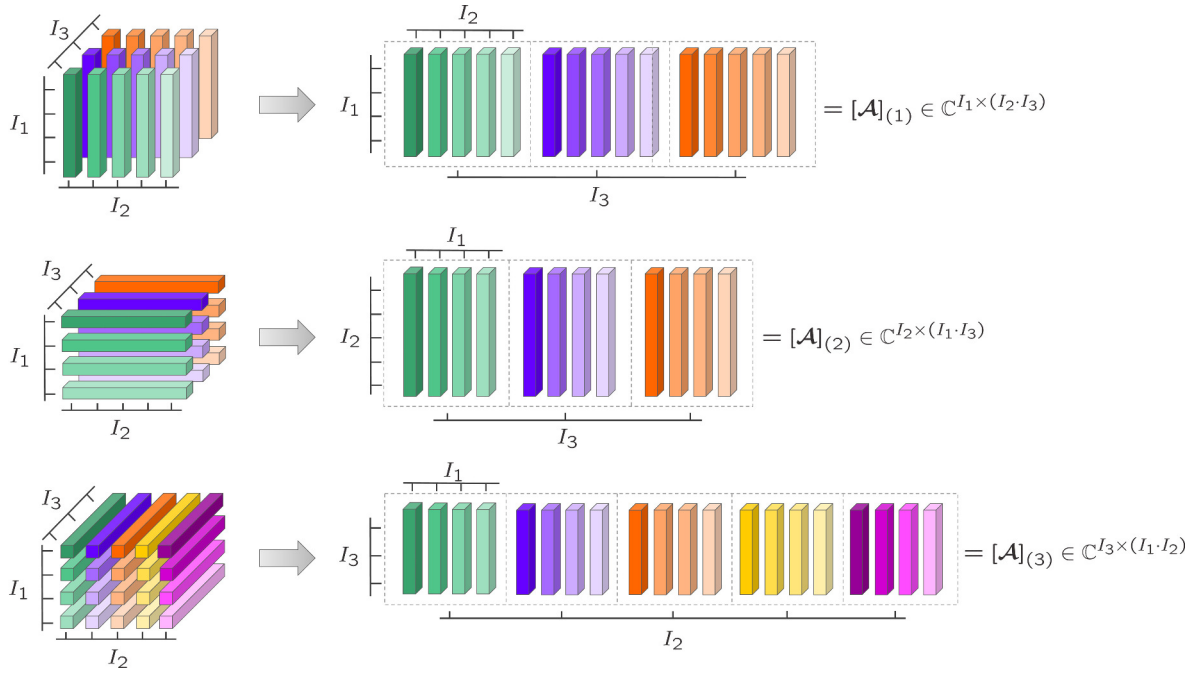
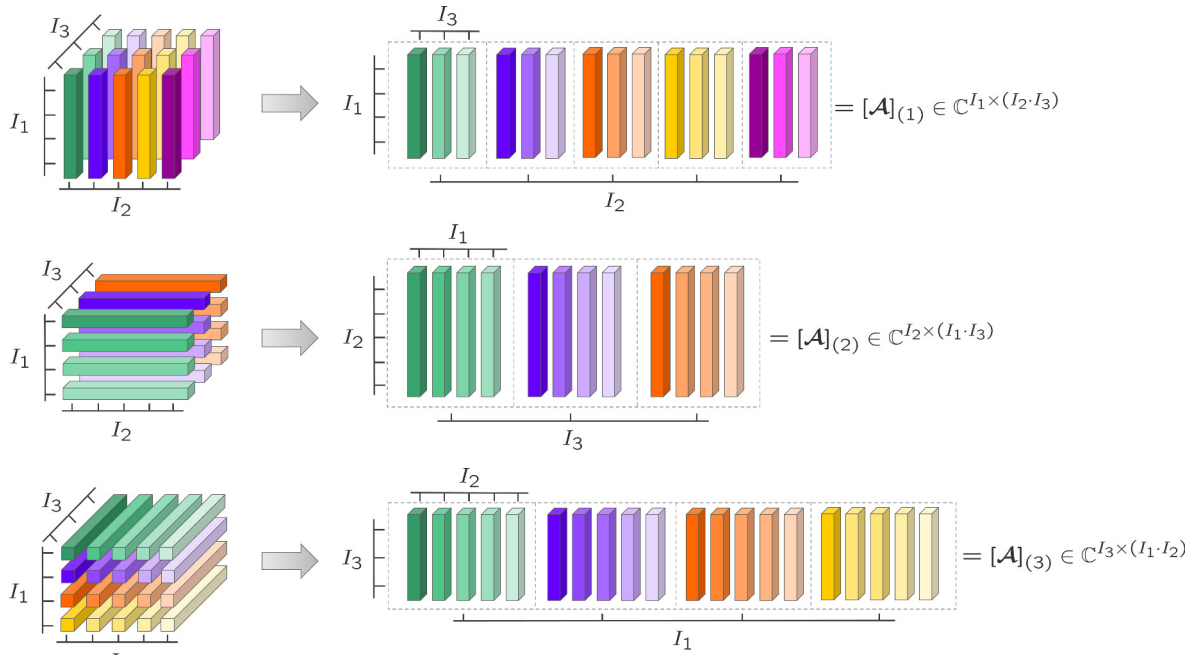
## 8.2. Tensor algebra

Throughout Part II of this thesis, the representation of multi-dimensional data in multi-way arrays is exploited. Consequently, the multi-dimensional structure inherent in the data is well preserved. In spite of the uses of the term tensor in various scientific fields, e.g., in physics, here we refer to a multi-way array of numbers as a tensor. An  $R$ -way,  $R$ -th-order, or  $R$ -D tensor is defined as a collection of numbers referenced by  $R$  indices. A first-order tensor ( $R = 1$ ) is a vector, whereas a second-order tensor ( $R = 2$ ) is a matrix. In the sequel, we focus on the case where  $R > 2$ , i.e., higher-order tensors, and briefly introduce notation as well as operations that belong to multi-linear algebra and are used in Part II of this thesis.

An  $R$ -way tensor with size  $I_r$  along mode  $r = 1, 2, \dots, R$  is represented as  $\mathcal{A} \in \mathbb{C}^{I_1 \times I_2 \times \dots \times I_R}$ . We use  $\mathcal{A}(i_1, i_2, \dots, i_R)$  to denote its  $(i_1, i_2, \dots, i_R)$ -th element. The  **$r$ -mode vectors** of  $\mathcal{A}$  are obtained by varying the  $r$ -th index from 1 to  $I_r$  and keeping all other indices fixed. In Figure 8.1 and Figure 8.2, the  $r$ -mode vectors are visualized with a three-way tensor used as an example. In addition, we call the vector space spanned by the  $r$ -mode vectors  **$r$ -mode subspace**. Aligning all  $r$ -mode vectors as the columns of a matrix yields the  **$r$ -mode unfolding** of  $\mathcal{A}$  which is denoted by  $[\mathcal{A}]_{(r)} \in \mathbb{C}^{I_r \times I_{r+1} \times \dots \times I_R \cdot I_1 \times \dots \times I_{r-1}}$ . The order of the columns is arbitrary as long as it is chosen consistently. We list four popular choices as follows:

- *Forward column ordering*: Start with varying the first index, keep increasing up to the  $(r - 1)$ -th index, then continue with the  $(r + 1)$ -th up to the  $R$ -th index. Note that this complies with the column ordering of the MATLAB's command, `reshape`. Taking a  $4 \times 5 \times 3$  tensor as an example, we illustrate its unfolding in the forward column ordering in Figure 8.1.
- *Reverse column ordering*: Similar to the forward column ordering but in a reverse order, i.e., start with the last index and keep decreasing to the first index, leaving out the  $r$ -th index.
- *Forward cyclical ordering*: Start with the  $(r + 1)$ -th index, keep increasing up to the  $R$ -th index followed by the first, then the second, and proceed forward up to the  $(r - 1)$ -th index.



Figure 8.1.: Illustration of the unfoldings of a  $4 \times 5 \times 3$  tensor in the forward column orderingFigure 8.2.: Illustration of the unfoldings of a  $4 \times 5 \times 3$  tensor in the reverse cyclical ordering

- *Reverse cyclical ordering*: Reverse the forward cyclical ordering to start with the  $(r-1)$ -th index instead, keep decreasing to the first index, continue with the  $R$ -th index, and proceed backwards until reaching the  $(r+1)$ -th index. This rule for the ordering of the  $r$ -mode vectors was proposed in [dLdMV00] and proves to be the most commonly used convention in the field of signal processing. In this thesis, we use the reverse cyclical ordering and visualize the corresponding unfoldings of a three-way tensor in Figure 8.2.

The  $r$ -mode product between a tensor  $\mathcal{A}$  and a matrix  $U$  is written as

$$\mathcal{A} \times_r U. \quad (8.1)$$

It is computed by multiplying all  $r$ -mode vectors of  $\mathcal{A}$  with  $U$ . In other words,

$$[\mathcal{A} \times_r U]_{(r)} = U \cdot [\mathcal{A}]_{(r)}. \quad (8.2)$$

Taking a three-way tensor  $\mathcal{A} \in \mathbb{C}^{I_1 \times I_2 \times I_3}$  as an example, we illustrate the  $r$ -mode products between  $\mathcal{A}$  and  $U_r \in \mathbb{C}^{P_r \times I_r}$  in Figure 8.3.

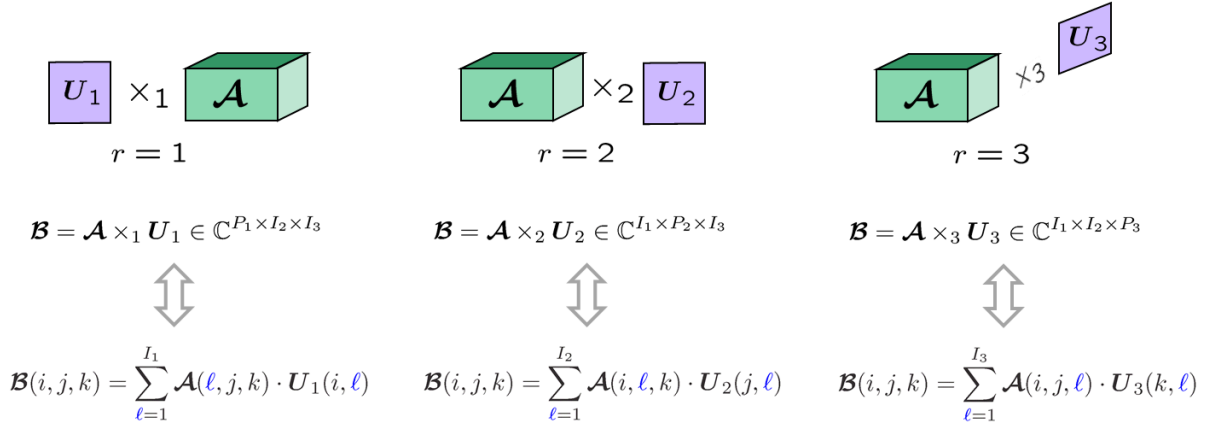


Figure 8.3.:  $r$ -mode products between a three-way tensor  $\mathcal{A}$  and a matrix

Some important properties of  $r$ -mode products and  $r$ -mode unfoldings are provided in the following. Given  $\mathcal{Y} \in \mathbb{C}^{I_1 \times \dots \times I_R}$  and  $U_r \in \mathbb{C}^{P_r \times I_r}$  ( $r = 1, \dots, R$ ), the  $r$ -mode unfolding of

$$\mathcal{X} = \mathcal{Y} \times_1 U_1 \times_2 U_2 \times_3 \dots \times_R U_R \in \mathbb{C}^{P_1 \times \dots \times P_R} \quad (8.3)$$

takes the form [dLdMV00]:

$$[\mathcal{X}]_{(r)} = U_r \cdot [\mathcal{Y}]_{(r)} \cdot (U_{r+1} \otimes U_{r+2} \otimes \dots \otimes U_R \otimes U_1 \otimes \dots \otimes U_{r-1})^T. \quad (8.4)$$

This property directly leads to [dLdMV00]

$$\mathcal{A} \times_r \mathbf{U}_r \times_p \mathbf{U}_p = \mathcal{A} \times_p \mathbf{U}_p \times_r \mathbf{U}_r, \text{ for } r \neq p \quad (8.5)$$

$$\mathcal{A} \times_r \mathbf{U}_r \times_r \mathbf{V}_r = \mathcal{A} \times_r (\mathbf{V}_r \cdot \mathbf{U}_r). \quad (8.6)$$

where  $\mathcal{A} \in \mathbb{C}^{I_1 \times \dots \times I_R}$ ,  $\mathbf{U}_r \in \mathbb{C}^{P_r \times I_r}$ , and  $\mathbf{V}_r \in \mathbb{C}^{N_r \times P_r}$ .

The  $r$ -**rank** of a tensor  $\mathcal{A}$  is the rank of the  $r$ -mode unfolding matrix  $[\mathcal{A}]_{(r)}$ . It is worth noting that, in contrast to the case of matrices (where the column rank is equal to the row rank), the  $r$ -ranks of a tensor can be different.

The tensor  $\mathcal{I}_{R,d}$  is an  $R$ -dimensional **identity tensor** of size  $d \times d \times \dots \times d$ , the elements of which are equal to one if all  $R$  indices are equal and zero otherwise [KB09]. A three-way identity tensor  $\mathcal{I}_{4,3}$  is illustrated in Figure 8.4.

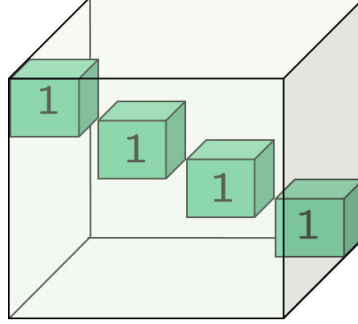


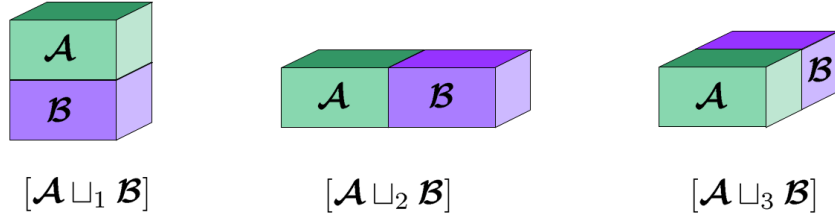
Figure 8.4.: Illustration of a three-way identity tensor  $\mathcal{I}_{4,3}$

In addition,  $[\mathcal{A} \sqcup_r \mathcal{B}]$  symbolizes the **concatenation** of two tensors  $\mathcal{A} \in \mathbb{C}^{I_1 \times \dots \times I_r \times \dots \times I_R}$  and  $\mathcal{B} \in \mathbb{C}^{I_1 \times \dots \times I_{r-1} \times P_r \times I_{r+1} \times \dots \times I_R}$  along the  $r$ -th mode [HRD08]. According to this definition, the  $r$ -mode unfolding of the concatenation of  $\mathcal{A}$  and  $\mathcal{B}$

$$[\mathcal{A} \sqcup_r \mathcal{B}]_{(r)} = \begin{bmatrix} [\mathcal{A}]_{(r)} \\ [\mathcal{B}]_{(r)} \end{bmatrix} \in \mathbb{C}^{(I_r + P_r) \times (I_1 \dots I_{r-1} \cdot I_{r+1} \dots I_R)}, \quad (8.7)$$

i.e., stacking the  $r$ -mode vectors of  $\mathcal{A}$  on top of those of  $\mathcal{B}$  gives the  $r$ -mode vectors of the resulting tensor. In Figure 8.5, we visualize the concatenation of two three-way tensors  $\mathcal{A}, \mathcal{B} \in \mathbb{C}^{I_1 \times I_2 \times I_3}$  along the  $r$ -modes.

In this section, we focus on the tensor notation and tensor operations that are used in this thesis. For a comprehensive survey on multi-linear algebra, tensor decompositions and their


 Figure 8.5.: Illustration of the concatenation of two three-way tensors along the  $r$ -modes

practical applications, the reader is refer to [KB09].

### 8.3. Data model

Let us consider a multi-dimensional harmonic retrieval problem where the data is sampled on an  $R$ -dimensional lattice. At a certain time instant, the measurement sample is modeled as a superposition of  $d$  undamped exponentials sampled on an  $R$ -dimensional grid of size  $M_1 \times M_2 \times \dots \times M_R$  [HN98]. In the context of array signal processing, the measurements under additive noise collected in  $N$  subsequent snapshots can be written in matrix form by stacking all  $R$  dimensions

$$\mathbf{X} = \mathbf{A} \cdot \mathbf{S} + \mathbf{W} \in \mathbb{C}^{M \times N}. \quad (8.8)$$

with  $M = \prod_{r=1}^R M_r$ . Here  $\mathbf{A} \in \mathbb{C}^{M \times d}$  is defined as the array steering matrix [HN98]

$$\mathbf{A} = \mathbf{A}^{(1)} \diamond \mathbf{A}^{(2)} \diamond \dots \diamond \mathbf{A}^{(R)} \quad (8.9)$$

$$\mathbf{A}^{(r)} = \begin{bmatrix} \mathbf{a}^{(r)}(\mu_1^{(r)}), & \mathbf{a}^{(r)}(\mu_2^{(r)}), & \dots & \mathbf{a}^{(r)}(\mu_d^{(r)}) \end{bmatrix},$$

where  $\mathbf{a}^{(r)}(\mu_i^{(r)}) \in \mathbb{C}^{M_r \times 1}$  and  $\mu_i^{(r)}$  represent the array steering vector and the spatial frequency for the  $i$ -th source ( $i = 1, 2, \dots, d$ ) in the  $r$ -th dimension, respectively. Here  $\diamond$  is used to denote the Khatri-Rao product (columnwise Kronecker product). The measurements are stacked in  $\mathbf{X} \in \mathbb{C}^{M \times N}$  in the same manner as in  $\mathbf{A}$ , while  $\mathbf{S} \in \mathbb{C}^{d \times N}$  and  $\mathbf{W} \in \mathbb{C}^{M \times N}$  contain the source symbols and the additive noise samples, respectively.

To exploit the multi-dimensional structure inherent in the measurement data, the measurement matrix  $\mathbf{X}$  is replaced by a measurement tensor  $\mathcal{X} \in \mathbb{C}^{M_1 \times M_2 \times \dots \times M_R \times N}$  such that the stacking operation used to construct the classical matrix-based data model is avoided [HRD08]. The measurement tensor  $\mathcal{X}$  is given by

$$\mathcal{X} = \mathcal{A} \times_{R+1} \mathbf{S}^T + \mathcal{W}, \quad (8.10)$$

where  $\mathbf{W}$  contains zero mean i.i.d. circularly symmetric Gaussian random variables with variance  $\sigma_n^2$ . Moreover,  $\mathcal{A}$  is the array steering tensor constructed as

$$\mathcal{A} = \mathcal{I}_{R+1,d} \times_1 \mathbf{A}^{(1)} \times_2 \mathbf{A}^{(2)} \dots \times_R \mathbf{A}^{(R)}, \quad (8.11)$$

where  $\mathcal{I}_{R+1,d}$  of size  $d \times d \times \dots \times d$  is a  $(R+1)$ -dimensional identity tensor. It is worth mentioning that the matrix-based data model and the tensor-based one are connected via

$$\mathbf{X} = [\mathcal{X}]_{(R+1)}^T, \quad (8.12)$$

and

$$\mathbf{A} = [\mathcal{A}]_{(R+1)}^T. \quad (8.13)$$

One typical example of the multi-dimensional harmonic retrieval problem is the parameter estimation step that follows channel sounding [HTR04]. In this case, the channel sampled in dimensions corresponding to time, frequency, polarization and space contributes to the multi-dimensional measurements via which the parameters are estimated. To show another example in the context of array signal processing, we consider  $d$  planar wavefronts impinging on a Uniform Rectangular Array (URA) of size  $M_1 \times M_2$ . The measurements collected in  $N$  subsequent snapshots can be arranged into a three-dimensional tensor  $\mathcal{X} \in \mathbb{C}^{M_1 \times M_2 \times N}$  as illustrated in Figure 8.6. Thereby, estimating the number of impinging wavefronts  $d$  is the task of model order selection approaches.

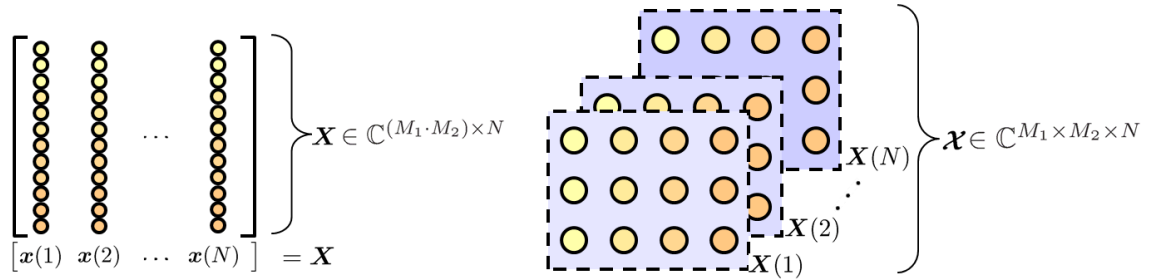


Figure 8.6.: Construction of the measurement tensor from the measurement matrix in the 2-D case

### 8.4. Robust multi-dimensional model order estimation

The original  $R$ -D AIC and  $R$ -D MDL algorithms [dCRHdS11] employ the sample covariance matrices of all  $r$ -mode unfoldings of the data tensor  $\mathcal{X} \in \mathbb{C}^{M_1 \times M_2 \times \dots \times M_R \times N}$

$$\hat{\mathbf{R}}_{xx}^{(r)} = \frac{M_r}{M \cdot N} [\mathcal{X}]_{(r)} \cdot [\mathcal{X}]_{(r)}^H \in \mathbb{C}^{M_r \times M_r}, \quad (8.14)$$

$$r = 1, 2, \dots, R + 1,$$

where we define the number of snapshots  $N$  alternatively as  $M_{R+1}$ . Then the eigenvalues of these sample covariance matrices are obtained. It is known that the influence function of a covariance estimator describes the bias impact of infinitesimal contamination at an arbitrary point on the estimator, standardized by the fraction of contamination [ZKCM12]. Boundedness and continuity are two desirable properties of the influence function of an estimator. The fact that the influence function is bounded indicates that a small fraction of contamination or highly deviating samples, known as outliers, only has a limited impact on the estimates. On the other hand, if the influence function exhibits a good continuity, it suggests that small changes in the data result in small changes in the estimates. An estimator whose influence function is both bounded and smooth is regarded as qualitatively robust against infinitesimal contamination. Figure 8.7 shows two examples of influence functions [ZKCM12]. We can see

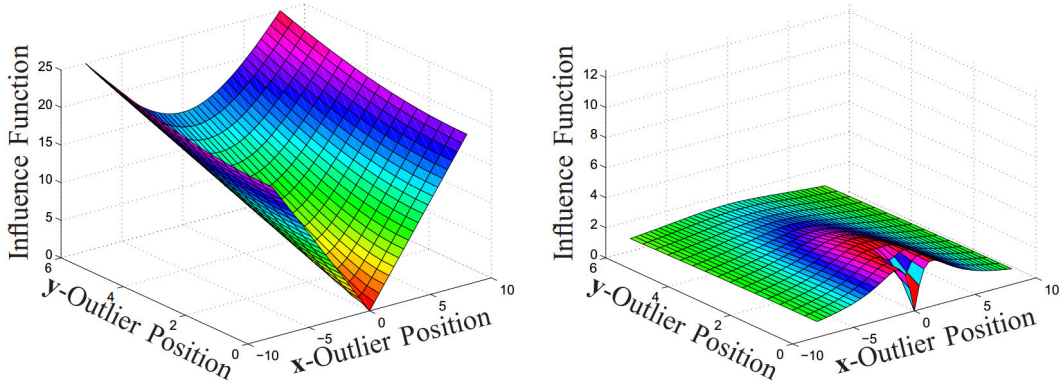


Figure 8.7.: Influence functions of two covariance estimators, the sample covariance estimator (left) and the M-estimator (right) at the bivariate complex normal distribution [ZKCM12]

that the influence function of the M-estimator is bounded and smooth. By comparison, for the sample covariance matrix, the influence function is not bounded. As a result, the impact of a contaminated data point, e.g., caused by a brief sensor failure, is unbounded [OK03]. Con-

sequently the classical model order estimation methods where sample covariance matrices are used are not robust against brief sensor failures, as also shown in [MCR<sup>+</sup>12] and in Section 8.6 via numerical results. Another important concept of robustness is the breakdown point which characterizes the quantitative robustness of an estimator [ZKCM12]. It identifies the maximal fraction of outliers that an estimator is able to handle without breaking down. The values of the breakdown point range from 0 to 50 %. A high breakdown point value indicates strong quantitative robustness and vice versa. More specifically, in the context of covariance estimation, the breakdown point is the smallest proportion of outliers (highly deviating observations) that renders the largest eigenvalue of the covariance matrix estimate over all bounds (towards infinity) or its smallest eigenvalue close to zero, leading to the fact that the covariance matrix is ill-conditioned. The breakdown point of the sample covariance estimator is zero, implying that even if only a very small portion of the measurement data is contaminated, it breaks down and fails to provide reliable covariance estimates [ZKCM12]. Hence, to obtain robustified versions of the classical model order estimation approaches, statistical robustness is introduced by replacing the sample covariance matrix of the  $r$ -mode unfolding of the data tensor (8.14) by a statistically more robust estimate of the covariance matrix.

The multivariate MM-estimator [TT00, SBAW06] is able to provide such estimates of the covariance matrices [MCR<sup>+</sup>12]. The principle of the estimator is based on a two-step procedure [ZKCM12]:

1. An initial estimate of the covariance is obtained by using an estimator that is endowed with a very high breakdown point, e.g., an S-estimator. S-estimators can be regarded as a robustification of LS-estimators, where the standard deviation is replaced by a robust scale estimate.
2. The final estimate of the covariance matrix is obtained by using an estimator efficient at the assumed model where the measurements are only corrupted by noise obeying a standard distribution [Ty183]. Note that the S-estimator, on the other hand, may suffer from a low efficiency [SBAW06]. In this step, a correctly tuned M-estimator can be employed. M-estimators are a generalization of Maximum Likelihood estimators where the log-likelihood function is replaced by a robustifying function such that the effect of the strongly deviating data points is bounded while the uncontaminated measurements remain unchanged.

In Table 8.1, we present the values of the breakdown points and the properties of the influence functions of the sample covariance matrix, the S-estimator, the M-estimator, the MM-estimator. The influence function of the MM-estimator is bounded and smooth, which means

Table 8.1.: Breakdown points and properties of the influence functions of the sample covariance matrix, the S-estimator, the M-estimator, the MM-estimator

Methods	Breakdown point	Influence function
sample covariance matrix	0	unbounded
S-estimator	0.5 [SBAW06]	bounded and continuous
M-estimator	may be low (decreasing with dimensions) [Mar76]	bounded and continuous
MM-estimator	0.5 [SBAW06]	bounded and continuous

that the bias impact of a large contamination is restricted and small changes in the data lead to small changes in the estimate. Combining the advantages of both the S-estimator and the M-estimator in the two steps described above, the MM-estimator experiences both a high statistical robustness and a high efficiency [SBAW06]. For a comprehensive survey on robust estimation, the reader is referred to [ZKCM12].

In order to render the MM-estimator originally designed for real-valued data applicable to complex-valued measurements, we propose in [MCR<sup>+</sup>12] to stack the real and imaginary parts of the  $r$ -mode unfoldings of the measurement tensor  $\mathcal{X}$ , i.e.,

$$[\tilde{\mathcal{X}}]_{(r)} = \begin{bmatrix} \text{Re} \left\{ [\mathcal{X}]_{(r)} \right\} \\ \text{Im} \left\{ [\mathcal{X}]_{(r)} \right\} \end{bmatrix} \in \mathbb{R}^{2M_r \times \frac{M \cdot N}{M_r}}. \quad (8.15)$$

The robust estimate of the covariance matrix of  $[\tilde{\mathcal{X}}]_{(r)}$  obtained by employing the MM-estimator on (8.15) can be further expressed as

$$\hat{\mathbf{R}}_{\tilde{x}\tilde{x}, \text{robust}}^{(r)} = \begin{bmatrix} \hat{\mathbf{R}}_{\tilde{x}\tilde{x}, A}^{(r)} & \hat{\mathbf{R}}_{\tilde{x}\tilde{x}, B}^{(r)} \\ \hat{\mathbf{R}}_{\tilde{x}\tilde{x}, C}^{(r)} & \hat{\mathbf{R}}_{\tilde{x}\tilde{x}, D}^{(r)} \end{bmatrix} \in \mathbb{R}^{2M_r \times 2M_r}, \quad (8.16)$$

where the four matrices  $\hat{\mathbf{R}}_{\tilde{x}\tilde{x}, A}^{(r)}$ ,  $\hat{\mathbf{R}}_{\tilde{x}\tilde{x}, B}^{(r)}$ ,  $\hat{\mathbf{R}}_{\tilde{x}\tilde{x}, C}^{(r)}$ , and  $\hat{\mathbf{R}}_{\tilde{x}\tilde{x}, D}^{(r)}$  all have the size of  $M_r \times M_r$ . Therefore, the robust estimate of the covariance matrix of the  $r$ -mode unfolding of the data tensor  $\mathcal{X}$  can be identified as

$$\hat{\mathbf{R}}_{xx, \text{robust}}^{(r)} = \hat{\mathbf{R}}_{\tilde{x}\tilde{x}, A}^{(r)} + \hat{\mathbf{R}}_{\tilde{x}\tilde{x}, D}^{(r)} + j(\hat{\mathbf{R}}_{\tilde{x}\tilde{x}, C}^{(r)} - \hat{\mathbf{R}}_{\tilde{x}\tilde{x}, B}^{(r)}) \in \mathbb{C}^{M_r \times M_r}. \quad (8.17)$$



### 8.4.1. Robustified $R$ -D Akaike's Information Criterion and $R$ -D Minimum Description Length

By incorporating the robust covariance matrix estimates of all  $r$ -mode unfoldings of the data tensor obtained above, the robust  $R$ -D AIC algorithm selects the model order as

$$\hat{d} = \arg \min_k \phi_{\text{AIC,rob}}(k), \quad k \in \{0, 1, \dots, K\} \quad (8.18)$$

$$\phi_{\text{AIC,rob}}(k) = -N(\alpha^{(\text{G})} - k) \ln \left( \frac{g_{\text{rob}}^{(\text{G})}(p)}{a_{\text{rob}}^{(\text{G})}(p)} \right) + k(2\alpha^{(\text{G})} - k),$$

where  $\alpha^{(\text{G})}$  is the total number of sequentially defined global eigenvalues [dCHRD07], [dCRHdS11],  $K = \alpha^{(\text{G})} - 1$ , and  $g_{\text{rob}}^{(\text{G})}(p)$  and  $a_{\text{rob}}^{(\text{G})}(p)$  are the geometric and arithmetic means of the smallest  $p = \alpha^{(\text{G})} - k$  global eigenvalues calculated using the robust estimates of the covariance matrices of the  $r$ -mode unfoldings, respectively. Here the model order is bounded by  $K$  which is smaller than  $\max(M_1, M_2, \dots, M_{R+1})$ . It is worth noting that the tensor rank can exceed all dimensions. Similarly, the robust  $R$ -D MDL estimates the model order as

$$\hat{d} = \arg \min_k \phi_{\text{MDL,rob}}(k), \quad k \in \{0, 1, \dots, K\} \quad (8.19)$$

$$\phi_{\text{MDL,rob}}(k) = -N(\alpha^{(\text{G})} - k) \ln \left( \frac{g_{\text{rob}}^{(\text{G})}(p)}{a_{\text{rob}}^{(\text{G})}(p)} \right) + \frac{1}{2}k(2\alpha^{(\text{G})} - k) \ln(N).$$

Assume that  $\hat{\mathbf{R}}_{xx,\text{robust}}^{(r)}$  has  $M_r$  eigenvalues, and they are ordered according to

$$\lambda_1^{(r)} > \lambda_2^{(r)} > \dots > \lambda_{M_r}^{(r)}. \quad (8.20)$$

The calculation of the global eigenvalues [dCHRD07], [dCRHdS11] is described as follows. For the case where  $M_1 = M_2 = \dots = M_{R+1}$ , the global eigenvalues are obtained as

$$\lambda_i^{(\text{G})} = \lambda_i^{(1)} \cdot \lambda_i^{(2)} \cdot \dots \cdot \lambda_i^{(R+1)}, \quad i = 1, 2, \dots, M_{R+1}. \quad (8.21)$$

In this case,  $\alpha^{(\text{G})} = M_{R+1}$ , the geometric and arithmetic means of the smallest  $p = \alpha^{(\text{G})} - k$  global eigenvalues are computed as

$$g_{\text{rob}}^{(\text{G})}(p) = \left( \prod_{\ell=k+1}^{M_{R+1}} \lambda_{\ell}^{(\text{G})} \right)^{1/p} \quad (8.22)$$

and

$$a_{\text{rob}}^{(\text{G})}(p) = \frac{1}{p} \sum_{\ell=k+1}^{M_{R+1}} \lambda_{\ell}^{(\text{G})}, \quad (8.23)$$

respectively. Without loss of generality, we assume  $M_1 \geq M_2 \geq \dots \geq M_{R+1}$ . In this case, we start by estimating  $d$  via AIC or MDL considering  $\lambda_i^{(1)}$  only, where  $i = 1, 2, \dots, M_1$ . If  $\hat{d} < M_2$ , we further run AIC or MDL on  $\lambda_i^{(1)} \cdot \lambda_i^{(2)}$ , where  $i = 1, 2, \dots, M_2$ , by taking advantage of the two-mode unfolding. If the new estimate  $\hat{d} < M_3$ , we continue by considering the first three unfoldings, i.e.,  $\lambda_i^{(1)} \cdot \lambda_i^{(2)} \cdot \lambda_i^{(3)}$ ,  $i = 1, 2, \dots, M_3$ , is used to estimate  $d$ . The model order estimation procedure continues until  $\hat{d} > M_r$  or  $r = R + 1$ . Figure 8.8 illustrates how the global eigenvalues are computed in a 3-D example.

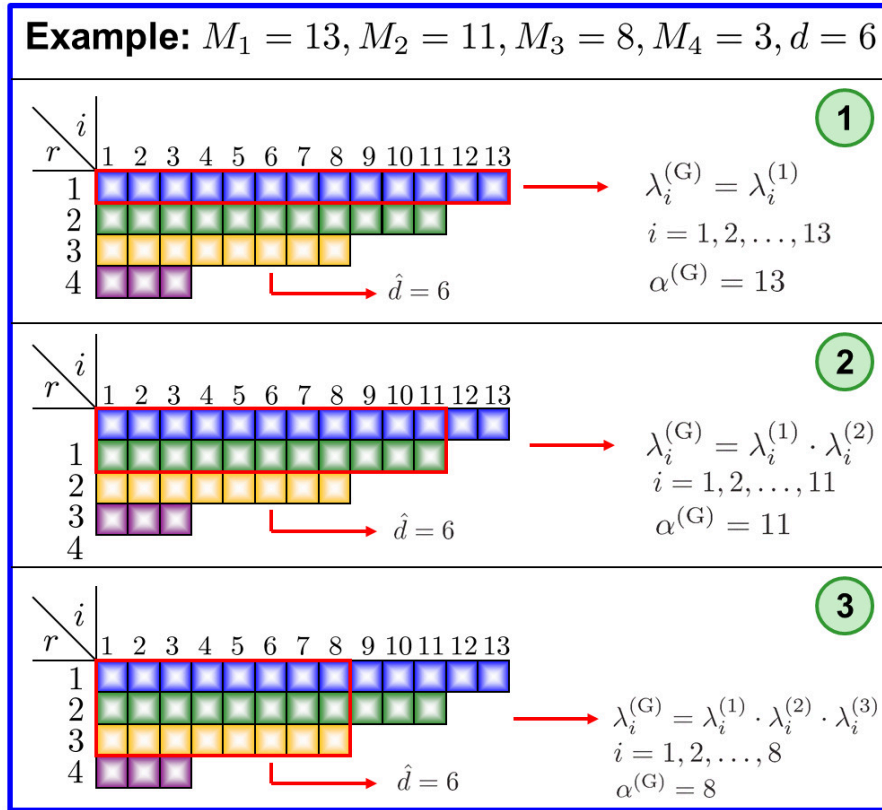


Figure 8.8.: Illustration of the calculation of the global eigenvalues

Note that robustified versions of the matrix-based model order selection schemes such as AIC or MDL [dCHRD07] can also be obtained by substituting the sample covariance matrix of the measurement matrix  $\mathbf{X}$  by a robust estimate of the covariance matrix.

#### 8.4.2. Enhancement by incorporating forward-backward averaging

It is known that when forward-backward averaging is employed as a preprocessing step in a matrix-based or tensor-based multi-dimensional parameter estimation scheme, complex-valued measurements can be further conveniently and efficiently transformed to real-valued data. Consequently real-valued subspace estimation can be performed, leading to an increased accuracy and a lower computational complexity [HN98], [HRD08]. This motivates the enhanced robust  $R$ -D model order selection schemes described in detail in the sequel.

Instead of stacking the real and imaginary parts of the  $r$ -mode unfoldings of the measurement tensor  $\mathcal{X}$ , we alternatively compute a real-valued measurement tensor, and its real-valued unfoldings naturally meet the requirement enforced by the MM-estimator. First, we calculate a forward-backward averaged version of the measurement tensor  $\mathcal{Z} \in \mathbb{C}^{M_1 \times M_2 \times \dots \times M_R \times 2N}$  [HRD08]

$$\mathcal{Z} = [\mathcal{X} \sqcup_{R+1} \mathcal{X}^* \times_1 \mathbf{\Pi}_{M_1} \times_2 \mathbf{\Pi}_{M_2} \times_3 \dots \times_{R+1} \mathbf{\Pi}_N] \quad (8.24)$$

where is  $\mathbf{\Pi}_p$  a  $p \times p$  exchange matrix which has ones on its anti-diagonal and zeros elsewhere. We further map this centro-Hermitian tensor to a real-valued tensor  $\mathcal{T}(\mathcal{X}) \in \mathbb{R}^{M_1 \times M_2 \times \dots \times M_R \times 2N}$  by using the transformation [HRD08]

$$\mathcal{T}(\mathcal{X}) = \varphi(\mathcal{Z}) = \mathcal{Z} \times_1 \mathbf{Q}_{M_1}^H \times_2 \mathbf{Q}_{M_2}^H \times_3 \dots \times_{R+1} \mathbf{Q}_{2N}^H, \quad (8.25)$$

where  $\mathbf{Q}_p$  is a left- $\mathbf{\Pi}$  real and unitary matrix. Then we further take the  $r$ -mode unfoldings of the real-valued tensor  $\mathcal{T}(\mathcal{X})$  and obtain the real-valued robust estimates of the their covariance matrices via the MM-estimator. Since the available number of snapshots is consequently doubled virtually, we replace  $N$  by  $2N$  in the cost functions  $\phi_{\text{AIC,rob}}$  in (8.18) and  $\phi_{\text{MDL,rob}}$  in (8.19) for robust  $R$ -D AIC and robust  $R$ -D MDL, respectively. It is worth mentioning that only real-valued computations are involved in the subsequent procedures of the model order estimation. In contrast, the robust estimates of the covariance matrices obtained by using (8.17) are complex-valued. Hence, the enhanced versions of the robust model order selection schemes have a lower computational complexity compared to the original ones. On the other hand, the additional symmetry relations inherent in the complex-valued measurements obtained from a sampling operation on centro-symmetric grids is exploited by incorporating forward-backward averaging. Thus, a performance improvement of the robust  $R$ -D model

order selection techniques can be expected.

## 8.5. Robust $R$ -D Exponential Fitting Test

Assume again that the  $M_r$  eigenvalues of the robust estimate of the covariance matrix  $\hat{\mathbf{R}}_{xx,\text{robust}}^{(r)}$  for the  $r$ -th mode are ordered as in (8.20). Similar as the matrix-based EFT [QBLH06], Modified EFT [dCHRD07], and the original  $R$ -D EFT algorithm [dCRHdS11], the robustified version of the  $R$ -D EFT technique is based on the observation that in the noise-only case the ordered eigenvalues display an exponential profile

$$\mathbb{E}\{\lambda_i^{(r)}\} = \mathbb{E}\{\lambda_1^{(r)}\} \cdot q(\alpha_r, \beta_r)^{i-1}, \quad (8.26)$$

where  $\alpha_r = \min\{M_r, \frac{M}{M_r}\}$ ,  $\beta_r = \max\{M_r, \frac{M}{M_r}\}$ , and

$$q(\alpha, \beta) = \exp \left\{ -\sqrt{\frac{30}{\alpha^2 + 2}} - \sqrt{\frac{900}{(\alpha^2 + 2)^2} - \frac{720\alpha}{\beta(\alpha^4 + \alpha^2 - 2)}} \right\}. \quad (8.27)$$

It is assumed in this technique that there exists at least one noise eigenvalue [dCRHdS11], i.e.,  $P \geq 1$ , where  $P$  denotes a candidate number of noise eigenvalues. In the light of the fact that the  $P$  noise eigenvalues exhibit the aforementioned decaying exponential profile, the  $(M_r - P)$ -th eigenvalue of the robust covariance matrix of the  $r$ -th mode can be predicted as [dCRHdS11]

$$\begin{aligned} \hat{\lambda}_{M_r-P}^{(r)} &= (P+1) \cdot \frac{1 - q\left(P+1, \frac{M}{M_r}\right)}{1 - q\left(P+1, \frac{M}{M_r}\right)^{P+1}} \cdot \hat{\sigma}_P^{(r)^2} \\ \hat{\sigma}_P^{(r)^2} &= \frac{1}{P} \sum_{i=0}^{P-1} \lambda_{M_r-i}^{(r)}. \end{aligned} \quad (8.28)$$

For simplicity, we first consider the setup where  $M_1 = M_2 = \dots = M_{R+1}$ . The predicted global eigenvalues are then calculated as

$$\hat{\lambda}_{M_r-P}^{(G)} = \lambda_{M_r-P}^{(1)} \cdot \lambda_{M_r-P}^{(2)} \cdot \dots \cdot \lambda_{M_r-P}^{(R+1)}, \quad 1 \leq P \leq M_r - 1. \quad (8.29)$$

To this end, we can see that the task of estimating the model order boils down to comparing the measured global eigenvalues with the predicted ones and finding the highest  $P$  in the case of which the measured global eigenvalue matches the theoretically predicted one based on the decaying exponential profile. In Figure 8.9, an example is shown, where  $M_1 = M_2 =$

$M_3 = N = 5$  and the model order is one, i.e.,  $d = 1$ . A brief sensor failure is present, and the contamination caused to the measurement data is modeled as in [MCR<sup>+</sup>12] and also explained later in Section 8.6. In the upper part of Figure 8.9, both the global eigenvalues calculated

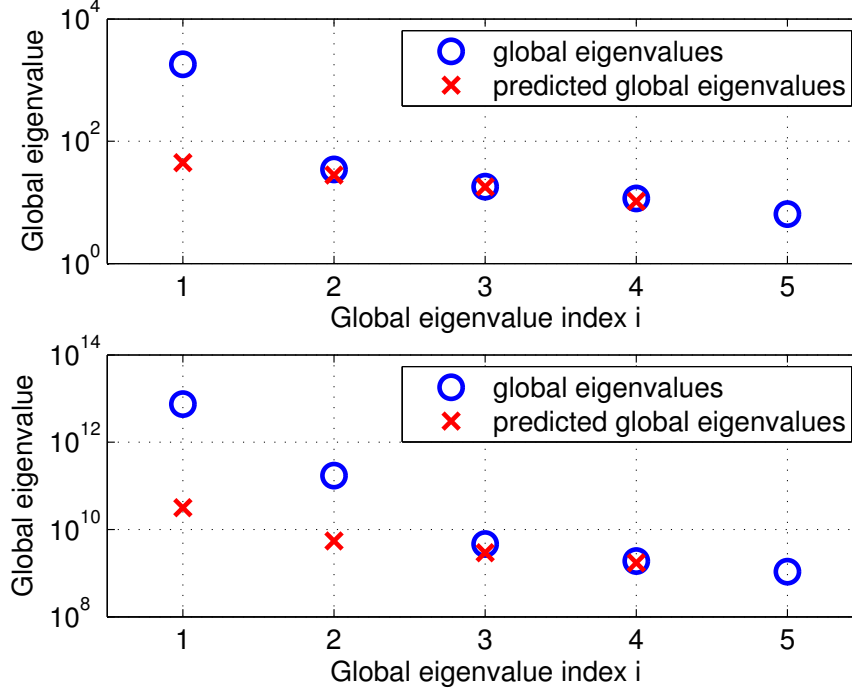


Figure 8.9.: Top: global eigenvalues and predicted global eigenvalues obtained in robust  $R$ -D EFT by applying the exponential approximation for  $M_1 = 5$ ,  $M_2 = 5$ ,  $M_3 = 5$ ,  $N = 5$ ,  $d = 1$ , and  $\text{SNR} = 0$  dB in the presence of a brief sensor failure; bottom: global eigenvalues and predicted global eigenvalues obtained in  $R$ -D EFT for the same scenario

by using the robust covariance matrices of all  $r$ -mode unfoldings of the measurement tensor and the predicted global eigenvalues are plotted. It can be observed that the model order is one as there is a gap only between the first global eigenvalue and its corresponding predicted one while for the rest the measured global eigenvalues and the predicted ones are well fitted to each other. For the purpose of comparison, the lower part of Figure 8.9 displays the global eigenvalues obtained by using the sample covariance matrices of all  $r$ -mode unfoldings of the data tensor according to (8.14) and the corresponding predicted ones as employed in the original non-robust  $R$ -D EFT algorithm. We observe gaps between the first two measured global eigenvalues and their corresponding predicted ones, leading to an incorrect estimate of the model order.

Similarly as in the original  $R$ -D EFT technique [dCRHdS11], the following two hypotheses are defined where the relative difference between each measured global eigenvalue and its corresponding predicted one is compared with a threshold

$$H_{P+1} : \lambda_{M_r-P}^{(G)} \text{ is a noise eigenvalue,}$$

$$\frac{\lambda_{M_r-P}^{(G)} - \hat{\lambda}_{M_r-P}^{(G)}}{\hat{\lambda}_{M_r-P}^{(G)}} \leq \eta_P^{(G)} \quad (8.30)$$

$$\hat{H}_{P+1} : \lambda_{M_r-P}^{(G)} \text{ is a signal eigenvalue,}$$

$$\frac{\lambda_{M_r-P}^{(G)} - \hat{\lambda}_{M_r-P}^{(G)}}{\hat{\lambda}_{M_r-P}^{(G)}} > \eta_P^{(G)}. \quad (8.31)$$

With the largest  $P$  denoted by  $\hat{P}$  in the case of which the test  $H_{P+1}$  fails, the model order estimate is determined as  $\hat{d} = M_r - \hat{P}$ . Note that the threshold  $\eta_P$  is obtained via Monte Carlo simulations in the noise-only case with respect to a pre-defined probability of false alarm and the sizes of a certain multi-dimensional measurement array [dCRHdS11].

Considering a more general case where the sizes of the measurement tensor along all of its  $(R+1)$  modes are not the same, the model order estimation in the proposed robust  $R$ -D EFT technique can be performed similarly as in robust  $R$ -D AIC and robust  $R$ -D MDL relying on the sequential definition of global eigenvalues [dCRHdS11]. Assume  $M_1 \geq M_2 \geq \dots \geq M_{R+1}$ . First, the Modified EFT [dCHRD07] is performed by using the eigenvalues of the robust covariance matrix of the one-mode unfolding of the data tensor  $\lambda_i^{(1)}$ , where  $i = 1, 2, \dots, M_1$ , and the obtained model order estimate is denoted by  $\hat{d}^{(1)}$ . For  $\hat{d}^{(r-1)} \leq M_r$ , where  $2 \leq r \leq R+1$  and  $\hat{d}^{(r-1)}$  represents the estimated model order by using Modified EFT on the previous computed set of global eigenvalues, the following set of eigenvalues are used such that the  $r$ -mode is exploited as well

$$\lambda_i^{(G)} = \lambda_i^{(1)} \cdot \lambda_i^{(2)} \dots \lambda_i^{(r)}, \quad i = 1, 2, \dots, M_r. \quad (8.32)$$

Such a model order estimation procedure continues until  $\hat{d}^{(r-1)} > M_r$  or  $r = R+1$ .

The assumption in the  $R$ -D EFT scheme that there exists at least one noise eigenvalue [dCRHdS11] is also true for the robust  $R$ -D EFT scheme, i.e.,  $P \geq 1$ . Therefore, the model order estimate is bounded by  $(\max(M_1, M_2, \dots, M_{R+1}) - 1)$ . Note that, nevertheless, the tensor rank can exceed all dimensions, i.e., it can take a value larger than  $\max(M_1, M_2, \dots, M_{R+1})$ .

## 8.6. Simulation results

In the first experiment, we consider a 3-D scenario with the following parameters:  $M_1 = 5$ ,  $M_2 = 7$ ,  $M_3 = 9$ ,  $N = 10$ , and  $d = 3$ . The spatial frequencies  $\mu_i^{(r)}$  are drawn from a uniform distribution in  $[-\pi, \pi]$ , for  $i = 1, 2, 3$  and  $r = 1, 2, 3$ . Moreover, the contamination caused by a very short sensor failure is modeled by randomly replacing a single entry of the measurement tensor with a complex i.i.d. impulsive noise that obeys a complex zero mean Gaussian distribution with variance of  $\kappa\sigma_n^2$  [MCR<sup>+</sup>12]. Here  $\sigma_n^2$  represents the variance of the noise, and we use  $\kappa = 50$ . A comparison between the proposed enhanced versions of robust  $R$ -D AIC as well as robust  $R$ -D MDL and the original versions is presented in Figure 8.10 in terms of the probability of correct detection. We observe a gain achieved by the enhanced

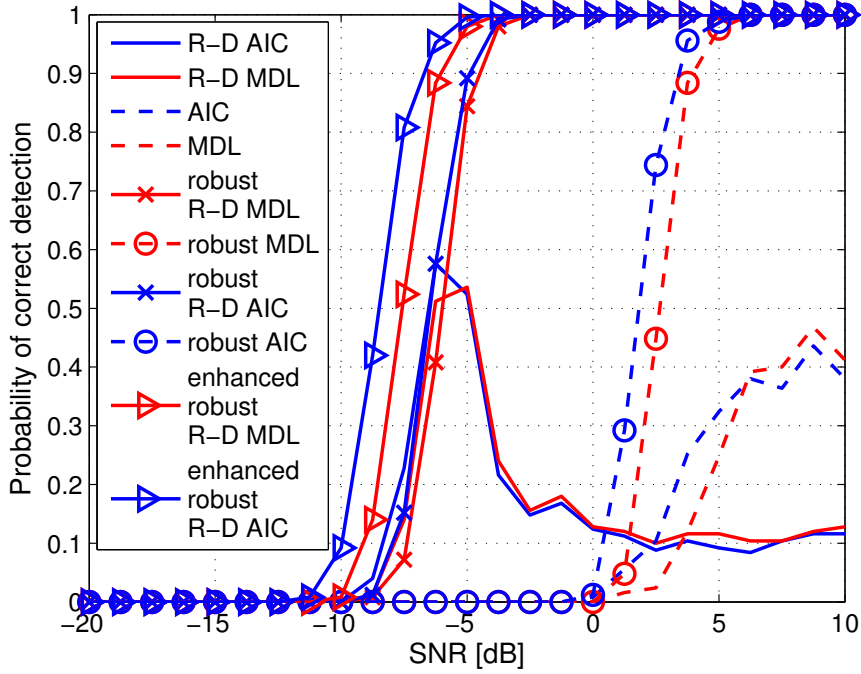


Figure 8.10.: Probability of correct detection versus SNR for  $M_1 = 5$ ,  $M_2 = 7$ ,  $M_3 = 9$ ,  $N = 10$ ,  $d = 3$  in the presence of a brief sensor failure modeled by randomly replacing a single entry of the measurement tensor with a complex i.i.d. impulsive noise that obeys a complex zero mean Gaussian distribution with variance of  $\kappa\sigma_n^2$ , where  $\sigma_n^2$  represents the variance of the noise, and  $\kappa = 50$

robust  $R$ -D AIC and enhanced robust  $R$ -D MDL which results from the forward-backward averaging procedure inherent in the construction of the real-valued data tensor. In addition,

the performances of *R-D* AIC, *R-D* MDL [dCRHdS11], and the matrix-based model order selection schemes AIC as well as MDL [WK85] are also shown in Figure 8.10. In the presence of brief sensor failures, these techniques break down and fail to perform accurate and reliable model order estimation. Furthermore, it can be seen that the robust versions of AIC and MDL also exhibit robustness against the contamination caused by brief sensor failures. However, their performances are much worse compared to their higher-dimensional counterparts, as the matrix-based techniques fail to exploit the multi-dimensional structure residing in the data. In the second example, the performances of robust *R-D* AIC and robust *R-D* MDL are further

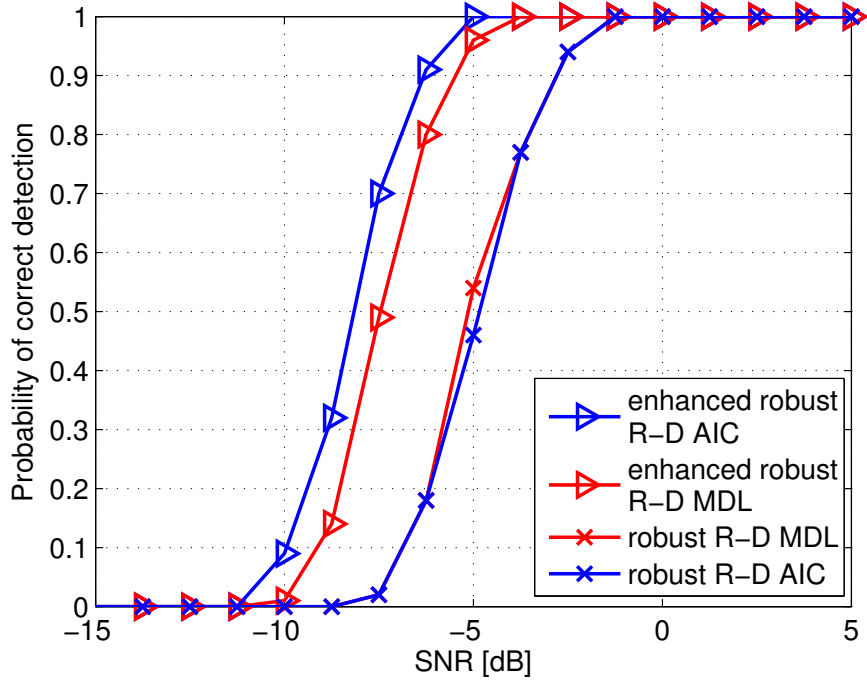


Figure 8.11.: Probability of correct detection versus SNR for  $M_1 = 7$ ,  $M_2 = 7$ ,  $M_3 = 7$ ,  $M_4 = 7$ ,  $N = 7$ ,  $d = 4$  in the presence of a brief sensor failure modeled by randomly replacing a single entry of the measurement tensor with a complex i.i.d. impulsive noise that obeys a complex zero mean Gaussian distribution with variance of  $\kappa\sigma_n^2$ , where  $\sigma_n^2$  represents the variance of the noise, and  $\kappa = 50$

compared with those provided by their enhanced versions in a 4-D scenario, where  $M_1 = 7$ ,  $M_2 = 7$ ,  $M_3 = 7$ ,  $M_4 = 7$ ,  $N = 7$ , and  $d = 4$  in the presence of brief sensor failures. The other parameters are the same as described in the first experiment. It can be observed in Figure 8.11 that the enhanced robust *R-D* AIC and the enhanced robust *R-D* MDL schemes significantly



outperform the original robustified versions of  $R$ -D AIC and  $R$ -D MDL, respectively.

In what follows, we continue to evaluate the performances of the proposed robustified version of  $R$ -D EFT. A 3-D scenario where  $M_1 = 5$ ,  $M_2 = 5$ ,  $M_3 = 5$ ,  $N = 5$ , and  $d = 3$  is considered. This example aims at demonstrating the efficiency of the robust  $R$ -D EFT scheme in an assumed model where the measurement data is only corrupted by Gaussian noise. In Figure 8.12, we present the probabilities of correct detection with respect to different SNR values obtained by employing AIC, MDL,  $R$ -D AIC,  $R$ -D MDL,  $R$ -D EFT and their corresponding robustified versions. It can be found that without the presence of brief sensor failures the proposed

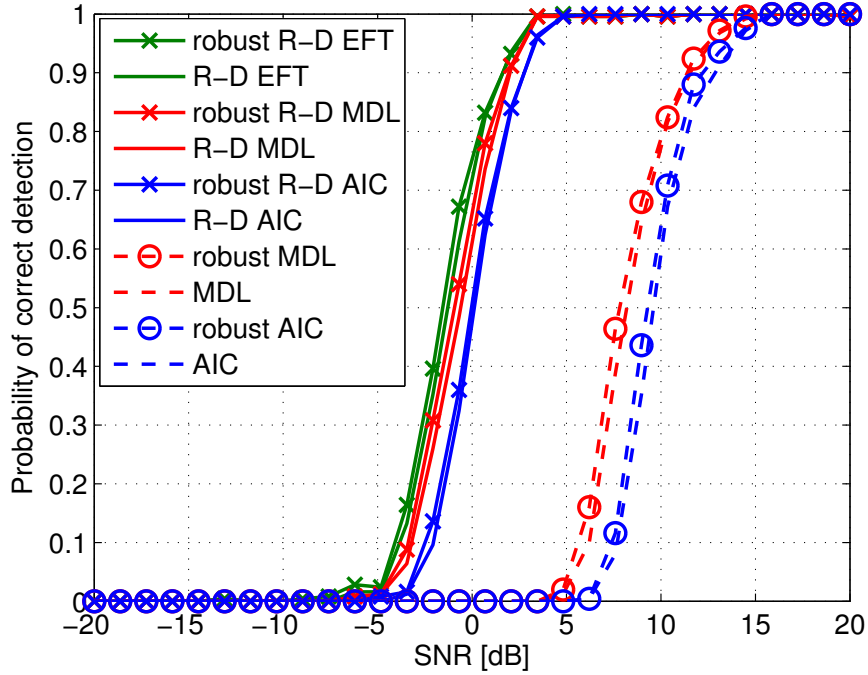


Figure 8.12.: Probability of correct detection versus SNR for  $M_1 = 5$ ,  $M_2 = 5$ ,  $M_3 = 5$ ,  $N = 5$ ,  $d = 3$  without sensor failure and the performances of the original  $R$ -D EFT and the robustified  $R$ -D EFT are compared

robustified  $R$ -D EFT scheme is able to provide a similar performance as the original  $R$ -D EFT algorithm. The same observation can be obtained based on the performance comparison of other robust model order selection schemes and their original unrobustified counterparts considered in this example. Therefore, it is verified that the proposed concept of introducing robustness to the model order estimation leads to robustified model order selection schemes endowed with a high efficiency.

To further demonstrate the performance of the proposed robust  $R$ -D EFT in a critical scenario where the measurements are severely contaminated, the same 3-D scenario as considered in the previous example is simulated. Here 2 % of the measurement data is contaminated due to brief sensor failures, and the effects are simulated by randomly replacing 2 % of the entries of the measurement tensor with impulsive noises as described in the first example. As

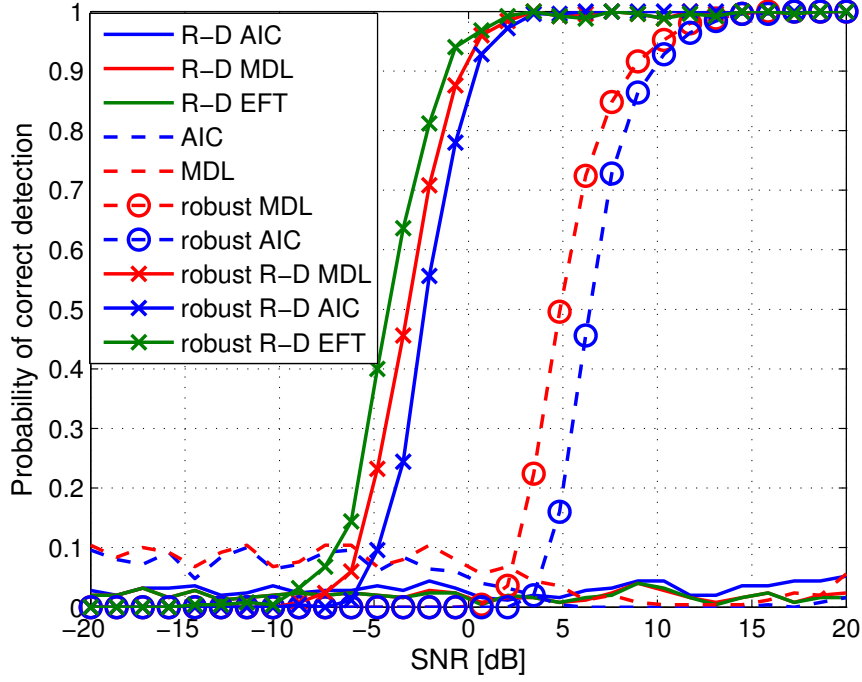


Figure 8.13.: Probability of correct detection versus SNR for  $M_1 = 5$ ,  $M_2 = 5$ ,  $M_3 = 5$ ,  $N = 5$ ,  $d = 3$  in the presence of a brief sensor failure modeled by randomly replacing 2 % of the entries of the measurement tensor with a complex i.i.d. impulsive noise that obeys a complex zero mean Gaussian distribution with variance of  $\kappa\sigma_n^2$ , where  $\sigma_n^2$  represents the variance of the noise, and  $\kappa = 50$

illustrated in Figure 8.13, the robustified  $R$ -D EFT algorithm is able to perform reliable model order estimation in spite of the fact that the measurement data is critically corrupted due to brief sensor failures. The non-robust  $R$ -D EFT scheme, on the other hand, completely breaks down.

A 4-D scenario where  $M_1 = 5$ ,  $M_2 = 5$ ,  $M_3 = 5$ ,  $M_4 = 5$ ,  $N = 5$ , and  $d = 2$  is also presented. The impact of a brief sensor failure is simulated as in the first experiment, i.e., a single random entry of the measurement tensor is replaced by a complex i.i.d. impulsive noise that obeys a

complex zero mean Gaussian distribution with variance of  $\kappa\sigma_n^2$ . Similarly, it can be seen in Figure 8.14 that the enhanced versions of the robustified  $R$ -D EFT,  $R$ -D AIC, and  $R$ -D MDL provide much better performances compared to the original robust  $R$ -D EFT,  $R$ -D AIC, and  $R$ -D MDL, respectively. Moreover, the EFT-based schemes outperform the AIC-based and MDL-based ones.

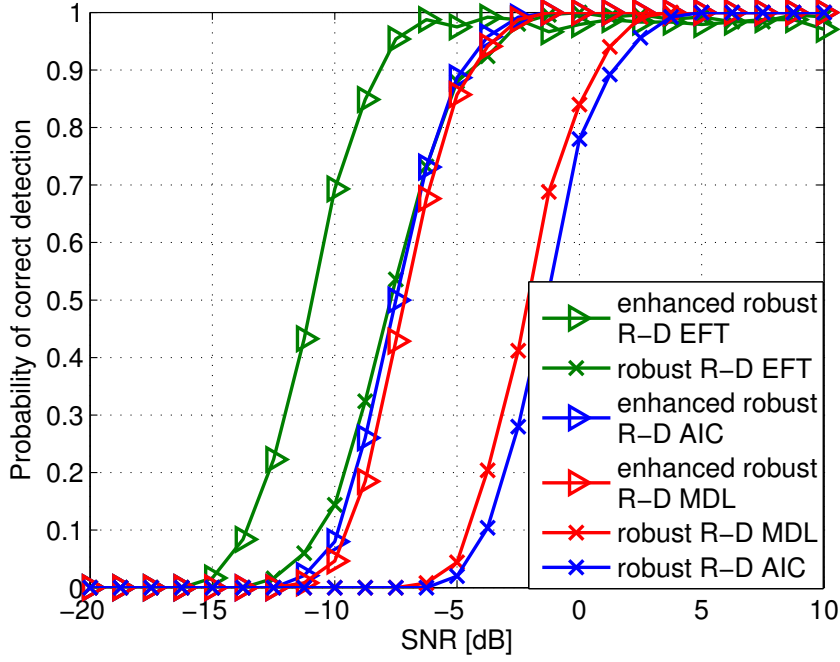


Figure 8.14.: Probability of correct detection versus SNR for  $M_1 = 5$ ,  $M_2 = 5$ ,  $M_3 = 5$ ,  $M_4 = 5$ ,  $N = 5$ ,  $d = 2$  in the presence of a brief sensor failure modeled by randomly replacing a single entry of the measurement tensor with a complex i.i.d. impulsive noise that obeys a complex zero mean Gaussian distribution with variance of  $\kappa\sigma_n^2$ , where  $\sigma_n^2$  represents the variance of the noise, and  $\kappa = 50$

Finally, we investigate the impact of the percentage of the severe contamination in the measurement data on the performance of the robust multi-dimensional model order estimation schemes. It is of great interest to see if and to what extent the quantitative robustness (represented via the breakdown point) of the robust covariance estimator, i.e., in our case the MM-estimator, is translated into these robustified  $R$ -D model order estimation algorithms. The same 3-D scenario as for Figure 8.13 is simulated, where  $M_1 = 5$ ,  $M_2 = 5$ ,  $M_3 = 5$ ,  $N = 5$ , and  $d = 3$ . The effect of the brief sensor failures is modeled by randomly replacing a certain percentage of the entries in the measurement tensor (referred to as “Percentage of contamina-

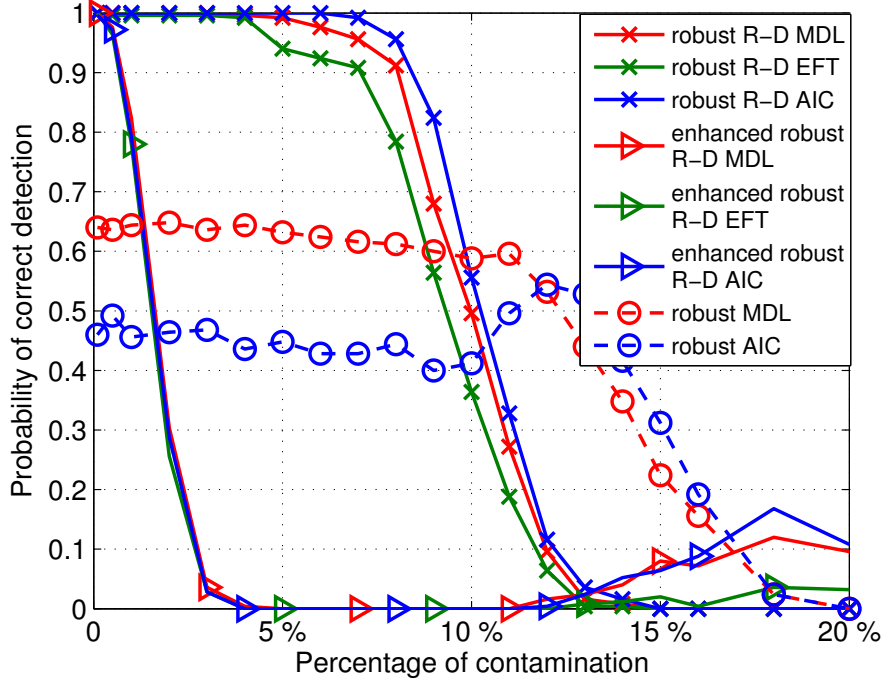


Figure 8.15.: Probability of correct detection versus the percentage of contamination at SNR = 0 dB for a 3-D scenario  $M_1 = 5$ ,  $M_2 = 5$ ,  $M_3 = 5$ ,  $N = 5$ , and  $d = 3$  in the presence of a brief sensor failure modeled by randomly replacing a certain percentage of the entries in the measurement tensor with a complex i.i.d. impulsive noise that obeys a complex zero mean Gaussian distribution with variance of  $\kappa\sigma_n^2$ , where  $\sigma_n^2$  represents the variance of the noise, and  $\kappa = 50$

tion” in the x-label of Figure 8.15) by a complex i.i.d. impulsive noise that obeys a complex zero mean Gaussian distribution with variance of  $\kappa\sigma_n^2$  and  $\kappa = 50$ . The SNR is set to 0 dB, whereas the percentage of contamination varies, ranging from 0.1 % to 20 %. We present the results in Figure 8.15. It can be observed that when the percentage of contamination is below around 5 %, robust  $R$ -D MDL, robust  $R$ -D AIC, and robust  $R$ -D EFT are able to provide very reliable estimates of the model order. As the percentage of contamination approaches 15 %, these three schemes tend to break down completely. Robust  $R$ -D AIC has a slightly stronger quantitative robustness compared to robust  $R$ -D MDL and robust  $R$ -D EFT. On the other hand, the percentage of severe contamination that enhanced robust  $R$ -D MDL, enhanced robust  $R$ -D AIC, and enhanced robust  $R$ -D EFT are able to handle is much smaller than that of robust  $R$ -D MDL, robust  $R$ -D AIC, and robust  $R$ -D EFT. It is due to the fact that including

forward-backward-averaging not only enhances the desired signal components but also brings the side effect in terms of the aggravation of the corruption in the measurements. As the percentage of contamination increases, the latter consequence becomes the dominant factor in the performance. Nevertheless, these enhanced versions show a significant performance superiority in case of a low percentage of contamination as observed in Figure 8.11 and Figure 8.14. The robustified matrix-based model order estimation approaches, robust MDL and robust AIC, totally break down as the percentage of contamination reaches 20 %. But even when only a very modest fraction of the data is corrupted, these matrix-based schemes fail to accurately estimate the model order for SNR = 0 dB. The probability of correct detection that they are able to achieve is much lower compared to the tensor-based schemes.

## 8.7. Summary

In this chapter, the multi-dimensional model order estimation problem is investigated in the presence of brief sensor failures. First, we introduce the concept of the robustified multi-dimensional model order estimation and present two examples, robust versions of  $R$ -D AIC and  $R$ -D MDL. Then, we propose enhanced versions of robust  $R$ -D AIC and robust  $R$ -D MDL by mapping the complex-valued measurement tensor to a real-valued one. In this transformation, forward-backward averaging is also incorporated, which leads to a noticeable performance improvement. In addition to such an enhancement of the performance, the resulting real-valued computations in the subsequent procedures of the model order estimation contribute to a reduced computational complexity compared to the original robust  $R$ -D model order selection schemes. Moreover, a robustified version of the  $R$ -D EFT algorithm is also developed following a similar concept of introducing the statistical robustness as used in robust  $R$ -D MDL and robust  $R$ -D AIC. The proposed robust  $R$ -D EFT achieves reliable model order estimation in spite of the fact that the measurements suffer from severe contamination caused by brief sensor failures, while the original  $R$ -D EFT breaks down in such a situation. Furthermore, the enhanced version of robust  $R$ -D EFT also provides a significant gain in contrast to the originally proposed robust  $R$ -D EFT.

## 9. Tensor subspace Tracking via Kronecker structured projections (TeTraKron)

In this chapter, we present a framework for Tensor-based subspace Tracking via Kronecker-structured projections (TeTraKron). TeTraKron allows to extend arbitrary matrix-based subspace tracking schemes to track the tensor-based subspace estimate. The latter can be computed via a structured projection applied to the matrix-based subspace estimate which enforces the multi-dimensional structure in a computationally efficient fashion. This projection is tracked by considering all matrix rearrangements of the signal tensor jointly, which can be efficiently realized via parallel processing. In addition, we incorporate forward-backward-averaging and find a similar link between the real-valued matrix-based and tensor-based subspace estimation. This enables the tracking of the real-valued tensor-based subspace estimate via a similar Kronecker-structured projection applied to the real-valued matrix-based subspace estimate. In time-varying multidimensional harmonic retrieval problems, the TeTraKron-based subspace tracking schemes outperform the original matrix-based subspace tracking algorithms as well as the batch solutions provided by the Singular Value Decomposition (SVD) and the Higher-Order Singular Value Decomposition (HOSVD). Moreover, incorporating forward-backward-averaging leads to an improved accuracy of the subspace tracking, and only real-valued processing is involved. Furthermore, we evaluate the performances of ESPRIT-type parameter estimation schemes where the subspace estimates obtained by the proposed TeTraKron-based subspace tracking algorithms are used for the tracking of spatial frequencies in time-varying scenarios. The aforementioned results have been published in [RKCH13] and [CRKH14].

### 9.1. Introduction

The design of adaptive algorithms to track the subspace of an instationary random signal has a long standing history in signal processing. The main challenges are achieving a fast adaptation and a good steady-state behavior while keeping the computational complexity low. The first subspace-tracking schemes like [Ows78] still had a complexity of  $\mathcal{O}\{M^2 \cdot d\}$  where  $M$  is the number of channels (sensors) and  $d$  is the rank of the signal subspace. Later as a Singular Value Decomposition (SVD) technique and a data projection method (DPM) were proposed in [Kar86] and [YK88], respectively, the complexity was lowered to  $\mathcal{O}\{M \cdot d^2\}$ . Approaches

that belong to a low complexity class with  $\mathcal{O}\{M \cdot d\}$  operations have been developed, such as the scheme in [Oja82] that estimates the eigenvector associated with the largest eigenvalue. Classified into the category of power-based methods similarly as DPM, the fast Rayleigh quotient-based adaptive noise subspace (FRANS) algorithm [AAM02] combines DPM with a fast orthonormalization procedure. Another power-based approach that has the complexity of  $\mathcal{O}\{M \cdot d\}$  as well, the fast approximated power iteration (FAPI) algorithm [BDR05], is based on the power iteration method and a novel projection approximation. On the other hand, belonging to the category of projection approximation-based methods, the well-known projection approximation subspace tracking (PAST) algorithm [Yan95b] is one of the first low complexity subspace tracking schemes with  $\mathcal{O}\{M \cdot d\}$  operations. PAST interprets the signal subspace estimate as the solution of a minimization problem which can be simplified via an appropriate projection approximation and then applies a recursive least squares (RLS) procedure to track the signal subspace. A deflation-based version of PAST (PASTd) with an even lower complexity was proposed in [Yan95b]. In the literature, variants of some of the aforementioned algorithms have been developed to improve the numerical stability or to track the minor subspace. In addition to complexity, there exist other aspects based on which matrix-based subspace tracking algorithms can be categorized. One of such aspects is the windowing of the measurement data. Two popular types of windowing that are often employed in subspace tracking algorithms are the exponential windowing and the sliding windowing. For instance, the PAST algorithm [Yan95b] employs an exponential window with a forgetting factor  $0 < \beta < 1$ . A modified version of PAST with a sliding window is also discussed in [Yan95b]. For the FAPI scheme [BDR05] mentioned previously, there are two versions that use an exponential window and a sliding window, respectively. On the other hand, whether the rank tracking is enabled is another important feature of subspace tracking algorithms. The rank is assumed to be known a priori in many schemes [Yan95b], [AAM02], [BDR05]. This assumption also applies to the results presented in this chapter. Model order selection algorithms, as discussed in Chapter 8, can be adopted to obtain rank estimates. Although beyond the scope of this thesis, it is worth mentioning that the tracking of the rank is incorporated in some approaches such as the URV scheme [Ste92], [Ste93] and the signed URV algorithm [ZvdV12]. In addition, an extension of the PASTd scheme has been proposed in [Yan95a] for both the rank and the subspace tracking. For a more detailed survey the reader is referred to [Del10].

For stationary multi-dimensional signals, it has been shown that the subspace estimation accuracy can be significantly improved if tensors are used to store and manipulate the signals. A signal subspace estimate based on the Higher-Order Singular Value Decomposition (HOSVD) [dLdMV00] was introduced in [HRD08]. Therefore, extending this subspace estimation scheme

to the tracking of the subspace of a time-varying multidimensional signal is of significant interest.

To this end we introduce the tensor-based subspace tracking via Kronecker structured projections (TeTraKron) framework. TeTraKron allows to exploit the rich heritage of matrix-based subspace tracking. It flexibly extends arbitrary matrix-based subspace tracking schemes to the tracking of the HOSVD-based subspace estimate defined in [HRD08] by running them on all the unfoldings of the data tensor in parallel. The form of windowing of the resulting tensor-based subspace tracking algorithms is determined by that of the corresponding matrix-based methods. Note that tracking the subspaces of all unfoldings of a tensor has been proposed before, e.g., in [HLZ<sup>+</sup>11, STP<sup>+</sup>08]. For the computer vision application, the incremental tensor subspace learning algorithm developed in [HLZ<sup>+</sup>11] tracks the subspace of the unfoldings by using an incremental SVD approach. The unfoldings of the data tensor are projected onto the subspaces. An incremental tensor analysis framework and its variants were introduced in [STP<sup>+</sup>08] to efficiently compute a compact summary of high-dimensional data and to reveal the hidden correlations. However, these approaches do not consider the recombination of these subspaces to the HOSVD-based subspace estimate from [HRD08]. The computationally efficient recombination is the main focus of the TeTraKron framework. Moreover, [HLZ<sup>+</sup>11, STP<sup>+</sup>08] require to track the core tensor of the HOSVD which TeTraKron does not need at all.

The incorporation of forward-backward-averaging is also investigated. Employed by many parameter estimation algorithms as a preprocessing step, forward-backward-averaging virtually augments the observations and leads to an enhanced estimation accuracy. In addition, complex-valued measurements can be further conveniently and efficiently transformed to real-valued data [HRD08]. Due to the fact that only real-valued computations are involved in the subsequent steps, the complexity is reduced. In this chapter, we show that after incorporating forward-backward-averaging, the real-valued HOSVD-based subspace estimate can be obtained by applying a structured projection to the real-valued matrix-based subspace estimate as well. Consequently, the TeTraKron framework enables the extension of matrix-based subspace tracking schemes to realize real-valued tensor-based subspace tracking where forward-backward-averaging is included and provides benefits in terms of both the performance and the complexity. In time-varying multidimensional harmonic retrieval problems, we use the subspace estimates tracked via the TeTraKron-based subspace tracking schemes in ESPRIT-type parameter estimation algorithms [HRD08] and evaluate their resulting performances.

This chapter is organized as follows: Section 9.2 introduces the data model for the matrix-based and the tensor-based subspace estimation. The TeTraKron framework is described



in detail in Section 9.3. The incorporation of forward-backward-averaging and real-valued subspace tracking are also discussed. Section 9.4 provides examples of how TeTraKron can be employed to develop tensor-based subspace tracking schemes based on PAST, PASTd, and FAPI. Section 9.5 presents numerical results before the conclusions are drawn in Section 9.6.

## 9.2. Data model for the matrix-based and the tensor-based subspace estimation

In this section we introduce the data model for both the matrix-based and the tensor-based subspace estimation. To this end, we start with the non-adaptive case where the subspaces are estimated once, based on  $N$  observations in a stationary window. We consider a linear mixture of  $d$  sources superimposed by additive noise, which can be expressed as

$$\mathbf{X} = \mathbf{A} \cdot \mathbf{S} + \mathbf{W}. \quad (9.1)$$

Here,  $\mathbf{X} \in \mathbb{C}^{M \times N}$  is the matrix of observations from  $M$  channels at  $N$  subsequent time instants,  $\mathbf{A} \in \mathbb{C}^{M \times d}$  is the unknown mixing matrix or the array steering matrix,  $\mathbf{S} \in \mathbb{C}^{d \times N}$  contains the unknown source symbols, and  $\mathbf{W}$  represents the additive noise samples. Then, the SVD of  $\mathbf{X}$  can be expressed as

$$\mathbf{X} = [\hat{\mathbf{U}}_s \ \hat{\mathbf{U}}_n] \cdot \begin{bmatrix} \hat{\mathbf{\Sigma}}_s & \mathbf{0} \\ \mathbf{0} & \hat{\mathbf{\Sigma}}_n \end{bmatrix} \cdot [\hat{\mathbf{V}}_s \ \hat{\mathbf{V}}_n]^H, \quad (9.2)$$

where the columns of  $\hat{\mathbf{U}}_s \in \mathbb{C}^{M \times d}$  represent an orthonormal basis for the estimated signal subspace, i.e.,  $\text{span}\{\hat{\mathbf{U}}_s\} \approx \text{span}\{\mathbf{A}\}$ .

We can arrange the elements of the matrix  $\mathbf{X} \in \mathbb{C}^{M \times N}$  into a tensor  $\mathcal{X} \in \mathbb{C}^{M_1 \times M_2 \dots \times M_R \times N}$ , where  $M = M_1 \cdot M_2 \dots \cdot M_R$ . While such a rearrangement is always possible it only provides a benefit if the actual underlying signal has a corresponding multidimensional structure, e.g., it resembles a signal sampled on a multidimensional lattice. These dimensions can for instance relate to space (1-D or 2-D arrays at transmitter or receiver), frequency, time, or polarization, depending on the application. The corresponding tensor-valued data model takes the following form [HRD08]

$$\mathcal{X} = \mathcal{A} \times_{R+1} \mathbf{S}^T + \mathcal{W}, \quad (9.3)$$

where  $\mathcal{A} \in \mathbb{C}^{M_1 \times M_2 \dots \times M_R \times d}$  and  $\mathcal{W} \in \mathbb{C}^{M_1 \times M_2 \dots \times M_R \times N}$  represent the mixing tensor and the noise

tensor, respectively. Since (9.3) is a rearranged version of (9.1), the corresponding quantities are linked via the relations  $\mathbf{X} = [\mathcal{X}]_{(R+1)}^T$ ,  $\mathbf{A} = [\mathcal{A}]_{(R+1)}^T$ , and  $\mathbf{W} = [\mathcal{W}]_{(R+1)}^T$ , respectively. Throughout this chapter, for the  $r$ -mode unfolding, the reverse cyclical ordering of the  $r$ -mode vectors [dLdMV00] as introduced in Section 8.2 is used.

As shown in [HRD08], based on (9.3) we can define a tensor-based subspace estimate by computing a truncated Higher-Order SVD (HOSVD) [dLdMV00],

$$\mathbf{X} \approx \hat{\mathcal{S}}^{[s]} \times_1 \hat{\mathbf{U}}_1^{[s]} \times_2 \hat{\mathbf{U}}_2^{[s]} \dots \times_{R+1} \hat{\mathbf{U}}_{R+1}^{[s]}, \quad (9.4)$$

where  $\hat{\mathbf{U}}_r^{[s]} \in \mathbb{C}^{M_r \times p_r}$  has unitary columns and denotes the matrix of the estimated  $r$ -mode singular vectors. Moreover,  $p_r$  is the  $r$ -rank of the mixing tensor  $\mathcal{A}$ , and  $\hat{\mathcal{S}}^{[s]} \in \mathbb{C}^{p_1 \times p_2 \dots \times p_{R+1}}$  represents the truncated core tensor that can be computed from  $\mathbf{X}$  via

$$\hat{\mathcal{S}}^{[s]} = \mathbf{X} \times_1 \hat{\mathbf{U}}_1^{[s]H} \times_2 \hat{\mathbf{U}}_2^{[s]H} \dots \times_{R+1} \hat{\mathbf{U}}_{R+1}^{[s]H}. \quad (9.5)$$

Based on the HOSVD, an improved signal subspace estimate is given by  $\left[\hat{\mathbf{u}}^{[s]}\right]_{(R+1)}^T \in \mathbb{C}^{M \times d}$ , where  $\hat{\mathbf{u}}^{[s]}$  is [HRD08]

$$\hat{\mathbf{u}}^{[s]} = \hat{\mathcal{S}}^{[s]} \times_1 \hat{\mathbf{U}}_1^{[s]} \times_2 \hat{\mathbf{U}}_2^{[s]} \dots \times_R \hat{\mathbf{U}}_R^{[s]} \times_{R+1} \hat{\mathbf{S}}_s^{-1}, \quad (9.6)$$

where  $\hat{\mathbf{S}}_s$  contains the  $(R+1)$ -mode singular values as defined in (9.2). Compared to the tensor-based subspace estimation in [HRD08], the multiplication with  $\hat{\mathbf{S}}_s^{-1}$  in mode  $(R+1)$  represents only a normalization [RHD14]. As discussed in [HRD08], (9.6) leads to a better signal subspace estimate than  $\hat{\mathbf{U}}_s$  if and only if  $\mathcal{A}$  is  $r$ -rank deficient in at least one mode  $r = 1, 2, \dots, R$ , i.e.,  $p_r < M_r$ .

Let us consider an  $R$ -D harmonic retrieval problem [HRD08] with a superposition of  $d$  harmonics sampled on an  $R$ -D lattice. This gives rise to a mixing matrix  $\mathbf{A}$  and a mixing tensor  $\mathcal{A}$  of the following form

$$\mathbf{A} = \mathbf{A}_1 \diamond \mathbf{A}_2 \diamond \dots \diamond \mathbf{A}_R \quad (9.7)$$

$$\mathcal{A} = \mathcal{I}_{R+1,d} \times_1 \mathbf{A}_1 \times_2 \mathbf{A}_2 \dots \times_R \mathbf{A}_R, \quad (9.8)$$

where  $\mathbf{A}_r \in \mathbb{C}^{M_r \times d}$  represents the mixing matrix in the  $r$ -th mode. In this case we have  $p_r \leq d$  and, therefore, the tensor-based subspace estimate is superior to the matrix-based subspace estimate if  $d < M_r$  for at least one  $r = 1, 2, \dots, R$  [HRD08]. However, there are applications

with  $r$ -rank deficiencies where the observed signal obeys (9.3) but not (9.8), for instance, the tensor-based blind channel estimation scheme in [SRH10a].

### 9.3. Tensor subspace Tracking via Kronecker structured projections (TeTraKron)

In a time-varying scenario, the observation matrix  $\mathbf{X}$  is augmented by a new column  $\mathbf{x}(n) \in \mathbb{C}^{M \times 1}$  with every new snapshot  $n$

$$\mathbf{x}(n) = \mathbf{A}(n) \cdot \mathbf{s}(n) + \mathbf{w}(n), \quad n = 1, 2, \dots, N, \quad (9.9)$$

where  $\mathbf{A}(n)$  is the mixing matrix or the array steering matrix for the  $n$ -th snapshot. By employing a subspace tracking scheme, an estimate of the signal subspace  $\hat{\mathbf{U}}_s(n)$  is obtained for each new snapshot  $n$ . In the tensor case,  $\mathbf{x}(n) \in \mathbb{C}^{M \times 1}$  is rearranged into  $\mathcal{X}(n) \in \mathbb{C}^{M_1 \times M_2 \times \dots \times M_R}$ . A tensor-based subspace tracking algorithm aims at estimating the HOSVD-based subspace estimate  $\left[ \hat{\mathcal{U}}^{[s]}(n) \right]_{(R+1)}^T \in \mathbb{C}^{M \times d}$  for each new snapshot. The type of windowing of the tensor-based subspace tracking scheme is determined by that of its corresponding matrix-based subspace tracking approach (cf. some examples in Section 9.4).

#### 9.3.1. Tensor subspace estimation via structured projections

At first sight (9.6) suggests that in order to track the signal subspace, we need to track the  $r$ -mode singular vectors as well as the core tensor. However, we show that tracking the core tensor is indeed unnecessary, since the tensor-based subspace estimate can be computed from the matrix-based subspace estimate via a structured projection which does not involve the core tensor. This was first pointed out in [RBHW09] for the 2-D case. However, it can be generalized to an arbitrary number of dimensions. This claim is summarized in the following theorem:

**Theorem 9.3.1.** *The HOSVD-based subspace estimate can be computed by projecting the unstructured matrix-based subspace estimate obtained via the SVD onto a Kronecker structure in the following manner*

$$\left[ \hat{\mathcal{U}}^{[s]} \right]_{(R+1)}^T = (\hat{\mathbf{T}}_1 \otimes \hat{\mathbf{T}}_2 \dots \otimes \hat{\mathbf{T}}_R) \cdot \hat{\mathbf{U}}_s, \quad (9.10)$$

where  $\hat{\mathbf{T}}_r = \hat{\mathbf{U}}_r^{[s]} \cdot \hat{\mathbf{U}}_r^{[s]H}$  is a projection matrix onto the space spanned by the  $r$ -mode vectors.

*Proof.* cf. Appendix F and [RHD14]. □

In the proof, the core tensor in (9.6) is first eliminated by substituting (9.5) into (9.6), and  $\left[\hat{\mathcal{U}}^{[s]}\right]_{(R+1)}^T$  is then computed as

$$\left[\hat{\mathcal{U}}^{[s]}\right]_{(R+1)}^T = (\hat{T}_1 \otimes \hat{T}_2 \dots \otimes \hat{T}_R) \cdot [\mathcal{X}]_{(R+1)}^T \cdot \hat{\mathcal{U}}_{R+1}^{[s]*} \cdot \hat{\Sigma}_s^{-1}.$$

Relying on the observation that  $\mathbf{X} = [\mathcal{X}]_{(R+1)}^T$ ,  $\hat{\mathbf{V}}_s = \hat{\mathcal{U}}_{R+1}^{[s]*}$ , and

$$\mathbf{X} = \hat{\mathcal{U}}_s \cdot \hat{\Sigma}_s \cdot \hat{\mathbf{V}}_s^H,$$

which follows (9.2), the identity (9.10) is proved. Equation (9.10) provides the central idea behind the TeTraKron framework we introduce in this chapter. It shows that the tensor-based subspace estimate can be understood as a projection of the unstructured matrix-based subspace estimate onto the Kronecker structure inherent in the data. It also shows that for all modes where  $p_r = M_r$  we have  $\hat{T}_r = \mathbf{I}_r$ , i.e., no projection is performed. Another consequence we can draw from (9.10) is that there is no need to compute (or track) the core tensor. We can find the tensor-based subspace estimate only based on the  $r$ -mode subspaces contained in  $\hat{\mathcal{U}}_r^{[s]}$ . These are the subspaces obtained from the  $r$ -mode unfoldings of  $\mathcal{X}$ , which are again matrices. Therefore, any matrix-based subspace tracking scheme can be applied to track these subspaces as well.

Consequently, the main idea can be summarized as follows: In addition to tracking the dominant column space (signal subspace) of the matrix  $\mathbf{X}$  (which is the same as tracking the dominant row space of the  $(R+1)$ -mode unfolding of  $\mathcal{X}$ ), we apply the same tracking algorithm to **all**  $r$ -mode unfoldings of the tensor which satisfy  $p_r < M_r$  for  $r = 1, 2, \dots, R$  in parallel. Note that even though this seems to increase the complexity by a factor equal to the number of modes we track, all these trackers can run in parallel which facilitates an efficient implementation. After each step, the tensor-based subspace estimate can be recombined via (9.10).

However, this recombination requires  $\mathcal{O}\{M^2 \cdot d\}$  multiplications, i.e., it is quadratic in  $M$ , which is undesirable. The definition of the notation  $\mathcal{O}\{\cdot\}$  has been given in Section 1.3. To lower the complexity, we rewrite (9.10) as

$$\left[\hat{\mathcal{U}}^{[s]}\right]_{(R+1)}^T = \mathbf{U}_{\text{Kron}}^{[s]} \cdot \hat{\mathcal{U}}_s, \quad (9.11)$$

where  $\mathbf{U}_{\text{Kron}}^{[s]} = \mathbf{U}_1^{[s]} \otimes \dots \otimes \mathbf{U}_R^{[s]} \in \mathbb{C}^{M \times d^R}$  and  $\hat{\mathbf{U}}_s = \mathbf{U}_{\text{Kron}}^{[s]H} \cdot \hat{\mathbf{U}}_s \in \mathbb{C}^{d^R \times d}$  assuming  $p_r = d \leq M_r$  for notational convenience, where  $r = 1, 2, \dots, R$ . This leads to the fact that  $d^R < M$ . Note that the matrix product in (9.11) requires only  $\mathcal{O}\{M \cdot d^R\}$  multiplications, i.e., it is linear in  $M$ . Moreover, (9.11) can be used for tensor-based subspace tracking as well: We track  $\mathbf{U}_r^{[s]}$  for  $r = 1, 2, \dots, R$  by applying matrix-based subspace tracking schemes to all unfoldings, then project our  $M$ -dimensional observations into a lower-dimensional subspace by premultiplying them with  $\mathbf{U}_{\text{Kron}}^{[s]H} \in \mathbb{C}^{d^R \times M}$  and finally run a matrix-based subspace tracker on the lower-dimensional data to track the  $d$ -dimensional subspace  $\hat{\mathbf{U}}_s \in \mathbb{C}^{d^R \times d}$ .

TeTraKron allows to readily extend arbitrary matrix-based subspace tracking schemes to tensors which yields an improved estimation accuracy as we demonstrate in Section 9.5. Therefore, we obtain novel tensor-based subspace trackers by building on known algorithms, which is a particularly attractive feature of the TeTraKron framework. In addition to running these trackers on all unfoldings in parallel and recombining the signal subspace estimate via (9.10) or (9.11), the only modification we have to apply to the matrix-based subspace tracking schemes is the following: As introduced at the beginning of this section, it is typically assumed that the observation matrix  $\mathbf{X}$  is augmented by a new column  $\mathbf{x}(n) \in \mathbb{C}^M$  with each new snapshot  $n$ . For the  $r$ -mode unfoldings of  $\mathcal{X}(n) \in \mathbb{C}^{M_1 \times M_2 \times \dots \times M_R}$  that are a rearranged version of  $\mathbf{x}(n)$ , every new snapshot generates not only one but several new columns. For instance, for the 1-mode unfolding we obtain  $\prod_{r=2}^R M_r$  new columns, each of size  $M_1$ . This new batch of columns can be processed sequentially, or, by modifying the tracking schemes, also in one batch. We demonstrate such a modification using the examples of the PAST algorithm, the PASTd algorithm [Yan95b], and the FAPI algorithm [BDR05] in Section 9.4.

### 9.3.2. Forward-backward-averaging and real-valued subspace tracking

Forward-backward-averaging and real-valued subspace estimation have been introduced for the matrix case in [HN95] and the tensor case in [HRD08], respectively. By employing forward-backward-averaging, the number of snapshots is virtually doubled. It also results in the decorrelation of two coherent sources. Moreover, the subsequent computations are real-valued, which contributes to a reduced complexity.

In this section, we revisit the concept of forward-backward-averaging and present real-valued subspace tracking. First, we define a forward-backward-averaged version of the measurement tensor  $\mathcal{X} \in \mathbb{C}^{M_1 \times M_2 \times \dots \times M_R \times N}$  [HRD08]

$$\mathcal{Z} = [\mathcal{X} \sqcup_{R+1} [\mathcal{X}^* \times_1 \mathbf{\Pi}_{M_1} \times_2 \mathbf{\Pi}_{M_2} \cdots \times_{R+1} \mathbf{\Pi}_N]] \in \mathbb{C}^{M_1 \times M_2 \times \dots \times M_R \times 2N}, \quad (9.12)$$

where  $\mathbf{\Pi}_p$  is a  $p \times p$  exchange matrix which has ones on its anti-diagonal and zeros elsewhere. We further map this centro-Hermitian tensor to a real-valued tensor  $\varphi(\mathbf{Z}) \in \mathbb{R}^{M_1 \times M_2 \times \dots \times M_R \times 2N}$  by using the transformation [HRD08]<sup>1</sup>

$$\varphi(\mathbf{Z}) = \mathbf{Z} \times_1 \mathbf{Q}_{M_1}^H \times_2 \mathbf{Q}_{M_2}^H \cdots \times_{R+1} \mathbf{Q}_{2N}^T, \quad (9.13)$$

where  $\mathbf{Q}_p$  is a  $p \times p$  left- $\mathbf{\Pi}$  real and unitary matrix, i.e., it satisfies  $\mathbf{\Pi}_p \cdot \mathbf{Q}_p^* = \mathbf{Q}_p$  [Lee80]. One way to construct such a unitary left- $\mathbf{\Pi}$  real matrix is given in [HN95]

$$\mathbf{Q}_{2n} = \frac{1}{\sqrt{2}} \begin{bmatrix} \mathbf{I}_n & j\mathbf{I}_n \\ \mathbf{\Pi}_n & -j\mathbf{\Pi}_n \end{bmatrix} \quad \text{and} \quad \mathbf{Q}_{2n+1} = \frac{1}{\sqrt{2}} \begin{bmatrix} \mathbf{I}_n & \mathbf{0}_{n \times 1} & j\mathbf{I}_n \\ \mathbf{0}_{n \times 1}^T & \sqrt{2} & \mathbf{0}_{n \times 1}^T \\ \mathbf{\Pi}_n & \mathbf{0}_{n \times 1} & -j\mathbf{\Pi}_n \end{bmatrix}, \quad (9.14)$$

for the even and the odd order, respectively.

For the matrix-based case, the matrix of observations  $\mathbf{X} \in \mathbb{C}^{M \times N}$  is mapped to the following centro-Hermitian matrix

$$\mathbf{Z} = \begin{bmatrix} \mathbf{X} & \mathbf{\Pi}_M \cdot \mathbf{X}^* \cdot \mathbf{\Pi}_N \end{bmatrix} \in \mathbb{C}^{M \times 2N}. \quad (9.15)$$

Then  $\mathbf{Z}$  is transformed to a real-valued matrix using the transformation [HN95]

$$\varphi(\mathbf{Z}) = \mathbf{Q}_M^H \cdot \mathbf{Z} \cdot \mathbf{Q}_{2N} \in \mathbb{R}^{M \times 2N}, \quad (9.16)$$

where  $\mathbf{Q}_M$  is defined as [HRD08]

$$\mathbf{Q}_M = \mathbf{Q}_{M_1} \otimes \mathbf{Q}_{M_2} \cdots \otimes \mathbf{Q}_{M_R}. \quad (9.17)$$

By computing a truncated HOSVD of  $\varphi(\mathbf{Z})$

$$\varphi(\mathbf{Z}) \approx \hat{\mathbf{S}}_Z^{[s]} \times_1 \hat{\mathbf{E}}_1^{[s]} \times_2 \hat{\mathbf{E}}_2^{[s]} \cdots \times_R \hat{\mathbf{E}}_R^{[s]} \times_{R+1} \hat{\mathbf{E}}_{R+1}^{[s]}, \quad (9.18)$$

a real-valued subspace estimate is obtained as  $\left[ \hat{\mathcal{E}}^{[s]} \right]_{(R+1)}^T \in \mathbb{R}^{M \times d}$ , where  $\hat{\mathcal{E}}^{[s]}$  has the following form [HRD08]

$$\hat{\mathcal{E}}^{[s]} = \hat{\mathbf{S}}_Z^{[s]} \times_1 \hat{\mathbf{E}}_1^{[s]} \times_2 \hat{\mathbf{E}}_2^{[s]} \cdots \times_R \hat{\mathbf{E}}_R^{[s]} \times_{R+1} \hat{\mathbf{\Sigma}}_s'^{-1}. \quad (9.19)$$

---

<sup>1</sup>Here  $\mathbf{Q}_{2N}^T$  is used instead of  $\mathbf{Q}_{2N}^H$  as originally proposed in [HRD08] where this transformation was introduced. This facilitates to build the link between the matrix-based data model and its tensor-based counterpart, i.e., (9.26).

The matrices  $\hat{\mathbf{E}}_r^{[s]}$ ,  $r = 1, 2, \dots, R+1$ , denote the estimates of the real-valued bases for the  $r$ -mode subspaces, and  $\hat{\Sigma}_s'$  represents the diagonal matrix of the  $(R+1)$ -mode singular values. The multiplication by  $\hat{\Sigma}_s'^{-1}$  in mode  $(R+1)$  is only a normalization procedure. By substituting the expression of the core tensor  $\hat{\mathcal{S}}_Z^{[s]}$

$$\hat{\mathcal{S}}_Z^{[s]} = \varphi(\mathbf{Z}) \times_1 \hat{\mathbf{E}}_1^{[s]\text{H}} \times_2 \hat{\mathbf{E}}_2^{[s]\text{H}} \dots \times_{R+1} \hat{\mathbf{E}}_{R+1}^{[s]\text{H}} \quad (9.20)$$

into (9.19),  $\left[\hat{\mathcal{E}}^{[s]}\right]_{(R+1)}^{\text{T}} \in \mathbb{R}^{M \times d}$  is further expressed as

$$\left[\hat{\mathcal{E}}^{[s]}\right]_{(R+1)} = \hat{\Sigma}_s'^{-1} \cdot \hat{\mathbf{E}}_{R+1}^{[s]\text{H}} \cdot [\varphi(\mathbf{Z})]_{R+1} \cdot (\hat{\mathbf{T}}_1' \otimes \hat{\mathbf{T}}_2' \dots \otimes \hat{\mathbf{T}}_R')^{\text{T}}, \quad (9.21)$$

where  $\hat{\mathbf{T}}_r' = \hat{\mathbf{E}}_r^{[s]} \cdot \hat{\mathbf{E}}_r^{[s]\text{H}}$ . Substituting (9.12) into (9.13) gives

$$\varphi(\mathbf{Z}) = \left[ \left[ \mathcal{X} \times_1 \mathbf{Q}_{M_1}^{\text{H}} \dots \times_R \mathbf{Q}_{M_R}^{\text{H}} \right] \sqcup_{R+1} \left[ \mathcal{X}^* \times_1 (\mathbf{Q}_{M_1}^{\text{H}} \cdot \mathbf{\Pi}_{M_1}) \dots \times_R (\mathbf{Q}_{M_R}^{\text{H}} \cdot \mathbf{\Pi}_{M_R}) \times_{R+1} \mathbf{\Pi}_N \right] \right] \times_{R+1} \mathbf{Q}_{2N}^{\text{T}}. \quad (9.22)$$

Notice that

$$\begin{aligned} (\mathbf{Q}_{M_1}^{\text{H}} \cdot \mathbf{\Pi}_{M_1}) \otimes (\mathbf{Q}_{M_2}^{\text{H}} \cdot \mathbf{\Pi}_{M_2}) \dots \otimes (\mathbf{Q}_{M_R}^{\text{H}} \cdot \mathbf{\Pi}_{M_R}) &= \mathbf{Q}_M^{\text{H}} \cdot (\mathbf{\Pi}_{M_1} \otimes \mathbf{\Pi}_{M_2} \dots \otimes \mathbf{\Pi}_{M_R}) \\ &= \mathbf{Q}_M^{\text{H}} \cdot \mathbf{\Pi}_M. \end{aligned} \quad (9.23)$$

Expanding the  $(R+1)$ -mode unfolding of (9.22) yields

$$[\varphi(\mathbf{Z})]_{(R+1)} = \mathbf{Q}_{2N}^{\text{T}} \cdot \begin{bmatrix} [\mathcal{X}]_{(R+1)} \cdot (\mathbf{Q}_M^{\text{H}})^{\text{T}} \\ \mathbf{\Pi}_N \cdot [\mathcal{X}]_{(R+1)}^* \cdot (\mathbf{Q}_M^{\text{H}} \cdot \mathbf{\Pi}_M)^{\text{T}} \end{bmatrix}. \quad (9.24)$$

As there exists a link between the matrix-based data model and its tensor-based counterpart such that  $\mathbf{X} = [\mathcal{X}]_{(R+1)}^{\text{T}}$ , we can express  $[\varphi(\mathbf{Z})]_{(R+1)}^{\text{T}}$  as

$$[\varphi(\mathbf{Z})]_{(R+1)}^{\text{T}} = \mathbf{Q}_M^{\text{H}} \cdot \begin{bmatrix} \mathbf{X} & \mathbf{\Pi}_M \cdot \mathbf{X}^* \cdot \mathbf{\Pi}_N \end{bmatrix} \cdot \mathbf{Q}_{2N}. \quad (9.25)$$

Recall that  $\varphi(\mathbf{Z})$  is defined via (9.15) and (9.16), leading to the observation that

$$\varphi(\mathbf{Z}) = [\varphi(\mathbf{Z})]_{(R+1)}^{\text{T}}. \quad (9.26)$$

As a real-valued equivalent to Theorem 1, we have

$$\left[ \hat{\mathcal{E}}^{[s]} \right]_{(R+1)}^T = \left( \hat{\mathbf{T}}_1' \otimes \hat{\mathbf{T}}_2' \dots \otimes \hat{\mathbf{T}}_R' \right) \cdot \hat{\mathbf{E}}_s, \quad (9.27)$$

where the columns of  $\hat{\mathbf{E}}_s \in \mathbb{R}^{M \times d}$  represent a real-valued orthonormal basis for the estimated signal subspace in the matrix-based case. The proof proceeds along the lines of the proof of Theorem 9.3.1 in Appendix F and [RHD14].

Hence, (9.27) indicates that the real-valued tensor-based subspace estimate can be computed by applying a Kronecker-structured projection to the real-valued matrix-based subspace estimate similar to the complex-valued case. The calculation of the core tensor is also not required. Note that the obtained real-valued tensor-based subspace estimate can be employed in the Unitary Tensor-ESPRIT algorithm [HRD08] for parameter estimation in multidimensional harmonic retrieval problems. We show the corresponding numerical results in Section 9.5.

To summarize, in case that forward-backward-averaging is incorporated, the TeTraKron framework can be employed to extend a matrix-based subspace tracking scheme to tensors such that real-valued tensor-based subspace tracking is realized. For each new snapshot, a forward-backward-averaged version of the measurement tensor is mapped to a real-valued tensor similarly as (9.12) and (9.13). Then, any matrix-based subspace tracker can be run on all unfoldings of this tensor in parallel where only real-valued computations are involved. Finally, the real-valued subspace estimate is obtained via a recombination procedure such as (9.27)<sup>2</sup>. In Section 9.4, where the matrix-based algorithms PAST, PASTd [Yan95b], and FAPI [BDR05] are used as examples, we explain explicitly how real-valued tensor-based subspace tracking based on the TeTraKron framework is performed.

## 9.4. Examples

In this section we provide examples of how the TeTraKron framework can be used to devise tensor-based subspace tracking schemes. Since TeTraKron allows us to extend an arbitrary matrix-based subspace tracking scheme to the tensor case we choose three examples, namely the simple but widely used PAST and PASTd algorithms [Yan95b] as well as the FAPI scheme [BDR05] that is a fast implementation of the power iteration method for subspace tracking. Since an exponential window is used in PAST, PASTd, and FAPI, it also applies to their corresponding tensor extensions.

---

<sup>2</sup>Alternatively, after tracking the  $r$ -mode subspaces, a projected lower-dimensional subspace similar to  $\hat{\mathbf{U}}_s$  can be tracked, and a recombination procedure similar to (9.11) can be used, leading to a reduced complexity.



### 9.4.1. Tensor-based PAST/PASTd

The PAST algorithm for tracking the signal subspace is summarized in Table 9.1, where  $\mathbf{x}(n) \in \mathbb{C}^M$  is the new measurement vector at time  $n$ ,  $\mathbf{P}(n)$  corresponds to the inverse of the correlation matrix of the projected vector  $\mathbf{y}(n) = \hat{\mathbf{U}}_s^H(n) \cdot \mathbf{x}(n) \in \mathbb{C}^d$ , which is approximated as  $\mathbf{y}(n) = \hat{\mathbf{U}}_s^H(n-1) \cdot \mathbf{x}(n) \in \mathbb{C}^d$ . Moreover,  $\mathbf{g}(n)$  is the gain vector and  $\beta$  the forgetting factor of

$\mathbf{P}(0) = \mathbf{I}_d, \hat{\mathbf{U}}_s(0) = \mathbf{I}_{M \times d}$
FOR $n = 1, 2, \dots$ DO
$\begin{aligned} \mathbf{y}(n) &= \hat{\mathbf{U}}_s^H(n-1) \cdot \mathbf{x}(n) \\ \mathbf{h}(n) &= \mathbf{P}(n-1) \cdot \mathbf{y}(n) \\ \mathbf{g}(n) &= \mathbf{h}(n) / (\beta + \mathbf{y}^H(n) \cdot \mathbf{h}(n)) \\ \mathbf{P}(n) &= \beta^{-1} \cdot \text{Tri}\{\mathbf{P}(n-1) - \mathbf{g}(n) \cdot \mathbf{h}^H(n)\} \\ \mathbf{e}(n) &= \mathbf{x}(n) - \hat{\mathbf{U}}_s(n-1) \cdot \mathbf{y}(n) \\ \hat{\mathbf{U}}_s(n) &= \hat{\mathbf{U}}_s(n-1) + \mathbf{e}(n) \cdot \mathbf{g}^H(n) \end{aligned}$
END

Table 9.1.: Summary of the PAST algorithm [Yan95b]

the underlying RLS procedure. Finally,  $\mathbf{e}(n)$  is the approximation error and  $\mathbf{I}_{M \times d}$  symbolizes the first  $d$  columns of an  $M \times M$  identity matrix. Here the operator  $\text{Tri}\{\cdot\}$  computes the upper/lower triangular part of its input matrix and copies its Hermitian transpose to the other lower/upper triangular part such that the Hermitian symmetry property of the input matrix is preserved. Alternatively, in our simulations we implement  $\text{Tri}\{\cdot\}$  as

$$\text{Tri}\{\mathbf{A}\} = \frac{\mathbf{A} + \mathbf{A}^H}{2}, \quad (9.28)$$

where  $\mathbf{A}$  is assumed to be the input matrix.

Recall that the data tensor observed at each new snapshot  $\mathcal{X}(n) \in \mathbb{C}^{M_1 \times M_2 \times \dots \times M_R}$  is a rearranged version of  $\mathbf{x}(n) \in \mathbb{C}^{M \times 1}$ . In the TeTraKron extension of PAST we apply the same algorithm to all unfoldings of  $\mathcal{X}(n)$ , i.e.,  $[\mathcal{X}(n)]_{(r)} \in \mathbb{C}^{M_r \times \frac{M}{M_r}}$ ,  $r = 1, 2, \dots, R$ . For instance, in the  $R = 2$ -dimensional case, our data tensor  $\mathcal{X}$  is of size  $M_1 \times M_2 \times N$ . With each new observation vector  $\mathbf{x}(n) \in \mathbb{C}^{M_1 \cdot M_2 \times 1}$  we obtain a new matrix of observations for the 1-space and the 2-space of  $\mathcal{X}$  which is given by  $\tilde{\mathbf{X}}(n) \in \mathbb{C}^{M_1 \times M_2}$  for  $[\mathcal{X}]_{(1)}$  and  $\tilde{\mathbf{X}}^T(n)$  for  $[\mathcal{X}]_{(2)}$ . Note that  $\tilde{\mathbf{X}}(n)$  is a rearranged version of  $\mathbf{x}(n)$  which satisfies  $\text{vec}\{\tilde{\mathbf{X}}(n)\} = \mathbf{x}(n)$ .

Since PAST is based on RLS, it can be modified to process the entire new batch of observations at the same time. The modified update equations for the  $r$ -mode unfolding  $[\mathcal{X}(n)]_{(r)} \in \mathbb{C}^{M_r \times \frac{M}{M_r}}$  become

$$\mathbf{Y}_r(n) = \hat{\mathbf{U}}_r^{[s]H}(n-1) \cdot [\mathcal{X}(n)]_{(r)} \in \mathbb{C}^{d \times \frac{M}{M_r}} \quad (9.29)$$

$$\mathbf{H}_r(n) = \mathbf{P}_r(n-1) \cdot \mathbf{Y}_r(n) \in \mathbb{C}^{d \times \frac{M}{M_r}} \quad (9.30)$$

$$\mathbf{G}_r(n) = \mathbf{H}_r(n) \cdot \left( \beta \cdot \mathbf{I}_{M/M_r} + \mathbf{Y}_r^H(n) \cdot \mathbf{H}_r(n) \right)^{-1} \quad (9.31)$$

$$\mathbf{P}_r(n) = \beta^{-1} \cdot \text{Tri}\{\mathbf{P}_r(n-1) - \mathbf{G}_r(n) \cdot \mathbf{H}_r^H(n)\} \quad (9.32)$$

$$\mathbf{F}_r(n) = [\mathcal{X}(n)]_{(r)} - \hat{\mathbf{U}}_r^{[s]}(n-1) \cdot \mathbf{Y}_r(n) \quad (9.33)$$

$$\hat{\mathbf{U}}_r^{[s]}(n) = \hat{\mathbf{U}}_r^{[s]}(n-1) + \mathbf{F}_r(n) \cdot \mathbf{G}_r^H(n). \quad (9.34)$$

Notice that to process the batch of  $\frac{M}{M_r}$  columns, the inverse of a  $\frac{M}{M_r} \times \frac{M}{M_r}$  matrix is involved. Especially for  $R > 2$ , it is usually true that  $d < \frac{M}{M_r}$ . In such cases, it becomes computationally more efficient to update the  $d \times d$  correlation matrix of  $\mathbf{Y}_r(n)$  given by

$$\mathbf{C}_{y_r y_r}(n) = \beta \cdot \mathbf{C}_{y_r y_r}(n-1) + \mathbf{Y}_r(n) \cdot \mathbf{Y}_r^H(n), \quad (9.35)$$

and directly calculate its inverse  $\mathbf{P}_r(n) = \mathbf{C}_{y_r y_r}^{-1}(n)$ . Multiplying  $\left( \beta \cdot \mathbf{I}_{M/M_r} + \mathbf{Y}_r^H(n) \cdot \mathbf{H}_r(n) \right)$  to the right of both sides of (9.31) yields

$$\mathbf{G}_r(n) \cdot \left( \beta \cdot \mathbf{I}_{M/M_r} + \mathbf{Y}_r^H(n) \cdot \mathbf{H}_r(n) \right) = \mathbf{H}_r(n). \quad (9.36)$$

Then,  $\mathbf{G}_r(n)$  is expressed as

$$\mathbf{G}_r(n) = \beta^{-1} \cdot \left( \mathbf{H}_r(n) - \mathbf{G}_r(n) \cdot \mathbf{Y}_r^H(n) \cdot \mathbf{H}_r(n) \right). \quad (9.37)$$

Substituting (9.30) into (9.37) gives

$$\begin{aligned} \mathbf{G}_r(n) &= \beta^{-1} \cdot \left( \mathbf{P}_r(n-1) - \mathbf{G}_r(n) \cdot \mathbf{Y}_r^H(n) \cdot \mathbf{P}_r(n-1) \right) \cdot \mathbf{Y}_r(n) \\ &= \beta^{-1} \cdot \left( \mathbf{P}_r(n-1) - \mathbf{G}_r(n) \cdot \mathbf{H}_r^H(n) \right) \cdot \mathbf{Y}_r(n). \end{aligned} \quad (9.38)$$

Knowing that

$$\mathbf{C}_{y_r y_r}^{-1}(n) = \mathbf{P}_r(n) = \beta^{-1} \cdot \left( \mathbf{P}_r(n-1) - \mathbf{G}_r(n) \cdot \mathbf{H}_r^H(n) \right), \quad (9.39)$$

while the operation  $\text{Tri}\{\cdot\}$  in (9.32) is only employed to preserve the Hermitian symmetry of  $\mathbf{P}_r(n)$  in the presence of rounding errors [Yan95b],  $\mathbf{G}_r(n)$  is alternatively updated as

$$\mathbf{G}_r(n) = \mathbf{C}_{y_r y_r}^{-1}(n) \cdot \mathbf{Y}_r(n). \quad (9.40)$$

Equations (9.30), (9.31), and (9.32) are replaced by (9.35) and (9.40). Therefore, the inverse of the  $d \times d$  correlation matrix  $\mathbf{C}_{y_r y_r}(n)$  is computed instead of the  $\frac{M}{M_r} \times \frac{M}{M_r}$  matrix inversion in (9.31). This leads to a reduced computational complexity for  $d < \frac{M}{M_r}$ . In addition, we discuss how to further avoid the  $d \times d$  inversion in Appendix G, where a computational complexity analysis is included as well. To this end, the tensor-based PAST scheme for updating the  $r$ -mode subspace estimates is summarized in Table 9.2.

IF $d < \frac{M}{M_r}$ DO
$\begin{aligned} \mathbf{Y}_r(n) &= \hat{\mathbf{U}}_r^{[s]H}(n-1) \cdot [\mathcal{X}(n)]_{(r)} \\ \mathbf{C}_{y_r y_r}(n) &= \beta \cdot \mathbf{C}_{y_r y_r}(n-1) + \mathbf{Y}_r(n) \cdot \mathbf{Y}_r^H(n) \\ \mathbf{G}_r(n) &= \mathbf{C}_{y_r y_r}^{-1}(n) \cdot \mathbf{Y}_r(n) \\ \mathbf{F}_r(n) &= [\mathcal{X}(n)]_{(r)} - \hat{\mathbf{U}}_r^{[s]}(n-1) \cdot \mathbf{Y}_r(n) \\ \hat{\mathbf{U}}_r^{[s]}(n) &= \hat{\mathbf{U}}_r^{[s]}(n-1) + \mathbf{F}_r(n) \cdot \mathbf{G}_r^H(n) \end{aligned}$
ELSE
$\begin{aligned} \mathbf{Y}_r(n) &= \hat{\mathbf{U}}_r^{[s]H}(n-1) \cdot [\mathcal{X}(n)]_{(r)} \\ \mathbf{H}_r(n) &= \mathbf{P}_r(n-1) \cdot \mathbf{Y}_r(n) \\ \mathbf{G}_r(n) &= \mathbf{H}_r(n) \cdot \left( \beta \cdot \mathbf{I}_{M/M_r} + \mathbf{Y}_r^H(n) \cdot \mathbf{H}_r(n) \right)^{-1} \\ \mathbf{P}_r(n) &= \beta^{-1} \cdot \text{Tri}\{\mathbf{P}_r(n-1) - \mathbf{G}_r(n) \cdot \mathbf{H}_r^H(n)\} \\ \mathbf{F}_r(n) &= [\mathcal{X}(n)]_{(r)} - \hat{\mathbf{U}}_r^{[s]}(n-1) \cdot \mathbf{Y}_r(n) \\ \hat{\mathbf{U}}_r^{[s]}(n) &= \hat{\mathbf{U}}_r^{[s]}(n-1) + \mathbf{F}_r(n) \cdot \mathbf{G}_r^H(n) \end{aligned}$
END

Table 9.2.: Summary of the tensor-based PAST algorithm for updating the  $r$ -mode subspace estimates

The deflation-based version of PAST, PASTd [Yan95b], is presented in Table 9.3. It is an extension of the PAST approach based on the deflation technique whose basic idea is

$\hat{\mathbf{U}}_s(0) = \mathbf{I}_{M \times d}, \quad \mathbf{d}(0) = \mathbf{1}_{d \times 1}$
FOR $n = 1, 2, \dots$ DO
$\mathbf{x}_1(n) = \mathbf{x}(n)$
FOR $i = 1, 2, \dots, d$ DO
$y_i(n) = \hat{\mathbf{u}}_i^H(n-1) \cdot \mathbf{x}_i(n)$
$d_i(n) = \beta \cdot d_i(n-1) +  y_i(n) ^2$
$\mathbf{e}_i(n) = \mathbf{x}_i(n) - \hat{\mathbf{u}}_i(n-1) \cdot y_i(n)$
$\hat{\mathbf{u}}_i(n) = \hat{\mathbf{u}}_i(n-1) + \mathbf{e}_i(n) \cdot (y_i^*(n)/d_i(n))$
$\mathbf{x}_{i+1}(n) = \mathbf{x}_i(n) - \hat{\mathbf{u}}_i(n) \cdot y_i(n)$
END
END

Table 9.3.: Summary of the PASTd algorithm [Yan95b] where  $\hat{\mathbf{u}}_i(n)$  represents the  $i$ -th column of  $\hat{\mathbf{U}}_s(n)$ , and  $d_i(n)$  is the  $i$ -th element of  $\mathbf{d}(n)$

the sequential estimation of the principal components [Yan95b]. In fact, it has been pointed out in [Yan95b] that the main body of the second **FOR** loop in Table 9.3 can be regarded as a special case of the PAST algorithm where  $d = 1$ . The PASTd scheme computes the eigenvectors explicitly, i.e.,  $\hat{\mathbf{u}}_i(n)$  is an estimate of the  $i$ -th eigenvector of the correlation matrix of the measurement data, and  $d_i(n)$  is an exponentially weighted estimate of the corresponding eigenvalue. Since PASTd is also based on RLS, it can be modified in the same manner as PAST such that a tensor-based version is obtained. We summarize the tensor-based PASTd algorithm for updating the  $r$ -mode subspace estimates in Table 9.4, where  $\hat{\mathbf{u}}_{r,i}^{[s]}(n)$  denotes the  $i$ th column of  $\hat{\mathbf{U}}_r^{[s]}(n) \in \mathbb{C}^{M_r \times d}$ , and  $d_{r,i}(n)$  represents the  $i$ th entry of  $\mathbf{d}_r(n) \in \mathbb{R}^d$ . The initial values of the eigenvalue estimates in  $\mathbf{d}_r(n)$  are chosen to be one [Yan95b], i.e.,  $\mathbf{d}_r(0)$  is an all-ones vector.

When forward-backward-averaging is incorporated, each new observation vector  $\mathbf{x}(n)$  is augmented by a new virtual column. In the matrix-based case, the real-valued subspace estimate  $\hat{\mathbf{E}}_s(n)$  is obtained by applying the PAST algorithm to

$$\varphi(\mathbf{Z}(n)) = \mathbf{Q}_M^H \cdot \mathbf{Z}(n) \cdot \mathbf{Q}_{2\in} \in \mathbb{R}^{M \times 2}, \quad (9.41)$$

$\bar{\mathbf{X}}_{r,1}(n) = [\mathbf{X}(n)]_{(r)}, \quad \mathbf{d}_r(0) = \mathbf{1}_{d \times 1}$
<p>FOR <math>i = 1, 2, \dots, d</math> DO</p>
$\mathbf{y}_{r,i}^T(n) = \hat{\mathbf{u}}_{r,i}^{[s]H}(n-1) \cdot \bar{\mathbf{X}}_{r,i}(n)$
$d_{r,i}(n) = \beta \cdot d_{r,i}(n-1) + \ \mathbf{y}_{r,i}(n)\ ^2$
$\mathbf{F}_{r,i}(n) = \bar{\mathbf{X}}_{r,i}(n) - \hat{\mathbf{u}}_{r,i}^{[s]}(n-1) \cdot \mathbf{y}_{r,i}^T(n)$
$\hat{\mathbf{u}}_{r,i}^{[s]}(n) = \hat{\mathbf{u}}_{r,i}^{[s]}(n-1) + \mathbf{F}_{r,i}(n) \cdot (\mathbf{y}_{r,i}^*(n)/d_{r,i}(n))$
$\bar{\mathbf{X}}_{r,i+1}(n) = \bar{\mathbf{X}}_{r,i}(n) - \hat{\mathbf{u}}_{r,i}^{[s]}(n) \cdot \mathbf{y}_{r,i}^T(n)$
<p>END</p>

Table 9.4.: Summary of the tensor-based version of the PASTd algorithm for updating the  $r$ -mode subspace estimates

where  $\mathbf{Z}(n)$  is a forward-backward-averaged version of  $\mathbf{x}(n)$  given by

$$\mathbf{Z}(n) = \begin{bmatrix} \mathbf{x}(n) & \mathbf{\Pi}_M \cdot \mathbf{x}^*(n) \end{bmatrix} \in \mathbb{C}^{M \times 2}. \quad (9.42)$$

Note that  $\mathbf{Q}_M$  and  $\mathbf{Q}_2$  are unitary left- $\mathbf{\Pi}$  real matrices an example of which is given in (9.14).

In the tensor-based case, a real-valued tensor  $\varphi(\mathbf{Z}(n)) \in \mathbb{R}^{M_1 \times M_2 \times \dots \times M_R \times 2}$  is computed by using  $N = 1$  in (9.13)

$$\varphi(\mathbf{Z}(n)) = \mathbf{Z}(n) \times_1 \mathbf{Q}_{M_1}^H \times_2 \mathbf{Q}_{M_2}^H \cdots \times_{R+1} \mathbf{Q}_2^T, \quad (9.43)$$

where  $\mathbf{Z}(n)$  is a forward-backward-averaged version of  $\mathbf{X}(n)$

$$\mathbf{Z}(n) = [\mathbf{X}(n) \sqcup_{R+1} [\mathbf{X}^*(n) \times_1 \mathbf{\Pi}_{M_1} \times_2 \mathbf{\Pi}_{M_2} \cdots \times_R \mathbf{\Pi}_{M_R}]] \in \mathbb{C}^{M_1 \times M_2 \times \dots \times M_R \times 2}. \quad (9.44)$$

In the new real-valued tensor-based subspace tracking scheme that is an extension of PAST based on the TeTraKron framework, we run the PAST algorithm on all unfoldings of the real-valued tensor  $\varphi(\mathbf{Z}(n))$  in parallel. For the  $r$ -mode unfolding  $[\varphi(\mathbf{Z}(n))]_{(r)} \in \mathbb{R}^{M_r \times 2 \cdot \frac{M}{M_r}}$  where  $p_r < M_r$ , the update equations where only real-valued computations are involved are as follows

$$\mathbf{Y}_r(n) = \hat{\mathbf{E}}_r^{[s]T}(n-1) \cdot [\varphi(\mathbf{Z}(n))]_{(r)} \quad (9.45)$$

$$\mathbf{C}_{y_r y_r}(n) = \beta \cdot \mathbf{C}_{y_r y_r}(n-1) + \mathbf{Y}_r(n) \cdot \mathbf{Y}_r^T(n) \quad (9.46)$$

$$\mathbf{G}_r(n) = \mathbf{C}_{y_r y_r}^{-1}(n-1) \cdot \mathbf{Y}_r(n) \quad (9.47)$$

$$\mathbf{F}_r(n) = [\varphi(\mathcal{Z}(n))]_{(r)} - \hat{\mathbf{E}}_r^{[s]}(n-1) \cdot \mathbf{Y}_r(n) \quad (9.48)$$

$$\hat{\mathbf{E}}_r^{[s]}(n) = \hat{\mathbf{E}}_r^{[s]}(n-1) + \mathbf{F}_r(n) \cdot \mathbf{G}_r^T(n). \quad (9.49)$$

Afterwards, the real-valued signal subspace estimate can be recombined via<sup>3</sup> (9.27).

#### 9.4.2. Tensor-based FAPI

As an additional example of how to apply the TeTraKron framework to extend a matrix-based subspace tracker to the tensor case, we consider the exponential window FAPI algorithm [BDR05]. As before, to update the  $r$ -mode subspace estimate, the matrix-based subspace tracker has to be modified to process a batch of  $\frac{M}{M_r}$  observations. This can be carried out at the same time as in the aforementioned example of the extended PAST algorithm. Alternatively, each column of the  $r$ -mode unfolding of  $\mathcal{X}(n)$  can be treated as a new observation vector, and the columns are processed sequentially<sup>4</sup>. The  $r$ -mode subspace estimates can be updated via exactly the same procedures as in the matrix-based subspace tracking scheme. However, only when the first column of the  $r$ -mode unfolding of  $\mathcal{X}(n)$  is used as an equivalent new observation vector, the forgetting factor stays the same as that used in the matrix-based subspace tracking algorithm at each snapshot. Starting from the second column that is treated as the second equivalent observation vector, the forgetting factor is set to one. In the following, we explain in detail how this approach is applied to obtain a tensor-based version of the exponential window FAPI algorithm [BDR05] via the TeTraKron framework. Denote the  $\ell$ -th column of the  $r$ -mode unfolding  $[\mathcal{X}(n)]_{(r)} \in \mathbb{C}^{M_r \times \frac{M}{M_r}}$  as  $\mathbf{x}_\ell^{(r)} \in \mathbb{C}^{M_r}$ , where  $\ell = 1, 2, \dots, \frac{M}{M_r}$ . The details on updating  $\hat{\mathbf{U}}_r^{[s]}$  are given in Table 9.5. For each snapshot, after obtaining  $\hat{\mathbf{U}}_r^{[s]}$  ( $r = 1, 2, \dots, R$ ) via the procedures in Table 9.5 and the matrix-based subspace estimate  $\hat{\mathbf{U}}_s$  by employing exponential window FAPI [BDR05], we recombine them via (9.10) to obtain the tensor-based subspace estimate  $\left[\hat{\mathbf{U}}^{[s]}\right]_{(R+1)}^T$ .

In case that forward-backward-averaging is incorporated, similar procedures as in Table 9.5

---

<sup>3</sup>As an alternative, after tracking the real-valued  $r$ -mode subspaces, a projected lower-dimensional subspace similar to  $\hat{\mathbf{U}}_s$  can be tracked, and a recombination procedure similar to (9.11) can be used. This leads to a reduced complexity.

<sup>4</sup>Both approaches, namely the batch processing and the sequential processing, can be employed in the tensor-based PAST algorithm. We have performed simulations to compare these two methods. It has been observed that when they are used to modify the PAST algorithm to update the  $r$ -mode subspace estimates, they lead to the same performance. It should be noted that for some state-of-the-art matrix-based subspace tracking schemes, such as the exponential window FAPI algorithm [BDR05], they have been developed based on the fact that each new observation takes the form of a column vector. Compared to the batch processing, this important feature is better preserved in the sequential processing. Consequently, when extending these schemes to the tensor case via TeTraKron, it is more convenient to use the sequential processing.

$\mathbf{P}'_r(0) = \mathbf{P}_r(n-1) \in \mathbb{C}^{d \times d}, \hat{\mathbf{U}}'_r(0) = \hat{\mathbf{U}}_r^{[s]}(n-1) \in \mathbb{C}^{M_r \times d}$
<p>FOR <math>\ell = 1, 2, \dots, \frac{M}{M_r}</math> DO</p>
<p>    IF <math>\ell = 1</math></p>
<p>        <math>\beta' = \beta</math></p>
<p>    ELSE</p>
<p>        <math>\beta' = 1</math></p>
<p>        <u>exponential window FAPI [BDR05]</u></p>
$\mathbf{y}_r(\ell) = \hat{\mathbf{U}}_r'^H(\ell-1) \cdot \mathbf{x}_\ell^{(r)}$
$\mathbf{h}_r(\ell) = \mathbf{P}'_r(\ell-1) \cdot \mathbf{y}_r(\ell)$
$\mathbf{g}_r(\ell) = \mathbf{h}_r(\ell) / (\beta' + \mathbf{y}_r^H(\ell) \cdot \mathbf{h}_r(\ell))$
$\epsilon_r^2(\ell) = \ \mathbf{x}_\ell^{(r)}\ ^2 - \ \mathbf{y}_r(\ell)\ ^2$
$\tau_r(\ell) = \frac{\epsilon_r^2(\ell)}{1 + \epsilon_r^2(\ell) \cdot \ \mathbf{g}_r(\ell)\ ^2 + \sqrt{1 + \epsilon_r^2(\ell) \cdot \ \mathbf{g}_r(\ell)\ ^2}}$
$\eta_r(\ell) = 1 - \tau_r(\ell) \cdot \ \mathbf{g}_r(\ell)\ ^2$
$\mathbf{y}'_r(\ell) = \eta_r(\ell) \cdot \mathbf{y}_r(\ell) + \tau_r(\ell) \cdot \mathbf{g}_r(\ell)$
$\mathbf{h}'_r(\ell) = \mathbf{P}_r'^H(\ell-1) \cdot \mathbf{y}'_r(\ell)$
$\epsilon_r(\ell) = \frac{\tau_r(\ell)}{\eta_r(\ell)} \cdot \left( \mathbf{P}'_r(\ell-1) \cdot \mathbf{g}_r(\ell) - \left( \mathbf{h}_r'^H(\ell) \cdot \mathbf{g}_r(\ell) \right) \cdot \mathbf{g}_r(\ell) \right)$
$\mathbf{P}'_r(\ell) = \frac{1}{\beta'} \cdot \left( \mathbf{P}'_r(\ell-1) - \mathbf{g}_r(\ell) \cdot \mathbf{h}_r'^H(\ell) + \epsilon_r(\ell) \cdot \mathbf{g}_r^H(\ell) \right)$
$\mathbf{e}'_r(\ell) = \eta_r(\ell) \cdot \mathbf{x}_\ell^{(r)} - \hat{\mathbf{U}}_r'(\ell-1) \cdot \mathbf{y}'_r(\ell)$
$\hat{\mathbf{U}}_r'(\ell) = \hat{\mathbf{U}}_r'(\ell-1) + \mathbf{e}'_r(\ell) \cdot \mathbf{g}_r^H(\ell)$
<p>END</p>
$\mathbf{P}_r(n) = \mathbf{P}'_r(\frac{M}{M_r}), \hat{\mathbf{U}}_r^{[s]}(n) = \hat{\mathbf{U}}_r'(\frac{M}{M_r})$

Table 9.5.: Summary of the tensor-based version of the exponential window FAPI algorithm [BDR05] for updating the  $r$ -mode subspace estimates

are employed on the  $r$ -mode unfolding of the real-valued tensor,  $[\varphi(\mathbf{Z}(n))]_{(r)} \in \mathbb{R}^{M_r \times 2 \cdot \frac{M}{M_r}}$ , to update the real-valued estimate of the  $r$ -mode subspace  $\hat{\mathbf{E}}_r^{[s]}$ , i.e.,  $\hat{\mathbf{U}}_r^{[s]}(n-1)$ ,  $\frac{M}{M_r}$ , and  $\mathbf{x}_\ell^{(r)}$  in Table 9.5 are replaced by  $\hat{\mathbf{E}}_r^{[s]}(n-1)$ ,  $2 \cdot \frac{M}{M_r}$ , and the  $\ell$ -th column of  $[\varphi(\mathbf{Z}(n))]_{(r)}$ , where  $\ell = 1, 2, \dots, 2 \cdot \frac{M}{M_r}$ , respectively. Then, the real-valued signal subspace estimate can be recombined via (9.27).

### 9.4.3. Summary of the proposed tensor-based subspace tracking schemes

To this end, we summarize the tensor-based subspace tracking algorithms developed via the TeTraKron framework in Table 9.6 and Table 9.7. For the schemes<sup>5</sup> that have been employed in the simulations (cf. Section 9.5), the corresponding equations are specified. It is worth noting that one example of the multi-dimensional harmonic retrieval problems where the real-valued subspace tracking schemes with forward-backward-averaging are recommended is the case of parameter estimation with centro-symmetric arrays [HN95], e.g., Uniform Rectangular Arrays (URAs).

## 9.5. Simulation results

In this section we first demonstrate the performance of the tensor extension of PAST and PASTd achieved via the proposed TeTraKron framework. To this end, we choose a simulation scenario that represents an extension of the one shown in [Yan95b] to  $R = 2$  dimensions. We consider a URA with  $d = 3$  impinging wavefronts. The first two sources are moved by changing their spatial frequencies (direction cosines) as a function of the time index  $n = 1, 2, \dots, N$  according to

$$\begin{aligned} \mu_1^{(1)}[n] &= 0.3 - 0.1 \cdot t[n], \quad \mu_2^{(1)}[n] = 0.2 + 0.1 \cdot t[n], \\ \mu_1^{(2)}[n] &= 0.2 + 0.1 \cdot t[n], \quad \mu_2^{(2)}[n] = 0.2 + 0.1 \cdot t[n], \end{aligned}$$

for  $t[n] = \frac{n-1}{N-1}$ , whereas the third source remains stationary at  $\mu_3^{(1)} = \mu_3^{(2)} = 0.1$ . Therefore, for  $n$  close to  $N/2$  the first and the second sources cross. Note that  $\mu_i^{(r)}$  represents the spatial

---

<sup>5</sup>TeTraKron-PAST, TeTraKron-PASTd, and TeTraKron-FAPI refer to the tensor extensions of PAST [Yan95b], PASTd [Yan95b], and FAPI [BDR05] via the proposed TeTraKron framework based on (9.10), respectively. In case of the reduced-complexity version (9.11), the corresponding tensor extensions of PAST and PASTd are called TeTraKron-PAST II and TeTraKron-PASTd II, respectively. In addition, we use “TeTraKron-PAST with FBA” and “TeTraKron-FAPI with FBA” to refer to the real-valued subspace tracking schemes as tensor extensions of PAST and FAPI, respectively. Here the TeTraKron framework based on (9.27) is applied, and forward-backward-averaging is incorporated.



**Initialization:**

$$\hat{\mathbf{U}}_s(0) = \mathbf{I}_{M \times d}$$

$$\hat{\mathbf{U}}_r^{[s]}(0) = \mathbf{I}_{M_r \times d} \text{ for } r = 1, 2, \dots, R$$

TeTraKron-PAST / TeTraKron-PAST II:  $\mathbf{P}(0) = \mathbf{I}_d$ ,  $\mathbf{C}_{y_r y_r}(0) = \mathbf{I}_d$  for  $r = 1, 2, \dots, R$

TeTraKron-PASTd / TeTraKron-PASTd II: initialize  $\mathbf{d}(0)$  and  $\mathbf{d}_r(0)$  ( $r = 1, 2, \dots, R$ ) as  $d$ -dimensional all-ones vectors

TeTraKron-FAPI:  $\mathbf{P}(0) = \mathbf{I}_d$ ,  $\mathbf{P}_r(0) = \mathbf{I}_d$  for  $r = 1, 2, \dots, R$

FOR  $n = 1, 2, \dots$  DO

**Step 1:** Update the  $r$ -mode subspace estimates  $\hat{\mathbf{U}}_r^{[s]}(n)$  ( $r = 1, 2, \dots, R$ ) in parallel

**Step 2:** Update the matrix-based subspace estimate  $\hat{\mathbf{U}}_s(n)$  or  $\hat{\hat{\mathbf{U}}}_s(n)$

**Step 3:** Update the tensor-based subspace estimate  $\left[ \hat{\mathbf{u}}^{[s]}(n) \right]_{(R+1)}^T$

	Step 1	Step 2	Step 3
TeTraKron-PAST	Table 9.2	Table 9.1 or [Yan95b]	equation (9.10)
TeTraKron-PASTd	Table 9.4	[Yan95b]	
TeTraKron-FAPI	Table 9.5	[BDR05]	
TeTraKron-PAST II	equations (9.29), (9.35), (9.40), (9.33), and (9.34)	Table 9.1 or [Yan95b]	equation (9.11)
TeTraKron-PASTd II	Table 9.4	[Yan95b]	

END

Table 9.6.: Summary of TeTraKron-PAST, TeTraKron-PASTd, TeTraKron-PAST II, TeTraKron-PASTd II, and TeTraKron-FAPI

**Initialization:**

$$\hat{\mathbf{E}}_s(0) = \mathbf{I}_{M \times d}$$

$$\hat{\mathbf{E}}_r^{[s]}(0) = \mathbf{I}_{M_r \times d} \text{ for } r = 1, 2, \dots, R$$

$$\text{TeTraKron-PAST with FBA: } \mathbf{P}(0) = \mathbf{I}_d, \mathbf{C}_{y_r y_r}(0) = \mathbf{I}_d \text{ for } r = 1, 2, \dots, R$$

$$\text{TeTraKron-FAPI with FBA: } \mathbf{P}(0) = \mathbf{I}_d, \mathbf{P}_r(0) = \mathbf{I}_d \text{ for } r = 1, 2, \dots, R$$

FOR  $n = 1, 2, \dots$  DO

**Step 1:** Calculate the real-valued tensor  $\varphi(\mathbf{Z}(n))$  via (9.43) and (9.44)

**Step 2:** Update the real-valued  $r$ -mode subspace estimates  $\hat{\mathbf{E}}_r^{[s]}(n)$  ( $r = 1, 2, \dots, R$ ) in parallel

**Step 3:** Update the real-valued matrix-based subspace estimate  $\hat{\mathbf{E}}_s(n)$

**Step 4:** Update the real-valued tensor-based subspace estimate  $\left[ \hat{\mathcal{E}}^{[s]}(n) \right]_{(R+1)}^T$

	Step 1	Step 2	Step 3	Step 4
TeTraKron-PAST with FBA	equations (9.43) and (9.44)	equations (9.45) – (9.49)	Table 9.1 or [Yan95b]	equation (9.27)
TeTraKron-FAPI with FBA		Table 9.5	[BDR05]	

END

Table 9.7.: Summary of TeTraKron-PAST with FBA and TeTraKron-FAPI with FBA

frequency of the  $i$ -th source in the  $r$ -th dimension for  $i = 1, 2, \dots, d$  and  $r = 1, 2, \dots, R$ . The total number of snapshots  $N$  is set to 1000 in all examples. In Figure 9.1, we depict this crossing scenario. The source samples as well as the noise samples are drawn from a zero

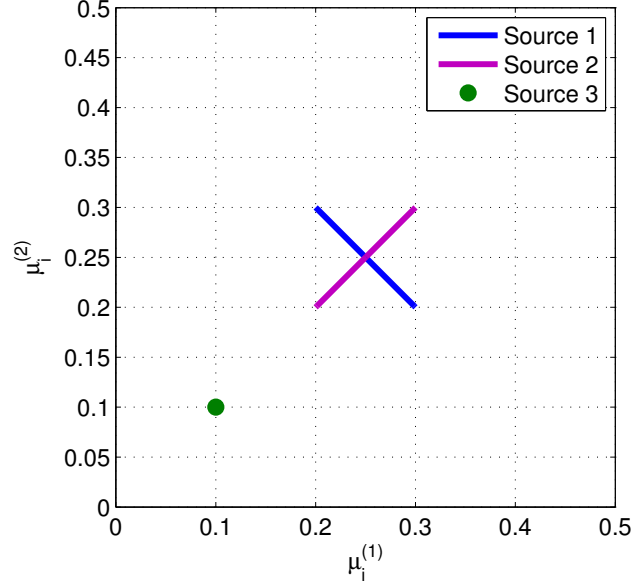


Figure 9.1.: Illustration of the spatial frequencies of the three sources over the course of 1000 snapshots. The first two sources cross, whereas the third source stays stationary

mean circularly symmetric complex Gaussian distribution with variance one (SNR = 0 dB). We choose the forgetting factor  $\beta = 0.97$  for all examples shown in this section. Similar to [Yan95b], we compare the algorithms based on the Largest Principal Angle (LPA) between the true and the estimated signal subspace since the LPA provides a measure for the agreement of the subspaces which is invariant to the particular choice of the basis. Figure 9.2 shows the LPA for a  $9 \times 9$  URA. The curve labeled “PAST” refers to the original matrix-based PAST algorithm from [Yan95b]. As summarized in Section 9.4.3, TeTraKron-PAST and TeTraKron-PAST II refer to the tensor extensions of PAST via the proposed TeTraKron framework based on (9.10) and the reduced-complexity version (9.11), respectively. For reference we display two curves labeled “SVD” and “HOSVD” where the entire matrix/tensor of observations<sup>6</sup> up to the current snapshot  $n$  is used to calculate a subspace estimate via the SVD and the HOSVD, respectively. In Figure 9.3 we replace PAST by PASTd. Moreover, we change the array size

<sup>6</sup>To render the comparison to the adaptive RLS-based schemes fair, the exponential weighting with a forgetting factor  $\beta$  is also applied here.

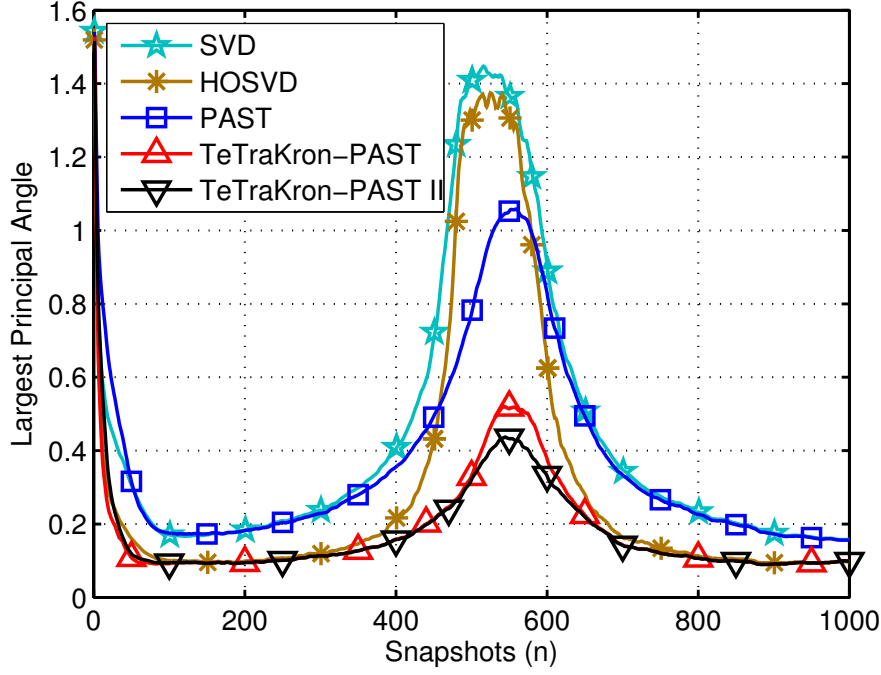


Figure 9.2.: LPA (in radians) for three moving sources on a  $9 \times 9$  URA at an SNR of 0 dB; averaged over 100 trials

to a  $7 \times 7$  URA to demonstrate that the tensor gain is present for different array sizes. Both simulation results show that the tensor-based subspace tracking algorithms outperform the matrix-based algorithms, as expected.

Using the same scenario as for Figure 9.2, we evaluate the performance of the tensor extensions of the FAPI algorithm [BDR05]. In Figure 9.4 where the LPA is plotted, the curves labeled “TeTraKron-FAPI” and “TeTraKron-FAPI with FBA” correspond to two tensor-based FAPI schemes that are extensions of the FAPI algorithm via the TeTraKron framework based on (9.10) and (9.27), respectively. The curve labeled “FAPI with FBA” corresponds to an extended version of FAPI where forward-backward-averaging is included (cf. (9.41)). It is observed that the performance of tensor-based FAPI is superior to that of the matrix-based FAPI algorithm. A gain is further obtained by incorporating forward-backward-averaging.

In the forth example, a three-dimensional harmonic retrieval problem of size  $7 \times 7 \times 7$  is simulated. As an extension of the two-dimensional scenarios shown previously, the spatial frequencies (direction cosines) of the first two sources are represented as a function of the time

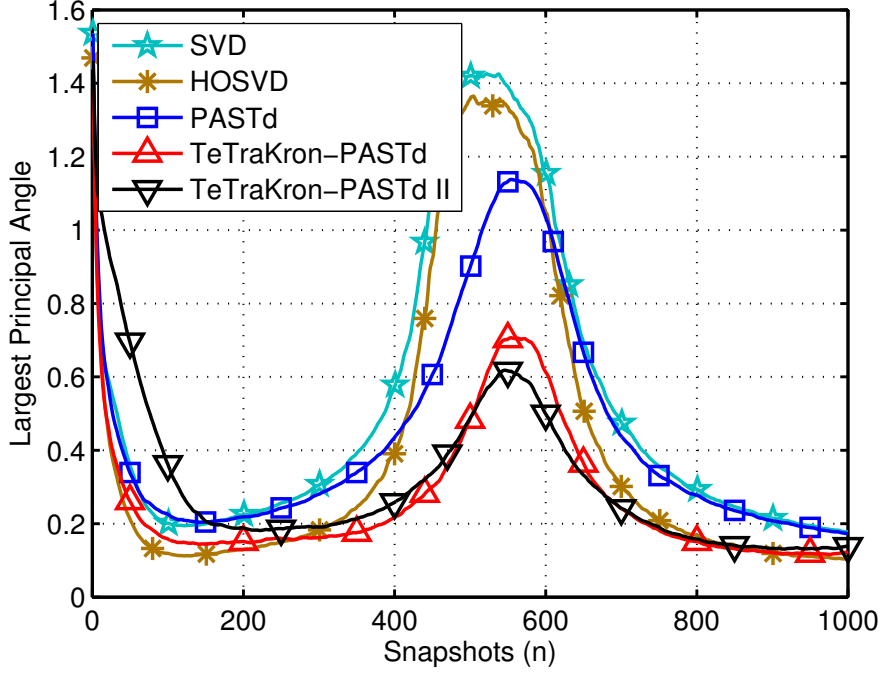


Figure 9.3.: LPA (in radians) for three moving sources on a  $7 \times 7$  URA at an SNR of 0 dB; averaged over 100 trials

index  $n = 1, 2, \dots, N$

$$\begin{aligned}\mu_1^{(1)}[n] &= 0.3 - 0.1 \cdot t[n], \quad \mu_2^{(1)}[n] = 0.2 + 0.1 \cdot t[n], \\ \mu_1^{(2)}[n] &= 0.2 + 0.1 \cdot t[n], \quad \mu_2^{(2)}[n] = 0.2 + 0.1 \cdot t[n], \\ \mu_1^{(3)}[n] &= 0.2 + 0.1 \cdot t[n], \quad \mu_2^{(3)}[n] = 0.2 + 0.1 \cdot t[n],\end{aligned}$$

for  $t[n] = \frac{n-1}{N-1}$ , whereas the third source remains stationary at  $\mu_3^{(1)} = \mu_3^{(2)} = \mu_3^{(3)} = 0.1$ . Similarly, as  $n$  approaches  $N/2$  the first and the second sources cross. Figure 9.5 depicts this crossing scenario. The LPA between the true and the estimated signal subspace is illustrated in Figure 9.6. The curve labeled “TeTraKron-PAST with FBA” refers to the real-valued subspace tracking scheme as a tensor extension of PAST via the proposed TeTraKron framework based on (9.27) where forward-backward-averaging is incorporated. On the other hand, the curve labeled “PAST with FBA” corresponds to an extended version of the matrix-based PAST algorithm with forward-backward-averaging included (cf. (9.41)). It can be observed that incorporating forward-backward-averaging contributes to a performance improvement for both the matrix-based and the tensor-based algorithms. Similarly as in the first three examples,

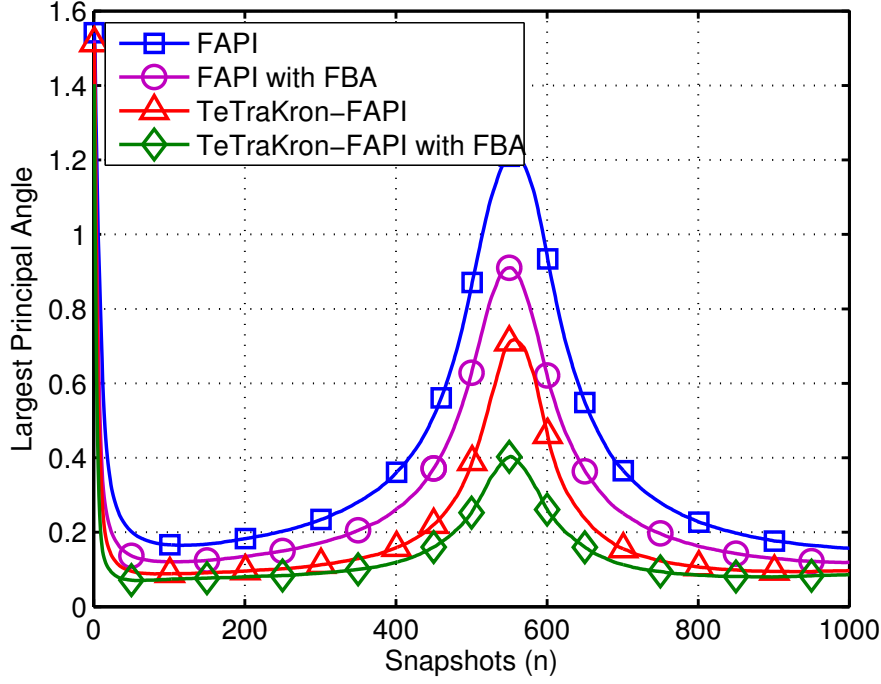


Figure 9.4.: LPA (in radians) for three moving sources on a  $9 \times 9$  URA at an SNR of 0 dB where FAPI and its tensor extensions are employed; averaged over 100 trials

the tensor-based subspace tracking schemes provide a better performance compared to the matrix-based schemes due to the fact that the former exploit the multidimensional structure inherent in the data in a better way.

Moreover, we assess the performance of various ESPRIT-type parameter estimation algorithms that use the subspace estimates obtained by the proposed subspace tracking schemes and least squares (LS) to solve the invariance equations [HRD08]. The evaluation criterion is the root mean square estimation error (RMSE). We define the RMSE in the spatial frequency domain as

$$\text{RMSE} = \sqrt{\mathbb{E} \left\{ \frac{1}{d} \frac{1}{R} \sum_{i=1}^d \sum_{r=1}^R \left( \mu_i^{(r)} - \hat{\mu}_i^{(r)} \right)^2 \right\}}, \quad (9.50)$$

where  $\hat{\mu}_i^{(r)}$  represents an estimate of  $\mu_i^{(r)}$ .

A two-dimensional scenario is considered where the sources are assumed to be correlated.

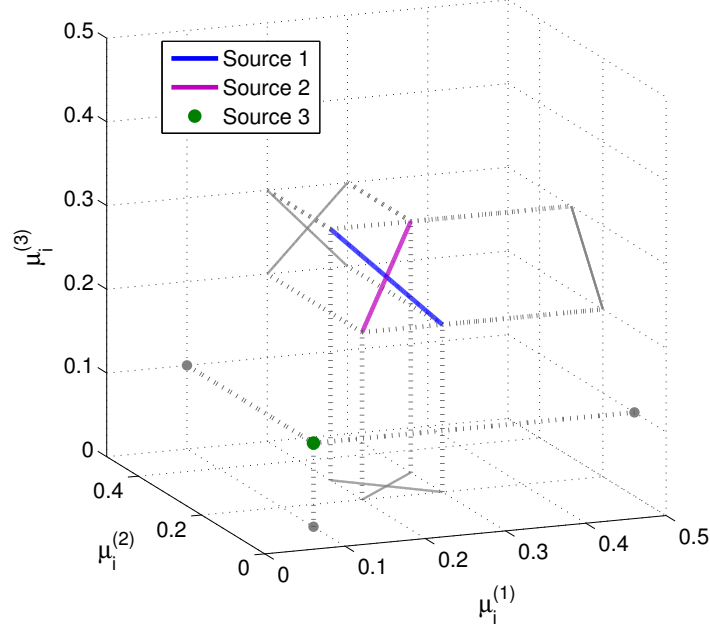


Figure 9.5.: Illustration of the spatial frequencies of the three sources over the course of 1000 snapshots. The first two sources cross, whereas the third source stays stationary

The source samples  $\mathbf{s}$  are generated such that  $\mathbf{R}_{\text{ss}} = \mathbb{E}\{\mathbf{s} \cdot \mathbf{s}^H\}$  has the form

$$\mathbf{R}_{\text{ss}} = \begin{bmatrix} 1 & \rho_{1,2} & \rho_{1,3} \\ \rho_{2,1} & 1 & \rho_{2,3} \\ \rho_{3,1} & \rho_{3,2} & 1 \end{bmatrix}, \quad (9.51)$$

where  $\rho_{i,j} = \rho \cdot e^{j\varphi_{i,j}}$ , and  $\varphi_{i,j} = -\varphi_{j,i}$  are drawn from a uniform distribution in  $[0, 2\pi]$  for  $i = 1, 2, 3$ ,  $j = 1, 2, 3$ , and  $i \neq j$ . Here  $\rho$  is chosen as 0.7. The other parameters are the same as for Figure 9.3. We plot the LPA in Figure 9.7. Similar observations as in the previous examples can be obtained. In addition, the performance improvement due to the incorporation of forward-backward-averaging is more significant in the presence of source correlation compared to the case of uncorrelated sources. The RMSE of the tracked spatial frequencies is shown in Figure 9.8. Four parameter estimation techniques, standard ESPRIT (SE) [RK89], Unitary ESPRIT (UE) [HN95], standard Tensor-ESPRIT (STE) [HRD08], and Unitary Tensor-ESPRIT (UTE) [HRD08] are employed where the subspace estimates are tracked by PAST, PAST with forward-backward-averaging, tensor extension of PAST via TeTraKron,

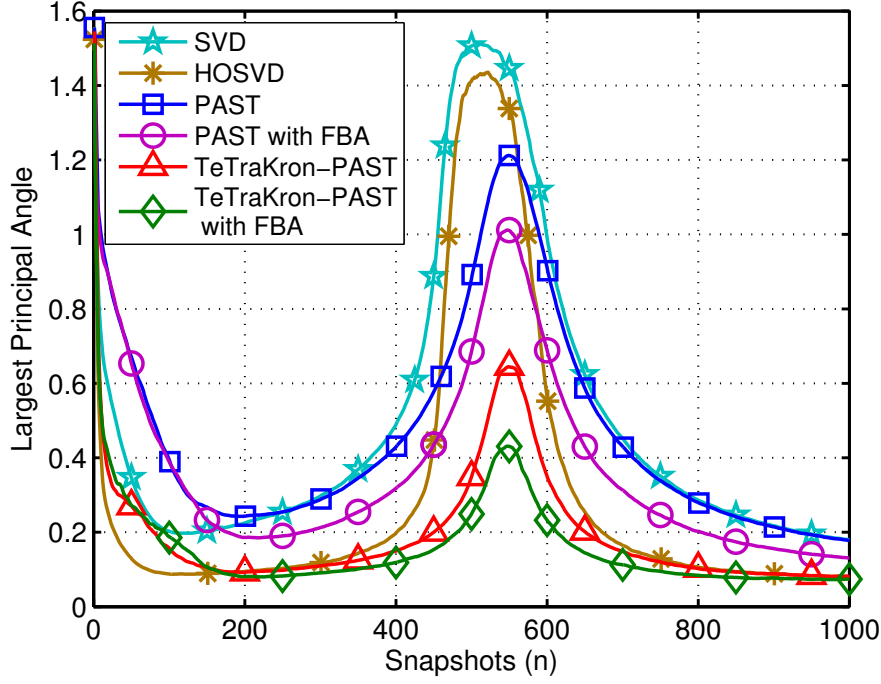


Figure 9.6.: LPA (in radians) for three-dimensional harmonic retrieval problem of size  $7 \times 7 \times 7$  at an SNR of 0 dB; three moving sources; FBA - forward-backward-averaging; averaged over 100 trials

and tensor extension of PAST via TeTraKron with forward-backward-averaging incorporated, respectively. It can be observed that the tensor-based parameter estimation algorithms combined with tensor-based subspace tracking schemes outperform the combinations of matrix-based parameter estimation and matrix-based subspace tracking algorithms. Moreover, a gain is achieved by incorporating forward-backward-averaging. This corroborates the benefits provided by forward-backward-averaging that it decorrelates coherent sources and contributes to an enhanced accuracy of the parameter estimation. In Figure 9.9 and Figure 9.10, the corresponding spatial frequency estimates of the first mode and the second mode averaged over 1000 trials are illustrated, respectively. To demonstrate the variation of the spatial frequency estimates around the averaged values, we plot the bars that represent the  $\pm 1$  standard deviation estimated from the 1000 trials as well. The two combinations of tensor-based subspace tracking and parameter estimation techniques (corresponding to the two plots labeled “STE + TeTraKron-PAST” and “UTE + TeTraKron-PAST with FBA”, respectively, at the bottom of Figure 9.9 and Figure 9.10) achieve an accurate estimation of the spatial frequencies. Even



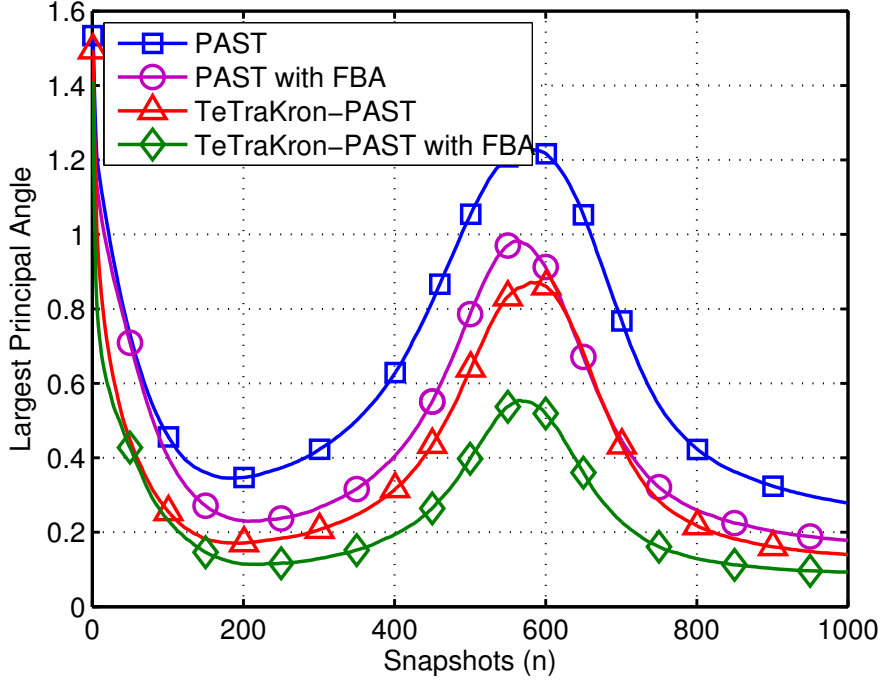


Figure 9.7.: LPA (in radians) for three moving sources on a  $7 \times 7$  URA at an SNR of 0 dB; sources correlated with  $\rho = 0.7$ ; FBA - forward-backward-averaging; averaged over 1000 trials

when the first two sources cross, their performances do not suffer much, and a fast adaptation is observed. In case of Unitary Tensor-ESPRIT combined with the TeTraKron extension of PAST where forward-backward-averaging is included, its performance is slightly better than that of the combination of standard Tensor-ESPRIT and the TeTraKron extension of PAST. By contrast, the matrix-based algorithms standard ESPRIT and Unitary ESPRIT combined with PAST adapt much slower at the beginning of the tracking as well as at the crossing point of the first two sources and fail to accurately estimate the spatial frequencies. The deviation of the spatial frequency tracks from the average is also much more severe compared to the deviation in case of the two combinations of tensor-based subspace tracking and parameter estimation techniques.

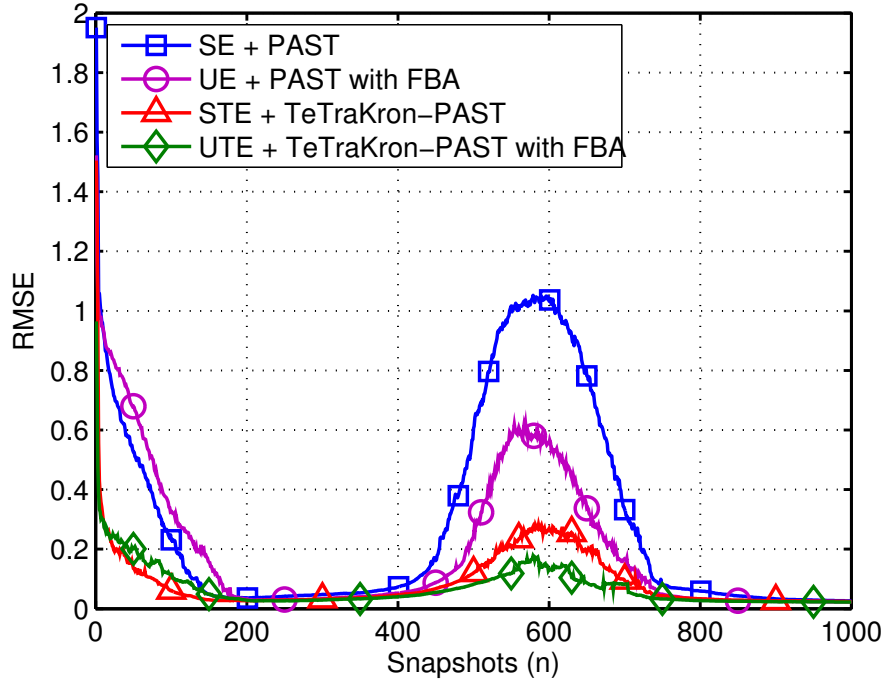


Figure 9.8.: RMSE of spatial frequencies for three moving sources on a  $7 \times 7$  URA at an SNR of 0 dB; sources correlated with  $\rho = 0.7$ ; FBA - forward-backward-averaging, SE - Standard ESPRIT, UE - Unitary ESPRIT, STE - Standard Tensor-ESPRIT, UTE - Unitary Tensor-ESPRIT; averaged over 1000 trials

## 9.6. Summary

In this chapter, we have presented the Tensor-based subspace Tracking via Kronecker structured projections (TeTraKron) framework. TeTraKron allows to extend arbitrary existing matrix-based subspace tracking schemes to the tracking of the HOSVD-based subspace estimate. Therefore, compared to previous matrix-based subspace tracking schemes, the subspace estimation accuracy is improved. The extension is based on an algebraic link between matrix-based and tensor-based subspace estimates via a Kronecker structured projection. Therefore, matrix-based subspace tracking schemes are applied to all tensor unfoldings and there is no need to track the core tensor. We have proposed a low-complexity approach for the recombination of the separate subspaces into one final estimate which is achieved in linear complexity. In addition, we have investigated the incorporation of forward-backward-averaging. To this end, a connection between the real-valued matrix-based and the HOSVD-based subspace estimate

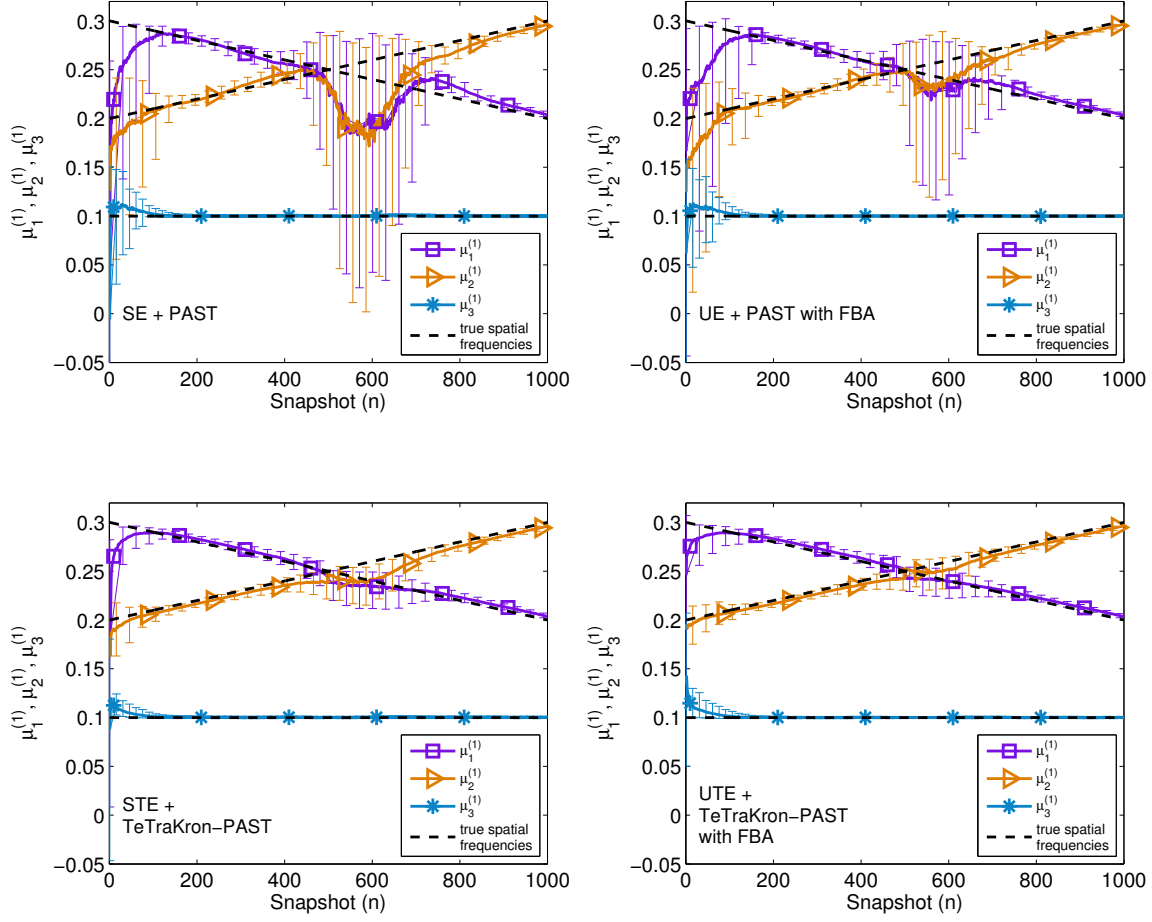


Figure 9.9.: Averaged spatial frequency estimates of the first mode and error bars for three moving sources on a  $7 \times 7$  URA at an SNR of 0 dB; sources correlated with  $\rho = 0.7$ ; FBA - forward-backward-averaging, SE - Standard ESPRIT, UE - Unitary ESPRIT, STE - Standard Tensor-ESPRIT, UTE - Unitary Tensor-ESPRIT; averaged over 1000 trials

via a similar Kronecker structured projection has been revealed. Consequently, the TeTraKron framework can also be employed to devise real-valued tensor-based subspace tracking schemes. As an example, we have used the TeTraKron framework to extend the PAST, the PASTd, and the FAPI algorithms to tensors and demonstrated the enhanced subspace estimation accuracy via numerical simulations. In time-varying multidimensional harmonic retrieval problems, we

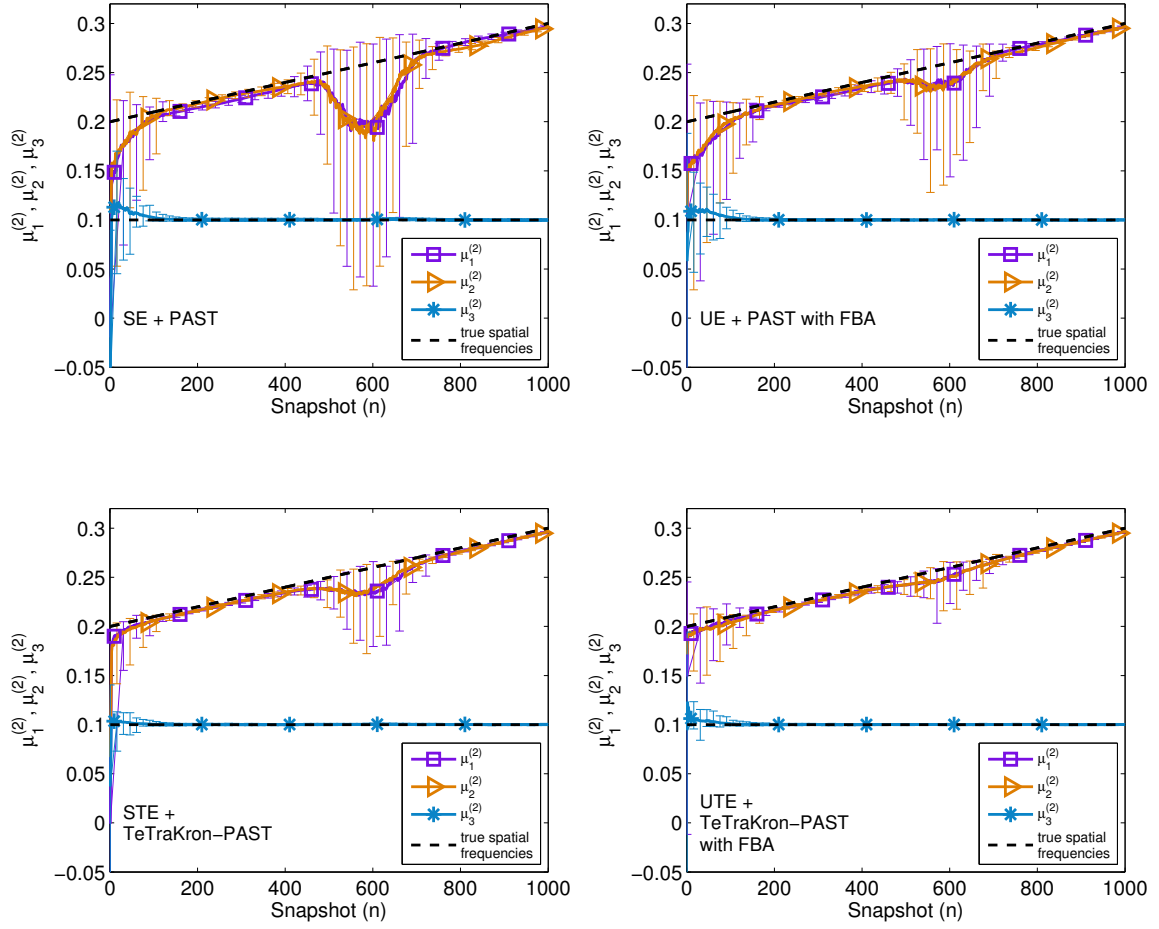


Figure 9.10.: Averaged spatial frequency estimates of the second mode and error bars for three moving sources on a  $7 \times 7$  URA at an SNR of 0 dB; sources correlated with  $\rho = 0.7$ ; FBA - forward-backward-averaging, SE - Standard ESPRIT, UE - Unitary ESPRIT, STE - Standard Tensor-ESPRIT, UTE - Unitary Tensor-ESPRIT; averaged over 1000 trials

have investigated the performances of standard Tensor-ESPRIT and Unitary Tensor-ESPRIT where the tensor-based subspace estimates tracked by the TeTraKron-based subspace tracking algorithms are used for direction-of-arrival estimation.

---

## 10. Conclusions and future work

This thesis presents novel and advanced signal processing techniques encompassing several aspects of wireless communication systems. Our goal is to fulfill the ever-growing demand for new innovations that feature an enhanced performance, a higher efficiency, a stronger robustness, a greater flexibility, etc.. As we show, this target has been well accomplished with respect to two important communications contexts, multi-carrier Multiple-Input Multiple-Output (MIMO) systems and multi-dimensional harmonic retrieval problems. In addition, the results presented in this thesis shed light upon future research directions in these fields and ignite great research interest in related topics.

Part I is dedicated to the development of new transmit-receive processing schemes for multi-carrier MIMO systems. Both the widely used Orthogonal Frequency Division Multiplexing with the Cyclic Prefix insertion (CP-OFDM) and its promising substitute multi-carrier modulation scheme, Filter Bank-based Multi-Carrier modulation (FBMC), are investigated. A variety of MIMO settings are covered, ranging from the single-user MIMO to Coordinated Multi-Point (CoMP) systems. In Chapter 2 we focus on the CP-OFDM-based multi-user MIMO downlink and present a highly efficient and flexible two-stage transmission strategy. In the spatial scheduling stage, the efficient multi-carrier ProSched (EMC-ProSched) algorithm is proposed to select a user group with an appropriate size and to assign users with a high spatial correlation to different groups. It employs a suboptimum but low-complexity tree-based sorting scheme. Inspired by the concept of link-to-system mapping, a novel and effective scheduling metric is tailored in light of the multi-carrier nature of the system with well-calibrated parameters. The precoding stage of the proposed transmission strategy alleviates the dimensionality constraint that many state-of-the-art precoding techniques suffer from. To handle the cases where the total number of receive antennas at the user terminals exceeds the number of transmit antennas at the base station, the low complexity coordinated beamforming (LoCCoBF) algorithm is designed to compute the transmit and receive beamformers in a joint and iterative manner. It experiences an enhanced efficiency by exploiting the correlation of adjacent subcarriers. On the other hand, when the number of transmit antennas at the base station is larger than or equal to the total number of receive antennas, a novel linear precoding-based geometric mean decomposition (LP-GMD) algorithm is employed to mitigate the Multi-User Interference (MUI) and to enable the implementation of the same Modulation and Coding Scheme (MCS) on all data streams for each user. It leads to a small signaling

overhead and is especially suitable for multi-user MIMO downlink systems that are compliant with the Wireless Local Area Network (WLAN) standard IEEE 802.11ac. Moreover, an MUI suppression scheme can be flexibly chosen in the LP-GMD algorithm. As examples, Block Diagonalization (BD) and Regularized Block Diagonalization (RBD) versions of the LP-GMD technique are introduced. In pursuit of an enhanced power efficiency, an MMSE-based power loading scheme is devised to wisely allocate the transmit power to the users such that the resulting number of padding bits is reduced. Furthermore, a system-level simulation tool for CP-OFDM-based multi-user MIMO downlink systems is developed where the parameters for the link-to-system interface can be calibrated according to the MCSs and the channel model specified in a certain standard such as IEEE 802.11ac. The extensive numerical results validate the performance superiority of the proposed transmission strategy over the state-of-the-art in terms of a significantly increased throughput and a lower computational complexity. It is demonstrated that by employing the proposed transmission scheme, a throughput of over one Gbps promised by IEEE 802.11ac for 80 MHz transmissions can be achieved.

The concept of the LP-GMD algorithm has sparked the interest in advanced multi-user MIMO downlink precoding schemes that support an equal MCS across all data streams of each user and thus require a modest signaling overhead. For instance, an adaptive uniform channel decomposition technique has been developed in [PRPF15] where the number of spatial streams per user can be flexibly selected. In addition to the pursuit of such a new degree of freedom, it is of great interest and importance to devise enhanced versions of the existing schemes or new precoding methods leading to an improved performance that is even closer to the dirty paper bound. Moreover, perfect knowledge of the Channel State Information at the Transmitter (CSIT) is assumed in Chapter 2. For future work, the impact of imperfect CSIT, e.g., due to limited feedback, on the proposed transmission strategy can be investigated. Accordingly, extensions aiming at an enhanced robustness against imperfect CSIT can be developed. In spite that the LoCCoBF algorithm features a lower computational complexity compared to the state-of-the-art, it belongs to the category of iterative schemes. As mentioned in Chapter 2, it has been shown in [YSRH12] that the coordinated beamforming task for the multi-user MIMO downlink can be transformed into a “sequentially drilled” joint congruence transformation (SeDJoCo). Although the joint and iterative calculation of the transmit and receive beamformers is avoided, an iterative process is still involved in the solutions of SeDJoCo [YSRH12]. Therefore, finding a closed-form solution of SeDJoCo, i.e., a closed-form semi-algebraic solution of coordinated beamforming, will be a significant breakthrough for the multi-user MIMO downlink precoding design.

The remaining chapters in Part I of this thesis are devoted to new progress and advances

---

in the design of transmit-receive processing strategies for FBMC-based MIMO systems. We start with an introduction of FBMC in Chapter 3. The strong motivation behind the use of FBMC is addressed. Among numerous applications of FBMC, we introduce the proposed future broadband Professional Mobile Radio (PMR) system in detail as an example to show the benefits due to the well-concentrated spectrum of FBMC. With a focus on Filter Bank-based Multi-Carrier with Offset Quadrature Amplitude Modulation (FBMC/OQAM), the FBMC scheme that has attracted the most research attention, we provide the data models of first Single-Input Single-Output (SISO) and then MIMO FBMC/OQAM systems. Different degrees of the frequency selectivity of the propagation channel are distinguished. Their crucial role in the design of transmit-receive processing schemes for FBMC/OQAM-based MIMO systems is stressed. Via a thorough review of the state-of-the-art, the demand for new and advanced transmit-receive processing strategies that are able to overcome the limits of the existing approaches is evident. Hence, we first investigate the incorporation of widely linear processing in FBMC/OQAM-based point-to-point MIMO systems in Chapter 4 considering the case of low frequency selective channels. A two-step receiver is proposed which combines linear and widely linear processing. The linear MMSE receiver in the first step serves to mitigate the intrinsic interference that hinders the exploitation of the benefits of widely linear processing. Then a widely linear MMSE receiver is employed in the second step. It is observed via numerical results that the two-step receiver significantly outperforms the linear MMSE receiver by taking advantage of the non-circularity in the signals of FBMC/OQAM-based systems. Chapter 5 concentrates on FBMC/OQAM-based point-to-point MIMO settings as well but takes one step further by investigating the case of intermediate frequency selective channels. Due to the fact that only the channel on each subcarrier is assumed to be flat fading, it is more challenging to achieve the suppression of the intrinsic interference in contrast to the case in Chapter 4. In spite of this, we develop two coordinated beamforming schemes to alleviate the dimensionality constraint that the number of receive antennas should be smaller than the number of transmit antennas imposed on the state-of-the-art. The designs of the precoders in these two schemes are based on a Zero Forcing (ZF) criterion and the maximization of the Signal-to-Leakage-plus-Noise-Ratio (SLNR), respectively. Different initialization strategies are devised by taking into account the dimensions of the system. Both algorithms yield a very promising Bit Error Rate (BER) performance comparable to that of a CP-OFDM-based counterpart, while an FBMC/OQAM-based MIMO system has a higher spectral efficiency owing to the fact that a CP is not required. The proposed coordinated beamforming scheme with the SLNR-maximizing precoder mitigates the intrinsic interference more effectively and therefore leads to an improved BER performance especially in the high Signal-to-Noise-Ratio

(SNR) regime compared to the method with the ZF-based precoder. But the joint-subcarrier processing involved in the former scheme results in a higher complexity as the price of a stronger capability of the intrinsic interference suppression.

The inspiring way of exploiting the benefits of widely linear processing in point-to-point MIMO FBMC/OQAM systems introduced in Chapter 4 opens up further enhancements and interesting extensions. A promising alternative to the linear MMSE receiver in the first step can be used to more effectively mitigate the intrinsic interference such that the performance of the two-step receiver is improved. The estimation of the covariance matrix of the residual intrinsic interference requires the use of training symbols. To overcome this drawback of the two-step receiver, effort can be spent on establishing an analytical expression for the covariance matrix of the residual intrinsic interference to avoid the loss of spectral efficiency and to enhance the applicability of the two-step receiver in practice. In addition, the use of widely linear processing in an FBMC/OQAM-based MIMO system where the propagation channel exhibits a higher frequency selectivity can be investigated. It calls for smart and powerful intrinsic interference mitigation schemes. There might also exist ways of translating the gain achieved by incorporating widely linear processing in a point-to-point MIMO FBMC/OQAM system to more sophisticated FBMC/OQAM-based communication scenarios, e.g., cooperative MIMO networks where the advantages of widely linear distributed beamforming algorithms have been identified [SH13]. On the other hand, the rationale of the intrinsic interference suppression in the SLNR-based coordinated beamforming scheme described in Chapter 5 can be extended to the downlink of an FBMC/OQAM-based multi-user MIMO system. It can be combined with the leakage-based precoding algorithm [STS07] to mitigate both the MUI and the intrinsic interference.

Other forms of FBMC/OQAM-based MIMO scenarios apart from the point-to-point case are studied in Chapter 6 and Chapter 7 of this thesis. For the downlink of an FBMC/OQAM-based single-cell multi-user MIMO system, two intrinsic interference mitigating coordinated beamforming (IIM-CBF) schemes are proposed in Chapter 6. They are very effective in mitigating both the MUI and the intrinsic interference inherent in FBMC/OQAM-based systems. In addition, the goal of relieving the dimensionality limit that the total number of receive antennas of the user terminals must be smaller than the number of transmit antennas of the base station is accomplished. In addition, a novel FBMC/OQAM-based CoMP technique, as a third IIM-CBF algorithm, is developed to enable the joint transmission of neighboring cells or clusters to cell edge users such that the cell edge throughput is boosted despite the heavy path loss and the strong interference. Both the BER performance and the sum rate performance of the proposed IIM-CBF schemes are evaluated, and their convergence behavior is



---

investigated. The corresponding results indicate that the IIM-CBF schemes are very promising transmit-receive processing strategies for the downlink of FBMC/OQAM-based single-cell and multi-cell multi-user MIMO systems. Furthermore, the stronger resilience against frequency misalignments of an FBMC/OQAM-based multi-user MIMO downlink system in contrast to its CP-OFDM-based counterpart is verified via simulation results, which again strengthens the motivation of using FBMC/OQAM. In Chapter 7, we turn to the case of highly frequency selective channels and demonstrate the use of multi-tap precoding techniques at the base station combined with efficient spatial receive filtering schemes at the user terminals to achieve the suppression of various types of interference, i.e., the inter-carrier interference, the inter-symbol interference, the MUI, and the inter-stream interference. The calculation of the multi-tap precoders is based on criteria such as the minimization of the MMSE, the maximization of the Signal-to-Leakage-Ratio (SLR) or the SLNR. At the user terminals with a weaker computational capability compared to the base station, Maximum Ratio Combining (MRC) or ZF-based single-tap spatial receive filters are employed. The satisfactory effectiveness of the proposed transmit-receive processing schemes in mitigating the aforementioned sources of interference is demonstrated via simulation results.

Compared to non-linear precoding, linear precoding for the multi-user MIMO downlink in general requires a lower computational complexity and leads to a stronger immunity against imperfect Channel State Information (CSI). Therefore, it is the major focus of Chapter 6. Nevertheless, non-linear precoding is still attractive owing to the remarkable performance that it promises. Although not included in this thesis, we have studied non-linear precoding for FBMC/OQAM-based multi-user MIMO downlink settings and have devised a Tomlinson-Harashima Precoding (THP)-based non-linear precoding scheme [CRH15]. Its superior performance over several linear precoding approaches is evident. This result motivates further investigations in this direction. For example, the coordinated THP algorithm in [CRH15] can be extended to the CoMP downlink. A performance gain over the linear IIM-CBF scheme introduced in Section 6.4 can be expected. Throughout Chapter 6 perfect synchronization in the time domain is assumed, whereas the strong robustness of FBMC/OQAM against residual carrier frequency offsets is demonstrated. It is worth noting, however, that the asynchronous nature of the interference in the CoMP downlink setting has been pointed out in [ZMM<sup>+</sup>08]. Thus, for future work, it will be interesting to assess the performance of an FBMC/OQAM-based CoMP scheme in the presence of asynchronous interference. A comparison can be made with its CP-OFDM-based counterpart, and robustified versions can be devised. Concerning the case of highly frequency selective channels, we come up with a coordinated beamforming-based extension of the SLNR-based multi-tap precoder and the ZF-based spatial receive filter

for overloaded multi-user MIMO downlink systems in Section 7.6. This concept can be adopted in the design of FBMC/OQAM-based CoMP schemes that are able to handle the critical highly frequency selective propagation conditions.

In Part II of this thesis, we present new advances in tensor-based signal processing for multi-dimensional harmonic retrieval problems highlighting statistical robustness or the applicability in time-varying scenarios. Chapter 8 introduces the concept of robustified multi-dimensional model order estimation where the statistical robustness is incorporated by replacing the sample covariance matrices of the  $r$ -mode unfoldings of the measurement tensor with robust covariance matrix estimates. The MM-estimator featuring a strong qualitative and quantitative robustness as well as a high efficiency is employed. Robust versions of  $R$ -D Akaike's Information Criterion (AIC),  $R$ -D Minimum Description Length (MDL), and the  $R$ -D Exponential Fitting Test (EFT) are developed. It is worth mentioning that following a similar philosophy devised here the statistical robustness can be introduced to other matrix-based and tensor-based model order selection methods. Moreover, we show that further incorporating forward-backward-averaging contributes to a noticeable performance improvement and a reduced computational complexity. In the presence of brief sensor failures that cause severe contamination to the measurement data, the original tensor-based schemes,  $R$ -D AIC,  $R$ -D MDL, and the  $R$ -D EFT break down, while their robust counterparts lead to a satisfactory performance and are able to provide model order estimates with a high accuracy. Finally, in Chapter 9, we consider time-varying multi-dimensional harmonic retrieval problems and devise a generic Tensor-based subspace Tracking via Kronecker structured projections (TeTraKron) framework. It enables the extension of existing matrix-based subspace tracking methods to track the Higher-Order SVD (HOSVD)-based subspace estimate owing to an algebraic link between matrix-based and tensor-based subspace estimates via a Kronecker structured projection. Therefore, matrix-based subspace tracking schemes are applied to all tensor unfoldings and there is no need to track the core tensor. A low-complexity approach is proposed for the recombination of the separate subspaces into one final estimate. In addition, by incorporating forward-backward-averaging, a similar connection between the real-valued matrix-based and the HOSVD-based subspace estimates is found, implying that the TeTraKron framework can also be employed to devise real-valued tensor-based subspace tracking schemes. It is then described in detail how TeTraKron is used to extend the projection approximation subspace tracking (PAST) algorithm, a deflation-based version of PAST (PASTd), and the fast approximated power iteration (FAPI) algorithm to tensors, while tensor-based versions of many other matrix-based subspace tracking approaches can be obtained in a similar manner thanks to the TeTraKron framework. Numerical simulations show that the resulting tensor-based subspace tracking

---

techniques lead to a significantly improved subspace estimation accuracy compared to their matrix-based counterparts. In time-varying multi-dimensional harmonic retrieval problems, we use the subspace estimates tracked via the TeTraKron-based subspace tracking schemes in ESPRIT-type parameter estimation algorithms and evaluate their resulting performances.

The success of the robustified multi-dimensional model order estimation schemes shown in Chapter 8 gives rise to the interest in incorporating statistical robustness into other tensor-based signal processing approaches in the context of multi-dimensional harmonic retrieval problems. Following a similar philosophy, for example, the sample covariance matrices of the unfoldings of the measurement tensor in the Tensor-ESPRIT [HRD08] can be replaced by the robust estimates of the covariance matrices. The resulting performance of this modified version of Tensor-ESPRIT can be evaluated in critical scenarios where the measurements are severely corrupted. Moreover, the manner of introducing robustness to model order estimation presented in Chapter 8 can potentially be exploited for the application of tensor imputation for big data analysis that has attracted tremendous research attention in recent years. In Chapter 9, we discuss several examples of devising tensor extensions of matrix-based subspace tracking methods via the TeTraKron framework. Apart from those investigated in Section 9.4, the Kalman filtering is recognized as a powerful tool for subspace tracking [CZZ06], [LZC10]. One interesting future step would be to study the use of TeTraKron for the design of a tensor-based Kalman filter-based subspace tracking algorithm. In addition, the TeTraKron framework offers an efficient way of tracking the HOSVD-based subspace estimate and also arouses the interest in investigating the tracking of the HOSVD and thereafter the Parallel Factor analysis (PARAFAC) decomposition. An analytical performance analysis of tensor-based subspace tracking algorithms devised via TeTraKron can be conducted as well. Furthermore, the tensor tool as the highlight of Part II can be adopted in the communications contexts considered in Part I. To name one example, let us recall an FBMC/OQAM-based point-to-point MIMO system with highly frequency selective channels. In the received signal, the time, frequency, and receive antennas constitute the three dimensions that can be exploited via tensors. Consequently, one interesting and seemingly promising direction would be to devise a tensor-based blind channel estimation scheme where, e.g., the HOSVD-based subspace estimate is used.

## Appendix A.

### Glossary of acronyms, symbols, and notation

#### A.1. Acronyms

<b>1-D</b>	one-dimensional
<b>2-D</b>	two-dimensional
<b>3-D</b>	three-dimensional
<b>4-D</b>	four-dimensional
<b>5G</b>	fifth generation of wireless communication systems
<b><math>R</math>-D</b>	$R$ -dimensional
<b>AFB</b>	Analysis Filter Bank
<b>ARQ</b>	Automatic Repeat Request
<b>ASK</b>	Amplitude Shift Keying
<b>AWGN</b>	Additive White Gaussian Noise
<b>BC</b>	Broadcast Channel
<b>BD</b>	Block Diagonalization
<b>BER</b>	Bit Error Rate
<b>BPSK</b>	Binary Phase Shift Keying
<b>BS</b>	Base Station
<b>CCDF</b>	Complementary Cumulative Distribution Function
<b>CDMA</b>	Code-Division Multiple Access
<b>CFO</b>	Carrier Frequency Offset
<b>CoMP</b>	Coordinated Multi-Point
<b>CP-OFDM</b>	Orthogonal Frequency Division Multiplexing with the Cyclic Prefix insertion
<b>CSI</b>	Channel State Information
<b>CSIR</b>	Channel State Information at the Receiver
<b>CSIT</b>	Channel State Information at the Transmitter
<b>DOA</b>	Direction-Of-Arrival
<b>DVB-T</b>	Digital Video Broadcasting-Terrestrial
<b>EESM</b>	Exponential Effective SINR Mapping
<b>EMPhAtiC</b>	Enhanced Multi-carrier Techniques for Professional Ad-Hoc and Cell-based Communications (European project)
<b>ESPRIT</b>	Estimation of Signal Parameters via Rotational Invariance Techniques
<b>EVD</b>	EigenValue Decomposition
<b>FBMC</b>	Filter Bank-based Multi-Carrier modulation
<b>FBMC/OQAM</b>	Filter Bank-based Multi-Carrier with Offset Quadrature Amplitude Modulation
<b>FEC</b>	Forward Error Correction

<b>FFT</b>	Fast Fourier Transform
<b>GMD</b>	Geometric Mean Decomposition
<b>HARQ</b>	Hybrid Automatic Repeat Request
<b>HOSVD</b>	Higher-Order Singular Value Decomposition
<b>IFFT</b>	Inverse Fast Fourier Transform
<b>ICI</b>	Inter-Carrier Interference
<b>ISI</b>	Inter-Symbol Interference
<b>LPA</b>	Largest Principle Angle
<b>LS</b>	Least Squares
<b>LTE</b>	Long Term Evolution
<b>LQM</b>	Link Quality Metric
<b>MCS</b>	Modulation and Coding Scheme
<b>MIMO</b>	Multiple-Input Multiple-Output
<b>MISO</b>	Multiple-Input Single-Output
<b>ML</b>	Maximum Likelihood
<b>MRC</b>	Maximum Ratio Combining
<b>MSE</b>	Mean Squared Error
<b>MMSE</b>	Minimum Mean Squared Error
<b>MUI</b>	Multi-User Interference
<b>OFDM</b>	Orthogonal Frequency Division Multiplexing
<b>OFDMA</b>	Orthogonal Frequency Division Multiplexing Access
<b>OQAM</b>	Offset Quadrature Amplitude Modulation
<b>PARAFAC</b>	Parallel Factor analysis
<b>PER</b>	Packet Error Rate
<b>PEP</b>	Pair-wise Error Probability
<b>PHY</b>	Physical Layer
<b>PHYDYAS</b>	Physical Layer for Dynamic Spectrum Access and Cognitive Radio (European project)
<b>PMR</b>	Professional Mobile Radio
<b>PSD</b>	Power Spectral Density
<b>PSDU</b>	Physical Layer Service Data Unit
<b>QAM</b>	Quadrature Amplitude Modulation
<b>QoS</b>	Quality of Service
<b>QPSK</b>	Quadrature Phase Shift Keying
<b>RBD</b>	Regularized Block Diagonalization
<b>RMSE</b>	Root Mean Squared Error
<b>SDMA</b>	Space-Division Multiple Access
<b>SFB</b>	Synthesis Filter Bank
<b>SIC</b>	Successive Interference Cancellation
<b>SINR</b>	Signal-to-Interference-plus-Noise-Ratio
<b>SISO</b>	Single-Input Single-Output
<b>SLR</b>	Signal-to-Leakage-Ratio
<b>SLNR</b>	Signal-to-Leakage-plus-Noise-Ratio
<b>SNR</b>	Signal-to-Noise-Ratio
<b>SVD</b>	Singular Value Decomposition
<b>THP</b>	Tomlinson-Harashima precoding
<b>ULA</b>	Uniform Linear Array

<b>URA</b>	Uniform Rectangular Array
<b>WINNER</b>	Wireless World Initiative New Radio (European project)
<b>WLAN</b>	Wireless Local Area Network
<b>ZF</b>	Zero Forcing

## A.2. Symbols and notation

$\mathbb{R}$	set of real numbers
$\mathbb{C}$	set of complex numbers
$a, b, c$	scalars
$\mathbf{a}, \mathbf{b}, \mathbf{c}$	column vectors
$\mathbf{A}, \mathbf{B}, \mathbf{C}$	matrices
$\mathcal{A}, \mathcal{B}, \mathcal{C}$	tensors
$A(m, n)$	$(m, n)$ -th entry of $\mathbf{A}$
$\mathbf{I}_m$	$m$ -by- $m$ identity matrix
$\mathbf{I}_{M \times d}$	a matrix that has the form $\mathbf{I}_{M \times d} = \begin{bmatrix} \mathbf{I}_d & \mathbf{0}_{d \times (M-d)} \end{bmatrix}^T$ for $M > d$
$\mathbf{\Pi}_m$	exchange matrix of size $m$ -by- $m$
$\mathbf{Q}_m$	left- $\mathbf{\Pi}$ -real matrix that satisfies $\mathbf{\Pi}_m \cdot \mathbf{Q}_m^* = \mathbf{Q}_m$
$(\cdot)^H$	conjugate transpose
$(\cdot)^T$	transpose
$(\cdot)^*$	conjugate
$(\cdot)^{-1}$	matrix inversion
$\text{blkdiag}\{\cdot\}$	a block-diagonal concatenation of its input matrices
$\text{Re}\{\cdot\}$	take the real part of the input argument
$\text{Im}\{\cdot\}$	take the imaginary part of the input argument
$ \cdot $	absolute value of the input argument
$\ \cdot\ $	two-norm of a vector
$\ \cdot\ _F$	Frobenius norm of a matrix
$\text{Tr}\{\cdot\}$	trace of the input matrix
$*$	discrete convolution
$\mathbf{A} \otimes \mathbf{B}$	Kronecker product between $\mathbf{A} \in \mathbb{C}^{M \times N}$ and $\mathbf{B} \in \mathbb{C}^{P \times Q}$
$\mathbf{A} \diamond \mathbf{B}$	Khatri-Rao product (columnwise Kronecker product) between $\mathbf{A} \in \mathbb{C}^{M \times N}$ and $\mathbf{B} \in \mathbb{C}^{P \times N}$
$\text{Tri}\{\cdot\}$	take the upper/lower triangular part of the input matrix and copy its Hermitian transpose to the other lower/upper triangular part

$\text{off}(\cdot)$	an operation of keeping all off-diagonal elements of its input matrix while setting its diagonal elements to zero
$\mathcal{P}\{\cdot\}$	compute the principal eigenvector of a matrix which corresponds to the maximal eigenvalue
$\mathbb{E}\{X\}$	expected value of the random variable $X$
$\mathcal{O}\{\cdot\}$	Big O notation frequently used in complexity theory describing the asymptotic behavior of a function
$\mathcal{A}(i_1, i_2, \dots, i_R)$	$(i_1, i_2, \dots, i_R)$ -th element of $\mathcal{A} \in \mathbb{C}^{I_1 \times I_2 \times \dots \times I_R}$
$[\mathcal{A}]_{(r)}$	$r$ -mode unfolding of tensor $\mathcal{A}$ in reverse cyclical column ordering
$\mathcal{A} \times_r \mathbf{U}$	$r$ -mode product between tensor $\mathcal{A}$ and a matrix $\mathbf{U}$
$[\mathcal{A} \sqcup_r \mathcal{B}]$	concatenation of $\mathcal{A}$ and $\mathcal{B}$ along the $r$ -th mode
$\mathcal{I}_{R,d}$	$R$ -dimensional identity tensor of size $d \times d \times \dots \times d$

### A.3. Frequently used notation in each chapter

#### A.3.1. Chapter 2

$M_T$	number of transmit antennas at the base station
$N$	total number of users in the multi-user MIMO downlink system
$K$	number of users assigned to one user group
$M_{R_i}$	number of receive antennas of the $i$ -th user, $i = 1, 2, \dots, K$
$M_R$	total number of receive antennas at the user terminals, $M_R = \sum_{i=1}^K M_{R_i}$
$d_i$	number of data streams transmitted to the $i$ -th user, $i = 1, 2, \dots, K$
$d$	total number of data streams, $d = \sum_{i=1}^K d_i$
$N_{SD}$	number of data subcarriers
$\mathbf{H}_i$	channel matrix between the base station and the $i$ -th user on a certain subcarrier
$\mathbf{F}_i$	precoding matrix for the $i$ -th user on a certain subcarrier
$\mathbf{D}_i$	decoding matrix of the $i$ -th user on a certain subcarrier
$\mathbf{y}_i$	received signal of the $i$ -th user on a certain subcarrier
$\mathbf{n}_i$	AWGN vector at the $i$ -th user terminal containing zero mean i.i.d. circularly symmetric Gaussian random variables with variance $\sigma_n^2$

### A.3.2. Chapter 4

$M_T$	number of transmit antennas in a point-to-point MIMO system
$M_R$	number of receive antennas in a point-to-point MIMO system
$K$	overlapping factor
$\mathbf{H}$	channel matrix on the $k$ -th subcarrier and at the $n$ -th time instant
$d$	real-valued desired signal on the $k$ -th subcarrier and at the $n$ -th time instant where $(k+n)$ is even
$ju$	pure imaginary intrinsic interference on the $k$ -th subcarrier and at the $n$ -th time instant where $(k+n)$ is even
$y$	received signal on the $k$ -th subcarrier and at the $n$ -th time instant
$\mathbf{n}$	AWGN vector on the $k$ -th subcarrier and at the $n$ -th time instant containing zero mean i.i.d. circularly symmetric Gaussian random variables with variance $\sigma_n^2$
$j\epsilon$	pure imaginary residual intrinsic interference on the $k$ -th subcarrier and at the $n$ -th time instant where $(k+n)$ is even
$c_{i,\ell}$	coefficients with respect to the impulse response of an FBMC/OQAM-based system determined by the synthesis and analysis filters, where $\ell = k-1, k, k+1, i = n-3, \dots, n+3$ , and $(\ell, i) \neq (k, n)$ with respect to the $k$ -th subcarrier and the $n$ -th time instant

### A.3.3. Chapter 5

$M_T$	number of transmit antennas in a point-to-point MIMO system
$M_R$	number of receive antennas in a point-to-point MIMO system
$d$	number of spatial streams
$K$	overlapping factor
$\mathbf{H}_k[n]$	channel matrix on the $k$ -th subcarrier and at the $n$ -th time instant
$\mathbf{F}_k[n]$	precoding matrix on the $k$ -th subcarrier and at the $n$ -th time instant
$\mathbf{D}_k[n]$	decoding matrix on the $k$ -th subcarrier and at the $n$ -th time instant
$d_k[n]$	real-valued desired signal on the $k$ -th subcarrier and at the $n$ -th time instant where $(k+n)$ is even
$y_k[n]$	received signal on the $k$ -th subcarrier and at the $n$ -th time instant
$\mathbf{n}_k[n]$	AWGN vector on the $k$ -th subcarrier and at the $n$ -th time instant containing zero mean i.i.d. circularly symmetric Gaussian random variables with variance $\sigma_n^2$



$c_{i,\ell}$	coefficients with respect to the impulse response of an FBMC/OQAM-based system determined by the synthesis and analysis filters, where $\ell = k - 1, k, k + 1, i = n - 3, \dots, n + 3$ , and $(\ell, i) \neq (k, n)$ with respect to the $k$ -th subcarrier and the $n$ -th time instant
$\mathbf{H}$	channel matrix on a certain subcarrier and at a certain time instant used in Section 5.2.2 and Section 5.3, where the time and the subcarrier indices are ignored as the precoding concept is on a per-subcarrier basis
$\mathbf{F}$	precoding matrix on a certain subcarrier and at a certain time instant used in Section 5.2.2 and Section 5.3
$\mathbf{D}$	decoding matrix on a certain subcarrier and at a certain time instant used in Section 5.2.2 and Section 5.3

#### A.3.4. Chapter 6

$M_T^{(\text{BS})}$	number of transmit antennas at the base station
$Q$	number of users in the multi-user MIMO downlink system served simultaneously
$M_{R_q}$	number of receive antennas of the $q$ -th user, $q = 1, 2, \dots, Q$
$M_R^{(\text{tot})}$	total number of receive antennas at the user terminals, $M_R = \sum_{q=1}^Q M_{R_q}$
$d_q$	number of data streams transmitted to the $q$ -th user, $q = 1, 2, \dots, Q$
$d$	total number of data streams, $d = \sum_{q=1}^Q d_q$
$K$	overlapping factor
$\mathbf{H}_{q,k}[n]$	channel matrix between the base station and the $q$ -th user on the $k$ -th subcarrier and at the $n$ -th time instant
$\mathbf{F}_{q,k}[n]$	first part of the precoding matrix for the $q$ -th user on the $k$ -th subcarrier and at the $n$ -th time instant calculated to mitigate the multi-user interference and thus decompose the multi-user MIMO downlink system into parallel equivalent single-user settings
$\mathbf{G}_{q,k}[n]$	second part of the precoding matrix for the $q$ -th user on the $k$ -th subcarrier and at the $n$ -th time instant that is treated as the transmit beamforming matrix for the equivalent single-user system with respect to the $q$ -th user
$\mathbf{D}_{q,k}[n]$	decoding matrix for the $q$ -th user on the $k$ -th subcarrier and at the $n$ -th time instant
$d_{q,k}[n]$	real-valued desired signal for the $q$ -th user on the $k$ -th subcarrier and at the $n$ -th time instant where $(k + n)$ is even

$y_{q,k}[n]$	received signal of the $q$ -th user on the $k$ -th subcarrier and at the $n$ -th time instant
$n_{q,k}[n]$	AWGN vector at the $q$ -th user terminal on the $k$ -th subcarrier and at the $n$ -th time instant containing zero mean i.i.d. circularly symmetric Gaussian random variables with variance $\sigma_n^2$
$c_{i,\ell}$	coefficients with respect to the impulse response of an FBMC/OQAM-based system determined by the synthesis and analysis filters, where $\ell = k - 1, k, k + 1, i = n - 3, \dots, n + 3$ , and $(\ell, i) \neq (k, n)$ with respect to the $k$ -th subcarrier and the $n$ -th time instant
$H_q$	channel matrix between the base station and the $q$ -th user on a certain subcarrier and at a certain time instant used in Chapter 6 starting from Section 6.2.2, where the time and the subcarrier indices are ignored as the precoding concept is on a per-subcarrier basis
$F_q$	first part of the precoding matrix for the $q$ -th user on a certain subcarrier and at a certain time instant used in Chapter 6 starting from Section 6.2.2
$G_q$	second part of the precoding matrix for the $q$ -th user on a certain subcarrier and at a certain time instant used in Chapter 6 starting from Section 6.2.2
$D_q$	decoding matrix of the $q$ -th user on a certain subcarrier and at a certain time instant used in Chapter 6 starting from Section 6.2.2

### A.3.5. Chapter 7

$M_T$	number of transmit antennas at the base station
$U$	number of users in the multi-user MIMO downlink system served simultaneously
$M_{R_j}$	number of receive antennas of the $j$ -th user, $j = 1, 2, \dots, U$
$M_R$	total number of receive antennas at the user terminals, $M_R = \sum_{j=1}^U M_{R_j}$
$M$	number of data subcarriers
$K$	overlapping factor
$d_\ell^{(j)}[n]$	signal transmitted to the $j$ -th user on the $\ell$ -th subcarrier after the OQAM staggering
$b_\ell^{(i,j)}[n]$	impulse response of the precoding filter for the $j$ -th user on the $\ell$ -th subcarrier with respect to the $i$ -th transmit antenna
$B$	length of the precoding filters

$x_\ell^{(i)}[n]$	precoded signal on the $\ell$ -th subcarrier with respect to the $i$ -th transmit antenna
$h_\ell[l_P]$	pulse shaping filter of the $\ell$ -th subcarrier
$L_P$	length of the prototype filter
$h_{\text{ch}}^{(i,j,r)}[l_P]$	impulse response of the propagation channel between the $i$ -th transmit antenna and the $r$ -th receive antenna of the $j$ -th user
$L_{\text{ch}}$	length of the channel impulse response
$h_{\ell,k}^{(i,j,r)}[n]$	equivalent channel impulse response for the signal that is transmitted on the $\ell$ -th subcarrier from the $i$ -th transmit antenna to the $r$ -th receive antenna and passed through the analysis filter for the $k$ -th subcarrier
$Q$	number of taps of the equivalent channel $h_{\ell,k}^{(i,j,r)}[n]$
$g_k^{(j,r)}[n]$	impulse response of the equalizer for the $r$ -th receive antenna of the $j$ -th user
$\eta^{(j,r)}[l_P]$	AWGN with variance $\sigma_n^2$
$\hat{\eta}_k^{(j,r)}[n]$	filtered AWGN
$\mathbf{d}_\ell^{(s)}[n]$	data vector containing consecutive data symbols for the $s$ -th user on the $\ell$ -th subcarrier defined for the matrix-vector formulation of the data model
$\mathbf{b}_\ell^{(s)}$	precoding vector containing the $M_T \cdot B$ coefficients of the precoding filter for the $s$ -th user on the $\ell$ -th subcarrier defined for the matrix-vector formulation of the data model
$\mathbf{H}_{\ell,k}^{(i,j,r)}$	Toeplitz matrix of the equivalent channel impulse response $h_{\ell,k}^{(i,j,r)}[n]$ defined for the matrix-vector formulation of the data model
$\mathbf{H}_{\ell,k}^{(j,r)}$	concatenation of $\mathbf{H}_{\ell,k}^{(i,j,r)}$ , $i = 1, 2, \dots, M_T$
$\alpha_\ell^{(s)}[m]$	in-phase component of the QAM modulated signal for the $s$ -th user on the $\ell$ -th subcarrier
$\beta_\ell^{(s)}[m]$	quadrature component of the QAM modulated signal for the $s$ -th user on the $\ell$ -th subcarrier
$D_j$	number of data streams transmitted to the $j$ -th user, $j = 1, 2, \dots, U$
$D$	total number of data streams, $D = \sum_{j=1}^U D_j$
$d_\ell^{(s,q)}[n]$	$q$ -th data stream transmitted to the $s$ -th user on the $\ell$ -th subcarrier after the OQAM staggering
$b_\ell^{(i,s,q)}[n]$	impulse response of the precoding filter for $q$ -th data stream transmitted to the $s$ -th user on the $\ell$ -th subcarrier with respect to the $i$ -th transmit antenna

$\mathbf{d}_\ell^{(s,q)}[n]$	data vector containing consecutive data symbols of the $q$ -th data stream for the $s$ -th user on the $\ell$ -th subcarrier defined for the matrix-vector formulation of the data model
$\mathbf{b}_\ell^{(s,q)}$	precoding vector containing the $M_T \cdot B$ coefficients of the precoding filter for the $q$ -th data stream transmitted to the $s$ -th user on the $\ell$ -th subcarrier defined for the matrix-vector formulation of the data model
$\alpha_\ell^{(s,q)}[m]$	in-phase component of the QAM modulated data symbols of the $q$ -th data stream for the $s$ -th user on the $\ell$ -th subcarrier
$\beta_\ell^{(s,q)}[m]$	quadrature component of the QAM modulated data symbols of the $q$ -th data stream for the $s$ -th user on the $\ell$ -th subcarrier
$\nu$	delay of the FBMC/OQAM-based multi-user MIMO downlink system with highly frequency selective channels where multi-tap precoding filters are employed
$\alpha$	regularization factor used to avoid the inversion of ill-conditioned matrices for the iterative design in Section 7.3 and the SLR-based design in Section 7.4

#### A.3.6. Chapter 8 and Chapter 9

$d$	number of the undamped exponentials in a multi-dimensional harmonic retrieval problem
$R$	number of dimensions of the lattice on which the data are sampled in a multi-dimensional harmonic retrieval problem
$M_r$	$r$ -th dimension of an $R$ -dimensional grid, $r = 1, 2, \dots, R$
$M$	product of the $R$ dimensions given by $M = \prod_{r=1}^R M_r$
$N$	number of subsequent snapshots
$\mathbf{A}$	mixing matrix or array steering matrix in the context of array signal processing
$\mathbf{S}$	containing the source symbols of the $N$ snapshots
$\mathbf{W}$	containing the additive noise samples of the $N$ snapshots with zero mean i.i.d. circularly symmetric Gaussian random variables with variance $\sigma_n^2$
$\mathbf{X}$	containing the measurements collected in the $N$ snapshots
$\mathcal{A}$	mixing tensor or array steering tensor in the context of array signal processing
$\mathcal{W}$	noise tensor containing zero mean i.i.d. circularly symmetric Gaussian random variables with variance $\sigma_n^2$

$\mathcal{X}$	measurement tensor
$\beta$	forgetting factor for the exponential window employed in, e.g., the PAST algorithm [Yan95b]
$\hat{U}_s$	containing columns that represent an orthonormal basis of the estimated signal subspace
$\hat{U}_r^{[s]}$	containing the estimated $r$ -mode singular vectors
$\left[\hat{\mathbf{u}}^{[s]}\right]_{(R+1)}^T$	containing columns that represent an orthonormal basis of the HOSVD-based estimate of the signal subspace
$\mathbf{x}(n)$	measurement of every new snapshot $n$ as a new column of the measurement matrix $\mathbf{X}$
$\mathbf{A}(n)$	mixing matrix or array steering matrix for the $n$ -th snapshot
$\mathcal{X}(n)$	measurement tensor of every new snapshot $n$
$\hat{U}_s(n)$	containing columns that represent an orthonormal basis of the estimated signal subspace for the $n$ -th snapshot
$\left[\hat{\mathbf{u}}^{[s]}(n)\right]_{(R+1)}^T$	containing columns that represent an orthonormal basis of the HOSVD-based estimate of the signal subspace for the $n$ -th snapshot
$\mu_i^{(r)}$	spatial frequency of the $i$ -th source in the $r$ -th dimension, $i = 1, 2, \dots, d$ and $r = 1, 2, \dots, R$

## Appendix B.

### Derivation of Exponential Effective SINR Mapping (EESM) for binary signaling

The Exponential Effective SINR Mapping (EESM) scheme is employed in the system-level simulator introduced in Section 2.6. For the case of binary signaling, the derivation of EESM is based on the Union-Chernoff bound of error probabilities [Eri03]. The union bound for coded binary transmissions and maximum-likelihood decoding is given by

$$P_e(\gamma) \leq \sum_{d=d_{\min}}^{\infty} \alpha_d P_2(d, \gamma), \quad (\text{B.1})$$

where  $\gamma$  is the SNR per symbol,  $d_{\min}$  denotes the minimum distance of the binary code, and  $\alpha_d$  represents the number of code words with Hamming weight  $d$ . Here  $P_2(d, \gamma)$  is the Pair-wise Error Probability (PEP) with respect to a certain Hamming distance  $d$  and a certain SNR  $\gamma$ . It takes the following form

$$P_2(d, \gamma) = Q(\sqrt{2\gamma d}). \quad (\text{B.2})$$

For BPSK transmissions over an AWGN channel, the PEP is upper bounded by

$$P_{2,\text{Chernoff}}(d, \gamma) = \left( P_{2,\text{Chernoff}}(1, \gamma) \right)^d = \exp(-\gamma d), \quad (\text{B.3})$$

leading to

$$P_e(\gamma) \leq \sum_{d=d_{\min}}^{\infty} \alpha_d P_2(d, \gamma) \leq \sum_{d=d_{\min}}^{\infty} \alpha_d \left( P_{2,\text{Chernoff}}(1, \gamma) \right)^d. \quad (\text{B.4})$$

Define

$$P_{e,\text{Chernoff}}(\gamma) = \sum_{d=d_{\min}}^{\infty} \alpha_d \left( P_{2,\text{Chernoff}}(1, \gamma) \right)^d \quad (\text{B.5})$$

as the Chernoff-bounded error probability that depends on the weight distribution of the code and the Chernoff-bounded symbol error probability  $P_{2,\text{Chernoff}}(1, \gamma)$ .

---

To explain the basic principles of the Union-Chernoff bound for a multi-state channel where different coded bits are subject to different SNRs, the case of a two-state channel is taken as an example. An extension to the case of the general multi-state channel can be conducted in a straightforward manner. A two-state channel is characterized by an SNR vector  $\boldsymbol{\gamma} = \begin{bmatrix} \gamma_1 & \gamma_2 \end{bmatrix}$ . The probabilities that the two states with respect to  $\gamma_1$  and  $\gamma_2$  occur are  $p_1$  and  $p_2$ , respectively. Moreover, it is assumed that these two SNRs are independent on each other. Considering two arbitrary code words with Hamming distance  $d$ , the exact PEP for these two code words in case of a two-state channel is determined by both the Hamming distance  $d$  and the position of the  $d$  different symbols. Nevertheless, the mean PEP that is averaged over all possible positions of the  $d$  different symbols is derived such that the detailed knowledge of the code is not required. In other words, an average is taken over all possible cases how the SNRs  $\gamma_1$  and  $\gamma_2$  are distributed among the  $d$  different symbols. Therefore, the Chernoff bounded PEP in a two-state channel is written as

$$P_{2,\text{Chernoff}}\left(d, \begin{bmatrix} \gamma_1 & \gamma_2 \end{bmatrix}\right) = \sum_{i=0}^d \binom{d}{i} p_1^i p_2^{d-i} \exp\left(-\left(i\gamma_1 + (d-i)\gamma_2\right)\right) \\ = \left(p_1 \exp(-\gamma_1) + p_2 \exp(-\gamma_2)\right)^d, \quad (\text{B.6})$$

where the final expression is obtained by using the binomial theorem, and the notation  $\binom{n}{r}$  represents the number of possible combinations of  $r$  objects from a set of  $n$  objects. Note that the term  $\left(p_1 \exp(-\gamma_1) + p_2 \exp(-\gamma_2)\right)$  is the averaged Chernoff-bounded symbol error probability for a two-state channel. Hence, similar as (B.3) for the case of a one-state channel, the following relationship is valid for the case of a two-state channel

$$P_{2,\text{Chernoff}}\left(d, \begin{bmatrix} \gamma_1 & \gamma_2 \end{bmatrix}\right) = \left(P_{2,\text{Chernoff}}\left(1, \begin{bmatrix} \gamma_1 & \gamma_2 \end{bmatrix}\right)\right)^d. \quad (\text{B.7})$$

According to the polynomial theorem, for the general multi-state channel that is characterized by an SNR vector  $\boldsymbol{\gamma} = \begin{bmatrix} \gamma_1 & \gamma_2 & \cdots & \gamma_N \end{bmatrix}$ , it can be shown that

$$P_{2,\text{Chernoff}}(d, \boldsymbol{\gamma}) = \left(P_{2,\text{Chernoff}}(1, \boldsymbol{\gamma})\right)^d. \quad (\text{B.8})$$

Now coming back to the derivation of the EESM, the goal is to obtain the expression of the effective SNR denoted by  $\gamma_{\text{eff}}$  of an equivalent one-state channel such that the Chernoff-

bounded error probability is equal to that of a multi-state channel characterized by  $\gamma$ , i.e.,

$$P_{\text{e,Chernoff}}(\gamma_{\text{eff}}) = P_{\text{e,Chernoff}}(\gamma). \quad (\text{B.9})$$

According to (B.8), equivalently, the desired  $\gamma_{\text{eff}}$  must render

$$P_{2,\text{Chernoff}}(1, \gamma_{\text{eff}}) = P_{2,\text{Chernoff}}(1, \gamma), \quad (\text{B.10})$$

which gives

$$\gamma_{\text{eff}} = -\ln \left( \sum_{n=1}^N p_n \exp(-\gamma_n) \right). \quad (\text{B.11})$$

In OFDM systems, the elements of  $\gamma$  can be the instantaneous SINRs measured on  $N$  subcarriers. The corresponding EESM is then given by

$$\gamma_{\text{eff}} = -\ln \left( \frac{1}{N} \sum_{n=1}^N \exp(-\gamma_n) \right). \quad (\text{B.12})$$



---

## Appendix C.

### Evaluation of the accuracy of Exponential Effective SINR Mapping (EESM)

In this appendix, we evaluate the accuracy of the Exponential Effective SINR Mapping (EESM) scheme that is employed in the system-level simulator introduced in Section 2.6. In Figure C.1, the EESM scheme [Eri03] is compared with the instantaneous SNR method where the effective SINR is computed as the average of the instantaneous SINRs of all the subcarriers. Recall

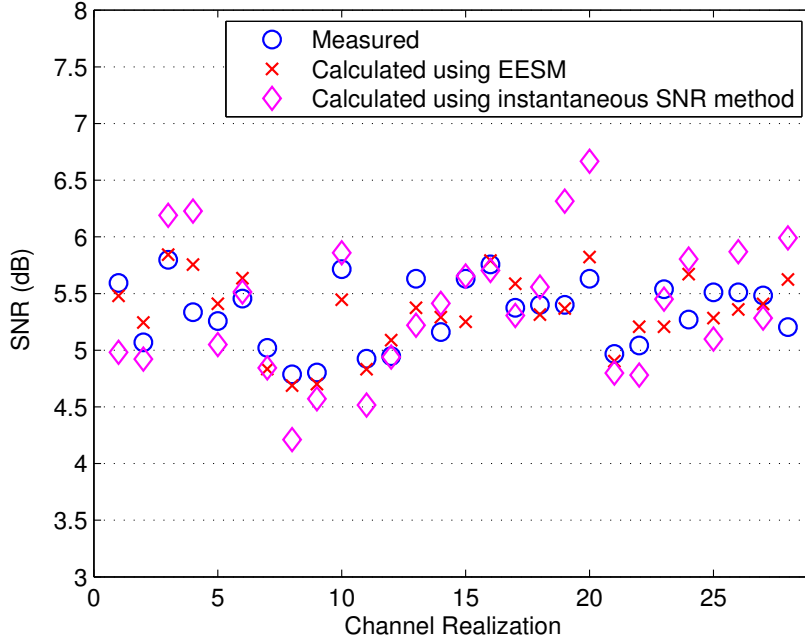


Figure C.1.: Comparison of EESM and the instantaneous SNR method for MCS 1

that when using EESM, the expression of the effective SINR is given by

$$\rho_{\text{eff}} = -\beta_2 \ln \left( \frac{1}{N_{\text{SS}} \cdot N_{\text{SD}}} \sum_{j=1}^{N_{\text{SD}}} \sum_{i=1}^{N_{\text{SS}}} \exp \left( -\frac{\rho_{i,j}}{\beta_1} \right) \right), \quad (\text{C.1})$$

where  $N_{\text{SS}}$  and  $N_{\text{SD}}$  denote the number of spatial streams and the number of subcarriers, respectively. The instantaneous SINR measured on the  $i$ -th stream and on the  $j$ th subcarrier is represented by  $\rho_{i,j}$ . Here  $\beta_1$  and  $\beta_2$  are the parameters that depend on the MCS and the channel model. They are obtained via calibration described in detail in Section 2.6. On the other hand, when the instantaneous SNR method is employed, the effective SINR is computed as

$$\rho_{\text{eff}} = \frac{1}{N_{\text{SS}} \cdot N_{\text{SD}}} \sum_{j=1}^{N_{\text{SD}}} \sum_{i=1}^{N_{\text{SS}}} \rho_{i,j}. \quad (\text{C.2})$$

It can be seen in Figure C.1 that the EESM algorithm provides a much more accurate estimate of the effective SINR than the instantaneous SNR method. This is due to the fact that well-tuned parameters are employed in the EESM scheme, where the frequency selectivity of the channel and the MCSs are taken into account. Therefore, it leads to a more accurate link-to-system mapping tool compared to the instantaneous SNR method.

In Figure C.2, the throughput CCDF is shown for MCS 3, in a single-user 4-by-4 MIMO system. Channel Model D [SD04], [IEE10] applicable to indoor (e.g., typical or large of-

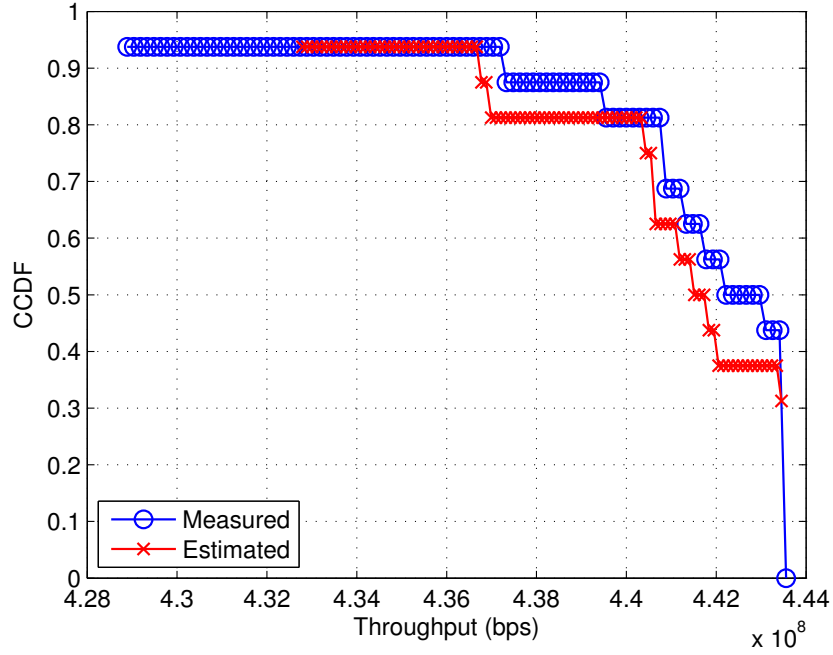


Figure C.2.: CCDF of the measured throughput and the estimated throughput by employing EESM for MCS 3 in a single-user 4-by-4 MIMO setting

fices) WLAN systems is considered in this simulation. Its frequency response is illustrated in Figure C.3. Note that this channel model is used in the numerical simulations discussed in Chapter 2. We can see that Model D exhibits obvious frequency selectivity. Considering that the OFDM symbol duration is  $4 \mu s$  for 80 MHz transmissions, this channel model has a slow variation in the time direction. The estimated performance is obtained via the EESM

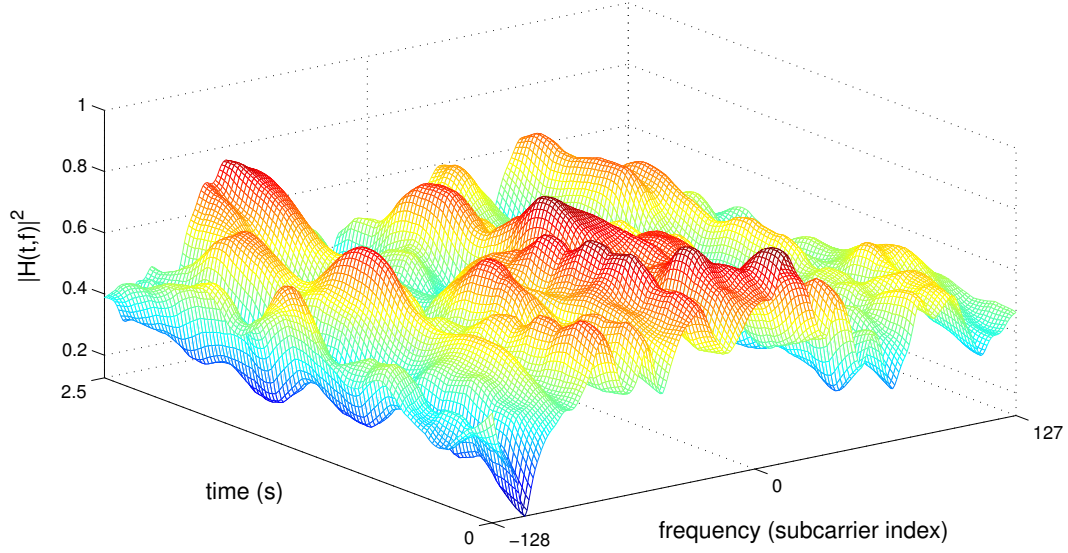


Figure C.3.: Channel frequency response of IEEE 802.11ac channel Model D

algorithm with the optimal values of  $\beta_1$  and  $\beta_2$  (cf. Appendix B). It can be observed that the estimated throughput is very close to the simulated one in the presence of such a frequency selective propagation channel. Therefore, when the EESM is employed in the system-level simulations with selected adjusting parameters  $\beta_1$  and  $\beta_2$  for a certain MCS, the estimated system throughput can model the real throughput with a satisfactory accuracy.

## Appendix D.

### Modulation and Coding Schemes (MCSs) specified in IEEE 802.11ac

Section 2.6 presents a system-level simulator for multi-user MIMO downlink settings, where the Modulation and Coding Schemes (MCSs)-dependent parameters for the link-to-system interface can be calibrated according to the IEEE 802.11ac specifications. As specified in IEEE 802.11ac [WG813], data subcarriers are modulated using Binary Phase Shift Keying (BPSK), Quadrature Phase Shift Keying (QPSK), 16 Quadrature Amplitude Modulation (16 QAM), 64 QAM, and 256 QAM. Forward Error Correction (FEC) coding (convolutional or LDPC coding) is used with coding rates of  $1/2$ ,  $2/3$ ,  $3/4$ , and  $5/6$ . The 10 MCSs are listed in Table D.1.

Table D.1.: IEEE 802.11ac MCSs (80 MHz, single data stream, and the length of CP is 800 ns);  $N_{\text{DBPS}}$  denotes the number of data bits per OFDM symbol

MCS index	Modulation	Coding rate	$N_{\text{DBPS}}$	Data rate (Mbit/s)
0	BPSK	$1/2$	117	29.3
1	QPSK	$1/2$	234	58.5
2	QPSK	$3/4$	351	87.8
3	16 QAM	$1/2$	468	117.0
4	16 QAM	$3/4$	702	175.5
5	64 QAM	$2/3$	936	234
6	64 QAM	$3/4$	1053	263.3
7	64 QAM	$5/6$	1170	292.5
8	256 QAM	$3/4$	1404	351.0
9	256 QAM	$5/6$	1560	390.0

---

## Appendix E.

### Derivation of the widely linear MMSE receiver

In Section 4.3, a two-step receiver has been presented. A linear MMSE receiver is employed in the first step for the intrinsic interference mitigation, whereas a widely linear MMSE receiver is used in the second step. The detailed derivation of the widely linear MMSE receiver is as follows. Let  $\mathbf{y} \in \mathbb{C}^{M_R}$  denote the received signal of a point-to-point MIMO system with  $M_T$  transmit antennas and  $M_R$  receive antennas. It is expressed as

$$\mathbf{y} = \mathbf{H} \cdot \mathbf{x} + \mathbf{n}, \quad (\text{E.1})$$

where  $\mathbf{H} \in \mathbb{C}^{M_R \times M_T}$  represents the channel matrix,  $\mathbf{x} \in \mathbb{C}^{M_T}$  is the transmit signal, and  $\mathbf{n} \in \mathbb{C}^{M_R}$  denotes the AWGN vector. The widely linear MMSE receiver given by

$$\hat{\mathbf{x}} = \begin{bmatrix} \mathbf{W}_1^H & \mathbf{W}_2^H \end{bmatrix} \cdot \begin{bmatrix} \mathbf{y} \\ \mathbf{y}^* \end{bmatrix}, \quad (\text{E.2})$$

where the matrices  $\mathbf{W}_1$  and  $\mathbf{W}_2$  are computed such that the MSE  $\mathbb{E}\{\|\mathbf{x} - \hat{\mathbf{x}}\|^2\}$  is minimized. Based on the orthogonality principle [PC95], each component of  $(\mathbf{x} - \hat{\mathbf{x}})$  is orthogonal to  $\mathbf{y}$  and  $\mathbf{y}^*$ , i.e.,

$$\mathbb{E}\{\mathbf{y} \cdot (x_i - \hat{x}_i)^*\} = \mathbf{0} \in \mathbb{R}^{M_R} \quad (\text{E.3})$$

$$\mathbb{E}\{\mathbf{y}^* \cdot (x_i - \hat{x}_i)^*\} = \mathbf{0} \in \mathbb{R}^{M_R}, \quad (\text{E.4})$$

where  $x_i$  and  $\hat{x}_i$  are the  $i$ -th element of  $\mathbf{x}$  and  $\hat{\mathbf{x}}$ , respectively, for  $i = 1, 2, \dots, M_T$ . Accordingly, the following can be obtained

$$\mathbb{E}\{\mathbf{y} \cdot (\mathbf{x} - \hat{\mathbf{x}})^H\} = \mathbf{0} \in \mathbb{R}^{M_R \times M_T} \quad (\text{E.5})$$

$$\mathbb{E}\{\mathbf{y}^* \cdot (\mathbf{x} - \hat{\mathbf{x}})^H\} = \mathbf{0} \in \mathbb{R}^{M_R \times M_T}, \quad (\text{E.6})$$

which then lead to

$$\mathbb{E}\{\mathbf{y} \cdot \mathbf{x}^H\} = \mathbb{E}\{\mathbf{y} \cdot \hat{\mathbf{x}}^H\} \quad (\text{E.7})$$

$$\mathbb{E} \{ \mathbf{y}^* \cdot \mathbf{x}^H \} = \mathbb{E} \{ \mathbf{y}^* \cdot \hat{\mathbf{x}}^H \}. \quad (\text{E.8})$$

Substituting (E.2) into the right-hand side of (E.7) yields

$$\begin{aligned} \mathbb{E} \{ \mathbf{y} \cdot \mathbf{x}^H \} &= \mathbb{E} \left\{ \mathbf{y} \cdot \left( \mathbf{W}_1^H \cdot \mathbf{y} + \mathbf{W}_2^H \cdot \mathbf{y}^* \right)^H \right\} \\ &= \mathbb{E} \{ \mathbf{y} \cdot \mathbf{y}^H \} \cdot \mathbf{W}_1 + \mathbb{E} \{ \mathbf{y} \cdot \mathbf{y}^T \} \cdot \mathbf{W}_2. \end{aligned} \quad (\text{E.9})$$

Let us define

$$\begin{aligned} \mathbf{R}_{yy} &= \mathbb{E} \{ \mathbf{y} \cdot \mathbf{y}^H \} \\ \mathbf{R}_{yy^*} &= \mathbb{E} \{ \mathbf{y} \cdot \mathbf{y}^T \} \\ \mathbf{R}_{yx} &= \mathbb{E} \{ \mathbf{y} \cdot \mathbf{x}^H \}. \end{aligned}$$

and consequently obtain

$$\mathbf{R}_{yy} \cdot \mathbf{W}_1 + \mathbf{R}_{yy^*} \cdot \mathbf{W}_2 = \mathbf{R}_{yx}. \quad (\text{E.10})$$

Similarly, substituting (E.2) into the right-hand side of (E.8) gives

$$\begin{aligned} \mathbb{E} \{ \mathbf{y}^* \cdot \mathbf{x}^H \} &= \mathbb{E} \left\{ \mathbf{y}^* \cdot \left( \mathbf{W}_1^H \cdot \mathbf{y} + \mathbf{W}_2^H \cdot \mathbf{y}^* \right)^H \right\} \\ &= \mathbb{E} \{ \mathbf{y}^* \cdot \mathbf{y}^H \} \cdot \mathbf{W}_1 + \mathbb{E} \{ \mathbf{y}^* \cdot \mathbf{y}^T \} \cdot \mathbf{W}_2 \\ &= \mathbb{E} \{ \mathbf{y} \cdot \mathbf{y}^T \}^* \cdot \mathbf{W}_1 + \mathbb{E} \{ \mathbf{y} \cdot \mathbf{y}^H \}^* \cdot \mathbf{W}_2 \\ &= \mathbf{R}_{yy^*}^* \cdot \mathbf{W}_1 + \mathbf{R}_{yy}^* \cdot \mathbf{W}_2. \end{aligned} \quad (\text{E.11})$$

Assuming that the desired signal and the noise are uncorrelated and  $\mathbb{E} \{ \mathbf{x} \cdot \mathbf{x}^H \} = \mathbf{I}_{M_T}$ , we have

$$\mathbb{E} \{ \mathbf{y} \cdot \mathbf{x}^H \} = \mathbf{H} \quad (\text{E.12})$$

$$\mathbb{E} \{ \mathbf{y}^* \cdot \mathbf{x}^H \} = \mathbf{H}^*, \quad (\text{E.13})$$

and consequently

$$\mathbf{R}_{yy} \cdot \mathbf{W}_1 + \mathbf{R}_{yy^*} \cdot \mathbf{W}_2 = \mathbf{H} \quad (\text{E.14})$$

$$\mathbf{R}_{yy^*}^* \cdot \mathbf{W}_1 + \mathbf{R}_{yy}^* \cdot \mathbf{W}_2 = \mathbf{H}^*. \quad (\text{E.15})$$

---

Finally,  $\mathbf{W}_1$  and  $\mathbf{W}_2$  are obtained as follows by solving (E.14) and (E.15)

$$\mathbf{W}_1 = \left( \mathbf{R}_{yy} - \mathbf{R}_{yy^*} \cdot \mathbf{R}_{yy}^{*-1} \cdot \mathbf{R}_{yy^*}^* \right)^{-1} \cdot \left( \mathbf{H} - \mathbf{R}_{yy^*} \cdot \mathbf{R}_{yy}^{*-1} \cdot \mathbf{H}^* \right) \quad (\text{E.16})$$

$$\mathbf{W}_2 = \left( \mathbf{R}_{yy}^* - \mathbf{R}_{yy^*}^* \cdot \mathbf{R}_{yy}^{-1} \cdot \mathbf{R}_{yy^*} \right)^{-1} \cdot \left( \mathbf{H}^* - \mathbf{R}_{yy^*}^* \cdot \mathbf{R}_{yy}^{-1} \cdot \mathbf{H} \right). \quad (\text{E.17})$$

## Appendix F.

### Proof of Theorem 9.3.1 [RHD14]

To show the identity (9.10) we first need to eliminate the core tensor in (9.6). This is achieved by observing that  $\hat{\mathcal{S}}^{[s]}$  can be computed from  $\mathcal{X}$  via

$$\hat{\mathcal{S}}^{[s]} = \mathcal{X} \times_1 \mathbf{U}_1^{[s]\text{H}} \dots \times_{R+1} \mathbf{U}_{R+1}^{[s]\text{H}}. \quad (\text{F.1})$$

Substituting (F.1) into (9.6) yields

$$\hat{\mathcal{U}}^{[s]} = \mathcal{X} \times_1 \hat{\mathbf{T}}_1 \dots \times_R \hat{\mathbf{T}}_R \times_{R+1} \left( \hat{\Sigma}_s^{-1} \cdot \hat{\mathcal{U}}_{R+1}^{[s]\text{H}} \right), \quad (\text{F.2})$$

where  $\hat{\mathbf{T}}_r = \hat{\mathcal{U}}_r^{[s]} \cdot \hat{\mathcal{U}}_r^{[s]\text{H}}$ . Expanding the  $(R+1)$ -mode unfolding of (F.2) based on the property (8.4) gives

$$\left[ \hat{\mathcal{U}}^{[s]} \right]_{(R+1)} = \hat{\Sigma}_s^{-1} \cdot \hat{\mathcal{U}}_{R+1}^{[s]\text{H}} \cdot [\mathcal{X}]_{(R+1)} (\hat{\mathbf{T}}_1 \otimes \hat{\mathbf{T}}_2 \dots \otimes \hat{\mathbf{T}}_R)^{\text{T}}.$$

Therefore, it remains to be shown that  $\hat{\Sigma}_s^{-1} \cdot \hat{\mathcal{U}}_{R+1}^{[s]\text{H}} \cdot [\mathcal{X}]_{(R+1)} = \hat{\mathcal{U}}_s^{\text{T}}$ . This is achieved by observing that  $[\mathcal{X}]_{(R+1)} = \mathbf{X}^{\text{T}}$  and therefore,  $\hat{\mathcal{U}}_{R+1}^{[s]} = \hat{\mathbf{V}}_s^*$  (as defined in (9.2)). Consequently,

$$[\mathcal{X}]_{(R+1)}^{\text{T}} \cdot \hat{\mathcal{U}}_{R+1}^{[s]*} \cdot \hat{\Sigma}_s^{-1} = \mathbf{X} \cdot \hat{\mathbf{V}}_s \cdot \hat{\Sigma}_s^{-1} = \hat{\mathcal{U}}_s, \quad (\text{F.3})$$

where the last step also follows from (9.2).



---

## Appendix G.

### Avoiding matrix inversion in TeTraKron-PAST

In Section 9.4, we discuss how to obtain a tensor extension of the matrix-based PAST algorithm [Yan95b] via TeTraKron. Note that in the resulting TeTraKron-PAST scheme, to update the  $r$ -mode subspace estimates, the inverse of the  $d \times d$  correlation matrix  $\mathbf{C}_{y_r y_r}(n)$  is involved. In the following, we show how to avoid this matrix inversion and present a computational complexity analysis.

Recall that the  $d \times d$  correlation matrix  $\mathbf{C}_{y_r y_r}(n)$  is given by

$$\mathbf{C}_{y_r y_r}(n) = \beta \mathbf{C}_{y_r y_r}(n-1) + \mathbf{Y}_r(n) \mathbf{Y}_r^H(n), \quad (\text{G.1})$$

where

$$\mathbf{Y}_r(n) = \begin{bmatrix} \mathbf{y}_{r,1} & \mathbf{y}_{r,2} & \dots & \mathbf{y}_{r,\frac{M}{M_r}} \end{bmatrix} \in \mathbb{C}^{d \times \frac{M}{M_r}} \quad (\text{G.2})$$

with  $\mathbf{y}_{r,m}$  denoting the  $m$ -th column of  $\mathbf{Y}_r(n)$ ,  $m = 1, 2, \dots, \frac{M}{M_r}$ . Alternatively,  $\mathbf{C}_{y_r y_r}(n)$  can be written as

$$\mathbf{C}_{y_r y_r}(n) = \beta \mathbf{C}_{y_r y_r}(n-1) + \sum_{m=1}^{\frac{M}{M_r}} \mathbf{y}_{r,m} \mathbf{y}_{r,m}^H. \quad (\text{G.3})$$

Define

$$\mathbf{C}_{y_r y_r}^{(m)}(n) = \mathbf{C}_{y_r y_r}^{(m-1)}(n-1) + \mathbf{y}_{r,m} \mathbf{y}_{r,m}^H, \quad m = 2, \dots, \frac{M}{M_r} \quad (\text{G.4})$$

$$\mathbf{C}_{y_r y_r}^{(1)}(n) = \beta \mathbf{C}_{y_r y_r}(n-1) + \mathbf{y}_{r,1} \mathbf{y}_{r,1}^H. \quad (\text{G.5})$$

Notice that consequently  $\mathbf{C}_{y_r y_r}^{(\frac{M}{M_r})}(n) = \mathbf{C}_{y_r y_r}(n)$ . Based on the matrix inversion lemma,  $\mathbf{C}_{y_r y_r}^{(1)-1}(n)$  is computed as

$$\mathbf{C}_{y_r y_r}^{(1)-1}(n) = \frac{1}{\beta} \left( \mathbf{P}_r(n-1) - \frac{\mathbf{P}_r(n-1) \mathbf{y}_{r,1} \mathbf{y}_{r,1}^H \mathbf{P}_r(n-1)}{\beta + \mathbf{y}_{r,1}^H \mathbf{P}_r(n-1) \mathbf{y}_{r,1}} \right), \quad (\text{G.6})$$

where  $\mathbf{P}_r(n-1) = \mathbf{C}_{y_r y_r}^{-1}(n-1)$  is known from the previous snapshot  $(n-1)$ . Let us use  $\mathbf{P}_r^{(m)}(n) = \mathbf{C}_{y_r y_r}^{(m)-1}(n)$  ( $m = 1, \dots, \frac{M}{M_r}$ ) as short-hand notation. Similarly, for  $m = 2, \dots, \frac{M}{M_r}$ ,  $\mathbf{P}_r^{(m)}(n) = \mathbf{C}_{y_r y_r}^{(m)-1}(n)$  is sequentially calculated according to the matrix inversion lemma as

$$\mathbf{P}_r^{(m)}(n) = \mathbf{P}_r^{(m-1)}(n) - \frac{\mathbf{P}_r^{(m-1)}(n) \mathbf{y}_{r,m} \mathbf{y}_{r,m}^H \mathbf{P}_r^{(m-1)}(n)}{1 + \mathbf{y}_{r,m}^H \mathbf{P}_r^{(m-1)}(n) \mathbf{y}_{r,m}}. \quad (\text{G.7})$$

Consequently, the inverse of  $\mathbf{C}_{y_r y_r}(n)$  is obtained as  $\mathbf{P}_r^{(\frac{M}{M_r})}(n)$ , and the direct matrix inversion is avoided. Considering a 2-D example where  $M_1 = M_2$ , we compute the FLOPs (floating point

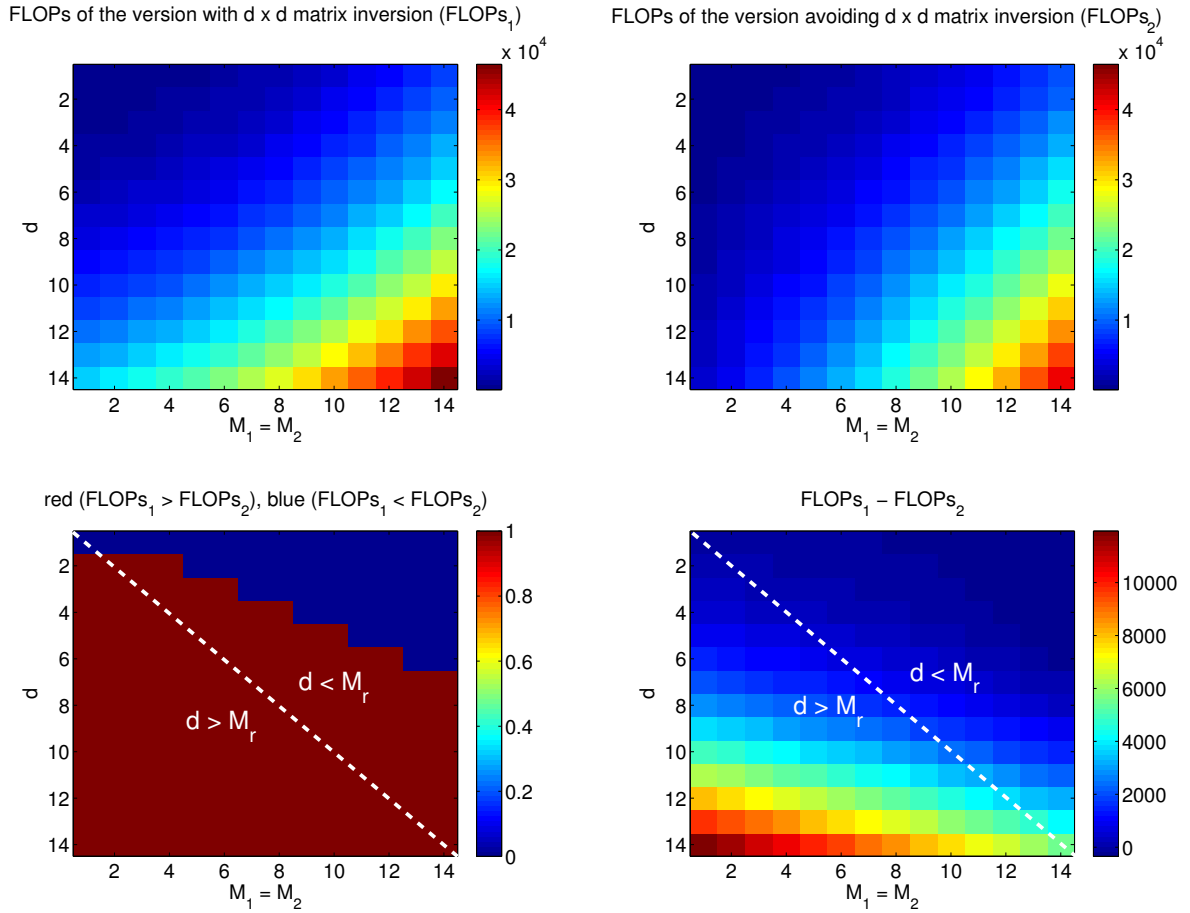


Figure G.1.: Complexity comparison between the version with the  $d \times d$  matrix inversion and the version of avoiding the matrix inversion in terms of FLOPs for updating the  $r$ -mode subspace estimates

---

operations) used for each update of the  $r$ -mode subspace estimates in the TeTraKron-PAST scheme using the Lightspeed toolbox [Min14]. Two versions are compared in Figure G.1. In one of them, the direct inverse of the  $d \times d$  correlation matrix is computed, whereas in the other version the method of avoiding the matrix inversion described above is employed. It is observed that for  $d < M_r$ , i.e., the cases that are relevant, as the gap between  $M_r$  and  $d$  is larger, it is more likely that the version with the  $d \times d$  matrix inversion leads to a lower computational complexity. Otherwise, e.g., when  $d$  is very close to  $M_r$  (corresponding to the region in the upper triangular part of the graphs in Figure G.1 that is near the diagonal), avoiding the matrix inversion as introduced above requires less computational effort.

## Bibliography

---

### Publications and Technical Documents as Co- or First Author

---

- [CBHN15a] Y. Cheng, L. G. Baltar, M. Haardt, and J. A. Nossek, "Downlink per-user multi-streaming for FBMC/OQAM based multi-user MIMO with highly frequency selective channels," in *Proc. International ITG Workshop on Smart Antennas (WSA 2015)*, Ilmenau, Germany, Mar. 2015.
- [CBHN15b] —, "Precoder and equalizer design for multi-user MIMO FBMC/OQAM with highly frequency selective channels," in *Proc. IEEE Int. Conference on Acoustics, Speech, and Signal Processing (ICASSP)*, Brisbane, Australia, Apr. 2015.
- [CH13a] Y. Cheng and M. Haardt, "Robust multi-dimensional model order estimation in the presence of brief sensor failures," in *Proc. 18-th International Conference on Digital Signal Processing (DSP 2013)*, Santorini, Greece, Jul. 2013.
- [CH13b] —, "Widely Linear Processing in MIMO FBMC/OQAM Systems," in *Proc. 10-th International Symposium on Wireless Communications Systems (ISWCS 2013)*, Aug. 2013.
- [CHH<sup>+</sup>13] Y. Cheng, M. Haardt, H. Henniger, R. Metzger, and E. Diedrich, "Interference suppression and electronic tracking using antenna arrays at satellite ground stations," in *Proc. International ITG Workshop on Smart Antennas (WSA 2013)*, Stuttgart, Germany, Mar. 2013.
- [CLH14a] Y. Cheng, P. Li, and M. Haardt, "Coordinated beamforming for the multi-user MIMO downlink using FBMC/OQAM," in *Proc. 6th International Symposium on Communications, Control, and Signal Processing (ISCCSP 2014)*, Athens, Greece, May 2014.
- [CLH14b] —, "Coordinated beamforming in MIMO FBMC/OQAM systems," in *Proc. IEEE Int. Conference on Acoustics, Speech, and Signal Processing (ICASSP)*, Florence, Italy, May 2014.
- [CLH14c] —, "FBMC/OQAM for the Asynchronous Multi-User MIMO Uplink," in *Proc. International ITG Workshop on Smart Antennas (WSA 2014)*, Erlangen, Germany, Mar. 2014.
- [CLH14d] —, "Intrinsic interference mitigating coordinated beamforming for the FBMC/OQAM based downlink," *EURASIP Journal on Advances in Signal Processing*, vol. 2014:86, May 2014.

- 
- [CLZ<sup>+</sup>12] Y. Cheng, S. Li, J. Zhang, F. Roemer, M. Haardt, Y. Zhou, and M. Dong, “Linear precoding-based geometric mean decomposition (LP-GMD) for multi-user MIMO systems,” in *Proc. 9-th International Symposium on Wireless Communications Systems (ISWCS 2012)*, Paris, France, Aug. 2012.
  - [CLZ<sup>+</sup>14] Y. Cheng, S. Li, J. Zhang, F. Roemer, B. Song, M. Haardt, Y. Zhou, and M. Dong, “An Efficient and Flexible Transmission Strategy for the Multicarrier Multiuser MIMO Downlink,” *IEEE Transactions on Vehicular Technology*, vol. 63, no. 2, pp. 628 – 642, Feb. 2014.
  - [CPNCH15] M. Caus, A. I. Pérez-Neira, Y. Cheng, and M. Haardt, “Towards a non-error floor multi-stream beamforming design for FBMC/OQAM,” in *Proc. of IEEE International Conference on Communications (ICC 2015)*, London, UK, June 2015.
  - [CRH15] Y. Cheng, V. Ramireddy, and M. Haardt, “Non-linear precoding for the downlink of FBMC/OQAM based multi-user MIMO systems,” in *Proc. International ITG Workshop on Smart Antennas (WSA 2015)*, Ilmenau, Germany, Mar. 2015.
  - [CRKH14] Y. Cheng, F. Roemer, O. Khatib, and M. Haardt, “Tensor subspace Tracking via Kronecker structured projections (TeTraKron) for time-varying multidimensional harmonic retrieval,” *EURASIP Journal on Advances in Signal Processing*, vol. 2014:123, Aug. 2014.
  - [CSR<sup>+</sup>12] Y. Cheng, N. Song, F. Roemer, M. Haardt, H. Henniger, R. Metzsig, and E. Diedrich, “Satellite ground stations with electronic beam steering,” in *Proc. 1st International IEEE-AESS Conference in Europe about Space and Satellite Telecommunications (ESTEL 2012)*, Rome, Italy, Oct. 2012.
  - [CYH16] Y. Cheng, A. Yeredor, and M. Haardt, “Extension of SeDJoCo and its use in a combination of multicast and coordinated multi-point systems,” in *Proc. IEEE Int. Conference on Acoustics, Speech, and Signal Processing (ICASSP 2016)*, Shanghai, China, Mar. 2016.
  - [CYWH15] Y. Cheng, A. Yeredor, A. Weiss, and M. Haardt, “Extension of the “Sequentially Drilled” Joint Congruence Transformation (SeDJoCo) Problem,” in *Proc. IEEE 6th Int. Workshop on Computational Advances in Multi-Sensor Adaptive Processing (CAMSAP 2015)*, Cancun, Mexico, Dec. 2015.
  - [DCL<sup>+</sup>a] M. Dong, Y. Cheng, S. Li, F. Roemer, J. Zhang, and M. Haardt, “Linear precoding method and device for multi-user multiple-input multiple-output systems,” patent WO/2013/034 088, 03 14, 2013. [Online]. Available: <http://patentscope.wipo.int/search/en/WO2013034088>
  - [DCL<sup>+</sup>b] —, “Method for SDMA transmission in multicarrier MU MIMO system and base station,” patent WO/2013/034 093, 03 14, 2013. [Online]. Available: <http://patentscope.wipo.int/search/en/WO2013034093>
-

- [DCL<sup>+</sup>c] M. Dong, Y. Cheng, S. Li, F. Roemer, J. Zhang, B. Song, and M. Haardt, “Linear precoding method and device for communication system,” patent WO/2013/029 561, 03 07, 2013. [Online]. Available: <http://patentscope.wipo.int/search/en/WO2013029561>
- [LCZ<sup>+</sup>12] S. Li, Y. Cheng, J. Zhang, F. Roemer, B. Song, M. Haardt, Y. Zhou, and M. Dong, “Efficient spatial scheduling and precoding algorithms for MC MU MIMO system,” in *Proc. 9-th International Symposium on Wireless Communications Systems (ISWCS 2012)*, Paris, France, Aug. 2012.
- [MCR<sup>+</sup>12] M. Muma, Y. Cheng, F. Roemer, M. Haardt, and A. M. Zoubir, “Robust source number enumeration for R-dimensional arrays in case of brief sensor failures,” in *Proc. IEEE Int. Conference on Acoustics, Speech, and Signal Processing (ICASSP)*, Kyoto, Japan, Mar. 2012, pp. 3709 – 3712.
- [PNCZ<sup>+</sup>16] A. I. Pérez-Neira, M. Caus, R. Zakaria, D. Le Ruyet, E. Kofidis, M. Haardt, X. Mestre, and Y. Cheng, “MIMO Signal Processing in Offset-QAM Based Filter Bank Multicarrier Systems,” *IEEE Transactions on Signal Processing*, vol. PP, no. 99, June 2016.
- [RKCH13] F. Roemer, E.-K. Kasnakli, Y. Cheng, and M. Haardt, “Tensor subspace Tracking via Kronecker structured projections (TeTraKron),” in *Proc. IEEE 5th Int. Workshop on Computational Advances in Multi-Sensor Adaptive Processing (CAMSAP 2013)*, Saint Martin, French Antilles, Dec. 2013.
- [YCH16] A. Yeredor, Y. Cheng, and M. Haardt, “On Multiple Solutions of the “Sequentially Drilled” Joint Congruence Transformation (SeDJoCo) Problem for Semi-Blind Source Separation,” in *Proc. IEEE Int. Conference on Acoustics, Speech, and Signal Processing (ICASSP 2016)*, Shanghai, China, Mar. 2016.

---

## References by Other Authors

---

- [5GN] “5th Generation Non-Orthogonal Waveforms for asynchronous signaling (5GNOW).” [Online]. Available: <http://www.5gnow.eu>
- [AAM02] S. Attallah and K. Abed-Meraim, “Low-cost adaptive algorithm for noise subspace estimation,” *Electronics Letters*, vol. 38, no. 12, pp. 609 – 611, 2002.
- [Ala98] S. Alamouti, “A simple transmit diversity technique for wireless communications,” *IEEE JSAC*, vol. 16, no. 8, pp. 1451 – 1458, Oct. 1998.
- [BCC<sup>+</sup>07] E. Biglieri, R. Calderbank, A. Constantinides, A. Goldsmith, A. Paulraj, and H. V. Poor, *MIMO wireless communications*. Cambridge University Press, 2007.

- 
- [BDR05] R. Badeau, B. David, and G. Richard, "Fast approximated power iteration subspace tracking," *IEEE Transactions on Signal Processing*, vol. 53, no. 8, pp. 2931 – 2941, 2005.
  - [Bel01] M. G. Bellanger, "Specification and design of a prototype filter for filter bank based multicarrier transmission," in *Proc. IEEE Int. Conf. Acoustics, Speech, and Signal Processing*, May 2001.
  - [Bel10] —, "FBMC physical layer: a primer," June 2010. [Online]. Available: [http://www.ict-phydyas.org/teamSPACE/internal-folder/FBMC-Primer\\_06-2010.pdf](http://www.ict-phydyas.org/teamSPACE/internal-folder/FBMC-Primer_06-2010.pdf)
  - [Bel11] —, "Specification and design of a prototype filter for filter bank based multicarrier transmission," in *Proc. IEEE Int. Conference on Acoustics, Speech, and Signal Processing (ICASSP)*, May 2011.
  - [BH07] F. Boccardi and H. Huang, "Limited downlink network coordination in cellular network," in *Proc. IEEE International Symposium on Personal Indoor and Mobile Radio Communications (PIMRC)*, Sept. 2007.
  - [BL86] A. Bax and L. Lerner, "Two-dimensional NMR spectroscopy," *J. Amer. Assoc. for the Advancement of Science*, vol. 232, pp. 960 – 967, May 1986.
  - [BNN12] L. G. Baltar, M. Newinger, and J. A. Nossek, "Structured subchannel impulse response estimation for Filter Bank based Multicarrier systems," in *Proc. 9-th International Symposium on Wireless Communications Systems (ISWCS 2012)*, Aug. 2012.
  - [BWN09] L. G. Baltar, D. Waldhauser, and J. Nossek, "MMSE subchannel decision feedback equalization for filter bank based multicarrier systems," in *Proc. IEEE Int. Symp. Circuits Syst. (ISCAS 2009)*, 2009, pp. 2802 – 2805.
  - [CCKC06] J. Cho, Y. Chang, Y. Kim, and J. Chon, "Analytic optimization of hybrid ARQ performance in wireless packet data systems," in *Proc. IEEE Global Telecommunications Conference*, Nov. 2006.
  - [CGN98] W. Chen, G. B. Giannakis, and N. Nandhakumar, "A Harmonic Retrieval Framework for Discontinuous Motion Estimation," *IEEE Transactions on Image Processing*, vol. 7, no. 9, Sept. 1998.
  - [CMIH08] C.-B. Chae, D. Mazzarese, T. Inoue, and R. W. Heath Jr., "Coordinated beamforming for the multiuser MIMO broadcast channel with limited feedforward," *IEEE Trans. Signal Process.*, vol. 56, no. 12, pp. 6044 – 6056, Dec. 2008.
  - [CMJH08] C.-B. Chae, D. Mazzarese, N. Jindal, and R. W. Heath Jr., "Coordinated beamforming with limited feedback in the MIMO broadcast channel," *IEEE Journal on Selected Areas in Communications*, vol. 26, no. 8, pp. 1505 – 1515, Oct. 2008.
-

- [CPN11] M. Caus and A. I. Pérez-Neira, “Transmit and receive filters for MISO FBMC systems subjected to power constraints,” in *Proc. IEEE Int. Conference on Acoustics, Speech, and Signal Processing (ICASSP)*, May 2011.
- [CPN13a] —, “Comparison of linear and widely linear processing in MIMO-FBMC systems,” in *Proc. 10-th International Symposium on Wireless Communications Systems (ISWCS 2013)*, Aug. 2013.
- [CPN13b] —, “Multi-stream transmission in MIMO-FBMC systems,” in *Proc. IEEE Int. Conference on Acoustics, Speech, and Signal Processing (ICASSP)*, May 2013.
- [CPN13c] —, “SDMA for filterbank with Tomlinson Harashima precoding,” in *Proc. ICC 2013*, June 2013.
- [CPN14a] —, “Experimental performance bounds of MIMO-FBMC/OQAM systems,” in *Proc. European Wireless 2014*, May 2014.
- [CPN14b] —, “Multi-stream transmission for highly frequency selective channels in MIMO-FBMC/OQAM systems,” *IEEE Trans. Signal Process.*, vol. 62, no. 4, pp. 786 – 796, Feb. 2014.
- [CPNM13] M. Caus, A. I. Pérez-Neira, and M. Moretti, “SDMA for FBMC with block diagonalization,” in *14-th IEEE Int. Workshop on Signal Processing Advances in Wireless Communications (SPAWC 2013)*, June 2013.
- [CZZ06] S. C. Chan, Z. G. Zhang, and Y. Zhou, “A New Adaptive Kalman Filter-Based Subspace Tracking Algorithm and Its Application to DOA Estimation,” in *Proc. IEEE International Symposium on Circuits and Systems (ISCAS 2006)*, May 2006.
- [dCHRD07] J. P. C. L. da Costa, M. Haardt, F. Roemer, and G. Del Galdo, “Enhanced model order estimation using higher-order arrays,” in *Proc. of the 40th Asilomar Conf. on Signals, Systems, and Computers*, Nov. 2007.
- [dCRHdS11] J. P. C. L. da Costa, F. Roemer, M. Haardt, and R. T. de Sousa Jr., “Multi-dimensional model order selection,” *EURASIP Journal on Advances in Signal Processing*, vol. 1, pp. 1 – 26, 2011.
- [Del10] J. P. Delmas, “Subspace tracking for signal processing,” in *Adaptive Signal Processing: Next Generation Solutions*, T. Adali and S. Haykin, Eds., 2010, pp. 211 – 270.
- [dLdMV00] L. de Lathauwer, B. de Moor, and J. Vanderwalle, “A multilinear singular value decomposition,” *SIAM J. Matrix Anal. Appl.*, vol. 21, no. 4, pp. 1253 – 1278, 2000.
- [DPS11] E. Dahlman, S. Parkvall, and J. Skold, *4G LTE/LTE-Advanced for Mobile Broadband*. Academic Press, 2011.



- 
- [EMP] “Enhanced Multicarrier techniques for professional ad-hoc and cell-based communications (EMPhAtiC).” [Online]. Available: <http://www.ict-emphatic.eu>
- [Eri03] Ericsson, “System-level evaluation of OFDM - further considerations,” Nov. 2003, 3GPP TSG-RAN WG1 No. 35, R1-031303.
- [FBL03] B. Farhang-Boroujeny and L. Lin, “Analysis of post-combiner equalizers in cosine-modulated filterbank-based transmultiplexer systems,” *IEEE Trans. Signal Process.*, vol. 51, no. 12, pp. 3249 – 3262, Dec. 2003.
- [FDH07] M. Fuchs, G. Del Galdo, and M. Haardt, “Low-complexity space-time-frequency scheduling for MIMO systems with SDMA,” *IEEE Trans. Veh. Technol.*, vol. 56, no. 5, pp. 2775 – 2784, Sept. 2007.
- [FK12] F. Frederiksen and T. E. Kolding, “Performance and modeling of WCDMA/HSDPA transmission/H-ARQ schemes,” in *Proc. IEEE 56th Vehicular Technology Conference*, Sept. 2012.
- [FPT08] T. Fusco, A. Petrella, and M. Tanda, “Sensitivity of multi-user filter-bank multicarrier systems to synchronization errors,” in *Proc. ISCCSP*, Mar. 2008.
- [GJJV03] A. Goldsmith, S. Jafar, N. Jindal, and S. Vishwanath, “Capacity Limits of MIMO Channels,” *IEEE JSAC*, vol. 21, no. 5, pp. 684 – 702, June 2003.
- [GSL03] W. H. Gerstacker, R. Schober, and A. Lampe, “Receivers with widely linear processing for frequency-selective channels,” *IEEE Transactions on Communications*, vol. 51, no. 9, pp. 1512 – 1523, Sept. 2003.
- [GSS<sup>+</sup>03] D. Gesbert, M. Shafi, D. Shiu, P. Smith, and A. Naguib, “From theory to practice: An overview of MIMO space-time coded wireless systems,” *IEEE JSAC*, vol. 21, no. 3, pp. 281 – 302, Apr. 2003.
- [GvL96] G. H. Golub and C. F. van Loan, *Matrix computations*, 3rd ed. John Hopkins University Press, Oct. 1996.
- [H<sup>+</sup>03] W. Hager *et al.*, “Matlab implementation of the Geometric Mean Decomposition,” Dec. 2003. [Online]. Available: <http://www.sal.ufl.edu/yjiang/papers/gmd.m>
- [Hal62] I. Halperin, “The product of projection operators,” *Acta. Sci. Math (Szeged)*, vol. 23, pp. 96 – 99, 1962.
- [HFDL13] F. Horlin, J. Fickers, T. Deleu, and J. Louveaux, “Interference-free SDMA for FBMC-OQAM,” *EURASIP Journal on Advances in Signal Processing*, vol. 46, Mar. 2013.

- [HLZ<sup>+</sup>11] W. Hu, X. Li, X. Zhang, X. Shi, S. Maybank, and Z. Zhang, “Incremental tensor subspace learning and its applications to foreground segmentation and tracking,” *Int. J. Computer Vision*, vol. 91, no. 3, pp. 303 – 327, 2011.
- [HMVS01] M. Haardt, C. F. Mecklenbräuker, M. Vollmer, and P. Slanina, “Smart antennas for UTRA TDD,” *European Transactions on Telecommunications (ETT)*, vol. 12, pp. 393 – 406, Sept. – Oct. 2001.
- [HN95] M. Haardt and J. A. Nossek, “Unitary ESPRIT: How to obtain increased estimation accuracy with a reduced computational burden,” *IEEE Trans. on Sig. Proc.*, vol. 43, no. 5, pp. 1232 – 1242, May 1995.
- [HN98] ———, “Simultaneous Schur decomposition of several non-symmetric matrices to achieve automatic pairing in multidimensional harmonic retrieval problems,” *IEEE Trans. Sig. Proc.*, vol. 46, no. 1, pp. 161 – 169, Jan. 1998.
- [HRD08] M. Haardt, F. Roemer, and G. Del Galdo, “Higher-order SVD based subspace estimation to improve the parameter estimation accuracy in multi-dimensional harmonic retrieval problems,” *IEEE Trans. on Sig. Proc.*, vol. 56, pp. 3198 – 3213, Jul. 2008.
- [HTR04] M. Haardt, R. S. Thomä, and A. Richter, “Multidimensional high-resolution parameter estimation with applications to channel sounding,” in *High-Resolution and Robust Signal Processing*, Y. Hua, A. Gershman, and Q. Chen, Eds. New York, NY: Marcel Dekker, 2004, pp. 255 – 338, chapter 5.
- [IEE04] IEEE 802.11 Working Group, “TGn channel models,” May 2004, doc.: IEEE 802.11-03/940r4.
- [IEE10] ———, “TGac channel model addendum,” Mar. 2010, doc.: IEEE 802.11-09/0308r12.
- [IILR11] T. Ihalainen, A. Ikhlef, J. Louveaux, and M. Renfors, “Channel Equalization for Multi-Antenna FBMC/OQAM Receivers,” *IEEE Transactions on Vehicular Technology*, vol. 60, no. 5, pp. 2070 – 2085, June 2011.
- [IL09] A. Ikhlef and J. Louveaux, “Per subchannel equalization for MIMO FBMC/OQAM systems,” in *Proc. IEEE Pacific Rim Conference on Communications, Computers and Signal Processing*, Aug 2009, pp. 559 – 564.
- [ISRR07] T. Ihalainen, T. H. Stitz, M. Rinne, and M. Renfors, “Channel equalization in filter bank based multicarrier modulation for wireless communications,” *EURASIP Journal on Advances in Signal Processing*, vol. 2007, 2007.
- [IST07] IST-4-027756 WINNER II, “D2.2.3 modulation and coding schemes for the WINNER II system,” Nov. 2007.

- 
- 265

- [LP01] Y. Lin and S. Phoong, "ISI free FIR filterbank transceivers for frequency selective channels," *IEEE Trans. Signal. Process.*, vol. 49, no. 11, pp. 2648 – 2658, Nov. 2001.
- [LSC<sup>+</sup>12] D. Lee, H. Seo, B. Clerckx, E. Hardouin, D. Mazzarese, S. Nagata, and K. Sayana, "Coordinated multipoint transmission and reception in LTE-advanced deployment scenarios and operational challenges," *IEEE Communications Magazine*, vol. 50, no. 2, pp. 148 – 155, Feb. 2012.
- [LSS02] X. Liu, N. D. Sidiropoulos, and A. Swami, "Blind High-Resolution Localization and Tracking of Multiple Frequency Hopped Signals," *IEEE Transactions on Signal Processing*, vol. 50, no. 4, Apr. 2002.
- [LTSL10] X. Li, H. Tian, Q. Sun, and L. Li, "Utility based scheduling for downlink OFDMA/SDMA systems with multimedia traffic," in *Proc. WCNC*, April 2010.
- [LZC10] B. Liao, Z. G. Zhang, and S. C. Chan, "A New Robust Kalman Filter-Based Subspace Tracking Algorithm in an Impulsive Noise Environment," *IEEE Transactions on Circuits and Systems II: Express Briefs*, vol. 57, no. 9, pp. 740 – 744, Sept. 2010.
- [Mar76] R. A. Maronna, "Robust M-Estimators of Multivariate Location and Scatter," *The Annals of Statistics*, vol. 4, no. 1, pp. 51 – 67, Jan. 1976.
- [MET] "Mobile and wireless communications Enablers for the Twenty-twenty Information Society (METIS)." [Online]. Available: <https://www.metis2020.com>
- [MG14] X. Mestre and D. Gregoratti, "A parallel processing approach to filterbank multicarrier MIMO transmission under strong frequency selectivity," in *Proc. IEEE Int. Conference on Acoustics, Speech, and Signal Processing (ICASSP)*, May 2014.
- [Min14] T. Minka, "Lightspeed Matlab toolbox version 2.7," Oct. 2014. [Online]. Available: <http://research.microsoft.com/en-us/um/people/minka/software/lightspeed>
- [MMP13] X. Mestre, M. Majoral, and S. Pfletschinger, "An Asymptotic Approach to Parallel Equalization of Filter Bank Based Multicarrier Signals," *IEEE Transactions on Signal Processing*, vol. 61, no. 14, pp. 3592 – 3606, July 2013.
- [Moo94] P. H. Moose, "A technique for orthogonal frequency division multiplexing frequency offset correction," *IEEE Transactions on Communications*, vol. 42, pp. 2908 – 2914, 1994.
- [NBSN14] M. Newinger, L. G. Baltar, A. L. Swindlehurst, and J. A. Nossek, "MISO Broadcasting FBMC System for Highly Frequency Selective Channels," in *Proc. International ITG Workshop on Smart Antennas (WSA 2014)*, Mar. 2014.

- 
- [NM93] F. D. Neeser and J. L. Massey, “Proper complex random processes with applications to information theory,” *IEEE Transactions on Information Theory*, vol. 39, no. 4, pp. 1293 – 1302, 1993.
  - [NS10] D. Nion and N. D. Sidiropoulos, “Tensor algebra and multidimensional harmonic retrieval in signal processing for MIMO radar,” *IEEE Signal Process. Lett.*, vol. 58, no. 11, pp. 5693 – 5705, Nov. 2010.
  - [Oja82] E. Oja, “A simplified neuron model as a principal components analyzer,” *Journal of Mathematical Biology*, vol. 15, no. 3, pp. 267 – 273, 1982.
  - [OK03] E. Ollila and V. Koivunen, “Influence functions for array covariance matrix estimators,” in *Proc. IEEE Workshop Statist. Signal Processing (SSP)*, 2003, pp. 462 – 465.
  - [Ows78] N. Owsley, “Adaptive data orthogonalization,” in *Proc. IEEE Int. Conference on Acoustics, Speech, and Signal Processing (ICASSP)*, vol. 3, Apr. 1978, pp. 109 – 112.
  - [PC95] B. Picinbono and P. Chevalier, “Widely linear estimation with complex data,” *IEEE Transactions on Signal Processing*, vol. 43, pp. 2030 – 2033, Aug. 1995.
  - [PGNB04] A. J. Paulraj, D. A. Gore, R. U. Nabar, and H. Bolcskei, “An overview of MIMO communications—a key to gigabit wireless,” *Proceedings of IEEE*, vol. 92, no. 2, pp. 198 – 218, Feb. 2004.
  - [PHY] “PHYsical layer for DYnamic spectrum AccesS and cognitive radio (PHY-DYAS).” [Online]. Available: <http://www.ict-phydyas.org>
  - [PKP11] M. Pun, V. Koivunen, and H. V. Poor, “Performance analysis of joint opportunistic scheduling and receiver design for MIMO-SDMA downlink systems,” *IEEE Trans. Commun.*, vol. 59, no. 1, pp. 268 – 280, Jan. 2011.
  - [PNG03] A. Paulraj, R. Nabar, and D. Gore, *Introduction to space time wireless communications*. Cambridge University Press, 2003.
  - [PRPF15] A. Panajotović, F. Riera-Palou, and G. Femenias, “Adaptive Uniform Channel Decomposition in MU-MIMO-OFDM: Application to IEEE 802.11ac,” *IEEE Trans. Wireless Commun.*, vol. 14, no. 5, pp. 2896 – 2910, May 2015.
  - [QBLH06] A. Quinlan, J.-P. Barbot, P. Larzabal, and M. Haardt, “Model order selection for short data: An exponential fitting test (EFT),” *EURASIP Journal on Applied Signal Processing*, vol. 2007, Oct. 2006.
  - [RBB<sup>+</sup>13] M. Renfors, F. Bader, L. Baltar, D. Le Ruyet, D. Roviras, P. Mege, and M. Haardt, “On the use of filter bank based multicarrier modulation for professional mobile radio,” in *Proc. 77th IEEE Vehicular Technology Conf. (VTC 2013 Spring)*, June 2013.
-

- [RBHW09] F. Roemer, H. Becker, M. Haardt, and M. Weis, “Analytical performance evaluation for HOSVD-based parameter estimation schemes,” in *Proc. of the IEEE Int. Workshop on Comp. Adv. in Multi-Sensor Adaptive Proc. (CAMSAP 2009)*, Aruba, Dutch Antilles, Dec. 2009.
- [RFH08] F. Roemer, M. Fuchs, and M. Haardt, “Distributed MIMO systems with spatial reuse for high-speed-indoor mobile radio access,” in *Proc. 20-th Meeting of the Wireless World Research Forum (WWRF)*, Apr. 2008.
- [RHD14] F. Roemer, M. Haardt, and G. Del Galdo, “Analytical performance assessment of multi-dimensional matrix- and tensor-based ESPRIT-type algorithms,” *IEEE Transactions on Signal Processing*, vol. 62, no. 10, pp. 2611 – 2625, May 2014.
- [RK89] R. Roy and T. Kailath, “ESPRIT – Estimation of signal parameters via rotational invariance techniques,” *IEEE Trans. Acoust., Speech, Signal Process.*, vol. 37, pp. 984 – 995, Jul. 1989.
- [SB10] M. Shaat and F. Bader, “Computationally efficient power allocation algorithm in multicarrier-based cognitive radio networks: OFDM and FBMC systems,” *EURASIP Journal on Advances in Signal Processing*, vol. 2010, Mar. 2010.
- [SB12] ———, “Comparison of OFDM and FBMC performance in multi-relay cognitive radio network,” in *Proc. 9-th International Symposium on Wireless Communications Systems (ISWCS 2012)*, Aug. 2012.
- [SBAW06] M. Salibian-Barrera, S. V. Aelst, and G. Willems, “Principal components analysis based on multivariate MM estimators with fast and robust bootstrap,” *J. Am. Statist. Assoc.*, vol. 101(475), pp. 1198 – 1211, 2006.
- [SCA<sup>+</sup>05] Z. Shen, R. Chen, J. G. Andrews, R. W. Heath Jr., and B. L. Evans, “Low complexity user selection algorithms for multiuser MIMO system with block diagonalization,” *IEEE Trans. Signal Process.*, vol. 54, no. 9, pp. 3658 – 3663, Sept. 2005.
- [SD04] L. Schumacher and B. Dijkstra, “Description of a MATLAB implementation of the indoor MIMO WLAN channel model proposed by the IEEE 802.11 TGn Channel Model Special Committee,” Jan. 2004. [Online]. Available: [https://staff.info.unamur.be/lsc/Publications/2004/implementation\\_note-TGn\\_v31.pdf](https://staff.info.unamur.be/lsc/Publications/2004/implementation_note-TGn_v31.pdf)
- [SH08] V. Stankovic and M. Haardt, “Generalized design of multi-user MIMO precoding matrices,” *IEEE Trans. Wireless Commun.*, vol. 7, no. 3, pp. 953 – 961, Mar. 2008.
- [SH13] J. Steinwandt and M. Haardt, “Optimal widely-linear distributed beamforming for relay networks,” in *Proc. IEEE Int. Conference on Acoustics, Speech, and Signal Processing (ICASSP)*, May 2013, pp. 4241 – 4245.

- 
- [SHGJ06] V. Stankovic, M. Haardt, S. Gale, and A. Jeffries, “Linear and non-linear multi-user MIMO downlink precoding,” in *Proc. WWRP*, Nov. 2006.
  - [SK10] S. Sigdel and W. A. Krzymień, “Antenna and user subset selection in downlink multiuser orthogonal space-division multiplexing,” *Wireless Personal Communications*, vol. 52, no. 1, pp. 227 – 240, Jan. 2010.
  - [SPSH04] Q. H. Spencer, C. B. Peel, A. L. Swindlehurst, and M. Haardt, “An introduction to the multi-user MIMO downlink,” *IEEE Commun. Mag.*, vol. 42, no. 10, pp. 60 – 67, Oct. 2004.
  - [SRH10a] B. Song, F. Roemer, and M. Haardt, “Blind estimation of SIMO channels using a tensor-based subspace method,” in *Proc. 44-th Asilomar Conf. on Signals, Systems, and Computers*, Pacific Grove, CA, Nov. 2010.
  - [SRH10b] —, “Flexible coordinated beamforming (FlexCoBF) algorithm for the downlink of multi-user MIMO systems,” in *Proc. International ITG Workshop on Smart Antennas (WSA 2010)*, Feb. 2010, pp. 114 – 420.
  - [SRH13] —, “Flexible coordinated beamforming (FlexCoBF) for the downlink of multi-user MIMO systems in single and clustered multiple cells,” *Elsevier Signal Processing*, vol. 93, pp. 2462 – 2473, Sept. 2013.
  - [SSH04] Q. H. Spencer, A. L. Swindlehurst, and M. Haardt, “Zero-forcing methods for downlink spatial multiplexing in multi-user MIMO channels,” *IEEE Trans. Signal Process.*, vol. 52, no. 2, pp. 461 – 471, Feb. 2004.
  - [SSL02] P. Siohan, C. Siclet, and N. Lacaille, “Analysis and design of OFDM/OQAM systems based on filterbank theory,” *IEEE Transactions on Signal Processing*, vol. 50, no. 5, pp. 1170 – 1183, May 2002.
  - [SSWB<sup>+</sup>11] H. Saeedi-Sourck, Y. Wu, J. W. M. Bergmans, S. Sadri, and B. Farhang-Boroujeny, “Complexity and performance comparison of filter bank multicarrier and OFDM in uplink of multicarrier multiple access networks,” *IEEE Transactions on Signal Processing*, vol. 59, no. 4, pp. 1907 – 1912, Apr. 2011.
  - [Ste92] G. W. Stewart, “An updating algorithm for subspace tracking,” *IEEE Trans. Signal Process.*, vol. 40, no. 6, pp. 1535 – 1541, 1992.
  - [Ste93] —, “Updating a rank-revealing ULV decomposition,” *SIAM J. Matrix Anal. Appl.*, vol. 14, no. 2, pp. 494 – 499, 1993.
  - [STP<sup>+</sup>08] J. Sun, D. Tao, S. Papadimitriou, P. S. Yu, and C. Faloutsos, “Incremental tensor analysis: Theory and applications,” *ACM Transactions on Knowledge Discovery from Data (TKDD)*, vol. 2, no. 3, Oct. 2008.
-

- [STS07] M. Sadek, A. Tarighat, and A. Sayed, "A Leakage-Based Precoding Scheme for Downlink Multi-User MIMO Channels," *IEEE Trans. Wireless Commun.*, vol. 6, no. 5, pp. 1711 – 1721, May 2007.
- [SW14] I. Soloveychik and A. Wiesel, "Tyler's covariance matrix estimator in Elliptical models with convex structure," *IEEE Trans. on Signal Processing*, vol. 62, no. 20, Oct. 2014.
- [Tel99a] E. Telatar, "Capacity of multi-antenna Gaussian channels," *Eur. Trans. Telecomm.*, vol. 10, no. 6, pp. 585 – 596, Nov. 1999.
- [Tel99b] I. E. Telatar, "Capacity of multi-antenna Gaussian channels," *Eur. Tran. Telecommun.*, vol. 10, no. 6, pp. 585 – 595, Nov. – Dec. 1999.
- [TJC02] V. Tarokh, H. Jafarkhani, and A. R. Calderbank, "Space-time block codes from orthogonal designs," *IEEE Transactions on Information Theory*, vol. 45, no. 5, pp. 1456 – 1467, Aug. 2002.
- [TT00] K. S. Tatsuoka and D. E. Tyler, "On the uniqueness of S and constrained M-functionals under non-elliptical distributions," *Ann. Statist.*, vol. 28, pp. 1219 – 1243, 2000.
- [Tyl83] D. E. Tyler, "Efficiency and Robustness of Scatter Matrices," *Biometrika*, vol. 70, no. 2, 1983.
- [VPW10] L. Venturino, N. Prasad, and X. Wang, "Coordinated linear beamforming in downlink multi-cell wireless networks," *IEEE Trans. on Wireless Communications*, vol. 9, no. 4, pp. 1536 – 1276, Apr. 2010.
- [WBN08a] D. S. Waldhauser, L. G. Baltar, and J. A. Nossek, "MMSE subcarrier equalization for filter bank based multicarrier systems," in *Proc. IEEE Workshop on Signal Processing Advances in Wireless Communications (SPAWC 2008)*, July 2008.
- [WBN08b] D. S. Waldhauser, L. Baltar, and J. A. Nossek, "Adaptive equalization for filter bank based multicarrier," in *Proc. IEEE Int. Symp Circuits Syst. (ISCAS 2008)*, May 2008.
- [WG809] WG802.11 - Wireless LAN Working Group, "802.11n – 2009 – IEEE Standard for Information technology – Local and metropolitan area networks – Specific requirements – Part 11: Wireless LAN Medium Access Control (MAC) and Physical Layer (PHY) Specifications Amendment 5: Enhancements for Higher Throughput," 2009.
- [WG813] —, "802.11ac-2013 – IEEE Standard for Information technology – Telecommunications and information exchange between systems – Local and metropolitan area networks – Specific requirements—Part 11: Wireless LAN Medium Access



- 
- Control (MAC) and Physical Layer (PHY) Specifications—Amendment 4: Enhancements for Very High Throughput for Operation in Bands below 6 GHz,” 2013.
- [WK85] M. Wax and T. Kailath, “Detection of signals by information theoretic criteria,” *IEEE Trans. Acoustics, Speech and Signal Processing*, vol. 33, no. 2, pp. 387 – 392, 1985.
- [Yan95a] B. Yang, “An extension of the PASTd algorithm to both rank and subspace tracking,” *IEEE Signal Process. Lett.*, vol. 2, no. 9, pp. 179 – 182, Sept. 1995.
- [Yan95b] —, “Projection approximation subspace tracking,” *IEEE Trans. on Signal Processing*, vol. 43, no. 1, pp. 95 – 107, Jan. 1995.
- [YK88] J.-F. Yang and M. Kaveh, “Adaptive eigensubspace algorithms for direction or frequency estimation and tracking,” *IEEE Transactions on Acoustics Speech and Signal Processing*, vol. 36, no. 2, pp. 241 – 251, 1988.
- [YSRH12] A. Yeredor, B. Song, F. Roemer, and M. Haardt, “A sequentially drilled joint congruence (SeDJoCo) transformation with applications in blind source separation and Multi-User MIMO systems,” *IEEE Transactions on Signal Processing*, vol. 60, pp. 2744 – 2757, June 2012.
- [ZCA09] J. Zhang, R. Chen, and J. G. Andrews, “Networked MIMO with clustered linear precoding,” *IEEE Trans. on Wireless Communications*, vol. 8, no. 4, pp. 1910 – 1921, Apr. 2009.
- [ZdH13] K. Zu, R. C. de Lamare, and M. Haardt, “Generalized design of low-complexity block diagonalization type precoding algorithms for multiuser MIMO systems,” *IEEE Transactions on Communications*, vol. 61, pp. 4232 – 4242, Oct. 2013.
- [ZKCM12] A. M. Zoubir, V. Koivunen, Y. Chakhchoukh, and M. Muma, “Robust estimation in signal processing,” *IEEE Signal Proc. Magazine*, May 2012.
- [ZKMW02] J. Zhang, A. Kačić, X. Ma, and K. M. Wong, “Design of unitary precoders for ISI channels,” in *Proc. IEEE Int. Conference on Acoustics, Speech, and Signal Processing (ICASSP)*, Orlando, FL, USA, May 2002.
- [ZL11a] R. Zakaria and D. Le Ruyet, “On spatial data multiplexing over coded filter-bank multicarrier with ML detection,” in *Proc. IEEE 22nd International Symposium on Personal Indoor and Mobile Radio Communications (PIMRC)*, Sept. 2011, pp. 1391 – 1395.
- [ZL11b] —, “Partial ISI cancellation with viterbi detection in MIMO filter-bank multicarrier modulation,” in *Proc. 8th International Symposium on Wireless Communication Systems (ISWCS 2011)*, Nov. 2011, pp. 322 – 326.
-

- [ZLB10] R. Zakaria, D. Le Ruyet, and M. Bellanger, “Maximum Likelihood Detection in spatial multiplexing with FBMC,” in *Proc. 2010 European Wireless Conference*, June 2010.
- [ZMM<sup>+</sup>08] H. Zhang, N. B. Mehta, A. F. Molisch, J. Zhang, and H. Dai, “Asynchronous Interference mitigation in Cooperative Base Station Systems,” *IEEE Trans. on Wireless Communications*, vol. 7, no. 1, pp. 155 – 164, Jan. 2008.
- [ZT03] L. Zheng and D. N. C. Tse, “Diversity and multiplexing: a fundamental trade-off in multiple-antenna channels,” *IEEE Transactions on Information Theory*, vol. 49, no. 5, pp. 1073 – 1096, May 2003.
- [ZV05] H. Zheng and H. Viswanathan, “Optimizing the ARQ performance in downlink packet data systems with scheduling,” *IEEE Trans. Wireless Commun.*, vol. 4, no. 2, pp. 495 – 506, Mar. 2005.
- [ZvdV12] M. Zhou and A.-J. van der Veen, “Stable subspace tracking algorithm based on a signed URV decomposition,” *IEEE Trans. Signal Process.*, vol. 60, no. 6, pp. 3036 – 3051, Jun. 2012.